New Results in Numerical and Experimental Fluid Mechanics VII

Contributions to the 16th STAB/DGLR Symposium Aachen, Germany 2008

Andreas Dillmann   Gerd Heller
Michael Klaas   Hans-Peter Kreplin
Wolfgang Nitsche   Wolfgang Schröder (Editors)

Springer

New Results in Numerical and Experimental Fluid Mechanics VII

Contributions to the 16th STAB/DGLR
Symposium Aachen, Germany 2008

Andreas Dillmann, Gerd Heller, Michael Klaas,
Hans-Peter Kreplin, Wolfgang Nitsche,
and Wolfgang Schröder (Editors)

Springer

Prof. Dr. Dr. habil. Andreas Dillmann
Deutsches Zentrum für Luft- und
Raumfahrt (DLR)
Institut für Aerodynamik
und Strömungstechnik
Bunsenstraße 10
37073 Göttingen
Germany

Dr. Gerd Heller
Airbus Deutschland
Airbusallee 1
28199 Bremen
Germany

Dr. Michael Klaas
Aerodynamisches Institut und
Lehrstuhl für Strömungslehre
RWTH Aachen
Wüllnerstr. 5a
52062 Aachen
Germany

Dr. Hans-Peter Kreplin
Deutsches Zentrum für Luft- und
Raumfahrt (DLR)
Institut für Aerodynamik
und Strömungstechnik
Bunsenstraße 10
37073 Göttingen
Germany

Prof. Dr. Wolfgang Nitsche
Institut für Luft- und Raumfahrt
TU Berlin
Marchstraße 12
10587 Berlin
Germany
E-mail: wolfgang.nitsche@tuberlin.de

Prof. Dr. Wolfgang Schröder
Aerodynamisches Institut und
Lehrstuhl für Strömungslehre
RWTH Aachen
Wüllnerstr. 5a
52062 Aachen
Germany
E-mail: office@aia.rwth-aachen.de

NNFM Editor Addresses

Prof. Dr. Wolfgang Schröder
(General Editor)
RWTH Aachen
Lehrstuhl für Strömungslehre und
Aerodynamisches Institut
Wüllnerstr. 5a
52062 Aachen
Germany
E-mail: office@aia.rwth-aachen.de

Prof. Dr. Kozo Fujii
Space Transportation Research Division
The Institute of Space
and Astronautical Science
3-1-1, Yoshinodai, Sagamihara
Kanagawa, 229-8510
Japan
E-mail: fujii@flab.eng.isas.jaxa.jp

Dr. Werner Haase
Höhenkirchener Str. 19d
D-85662 Hohenbrunn
Germany
E-mail: office@haa.se

Prof. Dr. Ernst Heinrich Hirschel
(Former General Editor)
Herzog-Heinrich-Weg 6
D-85604 Zorneding
Germany
E-mail: e.h.hirschel@t-online.de

Prof. Dr. Ir. Bendiks Jan Boersma
Chair of Energytechnology
Delft University of Technology
Leeghwaterstraat 44
2628 CA Delft
The Netherlands
E-mail: b.j.boersma@tudelft.nl

Prof. Dr. Michael A. Leschziner
Imperial College of Science
Technology and Medicine
Aeronautics Department
Prince Consort Road
London SW7 2BY
U.K.
E-mail: mike.leschziner@ic.ac.uk

Prof. Dr. Sergio Pirozzoli
Università di Roma "La Sapienza"
Dipartimento di Meccanica e Aeronautica
Via Eudossiana 18
00184, Roma, Italy
E-mail: sergio.pirozzoli@uniroma1.it

Prof. Dr. Jacques Periaux
38, Boulevard de Reuilly
F-75012 Paris
France
E-mail: jperiaux@free.fr

Prof. Dr. Arthur Rizzi
Department of Aeronautics
KTH Royal Institute of Technology
Teknikringen 8
S-10044 Stockholm
Sweden
E-mail: rizzi@aero.kth.se

Dr. Bernard Roux
L3M – IMT La Jetée
Technopole de Chateau-Gombert
F-13451 Marseille Cedex 20
France
E-mail: broux@l3m.univ-mrs.fr

Prof. Dr. Yurii I. Shokin
Siberian Branch of the
Russian Academy of Sciences
Institute of Computational
Technologies
Ac. Lavrentyeva Ave. 6
630090 Novosibirsk
Russia
E-mail: shokin@ict.nsc.ru

Foreword

This volume contains the papers presented at the 16th DGLR/STAB-Symposium held at the Eurogress Aachen and organized by RWTH Aachen University, Germany, November, 3 - 4, 2008. STAB is the German Aerospace Aerodynamics Association, founded towards the end of the 1970's, whereas DGLR is the German Society for Aeronautics and Astronautics (Deutsche Gesellschaft für Luft- und Raumfahrt - Lilienthal Oberth e.V.).

The mission of STAB is to foster development and acceptance of the discipline "Aerodynamics" in Germany. One of its general guidelines is to concentrate resources and know-how in the involved institutions and to avoid duplication in research work as much as possible. Nowadays, this is more necessary than ever. The experience made in the past makes it easier now, to obtain new knowledge for solving today's and tomorrow's problems. STAB unites German scientists and engineers from universities, research-establishments and industry doing research and project work in numerical and experimental fluid mechanics and aerodynamics for aerospace and other applications. This has always been the basis of numerous common research activities sponsored by different funding agencies.

Since 1986 the symposium has taken place at different locations in Germany every two years. In between STAB workshops regularly take place at the DLR in Göttingen. The changing meeting places were established as focal points in Germany's Aerospace Fluid Mechanics Community for a continuous exchange of scientific results and their discussion. Moreover, they are a forum where new research activities can be presented, often resulting in new commonly organized research and technology projects.

It is the seventh time now that the contributions to the Symposium are published after being subjected to a peer review. The material highlights the key items of integrated research and development based on fruitful collaboration of industry, research establishments and universities. Some of the contributions still present results from the "Luftfahrtforschungsprogramm der Bundesregierung (German Aeronautical Research Program)". Some of the papers report on work sponsored by the Deutsche Forschungsgemeinschaft (DFG, German Research Council) in some of their Priority Programs (Verbundschwerpunkt-Programm) as well as in their Collaborative Research Centres (Sonderforschungsbereiche). Other articles are sponsored by the European Community and are therefore results of cooperation among different organizations. The main areas include numerical simulation, experimental simulation and test techniques, flow control, airplane aerodynamics, hypersonic flows and aerothermodynamics, aeroacoustics and the rather new fields of convection mixing and biomedical flows. This volume gives an almost complete review of the ongoing

aerodynamics research work in Germany. The order of the papers in this book corresponds closely to that of the sessions of the Symposium.

From 100 lectures presented at the Symposium 75 are included in this book.

The Review-Board, partly identical with the Program-Committee, consisted of N. Adams (München), J. Ballmann (Aachen), C. Bartels (Hamburg), S. Becker (Erlangen), H. Bieler (Bremen), C. Breitsamter (Garching), G. Brenner (Clausthal), M. Breuer (Hamburg), C. Brücker (Freiberg), J. Delfs (Braunschweig), K. Ehrenfried (Göttingen), R. Ewert (Braunschweig), H. Foysi (Aachen), J. Fröhlich (Dresden), A. Gardner (Göttingen), N. Gauger (Berlin), A. Gülhan (Köln), D. Hänel (Duisburg), K. Hannemann (Göttingen), H. Hansen (Bremen), S. Hein (Göttingen), A. Henckels (Köln), R. Henke (Aachen), D. Hennecke (Darmstadt), P. Hennig (Unterschleißheim), M. Hepperle (Braunschweig), H. Herwig (Hamburg), R. Höld (Unterschleißheim), F. Holzäpfel (Weßling), K. H. Horstmann (Braunschweig), T. Indinger (Garching), S. Jakirlic (Darmstadt), C. Kähler (Neubiberg), R. Kessler (Göttingen), W. Khier (Braunschweig), M. Klaas (Aachen), L. Kleiser (Zürich), M. Kloker (Stuttgart), M. Konstantinov (Göttingen), W. Kordulla (Nordwijk), F. Kost (Göttingen), H. Krain (Köln), E. Krämer (Stuttgart), D. Kröner (Freiburg), N. Kroll (Braunschweig), W. Kühn (Bremen), H. Lienhart (Erlangen), J. Longo (Braunschweig), T. Lutz (Stuttgart), J. Martinez Schramm (Göttingen), M. Meinke (Aachen), F. Menter (Otterfing), D. Müller (Aachen), C. Mundt (Neubiberg), C.-D. Munz (Stuttgart), K.-P. Neitzke (Bremen), G. Neuwerth (Aachen), S. Niebergall (Merkers-Kieselbach), W. Nitsche (Berlin), H. Olivier (Aachen), H.-D. Papenfuß (Bochum), R. Radespiel (Braunschweig), H.-J. Rehder (Göttingen), M. Rein (Göttingen), C. Resagk (Ilmenau), K. Richter (Göttingen), U. Rist (Stuttgart), H. Rosemann (Göttingen), C.-C. Rossow (Braunschweig), R. Rudnik (Braunschweig), T. Rung (Hamburg), E. Sarradj (Cottbus), A. Schröder (Göttingen), W. Schröder (Aachen), E. Schülein (Göttingen), D. Schwamborn (Göttingen), F. Seiler (Saint-Louis), A. Seitz (Braunschweig), W. Send (Göttingen), J. Sesterhenn (Neubiberg), J. Srulijes (Saint-Louis), C. Stemmer (Garching), J. Stiller (Dresden), A. Thess (Ilmenau), F. Thiele (Berlin), C. Tropea (Darmstadt), R. Voß (Göttingen), C. Wagner (Göttingen), C. Weiland (Bruckmühl), H. Wengle (Neubiberg), J. Wild (Braunschweig) and W. Würz (Stuttgart).

Nevertheless, the authors sign responsible for the contents of their contributions.

The editors are grateful to Prof. Dr. W. Schröder as the General Editor of the "Notes on Numerical Fluid Mechanics and Multidisciplinary Design" and to the Springer-Verlag for the opportunity to publish the results of the Symposium.

November 2009

W. Schröder, Aachen
M. Klaas, Aachen
A. Dillmann, Göttingen
G. Heller, Bremen
H.-P. Kreplin, Göttingen
W. Nitsche, Berlin

Table of Contents

Numerics

Flow Control

Laminar Flow Control and Transition

Experimental Simulation and Test Techniques

Hypersonic Flows and Aerothermodynamics

Aeroacoustics

Biomedical Flows

Airplane Aerodynamics

Convection and Mixing

Miscellaneous

Interfacial Area Transport Equation in Statistical-Eulerian-Eulerian Simulations of Multiphase Flow

Daniel T. Banuti and Klaus Hannemann

German Aerospace Center DLR, Institute of Aerodynamics and Flow Technology,
Spacecraft Section, Bunsenstr. 10, 37073 Göttingen, Germany

Summary

This paper discusses the ongoing extension of the DLR TAU Code with a multiphase flow model. The reasoning behind choosing a Statistical Eulerian Eulerian (SEE) model with Interfacial Area Transport Equation (IATE) is covered. Properties of the model are introduced, especially concerning the less known IATE concept which provides information about interphasic interfacial area (IA) available in a computational cell. This allows for a more elaborate sub grid scale modeling. An general IA convection velocity is derived which holds for the limiting cases of stratified flow and disperse flow. As an exemplary application, the development of a spray injection IATE is discussed. This includes interfacial growth due to velocity gradients and a new IA detection term which resolves ambiguities with boundary conditions.

1 Introduction

Originally developed for ideal gas transonic flow problems, the DLR TAU code has been continuously extended to meet scientific and industry demands [2, 6]. Within the section 'Spacecraft', naturally space flight related developments have been pursued. Additional simulation capabilities are in demand now, covering almost the whole process chain of propellant supply in a spacecraft from sloshing of cryogenic fuels in tanks in microgravity environments to liquid and supercritical propellant injection in combustion chambers. This includes a wide range of phenomena from negligible velocities with dominating surface tension and relevant acceleration forces to primary and secondary atomization and evaporation.

1.1 Flow Model

All these phenomena have one thing in common: their multiphase nature. Thus, an appropriate multiphase flow model has to be employed that is capable of covering all flow regimes from disperse to stratified flow. A useful concept to describe multiphase flow is the phase volume fraction α_j, defined as the ratio of the volume of phase j to the total volume in an averaging regime such as a computational cell.

Multiphase Models: Different approaches are discussed by Wörner [11]. E.g., dilute spray flow is traditionally computed using a Lagrangian description. I.e. individual droplets are tracked as they move through the flow field, their trajectory determined by the drag due to the velocity difference between carrier and disperse phase. These methods are termed 'Statistical Eulerian Lagrangian' (SEL), because the carrier phase is computed in an Euler description and not all features are resolved but only an average is computed. However, with increasing liquid volume fraction it is apparent that there has to be a point where the description of the flow as individual particles seems not physically appropriate anymore. Regarding injection into liquid rocket engines (Mayer et al. [7]) it can be seen how the propellants enter the combustion chamber as a compact stream. While Lagrangian solvers amazingly still are capable of producing reasonable results in these cases (Preclik et al. [9]), it seems justifiable to look for alternative, physically more appropriate flow models. This appears even more important for other flow cases such as the propellant tank. In this case, the liquid phase is clearly a continuum, separated from the continuous gaseous phase. Cases like these lend themselves naturally to a physical frame where both phases are treated as Eulerian continua, hence their name 'Statistical Eulerian Eulerian' (SEE). Again, the statistical description is to be understood as opposed to resolution of all features, such as the surface reconstruction found in volume of fluid (VOF) methods. SEE methods have been successfully applied to both stratified flow cases (Ishii [3]) and liquid rocket engine propellant injection (Jay et al. [5]).

Eulerian Description of Multiphase Flow: While all SEE methods share the concept of regarding every involved phase as a continuum, there are different degrees of complexity of how to treat these flows depending on the character of the expected flow problems. Three main approaches can be distinguished, homogeneous, drift-flux, and two-fluid. The homogeneous flow model is the simplest of the three. The flow field of the carrier phase is computed from the governing equations (e.g. Navier-Stokes). The dilute phase velocity is then determined assuming that the disperse droplets follow the carrier phase without slip. The drift-flux model allows for some relative velocity between the phases, if it can be described by a suitable relation. The velocity field of the mixture is computed, the phase velocities are then calculated from this relation. The most general - and complex - model is the two-fluid model. Here, both phases are treated equally, a full set of governing equations is solved for *each* phase. The phases are coupled by source terms, modeling exchange of mass, momentum, and energy.

Interfacial Area Transport Equation: The Interfacial Area Transport Equation (IATE) is an additional equation to the system of governing equations. Interfacial area (IA) is understood as the area in between the phases, such as the surface of a droplet. As suggested by Ishii [3], the IATE in its general form can be written as $\partial a_i / \partial t + \boldsymbol{u}_i \, \nabla a_i = \phi$. Index i denotes states at the interface, ϕ represents source terms that cause interfacial area growth or destruction. Interfacial area density a_i is IA per unit volume. Together with the phase volume fractions this approach allows for a topological interpretation of the state inside a computational cell: with surface area *and* volume known, information about the tortuosity of the interface inside a cell can be deduced.

Conclusion for Chosen Model: Due to the initially discussed needed versatility, the most general models are chosen for the extension of the DLR TAU code. Because of their range from stratified to disperse flow, the SEE approach is chosen over the SEL approach. As a first step, a homogeneous flow model is implemented. Ultimately, a full two-fluid model with IATE is aspired, where IATE source terms have to be developed for each particular application.

2 Implementation

The introduced models can be expressed in the form $\partial \mathbf{U}/\partial t + \nabla \mathbf{F} = 0$ without source terms. The vectors of conservative variables $\mathbf{U}$ and inviscid fluxes $\mathbf{F}$ have to be chosen according to the selected model. These equations are then implemented into the AUSM+ scheme of TAU (Liou [4]). Equation (1) represents the homogeneous flow model (index hom) with IATE. It is the first step towards the general two-fluid model. The Euler equations are supplemented with two additional equations, describing the transport of liquid volume fraction and interfacial area. Index g and l denote the gaseous and liquid phase, i the interface, and t total conditions. In this model, the liquid volume fraction α_l behaves as a passive scalar, being convected with the gas phase flow but not affecting it.

$$\mathbf{U_{hom}} = \begin{pmatrix} \rho_g \\ \rho_g u_g \\ \rho_g e_{t,g} \\ \alpha_l \\ a_i \end{pmatrix}, \quad \mathbf{F_{hom}} = \begin{pmatrix} \rho_g u_g \\ \rho_g u_g^2 + p \\ \rho_g u_g h_{t,g} \\ \alpha_l u_g \\ a_i u_g \end{pmatrix} \tag{1}$$

The full two-fluid model with additional IATE is more elaborate. It can be seen in Eq. (2), two-fluid labeled with index tf. It is an extension to the AUSM+ two-fluid model as discussed by Paillère et al. [8]. Index j designates the phase (e.g. liquid or gaseous), index i labels a condition at the interface. A common pressure p is assumed to be shared by all phases present in a computational cell. Each phase has its own velocity field, making u_i, the interfacial velocity, not an obvious choice anymore. A suggestion will be derived in Chapter 2.1.

$$\mathbf{U_{tf}} = \begin{pmatrix} \alpha_j \rho_j \\ \alpha_j \rho_j u_j \\ \alpha_j \rho_j e_{t,j} \\ a_i \end{pmatrix}, \quad \mathbf{F_{tf}} = \begin{pmatrix} \alpha_j \rho_j u_j \\ \alpha_j \rho_j u_j^2 + \alpha_j p \\ \alpha_j \rho_j u_j h_{t,j} \\ a_i u_i \end{pmatrix} \tag{2}$$

2.1 Development of an IATE

The IATE is a modeled equation. Source terms are derived based on physical reasoning. While the growth term is best modeled for a particular application, the convection velocity is of a more general nature:
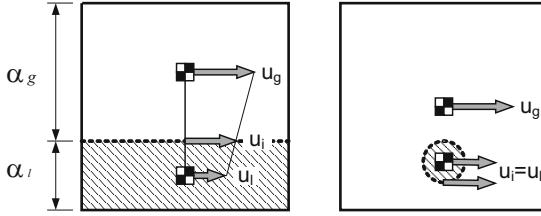
Fig. 1. Interfacial area convection velocity in a) stratified flow; b) vanishing phase case

Interfacial Area Convection Velocity: Interfacial area convection is clearly associated with the two fluids that form the interface; a choice based on their convection velocities appears mandatory. It should hold in the limiting cases of dispersed flow (interfacial area is bound to the dispersed phase: the surface of a single droplet falling in a gas falls with the same velocity as the droplet) and stratified flow (both phases move parallel to one another; an arithmetic mean seems appropriate). Several approaches are pursued in the literature [1]. SEE methods usually employ an averaging scheme $\boldsymbol{u}_i = c_1 \boldsymbol{u}_g + c_2 \boldsymbol{u}_l$, where typical choices for c_1, c_2 are $c_1 = c_2 = \frac{1}{2}$, $c_1 = \alpha_l, c_2 = \alpha_g$ or $c_1 = \alpha_g, c_2 = \alpha_l$. A methodical derivation is carried out here, where the phases are assumed to be stratified within the statistically averaged regime (e.g. a finite volume cell, Fig. 1a). The phase volume fractions and the phase velocities are given as solutions of the computational method. If the phase velocities hold in the phase centers of gravity, a linear interpolation between the phase velocities leads to

$$\boldsymbol{u}_i = \alpha_g \boldsymbol{u}_l + \alpha_l \boldsymbol{u}_g \tag{3}$$

at the interface. This velocity is interpreted as the convection velocity of the interfacial area. All listed choices for c_1, c_2 yield identical results for equal phase volume fractions and equal velocity fields. Differences can be found in the case of one dispersed phase. Only the cross volume fraction weighted scheme Eq. (3) gives the phenomenologically correct answer. This is a quite noticeable result: an averaging scheme derived specifically to hold for the case of equally distributed phases also holds for the other extreme of one vanishing phase. Furthermore, it is the *only* one of the common schemes that holds for the vanishing phase case.

2.2 Exemplary IATE: Supercritical Injection

The source term ϕ of the IATE has to be modelled for specific flow cases. As an example, supercritical injection is regarded, a practical application of which is injection into high pressure rocket combustion chambers. To study general properties of this particular type of flow, Mayer et al. [7] carried out cold flow studies in which cryogenic nitrogen is injected into a nitrogen environment at room temperature and at supercritical pressure. It is found that with vanishing surface tension, the cryogenic nitrogen stream behaves more like a dense gas, atomization is replaced by a mixing process.

Vallet et al. [10] followed this result in their modeling of atomization and additionally assumed that convection is dominant over diffusion[1]. This leads to

$$\frac{\partial a_i}{\partial t} + \boldsymbol{u}_i \, \nabla a_i = \phi = (\mathcal{M} + \mathcal{T})a_i - \mathcal{S} \cdot a_i^2 \tag{4}$$

In Eq. (4) $\mathcal{M}$ and $\mathcal{T}$ represent interfacial growth due to macroscopic and turbulent mixing, respectively. Hence $\mathcal{M}$ is the effect of velocity gradients, $\mathcal{T}$ is based on sub grid scale models. The nonlinear destruction term $\mathcal{S} \cdot a_i^2$ limits this growth by modeling saturation.

However, a difficulty with the IATE inflow boundary condition remains, as interfacial area has to be created in the instant that both phases meet and is not injected with the fluid. In the following, an alternative interfacial area creation mechanism is suggested that replaces the usual inflow boundary condition (Jay et al. [5]). Furthermore, a new model term for macroscopic IA growth in a shear layer will be derived, departing from Vallet's vorticity formulation.

Interfacial Area Detection: In the case of coaxial injection, which is widely used in rocket engines, one possible approximation to the initial interfacial area is a cylindrical interface, determined by the injector geometry. However, since the inner injector tube has a finite thickness, the position where the two streams meet and thus the radius of the cylindrical interface is not known a priori. Modeling the injector with zero thickness or simply assuming a meeting position could be used to overcome this problem. Several drawbacks are associated with these approaches: As the recirculation region behind the LOX post is important, it should be represented in the computation. Further, an unsteady contact position of the two phases cannot be taken into account. All of this can be overcome by an interfacial area detection algorithm that acts like a source term, following the concept that a certain surface area is needed to enclose a given volume. The volume of the phase to be enclosed is given as a solution by the computational method. In the case of the coaxial injector immediately after injection, a condition close to stratified flow can be expected. The formulation of a characteristic surface area $a_i V = (\alpha_{\mathbf{min}} V)^{2/3}$ is thus chosen, where V is the finite discretized cell volume and $\alpha_{\mathbf{min}} V$ the volume fraction occupied by the dispersed phase. The flow solver is then extended by a routine that ensures that at least this amount of IA is present in each computational cell.

Interfacial Area Growth due to Fluid Element Distortion: In order to evaluate interface stretching due to velocity gradients, a fluid element in a non-homogeneous flow is regarded. The interface will be distorted when the fluid element's shape is altered. For simplicity, a 2-D case is investigated. Interfacial area then collapses to a line which will be assumed to be straight at $t_0 = 0$ in the finite domain. This represents stratified, unmixed flow. Interfacial growth due to distortion is proportional to the initially present interface length because its mechanism is stretching and folding existing IA. In order to evaluate a maximum growth case, the diagonal as the longest straight line in the

---

[1] Strictly, with no surface tension acting, there is no clear distinction between the components and thus no clear multiphase flow. However, the concept of interfacial area as the meeting position of oxidizer and fuel is a reasonable one, e.g. for combustion models.

fluid element will be regarded. The distorted diagonal in the shear flow field (Fig. 2b)
and the dilatational flow (Fig. 2c) will be elongated. The rotational flow field (Fig. 2a)
merely rotates the element, leaving its shape unaltered. Therefore, dilatation and shear
together appear to be more appropriate to evaluate interface stretching and growth than
vorticity. In the limit of vanishing surface tension, no force acts to stabilize or mini-
mize this interfacial area. It can thus be assumed that any distortion to the interface will
not be reverted later in time. Contributions to interface stretching then depend on the
type of distortion. Dilatation only increases interfacial area when the fluid element is
expanded, i.e. when the value of the dilatation $\nabla \cdot v$ is positive. Shear however stretches
one diagonal as it contracts the other and thus always causes interfacial growth making
the absolute value of the shear an appropriate measure of growth. Consistent with this
non-demixing assumption, these two terms are summed up to evaluate the interfacial
growth due to distortion of the fluid cell. For the two dimensional case this results in
Eq. (5).

$$\mathcal{M} = G \left(\left(\frac{\partial u}{\partial x} + \frac{\partial v}{\partial y} \right)_+ + \left| \frac{\partial u}{\partial y} + \frac{\partial v}{\partial x} \right| \right); \qquad \xi_+ = \frac{1}{2} \left(\xi + |\xi| \right) \qquad (5)$$

The geometrical coefficient G relates the lengthening of the diagonal with the distortion
of the fluid element and can be shown (Banuti et al. [1]) to equal $1/\sqrt{2}$.
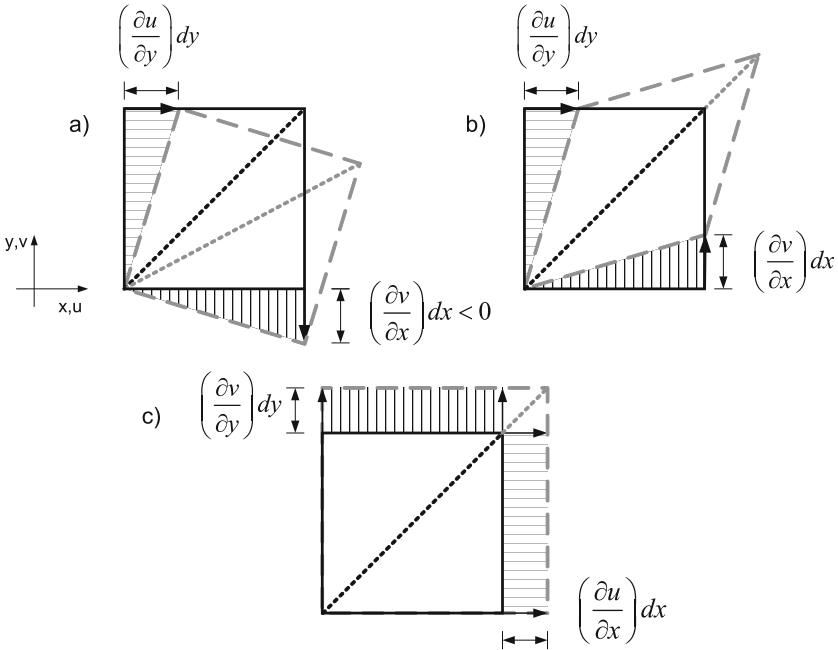
Fig. 2. a) Fluid element in rotational flow b) Fluid element in shear flow c) Fluid element in
dilatational flow
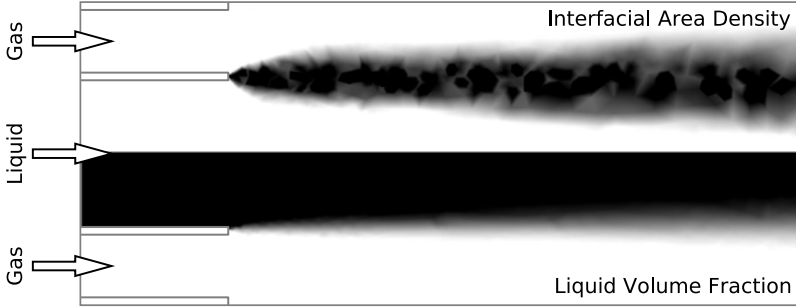
Fig. 3. Computation of coaxial injection using a homogeneous spray model. Depicted is a cut through the coaxial injector with a central liquid flow surrounded by a gas flow, entering from the left. Two variables are displayed, split by the injector symmetry axis. The upper half shows the evolution of interfacial area density a_i in the shear layer behind the liquid post. The lower half shows the spreading of liquid volume fraction α_l. Darker regions mark higher values.

Computation: The IATE described above along with the governing equation for the liquid volume fraction have been implemented in the DLR Navier-Stokes solver TAU [2]. TAU is a finite volume second order flow solver which has been validated for a variety of steady and unsteady flow cases, ranging from sub- to hypersonic Mach numbers. All calculations described in this article are based on the Reynolds averaged Navier Stokes equations (RANS) applying the one-equation Spalart-Allmaras turbulence model in a homogeneous two phase model. The effect of turbulence on the IATE has not been regarded in order to point out the effects of the discussed model terms ($\mathcal{T} = 0$). A result of a computation with this model can be seen in Fig. 3. The bottom part of the figure shows the spreading of the liquid volume fraction α_l in the shear layer following the coaxial injector. It can be seen how the pure phases mix in the shear layer, causing a gradually changing liquid volume fraction. The upper half shows the interfacial area density a_i. No interfacial area inflow boundary condition is used. The flow field is void of interfacial area inside the injector and outside the mixing regime. It can be seen how interfacial area is created by the detection term immediately after the injector. It is then convected with the flow. The interface growth term $\mathcal{M}$ causes a_i to increase in the shear layer. Finally, the saturation term stabilizes the solution by limiting interfacial area growth.

3   Conclusion

Statistical Eulerian Eulerian methods extended with an Interfacial Area Transport Equation have been argued to be a reasonable choice to simulate a wide range of flow cases. Several characteristics of a generic interfacial area density transport equation have been discussed in this article. The volume fraction cross weighted average has been shown to be a reasonable approach to determine the interfacial convection velocity. It has

further been shown to be the only common scheme discussed to hold in the important limiting cases of stratified flow, homogeneous flow, and dispersed flow. Shear rather than vorticity has been suggested to be the driving force in interfacial area growth. Following this reasoning, a new model term has been introduced based on a non-demixing hypothesis. An interfacial area detection algorithm has been proposed, which makes the definition of an unphysical interfacial area influx boundary condition unnecessary. The advantage of SEE methods of using physical boundary conditions is thus strengthened. This approach also allows a physical representation in computations where the position of the interface at the injector is unsteady. Calculations show the qualitative validity of the approach.

Acknowledgments

References

[1] Banuti, D.T., Karl, S., Hannemann, K.: Interfacial Area Modeling for Eulerian Spray Simulations in Liquid Rocket Engines. AIAA 2008-5231 (2008)

[2] Gerhold, T., Friedrich, O., Evans, J., Galle, M.: Calculation of Complex Three-Dimensional Configurations Employing the DLR-TAU-Code. AIAA 97-0167 (1997)

[3] Ishii, M., Hibiki, T.: Thermo-Fluid Dynamics of Two-Phase-Flow. Springer, Heidelberg (2006) ISBN 0-387-28321-8

[4] Liou, M.-S.: A Sequel to AUSM: AUSM+. Journal of Computational Physics 129, 364–382 (1996)

[5] Jay, S., Lacas, F., Candel, S.: Combined surface density concepts for dense spray combustion. Combustion and Flame 144, 558–577 (2006)

[6] Mack, A., Hannemann, V.: Validation of the Unstructured DLR TAU-Code for Hypersonic Flows. AIAA 2002-3111 (2002)

[7] Mayer, W., Schik, A., Schäffler, M., Tamura, H.: Injection and Mixing Processes in High-Pressure Liquid Oxygen/Gaseous Hydrogen Rocket Combustors. Journal of Propulsion and Power 16(5), 823–828 (2000)

[8] Paillère, H., Corre, C., García Cascales, J.R.: On the extension of the AUSM+ scheme to compressible two-fluid models. Computers & Fluids 32, 891–916 (2003)

[9] Preclik, D., Knab, O., Görgen, J., Hagemann, G.: Simulation and Analysis of Thrust Chamber Flowfields: Cryogenic Propellant Rockets. In: AIAA Progress in Astronautics and Aeronautics, 2006, Liquid Rocket Thrust Chambers (2006) ISBN-13: 978-1563472237

[10] Vallet, A., Burluka, A.A., Borghi, R.: Development of a Eulerian model for the "atomization" of a liquid jet. Atomization and Sprays 11, 619–642 (2001)

[11] Wörner, M.: A Compact Introduction to the Numerical Modeling of Multiphase Flows. Forschungszentrum Karlsruhe, Wissenschaftliche Berichte FZKA 6932 (2003)

Application of the Multi-Scale-Finite-Volume Method to the Simulation of Incompressible Flows with Immersed Boundaries

Giuseppe Bonfigli and Patrick Jenny

ETH Zurich, Sonneggstrasse 3, CH-8092 Zurich, Switzerland
bonfigli@ifd.mavt.ethz.ch

Summary

A second-order accurate numerical procedure is presented for the solution of the incompressible Navier-Stokes equations with immersed boundaries in the formulation proposed by Peller et al. [5]. In particular we derive exact constraints for the pressure at immersed solid walls and show that the resulting Poisson equation is formally identical to the elliptic problems governing flows in porous media. An efficient iterative procedure for the computation of the pressure is then obtained by adapting the iterative-multi-scale-finite-volume procedure by Hajibeygi et al. [2].

1 Introduction

The generation of body-fitted grids for finite-volume computations is typically the most time-consuming task in the work-flow of industrial CFD applications. Furthermore, geometries are frequently so complex, that high-quality grids are not affordable. The immersed-boundary method (IBM) [6] removes these difficulties by considering non-fitted orthogonal meshes and representing immersed bodies by means of concentrated volume forces. However, IBM are relatively inaccurate for problems considering immersed rigid bodies, due to the singular character of the solution at solid walls. An alternative to IBM is provided by the ghost-node method (GNM) [5, 1], where boundary conditions at immersed solid walls are imposed indirectly by extrapolating the velocity field at ghost nodes inside the solid body. GNM is quite promising with respect to accuracy issues, but it is less efficient than classical volume-force-based methods. Indeed, the velocity extrapolation at immersed boundaries modifies the structure of the Poisson equation governing the flow and prevents the straightforward use of standard solvers for structured grids.

We combine the primitive-variable GNM implementation by Peller et al. [5] with an efficient Poisson solver derived from the iterative-multi-scale-finite-volume (IMSFV) method by Hajibeygi et al. [2]. The latter was developed for the simulation of flows in porous media, where the pressure is governed by the elliptic problem

$$-\nabla \cdot \lambda \nabla p = q. \tag{1}$$
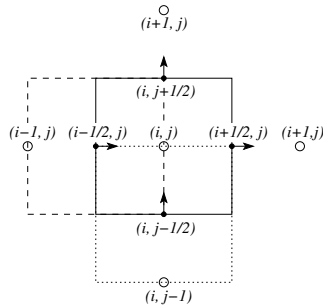
Fig. 1. Staggered grids for p (circles) u (horizontal arrows) and v (vertical arrows). Control volumes for mass (solid line), momentum in x-direction (dashed line) and momentum in y-direction (dotted line).

The coefficient λ represents thereby the medium permeability and may rapidly vary in space, making standard methods inefficient or inapplicable also in this case.

The paper is structured as follows. The finite-volume implementation of the Navier-Stokes solver with GNM capabilities is presented in section 2. The inclusion of immersed boundaries in the pressure Poisson equation and the equivalence of the resulting problem with equation (1), for $\lambda = 1$ within the flow region and $\lambda = 0$ inside solid bodies, is discussed in section 3. A brief discussion of the IMSFV procedure and of the modifications needed for its application to the present problem is also given in the same section. Numerical results to validate the modified IMSFV procedure as a stand alone solver and the complete Navier-Stokes implementation are provided in section 4. Concluding remarks are given in section 5.

2   Discretization of the Navier-Stokes Equations

The numerical procedure is based on a finite-volume discretization on staggered equidistant grids [3] (see figure 1, where also the indexing for pressure and velocity grids is defined). The integration domain Ω is rectangular and the following conservative non-dimensional formulation of the Navier-Stokes equations in primitive variables is considered:

$$\frac{\partial \underline{u}}{\partial t} + \nabla \cdot (\underline{u} \otimes \underline{u}) = -\nabla p + \frac{1}{Re}\Delta \underline{u}, \qquad \forall t, \forall \underline{x} \in \Omega, \qquad (2a)$$

$$\nabla \cdot \underline{u} = 0, \qquad \forall t, \forall \underline{x} \in \Omega, \qquad (2b)$$

$$\underline{u} = \underline{\bar{u}}, \qquad \forall t, \ \forall \underline{x} \in \partial\Omega. \qquad (2c)$$

Thereby $\underline{x} = (x, y)^T$, $\underline{u} = (u, v)^T$ and $\underline{\bar{u}}$ is a prescribed function defined on the boundary $\partial\Omega$ of Ω, including the surface of immersed bodies. A Poisson equation for the pressure is obtained by requiring the velocity field at the end of any time step to be exactly divergence free. Neumann boundary conditions for p follow thereby from the Dirichlet condition (2c) on the velocity.
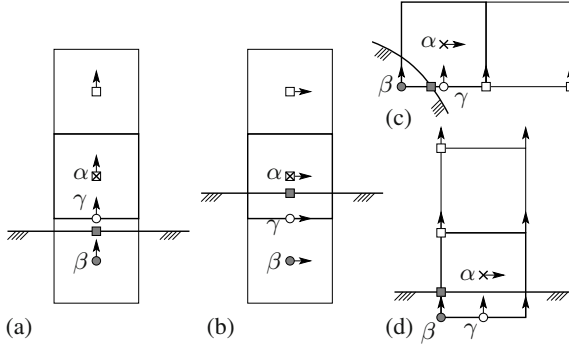
Fig. 2. Example of ghost node configurations. The evaluation of the momentum equation (2a) at nodes α (cross) requires the value of the velocity at the ghost nodes β (filled circle) in order to evaluate the same quantity (or its derivative) in γ (empty circle). Squares indicate nodes included in the extrapolation stencil. Empty squares are grid nodes, filled squares are boundary nodes where equation (2c) is applied.

Centered second-order stencils are used both for derivation and interpolation, and the standard fourth-order Runge-Kutta scheme is used for explicit time integration. In order to account for immersed boundaries, the value of the velocity components are defined by means of fourth-order extrapolation at ghost nodes lying next to the boundary within the region occupied by the solid bodies[1]. Only extrapolation along grid lines is considered and each extrapolation stencil includes nodes in the fluid region, as well as the intersection point between the grid line and the boundary. This allows the indirect imposition of the Dirichlet boundary condition (2c) and decouples the solution at nodes within the flow regions from that in the inner part of solid bodies. Examples of extrapolation stencils for different relative positions between grid and immersed boundaries are provided in figure 2. Results confirming the above statements about the accuracy of the method can be found in [7].

3   Pressure Computation with the IMSFV-Procedure

The equivalence between the Pressure-Poisson equation for the case with immersed boundaries and the elliptic problem (1) with proper definition of λ can be seen by considering the mass balance for the control volume (i, j) at the time step $(l + 1)$ (c.f. figure 1):

$$\frac{u_{(i+1/2,j)}^{(l+1)} - u_{(i-1/2,j)}^{(l+1)}}{\Delta x} + \frac{v_{(i,j+1/2)}^{(l+1)} - v_{(i,j-1/2)}^{(l+1)}}{\Delta y} = 0. \tag{3}$$

---

[1] Exceptions occur when extrapolation is carried out in the direction parallel to the velocity component, in which case also nodes in the flow field are treated as ghost nodes, if a neighbouring pressure node lies inside the body.
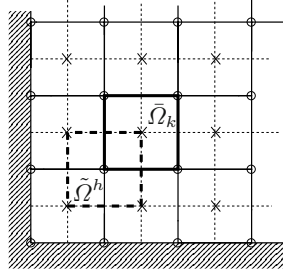
Fig. 3. Primal (solid lines) and dual (dashed lines) coarse grids; bold lines highlight the coarse cell $\bar{\Omega}_k$ and the dual cell $\tilde{\Omega}^h$. Each coarse cell is obtained as union of fine-grid cells.

To discuss the treatment of immersed boundaries, we assume that node $(i + 1/2, j)$ is a ghost node, so that the value $u^{(l+1)}_{(i+1/2,j)}$ of u at the time step $(l + 1)$ is evaluated by extrapolation and may be assumed to be known at this stage (it is iteratively improved in a further step as discussed below). Using the momentum equation (2a) to express $u^{(l+1)}$ as functions of p and $u^{(l)}$, and collecting all known terms (including $u^{(l+1)}_{(i+1/2,j)}$) into the right-hand side, we can recast equation (3) into the form

$$\frac{p_{(i-1,j)} - p_{(i,j)}}{\Delta x^2} + \frac{p_{(i,j+1)} - p_{(i,j)}}{\Delta y^2} + \frac{p_{(i,j-1)} - p_{(i,j)}}{\Delta y^2} = q_{(i,j)}, \tag{4}$$

which provides the needed equation for p at the node (i, j). An equation with the same left-hand-side as equation (4) is obtained by imposing Neumann boundary conditions for p at node $(i + 1/2, j)$, but also from the elliptic problem (1), if $\lambda = 0$ in the cell $(i + 1, j)$. More in general the pressure Poisson-equation for the Navier-Stokes implementation with immersed bodies and the elliptic problem (1) lead to systems of equations with identical matrices, if λ in (1) is set to zero for cells whose center lies within solid bodies, and to one elsewhere.

According to the IMSFV procedure, the solution p of equation (1) is approximated at the iteration step n as a superposition $p'^{[n]}$ of two sets of functions called basis functions (Φ^h_k, in the notation by [2]) and correction functions ($\Phi^{h\,[n]}$), respectively:

$$p \approx p'^{[n]} = \sum_{h=1}^{N} \left[\sum_{k=1}^{M} \Phi^h_k \bar{p}^{[n]}_k + \Phi^{h\,[n]} \right]. \tag{5}$$

Each Φ^h_k and $\Phi^{h\,[n]}$ is computed independently solving equation (1) on rectangular sub-domains $\tilde{\Omega}^h$, $h = 1, \ldots, N$ corresponding to the cells of a coarse grid (figure 3), which will be called dual coarse grid to distinguish it from the original fine grid and from the primal coarse grid also used in the following (primal coarse cells are $\bar{\Omega}_k$, $k = 1, \ldots, M$). While a homogeneous problem is solved for Φ^h_k, the original

right-hand side from equation (1) is considered for $\varPhi^{h\,[n]}$. The approximated boundary conditions (localization boundary condition)

$$\frac{\partial}{\partial n}\left(\lambda\frac{\partial \varPhi_k^h}{\partial n}\right) = 0, \qquad\qquad \forall t,\ \forall \underline{x},\ \in \partial\tilde{\varOmega}^h \qquad (6a)$$

$$\frac{\partial}{\partial n}\left(\lambda\frac{\partial \varPhi^{h\,[n]}}{\partial n}\right) = \frac{\partial}{\partial n}\left(\lambda\frac{\partial p'^{\,[n-1]}}{\partial n}\right), \qquad \forall t,\ \forall \underline{x},\ \in \partial\tilde{\varOmega}^h \qquad (6b)$$

are imposed on boundaries of $\tilde{\varOmega}^h$, which do not lie on the outer boundary of $\varOmega$. Furthermore, each $\varPhi^{h\,[n]}$ is required to be zero at corners of $\tilde{\varOmega}^h$. The same is true for $\varPhi_k^h$, except at the corner lying within the primal coarse cell $\bar{\varOmega}_k$, if any, where it is set to one. Both $\varPhi_k^h$ and $\varPhi^{h\,[n]}$ are zero outside $\tilde{\varOmega}^h$ and $\varPhi_k^h$ is identically zero if no corner of $\tilde{\varOmega}^h$ lies in $\bar{\varOmega}_k$. Finally, the coefficients $\bar{p}_k^{[n]}$ multiplying the basis functions in (5) are estimated requiring integral mass balance (e.g. the integral form of equation (3) for the Navier-Stokes context) for each primal coarse cell $\bar{\varOmega}_k$, $k = 1,\ldots,M$ (coarse system). Additional line relaxation applied onto $p'^{\,[n]}$ between each IMSFV iteration may greatly improve convergence rates and ensures stability also in critical cases (anisotropic problems). Notice also, that equation (6b) in the only algorithmic step, where the previous approximated solution $p'^{\,[n-1]}$ enters the computation of the new one. More details on the IMSFV-procedure can be found in [2].

Basis functions represent the key-element of the IMSFV-procedure. They allow the definition of the coarse system, which honors the elliptic character of the problem by coupling the solution over the whole integration domain. Thereby they also account for the fine-scale distribution of the permeability λ, which enters their definitions by means of the localized fine-scale problems. On the other hand, correction functions are necessary for the accurate representation of non-homogeneous terms.

The IMSFV procedure described above may fail when the permeability λ becomes zero or varies over several orders of magnitude within the integration domain. Two main reasons can be found for that. First, the condition number of the coarse system worsens proportionally to the ratio $\lambda_{max}/\lambda_{min}$. Second, the quality of the localization boundary conditions (6b) for the correction functions also deteriorates for increasing $\lambda_{max}/\lambda_{min}$. The first problem is a consequence of the fact that basis functions $\varPhi_k^h$, for which the node k lies within a low permeability region, rapidly decay within that region and are virtually zero outside of it. Therefore they produce negligible fluxes through the coarse-cell boundaries and the corresponding coefficients in the matrix of the coarse system become very small. The second aspect is due to the critical situations in which a permeable region on the edge of a dual cell $\tilde{\varOmega}^h$ is disconnected from the cell corners due to the interposition of impermeable cells. Since fluxes in the direction normal to the edge are prescribed by the boundary condition (6b), large gradients in $\varPhi^{h\,[n]}$ might be needed to fulfill the modified elliptic problem by generating fluxes along the edge, i.e. through the impermeable region, while in the exact solution flux balance would be rather achieved by means of fluxes in the transverse direction.

Modified basis and correction functions may be introduced to remove the mentioned difficulties. The former can be computed considering a modified permeability field (clipped below), so that the maximum ratio $\lambda_{max}/\lambda_{min}$ remains limited. If the lower bound for λ is chosen properly, the resulting basis functions preserve all the
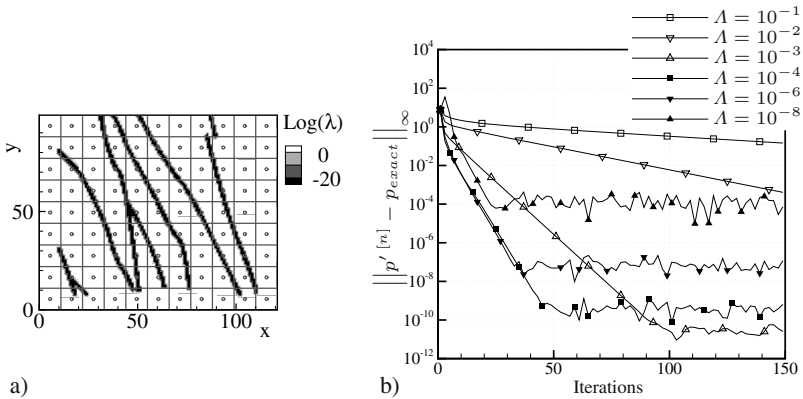
Fig. 4. Left: permeability distribution and primal coarse grid. The grid contains 121×99 fine cells and 11×9 coarse cells. Right: convergence behaviour of the modified IMSFV procedure for different values of the lower bound Λ. Correction functions were discarded and 5 line-relaxation steps were applied after each IMSFV step.

properties, which make them a suitable tool for the definition of the coarse system. Correction functions can be computed replacing the critical boundary condition (6b) with the more robust Dirichlet condition

$$\Phi^{h\,[n]} = 0, \qquad\qquad \forall t,\ \forall \underline{x} \in \partial\tilde{\Omega}^h. \qquad (7)$$

Finally, a residuum-correction formulation has to be introduced, since the solution can not be represented by superposing the modified basis and correction functions as in equation (5). In this context line relaxation may also be used to ensure local convergence on the fine scale and the computation of the correction functions is not strictly necessary any more.

We conclude by pointing out that interpolated values of the velocity at ghost nodes also depend on the pressure solution, they contribute to determine. This introduces a coupling between pressure and velocity, so that an iterative loop has to be carried out to improve both quantities in alternating sequence. We achieved most efficient convergence of the overall procedure, when the update of ghost nodes was carried out after each recomputation of the pressure field, i.e. after each line-relaxation step performed between the IMSFV steps.

4   Numerical Results

4.1   IMSFV for Elliptic Problems with Impermeable Regions

The performance of the modified IMSFV implementation proposed in the previous section is verified on the basis of a critical test case, where $\lambda = 1$ in most part of the integration domain, but $\lambda = 10^{-20}$ (i.e. numerically zero for double-precision computations) within thin layers of complex topology (figure 4-a). Neumann conditions are set on the whole boundary and concentrated sources and sinks are introduced at
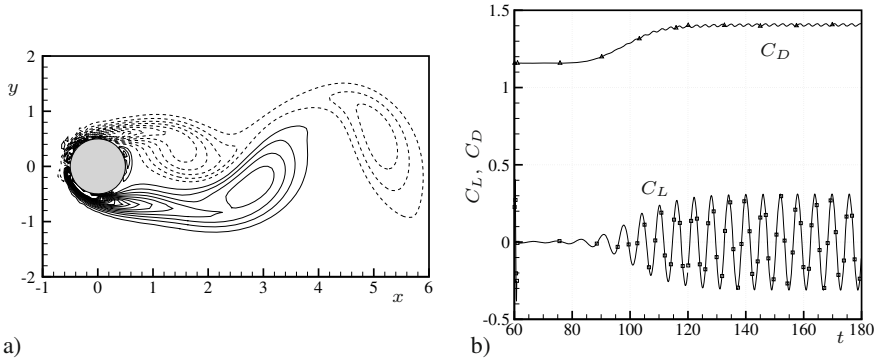
Fig. 5. Left: Isocontours of spanwise vorticity ω_z ($\Delta\omega_z = 0.5$). Right: Time development of drag and lift coefficients.

opposite corners of the integration domain. The standard IMSFV procedure fails for the given problem, while the modified procedure can still achieve sustained converge rates, depending on the choice of the lower bound Λ set for λ when computing the basis functions (figure 4-b). Best results are observed when Λ is 3 to 4 orders of magnitude lower than the maximum permeability.

4.2 Navier-Stokes Solver with IMSFV

The flow around a circular cylinder at $Re_D = 100$ is simulated for validation of the Navier-Stokes solver. Constant velocity is prescribed at the inflow and outflow boundaries, while symmetry is assumed at the upper and lower boundaries. The cylinder is located at the origin and the integration domain spans the region $-10 \leq x \leq 20$, $-10 \leq y \leq 10$ with grid spacing $\Delta x = \Delta y = 0.075$ (coordinates are made non-dimensional with the cylinder diameter D). Each coarse cell in the IMSFV procedure contains 5×5 fine cells and 5 IMSFV iterations with 5 line-relaxation steps each are carried out each time step. This is enough to achieve an error $\epsilon < 10^{-10}$ in the continuity equation. The time step size is $\Delta t = 0.02$.

The unstable steady wake is perturbed at $t = 60$ triggering the onset of a periodic motion resulting in the Karman vortex street (figure 5-a) . The Strouhal number $Sr = 0.168$ is in good agreement with results from the literature [4]. Mean value and oscillation amplitudes for lift and drag coefficients, $C_L = \pm0.31$ and $C_D = 1.405 \pm 0.00797$ (figure 5-b), deviate by up to 7% with respect to established values. However, this is quite satisfactory considering the relatively coarse discretization level (c.f. [4]).

In conclusion, we verify the possibly negative influence of the iterative velocity update at ghost nodes on the convergence of the pressure solution. The integration domain is $-1 \leq x, y \leq 1$ and a solid cylinder of diameter $D = 0.4$ is set in the origin. Highly unsteady boundary conditions are imposed at the immersed boundary to enhance the work load of the solver. Different discretization levels and numbers of smoothing steps are considered. Convergence rates of the IMSFV procedure is documented both for computations with (figure 6-a) and without (figure 6-b) iterative update. Performance reduction in the former case is very moderate.
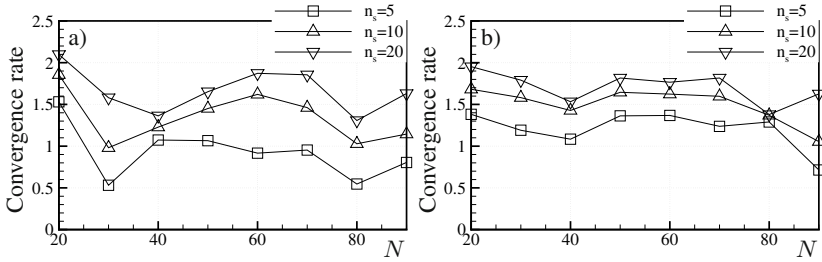
Fig. 6. Convergence rates for the pressure Poisson equation for different discretization levels (number of fine cells in each spatial direction N) and numbers of line-relaxation steps (n_s). Ghost nodes values are updated after each line-relaxation step (a) or kept constant (b).

5   Conclusions

The ghost-node method by Peller et. al. [5] for the solution of the incompressible Navier-Stokes equations with immersed boundaries has been been combined with a generalized version of the iterative-multi-scale-finite-volume method by Hajibeygi et al. [2]. In doing that the analogy between the resulting pressure Poisson equation and the elliptic problem governing flows in porous media has been highlighted and exploited. The iterative loop of IMSFV and the iterative update of extrapolated velocity values at ghost nodes, which is needed to impose the no-slip condition at immersed boundary exactly, could be combined without relevant loss of performance. Second-order accuracy in space and fourth order in time have been achieved. Good agreement with results from the literature for the unsteady flow around a circular cylinder at $Re = 100$ have been achieved in spite of a relatively coarse discretization level.

References

[1] Gibou, F., Fedkiw, R.: A fourth order accurate discretization for the laplace and heat equations on arbitrary domains with applications to the stefan problem. J. Comp. Phys. 202, 577–601 (2005)
[2] Hajibeygi, H., Bonfigli, G., Hesse, M.A., Jenny, P.: Iterative multiscale finite-volume method. J. Comp. Phys. 277, 8604–8621 (2008)
[3] Harlow, F.H., Welch, J.E.: Numerical calculation of time-dependent viscous incompressible flow of fluid with free surface. Phys. Fluids 8, 2182–2189 (1965)
[4] Linnick, M., Fasel, H.: A high-order immersed interface method for simulating unsteady incompressible flows on irregular domains. J. Comp. Phys. 204, 157–192 (2005)
[5] Peller, N., Duc, A.L., Tremblay, F., Manhart, M.: High-order stable interpolation for immersed boundary methods. Int. J. Num. Meth. Fluids 52, 1175–1193 (2006)
[6] Peskin, C.S.: Flow patterns around heart valves: a numerical method. J. Comp. Phys. 10, 252–271 (1972)
[7] Bonfigli, G., Jenny, P.: An efficient multi-scale poisson solver for the incompressible navier-stokes equations with immersed boundaries. J. Comp. Phys. 277, 8604–8621 (2009)

A Variable-Fidelity Modeling Method for Aero-Loads Prediction

Z.-H. Han, S. Görtz, and R. Hain

Deutsches Zentrum für Luft- und Raumfahrt e.V.,
Institut für Aerodynamik und Strömungstechnik,
Lilienthalplatz 7, 38108, Braunschweig, Germany
Zhong-hua.Han@dlr.de, Stefan.Goertz@dlr.de

Summary

A Variable-Fidelity Modeling (VFM) method has been developed as an efficient and accurate aerodynamic data modeling strategy. In this approach, a set of CFD methods with varying degrees of fidelity and computational expense is exercised to reduce the number of expensive high-fidelity computations. Kriging-based bridge functions are constructed to match the low- and high fidelity CFD data. The method is demonstrated by constructing a global approximation model of the aerodynamic coefficients of an RAE 2822 airfoil based on sampled data. The model is adaptively refined by inserting additional samples. It is shown that the method is promising for efficiently generating accurate aerodynamic models that can be used for the rapid prediction of aerodynamic data across the flight envelope.

1 Introduction

From an aerodynamic point of view, an aircraft is defined by comprehensive datasets regarding performance, loads and handling characteristics. This data, which needs to be determined for every possible flight condition, is used to design the structure of the aircraft and the flight control system. Currently, this data is obtained mainly from costly wind tunnel tests or using hand-book methods. The use of higher-fidelity and thus more time consuming CFD methods has been, up to now, impossible due to the large volume of data required. The long-term goal of the work described here is the development of a process chain for the efficient numerical prediction of all relevant aerodynamic data for the elastic aircraft over the entire flight envelope, based on a hierarchy of CFD methods of increasing fidelity. The idea is to use Variable-Fidelity Modeling (VFM).

The idea of VFM is not entirely new since it has been used in the aircraft design optimization community for more than ten years. Examples of local VFM, where an approximation model is constructed using only a few data points nearest to the design point of interest and refined during optimization, can be found in Ref. [1-4].

Examples of global VFM, where the approximation model is constructed with all the available points throughout the parameter space, can be found in Ref. [5-6]. Very few publications on VFM in the context of aerodynamic data for loads are available. In Ref. [7], e.g., a so called "data fusion" method was developed for the generation of an aerodynamic database by using CFD tools of varying fidelity.

This paper focuses on the development a VFM method that is especially well suited for predicting and modeling the aerodynamic data of aircraft throughout the entire flight envelope. Kriging-based global approximation of the aerodynamic data and Kriging-based bridge functions are studied and used to construct a global surrogate model of the aerodynamic data in the parameter space. A novel sample-point refinement strategy is proposed to adaptively refine the model, which makes it more accurate and the VFM method more efficient. The developed method is demonstrated for the prediction of the aerodynamic coefficients and the drag polar of an RAE 2822 airfoil at different Mach numbers and angles of attack.

2   Framework of the Variable-Fidelity Modeling Method

The framework for VFM was designed for constructing a model that can approximate the high-fidelity data throughout the parameter space. It is depicted in Figure 1.
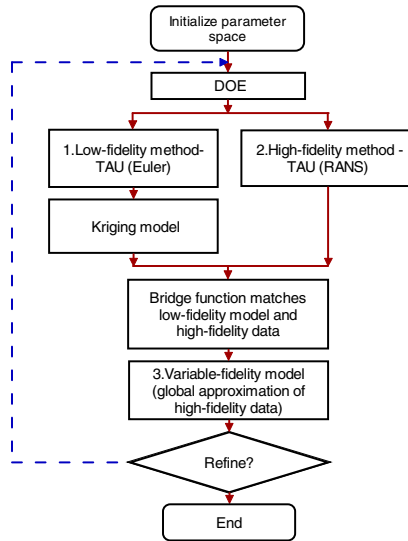
Fig. 1. Framework of VFM for aero-loads prediction

The basic steps of this framework are as follows:

- **Step 1 Initialization:** Define the unknown aero-loads (integrated or distributed) to be modeled; specify the parameter space by defining the independent variables and their range.

- **Step 2 Sampling:** Two sets of sample points (called samples in the following) are generated based on Design of Experiment (DoE) theory; one is for the intensively samples parameter space to be computed with the low-fidelity method, the other is for the less intensively samples parameter space to be evaluated with the high-fidelity method.
- **Step 3 Sample point evaluation:**   The aerodynamic data at the samples are calculated by low- and high-fidelity CFD methods, respectively.
- **Step 4 Low-fidelity surrogate model and bridge function:** Based on the low-fidelity sampled data, a Kriging model is constructed as a surrogate model to the low-fidelity CFD method (called low-fidelity Kriging). Based on the difference between the low-fidelity surrogate model and the high-fidelity data at the locations of the high-fidelity samples, a Kriging-based bridge function is constructed to match the low- and high-fidelity CFD methods.
- **Step 5 Initial VFM construction:** The low-fidelity surrogate model is corrected with the bridge function and an initial VFM is constructed.
- **Step 6 Refinement:** iterative refinement is performed by adding additional samples until a criterion for termination is fulfilled.
- **Step 7 Final VFM for aero-loads prediction:** Based on the final VFM, the parameter space can be probed in "real-time" for aerodynamic data at any point in the parameter space within the limits prescribed in Step 1 or a database of aerodynamic data can be efficiently generated by filling in the remainder of the parameter space using the VFM.

3   Kriging Model and Bridge Function

One of the key issues for VFM is how to create the global surrogate models. The Kriging method [9], a geostatistical technique, was used here due to its good global approximation characteristics. For a problem with n_v variables and n_s samples, the Kriging method approximates the unknown function y by a linear combination of the known values at samples as follows

$$\hat{y}(\mathbf{x}_p) = \sum_{i=1}^{n_s} w_i(\mathbf{x}_p) y(\mathbf{x}_i), \mathbf{x} \in R^{n_v} \tag{1}$$

where $\hat{y}(\mathbf{x}_p)$ is the predicted value at the location denoted by $\mathbf{x}_p$, $\mathbf{x}$ is vector of independent variable and w_i are the weight functions. For the ordinary Kriging used in this study, the weight functions fulfill the unbiasedness condition

$$\sum_{i=1}^{n_s} w_i(\mathbf{x}_p) = 1 \tag{2}$$

By minimizing the mean squared error of the predictor with the above equivalent constraint, the ordinary Kriging predictor can be expressed as

$$\hat{y}(\mathbf{x}_p) = \begin{bmatrix} y_1 \\ \vdots \\ y_{n_s} \\ 0 \end{bmatrix}^T \begin{bmatrix} R(\mathbf{x}_1,\mathbf{x}_1) & \cdots & R(\mathbf{x}_1,\mathbf{x}_{n_s}) & 1 \\ \vdots & \ddots & \vdots & \vdots \\ R(\mathbf{x}_{n_s},\mathbf{x}_1) & \cdots & R(\mathbf{x}_{n_s},\mathbf{x}_{n_s}) & 1 \\ 1 & \cdots & 1 & 0 \end{bmatrix}^{-1} \begin{bmatrix} R(\mathbf{x}_1,\mathbf{x}_p) \\ \vdots \\ R(\mathbf{x}_{n_s},\mathbf{x}_p) \\ 1 \end{bmatrix} \tag{3}$$

where y_1, ..., y_n are the function values at samples; $R(x_i,x_j)$ is the spatial correlation function [9] between any two points ($\mathbf{x}_i$ and $\mathbf{x}_j$).

Another key issue for VFM is how to manage the different models of varying fidelity or how to correct the low-fidelity surrogate to approximate the high-fidelity data by making use of so called "bridge functions", which are sometimes called "scaling functions". The existing bridge functions can be divided into three categories: multiplicative [3], additive [5, 8] and hybrid [7]. All three approaches require the construction of an unknown function to correct the lower-fidelity model, which in turn will approximate the high-fidelity model. Note that the bridge functions can take the form of first- or second-order polynomials or Kriging models. To avoid the possible problem of diving by zero when using multiplicative bride functions, an additive bridge function was used in this study. The additive bridge function can be expressed as

$$\gamma(\mathbf{x}) = y_{hf}(\mathbf{x}) - y_{lf}(\mathbf{x}) \tag{4}$$

where $y_{lf}(\mathbf{x})$ and $y_{hf}(\mathbf{x})$ denote the low- and high-fidelity models, respectively. After an additive bridge function $\gamma(\mathbf{x})$ is approximated by Kriging, the high-fidelity model can be approximated by the following VFM:

$$\hat{y}_{VFM}(\mathbf{x}) = \hat{y}_{lf}(\mathbf{x}) + \hat{\gamma}(\mathbf{x}) \tag{5}$$

4   Sample-Point Refinement Strategy

A refinement strategy dedicated to VFM has been developed. The method assumes that the VFM is always more accurate than the Kriging model constructed directly from the high-fidelity samples (called high-fidelity Kriging). Only in the limit of a very large number of high-fidelity samples, the VFM and the high-fidelity Kriging model will converge to the same result. Hence, one can measure the error between the VFM and the high-fidelity Kriging model to avoid the difficulty of having to estimate the error between the VFM and the exact underlying functional relationship, which is unknown. The error is defined as

$$e_i = \left| y_{VFM}^i - y_h^i \right|, i = 1,2,...,n_t \tag{6}$$

where n_t is the number of test points, y_{VFM}^i and y_h^i denote the VFM and high-fidelity Kriging value at the ith test point, respectively. The maximum, average error in % and the RMS error are defined as

$$e_{max} = \max(e_i), \bar{e} = \frac{1}{n_t}\sum_{i=1}^{n_t}(\frac{e_i \times 100}{y_{VFM}^i}), RMS = \sqrt{(\sum_{i=1}^{n_t} e_i^2)/n} \tag{7}$$

Since all the values used in the error estimation are obtained from the surrogate models, the computational cost is negligible even for a large number of test points. The location with the maximum error is selected for refinement, and the VFM is reconstructed. The refinement is repeated until the average error is below a certain threshold, here 5%. This refinement method will be demonstrated and evaluated in the next section.

5   Results and Discussion

The VFM method is demonstrated by modeling the aerodynamic coefficients of an RAE 2822 airfoil as a function of one and two free stream flow parameters. The VFM framework was built around the DLR TAU code [10]. The low- and high-fidelity computations were performed with the Euler and RANS versions of the TAU code, respectively. Jameson's central scheme was used for space discretization, and an LU-SGS implicit scheme was used for time stepping. The Spalart-Allmaras one-equation model was utilized for the simulation of fully turbulent flow. The grids around the RAE 2822 airfoil used for the Euler and RANS computations are illustrated in Figure 2.

Number of points: 13,124

Number of points: 27,884
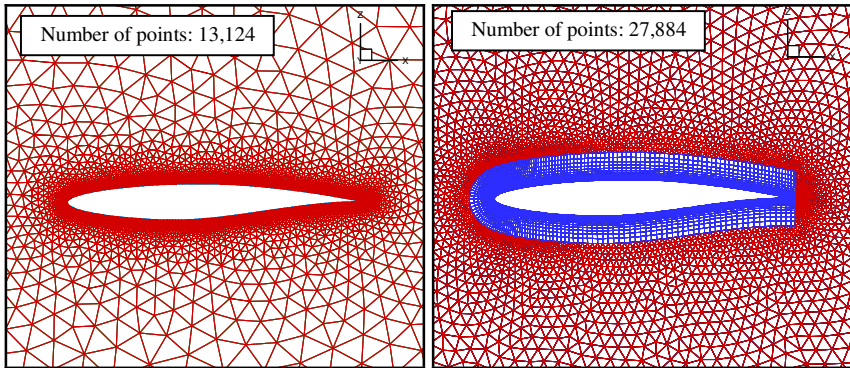
Fig. 2. Computational grids for Euler and N-S calculation

A VFM framework based on a single physical model (TAU Euler) evaluated on meshes of varying refinement was also demonstrated for the RAE 2822 airfoil (not shown here). It was shown that in this case VFM works very well even without sample-point refinement as the low-fidelity model captures the overall trend of the high-fidelity model.

5.1   VFM for RAE 2822 with One Independent Variable

At first, the VFM was applied to model the aerodynamics of the RAE 2822 airfoil as a function of a single variable, angle of attack, α, in the range from -4° to 16.5°. The Mach number was fixed at 0.2. A Reynolds number of 6.5×10^6 was assumed for the RANS computations. 26 samples were selected for the Euler computations, whereas only 4 initial

samples were selected for the RANS computations. The RANS computations were also performed at the locations of the 26 low-fidelity samples to validate the constructed VFM. The VFM was used to model the lift, drag and moment coefficients, as well as the drag polar. The VFMs for the lift and the drag polar are shown Figure 3. Reasonably good
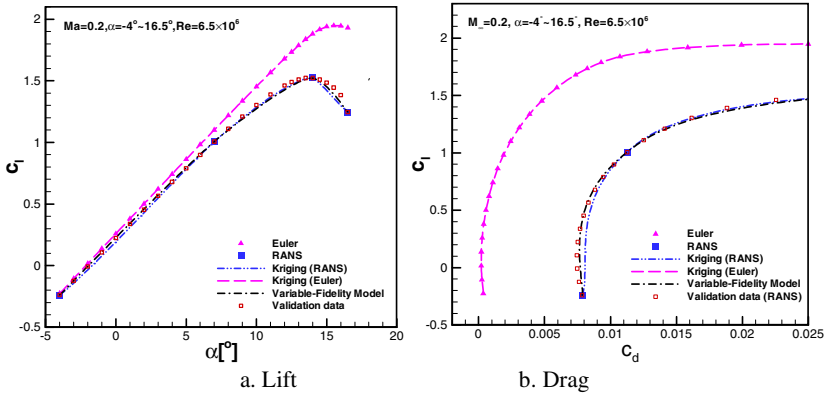
Fig. 3. VFM for lift and drag polar of RAE 2822 airfoil ($Ma = 0.2, \alpha = -4^o \sim 16.5^o$)
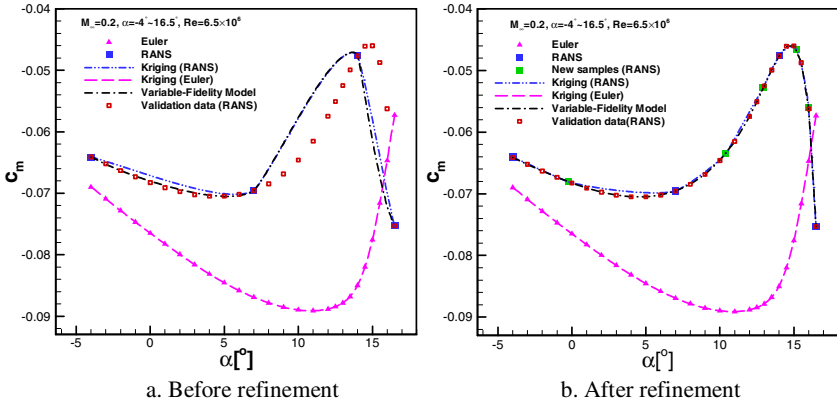
Fig. 4. VFM for C_m of RAE 2822 airfoil ($Ma = 0.2, \alpha = -4^o \sim 16.5^o$)

agreement between the VFM (without refinement) and the validation data is observed. Figure 4 shows the VFM for the moment coefficient as a function of angle of attack. The key features of VFM are clearly shown here: at low angles of attack the VFM is in very good agreement with the validation data, since the Euler method can capture the trend of the RANS method. At high angles of attack (especially near stall), the Euler method misses the trend, and the VFM is no longer better (but also not worse) than the high-fidelity Kriging model directly constructed from the high-fidelity samples. In such a case, refinement becomes necessary. The initial VFM was refined by adding new samples adaptively until the criterion for termination was fulfilled (see

section 4). Five new samples were added to refine the VFM, mainly in the region in which the flow is dominated by nonlinear effects. The refined VFM is in very good agreement with the validation data. As one of the results of refinement, the accuracy of high-fidelity Kriging was also increased. Although the final VFM is only slightly better than the high-fidelity Kriging model, VFM can be used to adaptively refine the approximation model.

5.2   VFM for RAE 2822 with Two Independent Variables

The VFM was then demonstrated for a problem with two variables (or a two-dimensional parameter space), angle of attack, α, and Mach number, Ma. The range of the variables was specified with Ma ranging from 0.1 to 1.2 and α ranging from -4° to 10°. 345 samples were selected manually for the Euler computations, while 32 initial samples were specified for the RANS computations using a Quasi-Monte Carlo DoE method. Refinement had to be performed since the Euler method missed the trend in the transonic regime and at high angles of attack. Based on the VFMs for the lift, drag and moment coefficients, respectively, 3 new samples were specified at each refinement iteration step. 15 steps of refinement were performed, and a total of 44 new samples were added. All the samples are plotted in Figure 5. It is clear that most of the samples were added in the region in which the flow is dominated by nonlinear effects. The remaining samples were added at the border of the parameter space. The 3-D hypersurfaces of the drag coefficient versus Mach number and angle of attack are shown in Figure 6. The low-fidelity Kriging model constructed from the 345 Euler computations is shown in Figure 6a; the high-fidelity Kriging model constructed from the 32 RANS computations is shown in Figure 6b. The difference between the low-fidelity Kriging model and the high-fidelity samples was used to construct the Kriging-based bridge function, and the VFM was obtained by correcting the low-fidelity Kriging model with the additive bridge function. The comparison of the final VFM and the validation data is also shown in Figure 6c, and very good agreement is observed. By comparing the number of high fidelity samples needed to construct an accurate VFM and that need for validation, one can conclude that the number of RANS computations can be reduced by a factor of about 5.
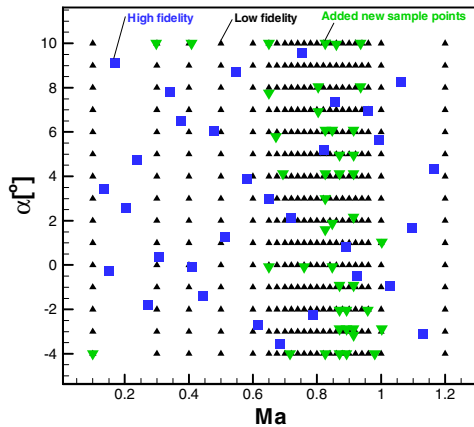
Fig. 5. Samples used to construct VFM ($Ma = 0.1 \sim 1.2, \alpha = -4^o \sim 10^o$)

a. Low fidelity model (Euler, 345 samples)

b. High fidelity model (RANS, 32 initial samples)

c. Variable-Fidelity Model refined by adding
44 additional high-fidelity samples
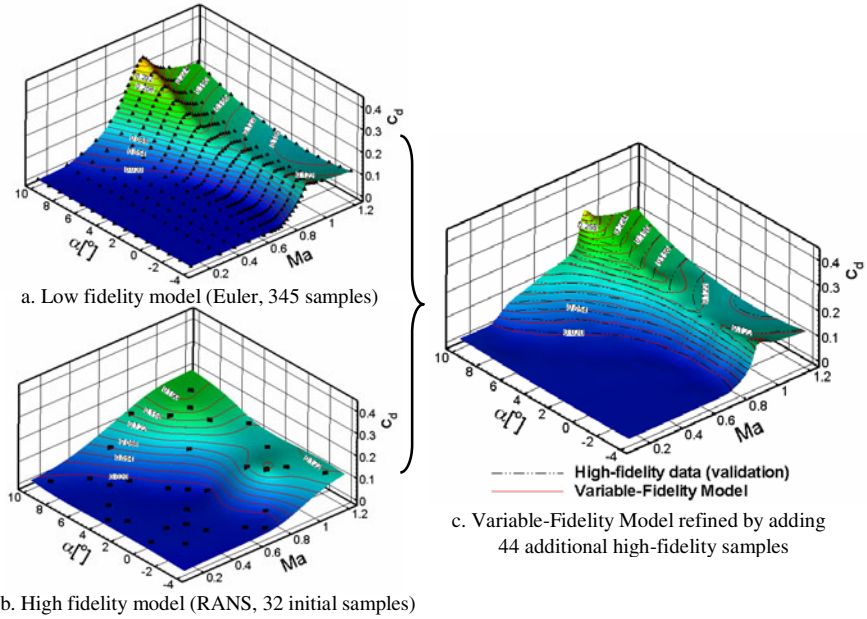
Fig. 6. Variable-fidelity model for C_d of RAE 2822 airfoil ($Ma = 0.1 \sim 1.2, \alpha = -4^o \sim 10^o$)

6 Conclusions

An efficient and accurate Variable-Fidelity Modeling (VFM) method for aero-loads prediction has been developed. This method was demonstrated for the prediction of the aerodynamic coefficients of an RAE 2822 airfoil. Some preliminary conclusions can be made as follows:

- When the low-fidelity model misses the actual trend in a specific region of the parameter space, the VFM needs to be refined in this region.
- The proposed refinement strategy was proven to be efficient and robust. It can be used to adaptively refine the VFM.
- The VFM method offers the possibility to significantly reduce the computational cost in the aero-data for loads context.

To further improve the efficiency and accuracy of VFM, the so-called gradient-enhanced direct Cokriging method will be employed. Also, the range of fidelity will be extended to include panel methods and RANS with wall functions. The method will also be extended to distributed aero loads and will be applied to more complex configurations and across the entire flight envelope.

References

[1] Braibant, V., Fleury, C.: An Approximation-Concepts Approach to Shape Optimal Design. Computer Methods in Applied Mechanics and Engineering 53, 119–148 (1985)

[2] Haftka, R.T.: Combining global and local approximations. AIAA Journal 29(9), 1523–1525 (1991)

[3] Chang, K.J., Haftka, R.T., Giles, G.L., Kao, P.-J.: Sensitivity-based scaling for approximating structural response. Journal of Aircraft 30(2), 283–288 (1993)

[4] Alexandrov, N.M., Lewis, R.M., Gumbert, C.R., Green, L.L., Newman, P.A.: Optimization with variable-fidelity models applied to wing design. AIAA Paper 2000-0841 (January 2000)

[5] Cho, S., Alonso, J.J., Kroo, I.M., Wintzer, M.: Multi-fidelity Design Optimization of Low-boom Supersonic Business Jets. AIAA Paper 2004-1530,

[6] Hatanaka, H., Obayashi, S., Jeong, S.: Application of the Variable-fidelity MDO Tools to a Jet Aircraft Design. In: The 25th International Congress of the Aeronautical Science 2006 (2006)

[7] Gano, S.E., Renaud, J.E., Martin, J.D., Simpson, T.W.: Update Strategies for Kriging Models for Using in Variable Fidelity Optimization. AIAA Paper 2005-2057 (April 2005)

[8] Tang, C.Y., Gee, K., Lawrence, S.L.: Generation of Aerodynamic Data using a Design of Experiment and Data Fusion Approach. AIAA Paper 2005-1137 (January 2005)

[9] Sacks, J., Welch, W.J., Mitchell, T.J., Wynn, H.P.: Design and Analysis of Computer Experiments. Statistical Science 4, 409–423 (1989)

[10] Schwamborn, D., Gerhold, T., Heinrich, R.: The DLR TAU-Code: Recent Applications in Research and Industry. In: ECCOMAS CDF 2006, The Netherland (2006)

Modelling and Validation of Covariance Transport Equations for Large-Eddy-Simulation of Ternary, Turbulent Mixing

Frank Victor Fischer and Wolfgang Polifke

Lehrstuhl für Thermodynamik, Technische Universität München, Boltzmannstraße 15, 85748 Garching, Germany

Summary

Large-Eddy-Simulation (LES) of turbulent reactive flows have an unclosed term for the filtered reaction rate. In order to obtain this rate, the subgrid-scale mixing state needs to be modelled. For the present case of ternary mixing, like it appears in a coannular jet-in-crossflow configuration, multi-variate Filtered Density Functions (FDFs) are used to model this mixing state. These FDFs are parameterized by the first and second order statistical moments, which include the covariance. It has been shown in literature that the covariance can have a noticable impact on the filtered reaction rate. This work develops and test transport equations for these moments, which include a non-equilibrium model for the subgrid scale scalar dissipation and the subgrad scale scalar cross-dissipation rates. Mixing models are then used to particle ensembles which represent the FDFs with the required moments.

1 Introduction

Mixing processes play an important role in understanding and assessing the performance of reacting systems in combustion processes, chemical engineering and similar reacting flow systems. It has been shown that Large–Eddy–Simulation (LES) is a suitable method for the effective simulation of such systems [3], as the large-scale processes are directly simulated and only the smaller scale (i.e. subgrid) processes need to be modelled, placing a lower burden onto the models involved and allowing the use of simpler and more general models than in Reynolds–Averaged–Navier–Stokes (RANS) context. By mixing, reactants are brought into direct molecular contact, so that a chemical reaction can take place, thus the small scale processes are still of importance because the quality of the mixing ultimately determines the reaction rate, at least for fast reactions. Jaberi and Colucci [9, 10] show that for LES of turbulent mixing three closure problems occur: The subgrid–scale stresses, the subgrid–scale scalar fluxes and the subgrid–scale unmixedness. As the former two closures have already been extensively studied in LES context, this work focuses on the latter closure problem which occurs in the transport equation for a reactive species ϕ:

$$\frac{D\overline{\phi}}{Dt} = \frac{\partial^2 \overline{\phi}}{\partial x_i^2} - \frac{\partial \tau_{i\phi}}{\partial x_i} + \overline{\dot{\omega}}, \tag{1}$$

where $\overline{\omega}$ is the filtered reaction rate of the cell and $\frac{\partial \tau_{i\phi}}{\partial x_i}$ denotes the subgrid–scale scalar stress, which can be modelled, for example, by using an eddy–diffusivity–approach as suggested by [4]. A subgrid scale model describing the mixing state of each cell is needed to accurately predict reaction rates in the cell, as it has been shown that large errors are made when only the resolved (i.e. filtered) values are taken into account for the mixing state.

2   Motivation

The mixing state itself can be represented by Filtered Density Functions (FDFs). Several alternatives have been suggested to represent such FDFs:

1. In order to minimize computational effort, functions of presumed shape can be employed. This approach has been proposed, for example, by Gutheil, Bockhorn [7, 8] and others using clipped Gaussian or β-functions.
2. For high accuracy, a transported PDF is used involving the tracking of a very large number of particles. The interaction between particles is determined by mixing models which describe the physical mixing process. However, this approach poses a large computational overhead on the simulation compared to the non–reacting and non–mixing LES of the velocity and pressure fields.

The present work uses Filtered Density Functions (FDF) represented by particle ensembles to model the subgrid–scale mixing state. A Monte Carlo approach as suggested for RANS context by Brandt and Polifke [1, 2] is used, where transport equations for the statistical moments are combined with a representation of the mixing state using a joint presumed discrete distribution (jpDD, i.e. an ensemble of particles) that are generated using mixing models. It is assumed that, at least in an approximate manner, the statistical state can be characterized uniquely by only the first and second order moments of the distribution.

Using a given jpDD of the mixture fractions within a computational cell, the filtered reaction rate inside the cell is computed by averaging over the individual reaction rates of each particle (as an example of a filtered value that takes into account subgrid–scale fluctuations):

$$\overline{\omega} \left(\overline{f_1}, \overline{f_2}, \overline{f_1'^2}, \overline{f_2'^2}, \overline{f_1'f_2'} \right) = \frac{1}{N} \sum_{i=1}^{N_{part}} \dot{\omega}_i(f_1, f_2). \tag{2}$$

This suggested approach is adapted for use in LES as follows and illustrated in figure 1:

1. The LES computes the velocity and pressure fields as well as transport equations for the first and second order moments of the distribution as it is done for presumed PDF approaches.
2. A mixing model generates jpDDs with given first and second order moments. For each of these distributions, a filtered reaction rate is computed as a sum over the individual particle reaction rates.

3. The LES uses these filtered reaction rates to compute the new mass fractions or concentrations of the species.
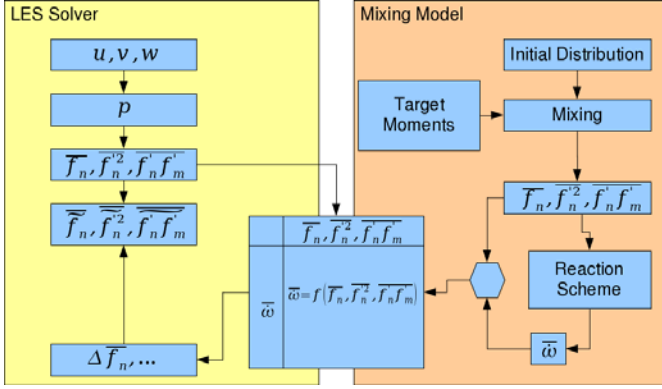
Fig. 1. Solver Approach

During LES, sets of similar first and second order moments are encountered repeatedly, so that further speedup can be obtained by storing the filtered rates in a table and computing the filtered quantities only once in a preprocessing step. Every access to the same set of moments results in a table lookup as shown in figure 1.

The authors have previously shown [5] that jpDDs with sufficient accuracy can be obtained using mixing models, which need the first and second order moments of the distribution to be supplied by the LES solver. As such, the present work focuses on the derivation and validation of the transport equations for the second order moments, as the precision of the first and second-order moments will ultimately determine the overall precision of the model.

3   Transport Equations

The fundamental transport equation for a conserved scalar ϕ reads [6]:

$$\frac{D\phi}{Dt} = \Gamma \frac{\partial^2 \phi}{\partial x_j \partial x_j}. \tag{3}$$

Filtering equation (3) for the LES approach and using a conventional eddy-diffusivity approach for the subgrid-scale transport as suggested by Eidson [4], or its dynamic counterpart yields a transport equation for the filtered scalar

$$\frac{D\overline{\phi}}{Dt} = \frac{\partial}{\partial x_j} \left((\Gamma + \Gamma_T) \frac{\partial \overline{\phi}}{\partial x_j} \right). \tag{4}$$

Here, Γ_T is the subgrid-scale diffusivity from the model. This equation can be used to derive a transport equation for the subgrid-scale variance of a scalar $\overline{\phi'^2}$ that reads, including the same model for the turbulent diffusivity:

$$\frac{\partial \overline{\phi'^2}}{\partial t} + \frac{\partial \overline{u_i}\overline{\phi'^2}}{\partial x_i} = \frac{\partial}{\partial x_i}\left((\Gamma + \Gamma_T)\frac{\partial \overline{\phi'^2}}{\partial x_i}\right) + 2(\Gamma + \Gamma_T)\frac{\partial \overline{\phi}}{\partial x_i}\frac{\partial \overline{\phi}}{\partial x_i} - \overline{\chi}. \quad (5)$$

The first term on the right-hand side represents the transport of variance by molecular and turbulent diffusion, the second term is the production of variance by gradients of the scalar field itself. Thus the only unclosed term in this transport equation is the third term, the *scalar dissipation rate*:

$$\overline{\chi} = 2\Gamma \overline{\frac{\partial \phi}{\partial x_i}\frac{\partial \phi}{\partial x_i}}. \quad (6)$$

Modeling of this term is thus crucial to predict the variance evolution.

4 Scalar Dissipation Rate

It has been suggested [13] to assume that the scalar dissipation and the variance production are in equilibrium. However, this assumption will conserve variance, whereas mixing is a process that is known to reduce variance [12]. Jimenez et al [11] have suggested a non-equilibrium approach that models the scalar dissipation rate using the mechanical-to-scalar time-scale ratio:

$$\frac{\overline{\chi}}{\overline{\phi'^2}} \propto \frac{\overline{\epsilon}}{\overline{k}}. \quad (7)$$

where $\overline{\epsilon}$ and $\overline{k}$ are taken from models by Smagorinsky [14] and Yoshizawa [15]:

$$\overline{\epsilon} = 2\left(\nu + C_S \overline{\Delta}^2\right)|\overline{S}| S_{ij} S_{ij}, \quad (8)$$

$$\overline{k} = 2C_I \overline{\Delta}^2 S_{ij} S_{ij}. \quad (9)$$

Fox [6] shows that at Schmidt numbers of around unity the mechanical-to-scalar time-scale ratio will be approximately constant for a given Taylor-scale Reynolds number.

$$\overline{\chi} = C_t \frac{\overline{\epsilon}}{\overline{k}} \overline{\phi'^2}. \quad (10)$$

However, this analysis is based on a fully developed scalar and turbulent energy spectrum. While such a spectrum will be obtained at sufficiently high Reynolds Numbers after some time, the spectra will look vastly different at the injection point of a jet-in-crossflow arrangement where the inflows are laminar, as no inertial sub-range will have developed yet.

5   Covariance Transport Equation and Cross-Dissipation Rate

The variance of a random variable X with an expected value μ reads:

$$\text{Var}(X) = E\left((X - \mu)^2\right), \tag{11}$$

while the covariance of two random variables X, Y with expected value μ, ν reads:

$$\text{Cov}(X, Y) = E\left((X - \mu)(Y - \nu)\right). \tag{12}$$

Thus, the variance can be regarded as a special case of the covariance:

$$\text{Var}(X) = \text{Cov}(X, X). \tag{13}$$

So the transport equation for the covariance $\overline{\phi_1' \phi_2'}$ can be derived from the transport equation of the variance, by replacing the quadratic terms by a term containing both scalars. The final form of the covariance transport equation thus reads:

$$\frac{\partial \overline{\phi_1' \phi_2'}}{\partial t} + \frac{\partial \overline{u_i}\, \overline{\phi_1' \phi_2'}}{\partial x_i} = \frac{\partial}{\partial x_i}\left((\Gamma + \Gamma_T)\frac{\partial \overline{\phi_1' \phi_2'}}{\partial x_i}\right) + 2\left(\Gamma + \Gamma_T\right)\frac{\partial \overline{\phi_1}}{\partial x_i}\frac{\partial \overline{\phi_2}}{\partial x_i} - \chi_c. \tag{14}$$

Where the term

$$\chi_c = 2\Gamma\overline{\frac{\partial \phi_1}{\partial x_i}\frac{\partial \phi_2}{\partial x_i}}. \tag{15}$$

is known as the *scalar cross-dissipation rate*.

6   Results and Conclusions

In order to validate the LES model, LES and DNS of co-annular jet-in-crossflows have been performed using a customized OpenFOAM 1.4.1 solver. Laminar inflow conditions have been chosen for all three inlets (crossflow and both jets) to match experimental results. The Reynolds number is 1200 (using the bulk velocity and the outer jet diameter, the Schmidt number of the flow is unity, so that the scalar field is fully resolved in the DNS. The geometric arrangement of the configuration can be seen in 2(b). Figure 6 shows one scalar with means, variances and dissipation rates.

The transport equations contain models for the subgrid scale scalar flux which is modelled by the eddy-diffusivity approach (see also [4]), which is validated well. Hence, the critical term to assess is the model for the scalar dissipation rate. To validate the presented model, the *total* scalar dissipation rate (on subgrid and resolved scales) has been compared against DNS data. Figure 6 shows this comparison.

It can be see that the DNS and LES data match well. As the LES grid contains significantly coarser cells, the steep gradients that are present in the DNS cannot be

(a) mean scalar

(b) instantaneous scalar

(c) scalar variance, logarithmic

(d) scalar dissipation rate, logarithmic
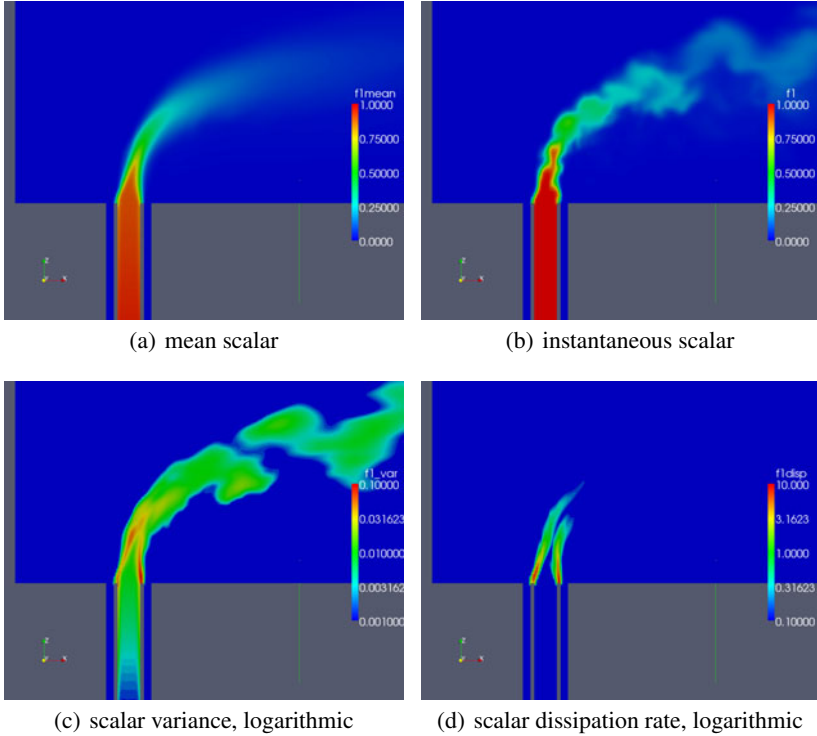
Fig. 2. Properties of scalar 1 in a coannular jet-in-crossflow, taken from DNS data. Main flow from left to right, coannular jet enters from the bottom, scalar value is set to unity for the central jet, and zero elsewhere

captured by the LES grid, hence the LES simulation show somewhat more 'blurred' gradients. However, this fact is a limitation of the grid used and not of the employed model.

The mechanical-to-scalar timescale ratio is shown in figure 6, with the associated mean scalar in figure 2(b). It can be observed that at the places where most of the mixing occurs (i.e. the gradients of the mean field), the timescale ratio takes values between zero and about unity. Thus in this case, assuming a mechanical-to-scalar timescale ratio of 2 will overestimate the mixing compared to the DNS data.

It has been previously shown that jpDDs can be used to accurately predict filtered reaction rates for turbulent ternary mixing in LES context. This work demonstrates that the second order moments can be computed with ample precision using a non-equilibrium approach for the scalar dissipation rate which assumes a fully developed spectrum for the turbulent and scalar energy. However, in the demonstrated test-case of a coannular jet-in-crossflow these conditions do not exist at the inflow of the jet. Further investigation is required to determine the influence of non-developed spectra on the prediction of the subgrid scale scalar variance and subgrid scale scalar covariance.

(a) DNS–Scalar 1

(b) DNS–Scalar 2

(c) LES–Scalar 1

(d) LES–Scalar 2
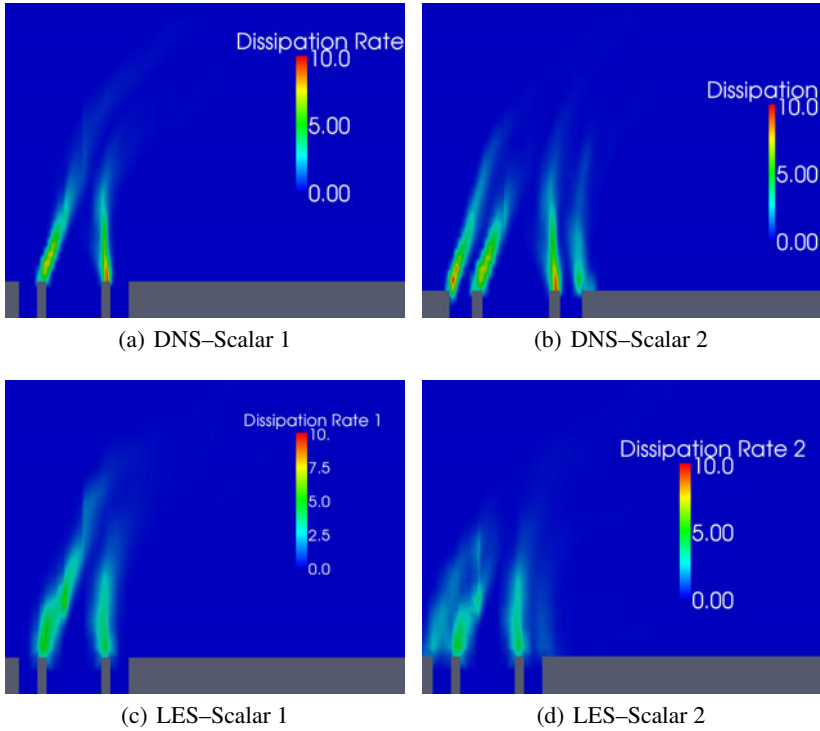
Fig. 3. Comparison of scalar dissipation rates between LES and DNS of a coannular jet-in-crossflow

(a) Scalar 1 – logarithmic

(b) Scalar 2 – logarithmic
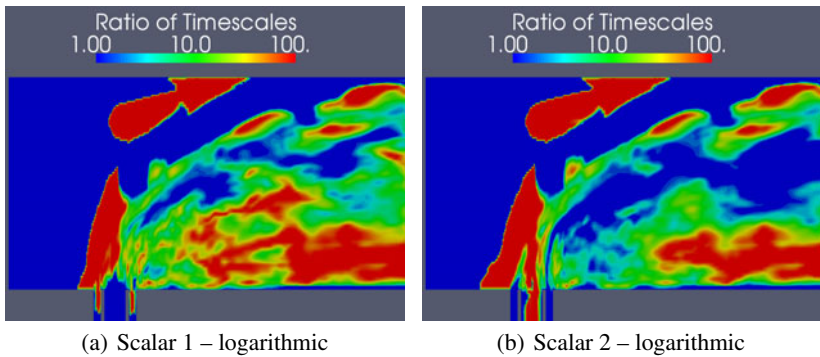
Fig. 4. Mechanical-to-scalar timescale ratio for a coannular jet-in-crossflow arrangement

Acknowledgments

References

[1] Brandt, M., Polifke, W., Flohr, P.: Approximation of joint PDFs by discrete distributions generated with Monte-Carlo methods. Combustion Theory and Modelling 10(4), 535–558 (2006)

[2] Brandt, M., Polifke, W., Ivancic, B., Flohr, P., Paikert, B.: Auto-ignition in a gas turbine burner at elevated temperature. In: Number 2003-GT-38224 in Proc. of ASME Turbo Expo 2003 Power for Land, Sea and Air, Atlanta, Georgia, USA, June 16-19, p. 11. ASME (2003)

[3] Colucci, Jaberi, Givi, Pope: Filtered density function for large eddy simulation of turbulent reacting flows. Phys. Fluids 10(2), 499–515 (1998)

[4] Eidson, T.M.: Numerical simulation of the turbulent rayleigh-benard problem using subgrid modelling. Journal of Fluid Mechanics 158, 245–268 (1985)

[5] Fischer, F.V., Muralidharan, B., Polifke, W.: Simulation of ternary mixing in a coannular jet in crossflow. JSME Int. J. of Fluid Science and Technology 4(2), 379–390 (2009)

[6] Fox, R.O.: Computational Models for Turbulent Reacting Flows, Cambridge (2003)

[7] Gutheil, E.: Multivariate PDF closure applied to oxidation of CO in a turbulent flow. In: Kuhl, A.L., Leyer, J.-C., Borisov, A.A., Sirignano, W.A. (eds.) Dynamics of Deflagrations and Reactive Systems. Progress in Astronautics and Aeronautics (1991)

[8] Gutheil, E., Bockhorn, H.: The effect of multi-dimensional PDFs on the turbulent reaction rate in turbulent reactive flows at moderate Damköhler numbers. Physico- Chemical Hydrodynamics 9(3/4), 525–535 (1987)

[9] Jaberi, F.A., Colucci, P.J.: Large Eddy Simulation of heat and mass transport in turbulent flows. Part 1: Velocity field. Int. J. Heat Mass Transf. 46(10), 1811–1825 (2003)

[10] Jaberi, F.A., Colucci, P.J.: Large Eddy Simulation of heat and mass transport in turbulent flows. Part 2: Scalar field. Int. J. Heat Mass Transf. 46(10), 1827–1840 (2003)

[11] Jimenez, C., Ducros, F., Cuenot, B., Bedat, B.: Subgrid scale variance and dissipation of a scalar field in large eddy simulations. Physics of Fluids 13, 1748–1754 (2001)

[12] Meyer, D.W., Jenny, P.: A mixing model for turbulent flows based on parameterized scalar profiles. Physics of Fluids 18(3), 035105 (2006)

[13] Pierce, C., Moin, P.: A dynamic model for subgrid-scale variance and dissipation rate of a conserved scalar. Physics of Fluids 10, 3041–3044 (1998)

[14] Smagorinsky, J.S.: General circulation experiments with the primitive equations, part I: The basic experiment. Monthly Weather Review 91, 99–152 (1963)

[15] Yoshizawa, A., Horiuti, K.: A Statistically-Derived Subgrid-Scale Kinetic Energy Model for the Large-Eddy Simulation of Turbulent Flows. J. Phys. Soc. Jpn. 54, 2834–2839 (1985)

An Efficient One-Shot Algorithm for Aerodynamic Shape Design

Emre Özkaya[1] and Nicolas R. Gauger[1,2]

[1] Humboldt University Berlin, Department of Mathematics,
Unter den Linden 6, 10099 Berlin, Germany
ozkaya@math.hu-berlin.de

[2] German Aerospace Center (DLR), Institute of Aerodynamics and Flow Technology,
Lilienthalplatz 7, 38108 Braunschweig, Germany
Nicolas.Gauger@dlr.de

Summary

In this paper we consider the shape optimization of a transonic airfoil whose aerodynamic properties are calculated by a structured Euler solver. The optimization strategy is based on a one-shot technique in which pseudo time-steps of the primal and the adjoint solver are iterated simultaneously with design corrections done on the airfoil geometry. The adjoint solver which calculates the necessary sensitivities is based on discrete adjoints and derived by using reverse mode of automatic differentiation (AD). A design example of drag minimization for an RAE2822 airfoil under transonic flight conditions and lift constraints is included.

1 Introduction

Computational Fluid Dynamics (CFD) is nowadays an essential part of aerodynamic design processes. During the past decades, CFD simulations evolved from basic inviscid potential solvers to Navier-Stokes solvers with complex turbulence and transition models. Along with the tremendous increase of computational power, CFD simulations, performed on meshes with several millions of grid points, are already state of the art. Mathematicians and engineers work on the goal to integrate efficiently CFD simulations into optimization strategies, even though derivative free optimization methods are preferred in industry, because of their simplicity. But derivative free optimization methods need several hundreds of function evaluations, even in the case of only a few design variables, and therefore they are inefficient, because in aerodynamics the simulation part is expensive in terms of computational costs. This is the reason why in detailed design one should prefer deterministic gradient-based optimization strategies. In our work, we focus on a special class of gradient-based methods, the so-called one-shot methods, where pseudo-time steps of the CFD solver and the design changes are performed simultaneously.

Let us consider the following optimization problem:

$$\min_{u} \; C_d(u, y) \;\; s.t. \; C_l(u, y) \geq C_{l,target} \;, \tag{1}$$

where C_d and C_l denote the drag and the lift coefficients respectively. $C_{l,target}$ is the target lift, i.e. the lift which is generated by the initial airfoil geometry. Furthermore, u is the vector of parameters defining the airfoil shape and y is the vector of the state variables. As the compressible Euler equations cannot be easily solved numerically due to the appearance of high nonlinearities, one usually uses quasi-unsteady formulations which are solved by explicit finite volume schemes stabilized by artificial dissipation and Runge-Kutta time integration. These pseudo timestepping schemes are most efficient in combination with geometric multigrid. That is to say, that our state equation $R(y, u) = 0$ is solved by a contractive fixed point iteration $y_{k+1} = G(y_k, u)$, i.e. $\|G_y\| \leq \rho < 1$. Here, k indicates the k-th pseudo time iterate.

A classical steepest descent algorithm (possibly with a penalty function for the lift constraint) would treat the problem (1) as follows:

Step 1: Iterate all through the pseudo timesteps ($k = 0, 1..$) in order to solve the flow equation, i.e. to get $R(u, y) = 0$.

Step 2: Calculate the gradient $\nabla_u C_d$ from the converged solution.

Step 3: Update the shape in the direction of the negative gradient with a suitable step size s, such that $u_{i+1} = u_i - s\nabla_u C_d$, in order to get a descent for C_d, and then return to Step 1 until convergence.

For the derivation of the one-shot approach, we treat the (fixed point iteration of the) state equation as an extra constraint. Therefore, we get:

$$\min_{u} \; C_d(u, y) \;\; s.t. \; y = G(y, u) \;\; and \;\; C_l(u, y) \geq C_{l,target} \tag{2}$$

For the moment we neglect the lift constraint and construct the Lagrangian function

$$L(u, y, \overline{y}) = C_d(y, u) + (G(y, u) - y)^T \overline{y} = N(y, \overline{y}, u) - y^T \overline{y} \tag{3}$$

for the optimization problem

$$\min_{u} \; C_d(u, y) \;\; s.t. \; y = G(y, u) \tag{4}$$

The lift constraint will be treated later on (by a so-called multiplier penalty method). The vector $\overline{y}$ denotes the Lagrangian multiplier and will become the adjoint state vector, if it fulfills the (necessary) optimality condition.

$$N(y, \overline{y}, u) := C_d(y, u) + G(y, u)^T \overline{y} \tag{5}$$

defines the so-called shifted Lagrangian.

If we derive the Karush-Kuhn-Tucker (KKT) or first order optimality conditions for the problem (4), a KKT point $(y^*, \overline{y}^*, u^*)$ has to satisfy $\nabla L(u, y, \overline{y}) = 0$, and therefore:

$$
\begin{aligned}
y^* &= G(y^*, u^*) \\
\overline{y}^* &= N_y(y^*, \overline{y}^*, u^*)^T = C_{dy}(y^*, u^*)^T + G_y(y^*, u^*)^T \overline{y}^* \\
0 &= N_u(y^*, \overline{y}^*, u^*)^T = C_{du}(y^*, u^*)^T + G_u(y^*, u^*)^T \overline{y}^*
\end{aligned}
\tag{6}
$$

Rather than first fully converging the primal state using

$$y_{k+1} = G(y_k, u) \rightarrow \text{primal feasibility at } y_* \tag{7}$$

and then fully converging the dual (or adjoint) state applying

$$\bar{y}_{k+1} = N_y(y, \bar{y}_k, u) \rightarrow \text{dual feasibility at } \bar{y}_* \tag{8}$$

before finally performing an "outer" optimization loop

$$u_{k+1} = u_k - B_k^{-1} N_u(y, \bar{y}, u_k) \rightarrow \text{optimality at } u_* , \tag{9}$$

we suggest a coupled iteration [4] of the form

$$\begin{aligned}
y_{k+1} &= G(y_k, u_k) \\
\bar{y}_{k+1} &= N_y(y_k, \bar{y}_k, u_k)^T \\
u_{k+1} &= u_k - B_k^{-1} N_u(y_k, \bar{y}_k, u_k)^T
\end{aligned} \tag{10}$$

For computing the optimization correction $\Delta u = u_{k+1} - u_k$, one has to choose a suitable preconditioner B_k.

Note, that these coupled iterations are done simultaneously for the updates of the state, adjoint and design vectors instead of first fully solving the state and adjoint equations and afterwards updating the design variables. As opposed to hierarchical methods like steepest descent or quasi-Newton, the convergence of the solvers and the object function optimality is reached simultaneously. Therefore, this method is called one-shot method.

In the next chapters, we will introduce first the one-shot algorithm in detail, then we will discuss several methods for the computation of derivative vectors needed for the one-shot method, and the implementation of lift constraints. Finally, results for the drag reduction problem under transonic flow conditions and lift constraints will be presented.

2   One-Shot Algorithm

The one-shot algorithm looks like the steepest descent algorithm that we have introduced in the first chapter. The only difference is, that the updates of the state, adjoint state and design vectors are done simultaneously. The algorithm can be summarized by these steps:

Step 0: Initialize the shape (u_0), the state (y_0) and the adjoint state ($\bar{y}_0 = 0$).
Step 1: Do one state update (one pseudo timestep) $y_{k+1} = G(y_k, u_k)$.
Step 2: Do one adjoint update $\bar{y}_{k+1} = N_y(y_k, \bar{y}_k, u_k)^T$.
Step 3: Compute the preconditioner (matrix) B_k.
Step 4: Update the shape to $u_{k+1} = u_k - B_k^{-1} N_u(y_k, \bar{y}_k, u_k)^T$.
Step 5: Increment k by one and return to Step 1 until convergence.

Now we discuss how to choose a set of suitable preconditioners B_k.

2.1   Preconditioner B

Griewank et al. [6] suggested the following preconditioner B in order to ensure the convergence of the coupled iterations (10):

$$B = \alpha G_u^T G_u + \beta N_{yu}^T N_{yu} + N_{uu} \,, \tag{11}$$

where α and β are positive reals. The precontioner B is defined such that it ensures descent of the following augmented Lagrangian function:

$$L^a(y, \overline{y}, u) = \frac{\alpha}{2} \left\| G(y, u) - y \right\|^2 + \frac{\beta}{2} \left\| N_y(y, \overline{y}, u) - \overline{y} \right\|^2 + N(y, \overline{y}, u) - \overline{y}^T y \quad (12)$$

This function is nothing but the Lagrangian with some added penalty terms for the so-called primal and dual feasibility (convergence of the solver and the adjoint solver) weighted by two positive real numbers α and β. The exact Hessian $\nabla_{uu} L^a$ of the augmented Lagrangian reads:

$$\nabla_{uu} L^a = \alpha G_u^T G_u + \beta N_{yu}^T N_{yu} + N_{uu} + \alpha (G - y)^T G_{uu} + \beta (N_y^T - \overline{y})^T \tag{13}$$

When primal and dual feasibility are satisfied, the last two terms are zero (since $G = y$ and $N_y^T = \overline{y}$). What remains is the expression (11) for B.

The parameters α and β are selected such that the "descent condition" is satisfied [6]. The descent condition says, that we have descent of L^a for the defined preconditioner B, if we choose α and β according to the following rule:

$$\beta = \frac{\theta}{2} \text{ and } \alpha = \frac{2\theta}{(1 - \rho)^2} \,, \tag{14}$$

where ρ is the contraction rate of the fixed point iteration:

$$\rho = \frac{\| G(y_k, u) - G(y_{k+1}, u) \|}{\| y_k - y_{k+1} \|} \tag{15}$$

Here, we might assume $\theta = \| N_{yy} \| = 1$. This assumption is tested and justified in [6] for contractive fixed point solvers based on elliptic PDEs. Since the computation of B derived from (11) involves matrix derivatives that may lead to expensive calculations, we aim to find an approximation by using BGFS updates [13] rather than computing it exact for each iteration. Since $B \approx \nabla_{uu} L^a$ we have

$$B \Delta u = \nabla_{uu} L^a(y, \overline{y}, u) \Delta u \approx \nabla_u L^a(y, \overline{y}, u + \Delta u) - \nabla_u L^a(y, \overline{y}, u) \tag{16}$$

Thus, we may employ the above approximation as a secant equation into the update of H (B^{-1}). Therefore, we may impose

$$H_{k+1} R_k = \Delta u_k, R_k := \nabla_u L^a(y_k, \overline{y}_k, u_k + \Delta u_k) - \nabla_u L^a(y_k, \overline{y}_k, u_k) \tag{17}$$

The secant equation (17) has a solution only if $R_k^T \Delta u_k > 0$ is satisfied. Therefore we check this condition in all iterates k and make a BFGS update whenever it is satisfied. Otherwise, we set simply B to identity matrix I. As far as the BFGS update is

concerned, there is no need to make an update of B and then inverse it; we can directly update the inverse of it by using the Sherman-Morrison-Woodburry formula (see [13])

$$H_{k+1} = (I - r_k \Delta u_k R_k^T) H_k (I - r_k R_k^T \Delta u_k) + r_k \Delta u_k \Delta u_k^T , \tag{18}$$

where $r_k = \frac{1}{r_k^T \Delta u_k}$. Now the only difficulty left for the implementation of the one-shot method is to calculate the term $\nabla_u L^a$. In the next section, we will introduce the computation of this term and other terms needed for the coupled iteration (10) by automatic differentiation (AD).

2.2 Computing Derivatives

There are three commonly used ways to calculate the gradient vectors for aerodynamic shape optimization applications.

The first and maybe the simplest way is to use the finite difference method (FD). This method is quite unsuitable for the one-shot method since we need gradient vectors with the size of the design space $(dim(u))$, which can be quite large. Other difficulties, such as tuning problems of the difference quotients, may be found in [2].

One can overcome these problems with the second approach, the continuous adjoint approach (see e.g. [11],[12],[3]), which has been already used in the context of one-shot methods [9], too. With the continuous adjoint approach one is independent of the dimension of the design vector with respect to numerical costs. But a problem with the continuous adjoint approach is, that on the discretized level, it is not necessarily consistent to the discretized primal state solver. Therefore, one needs more than one primal as well as adjoint update (see Step 1 and Step 2 of the one-shot algorithm) in order to get promising updates for the designs u in the one-shot method.

These inconsistency problems do not appear for the third approach, the automatic differentiation in reverse mode (see [7] for detailed information), which can be interpreted as a discrete adjoint approach. Here, on the discrete level, the gradients can be computed exactly at a computational cost that is independent of the size of the design space.

The automatic differentiation of a complete design chain for aerodynamic shape optimization is presented in [2]. In the following, we basically adopt exactly this (differentiated) design chain.

For the coupled iterations we need the gradient vectors N_u and N_y. The vector N_u is also needed for the computation of the preconditioner B. In order to calculate the preconditioner, we need $\nabla_u L^a$ as introduced in the previous chapter. It is given as:

$$\nabla_u L^a = \alpha \Delta y^T G_u + \beta \Delta \overline{y}^T N_{yu} + N_u \tag{19}$$

Note, that the terms N_u, N_y as well as all the terms of $\nabla_u L^a$ are either vectors or vector matrix products such that the reverse mode of AD might be applied in the same sense as discussed in [2]. For the term $\Delta \overline{y}^T N_{yu}$, second order adjoints [8] are used. The design chain has been differentiated with the AD tool ADOLC [15]. Since we use now the one-shot method, AD is directly applied to the problem, without using methods like the reverse accumulation approach, as discussed in [14] and introduced in [1].

2.3   Treatment of Lift Constraint

For the lift constraint $C_l \geq C_{l,target}$, a penalty function h can be defined:

$$h = C_{l,target} - C_l \tag{20}$$

The optimization problem is now written as:

$$\min_u \ \ C_d(u, y) + \lambda h \ \ s.t. \ y = G(y, u) \,, \tag{21}$$

where λ is the weighting coefficient for the penalty term h and can be updated in each iteration k as follows:

$$\lambda_{k+1} = \lambda_k(1 + ch) \tag{22}$$

The constant c should be adjusted according to the optimization problem. For the starting value of λ a suitable value is: $\lambda_0 = \frac{\|\nabla C_d\|}{\|\nabla h\|}$.

Whenever $C_l < C_{l,target}$, the penalty term h will be greater than zero causing an increase of the weighting coefficient λ. A larger value of λ will favor airfoil shapes which have larger lift values than the current one. For the steps in which C_l might be larger than $C_{l,target}$, h will be negative and λ will decrease, signaling the case that such a favoring of the lift is no more necessary. This method is called multiplier penalty method and details may be found in [5].

3   Numerical Results

The numerical test case is the drag minimization for an RAE2822 airfoil under transonic flight conditions. The primal CFD solver is TAUij from DLR(see [10]). The chosen Mach number is 0.73 and the angle of attack is set to be $2°$. The shape parameterization is based on camberline thickness decomposition. The thickness distribution is kept fixed and the camberline is parameterized by 40 Hicks-Henne functions. The computational grid has 161x33 grid points and we use three multigrid levels in order to accelerate the convergence. The applied optimization strategy is the one-shot method introduced in the previous chapter, while the lift constraint is tackled by the multiplier penalty method.

In Figure 1, the pressure distributions and the shapes of the optimal and the initial geometries are shown. The strong shock, typical for the RAE2822 airfoil under transonic flight conditions, is eliminated for the optimal shape. As can be seen in figure 2, the drag coefficient is reduced by more than 40%, while the lift constraint is satisfied. The primal residual $\|G(y_k, u_k) - y_k\|$ as well as the dual (adjoint) residual $\left\|N_y(y_k, u_k, \overline{y}_k)^T - \overline{y}_k\right\|$ are also plotted over the iterations k. The drag and lift coefficients show good convergence. Since the airfoil shape changes in each iteration, the behavior of the primal and dual residuals show oscillatory behavior but still satisfactory convergence behavior.

If we consider the fact that approximately 500 iterations are needed for a single simulation of the initial RAE2822 airfoil, the one-shot method needs just six times more iterations in order to find the optimal shape. In other words: With the one-shot approach, one can perform an optimization for the cost of six simulations. If we would apply a classical steepest descent method as optimization strategy, we would end up with much higher computational costs (see [2]).
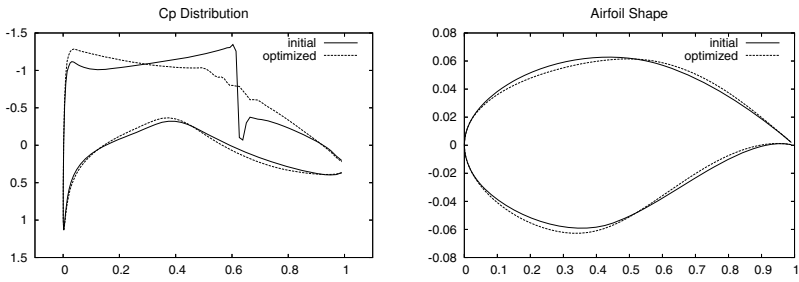
Fig. 1. Pressure distributions (left) and shapes (right) of the initial RAE2822 airfoil and the optimized shape
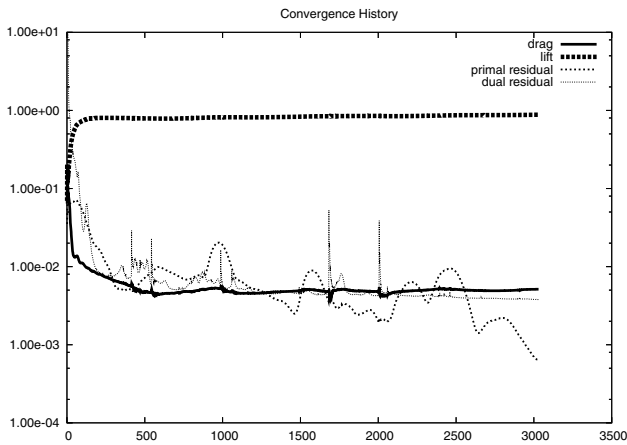
Fig. 2. Optimization history of C_d, C_l and the residuals of the primal and adjoint solvers

4   Conclusion

A one-shot methodology for constrained aerodynamic shape optimization, which makes use of automatic differentiation, has been presented in this paper. Furthermore, the related specific implementation issues have been discussed. It could be shown by numerical tests, that by the use of the presented one-shot methodology, one can gain a lot with respect to computational costs compared to hierarchical methods like steepest descent.

References

[1] Christianson, B.: Reverse accumulation and attractive fixed points. Optimization Methods and Software 3, 311–326 (1994)
[2] Gauger, N., Walther, A., Moldenhauer, C., Widhalm, M.: Automatic differentiation of an entire design chain for aerodynamic shape optimization. In: Notes on Numerical Fluid Mechanics and Multidisciplinary Design (NNFM), vol. 96, pp. 454–461 (2006)

[3] Gauger, N., Brezillon, J.: The continuous adjoint approach in aerodynamic shape optimization. In: MEGAFLOW-Numerical Flow Simulation for Aircraft Design, Notes on Numerical Fluid Mechanics and Multidisciplinary Design. NNFM, vol. 89, pp. 181–195. Springer, Heidelberg (2005)

[4] Gauger, N., Griewank, A., Riehme, J.: Extension of fixed point PDE solvers for optimal design by single-step one-shot method. European Journal of Computational Mechanics (REMN) 17, 87–102 (2008)

[5] Geiger, K., Kanzow, C.: Theorie und Numerik restringierter Optimierungsaufgaben. Springer, Heidelberg (2002)

[6] Griewank, A., Hamdi, A.: Properties of an augmented Lagrangian for design optimization. DFG SPP 1253 Preprints: SPP1253-11-01 (2008)

[7] Griewank, A.: Evaluating Derivatives: Principles and techniques of Algorithmic Differentiation. SIAM, Philadelphia (2000)

[8] Hamdi, A., Griewank, A.: Reduced quasi-Newton method for simultaneous design and optimization. DFG SPP 1253 Preprints: SPP1253-11-02 (2008)

[9] Hazra, S.B., Schulz, V., Brezillon, J., Gauger, N.: Aerodynamic shape optimization using simultaneous pseudo-time stepping. Journal of Computational Physics 204(1), 46–64 (2005)

[10] Heinrich, R.: Implementation and usage of structured algorithms within an unstructured CFD code. In: Notes on Numerical Fluid Mechanics and Multidisciplinary Design (NNFM), vol. 92 (2006)

[11] Jameson, A.: Aerodynamic design via control theory. Journal of Scientific Computing 3, 233–260 (1988)

[12] Mohammadi, B., Pironneau, O.: Applied shape optimization for fluids. Oxford Univ. Press, Oxford (2002)

[13] Nocedal, J., Wright, S.J.: Numerical Optimization. Springer Series in Operational Research (1999)

[14] Schlenkrich, S., Walther, A., Gauger, N., Heinrich, R.: Differentiating fixed point iterations with ADOL-C: Gradient calculation for fluid dynamics. In: Proceedings of Third International Conference on High Performance Scientific Computing Hanoi, March 6-10, pp. 489–508 (2006)

[15] Walther, A., Kowarz, A., Griewank, A.: ADOL-C: A package for the automatic differentiation of algorithms written in C/C++ (2008)

Application of a New Roughness Extension for $k - \omega$ Turbulence Models

Bernhard Eisfeld[1], Tobias Knopp[2], and Javier Bartolome Calvo[1]

[1] Institute of Aerodynamics and Flow Technology, German Aerospace Center (DLR),
Lilienthalplatz 7, D-38108 Braunschweig, Germany
bernhard.eisfeld@dlr.de, javier.bartolomecalvo@dlr.de
[2] Institute of Aerodynamics and Flow Technology, German Aerospace Center (DLR),
Bunsenstraße 10, D-37073 Göttingen, Germany
tobias.knopp@dlr.de

Summary

The roughness extension of Knopp, Eisfeld and Calvo (KEC) [4] for $k - \omega$ type turbulence models has been applied to the flow through rough pipes, over a flat plate and around the NACA 65_2-215 airfoil with a rough surface. The results are compared to predictions using the boundary condition originally devised by Wilcox [11] for rough surfaces, and to predictions with the Spalart-Allmaras model with the Boeing roughness extension by Aupoix and Spalart (ASB) [2]. Good agreement with experiments has been achieved with respect to the influence of the roughness on the velocity profile, the skin friction coefficient and the loss in lift.

1 Introduction

The influence of wall roughness on the characteristics of turbulent flow is of technical interest in the field of aircraft icing or turbine blade erosion. The fundamental experimental studies of Nikuradse [8] with densely glued sand grains on the walls of pipes have revealed three different regimes, depending on the roughness Reynolds number $k_r^+ = k_r u_\tau / \nu$, where k_r is the (equivalent) sand grain roughness, originally defined by the sieve size, u_τ is the friction velocity and ν the kinematic viscosity of the fluid.

In general the logarithmic law of the wall is found to hold also on rough surfaces which can be written under the following forms

$$\frac{U}{u_\tau} = \frac{1}{\kappa} \ln\left(\frac{y u_\tau}{\nu}\right) + C \tag{1}$$

$$= \frac{1}{\kappa} \ln\left(\frac{y}{k_r}\right) + \frac{1}{\kappa} \ln k_r^+ + C = \frac{1}{\kappa} \ln\left(\frac{y}{k_r}\right) + B, \tag{2}$$

where U is the velocity, y the wall distance and $\kappa \approx 0.41$ the von Kármán constant.

In the hydrodynamically smooth regime at values below $k_r^+ \approx 5$ the roughness elements are completely embedded into the viscous sublayer, so that they do not have

any influence on the flow, i. e. the logarithmic law of the wall holds in its original form (1) with $C \approx 5.1$.

In the transitionally rough regime, ranging from $k_r^+ \approx 5$ to $k_r^+ \approx 70$, an increasing part of the roughness elements extends into the buffer and log-layer, producing extra drag. In this regime B in Eq. (2) is a function of k_r^+ and the geometry of the roughness elements [5] which in case of sand grain roughness considered here exhibits a maximum around $k_r^+ \approx 10$.

In the fully rough regime above $k_r^+ \approx 70$ the viscous sublayer thickness is neglibible with respect to the height of the roughness elements. Under these conditions $B \approx 8.5$ becomes constant.

Note that despite of the maximum in B the velocity profile in the log-layer is monotonically shifted towards lower values and that the wall friction is monotonically increasing with k_r^+. These two effects have to be covered simultaneously by modifications of any turbulence model to account for surface roughness.

2   Roughness Modeling

Various approaches have been published to account for the effects of wall roughness, mainly by altering the boundary conditions of the turbulence equations. E. g. for his $k-\omega$ model Wilcox [11] prescribes ω at the wall depending on k_r^+, while keeping $k = 0$ at the wall. In contrast Aupoix and Spalart [2] derive a hydrodynamic roughness length d_0 by which the wall is effectively shifted. From Eq. (2) they obtain $d_0 = k_r \exp(-B\kappa)$ with $B = 8.5$, assuming fully rough conditions. In particular, they conclude on a non-zero wall value of the transported quantity $\widetilde{\nu}$ of the Spalart-Allmaras model [10], since for fully rough surfaces the model reduces to the modified mixing length relation $\widetilde{\nu} = \kappa u_\tau (y + d_0)$ down to the wall.

Only recently it has been found out that enforcing $k = 0$ at rough walls shifts the region, where the k-gradient is significant and has to be resolved, closer to the wall [4]. For this reason the Wilcox boundary condition requires an extremely fine near-wall grid for obtaining grid-converged solutions with roughness, whereas the Aupoix-Spalart approach can be used on meshes designed for smooth walls, see Section 3. Furthermore the Wilcox boundary condition for rough walls has been observed to erroneously trigger the eddy viscosity limitation when applied to Menter's SST model [3], thus deteriorating the predictions.

For these reasons the concept of the hydrodynamic roughness length has been transferred to $k - \omega$ type models [4]. Beyond $k_r^+ = 90$ the standard log-layer solution at a wall distance $y = d_0$ is set as boundary condition for k and ω, whereas for smaller values of k_r^+ this boundary condition is suitably modified towards the smooth wall boundary condition, where special care has been taken, in order to yield the monotoneous velocity shift and shear stress increase with k_r^+ as described in the Introduction. The boundary condition at rough walls devised by Knopp et al. [4] reads

$$k_w = \frac{u_\tau^2}{\sqrt{\beta_k}} \; \min\left(1, \frac{k_r^+}{90}\right), \tag{3}$$

$$\omega_w = \frac{u_\tau}{\sqrt{\beta_k}\kappa d_0 \phi_{r2}}, \tag{4}$$

where $\beta_k = 0.09$ and

$$\phi_{r2} = \min\left[1, \left(\frac{k_r^+}{30}\right)^{2/3}\right] \min\left[1, \left(\frac{k_r^+}{45}\right)^{1/4}\right] \min\left[1, \left(\frac{k_r^+}{60}\right)^{1/4}\right]. \tag{5}$$

Note that ω_w is limited by the corresponding smooth wall value suggested by Menter [7]. This boundary condition (KEC-extension) is applied in the following to a couple of test cases and compared to predictions with the Spalart-Allmaras model (SAO) with the ASB-extension [2].

3   Results

In the following simulation results obtained with the DLR TAU code [9] are presented in comparison to experiments. The DLR TAU code is based on a Finite Volume method, using central space discretisation and artificial dissipation of second order accuracy. (Time) integration is carried out by an implicit LUSGS scheme accelerated by multigrid.

3.1   Flow through a Rough Pipe (Nikuradse [8])

Nikuradse [8] carried out his fundamental experiments in pipes with densely glued sand grains at the walls, where the roughness with respect to the pipe radius R has been varied by the sieve size for the sand. A subset of these experiments has been simulated, where the conditions have been chosen in such a way that the whole range from almost hydraulically smooth to fully rough is covered, as one can see from Table 1.

Fig. 1 shows the velocity profiles obtained with the Wilcox $k - \omega$ [11] and the Menter SST model [7], using the KEC-extension [4], together with the experiments by Nikuradse [8]. Additionally the results for the SAO model [10] with the ASB-extension [2] are shown for comparison. As one can see, the predictions with the two-equation models with the KEC-extension are in good agreement with the experiments as well

Table 1. Simulated experimental conditions for rough pipes [8].

R/k_r	Re_1 (low)	k_r^+	Re_2 (high)	k_r^+
252	51000	5.34	624000	66.98
60	–	–	677000	369.83
30.6	43000	52.48	638000	805.38
15	43000	124.45	–	–
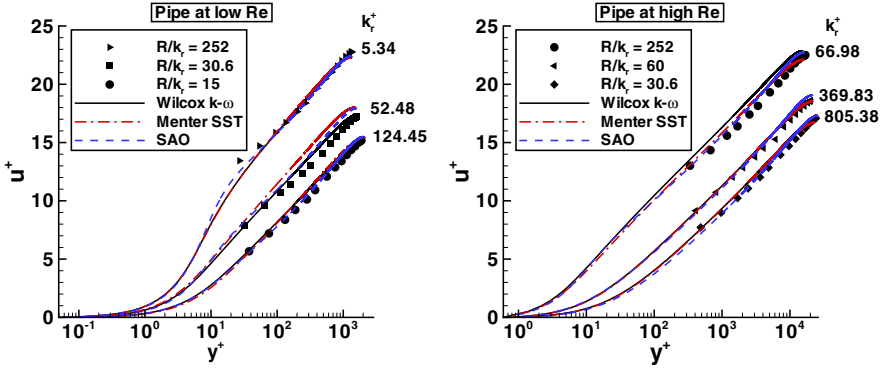
Fig. 1. Flow through a rough pipe at low (left) and high Reynolds numbers (right) for varying sand roughness. Comparison of predictions with experiments by Nikuradse [8].

as with the predictions of the SAO model. Larger discrepancies occur only in the transitionally rough regime, i. e. for $k_r^+ = 52.48$ and $k_r^+ = 66.98$, where the KEC-extension is modelled by an empirical modification of the fully rough conditions, compromising between the predicted increase in wall shear stress and the shift of the velocity profile. This may explain part of the deviations. Nevertheless, the general trend how the velocity profile is shifted by the wall roughness in the Nikuradse experiments [8] is predicted very well, which is considered a minimum requirement to any roughness modification of turbulence models.

3.2   Flow over a Rough Flat Plate (Ligrani and Moffat [5])

Ligrani and Moffat [5] conducted experiments on a flat plate with roughness elements of equivalent sand grain roughness $k_r = 0.79$mm. By varying the free stream velocity U_∞ they obtained different conditions along the surface, particularly covering the transitionally rough regime from $k_r^+ = 20.5$ to $k_r^+ = 63$.

The experiments of Ligrani and Moffat [5] have been simulated on a fine cartesian grid with 50 points ahead the leading edge, 90 points on the flat plate and 250 points normal to the wall. The near wall resolution has been manually adapted to the different computations, ensuring grid independent solutions. It appeared that, in order to ensure grid converged solutions, the Wilcox $k - \omega$ model with the original boundary condition for rough surfaces by Wilcox [11] required a wall distance of the wall nearest grid points, y_1, corresponding to $y_1^+ = y_1 u_\tau / \nu = 0.01$ compared to $y_1^+ = 0.3$ for the Wilcox $k - \omega$ model with the KEC-extension [4] and the SAO model with the ASB-extension [2].

Fig. 2 shows the skin friction coefficient along the flat plate for different onflow velocities and a constant equivalent sandgrain roughness of $k_r = 0.79$mm obtained with the different turbulence models and roughness extensions compared to the experiments by Ligrani and Moffat [5]. As one can see, the Wilcox $k - \omega$ model with the Wilcox roughness boundary condition yields considerably higher friction factors C_f than the SAO with the ASB-extension [2] and the Wilcox $k - \omega$ model with the
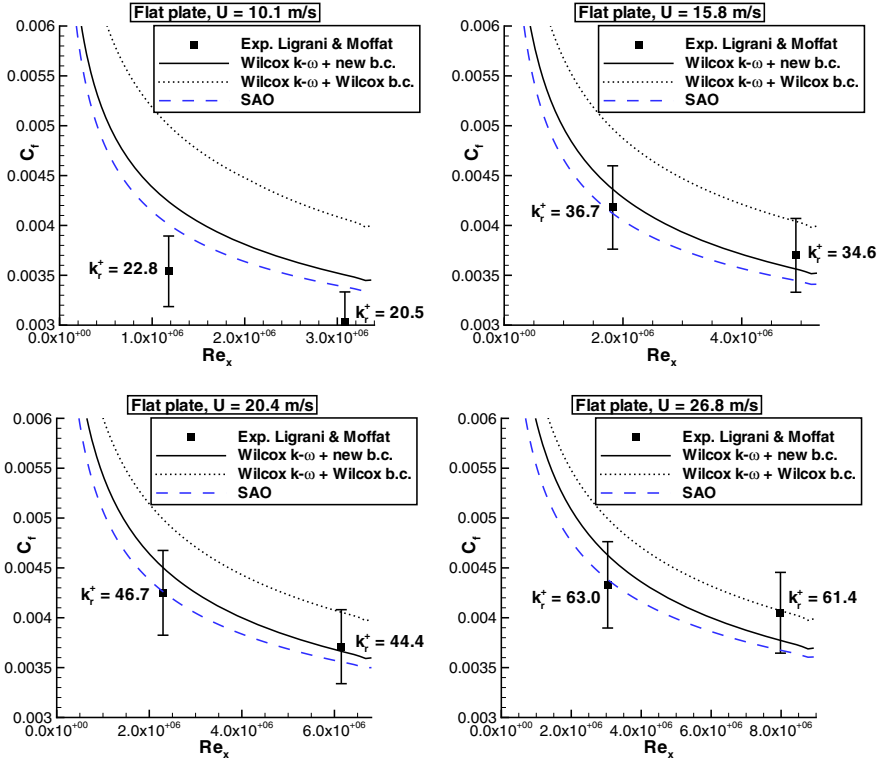
Fig. 2. Flow over a rough flat plate with $k_r = 0.79$mm at different onflow velocities. Comparison of skin friction predictions with experiments by Ligrani and Moffat [5].

KEC-extension [4]. The latter are not only in fair agreement with each other, but also with the majority of the experiments, considering the experimental uncertainty of $\pm 10\%$ [5]. Larger deviations occur only for $U = 10.1$m/s which might be due to the empirical nature of the modelling in the transitionally rough regime. Thus the KEC-extension [4] is considered clearly an improvement of the roughness treatment for $k - \omega$ type models.

3.3 Flow over a Rough Airfoil (Ljungström [6])

The flow over a NACA 65_2-A215 airfoil with different roughness heights has been investigated experimentally by Ljungström [6] at a Mach number of $Ma = 0.182$ and a Reynolds number of $Re = 2.6 \cdot 10^6$ based on the chord length c. However, comparing with the classical experiments by Abbott and von Doenhoff [1] for the closely related NACA 65_2-215 airfoil with smooth surface, Hellsten [3] observed a systematically lower lift in the Ljungström measurements that he considered being caused by a geometrical imperfection due to a retracted flap. Fig. 3 shows the experiments together with simulations for the NACA 65_2-215 airfoil. As one can see, in particular
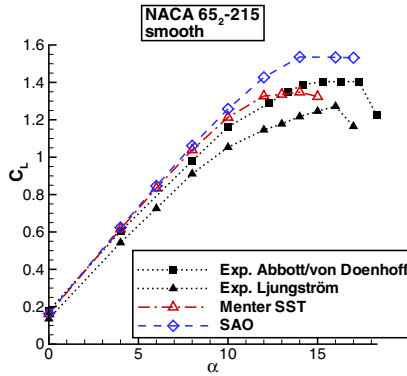
Fig. 3. NACA 65_2-215 airfoil, $Ma = 0.182$, $Re = 2.6 \cdot 10^6$. Lift curves for smooth airfoil. Experiments by Abbott and von Doenhoff [1] and by Ljungström [6].

the result for the Menter SST model is in fairly good agreement with the Abbott and von Doenhoff experiment, except that the lift breakdown occurs at a lower incidence.

In the following the computations have been repeated with two different roughness heights of $k_r/c = 1.54 \cdot 10^{-4}$ and $k_r/c = 3.08 \cdot 10^{-4}$, both corresponding to the most difficult transitionally rough regime [4]. In the experiment the roughness covered the complete suction side of the airfoil and was assumed to extend until 15% chord on the pressure side, following Hellsten [3]. The hybrid grid consisted of 29361 nodes with 512 of them on the surface and 46 layers of quadrilateral cells around the airfoil. It has been checked that for the largest incidence the wall distance of the wall nearest grid
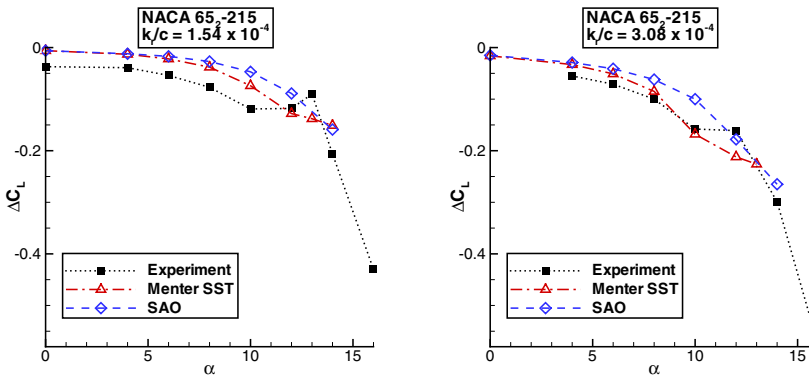
Fig. 4. NACA 65_2-215 airfoil, $Ma = 0.182$, $Re = 2.6 \cdot 10^6$. Difference in lift coefficient with respect to the smooth airfoil for $k_r/c = 1.54 \cdot 10^{-4}$ (left) and $k_r/c = 3.08 \cdot 10^{-4}$ (right). Experiments by Ljungström [6] are also shown.

points, y_1, corresponded to a value of $y_1^+ = y_1 u_\tau / \nu < 0.54$ at the suction peak and to $y_1^+ \approx 0.25$ on the remaining airfoil surface. Thus the results should be fairly grid independent.

In order to remove the uncertainties with respect to the experiments, only the decrease in lift with respect to the smooth airfoil, $\Delta C_L = C_L^{(\text{rough})} - C_L^{(\text{smooth})}$, is considered. As one can see from Fig. 4, both the SAO model with ASB-extension as well as the Menter SST model with the KEC-extension [4] predict the increasing loss in lift with increasing α in qualitative agreement with the experiment. Nevertheless the Menter SST predictions are generally closer to the experiments. In particular, in contrast to the SAO predictions, the Menter SST results indicate the characteristic change of sign in the curvature of $\Delta C_L(\alpha)$ in the experiments, which is caused by a shift of maximum lift towards lower incidences with increasing roughness. This probably reflects the superiority of the underlying Menter SST model for flows with separation at high incidence angles and underlines the necessity for a suitable extension of $k - \omega$ type turbulence models for the flow over rough surfaces. In particular it should be noted that the KEC-extension [4] does not require any modification of Menter's SST model in contrast to the findings of Hellsten [3], using the Wilcox roughness boundary condition.

4 Conclusion

The roughness extension by Knopp, Eisfeld and Calvo (KEC) [4] for $k - \omega$ type turbulence models has been applied to the flow through rough pipes, over a rough flat plate and around a rough airfoil. The focus of the present work is on the comparison between the new roughness extension, the roughness modification by Wilcox [11] for k-ω models and the Spalart-Allmaras model with Boeing roughness extension by Aupoix and Spalart (ASB) [2] in terms of numerical resolution requirements and predictive quality. The latter aspect was considered only in parts in [4].

Regarding the flow through rough pipes the influence of the roughness on the velocity profiles has been studied. Good agreement with the classical experiments by Nikuradse [8] has been achieved for roughness Reynolds numbers in the range $5.34 \leq k_r^+ \leq 805.38$, thus covering the whole regime from almost hydrodynamically smooth to fully rough conditions.

In case of the flow over a rough flat plate the influence of surface roughness on the skin friction has been investigated in comparison with the experiments by Ligrani and Moffat [5] for transitionally rough conditions ($20.5 \leq k_r^+ \leq 63.0$). For transitional roughness values, the KEC-extension [4] remedies the overprediction of skin friction observed for the roughness modification by Wilcox [11], leading to a better agreement with the predictions of the Spalart-Allmaras model with the ASB-extension [2] and the experiments, when accounting for the experimental uncertainty. In particular it has been found out that the KEC-extension [4] and the ASB-extension [2] require a significantly lower near wall resolution for obtaining grid independent solutions than the Wilcox roughness boundary condition [11], making the latter rather impractical for complex technical applications.

Finally, the influence of roughness on the lift curve until stall has been studied for the flow around the NACA 65_2-215 airfoil with smooth and rough surfaces with two

different roughness heights. In this case the capability of the underlying turbulence model to predict separation is of major importance. As it appears, the Menter SST model with the KEC-extension [4] predicts the loss in lift with respect to the smooth airfoil in better agreement with the measurements by Ljungström [6] than the Spalart-Allmaras model with the ASB-extension [2].

Acknowledgements

References

[1] Abbott, I.H., von Doenhoff, A.S.: Theory of Wing Sections. Dover Publications, New York (1959)

[2] Aupoix, B., Spalart, P.R.: Extensions of the Spalart-Allmaras model to account for wall roughness. International Journal of Heat and Fluid Flow 24, 454–462 (2003)

[3] Hellsten, A., Laine, S.: Extension of the $k\omega$-SST turbulence models for flows over rough surfaces. AIAA-Paper 97-3577 (1997)

[4] Knopp, T., Eisfeld, B., Calvo, J.B.: A new extension for $k-\omega$ turbulence models to account for wall roughness. International Journal of Heat and Fluid Flow 30, 54–65 (2009)

[5] Ligrani, P.M., Moffat, R.J.: Structure of transitionally rough and fully rough turbulent boundary layers. Journal of Fluid Mechanics 162, 69–98 (1986)

[6] Ljungström, B.: Wind tunnel investigations of simulatied hoar frost on a 2-dimensional wing section with and without high lift devices. FFA, Report AU-902 (1972)

[7] Menter, F.R.: Two-Equation Eddy-Viscosity Turbulence Models for Engineering Applications. AIAA Journal 32, 1598–1605 (1994)

[8] Nikuradse, J.: Strömungsgesetze in rauhen Rohren. VDI-Forschungsheft 361 (1933)

[9] Schwamborn, D., Gerhold, T., Heinrich, R.: The DLR TAU-Code: Recent Applications in Research and Industry. In: Wesseling, P., Oñate, P.J. (eds.) Proceedings of ECCOMAS (2006)

[10] Spalart, P.R., Allmaras, S.R.: A One-Equation Turbulence Model for Aerodynamic Flows. AIAA-Paper, 92-439 (1992)

[11] Wilcox, D.C.: Reassessment of the Scale Determining Equation for Advanced Turbulence Models. AIAA Journal 26, 1299–1310 (1988)

Improved Wall Functions Based on the 1D Boundary Layer Equations for Flows with Significant Pressure Gradient

Tobias Knopp

German Aerospace Center (DLR), Dept. $C^2A^2S^2E$,
Bunsenstr. 10, 37073 Göttingen, Germany
Tobias.Knopp@dlr.de

Summary

This paper presents an improved wall function method for unstructured flow solvers using the DLR TAU Code based on the one-dimensional boundary-layer equations for wall-parallel velocity, including pressure gradient term and convective term, and turbulence quantities in wall normal direction. For each wall node, this system of equations is integrated numerically on an embedded subgrid between wall node and first node above the wall. The method is verified for a flat plate turbulent boundary layer flow at zero pressure gradient. Then the method is applied to the flow in a diffusor at adverse pressure gradient without separation to assess different levels of approximation of the boundary layer model for wall-parallel velocity and to demonstrate the improvement of results compared to universal wall-functions.

1 Introduction

Statistical turbulence models based on the Reynolds averaged Navier-Stokes (RANS) equations together with the Boussinesq hypothesis and a one- or two-equation model of Spalart-Allmaras (SA) and k-ω type for computing the eddy-viscosity are a standard tool for aerodynamic research and design. Integration of these equations down to the wall on a so-called low-Re grid requires a spacing in universal units of $y^+(1) = 1$ for the first node above the wall $y(1)$ and several grid nodes in the viscous sublayer, leading to a large number of nodes for resolving the boundary layer, increased numerical stiffness and therefore slower convergence of the solver. Moreover, mesh generation becomes more costly, in particular for complex geometries.

Recent wall-functions [3, 4] are based on the turbulence model specific universal near-wall solution of SA and k-ω model in zero-pressure gradient (ZPG) boundary layer flow. These wall-functions are called adaptive, as for flows with negligible pressure gradient, the solution is (almost) independent of $y^+(1)$, provided $y(1)$ is in the log-layer or below. For transonic flows at high Reynolds number and at moderate angle of attack with separation and reattachment, the solution using these wall-functions is in very

close agreement with the low-Re solution. The crucial parameter that governs the range of validity of universal wall-functions was shown to be the pressure gradient parameter $p^+ = \nu/(\rho u_\tau^3)\mathrm{d}p/\mathrm{d}x$ with streamwise pressure gradient $\mathrm{d}p/\mathrm{d}x$, viscosity ν, density ρ and friction velocity u_τ. The deviation of the near-wall RANS solution increases with p^+ and p^+ determines the maximum value for $y^+(1)$ for which the universal solution is reasonable. For cruise flight conditions, due to high Reynolds number and small angle of attack, p^+ is not too large and on meshes with $y^+(1) = 60$ very good agreement with the low-Re solution can be obtained. But for cases at small Reynolds number and large angle of attack (e.g., high-lift configurations), p^+ takes values of $\mathcal{O}(10^{-1})$ causing the near-wall RANS solution to deviate significantly from their universal behaviour and $y^+(1) \lesssim 10$ is the restriction.

Since noticeable acceleration of the flow solver and mesh generation is obtained only for $y + (1) \gtrsim 50$, it is worth to consider improved wall-function methods that admit such large $y^+(1)$-values even for flows with large pressure gradient parameter. The aim is to design a method based only on the one-dimensional boundary layer (1d-BL) equation in wall-normal direction on an embedded sub-grid for wall-parallel velocity and turbulence quantities. This allows, in a later step, to use the method as near-wall model for LES, since it relates locally the wall-shear stress to the instantaneous velocity at the matching node. Since the method should be applicable directly for unstructured methods, an approach based on the so-called thin-boundary-layer equation (TBLE), see e.g. [1], is not used.

For the design of a new wall-function method, first a term by term investigation of the boudary layer equation for wall-parallel momentum is presented, showing that, in the log-layer, the convective term becomes of similar magnitude as the pressure gradient term. Therefore this term needs to be considered also in the improved wall-function model. The second step is to develop an approximation for the convective term $u\mathrm{d}u/\mathrm{d}x$ which is not available for a one-dimensional (in wall-normal direction) method. The importance of the convective term will be confirmed by numerical results for adverse pressure gradient flow in a diffuser. A method based only on the pressure gradient term allows for an analytical modification of universal wall-functions [6], but shows a clear modelling error for large values for $y^+(1)$.

2   Study of Dominant Terms in the Boundary Layer Equation

The first step in the design of an improved wall-function model is an order of magnitude analysis of the different terms in the boundary layer equation for the wall-parallel velocity component u

$$-\frac{\partial}{\partial y}\left((\nu + \nu_{\mathrm{t}})\frac{\partial u}{\partial y}\right) = -\frac{1}{\rho}\frac{\partial p}{\partial x} - u\frac{\partial u}{\partial x} - v\frac{\partial u}{\partial y} \qquad (1)$$

in a wall-fitted coordinate system with x denoting streamwise and y the wall-normal direction, v is the wall-normal component of velocity. Instead of the classical approach for estimates, here we investigate these terms from RANS solutions.

We consider the solution for the SA model with Edwards modification (SA-E) for the flow over a flat plate of length $L = 8\mathrm{m}$ with farfield data $u_\infty = 78\mathrm{m/s}$, $\nu_\infty = 1.5\times$
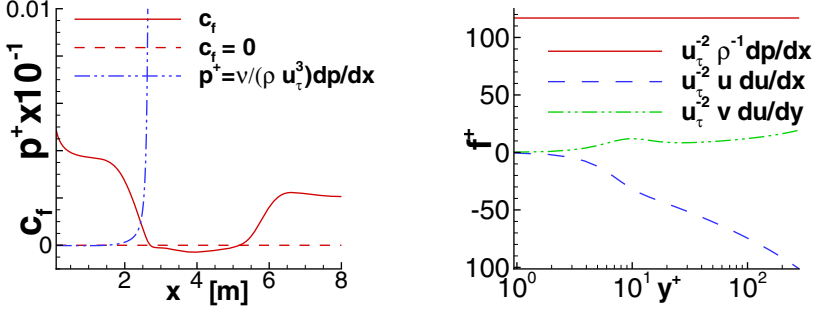
Fig. 1. Testcase APG flow by [3]. Left: Plot of c_f and p^+. Right: Profiles of the different right hand side terms in the boundary layer equation (2) at $x = 2.50$m

10^{-5}m^{2}s^{-1}. An adverse pressure gradient (APG) is imposed by suction and blowing at a distance $y = 0.5$m above the wall, see [3]. For an illustration, Fig. 1 (left) shows c_f, hence separation and reattachment point, and p^+. At $x = 2.5$m, where $p^+ = 0.015$ is still moderate, at a certain distance before separation at $x = 2.71$m the right hand side terms of (1) normalised by u_τ^2 are plotted as a function of wall-distance in plus units $y^+ = yu_\tau/\nu$, see Fig. 1 (right). As predicted by classical theory, pressure gradient $\partial p/\partial x$ is constant in wall-normal direction. The term $u\partial u/\partial x$ becomes of the same size as the pressure gradient term in the log-layer. The term $v\partial u/\partial y$ is significantly smaller than the other two terms, also very close before the separation point and in the region of separated flow. For the SST k-ω model a similar result is obtained.

We conclude that an improved wall-function model based on the dominant terms of (1) can neglegt the term $v\partial u/\partial y$ but needs to incorporate $u\partial u/\partial x$.

3   Improved Wall-Function Modelling

Similar to standard wall-function methods, the no-slip condition at the wall of the global problem for the RANS equations is replaced by prescribing the wall-tangential stresses, i.e., the wall-shear stress τ_w, and imposing no-penetration condition $\boldsymbol{u}\cdot\boldsymbol{n} = 0$. For each wall node $\boldsymbol{x}(0)$, τ_w is computed from the wall-function model, i.e. a non-linear coupled system of diffusion-reaction problems in wall-normal direction to be solved between $\boldsymbol{x}(0)$ and $\boldsymbol{x}(1)$, being the corresponding first node above the wall at wall distance y_δ, see Fig. 2 (right). Then, e.g., for the SA-E type model (see [2] for a full description), the 1D-boundary layer problem to be solved is

$$-\frac{\mathrm{d}}{\mathrm{d}y}\left((\nu + \nu_t)\frac{\mathrm{d}u}{\mathrm{d}y}\right) = -\frac{1}{\rho}\frac{\mathrm{d}p}{\mathrm{d}x} - u\frac{\mathrm{d}u}{\mathrm{d}x} \tag{2}$$

$$-\frac{\mathrm{d}}{\mathrm{d}y}\left(\frac{\nu + \tilde{\nu}}{\sigma}\frac{\mathrm{d}\tilde{\nu}}{\mathrm{d}y}\right) = \frac{c_{b2}}{\sigma}\left(\frac{\mathrm{d}\tilde{\nu}}{\mathrm{d}y}\right)^2 + c_{b1}\rho\tilde{S}\tilde{\nu} - c_{w1}f_w\left(\frac{\tilde{\nu}}{y}\right)^2 \tag{3}$$

$$u = 0\,, \quad \tilde{\nu} = 0 \quad \text{for } y = 0\,, \qquad u = u_\delta\,, \quad \tilde{\nu} = \tilde{\nu}_\delta \quad \text{for } y = y_\delta\,. \tag{4}$$
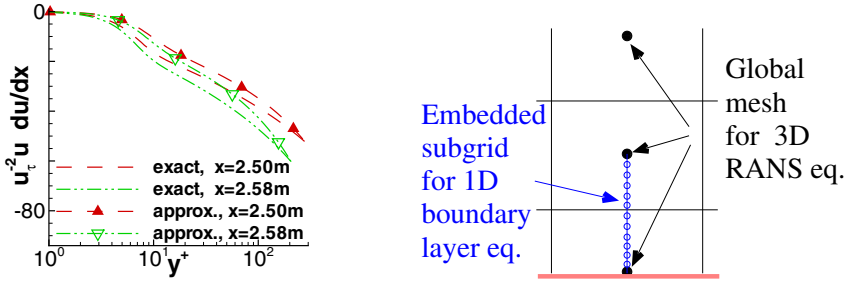
Fig. 2. Left: Profiles of exact term $u\partial u/\partial x$ and using approximation (5) for APG flow by [3]. Right: Sketch of coupling between global RANS problem and wall-function problem.

The near-wall problem (2)-(4) satisfies the low-Re boundary condition $u = 0$ and $\tilde{\nu} = 0$ on the wall and is matched with the global RANS solution at the first node y_δ. Alternative boundary conditions at y_δ will be studied in future work. For the coupling with the global problem see Section 4. In (2)-(4) u_δ, $\tilde{\nu}_\delta$ are given by the global RANS solution at y_δ, d is the wall distance and ν_t is computed from

$$\nu_{\mathrm{t}} = \nu_{\mathrm{t}} \ , \quad \nu_{t} = f_{v1} \max(\tilde{\nu}; 0) \ , \quad f_{v1} = \frac{\chi^3}{\chi^3 + c_{v1}^3} \ , \quad \chi = \frac{\tilde{\nu}}{\nu_l} \ .$$

Only the contribution of the derivative in wall-normal direction is used for $\tilde{S}$ and f_w, since the gradient in streamwise direction was found to be much smaller than the gradient in wall-normal direction even in regions of separation.

The model (2)-(4) is elliptic and takes into account directly only diffusion in wall-normal direction; hyperbolic transport of information is due to the close coupling with the global RANS problem via the boundary conditions. The term $u\,du/dx$ needs to be approximated, since du/dx in not known for a 1D method

$$u\, \frac{\mathrm{d}u}{\mathrm{d}x} \ \approx \ u^2 \ \times \ \frac{\frac{\mathrm{d}u}{\mathrm{d}x}\big|_{y=y_\delta}}{u\big|_{y=y_\delta}} \ . \tag{5}$$

Figure 2 (left) gives a comparison between exact and approximated term for the APG flow shown in Fig. 1. The approximation is satisfactory. The full right hand side f in (2) will be referred to as *full-approximation*, the choice $f = \mathrm{d}p/\mathrm{d}x$ will be called *pressure gradient*, and $f = 0$ is the *stress-equilibrium* assumption.

4   Numerical Method

In this section the numerical solution method including the coupling between global RANS problem and near-wall wall-function model is described. The method has been implemented into the DLR TAU-Code. The global RANS problem is solved using a finite-volume method of cell-vertex type, i.e., of cell-centred type with respect to the

dual mesh of control volumes. For steady state problems, the non-linear problem is solved using an explicit Runge-Kutta scheme in a pseudo-time. After a certain number of iterations, the wall-function model (2)-(4) is solved using an implicit finite element method of piecewise linear test- and ansatz functions. The arising linear system is tridiagonal and can be solved directly. For the production and destruction terms, a Newton-Raphson type linearization and mass lumping is used to increase diagonal dominance of the equations. The non-linearity of the wall-function model is solved iteratively during the coupling procedure, i.e., only one linearisation step is performed per call of the wall-function routines.

The wall-function solution is provided to the global RANS method. On the subgrids, the wall-normal gradients of velocity and turbulence quantities can be computed very exactly. From this, we compute the wall-shear stress as boundary condition for momentum and the flux of turbulence quantities across the first inner face as boundary condition for $\tilde{\nu}$ resp. for k and ω. The production term in the first off-wall cell and the viscous flux of momentum across the first inner face are also computed on the subgrid. Thus, regarding the turbulence quantities, a Dirichlet-Neumann type coupling between global RANS and boundary layer problem is used.

5   Results

The method is applied first to the turbulent boundary layer flow at zero pressure gradient (ZPG) over a flat plate of length $l = 5$m studied experimentally by Wieghardt and Tillmann and recorded in [7] as Flow 1400 with $u_\infty = 33$m/s, $\nu = 1.51 \times 10^{-5}$m^2/s and an adiabatic wall. The wall is treated fully turbulent.

The first goal is to verify the method. Whereas universal wall-functions use an analytical formula for computing u_τ, the present method relies on a numerical procedure. An improper coupling between global RANS and wall-function model can lead to large errors at the interface, i.e., at the first off-wall node. This causes solutions which are significantly worse than using universal wall-functions, since the increase in physical modelling is contaminated by a large numerical error. For the ZPG flow, pressure gradient term and convective term are small and the three levels of approximation of (2), i.e., stress-equilibrium, pressure gradient, and full-approximation yield the same result. The agreement with the low-Re solution and the solution using universal wall-functions is very good, see Fig. 3. The prediction for k shows an improvement compared to universal wall-functions, see Fig. 4 (left). The deviation between the 1d-BL wall-function and the low-Re solution is due to the numerical error on the coarse global RANS grid. Using a grid refinement in the region between first off-wall node and the boundary layer edge, this deviation can be removed. For the SST model, it was found mandatory to compute the production term and also the viscous momentum flux across the first face using the subgrid solution. The predictions for c_f are little improved compared to universal wall-functions, see Fig. 4 (right). However, it has to be admitted that here the universal wall-function boundary condition for ω was imposed, i.e., the exact value for ω in ZPG flows, see [4]. If the flux of ω across the first inner face using the subgrid solution for ω is prescribed as boundary condition for the global RANS problem, then the deviation from the low-Re solution becomes little larger than for the universal wall-functions, see also Fig. 3.
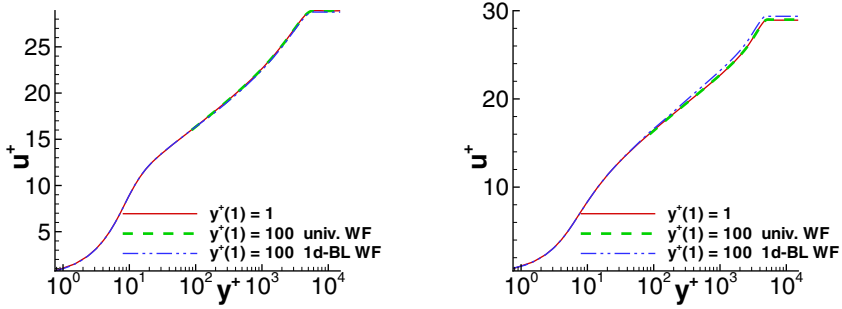
Fig. 3. Turbulent boundary layer flow at zero-pressure gradient by [7]: Velocity profiles for SA-E model (left) and SST k-ω model (right).
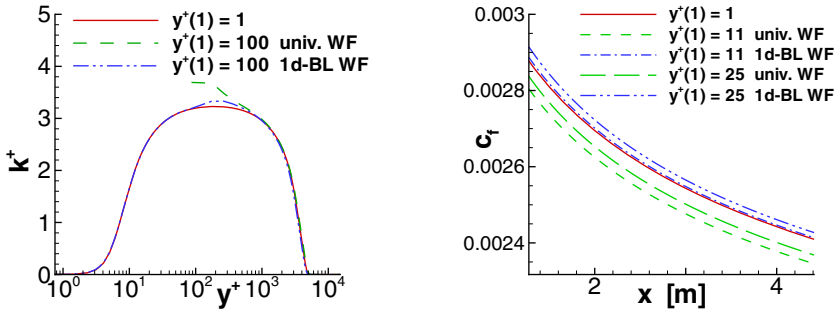
Fig. 4. Turbulent boundary layer flow at zero-pressure gradient by [7] using the SST k-ω model: Profile for turbulent kinetic energy k (left) and prediction for c_f (right).

Question of grid independence of the results is threefold. First, grid convergence on the near-wall subgrid needs to be ensured, which was always checked. Secondly, the dependence on $y^+(1)$ of the global mesh needs to be tested where the spreading in c_f is similar to the results in [4] using universal wall functions and thus much smaller than for most other existing methods. The third aspect is the role of the coarse mesh for the global RANS solution, which is subject to present research.

Finally the method is applied to the attached boundary flow in a 2D symmetric diffusor using the SA-E model. The geometry is sketched in Fig. 5 (left). Inlet height is $H = 0.075$m and corner radius $R = 0.5$m. At the inlet, constant inflow velocity is 25m/s and viscosity $\nu = 1.51 \times 10^{-5}$m^2/s. The velocity profiles along a wall-normal ray at $x/H = 1.61$ for different approximations of the right hand side of equation (2) are shown in Fig. 5 (right) on a mesh with $y^+(1) = 100$ (measured at $x/H = 0$). Clearly, for the stress-equilibrium approximation the wall-function solution and the global RANS solution do not match smoothly at $y(1)$. Results are significantly improved by using the pressure gradient term and the full approximation. The predictions for c_f using different approximations of the right hand side of eq. (2) on meshes with
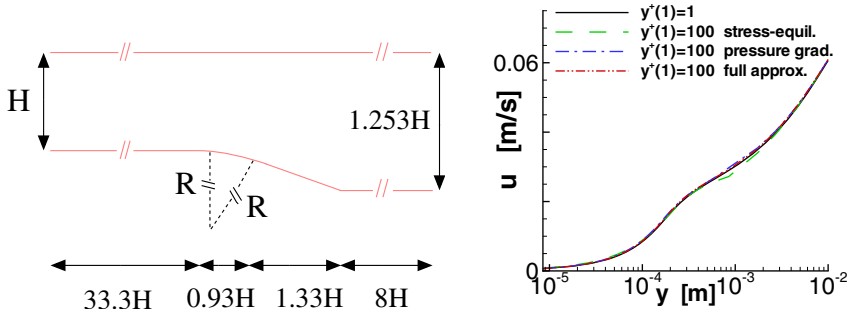
Fig. 5. Left: Sketch of the diffuser geometry for APG flow. Right: Velocity profiles at $x/H = 1.61$ for different approximations of the right hand side of eq. (2).

$y^+(1) = 100$ and $y^+(1) = 200$ are shown in Figure 6. The solution using universal wall functions is also shown. In the region before the expansion, all models give close results. The flow acceleration in the region of the corner fairing at $x/H = 0$ can be predicted only using the full approximation. In the region of adverse pressure gradient the agreement of the full approximation and the low-Re solution is also best. Skin friction is overpredicted using the stress-equilibrium model and universal wall functions and little underpredicted using the pressure-gradient model. On the mesh with $y^+(1) = 200$ differences become more discernible than on the mesh with $y^+(1) = 100$.

For the SST k-ω model, additional research work is needed before showing results. An investigation not shown here has revealed that the coupling of global problem and wall-function model for the ω equation has a significant influence on the results. Whereas for equilibrium boundary layer flows, this leads only to a little underprediction of u_τ, see Fig. 3 (right), for the diffusor flow the influences are more significant.
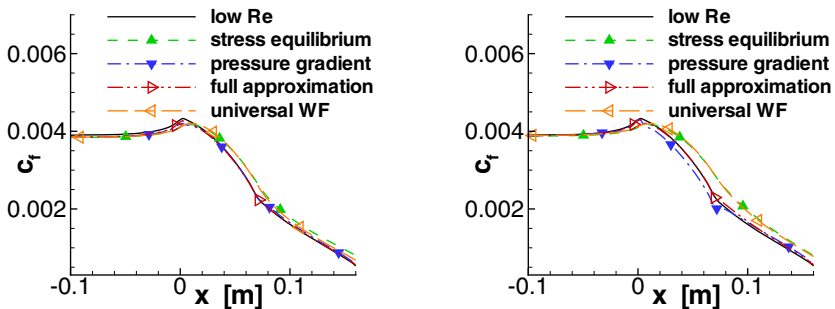
Fig. 6. Diffusor flow: Predictions for c_f using different approximations of the right hand side of eq. (2) on meshes with $y^+(1) = 100$ (left) and $y^+(1) = 200$ (right).

6   Conclusion

This paper presented an improved wall function method suitable for unstructured flow solvers based on the numerical integration of the turbulence model specific one-dimensional boundary-layer equations for wall-parallel velocity, including pressure gradient term and convective term, and turbulence quantities in wall normal direction. An investigation of the different terms in the boundary layer equation of the near-wall RANS solution for SA-E and SST k-ω model for a turbulent boundary layer flow at adverse pressure gradient with separation showed that in the viscous sublayer the streamwise convective term is much smaller than the pressure gradient term, but in the log-layer both terms are of comparable size. Therefore the convective term needs to be included into an improved wall-function model. For turbulent boundary layer flow at zero pressure gradient, the agreement with the low-Re solution using the present method is close to the results using turbulence model specific universal wall-functions, which have been designed for this test case. For the attached boundary layer flow in a diffusor at adverse pressure gradient the improvement of the results using the present method compared to universal wall function has been clearly shown for the SA-E model. Regarding the SST model, additional research work on the coupling for the ω-equation is needed.

References

[1] Craft, T.J., Gant, S.E., Iacovides, H., Launder, B.E.: Development and application of a new wall function for complex turbulent flows. In: Proceedings of the European Conference on Computational Fluid Dynamics, ECCOMAS CFD (2001)
[2] Edwards, J.R., Chandra, S.: Comparison of eddy viscosity-transport turbulence models for three-dimensional, shock separated flowfields. AIAA Journal 34, 756–763 (1996)
[3] Kalitzin, G., Medic, G., Iaccarino, G., Durbin, P.: Near-wall behaviour of RANS turbulence models and implications for wall functions. J. Comput Phys. 204, 265–291 (2005)
[4] Knopp, T., Alrutz, T., Schwamborn, D.: A grid and flow adaptive wall-function method for RANS turbulence modelling. J. Comput Phys. 220, 19–40 (2006)
[5] Menter, F.R.: Zonal two equation k/ω turbulence models for aerodynamic flows. AIAA Paper 1993-2906 (1993)
[6] Shih, T.-H., Povinelli, L.A., Lumley, J.A.: A generalized wall function. In: NASA TM-1999-209398 (1999)
[7] Wieghardt, K., Tillmann, W.: On the turbulent friction layer for rising pressure. In: Coles, D.E., Hirst, E.A. (eds.) Computation of Turbulent Boundary Layers - 1968 AFOSR-IFP-Stanford Conference, Stanford, pp. 98–123 (1969)

A Wall Model Based on Simplified Thin Boundary Layer Equations for Implicit Large Eddy Simulation of Turbulent Channel Flow

ZhenLi Chen[1,2], Antoine Devesa[1], Stefan Hickel[1],
Christian Stemmer[1], and Nikolaus A. Adams[1]

[1] Institute of Aerodynamics, Technische Universität München, 85748 Garching, Germany
zhenli.chen@aer.mw.tum.de
[2] Institute of Fluid dynamics, Northwestern Polytechnical University,
710072 Xi'an, Shaanxi, P.R. China

Summary

In order to perform implicit Large Eddy Simulation (LES) of high Reynolds number wall-bounded flows, a wall model based on simplified Thin Boundary Layer Equations (TBLE) is designed and applied to turbulent channel flow for a wide range of friction Reynolds numbers up to Re_τ=20,000. The prediction capability of the employed wall model concerning mean velocities and Reynolds stresses is satisfactory, even on very coarse LES grids. The coupling position between the simplified TBLE model and the LES should be located at the bottom of the logarithmic region. The grid resolution requirement depends mainly on the embedded TBLE grids and is only weakly dependent on the Reynolds number.

1 Introduction

In Large Eddy Simulation (LES), the large energy-containing eddies are computed directly, while the small subgrid-scales of motion are modeled by a subgrid-scale (SGS) model, in order to avoid the prohibitive resolution requirements of direct numerical simulation (DNS). LES have been successfully applied to many types of flows, especially for free shear flows. However, SGS models can not accurately represent the turbulent stresses in the vicinity of the wall on coarse meshes [1]. That is because the near-wall viscous and buffer regions contain a lot of those small-scale structures that are known to play a significant role in the generation and transport of turbulent kinetic energy and shear stress. A fully resolved LES must simulate the bulk of these features. However, the number of grid points increases as Re_τ^2 [2], and correspondingly a small time step is required by numerical stability and the characteristic time of the smallest eddies, therefore a large amount of computational resources is required. This turns LES to be hardly affordable for the simulation of wall-bounded flows at high Reynolds number.

To circumvent these problems and diminish the grid resolution requirements near the wall, wall models have been introduced. This approach allows to resolve only the

outer part of the boundary layer. The cost of the computation based on the outer flow exclusively, becomes then weakly dependent on the Reynolds number [3]. Since the time step and grid size are much larger than the characteristic time and length scales of near-wall small structures respectively, wall models provide the near-wall flow information to the outer flow in a statistical sense.

A large number of approximate boundary conditions based on wall-shear stresses can be found in the literatures, including algebraic, two-layer and control-based models. The main property of these models is the prescription of wall-shear stresses, while setting the wall-normal velocity to zero. Another alternative considered is the off-wall Dirichlet boundary conditions. Using these boundary conditions, it is possible to use a grid designed only to capture the outer scales of the flow. Unfortunately, prescription of these velocities was shown to be challenging [4]. A third alternative to wall modeling consists in merging LES and Reynolds Average Navier-Stokes (RANS) into a hybrid simulation. The difficulty with the RANS/LES hybrid approach comes from providing the matching conditions at the boundary between the two domains. A spurious buffer layer in the logarithmic region is developed, which makes the skin friction coefficient under-predicted, and therefore, shifts the mean velocity upwards. This problem was mitigated by using stochastic forcing [5]. Recently, a RANS eddy-viscosity, which was obtained from a resolved LES of channel flow and then was stored in a look-up table, was used with a wall-stress model. This technique enabled LES to be performed on coarse grids [6]. Although some encouraging results were obtained, the priority was the resolved near-wall flow information.

All the wall models mentioned above are based on the assumption that the viscous and buffer layers over smooth walls are essentially independent of the outer flow and the interaction between the inner and outer layers is weak for the attached flow [7]. Therefore, it is essential to know what information provided by the near-wall region does the outer flow need. However, the SGS model near the wall and numerical errors are important for LES on coarse grids, since they mostly cause the deficiencies of the wall models [8].

In the present work, the information from the wall provided to the outer flow are the wall-shear stresses and zero velocity in wall-normal direction. These are obtained by solving simplified Thin Boundary Layer Equations (TBLE) as a two-layer model on an embedded grid. The flow features far from the wall are obtained by implicit LES. A finite volume method based on a nonlinear deconvolution operator and a numerical flux function called Adaptive Local Deconvolution Method (ALDM) is used in implicit LES to formulate the truncation error as an implicit SGS model [9]. The prediction capability of this two-layer wall model in the framework of implicit LES is assessed for turbulent channel flow. Results are compared with available DNS results for a wide range of friction Reynolds numbers. The influence of the coupling position between the LES and the simplified TBLE on mean velocity and Reynolds stresses is investigated. A particular attention is given to the Reynolds-number dependency of the grid resolution requirement.
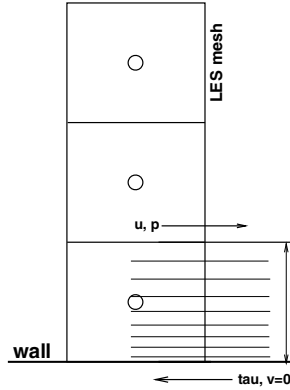
Fig. 1. A sketch of simplified TBLE model coupling with LES.

2 Simplified Thin Boundary Layer Equation

The unsteady Thin Boundary Layer Equations (TBLE) are a set of simplified partial differential equations derived from the Navier-Stokes equations under the assumption that in the very thin wall region, the wall-tangential length scales are much larger than the wall-normal ones, and wall-normal direction derivatives are much bigger than derivatives of wall-tangential directions. Interested in including more dynamics in the near-wall region and computational efficiency, we base our work on [8]. The following simplified equations are used:

$$\frac{\partial}{\partial y}(\nu + \nu_t)\frac{\partial u_i}{\partial y} = \frac{\partial u_i}{\partial t} + \frac{1}{\rho}\frac{\partial p}{\partial x_i}, \quad (i = 1, 3). \tag{1}$$

The mixing-length eddy-viscosity model with damping function is used, which accounts for all near-wall turbulent scales:

$$\nu_t = \kappa y u_\tau (1 - e^{-y^+/A})^2, \tag{2}$$

where $\kappa = 0.4$, and $A = 19.0$. The wall-normal velocity is obtained from the continuity equation:

$$v(x, y, z) = -\int_0^y (\frac{\partial u}{\partial x} + \frac{\partial w}{\partial z})\, dy'. \tag{3}$$

The simplified boundary layer equations neglecting the convective terms are ordinary differential equations that are solved algebraically every time step on embedded grids with the same streamwise and spanwise grid distribution as in the LES. A no-slip boundary condition is imposed at the wall. The upper boundary condition for velocity and pressure is given by the LES. As output, the TBLE model provides the LES algorithm with the streamwise and spanwise wall-shear stresses. The sketch of the simplified TBLE model coupling with LES is shown in Figure 1.

3   Numerical Method

The turbulent channel flow is described by the incompressible Navier-Stokes equations which are discretized on a staggered Cartesian mesh. An explicit third-order Runge-Kutta scheme is used for time advancement. The time step is dynamically adapted to satisfy a Courant-Friedrichs-Lewy condition with $CFL = 1.0$. The pressure Poisson equation and diffusive terms are discretized by second-order centered differences, whereas the convective terms are discretized by Simplified Adaptive Local Deconvolution method (SALD) for improved computational efficiency[10]. The validation of this numerical methodology has been established for plane channel flow, separated channel flow, passive-scalar mixing, and massively separated turbulent boundary layer under adverse pressure gradient [10]. In the simulations of this paper, the Poisson solver employs fast Fourier transforms in the spanwise and streamwise directions, and direct tridiagonal matrix inversion in wall-normal direction. The Poisson equation is solved at every Runge-Kutta substep. The wall-shear stresses are updated at every Runge-Kutta substep by solving the simplified Thin Boundary Layer Equations.
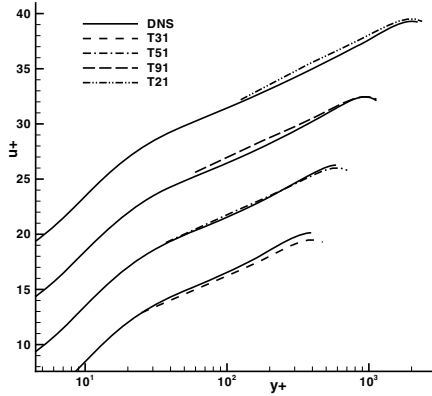
Fig. 2. Mean velocity profiles comparison between wall-modeled LES and DNS.

4   Results

The reference validation case considered and presented here is the turbulent flow in a bi-periodic plane channel. The computations are undertaken for a wide range of friction Reynolds numbers, from Re_τ=395 up to 20,000, as shown in Table 1. The streamwise, wall-normal and spanwise dimensions of the computational domain are $2\pi h \times 2h \times \pi h$. The LES grid points are regularly distributed in three directions of space. The TBLE grids are stretched using the same coefficient 1.25 in the wall-normal direction. Friction velocity defined as $u_\tau = \sqrt{\tau_w/\rho}$ and wall units $y_\tau = \nu/u_\tau$ obtained by the simplified TBLE are used as characteristic velocity and length scales.

Table 1. Computational cases

case	Re_τ	LES grid	TBLE resolution	Coupling position
T31	395	$16 \times 16 \times 16$	20	C1
T32	395	$16 \times 16 \times 16$	20	C2
T33	395	$16 \times 16 \times 16$	20	C3
T34	395	$16 \times 16 \times 16$	30	C3
T51	590	$16 \times 16 \times 16$	20	C1
T91	950	$16 \times 16 \times 16$	20	C1
T21	2000	$16 \times 16 \times 16$	20	C1
T41	4000	$16 \times 16 \times 16$	20	C1
T201	20,000	$16 \times 16 \times 16$	20	C1
T202	20,000	$16 \times 16 \times 16$	30	C1
T203	20,000	$32 \times 32 \times 32$	20	C2
T204	20,000	$32 \times 32 \times 32$	30	C1
T205	20,000	$48 \times 48 \times 48$	20	C1
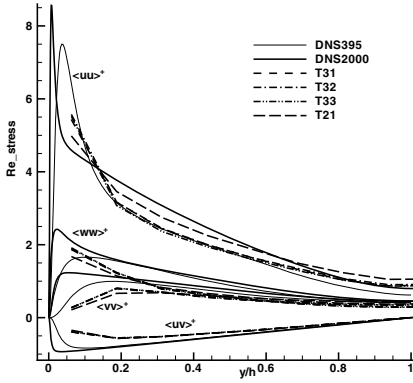
Fig. 3. Reynolds stresses of wall-modeled LES and DNS.
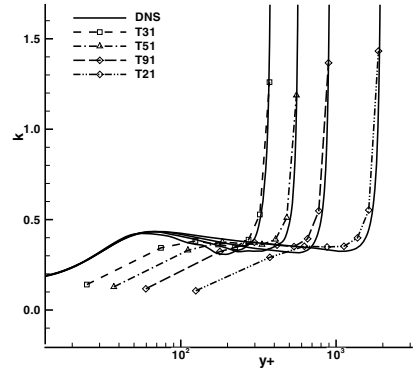
Fig. 4. Von-Kármán parameter κ comparison between wall-modeled LES and DNS.

4.1   Prediction Capability

In order to verify the prediction capability of the presented wall model, the mean velocity profiles of cases T31, T51, T91 and T21 are compared with DNS results of Moser *et al.* at Re_τ=395 and 590, del Alamo *et al.* at Re_τ=950 and Hoyas & Jimenez at Re_τ=2000. The comparison in Figure 2 shows that the outer flow can be predicted well even on very coarse LES grids. The Reynolds stresses of cases T31 and T21 are compared with DNS in Figure 3, which show reasonable agreement. The logarithmic region parameter $\kappa = 1/(y^+ du^+/dy^+)$, corresponding to the Kármán constant, is compared with DNS in Figure 4. It can be seen that the trend is reasonable, with values around 0.4 in the logarithmic region.
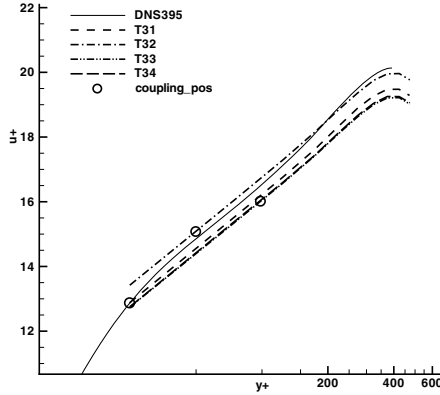
Fig. 5. Effect of the coupling positions on the mean velocity at Re_τ=395.

4.2   The Effect of LES/TBLE Coupling Positions

The influence of the coupling position on the prediction of mean velocity and Reynolds stresses is investigated here. Three different coupling positions (C1, C2 and C3) are used in the simulations T31, T32, T33 respectively. C1 corresponds to a coupling position at the 1st LES off-wall point, C2 at the middle of 1st and 2nd LES off-wall points, and C3 at the middle of the 2nd and 3rd ones. In these three cases, almost the same friction velocity is obtained. The mean velocity profiles are compared in Figure 5. In the embedded TBLE part, the mean velocity profile can be correctly predicted in T31 and T32, but is under-predicted in T33. That is because strong convection is present in the outer part of TBLE in T33, which can not be accounted for by the simplified TBLE. T34 is implemented to verify that the resolution of the TBLE is sufficient. In the outer LES part, the mean velocity profiles are under-estimated in cases T31 and T33, which means that the LES feels the inner near-wall flow not only through the wall stresses but also through the velocities at the coupling position. Reynolds stresses compared in Figure 3 are almost the same, which proves that as long as the TBLE provide correct wall-shear stresses, the coupling position has almost no influence on Reynolds stresses. Therefore, the coupling position should be not too close to the wall, or where convection is strong, ideally at the bottom of the logarithmic region.

4.3   Reynolds Number Dependency of Grid Resolution Requirements

Figure 2 shows that up to Re_τ=2000, the grid resolution of 16^3 is enough for LES to simulate the large scales in the logarithmic and core flow region. In order to investigate the Reynolds-number dependency of grid resolution, the calculations of T41 and T201 at Re_τ=4000 and 20,000 are carried out and compared with the logarithmic law in Figure 6. The mean velocity profile of T41 is correctly predicted, which shows that the LES grid resolution for outer flow is still sufficient. In case T201, the outer mean velocity is significantly under-estimated, and the TBLE fails to catch the mean flow
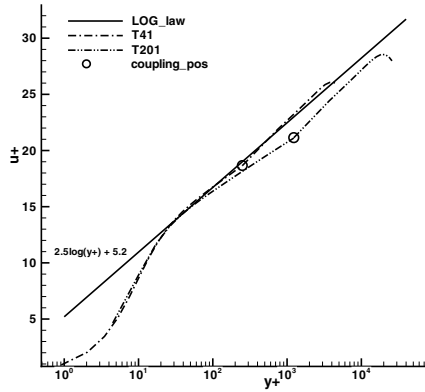
Fig. 6. Mean velocity profiles comparison between wall-modeled LES and logarithmic law at Re_τ=4000 and 20,000.

at its outer part, as the case T33 in Section 4.2 at Re_τ=395, which shows Reynolds number dependency. In this case, with coupling position C1, the simplified TBLE has the ability to obtain the mean flow feature. Therefore, its failure is caused by the insufficient resolution of the embedded grid and the outer coarse LES. In order to know which one is crucial, firstly, from case T201 to T202, the resolution of the LES is fixed. Secondly, from case T201 to T203, the resolution of the TBLE is fixed. The mean velocity profiles are compared in Figure 7, which shows that the case T202 shifts the profile towards the logarithmic law significantly, while the case T203 has not much effect on the mean velocity profile. This means that not the expensive outer LES part but the less costly near-wall embedded TBLE mainly accounts for the Reynolds-number dependence of the grid resolution. To obtain well-predicted mean velocity profile, cases T204 and T205 are carried out, and are compared in Figure 7. They are almost same
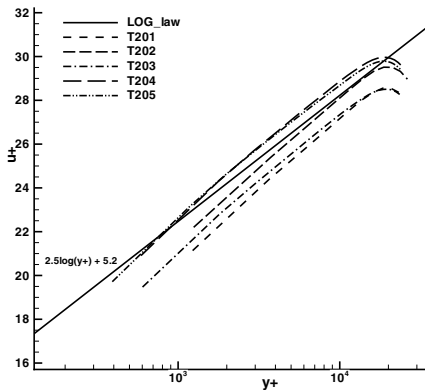
Fig. 7. Effect of grid resolution on the mean velocity at Re_τ=20,000.

and compared well with the logarithmic law. This means that well-predicted results can be obtained by increasing the resolution of TBLE only or the resolution of LES and TBLE together. The overall computational cost then weakly depends on the Reynolds number.

5   Conclusions

A wall model designed and implemented in the framework of implicit Large Eddy Simulation has been investigated and assessed for the turbulent channel flow. This wall model is based on the simplified Thin Boundary Layer Equations. Using this wall model, well-predicted mean velocity profiles, and reasonable Reynolds stresses can be obtained on coarse LES grids. Not only the wall stresses provided by TBLE, but also the coupling position between embedded TBLE and outer coarse LES is crucial for the mean velocity. The coupling position at the bottom of the logarithmic region is required. The grid resolution requirement depends mainly on the embedded TBLE and exhibits weak Reynolds-number dependence.

Acknowledgements

References

[1] Jimenez, J., Moser, R.: LES: where we are and what we can expect. AIAA J. 38(4), 605–612 (2000)
[2] Baggett, J., Jimenez, J., Kravchenko, A.: Resolution requirements in large-eddy simulation of shear flows. CTR Annu. Res. Briefs, 51–66 (1997)
[3] Piomelli, U., Balaras, E.: Wall-layer models for Large-Eddy Simulation. Annu. Rev. Fluid Mech. 34, 349–374 (2002)
[4] Jimenez, J., Vasco, C.: Approximate lateral boundary conditions for turbulent simulations. In: Proceedings of the 1998 Summer Program, CTR, pp. 399–412 (1998)
[5] Piomelli, U., Balaras, E., Pasinato, H., Squires, K., Spalart, P.: The inner-outer layer interface in large-eddy simulations with wall-layer models. Int. J. Heat and Fluid Flow 24, 538–550 (2003)
[6] Medic, G., et al.: A formulation for near-wall RANS/LES coupling. International Journal of Engineering Science 44, 1099–1112 (2006)
[7] Jimenez, J.: Recent developments on wall-bounded turbulence. Rev. R. Acad. Cien. Serie A. Mat. 101(2), 187–203 (2007)
[8] Cabot, W., Moin, P.: Approximate wall boundary conditions in the large-eddy simulation of high Reynolds number flow. Flow, Turbulence and Combustion 63, 269–291 (1999)
[9] Hickel, S., Adams, N.A., Domaradzki, J.A.: An adaptive local deconvolution method for implicit LES. Journal of Computational Physics 213, 413–436 (2006)
[10] Hickel, S., Adams, N.A.: Implicit LES applied to zero-pressure-gradient and adverse-pressure-gradient boundary-layer turbulence. Int. J. Heat and Fluid Flow 29(3), 626–639 (2008)

Detached-Eddy Simulation of Supersonic Flow Past Cylindrical Aft Body with and without Base Bleed

Vamshi Togiti[1], Michael Breuer[2], and Heinrich Lüdeke[1]

[1] DLR, Institute of Aerodynamics and Flow Technology, Branch: Spacecrafts
D-38108 Braunschweig, Germany
{vamshi.togiti,heinrich.luedeke}@dlr.de
[2] Department of Fluid Mechanics (PfS), Institute of Mechanics
Helmut–Schmidt–University Hamburg, Germany
breuer@hsu-hh.de

Summary

In the present work supersonic base flows with and without base bleed are studied to investigate the influence of the bleed on the flow field. To this end, simulations are performed using detached-eddy simulation. To evaluate the performance of DES, numerical predictions are compared with computations based on RANS and experimental data for the base flow without bleed. To understand the influence of the bleed on the flow and the base pressure distribution, predictions of the base flow with bleed are compared with numerical data of the case without bleed.

1 Introduction

The supersonic flow over a cylindrical afterbody represents the kind of flow phenomenon which occurs in flows around rockets, projectiles and missiles. The most important issue for the above mentioned vehicles is total drag. The total drag can be divided into three components. The first is the pressure drag (excluding base drag), the second is the viscous drag and, finally, the base drag, which is due to the low pressure acting on the area of the afterbody. The base drag yields a major contribution which can be up to 50–60% of the total drag. In the past, several methods to reduce the base drag have been developed, including afterbody boat-tailing, base bleed and base cavities. These methods modify the wake flow field in a way that the pressure along the base increases which eventually decreases the base drag.

In supersonic afterbody flows (base flow without bleed), the on-coming turbulent boundary layer separates at the base corner, undergoes an expansion and forms a free shear layer which separates the outer inviscid flow from the large recirculation downstream of the base. As the free shear layer approaches the axis of symmetry, the flow tries to realign with the axis undergoing a re-compression process which subjects the shear layer to a strong pressure gradient. A part of the free shear layer, which can not

overcome the pressure gradient, is forced towards the cylinder base. A free stagnation point, where the mean streamwise velocity vanishes along the axis, separates the recirculation region behind the base and the turbulent wake. In the flow case with base bleed, where low speed air is injected through the base region, the recirculation behind the base is moved downstream of the base and an additional forward stagnation point is created. This shift in the location of the recirculation region weakens the re-compression shock, resulting in an increase of the base pressure and leading to a reduction in the base drag.

The main objective of the present work is to investigate supersonic base flow with and without bleed using detached-eddy simulation (DES) proposed by Spalart et al. [1] and to evaluate the predictive capabilities of DES by comparing numerical predictions with available experimental data.

2   Numerical Methodology

In the current investigation the DLR-TAU code is used, which is an unstructured compressible flow solver. Details about the finite-volume flow solver can be found in [4]. In the present study the convective fluxes are approximated by an advection upstream splitting method AUSM$^+$-UP, and the diffusion fluxes are evaluated by a central scheme. The time advancement is done using an implicit dual time-stepping scheme of second-order accuracy with an implicit lower-upper symmetric Gauß-Seidel algorithm, LUSGS.

3   Details of the Test Case

The configuration investigated is based on the experimental work done by Herrin & Dutton [2] and Mathur & Dutton [3]. In the experiments the free-stream Mach number is set to 2.46 and the free-stream pressure and temperature are 31,415 Pa and 145 K, respectively. The Reynolds number per unit meter is 45×10^6. In these studies [2, 3] a cylindrical afterbody with a radius R of 31.75 mm and the base bleed hole radius of 12.7 mm through which low speed air is injected into the base region in the case of base flow with bleed is used. The base flow with and without bleed can be categorized based on the mass injection parameter defined as $I = \dot{m}_j/(\rho_\infty u_\infty A_b)$, where $\dot{m}_j$ is the bleed mass flow rate and ρ_∞, u_∞ and A_b are the free-stream density, velocity and the area of the base. In the present study, supersonic base flow with a mass injection parameter of zero for the case without bleed and $I = 0.0075$ for the case with bleed are investigated.

The computational domain covers a region of $4R$ upstream of the base, where a steady turbulent boundary layer profile is set. This distance was chosen to match the experimental boundary layer thickness of 3.2 mm close to the cylinder base. The outflow boundary is placed $12R$ downstream of the base, where supersonic outflow conditions are prescribed. In the radial direction, the outside boundary is a conical frustum, with radius $4R$ at the inflow plane and $8R$ at the outflow plane, where the farfield boundary condition is imposed. At the base bleed hole, a constant mass flow with total conditions is prescribed. The computational grid used in the present study ia a structured grid which consists of 128 points in azimuthal direction. The total number of nodes is about 3.5 million.

In the current investigation the on-coming flow is turbulent. Here the DES approach is used in which LES falls inside the boundary layer if the grid is fine. In the present case the model switches from RANS to LES mode at y^+ equal to about 520. It is required to check whether the grid resolution is fine enough to resolve the boundary layer properly. For this purpose, the time-averaged turbulent boundary layer profile at a radial cross-section 1 mm upstream of the cylinder base is compared with the experiments and the law of the wall (see Fig. 1). A very good agreement is observed.

(a)   (b)
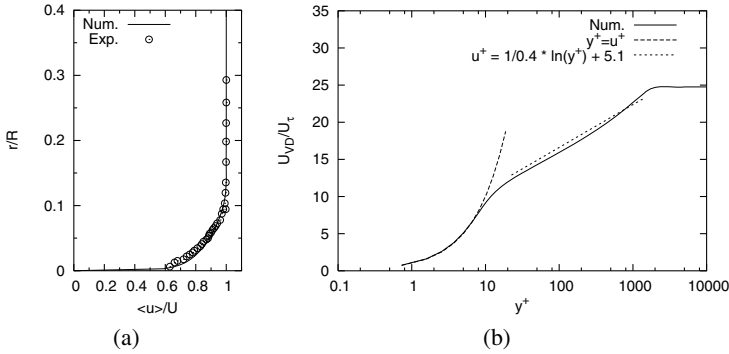
Fig. 1. Predicted time-averaged boundary layer profile at a radial cross-section 1 mm before the base corner; (a) comparison with experiments, (b) comparison with the law of the wall

4   Results

In this section, first the predictions of supersonic base flow without bleed produced by Spalart-Allmaras RANS and DES models are discussed and compared with the experimental data. Later, the DES predictions of the base flow with bleed are compared with the predictions without bleed to understand the influence of mass injection on the flow field. Furthermore, the results are also compared with the available experimental data.

4.1   Aft Body without Bleed

Instantaneous vorticity magnitude contours predicted by DES are depicted in Fig. 2 where the contour lines of the mean pressure are superimposed. The resolved large-scale structures are apparent and indicate the unsteadiness of the flow. The mean pressure contour lines render the expansion fan at the base corner where the flow separates and further downstream of the base the re-compression during which the free shear layer tries to realign with the flow axis.

The time-averaged streamwise and radial velocity profiles produced by RANS and DES are depicted in Fig. 3 and compared with the experimental data. These profiles show that the RANS predictions poorly agree with the experiments while the DES predictions not only follow the trends of the measurements but also agree rather well with the experiments. The mean streamwise velocity along the wake axis behind the base
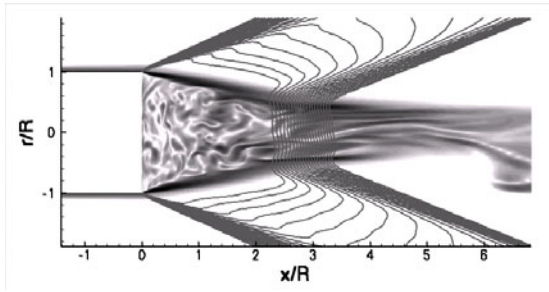
Fig. 2. Instantaneous vorticity magnitude contours along with the mean pressure contours for the afterbody without bleed
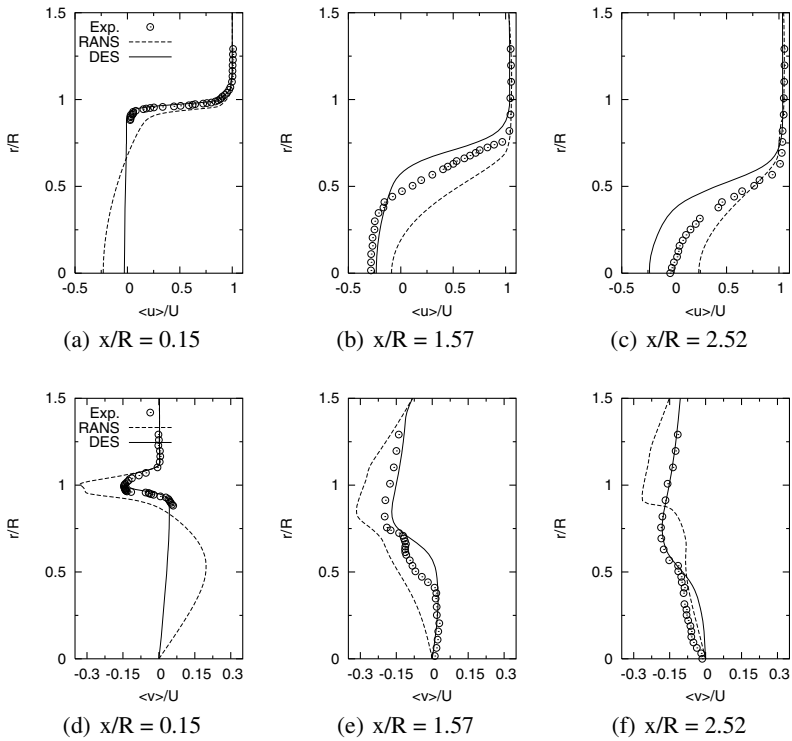
Fig. 3. Mean streamwise [(a)–(c)] and radial [(d)–(f)] velocity profiles at different streamwise locations behind the base; flow without base bleed

predicted by both techniques (RANS and DES) are shown in Fig. 4(a) and compared with the experiments. The profiles illustrate that based on the RANS approach the length of the recirculation is underpredicted and the maximum reverse velocity is overpredicted, whereas DES slightly overpredicts the length of the recirculation

and almost yields the right level of reverse velocity. The shorter recirculation is possibly due to higher turbulent viscosity behind the base predicted by RANS, which forces the free shear layer to deflect towards the axis of the cylinder earlier. Based on the DES approach the length of the recirculation is overpredicted by about 30%. A similar trend was also observed by Simon et al. [5] using the DES approach on a structured grid with about five million nodes.

The vital parameter for aerospace industry regarding blunt bodies is the pressure distribution behind the body, as it has large impact on the total drag. The mean pressure coefficient along the base is depicted in Fig. 4(b). A flat pressure coefficient typical for large separation regions is apparent from the experimental data. The DES prediction also delivers a flat pressure distribution as expected. The predicted level slightly deviates from the experimental one. The RANS prediction, however, predicts a much lower pressure coefficient and the distribution along the base differs considerably from the experimental data. The reason for this lower pressure coefficient is clearly visible from the distribution of the centerline velocity which shows a higher reverse velocity and a shorter recirculation length leading to a lower pressure level. Resolved turbulent
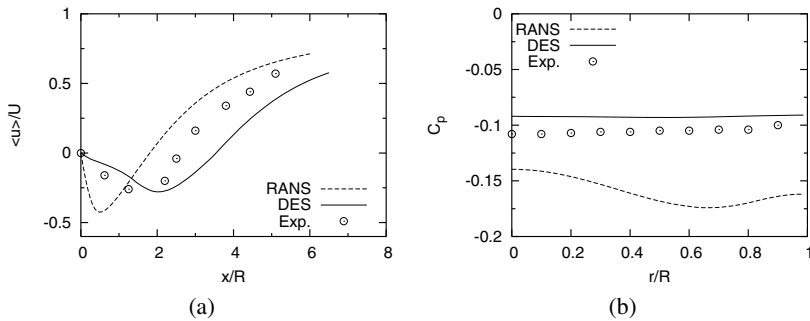
Fig. 4. Mean streamwise velocity along the wake axis (a) and mean pressure coefficient along the base (b); flow without base bleed

kinetic energy (TKE) profiles at different streamwise locations predicted by DES are depicted in Fig. 5 and compared with the experiment. The profile at $x/R = 0.15$ shows that the peak level is not predicted correctly by DES. The reason is that at this location most of the turbulence is modeled. Thus the resolved part is too low compared to the total turbulent kinetic energy determined in the measurements. Along the downstream direction, the TKE levels increase and even higher turbulent kinetic energy levels than in the experiment are predicted at $x/R = 2.52$.

4.2   Aft Body with Bleed, $I = 0.0075$

Contours of the mean streamwise velocity normalized with the free-stream velocity for the base flow with and without bleed are shown in Fig. 6. The low values of mean velocity show the extent of the recirculation. From the contours it is apparent that the location at which a positive mean streamwise velocity is observed behind the body,

(a) x/R = 0.15   (b) x/R = 1.57   (c) x/R = 2.52
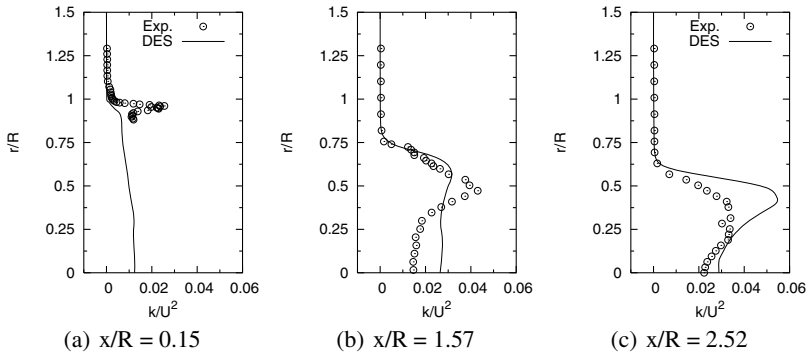
Fig. 5. Resolved turbulent kinetic energy at different streamwise locations behind the base; flow without base bleed

(a) I = 0   (b) I = 0.0075
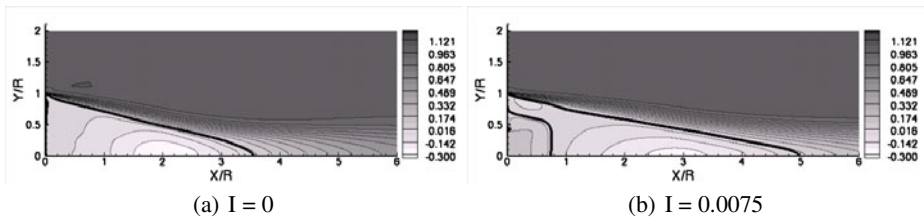
Fig. 6. Contours of mean non-dimensional steamwise velocity $\langle u \rangle /U$ behind the base; (a) without bleed, (b) with bleed; Thick contour line represents $\langle u \rangle /U = 0$

(a) I = 0   (b) I = 0.0075
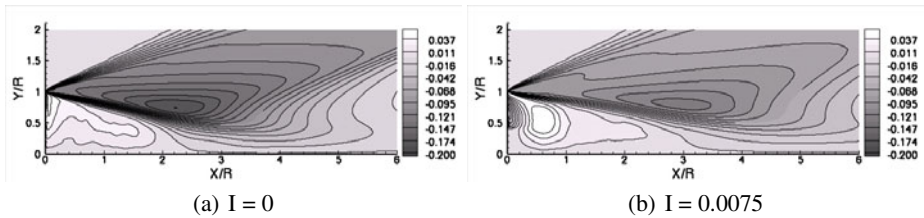
Fig. 7. Contours of the mean non-dimensional radial velocity $\langle v \rangle /U$ behind the base; (a) without bleed, (b) with bleed

moved downstream in the case with bleed in relation to the case without bleed. Furthermore, the height of the recirculation is reduced in the case with bleed. In the present numerical investigation the recirculation is displaced from the base till x/R of 0.75, whereas in the experiment it is 0.85.

In Fig. 7 contours of the mean radial velocity normalized with the free-stream velocity are depicted for both cases. These contours clearly show the expansion fan centered at the base corner. In the case of base flow with bleed low values of the radial velocity are predicted very close to the base where a secondary recirculation is
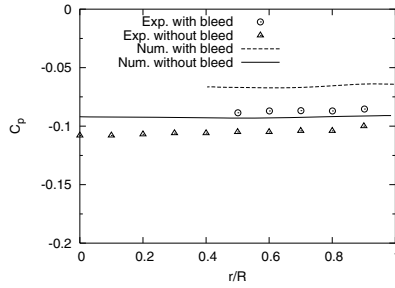
Fig. 8. Mean pressure coefficient along the base

(a) I = 0   (b) I = 0.0075
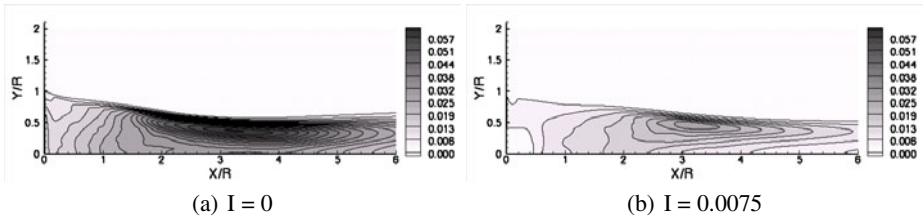
Fig. 9. Non-dimensional resolved turbulent kinetic energy (k/U^2) contours behind the base

observed. In the inviscid region behind the base, negative values of the radial velocity indicate that the flow turns towards the axis after the separation at the base corner. A large zone of low radial velocity is observed in the case without bleed. The reason for this behavior is assumed to be a change in the angle of the expansion fan. In the case with bleed, the angle of the expansion fan is reduced as a secondary recirculation formed along the base.

The mean pressure coefficient along the base is shown for the base flow with and without bleed in Fig. 8 and compared with the experimental pressure distribution. In the experiment [3] higher pressure values along the base were observed when injecting a low-speed mass flow through the bleed hole. The rise in the pressure coefficient (ΔC_p) along the base was about 0.02. In the numerical results a similar trend is observed but the increment is slightly higher and about 0.025. The comparison with the experimental results for both cases with and without bleed shows that the pressure coefficient is overpredicted, which is consistent with the overestimation of the length of the recirculation region *(saddle point)* behind the afterbody.

Contours of the resolved turbulent kinetic energy normalized with the square of the free-stream velocity are shown in Fig. 9. For both cases peak TKE values are evident in the free shear layer at a distance from the base equal to the location of the saddle point. Higher values of TKE are predicted in the case without bleed. The same trend is also known from the experiment [6].

5   Conclusions

In the current investigation, DES was applied to supersonic base flow with and without bleed and the influence of bleed on the flow field was studied. The base flow without bleed was studied using RANS and DES and the predictions were compared with each other and with the experiments. The comparison with the experiments showed that RANS predicted a smaller recirculation which compelled higher reverse velocity and lower base pressure. The reason for such a trend was found to be a high turbulent viscosity behind the base. DES predictions not only followed the trends of the experiments but also agree well with the measurements concerning the mean flow field and the base pressure. The turbulent kinetic energy level in the free shear layer very close to the base corner is underpredicted as most of turbulence is modeled. Further downstream, the TKE trends of the experiment are reproduced. However, the TKE levels are overpredicted near the free stagnation point.

The base flow with bleed was studied using DES and compared with predictions without bleed. By introducing the bleed, a displacement of the recirculation behind the base and an increase of the pressure along the base was observed. Comparisons with the experiments showed that a higher pressure coefficient along the base was predicted. Furthermore, a lower level of the turbulent kinetic energy in the shear layer was found in the case with bleed compared to the case without bleed, which is consistent with the experimental findings.

References

[1] Spalart, P.R., Jou, W.-H., Strelets, M., Allmaras, S.R.: Comments on the Feasibility of LES for Wings, and on a Hybrid RANS/LES Approach. In: Advances in DNS/LES, 1st AFSOR Int. Conf. on DNS/LES. Greyden Press, Col (1997)

[2] Herrin, J.L., Dutton, J.C.: Supersonic Base Flow Experiments in the Near Wake of a Cylindrical Afterbody. AIAA Journal 32(1), 77–83 (1994)

[3] Mathur, T., Dutton, J.C.: Base Bleed Experiments With a Cylindrical Afterbody in Supersonic Flow. AIAA Paper No. 95-0062 (1995)

[4] Mack, A., Hannemann, V.: Validation of the Unstructured DLR TAU-Code for Hypersonic Flows. AIAA Paper No. 2002-3111 (2002)

[5] Simon, F., Deck, S., Guillen, P.: Reynolds-Averaged Navier-Stokes/Large-Eddy Simulation of Supersonic Base Flow. AIAA Journal 44(11), 2578–2590 (2006)

[6] Mathur, T., Dutton, J.C.: Base Bleed Experiments With a Cylindrical Afterbody in Supersonic Flow. J. Spacecrafts and Rockets 33, 30–37 (1996)

Prediction of the Wind Tunnel Sidewall Effect for the iGREEN Wing-Tailplane Interference Experiment

A.D. Gardner, K. Richter, and H. Rosemann

German Aerospace Center (DLR), Institute of Aerodynamics and Flow Technology (AS),
Bunsenstrasse 10, 37073 Göttingen, Germany
`tony.gardner@dlr.de`

Summary

Computations using the DLR TAU code are presented to predict the effect of the wind tunnel on models which are directly attached to the wind tunnel side-wall. Results show that the effect of the sidewalls is similar to an offset in the angle of attack (but can only partially be corrected by a change in α), and that this effect is proportional to the lift and Mach number. These results were used in the design phase for the iGREEN wing-tailplane interference experiment.

1 Introduction

The DLR project iGREEN (Integrated Green Aircraft; 2007-2011) investigates the effects of increased aircraft elasticity from optimised structures or new aerodynamic configurations. One work package concerns the wing-tailplane interference through buffet processes and includes experiments in the adaptive test section of the Transonic Wind Tunnel Göttingen (TWG) in 2010. An NLR7301 airfoil is to be attached to a flutter rig [3] providing high-frequency pitching oscillations upstream of an elastic swept wing [2] previously used in the Aerostabil project (Figure 1). The aim of this numerical investigation was to identify which parts of the wind tunnel need to be modelled so that URANS and DES computations will be accurate, and to decide on the instrumentation for the wind tunnel experiment [5].

The two models are to be mounted in the TWG adaptive wall test section. This is a 1 m x 1 m test section where the top and bottom walls can be adapted such that the Mach gradient due to the boundary layer growth on the wind tunnel wall is minimised, and the interference of the walls on the model, due to the model lift and displacement, is compensated. For this investigation it was assumed that there are no interference effects from the top and bottom walls. The side-wall effects will be significant, since both the NLR7301 and the Aerostabil wing model are mounted directly on the wall of the TWG. The NLR7301 can be statically rotated and dynamically pitch-oscillated and the Aerostabil wing model can be statically rotated or statically translated in the z-direction (vertically), although z-movement was not used for these computations. The distance between the centers of the models is 1154 mm.
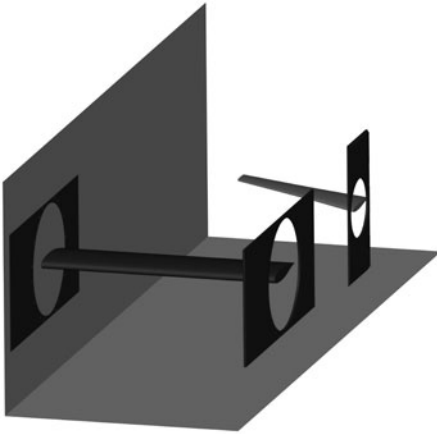
Fig. 1. Diagram of both wings in the experimental setup.
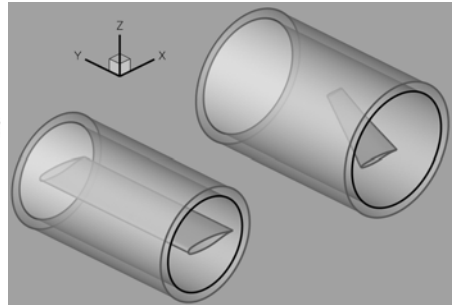
Fig. 2. The chimera surfaces with 50 mm overlaps.

2   Grid and Solver

Computations were performed with the DLR-TAU code [6] 2006.1.0 patch 3. An LUSGS finite-volume solver was used on a hybrid unstructured 3-D grid consisting of structured prism layers of y^+=1 and stretching 1.2 close to the surfaces, and a field discretised with tetrahedral cells, generated using the CENTAUR^{TM}[1] 7.0b1 unstructured grid generator. Computations were fully turbulent, using the Wilcox kω turbulence model ([12] p121, p129). In this case the Wilcox kω turbulence model was chosen for its high dissipation, to help convergence where large separated regions were created. Pressures on the model midline were identical to those generated using the Spalart-Allmaras turbulence model [10] with the Edwards modification (SAE) [4], but required only half the computational time to convergence.

The grid was built in three parts, and assembled in TAU using the grid overset (chimera) method (Figure 2). This meant that the NLR7301 and Aerostabil wing grids were built in small cylinders, which were later inserted into holes in the external grid. The external grid was a field of 1 m width and a length x height of 20 m x 20 m. The wind tunnel sidewalls were modelled as large plates which could be set as symmetry boundaries to simulate the 2D case, or to viscous boundaries to simulate the side-wall boundary layer. The model was in the middle of this field, giving a 10 m lead-in for boundary layer development on the side-walls. This is consistent with the lead-in suggested by Loic [7] from the boundary layer data measured in the TWG by Poten [8]. The remaining four walls of the domain (upstream, downstream, top, bottom) were set to be farfield boundaries. The compression of the flow by the boundary layers on the viscous sidewalls produced a divergent flow at the model position, leading to outflow on the top and bottom walls of the domain. The size of the computational field was set to approximate the flow divergence of the TWG, which led to a computed flow divergence

of 0.055° at 0.5m from the centerline with no model. The Mach-number gradient at the model position was approximately 0.0003/m.

The effect of the NLR7301 on the Aerostabil wing was by the dip in the total pressure in the wake of the NLR7301, with large cells used between the models to damp any unsteady flow effects. The surface cells of the NLR7301 were limited to 1.7% of chord. Blank cylinders without a model were also built so that the models could be tested independently of each other. Complete grids had between 1 million and 10 million nodes, depending on the configuration.

A 2D reference grid, generated in Centaur, was used to give 2D angle offsets and to make the uncertainty due to the turbulence model visible. The grid used a circular farfield of radius 500 chord lengths and grid adaptation was used to ensure that the 2D results were converged. The 3D results with symmetry sidewalls were compared to the 2D results to ensure an accuracy in lift and drag of better than 0.1%. The geometry of the structured-unstructured grid interface near the model trailing edge was particularly important for correct grid convergence.

3   Results

This section presents the results of the computations. A large test matrix was computed, from Mach 0.50 to Mach 0.85, but only results from Mach 0.70 with a Reynolds number of 2 million (based on a chord length of 0.3 m) will be shown here, as having most of the interesting characteristics also seen at other conditions. This was equivalent to the lower of the two Mach number conditions tested on the NLR7301 in [3], and is a low transonic Mach number for the Aerostabil wing.

3.1   The NLR7301 at Mach 0.70

The contours of C_P on the top surface of the NLR7301 with viscous side-walls are in Figure 3 for α=0° and 2°. At 2°, a region of supersonic flow is terminated by a strong shock at x/c=0.3, and at 0° a weaker shock is at x/c=0.15. Note the uniform region between y/l=0.3 and y/l=0.7. The three-dimensionality of the flow, from the interaction of the airfoil with the boundary layer on the wind tunnel side wall, is caused by a separation at the rear of the airfoil at the join between the airfoil and the wall. This separation acts as a displacing body in the flow, causing the surface streamlines to divert around it. Although the width of the separation region at the trailing edge is only around y/l=0.06 in these cases, a direct three-dimensional effect is observable in the C_P contours out to a width of at least y/l=0.3.

The surface streamlines for the top of the NLR7301 are shown in Figure 4 for the top and bottom of the airfoil at α=0°. Here it can be seen that the maximum width of the separations are y/l=0.055 and y/l=0.035 for the top and bottom of the airfoil respectively, and that the sidewall separations cause the streamlines to curve towards the model centerline for all values of y/l. Figure 5 shows that increasing the Mach number increases the size of the separation regions, and that increasing the angle of attack increases the size of the separation on the top and decreases the size of the separation on the bottom. This is one cause of differences in lift-polar gradients measured in wind tunnels to those found in free flight.
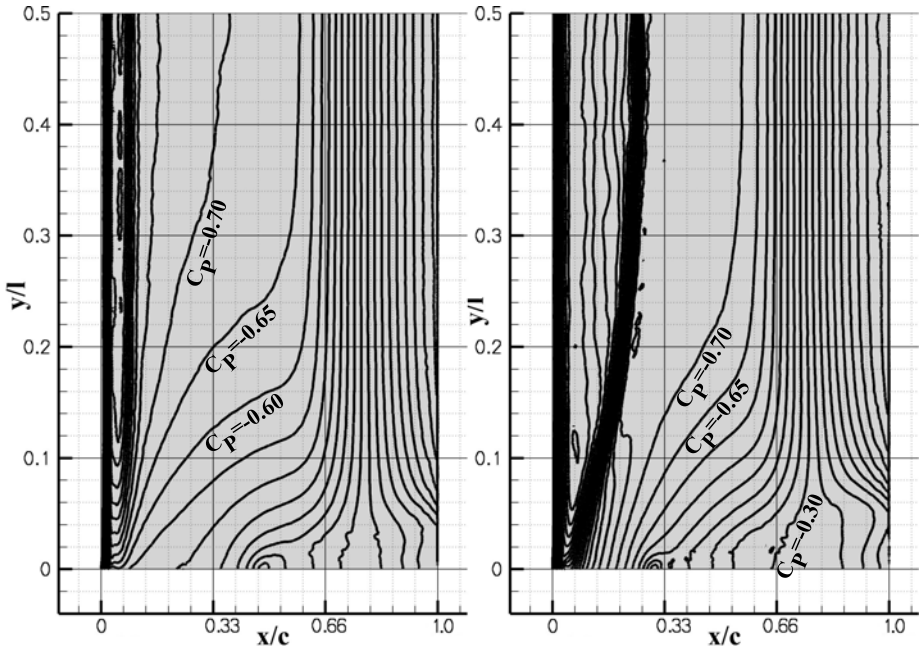
Fig. 3. Contours of C_P (0.05 step) for the NLR7301 top: Left: $\alpha_{NLR}=0°$, Right: $\alpha_{NLR}=2°$.

To quantify the interference effect of the wind-tunnel side-walls, cut planes were extracted from the airfoil on the model centerline at y/l=0.5. Although the region between y/l=0.3 and y/l=0.7 is relatively uniform, the 2D C_P distribution was not observed. For both $\alpha=0°$ and $2°$ (Figure 6), the effect of the viscous side walls is to increase the pressure on the model top side, pushing the shock forward, and to decrease the pressure on the bottom side of the model. The combined effect of these two changes is that the model computed with viscous side-walls has a changed circulation, making it appear to be at a lower angle of attack than the model with symmetry planes. This reduction in angle of attack has previously been estimated to be 0.5° to 0.7° for the WIONA model [9] and 0.6° for the COSDYNA model [11]. This well-known 3D sidewall effect causes a systematic error of the order of 20% in C_L for the NLR7301 tested at constant α. Historically this effect has been corrected by testing at constant C_L (variable α), which compensates for the change in circulation caused by the wall effects. This correction is increasingly invalid when transonic flow with shocks appears on the airfoil.

The problem with using a simple adjustment of the 2-D angle of attack is illustrated in Figure 6, Right. Here 2D computations for different angles of attack are compared with the 3D computations with either viscous or symmetry sidewalls. The 2D computation at $\alpha_{2D}=2°$ shows a similar shock position and similar pressures in the supersonic region and on the pressure side of the airfoil to the 3D case using the symmetry walls. Pressures behind the shock are different, mainly indicating that the 2D computation using the SAE turbulence model is closer to separation than the 3D computation with the Wilcox kω turbulence model. The computation for the viscous wall case is matched
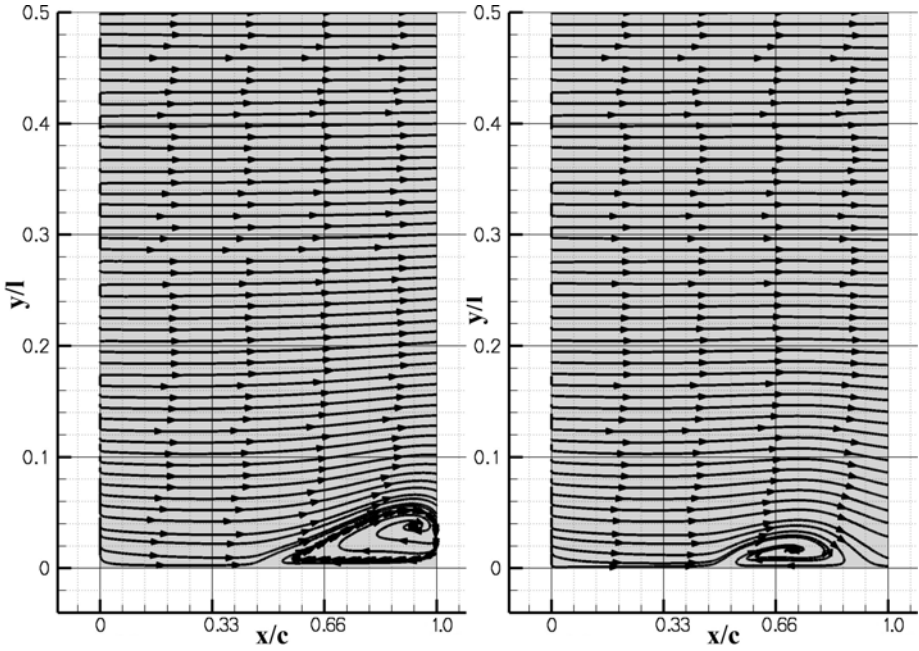
Fig. 4. Surface streamlines for the NLR7301 at α_{NLR}=0°. Left: Top, Right: Bottom.
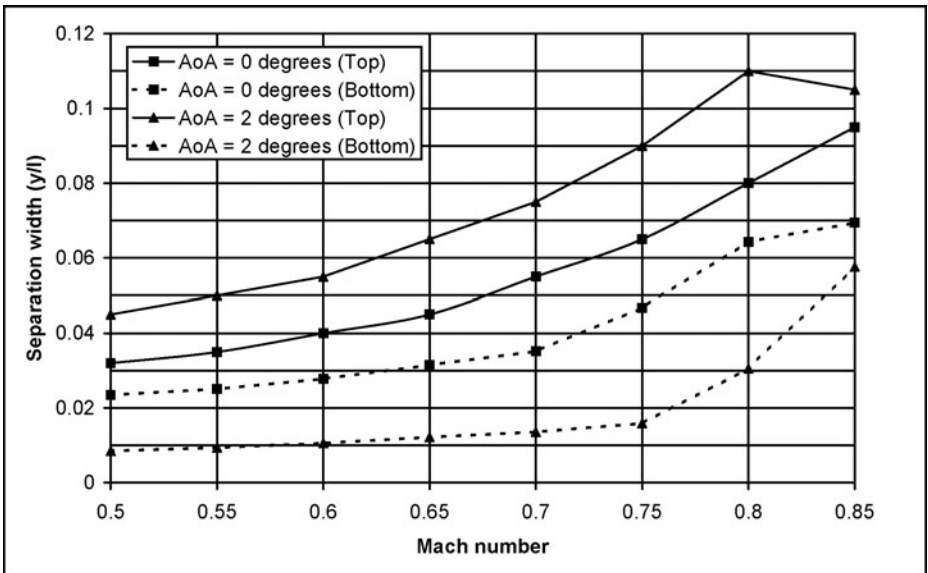
Fig. 5. Width of the NLR7301 corner separation by Mach number and angle of attack.
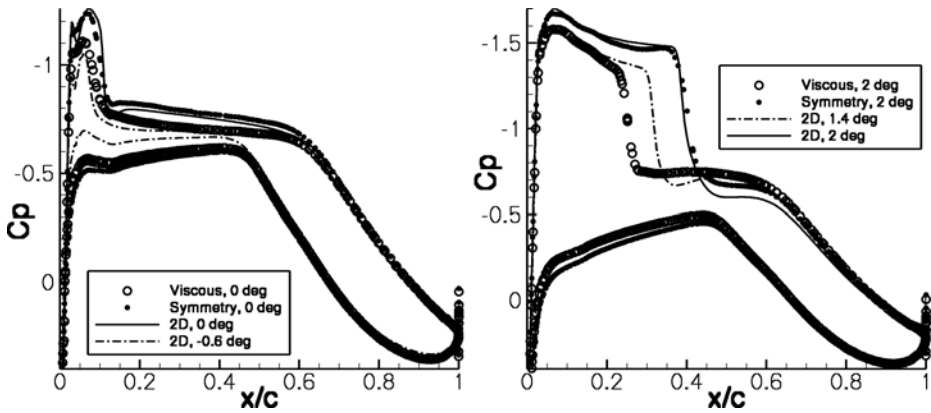
Fig. 6. Comparison of centerline pressures from computations with viscous and symmetry boundary conditions, compared with 2D computations. Left: $\alpha_{NLR}=0°$, Right: $\alpha_{NLR}=2°$.

best by the 2D computation with $\alpha_{2D}=1.4°$, an offset of -0.6°. Here the C_P on the pressure side of the airfoil, the pressure in the supersonic region, and the pressure after the shock are well matched, but the position of the shock is different. Figure 6 (Left) shows that, for $\alpha_{NLR}=0°$, the computation for the symmetric condition is relatively well matched by the 2D computation at $\alpha_{2D}=0°$, but the comparison for the viscous walls using $\alpha_{2D}=-0.6°$ has the C_P on the suction side of the airfoil is approximately correct, but the C_P on the pressure side of the airfoil completely wrong. It can be seen from Figure 5 that the "correct" α_{2D} will be a function of both Mach number and angle of attack. One solution is to use experimental models with a higher aspect ratio than 10/3, but stiffness and weight constraints often make this impossible.

3.2   The Aerostabil Wing at Mach 0.70

The Aerostabil 3D wing does not have the large corner separations seen on the NLR7301, with only a small corner separation at the trailing edge of the pressure side. The aeroelastic experiment requires the mounting of the model to be very stiff so that the elastic deformation of the model can be accurately measured. This means that peniches or splitter plates are avoided. The elastic wing is fixed directly to the TWG side-wall, with the wing root within the wind tunnel wall boundary layer. The result of this is that the model has an unusually high wall interference effect, which must be separated from the wake interference effect caused by the NLR7301. Thus the decision where to place the instrumentation in the wing depends on the extent of the effects of the boundary layer on the wing.

When the data for the symmetric wall condition is subtracted from the data for the viscous wall (Figure 7, left), it is clear that a large part of the wing is significantly affected by the wall. For a C_P difference on the order of 0.01, only positions on this model with y greater than 400 mm should be considered. Difference contours of C_P can also be used to show the effect of the NLR7301 wake on the Aerostabil wing at
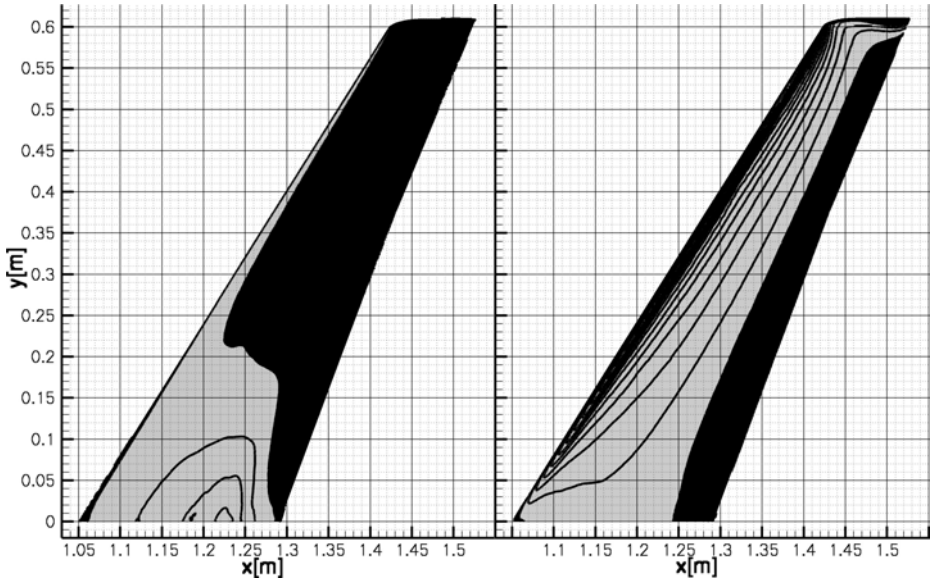
Fig. 7. Contours of C_P difference at $\alpha_{Aero}=0°$ Black is a difference of less than 0.05 and following contours are at steps of 0.05. Left: Differences due to the sidewall, Right: Differences due to wake of NLR7301 at $\alpha_{NLR}=2°$.

$\alpha_{Aero}=0°$ for $\alpha_{NLR}=2°$. Figure 7 (right) shows the difference contours between computations including the NLR7301, and computations with only the Aerostabil. Here it can be seen that the interference effect of the NLR7301 wake is to increase the pressures on the Aerostabil wing, similar to the effect of the sidewalls. While the effect of the sidewall is concentrated close to the wall, the wingtip shows a significant difference due to the NLR7301 wake. Thus separating the effects of the wing-tailplane interaction from the effect of the viscous wall will be challenge for the experimenters, but certainly possible in the outer portion of the wing.

4 Conclusion

Computations for the NLR7301 comparing viscous and symmetry sidewalls identified significant effects of the side-wall boundary layer separation. Here 3D separations form at the joint between the wall and both the upper and lower sides of the airfoil. These separations act as displacing bodies which accelerate the flow, changing the circulation around the airfoil, giving an effect similar to a reduction in angle of attack. Historically this effect has been corrected by testing at constant C_L (variable α), however further investigation using 2D computations with a corrected angle of attack could only approximately reproduce the effect shown, indicating that modelling the wind tunnel sidewalls is necessary. A comparison of the differences in pressure induced by the side-wall showed that positions on the Aerostabil model with distances from the wall greater

than 400 mm are best suited for instrumentation, helping considerably in preparing a successful validation experiment. The method of finding the optimal sensor positions is also applicable to other models and wind tunnels.

Acknowledgments

References

[1] http://www.centaursoft.com
[2] Dietz, G., Schewe, G., Kießling, F., Sinapius, M.: Limit-Cycle-Oscillation Experiments at a Transport Aircraft Wing Model. In: Proceedings IFASD 2003, Amsterdam (2003)
[3] Dietz, G., Schewe, G., Mai, H.: Experiments on heave/pitch limit cycle oscillations of a supercritical airfoil close to the transonic dip. J. Fluids and Structures 19 (2004)
[4] Edwards, J.R., Chandra, S.: Comparison of Eddy Viscosity-Transport Turbulence Models for Three-Dimensional, Shock-Separated Flowfields. AIAA Journal 34(4) (1996)
[5] Gardner, A.D.: Pre-Computations for the iGREEN Wing-Tailplane Interference Experiment in the TWG, DLR IB 224-2008 A19 (2008)
[6] Gerhold, T., Friedrich, O., Evans, J., Galle, M.: Calculation of Complex Three-Dimensional Configurations Employing the DLR-TAU-Code. AIAA 97-0167 (1997)
[7] Loic, L.B.: Calculation of Wall Contours for Interference Free Measurements of Flow Around Profiles, Diplomarbeit, DNW-GUK, Göttingen (1998)
[8] Poten, O.: Grenzschicht Untersuchung in Transsonische Windkanal Göttingen, DLR IB 29112-96B02
[9] Soda, A.: Numerical Investigation of Wing-Nacelle Interference Effects at Transonic Flow Conditions, DLR IB 232-2006 C02 (2006)
[10] Spalart, P.R., Allmaras, S.R.: A one-equation turbulence model for aerodynamic flows. AIAA Paper 92-0439 (1992)
[11] Voß, R. (ed.): Proceedings of the HighPerFlex Concluding Meeting, HighPerFlex CD (2006)
[12] Wilcox, D.C.: Turbulence Modeling for CFD. DCW Industries, California (1998)

The Influence of the Length Scale Equation on the Simulation Results of Aerodynamic Flows Using Differential Reynolds Stress Models

Bernhard Eisfeld

Institute of Aerodynamics and Flow Technology, German Aerospace Center (DLR),
Lilienthalplatz 7, 38108 Braunschweig, Germany
Bernhard.Eisfeld@dlr.de

Summary

The Stress-ω differential Reynolds stress model with the ω-equations of Wilcox, Kok and Menter and the SSG/LRR-ω, being always linked to the Menter ω-equation, have been applied to the transonic flow around the RAE 2822 airfoil and the ONERA M6 wing. Comparison with the Wilcox $k - \omega$ model shows the influence of replacing the k-equation and the Boussinesq hypothesis by the modeled Reynolds stress transport equation. Particularly for the M6 wing differential Reynolds stress models appear to be generally superior. Nevertheless the comparison between the different model variants reveals, that details of the length scale equation can have a larger influence than details of the re-distribution term modeling.

1   Introduction

The simulation quality of aerodynamic flows critically depends on the respective turbulence model, the strengths and weaknesses of which are particularly revealed in the case of separating flows. Except for massively separated flow, the concept of Reynolds averaged Navier-Stokes (RANS) equations is generally considered suitable for the simulation of technical flow problems. Within this framework mainly eddy viscosity models (EVM) are applied, that can be treated by standard CFD methods without particular problems at affordable additional cost. Nevertheless these models are of limited accuracy, especially for predicting separated flows [5].

A major reason for the failure of EVMs in complex flows is assumed to be the underlying Boussinesq hypothesis, setting the Reynolds stress tensor parallel to the strain rate tensor, where the eddy viscosity is a scalar scaling factor. Furthermore the production term, considered of major importance, needs to be modelled in EVMs, e. g. in the k-equation. In contrast, differential Reynolds stress models (DRSM) do not rely on the Boussinesq hypothesis but instead provide transport equations for the individual Reynolds stresses, where the production term is treated exactly. Having solved the problem of numerical robustness at still reasonable cost, DRSMs have been demonstrated to be applicable to complex aerodynamic flow problems [4], showing indeed improved predictions in many cases compared to EVMs [2].

However DRSMs need an additional equation for a length scale supplying variable, typically ϵ or ω, the influence of which on the model's accuracy is widely unknown. In the DLR TAU code different DRSMs are implemented, relying on different forms of the ω-equation. These equations can be integrated down to the wall (Low-Re models), avoiding wall-functions that might deteriorate the results in case of separation. In the following different ω-equations are combined with different DRSMs for investigating the influence of details of the length scale equation on the prediction of aerodynamic flows, in particular with separation.

2 Model Components

2.1 Reynolds Stress Equation

The modeled Reynolds stress equation applied here reads

$$\frac{\partial (\rho R_{ij})}{\partial t} + \frac{\partial}{\partial x_k} (\rho R_{ij} U_k) = -R_{ik}\frac{\partial U_j}{\partial x_k} - R_{jk}\frac{\partial U_i}{\partial x_k} - \frac{2}{3}\rho\epsilon\delta_{ij}$$
$$+\rho\Phi_{ij} + \frac{\partial}{\partial x_k}\left[\left(\mu\delta_{kl} + \mathcal{D}\frac{\rho}{\omega}R_{kl}\right)\frac{\partial R_{ij}}{\partial x_l}\right], \quad (1)$$

where ρ denotes the density, U_i the velocity components, μ the molecular viscosity, R_{ij} the components of the specific Reynolds stress tensor, $k = 0.5R_{ii}$ the specific kinetic turbulence energy, $\epsilon = 0.09k\omega$ the dissipation rate with ω the specific dissipation rate. The specific re-distribution tensor is written according to Speziale et al. [11] as

$$\Phi_{ij} = -\left(C_1\epsilon + C_1^* P^{(k)}\right) b_{ij} + C_2\epsilon\left(b_{ik}b_{kj} - \frac{1}{3}b_{mn}b_{mn}\delta_{ij}\right)$$
$$+ \left(C_3 - C_3^*\sqrt{b_{mn}b_{mn}}\right) kS_{ij} + C_4k\left(b_{ik}S_{jk} + b_{jk}S_{ik} - \frac{2}{3}b_{mn}S_{mn}\delta_{ij}\right)$$
$$-C_5k\left(b_{ik}W_{kj} - W_{ik}b_{kj}\right), \quad (2)$$

where $P^{(k)} = -R_{ij}\partial U_i/\partial x_j$ represents the production of kinetic turbulence energy, $b_{ij} = R_{ij}/(2k) - \delta_{ij}/3$ is the anisotropy tensor, and S_{ij} and W_{ij} are the symmeric and the antisymmetric part of the velocity gradient tensor $\partial U_i/\partial x_j$, respectively.

Two different DRSMs are considered, i. e. the Stress-ω model by Wilcox [13], using constant coefficients according to the Launder-Reece-Rodi (LRR) model [7], and the SSG/LRR-ω model [4], blending all coefficients $\varphi_{DRSM} = \mathcal{D}, C_i, C_i^*$ between the values of the LRR and the Speziale-Sarkar-Gatski (SSG) model [11] according to

$$\varphi_{DRSM} = F_1\varphi_{DRSM}^{(LRR)} + (1 - F_1)\varphi_{DRSM}^{(SSG)}, \quad (3)$$

where F_1 is the blending function of Menter's k-ω models [9], changing gradually from $F_1 = 1$ at the wall to $F_1 = 0$ further away. Table 1 shows the values of the closure coefficients refering to the LRR and SSG model, respectively.

Table 1. DRSM closure coefficients.

	$\mathcal{D}$	C_1	C_1^*	C_2	C_3	C_3^*	C_4	C_5
LRR	0.50	3.6	0	0	0.8	0	2.00	1.11
SSG	2.44	3.4	1.8	4.2	0.8	1.3	1.25	0.40

2.2   Length Scale Equation

The above Reynolds stress transport equation is supplemented with a ω-equation for supplying the length scale that can be written in the following generalized form

$$\frac{\partial (\rho\omega)}{\partial t} + \frac{\partial}{\partial x_k}\left(\rho\omega U_k\right) = -\alpha\frac{\omega}{k}R_{ik}\frac{\partial U_i}{\partial x_k} - \beta\rho\omega^2 + \frac{\partial}{\partial x_k}\left[\left(\mu + \sigma\frac{\rho k}{\omega}\right)\frac{\partial \omega}{\partial x_k}\right]$$
$$+ \sigma_d\frac{\rho}{\omega}\max\left(\frac{\partial k}{\partial x_k}\frac{\partial \omega}{\partial x_k}; 0\right). \tag{4}$$

The equations considered differ only in the coefficients $\varphi_\omega = \alpha, \beta, \sigma, \sigma_d$ where in case of Menter's ω equation their values vary from the wall ($\varphi_\omega^{(1)}$) to the outer edge of the boundary layer ($\varphi_\omega^{(2)}$) as the DRSM coefficients in eq. (3), i. e.

$$\varphi_\omega = F_1\varphi_\omega^{(1)} + (1 - F_1)\varphi_\omega^{(2)}. \tag{5}$$

Table 2 shows the values of the closure coefficients for the ω-equations by Wilcox [12], Kok [6] and Menter [9]. As one can see, the Kok equation only adds a cross-diffusion term to the Wilcox equation, whereas the Menter equation additionally involves a gradual change of the coefficient values. Note, that the Stress-ω model can be combined with any of these equations, whereas the SSG/LRR-ω model strictly requires the Menter ω-equation for closure.

Table 2. Closure coefficients of ω-equations.

	$\alpha^{(1)}$	$\alpha^{(2)}$	$\beta^{(1)}$	$\beta^{(2)}$	$\sigma^{(1)}$	$\sigma^{(2)}$	$\sigma_d^{(1)}$	$\sigma_d^{(2)}$
Wilcox [12]	0.5556	0.5556	0.075	0.075	0.5	0.5	0	0
Kok [6]	0.5556	0.5556	0.075	0.075	0.5	0.5	0.5	0.5
Menter [9]	0.5556	0.44	0.075	0.0828	0.5	0.856	0	1.712

3   Results

The Stress-ω model with the ω-equations by Wilcox, Kok and Menter as well as the SSG/LRR-ω model, always using the Menter ω-equation, have been applied to typical transonic test cases, particularly involving shock induced separation. The comparison of the results gives some insight into the influence of details of the length scale equation compared to the influence of the re-distribution model.

3.1   RAE 2822 Airfoil

The transonic flow around the RAE 2822 airfoil is a widespread test for turbulence models in aerodynamics, particularly the conditions refered to as Case 9 (Mach number $Ma = 0.73$, Reynolds number $Re = 6.5 \cdot 10^6$, incidence $\alpha = 2.8^0$) and Case 10 (Mach number $Ma = 0.75$, Reynolds number $Re = 6.2 \cdot 10^6$, incidence $\alpha = 2.8^0$) [1]. In particular for Case 10 the occurring shock on the suction side of the airfoil induces separation.

Case 9 and Case 10 have been computed on a very fine structured grid with 736×176 cells, yielding fairly grid independent solutions. Fig. 1 shows the corresponding pressure distributions obtained with the four DRSM variants and the Wilcox $k - \omega$ model for comparison. Replacing the k-equation and Boussinesq hypothesis by the Reynolds stress transport equation obviously improves the prediction of the shock location. However, exchanging the Wilcox by the Kok ω-equation, shifts the shock position upstream by roughly the same amount. Obviously the cross-diffusion term in the latter, supposed to be active only in the outer part of the boundary layer, has a significant influence. In contrast the difference between the SSG/LRR-ω and the Stress-ω model, both using the Menter ω-equation, is rather small, despite of the differing terms in the Reynolds stress transport equation, particularly the re-distribution tensor.

As one can see from Fig. 2, the predicted shock location is directly related to the predicted wall shear stress level upstream of the shock. The higher C_f, the further downstream the shock is located. As one can see, using a Reynolds stress transport model instead of a k-based EVM leads to a similar reduction in C_f as the cross-diffusion term, present in the ω-equations of Kok and Menter, confirming the above observation on the C_p-distribution.

3.2   ONERA M6 Wing

The ONERA M6 wing is a low aspect ratio tapered wing, representing a three-dimensional counterpart to the RAE 2822 airfoil for testing turbulence models. In particular the flow at a Mach number of $Ma = 0.84$ is considered here at incidences ranging from $\alpha = 0.04^o$ to $\alpha = 6.06^o$. The Reynolds number varies between $Re = 11.71 \cdot 10^6$ and $Re = 11.82 \cdot 10^6$. Only experimental pressure distributions in seven cross-sections are available [1], indicating no lift breakdown up to $\alpha = 6.06^o$.

The computations have been carried out on a grid, consisting of $4.5 \cdot 10^6$ nodes, which is considered fine enough for obtaining fairly grid independent solutions [3]. In particular it has been checked, that in all computations the wall distance of the wall nearest grid points, d_1, corresponds to a value of $y_1^+ = d_1 u_\tau / \nu < 1$ on the entire wing, where u_τ is the friction velocity, and ν is the kinematic viscosity of the fluid.

Fig. 3 shows the computed lift curves and polars for the different DRSM variants and the Wilcox $k - \omega$ model for comparison. As one can see, at lower incidences up to $\alpha = 4.08^o$ the results for the lift coefficient are virtually identical for all models, whereas at higher incidence, deviations can be observed. The same holds for the polar, except that at small angles of attack the Wilcox $k - \omega$ model yields a significantly larger drag coefficient C_D than any of the DRSMs. At $\alpha = 0.04^o$, which is close to zero lift, the C_D-value predicted by the Wilcox $k - \omega$ model is 9.5% higher than the lowest C_D predicted by the Stress-ω model with the Kok ω-equation.
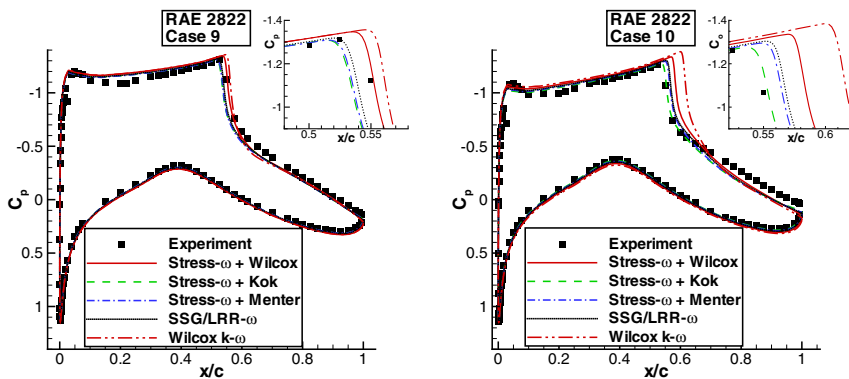
Fig. 1. RAE 2822. Pressure distributions for Case 9 and Case 10.
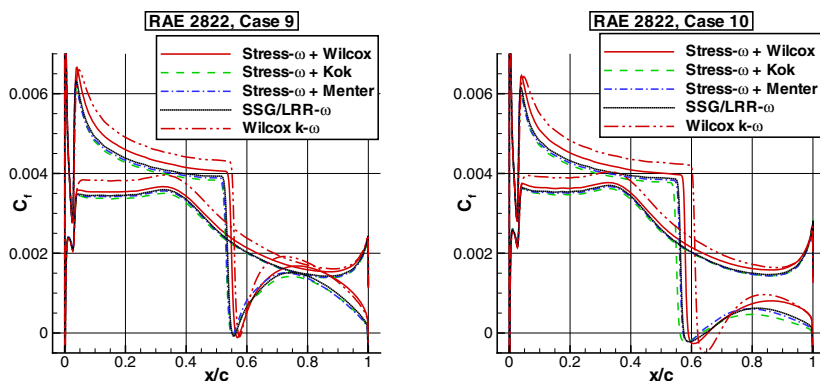
Fig. 2. RAE 2822. Shear stress distributions for Case 9 and Case 10.
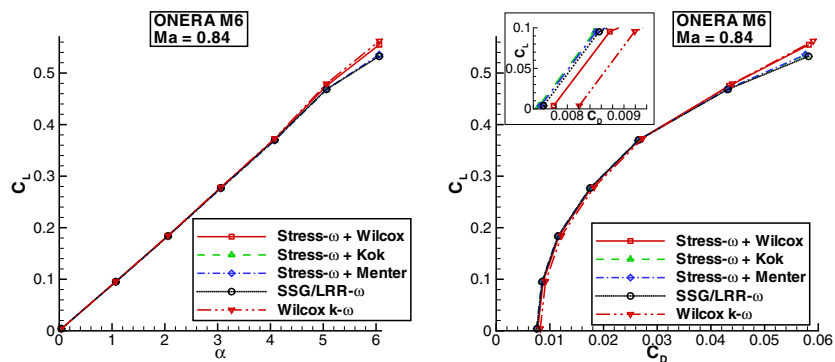
Fig. 3. ONERA M6 wing, $Ma = 0.84$. Computed lift curves (left) and polars (right).
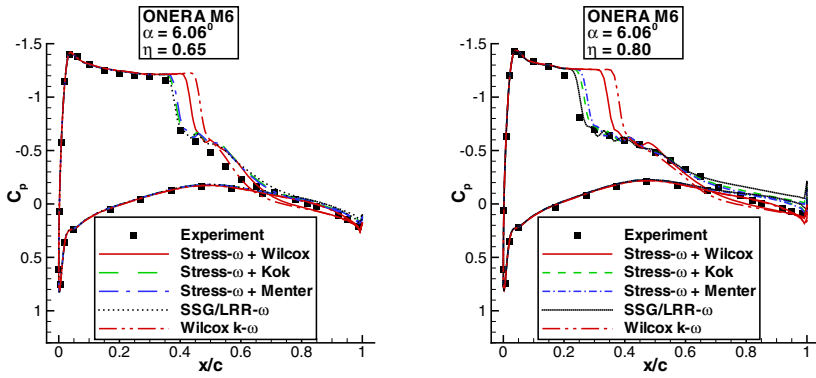
Fig. 4. ONERA M6 wing, $\alpha = 6.06^o$. Pressure distributions at 65% and 80% span.
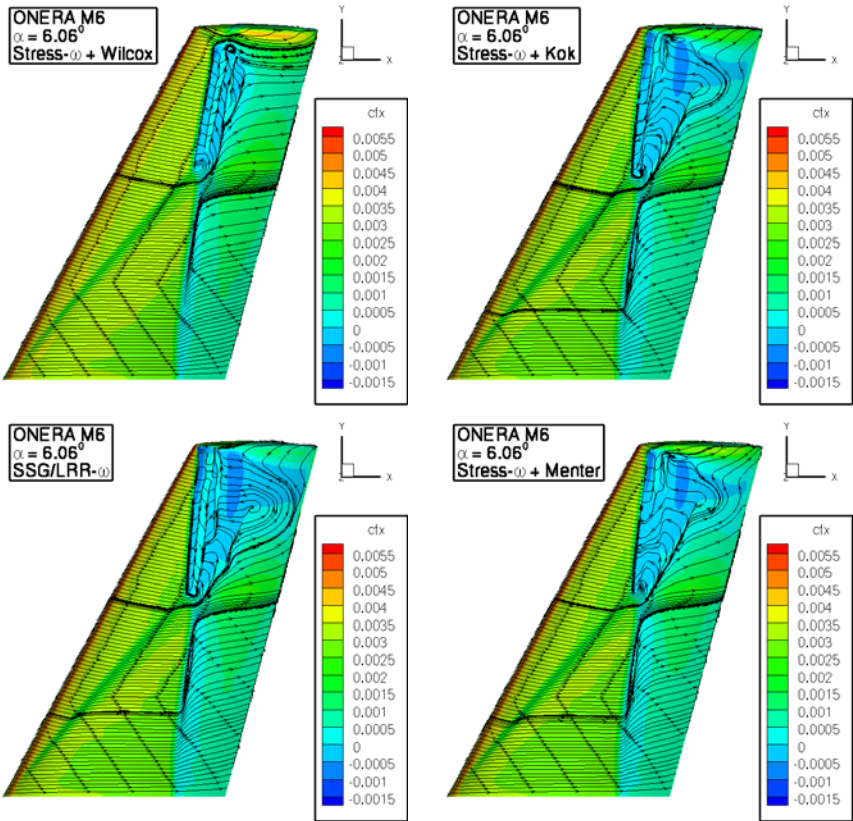
Fig. 5. ONERA M6 wing, $\alpha = 6.06^0$. Friction lines for different DRSM variants. Colors indicate x-component of friction coefficient, $C_{f,x}$.

Fig. 4 shows the pressure distributions in two sections at 65% and at 80% span at the highest incidence of $\alpha = 6.06^o$. Similar to the results for the RAE 2822 airfoil the Wilcox $k - \omega$ model predicts the shock the furthest downstream. Replacing the k-equation and the Boussinesq hypothesis by the Reynolds stress transport equation shifts the shock further upstream, thus improving the prediction. Anyway, replacing the Wilcox by the Kok ω-equation, i. e. adding a cross-diffusion term, leads to significantly better agreement with the experiment up to 80% span. In comparison the differences between the SSG/LRR-ω and the Stress-ω model with the Menter ω-equation are much smaller, indicating only little influence of the re-distribution modeling.

Fig. 5 shows the friction lines on the upper surface of the ONERA M6 wing at $\alpha = 6.06^o$ predicted by the four DRSM variants. As one can see, a complex, shock induced separation pattern forms, where the Stress-ω model with the Wilcox ω-equation predicts the smallest chordwise recirculation zone. Replacing the Wilcox by the Kok or Menter ω-equation this separation extends almost to the trailing edge, where the SSG/LRR-ω model yields a slightly larger spanwise width.

Note, that in the outboard sections beyond 90-95% span the Stress-ω model with the Wilcox ω-equation gives the best agreement with the experimental pressure distribution which is probably a positive countereffect of its tendency to underpredict separation. Note further, that with any other EVM tried, including Menter SST [9] and Spalart-Allmaras [10], a sudden lift breakdown has been observed below an incidence of $\alpha = 5.06^o$ which is in contradiction to the experimental pressure distributions. Thus these models completely fail to predict the flow at $\alpha = 6.06^o$.

4 Conclusion

Four different DRSM variants have been applied to the transonic flow around the RAE 2822 airfoil (Case 9 and 10) and the ONERA M6 wing at $Ma = 0.84$, exhibiting shock-induced separation. As it comes out, replacing the k-equation and the Boussinesq hypothesis in the Wilcox $k - \omega$ model by a modeled Reynolds stress transport equation (Stress-ω model), reduces the skin friction and moves the shock position upstream, thereby improving the predictions. Nevertheless, replacing the Wilcox by the Kok or Menter ω-equation, i. e. adding a cross-diffusion term, further improves the predictions by almost the same amount. In contrast the differences between the predictions by the SSG/LRR-ω and the Stress-ω model, both using the Menter ω-equation, are only minor. The results for the ONERA M6 wing at $\alpha = 6.06^o$ show a spanwise slightly wider separation zone with the SSG/LRR-ω model, that is supposed to be mainly attributed to the different re-distribution models in the Reynolds stress transport equation.

Thus one has to conclude that the length scale equation is of major importance for DRSM predictions. Wall normal ω-distributions upstream the shock (not shown due to restricted space) reveal lower ω in the outer part of the boundary layer, when using the Wilcox ω-equation. This indicates that the known freestream sensitivity of the latter due to a missing cross-diffusion term [8] is a major source of discrepancies. Nevertheless for the ONERA M6 wing the DRSMs have generally shown to be superior to EVMs, because, except the rather inaccurate Wilcox $k - \omega$ model, all other tested EVMs yield lift break down below an incidence of $\alpha = 5.06^o$, which is in contradiction to the experimental pressure distributions.

References

[1] Barche, J. (ed.): Experimental Data Base for Computer Program Assessment, AGARD-Report AGARD-AR-138 (1979)

[2] Eisfeld, B.: Numerical simulation of aerodynamic problems with a Reynolds stress model. In: Rath, H.-J., Holze, C., Heinemannm, H.-J., Henke, R., Hönlinger, H. (eds.) New Results in Numerical and Experimental Fluid Mechanics V, Notes on Numerical Fluid Mechanics and Multidisciplinary Design, vol. 92, pp. 413–419 (2006)

[3] Eisfeld, B.: Numerical Simulation of Aerodynamic Problems with the SSG/LRR-ω Reynolds Stress Model Using the Unstructured TAU Code. In: Tropea, C., Jakrilić, S., Heinemannm, H.-J., Henke, R., Hönlinger, H. (eds.) New Results in Numerical and Experimental Fluid Mechanics VI, Notes on Numerical Fluid Mechanics and Multidisciplinary Design, vol. 96, pp. 356–363 (2007)

[4] Eisfeld, B., Brodersen, O.: Advanced Turbulence Modelling and Stress Analysis for the DLR-F6 Configuration. AIAA-Paper 2005-4727 (2005)

[5] Haase, W., Aupoix, B., Bunge, U., Schwamborn, D. (eds.): FLOMANIA – A European Initiative on Flow Physics Modelling. Notes on Numerical Fluid Mechanics, vol. 94. Springer, Heidelberg (2006)

[6] Kok, J.C.: Resolving the Dependence on Freestream Values for the $k-\omega$ Turbulence Model. AIAA Journal 38(7), 1292–1295 (2000)

[7] Launder, B.E., Reece, G.J., Rodi, W.: Progress in the development of a Reynolds-stress turbulence closure. Journal of Fluid Mechanics 68, 537–566 (1975)

[8] Menter, F.R.: Influence of Freestream Values on k-ω Turbulence Model Predictions. AIAA Journal 30(6), 1657–1659 (1992)

[9] Menter, F.R.: Two-Equation Eddy-Viscosity Turbulence Models for Engineering Applications. AIAA Journal 32, 1598–1605 (1994)

[10] Spalart, P.R., Allmaras, S.R.: A One-Equation Turbulence Model for Aerodynamic Flows. AIAA-Paper, 92-439 (1992)

[11] Speziale, C.G., Sarkar, S., Gatski, T.B.: Modelling the pressure-strain correlation of turbulence: an invariant dynamical systems approach. Journal of Fluid Mechanics 227, 245–272 (1991)

[12] Wilcox, D.C.: Reassessment of the Scale Determining Equation for Advanced Turbulence Models. AIAA Journal 26, 1299–1310 (1988)

[13] Wilcox, D.C.: Turbulence Modeling for CFD, 2nd edn., DCW Industries, La Cañada, USA (1998)

Efficient Flow Computation Including Turbulent Transport

C.-C. Rossow[1] and R.C. Swanson[2]

[1] DLR, Institut für Aerodynamik und Strömungstechnik, Lilienthalplatz 7
D-38108 Braunschweig, Germany
`cord.rossow@dlr.de`
[2] NASA Langley Research Center, Hampton, Virginia, VA-23681-2199, USA
`r.c.swanson@nasa.gov`

Summary

Runge-Kutta/Implicit methods for the solution of the Navier-Stokes equations provide superior convergence rates, especially when combined with a multigrid framework. In previous investigations [7,8,10], the algebraic model of Baldwin and Lomax [1] was employed as turbulence model. In the present contribution, this model is replaced by the model of Spalart and Allmaras [9], where an additional partial differential equation has to be solved. The design of an appropriate solution strategy to solve this additional equation and account for the necessary coupling to the system of main flow equations to maintain the favorable convergence rates of the basic scheme are outlined and discussed. Different cases of turbulent subsonic and transonic flow around airfoils are considered to assess the convergence properties of the resulting algorithm. Comparison with results of previous investigations confirms that the high efficiency of the basic Runge-Kutta/Implicit method is not impaired when adding an equation for turbulent transport.

1 Introduction

Efficient solution of the Navier-Stokes equations still represents a significant challenge, especially when at high Reynolds numbers the resolution of thin boundary layers requires highly stretched meshes with very high cell aspect ratios. These problems are substantially aggravated when additional equations need to be solved to model the influence of turbulence. Here, not only the way of coupling these equations to the main equations is a matter of concern, but large source terms need to be properly taken care of, especially in the context of multigrid acceleration.

In previous work, the authors proposed Runge-Kutta/Implicit (RK/I) methods for efficient solution of the Euler and Navier-Stokes equations [7,8,10]. These methods showed superior performance with respect to standard solution techniques: the number of multigrid cycles required for a converged solution was reduced by more than an order of magnitude, and corresponding CPU times by a factor of 5.

In the present work the algorithm of Ref. [7,8] is extended to incorporate the partial differential equation based turbulence model of Spalart and Allmaras [9], instead of the purely algebraic model of Baldwin and Lomax [1] used in the previous investigations. In order to maintain the favorable convergence rates of the basic algorithm, special care has to be taken to efficiently solve the turbulence equation with its source terms, and to couple the solution of this equation into the algorithm for solution of the main equations. The performance of the resulting method will be assessed by computing turbulent, compressible and incompressible flow around airfoils at various Reynolds numbers.

2 Governing Equations

We consider the two-dimensional compressible Navier-Stokes equations. For a control volume fixed in time and space, the system of partial differential equations in integral form in a Cartesian reference frame is given by:

$$\iint_{Vol}\frac{\partial \vec{W}}{\partial t}\,dV \;+\; \int_{S}\overline{F}\cdot\vec{n}\;dS = 0 \; , \tag{1}$$

where $\vec{W}=[\rho,\rho u,\rho v,\rho E]^{T}$ represents the vector of conservative variables, $\overline{F}$ is the flux-density tensor, and Vol, S, and $\vec{n}$ denote volume, surface, and outward facing normal of the control volume.

For technically relevant flows, the scales of turbulent motion cannot be resolved, and the influence of turbulence has to be modeled. Spalart and Allmaras [9] define a transport equation for a turbulence variable $\tilde{v}$ to provide a turbulent eddy viscosity. Here, a rearranged form following Ref. [11] is used:

$$\begin{aligned}
\frac{\partial \tilde{v}}{\partial t}+u_j\frac{\partial \tilde{v}}{\partial x_j} &= C_{b1}(1-f_{t2})|\boldsymbol{\Omega}|\tilde{v}+\left\{C_{b1}\left[(1-f_{t2})f_{v2}+f_{t2}\right]\kappa^{-2}-C_{w1}f_w\right\}\!\left(\frac{\tilde{v}}{d}\right)^{2}\\
&\quad+\frac{1}{\sigma}\frac{\partial}{\partial x_j}\left[(v+(1+C_{b2})\tilde{v})\frac{\partial \tilde{v}}{\partial x_j}\right]-\frac{C_{b2}}{\sigma}\tilde{v}\frac{\partial^2 \tilde{v}}{\partial x_j^2}
\end{aligned} \tag{2}$$

where $\boldsymbol{\Omega}$ denotes vorticity, x_j and u_j denote Cartesian coordinates and velocity components using tensor notation, and d is the distance to the closest wall boundary. The definition of the model constants follows from Ref. [9,11].

3 Basic Solution Scheme

The basic solution scheme uses a cell centered, finite volume space discretization on structured meshes [6]. A semi-discrete form of equation (1) may be written as:

$$\frac{\partial \vec{W}_{i,j}}{\partial t}+\frac{1}{Vol_{i,j}}\sum_{k=1}^{K}\overline{F}_{\perp,k}\,S_k = 0 \; , \tag{3}$$
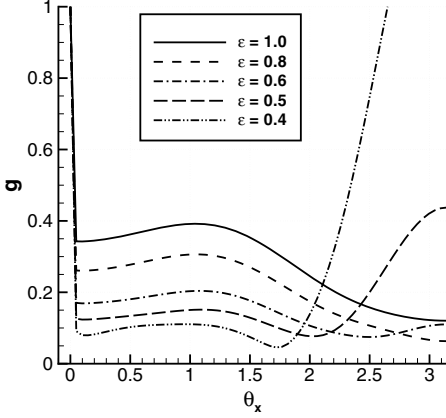
Fig. 1. Amplification of 3-stage RK/I scheme   **Fig. 2.** Pressure distribution (SA-model)
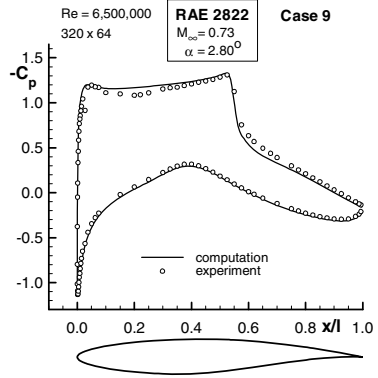
where the indices i,j denote a computational cell in the flow field, *Vol* is the volume of cell i,j, $\overline{F}_\perp$ is the flux density vector corresponding to the direction normal to a cell face S, and K represents the maximum number of cell faces of the control volume with k as running index. For discretization, Flux Difference Splitting [5] using the Mach number based implementation of Ref. [6] is used.

Time integration of Eq. (3) is achieved by the Runge-Kutta/Implicit (RK/I) method proposed in Ref. [7,8]. In a Runge-Kutta scheme, variables of $\vec{W}$ are updated by:

$$\vec{W}_{i,j}^{(m)} = \vec{W}_{i,j}^{(0)} + \alpha^{(m)} \cdot \vec{R}_{i,j}^{(m-1)} \; , \tag{4}$$

where superscript (m) denotes the stage count, and $\alpha^{(m)}$ is the coefficient of the mth-stage. The vector $\vec{R}_{i,j}^{(m-1)}$ represents residuals evaluated with the variables of the previous $(m\text{-}1)$-stage. Following Refs. [7,8], at each stage the explicit Runge-Kutta time stepping of Eq. (4) is augmented by an implicit preconditioning step:

$$\left(\bar{I} + \varepsilon \frac{\delta t_{i,j}}{Vol_{i,j}} \sum_{k=1}^{K} \overline{A}_{\perp,k}^{+} S_k \right) \tilde{\tilde{R}}_{i,j} = \vec{R}_{i,j}^{(m-1)} - \varepsilon \frac{\delta t_{i,j}}{Vol_{i,j}} \sum_{k=1}^{K} \overline{A}_{\perp,k}^{-} S_k \, \tilde{\tilde{R}}_{NB(k)} \; , \tag{5}$$

where $NB(k)$ indicates the neighbor of cell i,j corresponding to face k, $\bar{I}$ is the identity matrix, $\delta t_{i,j}$ the local time step of cell i,j, and ε a user specified smoothing parameter. The two matrices $\overline{A}_\perp^{+}$ and $\overline{A}_\perp^{-}$ represent the positive and negative parts of the flux Jacobian $\overline{A}_\perp$ corresponding to the direction normal to a cell face S.

The preconditioned residuals $\tilde{\tilde{R}}$ obtained from the solution of Eq. (5) are used in the Runge-Kutta framework given by Eq. (4) for updating conservative variables:

$$\vec{W}_{i,j}^{(m)} = \vec{W}_{i,j}^{(0)} + \alpha^{(m)} \cdot \tilde{\tilde{R}}_{i,j} \; , \tag{6}$$

Figure 1 shows the amplification factor g of a 3-stage scheme defined by Eqs. (5) to (6) determined from a one-dimensional Fourier analysis of Swanson et al. [10]. In the present investigation, ε is specified as $\varepsilon = 0.5$ on the finest mesh, and $\varepsilon = 0.4$ on all coarser meshes, being identical to previous investigations [7,8].

Since the RK/I scheme removes the CFL restriction of the basic explicit method, CFL numbers in the order of 1000 are used [7]. Time integration is further enhanced by employing multigrid following the ideas of Jameson [4].

4   Implementation of the One-Equation Turbulence Model

Following the original work of Spalart and Allmaras [9], a first order, non-conservative discretization of eq. (2) is employed. Considering an implicit notation, this leads to the discrete form:

$$\left(I + L_x + L_y + S\right)\Delta \tilde{\nu} = -R , \tag{7}$$

where L_x, L_y are first order linear operators, S is the source term containing production and destruction of turbulence, and R is the residual function.

The main equations (1) and the turbulence equation (2) are solved in a loosely coupled manner. When solving the main equations (1), eq. (2) is solved at each stage of the RK/I scheme on the finest mesh only. Turbulent viscosity is then transferred to the coarser meshes and frozen. Eq. (2) is solved in the framework of the RK/I scheme for the main equations by three different approaches:

1. A Diagonally Dominant Alternating Direction Implicit (DDADI) scheme following the work of Faßbender [3].
2. A Symmetric Line Gauss-Seidel (SLGS) method, which is employed along the grid lines perpendicular to the solid wall and wake-cut boundary to account for the direction of maximum stiffness.
3. A 2-stage RK/I scheme (RKI-SGS) with the same Symmetric Gauss-Seidel iteration as for the main equations. To appropriately treat the source term in eq. (2), this is augmented by a local line symmetric relaxation sweep in the boundary layer and in the wake.

To further enhance efficiency and robustness when solving eq. (2), the three different solution strategies, namely DDADI, SLGS, and RKI-SGS, are supported by a V-cycle multigrid algorithm. Here, a W-cycle did not offer advantages in efficiency. The multigrid algorithm to solve eq. (2) is called at each stage of the fine mesh RK/I scheme when solving the main equations (1).

5   Computational Results

Structured C-meshes around the RAE 2822 airfoil are used. Since grid lines are directly identified, implementation of the line-solves for DDADI and SLGS is straightforward. The line relaxation added to the RKI-SGS scheme is employed from the wall or wake-cut boundary to 1/4 of the computational domain in j-direction, with the j-direction being perpendicular to the wall or wake-cut boundary. A 4-level W-cycle is employed in the
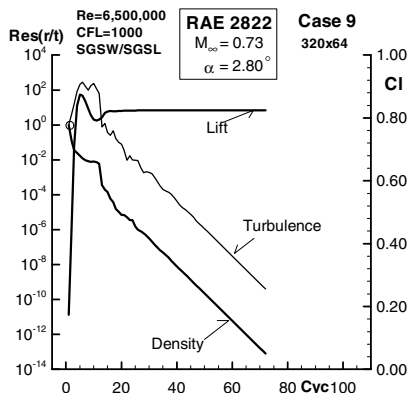
Fig. 3. Convergence for Case 9 (320x64)
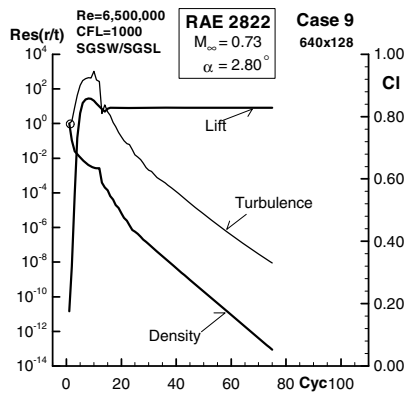
Fig. 4. Convergence for Case 9 (640x128)

multigrid algorithm for the main equations (1). The same number of levels is used in the V-cycle multigrid of the turbulence equation (2). On the finest mesh, a second order discretization is employed. On coarse meshes discretization for advection terms is reduced to first order.

5.1   Compressible, Turbulent Flow at Moderate Reynolds Numbers

First, the convergence properties at moderate Reynolds numbers are investigated using the C-meshes with 320x64 and 640x128 cells of Ref. [7,8]. Computations are terminated when the density residual is decreased by 13 orders of magnitude.

For the transonic Case 9 $(M_\infty = 0.73; \alpha = 2.31°; Re = 6,500,000)$ of Ref. [2], Figure 2 shows the pressure distribution obtained with the Spalart-Allmaras turbulence model. Table 1 summarizes the convergence behavior of the method with DDADI, SLGS, or RKI-SGS to solve the turbulence equation. Without employing multigrid for the turbulence equation, on the 320x64 mesh one call of DDADI or SLGS suffices. Refining the mesh to 640x128 cells, the number of calls has to be doubled; however, using the V-cycle multigrid leads to grid independent convergence with only one call of DDADI or SLGS. Computation times for DDADI and SLGS are very similar. Due to the point-implicit nature of the RKI-SGS scheme, it requires support from the V-cycle. With the multigrid the scheme exhibits grid independent convergence. Note that the computation times for the RKI-SGS scheme are only about 5-10% higher than for the fully line-implicit algorithms. Additionally, a computation of the same case with the well-tuned reference method used in Ref. [7,8] is included in Table 1. Following Ref. [3], the equation of the Spalart-Allmaras turbulence model is solved only once at the beginning of the 5-stage Runge-Kutta scheme by employing the DDADI scheme without multigrid. With respect to the reference method computation time is reduced by about a factor of five, confirming the superior performance of the RK/I scheme. In Figures 3 and 4, convergence histories for density and turbulence

Table 1. Comparison of time-integration strategies for turbulence equation (Case 9)

Method	Grid	MG	# Calls	# Cycles	Cpu Time
DDADI	320 x 64	None	1	71	199
DDADI	320 x 64	None	2	72	217
DDADI	320 x 64	4 V	1	72	214
DDADI	640 x 128	None	2	77	968
DDADI	640 x 128	4 V	1	74	913
SLGS	320 x 64	None	1	72	199
SLGS	320 x 64	None	2	71	208
SLGS	320 x 64	4 V	1	72	211
SLGS	640 x 128	None	2	80	976
SLGS	640 x 128	4 V	1	74	895
RKI-SGS	320 x 64	4 V	1	72	228
RKI-SGS	640 x 128	4 V	1	73	951
RK5/3-S	320x64	None	---	1648	1078

residuals are displayed when using the RKI-SGS scheme for solving the turbulence equation. The residual of the turbulence equation is reduced with an asymptotic convergence rate similar to that of the main equations.

For the more severe Case 10 $(M_\infty = 0.75; \alpha = 2.80°; \text{Re} = 6,200,000)$, Figures 5 and 6 show the convergence histories with the RKI-SGS scheme on the 320x64 and 640x128 meshes for solving the turbulence equation. Corresponding results for the subsonic Case 1 $(M_\infty = 0.676; \alpha = 1.93°; \text{Re} = 5,700,000)$ are displayed in Figures 7 and 8. Following the investigations of Ref. [7,8], here on the finest mesh a pure second order reconstruction of variables without limiting is employed.
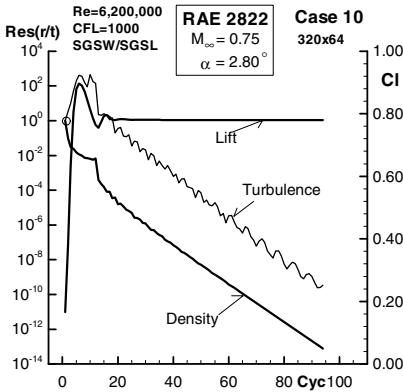
Fig. 5. Convergence for Case 10 (320x64)
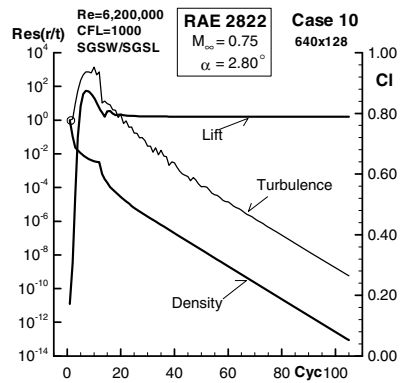
Fig. 6. Convergence for Case 10 (640x128)
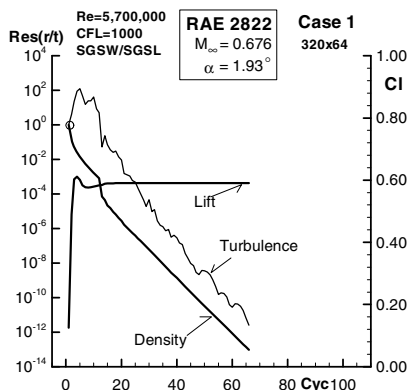
Fig. 7. Convergence for Case 1 (320x64)
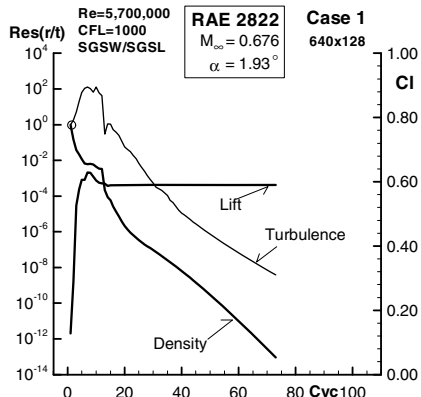
Fig. 8. Convergence for Case 1 (640x128)
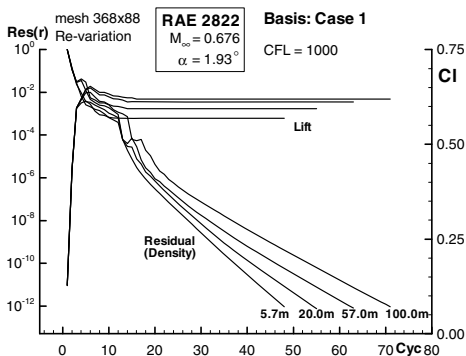
Fig. 9. Re-variation; density residual
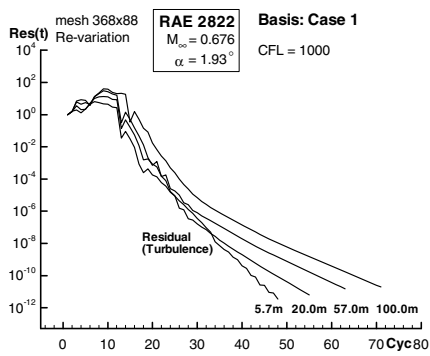
Fig. 10. Re-variation; turbulence residual

5.2 Compressible, Turbulent Flow at High Reynolds Numbers

Second, sensitivity of the method to variation in Reynolds number is investigated. Starting from the subsonic conditions of Case 1, Reynolds number is varied from $Re = 5.7x10^6$ to $Re = 100x10^6$. The C-meshes from Ref. [3] with 368x88 cells are used, which were adapted to Reynolds number, leading to cell aspect ratios varying from about 3,000 to over 50,000. Figures 9 and 10 show the convergence histories for density and turbulence residual, respectively. Despite a variation of Reynolds number by more than an order of magnitude, the number of cycles required to reduce the density residual by 12 orders of magnitude increased only by somewhat less than 50% with respect to computation at the lowest Reynolds number.
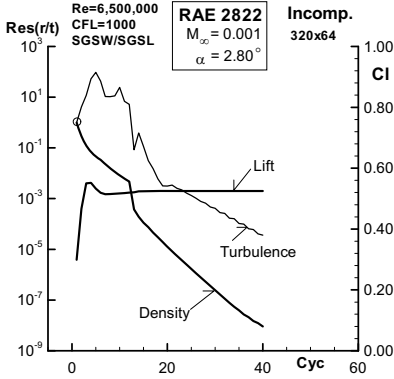
Fig. 11. Incompressible flow (320x64)   **Fig. 12.** Incompressible flow (640x128)
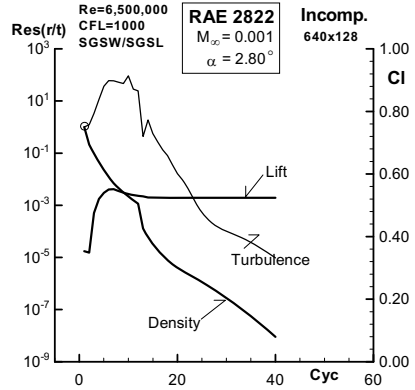
5.3 Incompressible, Turbulent Flow

Last, incompressible flow is computed on the 320x64 and 640x128 meshes. Except for the free-stream Mach number of $M_\infty = 0.001$, the on-flow conditions are similar to Case 1. Figures 11 and 12 show the convergence histories of density and turbulence residuals. Here the density residual is decreased by only eight orders of magnitude to avoid round-off errors [8].

6   Conclusion

The one-equation turbulence model of Spalart and Allmaras was integrated into a Runge-Kutta/Implicit scheme by loosely coupling the solutions of main equations and turbulence equation. For efficient computation, the turbulence equation was solved at each stage of the main equations Runge-Kutta/Implicit method on the finest mesh. Three different strategies for solving the turbulence equation, namely a Diagonal Dominant Alternating Direction Implicit, a Symmetric Line Gauss-Seidel, and a Runge-Kutta/Implicit method with local line solves were investigated. Adding a V-cycle multigrid algorithm for the solution of the turbulence equation, grid independent convergence was achieved. Computation times of the three strategies were similar, and comparison with a well-tuned reference method showed that the superior performance of the Runge-Kutta/Implicit method for solving the main equations was not degraded when adding the solution of a turbulence transport equation. Variation of Reynolds number by more than an order of magnitude showed a low sensitivity to discrete stiffness of large cell aspect ratios, and the applicability to incompressible flows was demonstrated by computing flow at a free-stream Mach number of $M_\infty = 0.001$.

References

1. Baldwin, B., Lomax, H.: Thin Layer Approximation and Algebraic Turbulence Model for Separated Turbulent Flows. AIAA-Paper 78-257 (1987)
2. Cook, P.H., McDonald, M.A., Firmin, M.C.P.: Aerofoil RAE2822 Pressure Distributions and Boundary Layer and Wake Measurements. AGARD-AR-138 (1979)
3. Faßbender, J.: Improved Robustness of Numerical Simulation of Turbulent Flows around Civil Transport Aircraft at Flight Reynolds Numbers. Ph.D. Thesis, Technical University of Braunschweig (2004),
   http://opus.tu-bs.de/opus/volltexte/2004/579
4. Jameson, A.: Multigrid Algorithms for Compressible Flow Calculations. In: Hackbusch, W., Trottenberg, U. (eds.) Second European Conference on Multigrid Methods, Cologne. Lecture Notes in Mathematics, vol. 1228. Springer, Berlin (1985/1986)
5. Roe, P.L.: Approximate Riemann Solvers, Parameter Vectors and Difference Schemes. J. Comput. Phys. 43, 357–372 (1981)
6. Rossow, C.-C.: A Flux Splitting Scheme for Compressible and Incompressible Flows. J. Comput. Phys. 164, 104–122 (2000)
7. Rossow, C.-C.: Convergence Acceleration for Solving the Compressible Naver-Stokes Equations. AIAA J. 44, 345–352 (2006)
8. Rossow, C.-C.: Efficient computation of Compressible and Incompressible Flows. J. Comput. Phys. 200, 879–899 (2007)
9. Spalart, P.R., Allmaras, S.R.: A One-Equation Turbulence Model for Aerodynamic Flows. La Rechereche Aerospatiale 1, 5–21 (1994)
10. Swanson, R.C., Turkel, E., Rossow, C.-C.: Convergence Acceleration of Runge-Kutta Schemes for Solving the Navier-Stokes Equations. J. Comput. Phys. 224, 365–388 (2007)
11. Swanson, R.C., Rossow, C.-C.: An Initial Investigation of the Effects of Turbulence Models on the Convergence of the RK/Implicit Scheme, NASA Technical Memorandum, NASA/TM-2008-215342 (2008)

Automatic Transition Prediction for Three-Dimensional Aircraft Configurations Using the DLR *TAU* Code

A. Krumbein[1], N. Krimmelbein[2], and G. Schrauf[3]

[1,2] Deutsches Zentrum für Luft- und Raumfahrt e.V. (DLR),
Institute of Aerodynamics and Flow Technology (AS), $C^2A^2S^2E$,
[1] Bunsenstraße 10, 37073 Göttingen, Germany
andreas.krumbein@dlr.de
[2] Lilienthalplatz 7, 38108 Braunschweig, Germany
normann.krimmelbein@dlr.de
[3] Airbus, Airbus Allee 1, 28199 Bremen, German
geza.schrauf@airbus.com

Summary

A Reynolds-averaged Navier-Stokes solver, a laminar boundary-layer code and a fully automated local, linear stability code for the prediction of Tollmien-Schlichting and cross-flow instabilities were coupled for the automatic prediction of laminar-turbulent transition on general aircraft configurations during the ongoing flow computation. The procedure is applied to a three-dimensional wing-body configuration and the sensitivity of the coupled system to a variety of coupling parameters is investigated.

1 Introduction

Besides wind tunnel testing and flight tests, computational fluid dynamics (CFD) simulation based on Reynolds-averaged Navier-Stokes (RANS) solvers has become a standard design approach in industry for the design of aircraft. For the design point of aircraft a positive assessment of the numerical results was achieved for many validation and application tests and the prediction capabilities of the software tools could be positively evaluated. As a consequence, high confidence in numerical simulations could be achieved in industry and will eventually allow more simulation and less physical testing. However, and despite of the progress that has been made in the development and application of RANS-based CFD tools, there is still the need for improvement, for example, with regard to the capability of a proper capturing of all relevant physical phenomena. This can only be achieved if capable and accurate physical models are available in the codes. On the one hand, the combined use of transition and turbulence models is indispensable for flows exhibiting separation,

because otherwise the close interaction between the laminar-turbulent transition and its impact on flow separation is not reproduced. On the other hand, it is not possible to fully exploit the high potential of today's advanced turbulence models if transition is not taken into account. Thus, in modern high-fidelity CFD tools a robust transition modeling must be established together with reliable and efficient turbulence models.

The unstructured/hybrid RANS solver *TAU*, [13], [5] and [14], has been equipped with a general transition prediction functionality which can be applied to general three-dimensional aircraft configurations. The development and first technical validation steps were carried out at the Institute of Fluid Mechanics of the University of Braunschweig, [9], [3] and [4]. The code can be used together with a laminar boundary-layer method, [1], for the calculation of highly accurate laminar boundary-layer data. Alternatively, the boundary-layer data can be directly extracted from the RANS solution. A fully automated, local linear stability code, [12], analyzes the laminar boundary layer and detects transition due to Tollmien-Schlichting or cross-flow instabilities. The stability code, which applies the e^N-method, [15] and [18], and the two-N-factor approach, [10], [17] and [11], for the determination of the transition points, uses a frequency estimator for the detection of the relevant regions of amplified disturbances for Tollmien-Schlichting instabilities and a wave length estimator for cross-flow instabilities. The stability code is now used instead of the e^N-database methods which have a more limited application range and which were applied usually in an automated process chain coupling a RANS solver and a transition prediction tool, [6]. Recently, the transition prediction module of the *TAU* code was applied to two-dimensional airfoil configurations, the horizontal tail plane of a generic aircraft configuration and a wing-body configuration with a three-element high-lift wing, [7], [8]. In this paper, the *TAU* code with transition prediction is applied to a three-dimensional wing-body configuration. The computations were carried out on big cluster systems. The main purpose of the investigations is the following: The sensitivity of the complete coupled system to a variety of the most important coupling parameters must be known in order to ensure fast and reliable computations. The setting of these parameters and possible interactions between their influences on the coupled computation procedure may have an impact on the convergence of the transition locations and the convergence of the computation as a whole and influence the quality of the solution. It is shown that for the parameters analysed in the present work certain range combinations can be found, so that they have either a positive or a negative influence on the overall behaviour of the coupled system. Eventually, a number of best-practice statements can be derived. The results represent a first step towards the industrialization of the *TAU* transition prediction module.

2 Transition Prediction Coupling

For production purposes, the transition prediction module applies a laminar boundary-layer method for a fast and highly accurate computation of the laminar boundary

layers. The *TAU* code communicates the surface c_p-distribution as input data to the laminar boundary-layer method COCO, [1], and COCO computes all of the boundary-layer parameters that are needed for the stability code LILO, [12]. Based on the stability analysis done by LILO e^N-methods for Tollmien-Schlichting and cross-flow instabilities determine transition locations that are communicated back to the *TAU* code. This coupling structure results in an iteration procedure for the transition locations within the iterations of the RANS equations. The structure is outlined graphically in Fig. 1. During the computation, the *TAU* code is stopped after a certain number of iteration cycles, usually when the lift has sufficiently converged, the transition module is called and transition points are determined and fixed in the computational grid. This is done consecutively for all upper and lower sides of all specified wing sections which are defined by 'line-in-flight' cuts, that is, the wing is cut through parallel to the oncoming flow, according to strip theory. When all new transition locations have been communicated back, each transition location is slightly underrelaxed to damp oscillations in the convergence history of the transition points. This means that only a certain percentage of the currently determined transition points are taken into account and the new transition location is fixed somewhat downstream of that position given by the prediction method. Then, all underrelaxed transition points – they represent a transition line on the upper or lower surface of a wing element in form of a polygonal line – are mapped onto the surface grid and the computation is continued. In so doing, the determination of the transition locations becomes an iteration process itself. With each transition location iteration step the effective underrelaxation is reduced until a converged state of all transition points has been obtained. In the last prediction step, no underrelaxation is applied.
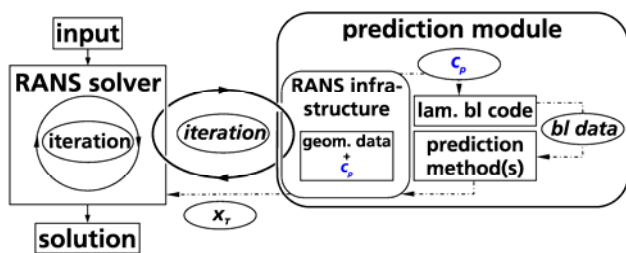
Fig. 1. Coupling structure.

In favour of the presentation of the current results the authors refer to the references [3], [4] and [6] - [9] for further and much more detailed information on the transition coupling structure, the backgrounds of its construction and its different application modes.

3   Computational Results

Two important coupling parameters which significantly influence the overall computational time are the underrelaxation factor and the interval length between two

consecutive calls of the transition prediction module during the coupled computation. These two are the main parameters whose settings can lead to a significant computational overhead in a computation with predicted transition compared to a fully turbulent one, because the time of an interval and the time until the transition lines have converged are the main sources contributing to the additional computing time. In comparison, the contribution of the execution of the software parts of the transition module itself (infrastructure part in the solver, boundary-layer code and stability code) is of much lower impact. For these investigations, the flow over a generic wing-body configuration at cruise conditions – $M_\infty = 0.75$, $Re_\infty = 18.4\times10^6$, $\alpha = 2.0°$ –, with settings for the critical N factors for quiet atmospheric conditions, $N^{TS}_{crit} = 12.0$ and $N^{CF}_{crit} = 9.0$, using the Spalart-Allmaras turbulence model [16] with Edwards modification [2] was computed parallel on a hybrid grid with 9.5 million points on the $C^2A^2S^2E$ Linux cluster using 96 processes, each on one processor core.

As depicted in Fig. 2, all transition lines at the end of the computations with underrelaxation factors $f_{relax} = 0.5$, 0.7, and 0.85 (where $f_{relax} = 0.7$ means that 70% of the displacement relative to the preceding iteration step are taken into account) have the same converged positions, which documents the independence of the final results of the transition prediction procedure over a wide range of f_{relax}.
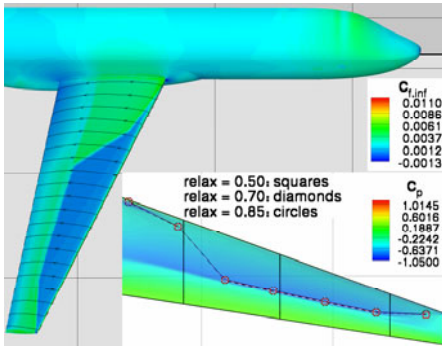
Fig. 2. c_f-distribution on wing-body configuration, c_p-distribution and transition lines on the wing upper side, different underrela-xation factors
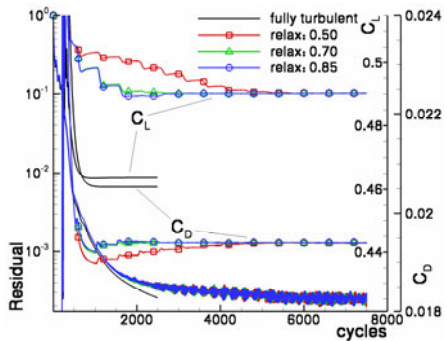
Fig. 3. RANS convergence histories of density residual and lift and drag coefficients for different underrelaxation factors

Fig. 3 shows the impact of f_{relax} on the global RANS convergence history in terms of the density residual and the lift and drag coefficients, C_L and C_D. In all computations the force coefficients converge to the same final values. This reflects the fact that the converged transition lines are finally identical. However, the computational effort to reach the converged values is very different. $f_{relax} = 0.7$ results in a significant convergence acceleration compared to the standard setting $f_{relax} = 0.5$. Both computations exhibit a monotonic behaviour from higher to lower values of C_L. For $f_{relax} = 0.85$, one obtains a slight negative influence. This setting leads to a visible intermediate overshoot of C_L to values lower than the final value. Although the overshoot vanishes after a while, it is not yet clear if this occurs for all flow cases

possible or if it might happen that the lift remains at this too low value. Additionally, one finds a mild oscillatory behaviour in the evolution of the drag affecting slightly the convergence of C_D to its final value. In the computations the prediction interval between two consecutive calls of the transition module was $\Delta cyc = 500$ cycles.

In Fig. 4, the results for $f_{relax} = 0.7$ (left) and 0.85 (right) are compared to those obtained for $\Delta cyc = 250$ and 150. As one can see, the convergence is accelerated once more leading to converged force coefficients after about 1,500 to 2,000 RANS cycles which is a factor 1.5 to 2 compared to a fully turbulent computation. The convergence histories of the fully turbulent computation are depicted as dashed lines without symbols in Fig. 4. In order to be able to do an estimation of the convergence velocities of the different computations the levels of the converged fully turbulent force coefficients have been shifted to the level of the converged values from the computations with predicted transition. Again for $f_{relax} = 0.85$, the intermediate overshoot of C_L occurs for $\Delta cyc = 250$ as well as for $\Delta cyc = 150$. The fastest convergence is obtained using the combination $f_{relax} = 0.7$ and $\Delta cyc = 150$. For this setting, however, the C_L overshoot occurs too. In all computations, this overshoot is correlated to a transition point on the wing upper side which is located a bit too far upstream of its converged position during the transient phase of the computation.
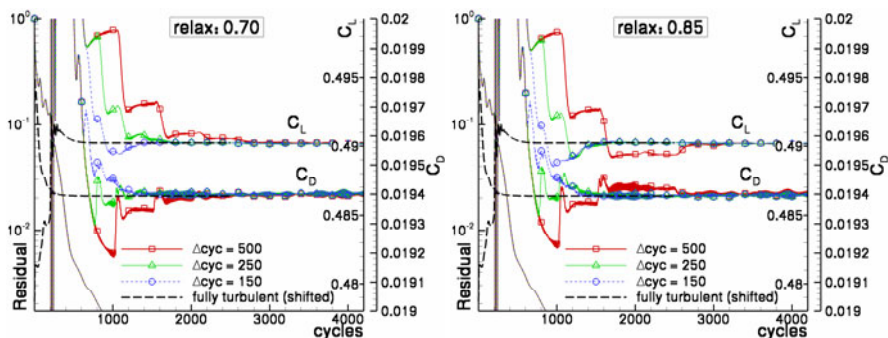
Fig. 4. RANS convergence histories of density residual and lift and drag coefficients for different underrelaxation factors and different iteration intervals.

This is shown in Fig. 5 where the transition lines from all transition prediction iteration steps are depicted. The picture shows the transition lines on the upper and lower sides of the wing using two different sets of coordinate axes with different scalings in each case. The x-direction specifies the longitudinal axis of the aircraft from the fuselage nose to the tail. The spanwise y-direction is perpendicular to the x-direction and is positive from the fuselage symmetry plane to the wing tip. In the penultimate wing section on the wing upper side towards the tip, one can see an overshoot of the transition point in the first iteration steps in upstream direction and that the overshoot is then shifted downstream to its final position. This effect is most pronounced for $f_{relax} = 0.85$ which explains the affection of the RANS convergence histories of the force coefficients in these cases and also in the case with the combination $f_{relax} = 0.7$ and $\Delta cyc = 150$. This behaviour that intermediate transition points located too far upstream are shifted to a more downstream position in the
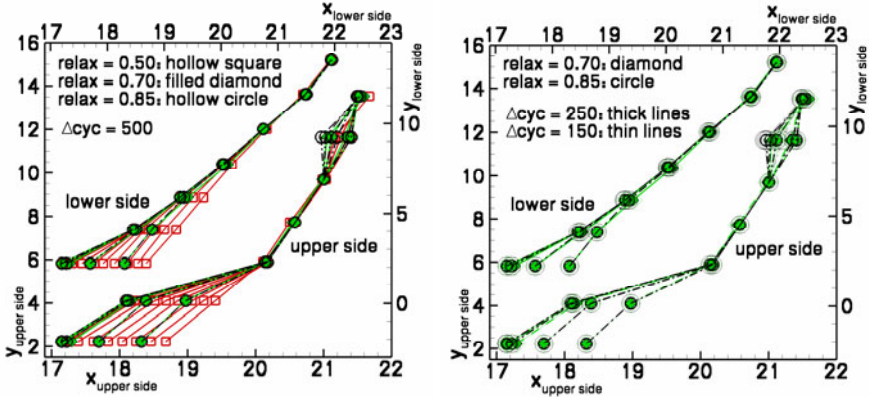
Fig. 5. Convergence histories of the transition lines for different underrelaxation factors for $\Delta cyc = 500$ (left) and $\Delta cyc = 250$ and 150 (right) iteration intervals; different coordinate axes with different scalings for upper and lower side.

subsequent transition iteration steps is significantly different from the behaviour of other transition prediction methods. With e^N-database methods, for example, it often occurs that an intermediate transition point located too far upstream stays at its incorrect or inaccurate position until the end of the computation, so that the transition point iteration converges to a wrong final value. In order to prevent such a kind of uncertainty the transition prediction algorithm is based on a downstream-to-upstream shifting of the sequence of predicted transition points realized by the underrelaxation technique. These results are the first indication, that the stability code does not exhibit this sensitivity. This issue will be subject to further investigations in the nearest future. The convergence histories of the transition lines in Fig. 5 show that with $f_{relax} = 0.7$ and 0.85 convergence is reached after four to five calls of the transition module and that the prediction intervals $\Delta cyc = 250$ and 150 lead to the same transition lines in each transition iteration step independent of the settings of Δcyc. It has to be noted that – except for the penultimate wing section on the wing upper side towards the tip – the movement of the transition points during the iteration is from greater to lower x-coordinates and that after four to five iteration steps all other predicted transition lines lie on top of each other. From these results it can be concluded that for this type of flow (attached, shock without separation) one can expect a smooth and fast convergence for the range $0.65 \leq f_{relax} \leq 0.8$. Additionally, it becomes clear that for a further industrialization of the transition prediction module a pointwise automatic shut-down of the transition iteration procedure, on the one hand, and sensors for a proper balancing of the settings of the underrelaxation factor and the interval length, on the other hand, are needed, whereas it is felt that the latter is of higher importance in this context.

In Fig. 6, the interaction between the transition prediction procedure and the iteration of the angle of attack for target lift computations ($C_L = 0.48$) is documented using target lift intervals $\Delta cyc_{lift} = 50$, 100, 200 cycles with the settings $f_{relax} = 0.7$ and
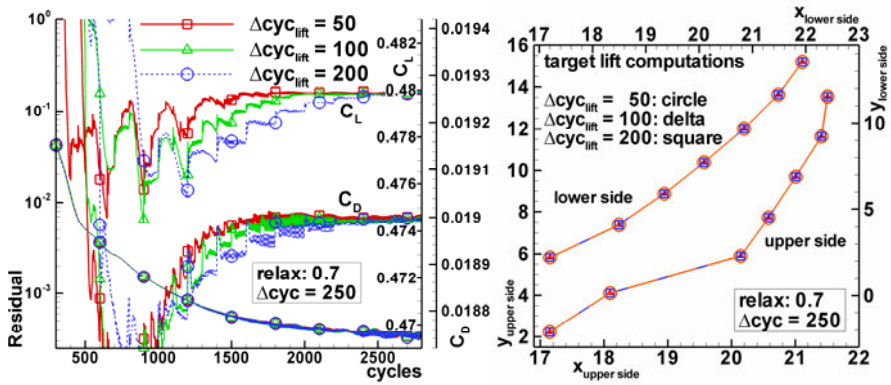
Fig. 6. RANS convergence histories for different angle adjustment intervals in target lift computations; Δcyc_{lift} = 50, 100, 200 cycles (left) and corresponding converged transition lines (right).

Δcyc = 250. One can see that all computations converge to the same solutions in terms of the force coefficients as well as the transition lines. The fastest convergence was found for Δcyc_{lift} = 50.

4   Conclusions

The behaviour of the *TAU* transition prediction module was investigated with respect to a number of coupling parameters which influence the convergence of the transition lines and the coupled computation. A high stability and parameter combinations for fast convergence were found. An unexpected insensitivity to intermediate transition locations located too far upstream was found and will be subject to further investigations.

Acknowledgements

References

[1] COCO – A Program to compute Velocity and Temperature Profiles for Local and Nonlocal Stability Analysis of Compressible, Conical Boundary Layers with Suction, ZARM Technik Report (November 1998)

[2] Edwards, J.R., Chandra, S.: Comparison of Eddy Viscosity–Transport Turbulence Models for Three-Dimensional, Shock-Separated Flowfields. AIAA Journal 34(4), 756–763 (1996)

[3] Krimmelbein, N., Radespiel, R., Nebel, C.: Numerical Aspects of Transition Prediction for Three-Dimensional Configurations. AIAA-2005-4764

[4] Krimmelbein, N., Radespiel, R.: Transition prediction for three-dimensional flows using parallel computation. Computers & Fluids 38, 121–136 (2009)

[5] Kroll, N., Rossow, C.-C., Schwamborn, D., Becker, K., Heller, G.: MEGAFLOW - A Numerical Flow Simulation Tool For Transport Aircraft Design. In: ICAS Congress 2002 [CD-Rom], ICAS, Toronto, Canada, pp. 1.105.1–1.105.20 (2002)

[6] Krumbein, A.: Automatic Transition Prediction and Application to Three-Dimensional High-Lift Configurations. Journal of Aircraft 44(3), 918–926 (2007), doi:10.2514/1.25528, also: AIAA-2006-3164 (June 2006)

[7] Krumbein, A., Krimmelbein, N., Schrauf, G.: Automatic Transition Prediction in a Hybrid CFD Code – Part 1: Methodology and Sensitivities" and "Automatic Transition Prediction in a Hybrid CFD Code – Part 2: Practical Application. both accepted at Journal of Aircraft, also: AIAA-2007-4284 and AIAA-2008-413

[8] Krumbein, A., Krimmelbein, N.: Navier-Stokes High-Lift Airfoil Computations with Automatic Transition Prediction using the DLR TAU Code. In: New Results in Numerical and Experimental Fluid Mechanics VI, Contributions to the 15th STAB/DGLR Symposium, Darmstadt, Germany. Notes on Numerical Fluid Mechanics and Multidisciplinary Design, vol. 96, pp. 210–218. Springer, Heidelberg (2007)

[9] Nebel, C., Radespiel, R., Wolf, T.: Transition Prediction for 3D Flows Using a Reynolds-Averaged Navier-Stokes Code and N-Factor Methods. AIAA-2003-3593

[10] Rozendaal, R.A.: Natural Laminar Flow Flight Experiments on a Swept Wing Business Jet-Boundary-Layer Stability Analysis, NASA CP 3975 (March 1986)

[11] Schrauf, G.: Large-Scale Laminar-Flow Tests Evaluated with Linear Stability Theory. Journal of Aircraft 41(2), 224–230 (2004)

[12] Schrauf, G.: LILO 2.1 User's Guide and Tutorial, Bremen, Germany, GSSC Technical Report 6, originally issued September 2004, modified for Version 2.1 July 2006

[13] Schwamborn, D., Gerhold, T., Hannemann, V.: On the Validation of the DLR-TAU Code. In: New Results in Numerical and Experimental Fluid Mechanics II. NNFM, vol. 72, pp. 426–433. Vieweg Verlag, Braunschweig (1999)

[14] Schwamborn, D., Gerhold, T., Heinrich, R.: The DLR TAU-Code: Recent Applications in Research and Industry. In: European Conference on Computational Fluid Dynamics, ECCOMAS CFD 2006, Egmond aan Zee, The Netherlands, 5 – 8 September. ECCOMAS CFD 2006 - CD-Rom Proceedings, TU Delft, The Netherlands (2006)

[15] Smith, A.M.O., Gamberoni, N.: Transition, Pressure Gradient and Stability Theory. Douglas Aircraft Company, Long Beach (1956)

[16] Spalart, P.R., Allmaras, S.R.: A one-equation turbulence model for aerodynamic flows. La Recherche Aérospatiale 1, 5–21 (1994)

[17] Stock, H.W.: Infinite Swept Wing RANS Computations with eN Transition Prediction – Feasibility Study, Rept. IB 124-2003/12, Deutsches Zentrum für Luft- und Raumfahrt (DLR), Braunschweig, Germany (August 2002)

[18] van Ingen, J.L.: A suggested Semi-Empirical Method for the Calculation of the Boundary Layer Transition Region, University of Delft, Dept. of Aerospace Engineering, Delft, The Netherlands, Rep. VTH-74 (1956)

Numerical Simulation of the Elastic and Trimmed Aircraft

Andreas Michler and Ralf Heinrich

DLR, Institute of Aerodynamics and Flow Technology,
Lilienthalplatz 7, 38108 Braunschweig, Germany
Andreas.Michler@dlr.de

Summary

A simulation environment has been developed enabling the computation of the elastic and trimmed aircraft. It consists of a trim algorithm which is coupled with a procedure to account for the interaction between fluid and structure. The trim algorithm is based on a Newton method with a discretized Jacobian. It incorporates the six degrees-of-freedom (DoF) flight-mechanics equations and thereby enables to compute different trimmed states. The fluid-structure interaction (FSI) procedure uses a partitioned approach to compute the flow around the configuration in static aeroelastic equilibrium. This simulation environment has been successfully applied to trim a rigid transport-aircraft configuration in viscous flow as well as in inviscid flow with rigid and flexible wing.

1 Introduction

Cruise constitutes the major phase of flight for a transport aircraft, in which most of the aircraft's fuel is consumed. Hence for this phase, it is of utmost importance to accurately predict the aerodynamic coefficients, which are closely related to fuel consumption. Their computation involves the disciplines fluid, structural and also flight mechanics. Firstly, during flight, especially the wing noticeably deforms and reaches an equilibrium position in cruise, the so-called *static aeroelastic equilibrium*. This is accounted for by a partitioned approach, enabling the application of specialized software tailored to each discipline and already in use in industry. Secondly, in cruise, the loads acting on the aircraft are balanced: a *trimmed state* is reached, in which the statically stable aircraft returns after perturbation. In order to simulate these interactions, a simulation environment has been developed coupling trim algorithm with an FSI procedure for the computation of the static aeroelastic equilibrium. The FSI procedure uses the hybrid RANS code TAU [8] for the flow computation and the commercial software ANSYS [10] for the solution of the structural equations. The trim algorithm is based on a Newton method, in which the derivatives of the Jacobian are discretized

by finite differences. For the deflection of control surfaces, prescribed by the trim algorithm, the Chimera technique is used. It provides a fast and reliable means of rigid-body component rotations even in the case of large rotations.

The outline of this paper is as follows. Section 2 describes the algorithm used for calculating the trimmed state, and Sect. 3 deals with the coupling between fluid and structure, as well as between FSI procedure and the trim algorithm. Section 4 explains the results for applications involving some or all of the disciplines mentioned above. This paper is concluded by Sect. 5.

2   Trim Algorithm

For stability reasons, a trimmed state is adopted in cruise [9]. It is achieved by deflecting so-called *control surfaces*, thereby cancelling moments acting on the aircraft, as noted in [9]; elevator, aileron, rudder and even the horizontal tail (HT) may act as such.

More generally, trim can be seen as the process of balancing forces and moments acting on the aircraft to achieve a certain state of flight. To this end, the aircraft is perceived as a system with input and output parameters: the output parameters are of interest to the observer and influenced by the input parameters, determining the state of the aircraft. This state is governed by the 6-DoF flight-mechanics equations [6], linking input and output parameters. These equations require the aerodynamic forces.

The trim problem can then be stated as follows. Let $\tilde{z} \in \mathbb{R}^n$ be the vector of trim input parameters and $\tilde{y} \in \mathbb{R}^m$ the vector of trim output parameters, composed of some or all the input or output parameters, respectively; find the values for the trim input parameters $\tilde{z}_i, i = 1, \dots, n$ such that the trim output parameters $\tilde{y}_j, j = 1, \dots, m$ are equal to prescribed values $\hat{y}_j$ specifying a certain trimmed state. In case the trim input vector $\tilde{z}$ does not contain all the components of the input vector, the other components not included are kept constant during the trim process. This problem is formulated as a root-finding problem and, for the solution, a Newton method is applied. The basic equation reads as follows:

$$\mathbf{J}^{(k)} \Delta\tilde{z}^{(k)} = q^{(k)}, \tag{1}$$

where k denotes the current trim iteration number, $\Delta\tilde{z}$ the vector of the step sizes of trim input parameters and q is the difference between current values of the trim output parameters and their prescribed values, $q = \hat{y} - \tilde{y}$, termed the *quality vector*. $\mathbf{J}$ is the Jacobian with the trim output parameters differentiated w.r.t. the trim input parameters as entries. Since, in general, these derivatives are not given explicitly, they are discretized using finite differences. This may be computationally expensive in case CFD methods are involved; fortunately, not every variation of the trim input parameters requires a CFD computation. For the solution of (1), singular value decomposition (SVD) is used, since it is also applicable to the general case of $m \neq n$, resulting in a non-square Jacobian; furthermore, it provides a means of coping with ill-conditioned Jacobians [2]. SVD factorizes the Jacobian and yields a product of three easily invertible matrices.

The new trim input parameters are then calculated as follows:

$$\tilde{z}^{(k+1)} = \tilde{z}^{(k)} + \kappa \cdot \Delta\tilde{z}^{(k)}, \tag{2}$$

where κ is not equal to 1 and scales the step size vector appropriately in the cases of violation of

(a) given maximally allowed changes of input parameters from one iteration to another (termed *relative bounds*), or
(b) given upper and lower limits on trim input parameters (termed *absolute bounds*).

The solution's quality is measured by the quality function $Q^{(k)}$, computed, e.g., as the ℓ^2-norm of the current quality vector $\boldsymbol{q}^{(k)}$.

The trim algorithm terminates if

(1) the given maximum iteration number is reached,
(2) the current value of the quality function reaches a prescribed tolerance,
(3) the ℓ^2-norm of the current step size vector $\Delta\tilde{\boldsymbol{z}}^{(k)}$ reaches a prescribed tolerance,
(4) the value of the quality function increases (more than allowed), or
(5) relative or absolute bounds are violated.

A successful trim calculation ends because of either stopping criterion (2) or (3). Although only one solution may be found at a time, starting from different values of input parameters may yield different solutions, due to the non-linearity of the underlying physics or due to a different number of trim input and output parameters. This can be avoided by imposing bounds on the trim input parameters.

Common trimmed states are cruise, i.e. steady level flight, climb or descent with constant acceleration. For cruise conditions, the translational and rotational body accelerations, $\dot{u}_b$, $\dot{w}_b$ and $\dot{q}$, respectively, as well as the flight path angle γ have to be zero, hence: $\tilde{\boldsymbol{y}} = [\dot{u}_b, \dot{w}_b, \dot{q}, \gamma]^T \overset{!}{=} [0, 0, 0, 0]^T$. This can be achieved by a certain combination of angle of attack (AoA) α, tail angle η, pitch angle Θ and thrust T, i.e. $\tilde{\boldsymbol{z}} = [\alpha, \eta, \Theta, T]^T$. The Jacobian is hence a 4×4-matrix. The results for such a trim calculation are shown at the beginning of Sect. 4. For small AoA and $\alpha \equiv \Theta$, the thrust balancing the drag and acting in the aircraft's center of gravity, as well as the pitching rate q being zero, the 3-DoF equations can be simplified to

$$L = G, \tag{3}$$

$$M = 0, \tag{4}$$

where L is the aerodynamic lift force balancing the aircraft's weight G, M its aerodynamic moment. Thus, the trim vectors are $\tilde{\boldsymbol{z}} = [\alpha, \eta]^T$ and $\tilde{\boldsymbol{y}} = [C_L, C_M]^T \overset{!}{=} \left[\hat{C}_L, 0\right]^T$ with C_M being the moment coefficient and C_L the lift coefficient. This yields a 2×2-Jacobian and reduces the number of necessary flow / FSI computations. Trim calculation with these parameters were also performed in Sect. 4.

3   FSI Procedure and Coupling between FSI and Trim Algorithm

Fluid-structure interaction constitutes a multi-physics problem in which two disciplines are coupled on the common boundary or *interface*. A *partitioned approach* [1] is

adopted here: each domain is spatially independently discretized and the equations governing each domain solved with a different solver. The solution of each set of governing equations is performed subsequently until the static aeroelastic equilibrium is reached. On the interface, coupling terms have to be exchanged: aerodynamic forces have to be transferred to the structural grid, and the nodal displacements of the structural grid have to be transferred to the CFD grid. For the first, a *nearest neighbor mapping* technique is used, for the latter a volume spline interpolation algorithm [3]. The subsequent deformation of the CFD grid is performed by an algorithm based on radial basis functions [3]. This coupling scheme reads as follows:

(1) **CFD:**
    Calculate the solution of the Euler- or Navier-Stokes equations
(2) **CFD → CSM:**
    transfer the aerodynamic forces to the nodes of the structure grid
(3) **CSM:**
    calculate the nodal displacements for the structure grid
(4) **CSM → CFD:**
    transfer the nodal displacements of the structure grid to the CFD grid
(5) **stopping criteria:**
    check if a stopping criterion is met
    `if YES`: end and take the aerodynamic coefficients of last CFD computation
    `if NO`: **deform** the CFD grid and go back to step (1)

The coupling procedure ends if

(A) a given maximum number of coupling iterations is reached;
(B) the aerodynamic coefficients of subsequent iterations do not change significantly, or
(C) the difference between maximum nodal displacements for the structure (and hence the distance between CFD meshes) of subsequent coupling iterations is negligible,

(C) being applicable for static aeroelastic equilibrium.

The speed of the modern transport aircraft in cruise falls in the transonic flight regime, governed by the non-linear compressible stationary Navier-Stokes equations. These equations can be adequately solved by modern CFD solvers, such as the hybrid RANS solver TAU, which is employed here. The software Centaur [11] was used for the generation of unstructured grids, consisting of tetrahedra for the case of inviscid flow described by the Euler equations, and additionally prisms for the resolution of the boundary layer for visous flow, as described by the Navier-Stokes equations. For the deflection of the horizontal tail necessary for trim, the Chimera technique was used, enabling the relative rotation of overlapping component grids [5]. Geometries have been created or modified with the CAD program CATIA [12]. The DLR-F12 (cf. Sect. 4) transport-aircraft model was cleaned using this program; furthermore, in order to use the Chimera technique, a gap between horizontal tail and fuselage was generated and Chimera cylinders around the horizontal tail defined.

The structure is governed here by the elastostatic equations. They are solved using the commercial software ANSYS. For now, solely the influences of the elasticity of

the wing is taken into account. The structure of the wing is modelled following the approach described in [7], where a model of the structure is generated based on the surrounding aerodynamic surface mesh. This model basically consists of skin, spars and ribs. As to the boundary conditions, no translation is allowed for the nodes at the root; this constitutes a simplification compared with a free-flying aircraft. The loads, transferred from the CFD solution, act on the nodes of the surface of the structure.

The trim algorithm acts as master program during the computation, setting the input parameters for the FSI procedure. The FSI procedure then computes the corresponding static aeroelastic equilibrium and passes the aerodynamic coefficients on to the trim algorithm.

The simulation environment was developed under Linux using the scripting language Python [4] to interface between stand-alone applications such as ANSYS or TAU and the routines for the transfer of coupling terms and deformation. It was also used for the communication with one of the institute's clusters, where the time-consuming flow calculations for the DLR-F12 were performed. The other applications were run on a local PC. The trim algorithm was written in Python, as well as the program for the generation of the model for the structure. ANSYS' scripting language APDL is used for the generation of the actual model within ANSYS, the mesh generation, the setting of the boundary conditions, the solution of the elastostatic equations and post-processing. For the generation of these scripts, templates stemming from [7] were adapted.

4   Applications

The applications are presented in the order of increasing number of disciplines involved: first, only flight mechanics, then CFD additionally and finally also structural mechanics.

The first test case involves four trim input and trim output parameters (cf. Sect. 2). It exemplifies the successful application of the trim procedure for more complex trim problems involving flight mechanics equations. The aerodynamic coefficients were provided by simple analytical models depending linearly on AoA α and tail angle η. As further simplification, the thrust was assumed to act at the center of gravity. The accelerations used as trim output parameters were computed by solving the 3-DoF flight-mechanics equations. Figure 1 shows that trim input and output parameters converge at the end of the trim calculations, and the trim output parameters reach the values initially prescribed.

The configuration used in the next test case is the rigid DLR-F12 transport-aircraft configuration, a windtunnel model scaled to real dimensions. Cruise conditions were assumed for a speed of Ma=0.85 at a height of about 10km. The grid is made up of about 4.25 million grid points, and prism layers were used to resolve the boundary layer (cf. Fig. 2). The Spalart-Allmaras turbulence model was chosen. On the right side of Fig. 2, the success of the trim calculation can be seen, as the *goal values* of $\hat{C}_L = 0.46$ and $\hat{C}_M = 0$ for cruise condition had been prescribed.

An FE model for the wing of the DLR-F12 was developed, which consists of spars, ribs and skin and is meshed with shell elements. The total number of nodes on the surface is about 10,300. Trim calculations were performed with and without considering the elastic deflection of the wing with this structural model. In both cases, viscosity was
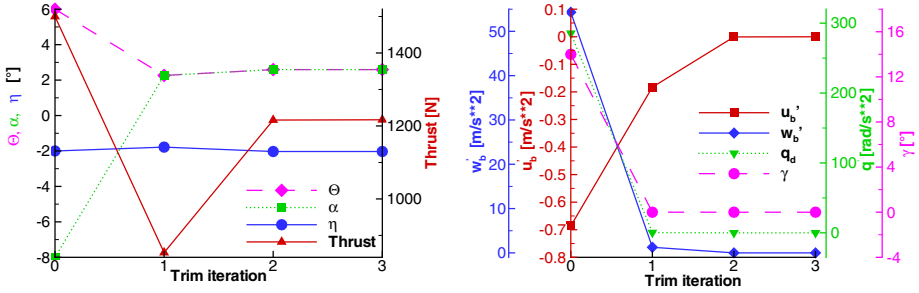
Fig. 1. Convergence of trim input (left) and trim output parameters (right)
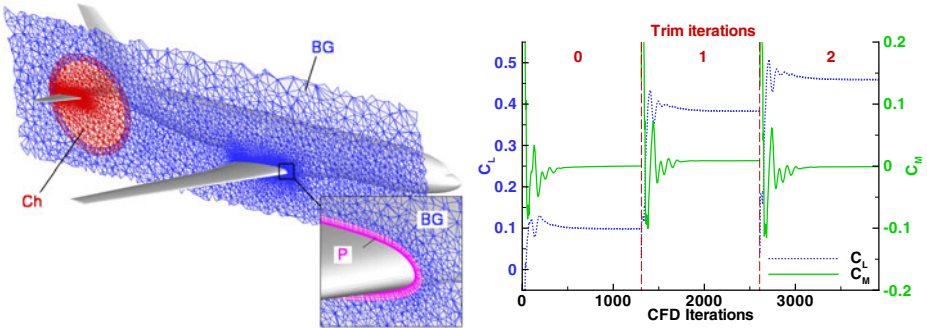
Fig. 2. A cut through the hybrid grid of the DLR-F12 is shown on the left side. The grid section, labeled "Ch", belongs to the Chimera block of the horizontal tail, overlapping the background grid ("BG"). The close-up shows prism layers ("P") near the wing root. On the right side, the convergence of the aerodynamic coefficients is plotted for CFD calculations of subsequent trim iterations.

neglected, but the same ambient conditions and goal values were prescribed as before. The CFD mesh was comprised of tetrahedra and had about 1.2 million points. For each trim iteration, FSI calculations had to be performed to obtain the values for C_L and C_M in static aeroelastic equilibrium. For the last trim iteration, Fig. 3 exemplarily shows the CFD meshes and the convergence of the aerodynamic coefficients for subsequent coupling iterations. Figure 4 (left) shows the convergence of trim input and output parameters during the trim process for both the rigid and the elastic case. Starting from different values for the aerodynamic coefficients C_L and C_M for the same angles α and η, the goal values of $\hat{C}_L = 0.46$ and $\hat{C}_M = 0$ were reached in both cases after just a few trim iterations. At the trimmed state, both the values for angle of attack and tail angle were higher in the case of the partially elastic configuration. Furthermore, as can be seen in Figure 4 (right), the vertical forces over the wing are shifted towards the wing root. An increase in drag (of about seven drag counts) was also found.
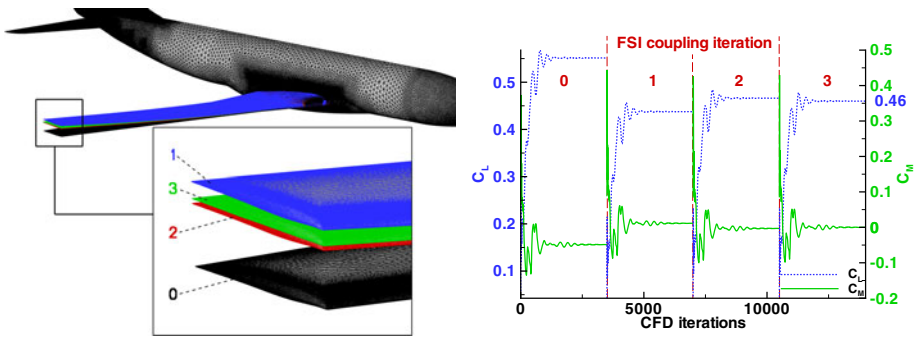
Fig. 3. On the left side, the surface meshes for subsequent FSI coupling iterations for the last trim iteration are presented: the undeformed mesh, labeled "0", and the deformed meshes after the first ("1"), the second ("2") and the third ("3") iteration. On the right side, the corresponding convergence histories of lift and moment coefficients are displayed.
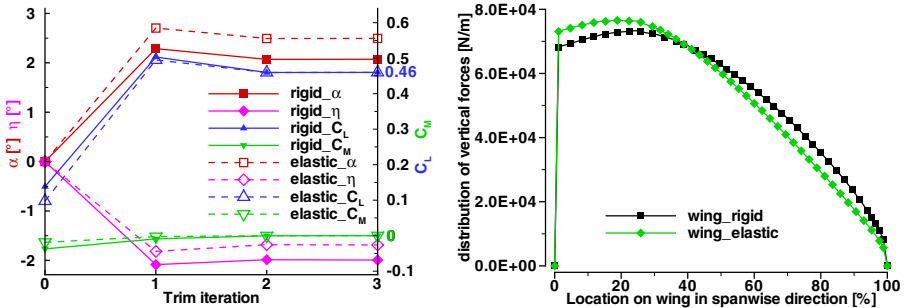
Fig. 4. On the left side, the convergence of trim input and output parameters are shown for the rigid and partially elastic DLR-F12 configuration in inviscid flow. On the right side, the distribution of vertical force in spanwise direction over the wing is displayed for the trimmed state. A location of 0% corresponds to the wing root, 100% to the wing tip.

5   Conclusions

A simulation environment has been presented enabling the computation of trimmed elastic configurations in static aeroelastic equilibrium. The trim algorithm uses a Newton method and can handle different trim conditions involving multiple trim input and output parameters. The simulation environment was applied to the DLR-F12 transport-aircraft configuration. First, the rigid configuration immersed in viscous flow was successfully trimmed for cruise conditions. Then, for inviscid flow, the same configuration was trimmed with a rigid wing and also for an elastic wing. For both cases, the trim algorithm succeeded in achieving the values for the aerodynamic coefficients prescribed for cruise conditions. For the same cruise conditions, the elastic case was found to require a higher angle of attack and tail angle, as well as to yield an increase

in drag. Furthermore, a shift of wing loading towards the wing root was observed. This clearly indicates that elasticity cannot be neglected when considering cruise conditions. In the near future, the partially elastic DLR-F12 in visous flow will be trimmed and the results compared to those of the rigid configuration, such that the effects of elasticity, especially on the drag, can be more accurately assessed.

Acknowledgements

References

[1] Felippa, C., Park, K., Farhat, C.: Partitioned Analysis of Coupled Mechanical Systems. Computer Methods in Applied Mechanics and Engineering 190, 3247–3270 (2001)

[2] Heath, M.T.: Scientific Computing: An Introductory Survey, 2nd edn. McGraw-Hill, New York (2002)

[3] Heinrich, R., Wild, J., Streit, T., Nagel, B.: Steady Fluid-Structure Coupling for Transport Aircraft. Deutscher Luft- und Raumfahrtkongress, Braunschweig (2006)

[4] Langtangen, H.P.: Python Scripting for Computational Science, 2nd edn. Texts in Computational Science and Engineering. Springer, Heidelberg (2006)

[5] Madrane, A., Raichle, A., Stürmer, A.: Parallel Implementation of a Dynamic Overset Unstructured Grid Approach. In: Neittaanmäki, P., Rossi, T., Majava, K., Pironneau, O. (eds.) Proceedings of the ECCOMAS 2004 Conference

[6] Murman, S.M., Aftosmis, M.J., Berger, M.J.: Simulations of 6-DOF Motion with a Cartesian Method. In: 41st AIAA Aerospace Sciences Meeting, Reno, NV, January 6-9, AIAA-2003-1246

[7] Nagel, B.: Berechnung der strukturmechanischen Geometrie von Tragflügeln auf Basis eines aerodynamischen Netzes. Diplomarbeit, DLR-Institut für Faserverbundleichtbau und Adaptronik

[8] Schwamborn, D., Gerhold, T., Heinrich, R.: The DLR TAU-Code: Recent Applications in Research and Industry. In: ECCOMAS CFD 2006, Egmond aan Zee, The Netherlands (2006)

[9] Tewari, A.: Atmospheric and Space Flight Dynamics. Birkhäuser, Boston (2007)

[10] ANSYS homepage, http://www.ansys.com/

[11] Centaur homepage, http://www.centaursoft.com/

[12] CATIA homepage in German language, http://www.3ds.com/de/

Chimera Simulations of Transported Large–Scale Vortices and Their Interaction with Airfoils

Christoph Wolf[1], Axel Raichle[2], Tobias Knopp[1], and Dieter Schwamborn[1]

[1] DLR Göttingen, AS − $C^2A^2S^2E$, Bunsenstraße 10, 37073 Göttingen, Germany
christoph.wolf@dlr.de
[2] DLR Göttingen, AS − $C^2A^2S^2E$, Lilienthalplatz 7, 38108 Braunschweig, Germany

Summary

A Chimera technique for moving grids is applied to simulate the transport of large-scale vortices convected by a mean velocity field over large distances and their interaction with an airfoil. While keeping the numerical dissipation at a minimum, the Chimera approach allows to resolve the vortex on a local fine grid whereas the unstructured global background grid can be relatively coarse. Having examined the vortex dissipation rate numerically, the interaction of a Rankine-like type vortex with a NACA 0012 airfoil and an ONERA-A airfoil near stall, respectively, is simulated. The interaction can be interpreted as a time-dependent variation in the effective angle of attack. A subsequent computation of a flapping NACA 0012 airfoil turns out to be an insufficient approximation of the vortex-airfoil interaction.

1 Introduction

The modeling and simulation of large-scale vortices in the onflow conditons and their interaction with airplanes pose an important challenge in today's air traffic. Such vortices can either evolve naturally in the atmosphere due to certain weather conditions or they are caused during take-off and landing by the airplanes themselves (so-called wake vortices [4]). Both types of disturbances pose a great danger for oncoming airplanes and even can cause fatal accidents. The status quo of avoiding the risks of wake vortices lies in waiting several minutes before allowing the next airplane to take-off or land on the same runway. In times of worldwide increasing air traffic, this limitation becomes more and more problematic.

The focus in this publication lies on the development and application of a numerical technique that enables firstly to preserve transported vortices for a sufficiently long time and secondly to compute their interaction with airfoils in order to predict the forces and moments acting at the wing. As both atmospheric vortices and wake vortices are highly three-dimensional, the 2D-examples in section 3 can only be seen as a first step towards a reliable prediction of a vortex-airfoil interaction. Nevertheless the presented technique can also be applied in 3D. In [3] tip vortices are captured and transported by

an overset grid technique, showing that this approach minimises the numerical dissipation. In [1] the collision of a sinusoidal gust and a NACA 0012 airfoil is examined numerically in 2D. This computation requires a globally fine grid, making an extension of [1] to a complex 3D test case impractical. As the simulation of a complete 3D wing-fuselage configuration with disturbed onflow conditions is subject to future research, an alternative approach is required.

The underlying principle of the technique can be described as follows: First an analytically defined vortex is inserted into the flow field, which is a standard procedure in literature [2]. The vortex must then be transported over a large distance within the computational domain. The use of a globally fine background grid or a constant grid refinement after each computational time step is too expensive. Another disadavantage lies in the possible decreasing grid quality caused by the refinement of tetrahedrons, leading to large numerical dissipation. Therefore a Chimera approach [8] is used instead, which consists in coupling the background grid with an additional cartesian vortex grid fine enough to represent the vortex. The vortex is initialised on the vortex grid and remains attached to it during the computation as both are moving with the free stream velocity through the background grid. If the computation furthermore includes the collision of the vortex and a solid object, a third computational step has to be performed. As the vortex grid and the object must not overlap, the vortex grid is stopped just before it reaches the object. The vortex is then interpolated onto the background grid, which is fine enough near the airfoil, where it can be transported farther towards the object.

2   Numerical Method

All computations have been performed within the DLR TAU Code [7], which is a finite volume computational fluid dynamics solver for the three-dimensional compressible RANS equations. As all flow variables are stored at the cell vertices (or respectively at the cell centers with respect to the dual grid cells) the code is independent of the type of grid cells, which allows the use of unstructured, structured or hybrid grids. For the discretization of the convective fluxes, several upwind, central or mixed upwind-central discretization methods are available. The present computations are performed by a second-order accurate central differencing scheme with artifical scalar dissipation using standard settings. The gradients of the flow variables are determined by a Green-Gauss formula. The time-accurate simulations are performed using dual-time. Within each time step the nonlinear problem is solved in pseudo time using an implicit LUSGS scheme. For convergence acceleration residual smoothing, multigrid methods and preconditioning have been used. The turbulence model used in examples 3.1 and 3.2 is the k-ω linearized explicit algebraic stress (LEA) model [6]. As several preliminary examinations showed only an neglible effect of the underlying turbulence model on the vortex dissipation rate, the numerically cheaper 1-equation Spalart-Allmaras turbulence model is applied in example 3.3. All examples in section 3 have been performed in 2D.

The Chimera technique allows flow solutions on overlapping grids, where the grids can be in relative motion to each other during a simulation. For the examples of this publication it is sufficient to combine a cartesian vortex grid and a large (not necessarily cartesian) background grid. The vortex grid is completely embedded within the

background grid. Those points of the background grid that are located in the interior of the vortex grid are blanked out, meaning that no flow solution is computed in this region. This procedure is commonly referred to as "hole cutting" [5]. After each time step the points situated in the boundary of the vortex grid and the points of the background grid lying next to the "hole" obtain their flow variables by bilinear interpolation of the conservative variables from the relative other grid. Using this Chimera interpolation the vortex is interpolated from the vortex grid onto the background grid during the third computational step of the presented technique.

3   Results

In order to test the numerical performance of the presented technique, several test cases in 2D have been computed. All vortices are rotating in counterclockwise direction and they are of Rankine-like type. In all examples the following notations are used: x and y denote the global coordinates of the background grid, whereas x_{local} and y_{local} are the local x- and y-coordinates of the vortex grid ($y_{local} = y$ in all examples). v is the velocity relative to the background grid and v_x and v_y are its x- and y-components. v_{vg} stands for the velocity of the vortex grid relative to the background grid and $v_{vg,x}$ and $v_{vg,y}$ are its x- and y-components. The free stream velocity is indicated by v_∞, whereas $v_{\infty,x}$ and $v_{\infty,y}$ denote its x- and y-components. Throughout all examples $v_{vg,y} = v_{\infty,y} = 0 \ m/s$. The local velocity v_{local} is defined by $v_{local} := ((v_x - v_{\infty,x})^2 + (v_y - v_{\infty,y})^2)^{\frac{1}{2}}$. The numerical setting is further described by the grid cell size h, chord length c and angle of attack α of an airfoil, Mach number Ma, Reynolds number Re, physical time t (i.e. nondimensionalised time $\tilde{t} := t \cdot v_\infty / c$) and time step size Δt. To ensure that initially all vortices are completely situated on the vortex grid, their tangential velocity is set to zero at a prescribed outer radius r_o. Additionally, vortices are characterised by their core radius r_c and the constant circulation Γ_0. c_l, c_d, c_m, and c_p denote the coefficients of lift, drag, moment and pressure.

3.1   Transported Vortices

In this first example a vortex defined by $r_c = 2\text{m}$, $r_o = 10\text{m}$ and $\Gamma_0 = 60 \ m^2/s$ is transported 100m to the right. As a vortex-airfoil interaction is excluded, no third part of the presented technique is required. The simulation is performed four times. In the first two computations the Chimera approach is applied, where the only difference is the use of a coarse and a fine background grid, respectively. In simulations three and four no utilisation of the Chimera technique is made, but the computations are performed solely on the fine and coarse backgrund grid from the first two simulations. The aim is to compare the numerical dissipation resulting from the different approaches. The equidistant background grids cover the rectangular area $(x, y) \in [-50\text{m}, 150\text{m}] \times [-50\text{m}, 50\text{m}]$. They contain 80601 and 5151 grid points, which results in a grid cell size of $h = 0.5m$, i.e. $h/r_c = 0.25$, and $h = 2m$, i.e. $h/r_c = 1$, respectively. The vortex grid in the first two simulations covers the domain $(x_{local}, y_{local}) \in [-25\text{m}, 25\text{m}] \times [-25\text{m}, 25\text{m}]$ and contains 40401 grid points, which is eqivalent to $h = 0.125m$, i.e. $h/r_c = 0.125$. The resolution ratio of the vortex grid and the two background grids is therefore $4 : 1$ and
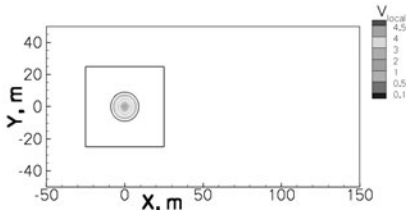
Fig. 1. Transported vortices. Vortex grid and v_{local} at $t = 0$s.
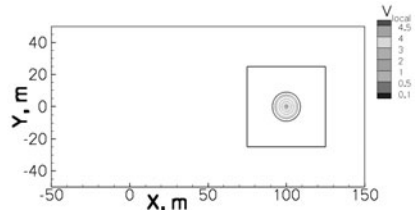
Fig. 2. Transported vortices. Vortex grid and v_{local} at $t = 2$s.

16 : 1, respectively, in each dimension. At the beginning of the first two computations $x_{local} = x$. Figure 1 shows the initial position of both grids and v_{local} of the already initialised vortex. Both $v_{\infty,x}$ and $v_{vg,x}$ are prescribed as 50 m/s and $\Delta t = 10^{-2}$s is chosen.

Figure 2 shows the relative position of both grids and v_{local} at the end of the first two computations. Although the displayed vortices in figures 1 and 2 are the result from the Chimera computation using the coarse background grid, no visible difference could be observed when regarding the computation with a fine background grid. Then the final two computations are performed with the same setting but without using a vortex grid. Figure 3 shows v_{local}, where only the values at points $(x_{local}, y_{local}) \in [0\text{m}, 20\text{m}] \times \{0\text{m}\}$ are displayed. One can see v_{local} at t = 0s, at t = 2s with application of the Chimera technique (v_{local} of both Chimera simulations looks exactly the same, so only one result is displayed), and at the end of the two non-Chimera computations. While both Chimera simulations preserve the vortex well, the computation on a fine background grid without using Chimera results in a significant reduction of the velocity maximum. In the non-Chimera simulation on the coarse background grid the vortex decays very rapidly.

This comparison shows firstly that a coarse background grid does not increase the numerical dissipation when using the Chimera approach. Secondly the Chimera technique is strictly required in order to minimise the numerical dissipation and at the same time compute efficiently, which is obvious due to the following consideration: To get as less dissipative results without Chimera, the background grid would globally have to be as fine as the vortex grid from the Chimera approach, which is numerically too expensive. A numerically cheaper local adaption of the background grid in the area of the vortex would on the other hand destroy the equidistant character of the background grid, resulting in an increase in dissipation.

3.2   NACA 0012 Airfoil

In this example the collision between a vortex, which is defined by $r_c = 1.5$m, $r_o = 7$m and $\Gamma_0 = 60 \ m^2/s$, and a NACA 0012 airfoil of chord length $c = 1$m at $\alpha = 0°$ is simulated. The hybrid background grid contains the airfoil in its centre and describes a circular area of radius 100c. It consists of 27779 points, the number of surface points equals 418 points and the structured part is composed of 27 prismatic layers. The quadratic vortex grid covers an area of $30c \times 30c$ and contains 22801 points, which results in a
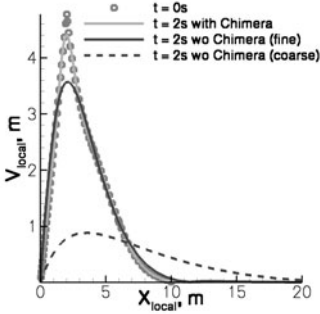
Fig. 3. Transported vortices. v_{local} of different computations, where $(\mathbf{x_{local}}, \mathbf{y_{local}}) \in [\mathbf{0}m, \mathbf{20}m] \times \{\mathbf{0}m\}$.
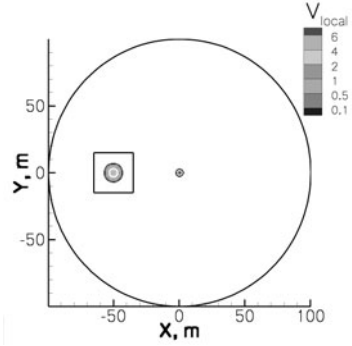
Fig. 4. NACA 0012, $\alpha = 0°$. Vortex grid and v_{local} at $\tilde{t} = 0$ within the background grid.

grid cell size of $h = 0.2c$. The flow conditions $Re = 3.8 \times 10^6$, $Ma = 0.15$, $v_{\infty,x} = v_{vg,x} = 50$ m/s and $\Delta t = 10^{-4}$s are chosen and the computation is performed until $t = 1.3$s, i.e. $\tilde{t} = 65$.

Figure 4 shows the relative position of the grids, the vortex and the airfoil at the beginning of the computation, where the vortex has already been initialised on the vortex grid. At this stage the volume of a cell of the vortex grid is approximately 50 times smaller than a cell of the subjacent part of the background grid.

First the simulation is performed until 0.66s of physical time, i.e. $\tilde{t} = 33$, have passed. As in the area of the right boundary of the vortex grid the resolution of the subjacent part of the background grid is at that time already finer than that of the vortex grid, the latter is stopped then. The vortex continues to move to the right, where it is then successively interpolated onto the background grid. Figure 5 shows the pressure distribution at the airfoil at $t = 1$s, i.e. $\tilde{t} = 50$. Due to the incidence angle of $\alpha = 0°$, no flow separation can be observed at the wing. The stagnation point has moved downwards, indicating that the vortex interaction can be interpreted as a change of the effective incidence angle. Figure 6, which shows the time history of c_l, c_d and c_m, further supports this assumption: During the first half period the effective α is increased, which results in positive values of c_l and c_m. Then α is effectively decreased in the second half period, leading to negative c_l and c_m-values. At $t = 0.981$s, i.e. $\tilde{t} = 49.05$, the lift coefficient reaches its maximal value of $c_l = 0.4097$ and the associated moment coefficient equals $c_m = 0.0966$.

At this point it is interesting to study which values of α and c_m correspond to $c_l = 0.4097$ in the case of undisturbed onflow conditions. For this purpose a steady computation without vortex is performed on the NACA 0012 grid, where a target c_l-value of 0.4097 is prescribed. Starting with $\alpha = 0°$, the angle of attack is iteratively increased until the target c_l-value has been obtained. The resulting values are $\alpha = 3.704°$ and $c_m = 0.1012$, which is in good agreement with the c_m-value from the vortex-airfoil interaction at $\tilde{t} = 49.05$. Another analogy of both computations can be seen when looking at the pressure distributions, which are shown in figure 7. Except at the leading edge of the airfoil, both curves almost coincide. In order to examine the reason
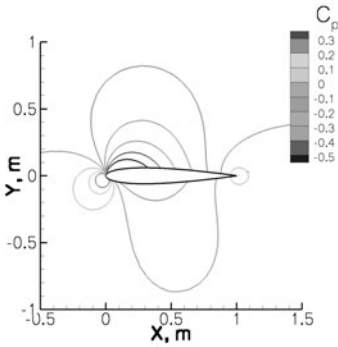
Fig. 5. NACA 0012, $\alpha = 0°$. c_p around the airfoil at $\tilde{t} = 50$.
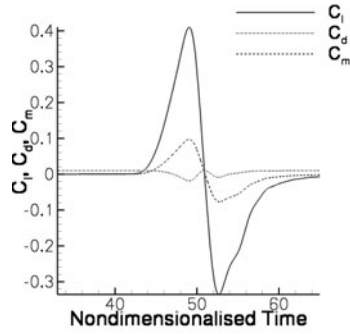
Fig. 6. NACA 0012, $\alpha = 0°$. Time history of c_l, c_d, c_m.
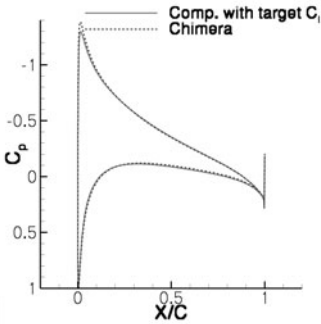
Fig. 7. NACA 0012, $\alpha = 0°$. c_p of Chimera simulation at $\tilde{t} = 49.05$ and of computation with target c_l-value.
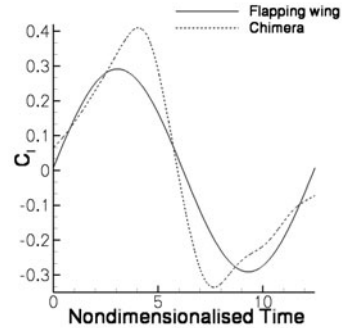
Fig. 8. NACA 0012, $\alpha = 0°$. Time history of c_l in Chimera simulation and in flapping wing computation.

for this surprisingly good agrement of the two c_p-distributions, several similar steady state simulations with undisturbed onflow conditions and prescribed target c_l-values, which belong to points of time shortly before and after $\tilde{t} = 49.05$ in the vortex-airfoil interaction, have been performed. When comparing the pressure distributions of these results with the corresponding pressure distributions of the vortex-airfoil interaction (not shown here due to space limitations) the curves again look similar but they visibly do not coincide. The extremely good agreement of the pressure distributions in figure 7 is therefore probably coincidence.

Finally a flapping wing simulation for the NACA 0012 grid is performed with an amplitude of the pitching motion of $\Delta\alpha = 3.704°$ and a period of $0.25s$, i.e. 12.5 in nondimensionalised time. Figure 8, which shows the c_l time histories of the Chimera simulation and of the flapping wing, indicates that the latter is not a satisfying approximation of the vortex-airfoil interaction.
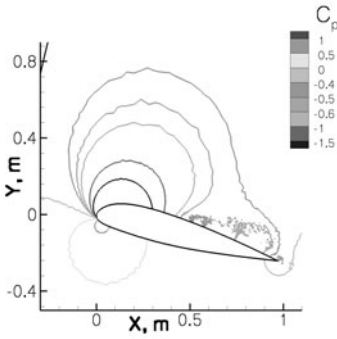
Fig. 9. Onera-A, $\alpha = 13.3°$. c_p at $\tilde{t} = 15.45$.
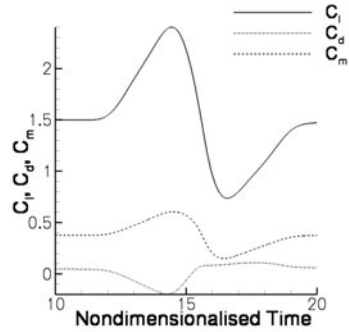
Fig. 10. Onera-A, $\alpha = 13.3°$. Time history of c_l, c_d, c_m.

3.3   ONERA-A Airfoil

In this final example the collision of a vortex, which is defined by $r_c = 1.5$m, $r_o = 7$m and $\Gamma_0 = 60 \ m^2/s$, and an ONERA-A airfoil of chord length $c = 1$m at $\alpha = 13.3°$ is simulated. The hybrid background grid contains the airfoil in its centre and describes a circular area of radius 100c. It consists of 38668 points, the number of surface points equals 530 points and the structured part contains 33 prismatic layers. The quadratic vortex grid covers an area of $12c \times 12c$ and contains 6561 points, resulting in $h = 0.15c$. The setting is described by $Re = 2.0 \times 10^6, Ma = 0.15, v_{\infty,x} = v_{vg,x} = 51.5$ m/s and $\Delta t = 2.5 \cdot 10^{-4}$s. For this configuration a small trailing edge separation occurs in the case of indisturbed flow separation. As the previous two examples showed that the vortex transport over a large distance does not have a huge impact on the simulation, the distance is shortened to reduce CPU-time. The computation is therefore only performed for 0.42s, i.e. $\tilde{t} = 21.63$. At the beginning of the simulation the volume of a cell of the vortex grid is approximately 25 times smaller than a cell of the subjacent part of the background grid.

First the simulation is performed until $t = 0.16$s i.e. $\tilde{t} = 8.24$, have passed. As in the area of the right boundary of the vortex grid the resolution of the subjacent part of the background is at that time already finer than that of the vortex grid, the latter is stopped then. Contrary to the previous example, the vortex interaction causes a significant increase in flow separation on the upper side of the airfoil. This is indicated in figure 9, which shows c_p at $t = 0.3s$, i.e. $\tilde{t} = 15.45$. Figure 10, which illustrates the time history of c_l, c_d and c_m, shows that the vortex interaction can again be interpreted as a change of the effective incidence angle.

4   Conclusion

A Chimera technique for moving grids has been successfully introduced and applied to simulate the transport of vortices and their interaction with airfoils.

The obtained results showed that the technique minimises the numerical dissipation of transported vortices, even when using a coarse background grid. Contrary to the

NACA 0012 case, flow separation could be observed at the ONERA-A airfoil due to the vortex interaction. The following computation of a flapping NACA 0012 wing turned out to be an inaccurate approximation of the vortex-airfoil interaction. Both the NACA 0012 and the ONERA-A test cases showed that the vortex-airfoil interaction can be interpreted as a change of the effective angle of attack.

Acknowledgements

References

[1] Abate, M.: Gust Boundary Condition for the TAU-Code, Technical Report IB 124–2007/9, DLR, Braunschweig, Germany (November 2007)
[2] Fabre, D., Sipp, D., Jacquin, L.: Kelvin Waves and the Singular Modes of the Lamb-Oseen Vortex. Journal of Fluid Mechanics 551, 235–274 (2006)
[3] Hariharan, N.: Rotary-Wing Wake Capturing: High-Order Schemes Toward Minimizing Numerical Vortex Dissipation. Journal of Aircraft 39(5), 822–829 (2002)
[4] Holzäpfel, F.: Probabilistic Two-Phase Aircraft Wake-Vortex Model: Furter Development and Assessment. Journal of Aircraft 43(3), 700–708 (2006)
[5] Petersson, N.A.: Hole-Cutting for Three-Dimensional Overlapping Grids. SIAM Journal on Scientific Computing, Society for Industrial and Applied Mathematics 21(2), 646–665 (1999)
[6] Rung, T., Lübcke, H., Franke, M., Xue, L., Fu, S.: Assessment of Explicit Algebraic Stress Models in Transonic Flow. In: Engineering Turbulence Modeling and Experiments, vol. 4, pp. 659–668. Elsevier, Amsterdam (1999)
[7] Schwamborn, D., Gerhold, T., Heinrich, R.: The DLR Tau-Code: Recent Applications in Research and Industry. In: Wesseling, P., Onate, E., Periaux, J. (eds.) ECCOMAS CFD 2006, Technical University Delft, The Netherlands (2006)
[8] Schwarz, T.: Ein blockstrukturiertes Verfahren zur Simulation der Umströmung komplexer Konfigurationen, DLR-Forschungsber. 2005-20, 122 S. (2005) ISSN 1434-8454

An Approach to the Gust Problem
with Interfering Profiles

W. Send

German Aerospace Center (DLR), Institute of Aeroelasticity
Bunsenstr. 10, D-37073 Göttingen, Germany
`wolfgang.send@dlr.de`

Summary

The mutual influence of two profiles is studied in subsonic and transonic 2D viscous flow. The profiles are arranged such that the second one is located downstream of the first one similar to the configuration of a tail plane behind a wing. The physical effect is that of a gust generator. The unsteady wake of the leading profile encounters the trailing profile and effects a load change. A first simplified attempt has been made using a rigid grid where both profiles execute a synchronous heaving motion.

1 Introduction

The physical phenomena occurring during a gust event have been investigated in the past primarily on an experimental basis. The very first experiment dates back to R. Katzmayr in 1922, who uses the new wind tunnel at the Aeromechanical Laboratory of the Royal Technical University in Vienna [1]. His work serves as an example for subsequent research using a gust generator [2]. An overview of research in the second half of the last century may be found in [3]. More recent work concentrates on the wake itself behind large transport aircraft [4].

Modern CFD provides access to a detailed analysis of the interaction between a gust field and an aircraft wing it effects on. The work presented here is a first step towards a broader numerical approach to a 3D configuration with more flexible kinematics. The numerical framework is the DLR Tau code [5].

The study prepares for several wind tunnel experiments in the DLR's 1x1 square meter transonic wind tunnel within the DLR project iGREEN. The results presented in this paper are based on a rigid grid where both profiles execute a synchronous heaving motion. In one of the cases the motion is turned off, and the vorticity shed from the leading profile carries a single gust event downstream to the second profile. The Fourier analysis of the load history shows the load spectrum. Besides the main purpose of the computations to predict gust loads, the unsteady flow field with the physical data given below shows interesting features like the interaction of two wakes (Figure 7), the generation and propagation of sound waves (Figure 9) and the impact of incoming vorticity on a shock front, where almost all of the supersonic domain literally is blown out (Figure 8).

2 Parameters and Steady Solution

The numerical characteristics of the solution scheme employed are

- central differences for the discretization of the fluxes for the Reynolds averaged Navier-Stokes equations (RANS) with the Spalart-Allmaras turbulence model applying Edwards' modification (SAE),

- dual time-stepping with 200 inner iterations during two subsequent physical time steps, which divide one period of motion into 360 steps,

- multi-grid procedure with 5 levels of resolution, using backward Euler relaxation for the implicit time integration and a symmetric Gauß-Seidel decomposition ((LUSGS).

The unstructured grid has been generated using CENTAUR software. The total number of points is 289 406. 325 762 triangles and 124 440 quadrilaterals for the boundary layer form the mesh. With 30 prismatic layers, each profile boundary is formed by 2 074 quadrilateral baselines. The geometric configuration shows Figure 2. The chord length c is 1 m. The kinematics are

- a synchronous heaving motion with an amplitude $h_0/c = 0.1$,

- two pairs of Mach number and Reynolds number $(Ma, Re) = (0.5, 10^6)$ and $(0.75, 10^7)$ for subsonic and transonic flow with velocities 165.8 m/s and 248.6 m/s, based on the speed of sound $c_S = 331.5$ m/s,

- the reduced frequency $\omega^* = 2\pi/5 = 1.257$ (based on c), leading to a natural frequency f of 33.3 Hz for Ma = 0.5 and of 50 Hz for Ma = 0.75.

The spatial distance between the trailing edge (TE) of the first profile and the leading edge (LE) of the second profile is 4 c (c = 1 m). The fairly high reduced frequency is chosen such that the wake length for one period of motion fits into the area of fine grid resolution covering the space around the two profiles.

The properties of the steady subsonic solution shows Figure 1. There is hardly any influence of the profiles on each other in steady flow. The two coefficients for pressure c_p and friction c_f look very similar. The characteristic numerical value y^+ is in the order of one as desired. The vorticity field $\mathbf{j}$ $(x,y,z) = curl \; \mathbf{v} \; (x,y,z)$ of the steady subsonic solution is displayed in Figure 2. The y-component of $\mathbf{j}$ points perpendicular into the paper plane. At various downstream positions x, the y-component of the vorticity in the upper half $(z > 0)$ of the flow field behind the respective TE is integrated from z/c = 0 to z/c = 1. The result is given in Figure 3. The x-coordinate in this figure is counted relative to the respective TE. Except the negative sign, the result in the lower half (not shown here) is almost equal to the one in the upper half. Both contributions are supposed to cancel each other like in the limiting case of infinite Reynolds number in 2D "inviscid" theory, where there is no wake at all. The rapid decay of the steady vorticity is surprising, because the unsteady vorticity is conserved much better.
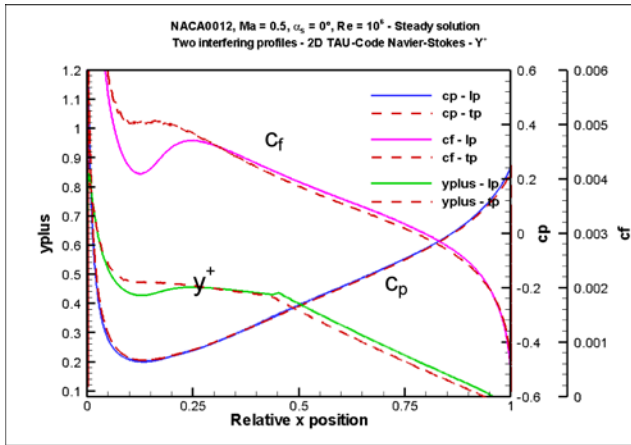
Fig. 1. Steady subsonic solution, Ma = 0.5, Re = 10^6, angle of incidence $\alpha_S = 0$ deg for both the leading profile (lp) and the trailing profile (tp).
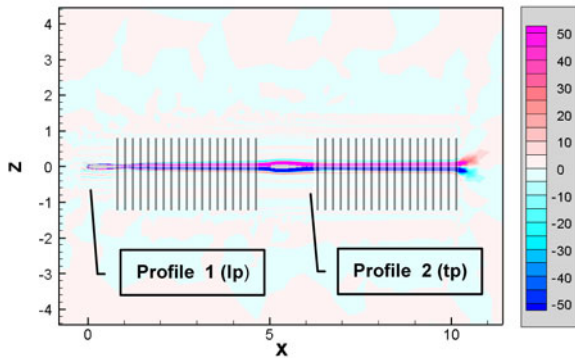
Fig. 2. Location of the 2 profiles, contours of the vorticity field of the steady solution ranging from -50 to 50 1/s for Ma = 0.5, integration paths.

3 Unsteady Subsonic and Transonic Solutions

Figures 4, 5 and 6 show the time history for the lift coefficient c_L, the moment coefficient c_M and the drag coefficient c_D. The first two figures display the results for the synchronous harmonic motion of both profiles in subsonic and in transonic flow. The unsteady heaving motion starts with an upstroke at the profiles' mean position $z = 0$. The lift history of the leading profile begins with the maximum negative value just passed at -8 deg. Except a delay in the phase position of about 25 deg for the transonic case, the two lift curves are very similar. The moment coefficients also behave like that. The trailing profile experiences a strong influence for both the subsonic and the transonic case.
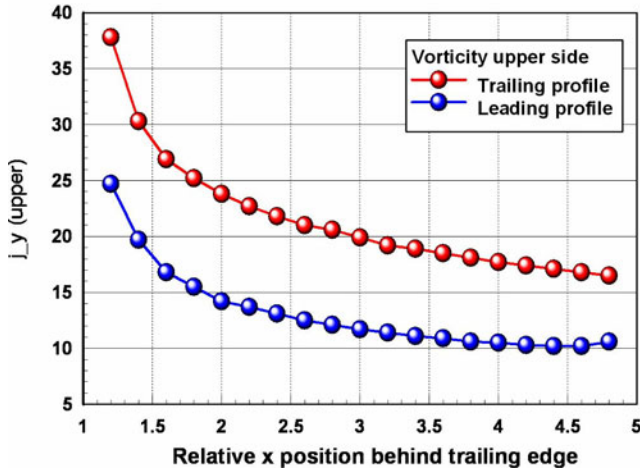
Fig. 3. Integration of vorticity in the upper half (z > 0) of the respective wake.
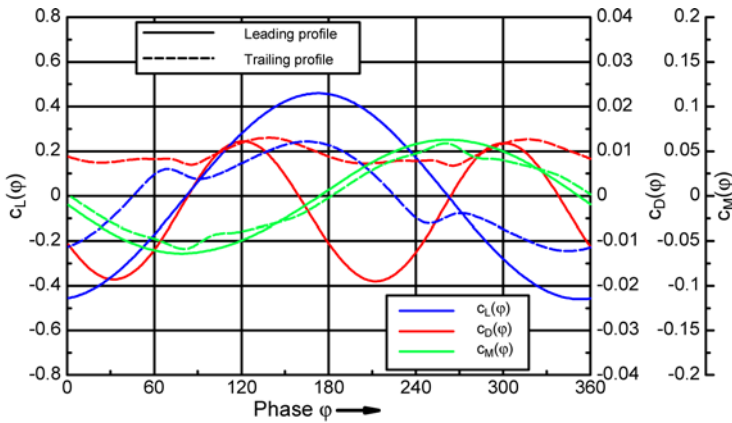
Fig. 4. Ma = 0.5, periodic motion.

The results in Figure 6 are a first approach to a single gust field. The unsteady motion is turned off and both profiles are at rest. The shed wake of the leading profile travels downstream and hits the trailing profile. The behaviour of the corresponding vorticity field is shown in Figure 7. The vorticity is accompanied by a strong vertical flow curling around the y-component of **j**, i.e. the gust. The maximum moment each time occurs right after the lift has changed its sign. The Fourier analysis of the load history shows the load spectrum (Table 1) with significant contributions to lift and moment over a wide range of frequencies.

Table 1. Fourier analysis of c_L of the trailing profile for Ma 0.75. Frequency *Freq*, percentage of contribution *p_cL* and magnitude *cL_abs*.

Harmonic motion				Gust field			
k	Freq	p_cL[%]	cL_abs	k	Freq	p_cL[%]	cL_abs
1	50.02	95.8022	0.229561	1	50.02	78.1246	0.149291
2	100.04	0.0334	0.004286	2	100.04	14.2861	0.063841
3	150.06	3.0980	0.041281	3	150.06	5.0945	0.038123
4	200.08	0.0031	0.001312	4	200.08	1.0918	0.017648
5	250.10	0.3842	0.014538	5	250.10	0.2513	0.008467
6	300.12	0.0081	0.002109	6	300.12	0.3571	0.010093
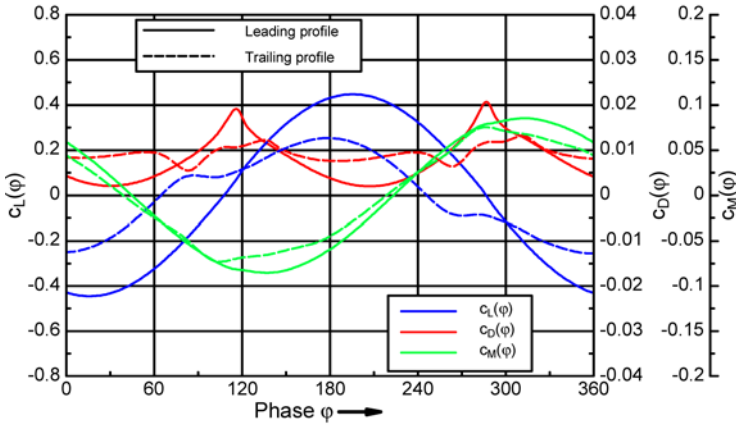
Fig. 5. Ma= 0.75, periodic motion.
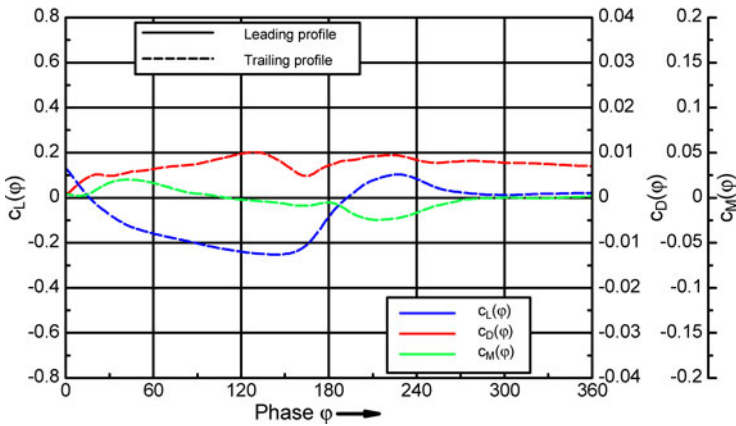
Fig. 6. Ma= 0.75, gust field.
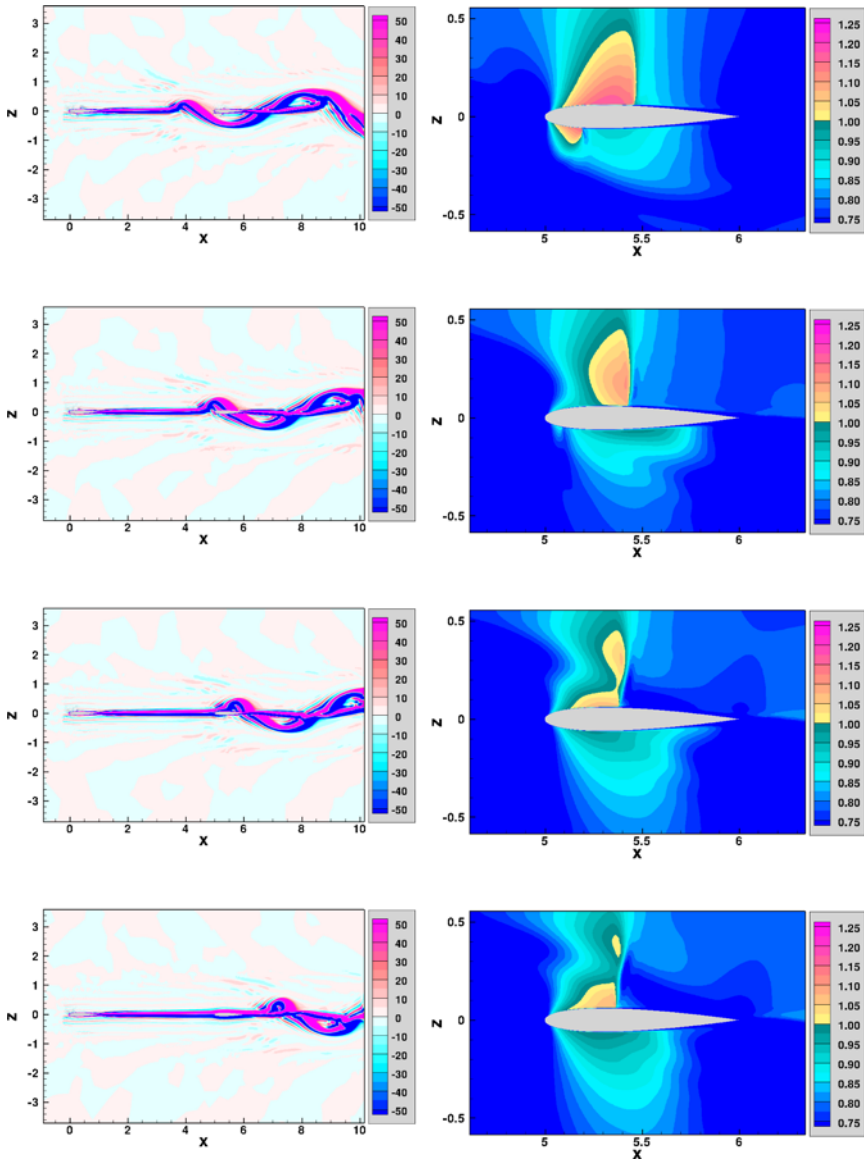
Fig. 7. Contours of the vorticity field j_y, ranging from -50 to +50 1/s. Vorticity generated by the leading profile.

Fig. 8. Contours of the Mach number Ma, ranging from 0.75 to 1.25. Sequence of frames not related to Fig. 7.

Parameters for both figures: Profile sections NACA0012 without angle of incidence, chord length c = 1 m, space between the profiles 4 c, Ma = 0.75, Re = 10^7, amplitude of heaving motion 0.1 c, red. frequency $\omega^* = 2\pi/5 = 1.257$, i.e. a wavelength 5c for the unsteady wake.
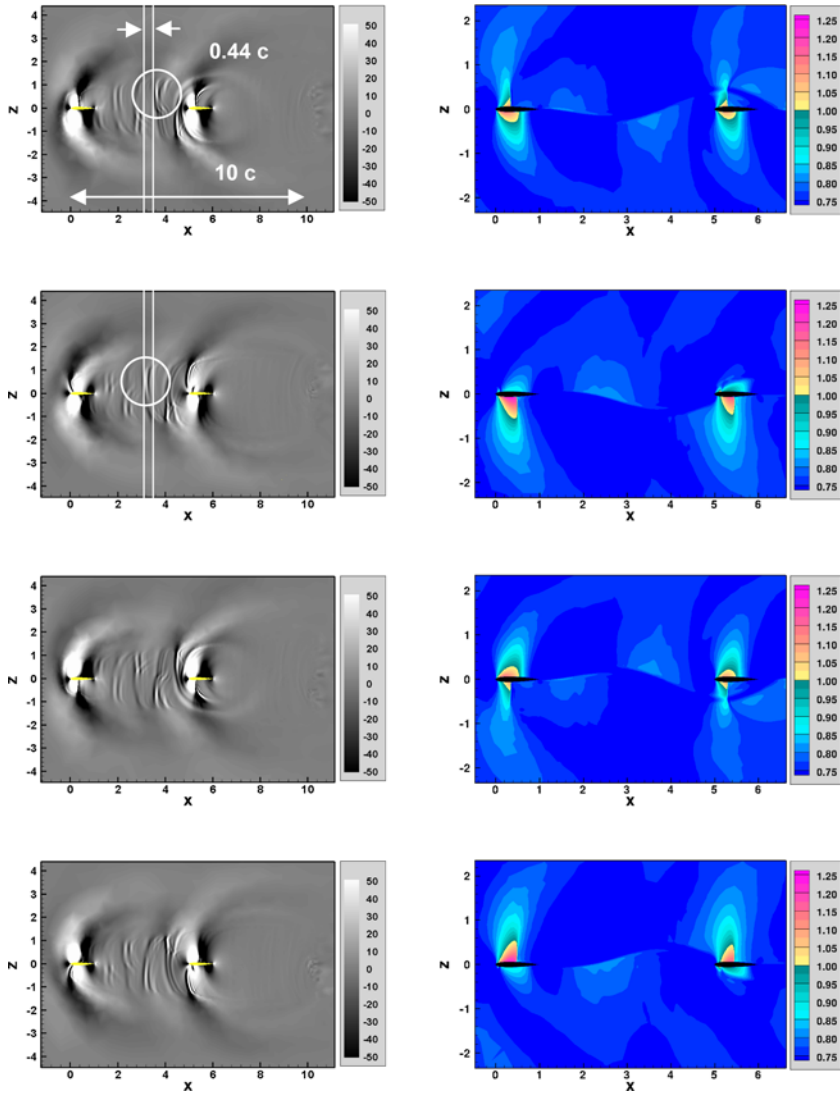
Fig. 9. Contours of the functions *div V* (left) *Ma* (right) for phase = 0, 90, 180, 270 deg.

Parameters for both figures: Profile sections NACA0012 without angle of incidence, chord length c = 1 m, space between the profiles 4 c, Ma = 0.75, Re = 10^7, amplitude of heaving motion 0.1 c, red. frequency $\omega^* = 2\pi/5 = 1.257$, i.e. a wavelength 5c for the unsteady wake.

4   Accuracy of the Unsteady Solution

The divergence of the flow field and its curl, $\delta = div\ \mathbf{v}$ and $\mathbf{j} = curl\ \mathbf{v}$, are employed to check the overall accuracy of the solutions, The curl already has been introduced. A fundamental theorem in vector analysis states that any vector field may be composed of two vector functions, the gradient of a scalar potential function and the curl of a vector potential function. δ and $\mathbf{j}$ serve as source functions for these two potential functions. They are related to the physical properties compressibility and viscosity. The propagation of sound waves is represented by unsteady divergence, the propagation and diffusion of momentum, transferred into the fluid from the moving surfaces, by vorticity. The speed of sound waves travelling upstream is estimated from the velocity of sound and the position of a disturbance in two subsequent frames displaying the divergence. Figure 9 is marked with the displacement of the encircled disturbance during the time interval T/4 with 1/T = f. The distance is roughly 0.44 c, the time interval 5 ms, which results in 88 m/s. From Ma = 0.75 and the speed of sound, a slightly different value of 83 m/s is expected, which is a good agreement.

The amplitude of vorticity $j_y(x,z,t)$ and its integral for one cycle of motion, the vanishing circulation $\Gamma = 0$, are calculated at various downstream positions *x-pos* in Table 2. The error *Err*, the ratio of Γ (*Gamma*) to the amplitude *Ampl* of the oscillating vorticity is less than 1 %. The amplitude is well preserved (Table 2).

Table 2. Circulation Γ and vorticity (Ampl) for Ma = 0.75 behind both profiles.

Wake of the leading profile				Wake of the trailing profile			
x-pos	Gamma	Ampl	Err %	x-pos	Gamma	Ampl	Err %
1.2000	−1.25	62.7	−1.99	6.2000	0.189	85.7	0.22
1.4000	−0.750	57.5	−1.31	6.4000	−0.248	83.2	−0.30
1.6000	−0.310	57.1	−0.54	6.6000	−0.179	83.8	−0.21
1.8000	−0.429	56.1	−0.76	6.8000	−0.261	83.9	−0.31
2.0000	−0.420	55.4	−0.76	7.0000	−0.444	83.4	−0.53
3.0000	−0.431	55.3	−0.78	8.0000	−0.090	82.2	−0.11
4.0000	−0.197	58.0	−0.34	9.0000	−0.096	86.4	−0.11

5   Conclusions

The interaction between a gust induced by a profile oscillating upstream and a downstream located profile can well be simulated using the simplification of a synchronous heaving motion. This first approach avoids additional numerical implications caused by the chimera grid generation technique, which needs to be applied for profiles being in motion relative to each other. The constraint will be released in the future work. The accuracy of the computation is investigated using inherent physical properties. The result of the circulation being preserved within an error in the order of one percent indicates a proper setting of the numerical parameters for the numerical computation of the flow field.

References

[1] Katzmayr, R.: Über das Verhalten der Flügelflächen bei periodischen Änderungen der Geschwindigkeitsrichtung. ZFM Heft 6(13), 80–82 (1922)

[2] Freymann, R.: Die Böensimulationsanlage des 3m x 3m – Niedergeschwindigkeitskanals der DFVLR in Göttingen, DFVLR-FB 85-04 (1985)

[3] Krag, B., Wegner, W.: Generation of Two-Dimensional Gust Fields in Subsonic Windtunnels. In: AGARD Conference Proc. 386, AGARD-CP-386, Joint Symposium of the Fluid Dynamics and Flight Mechanics Panels, Göttingen (FRG), May 6-9 (1985)

[4] de Bruin, A.C., Schrauf, G.: Wake Vortex Results From The AWIATOR Project. In: CEAS Congress 2007, Berlin, CEAS-2007-008, September 10-13 (2007)

[5] Suggested reference for more information, `http://tau.dlr.de`

Application of the Immersed Boundary Method for the Simulation of Incompressible Flows in Complex and Moving Geometries

Eike Hylla, Octavian Frederich, Johannes Mauß, and Frank Thiele

Berlin Institute of Technology, Institute of Fluid Mechanics and Engineering Acoustics,
Müller-Breslau-Str. 8, 10623 Berlin, Germany
`eike.hylla@cfd.tu-berlin.de`
`http://www.cfd.tu-berlin.de`

Summary

A new variant of the *Immersed Boundary Method* (IBM) has been implemented into an established flow solver. Important aspects of the implementation towards the application of this approach for flow simulations in complex and moving geometries are characterised. Simple validation test cases are addressed first, followed by a moving boundary example and more complex geometries like the Weibel lung model.

1 Introduction

The generation of structured body-fitted computational grids is time-consuming and runs into problems, when the geometry is complex. Moving geometries can be handled by grid deformation algorithms but are limited to small deviations in general. The IBM is a numerical approach, which can avoid these problems. The method was first introduced by Charles Peskin in 1972, for the simulation of blood flow through heart valves [1]. Instead of a body-fitted grid, two grids are used: a Cartesian computational grid and one to represent the surface of the body. Imposition of the boundary conditions at the surface grid, which is *immersed* into the Cartesian grid, is the main issue of the IBM. The essential advantage of this method is the distinction between the computational grid and the surface description. This makes it possible to consider complex and moving or deforming geometries during the simulation. Today, further developments and numerous variations of this method exist. While Peskin [2] applied a *continuous forcing approach* modifying the governing equations to satisfy the boundary conditions, most variations use a *discrete forcing approach* [3], where the boundary conditions are imposed following the discretization on the Cartesian grid. In the framework of the *ghost-cell-method* [4] cells outside of the flow field but next to the surface are used to fulfill the boundary conditions by interpolating appropriate velocities for these ghost-cells.
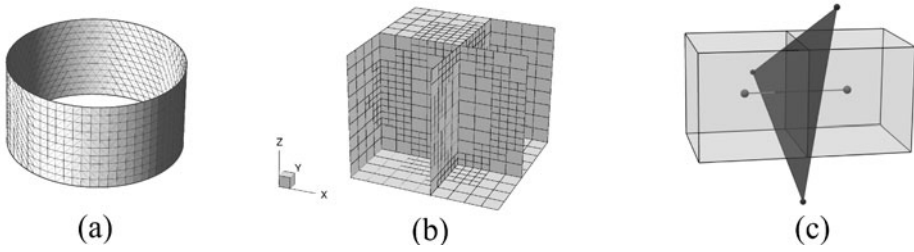
Fig. 1. Surface grid (a), Cartesian domain grid (b), adjacent cells hit by IB triangle (c)

2   Fundamentals of Implementation

A new kind of the ghost-cell-method [5] is implemented into the finite-volume based in-house flow solver [6]. The advantage compared to other established methods is, that the algorithm neglects the calculation of the non-fluid *and* the ghost-cells. Interpolated values of the ghost-cells are shifted to the source term of adjacent inner cells (cf. 2.3). In the following important aspects of the implementation are described.

2.1   Surface and Domain Grids

The surface of the geometry can be easily discretized using interconnected triangles (fig. 1 a). Complex or curved surfaces may require a finer resolution to give an appropriate discretization of the geometry. To distinguish between different kinds of boundary conditions, the associated triangles are grouped separately.

The domain grid (fig. 1 b) has a strict Cartesian 3d structure with orthogonal cells aligned to the Cartesian directions x, y, z. Isotropic grid refinement employing hanging node elements (with a split ratio of 1:2) can be used to effect a higher resolution near the IB. Therefore a mesh generator has been set up, which improves the local mesh resolution by subdividing cells depending on given threshold distances to the surface. The high number of possible refinement levels requires an unstructured data format for the domain grid, leading to the necessity of an unstructured solver for the equation system (see section 2.5). The computational grid passes a preprocessing step, where the decomposition for multiprocessing purpose is done. The shape and structure of the coefficient matrix is detected and stored in *Compressed Row Storage* format [7], which is best suited for sparse matrix handling.

2.2   Domain Identification and Marking Algorithm

Before the simulation, the identification and marking of the computational domain is necessary to distinguish between fluid and non-fluid regions. The neighboring cells of element faces to be divided by the IB must therefore be found (fig. 1 c). To achieve that, each domain face has to be checked with every IB triangle for possible intersection points. Those points and hit faces are stored. The areas intersected by the immersed boundary are gradually marked with a painter variable [5].
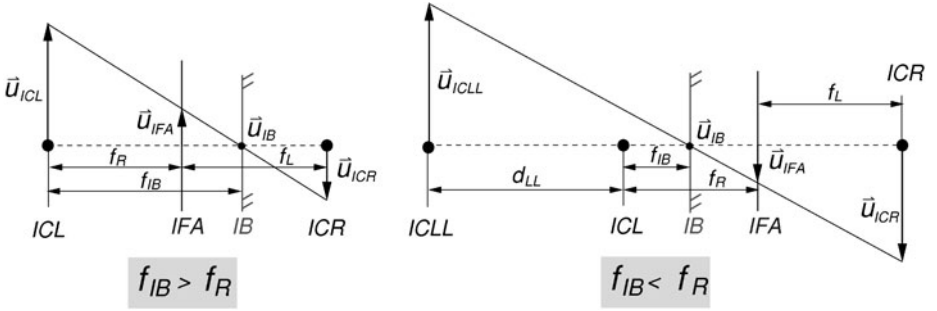
Fig. 2. Different velocity interpolations at IB walls, depending on the intersection point

2.3   Imposition of Boundary Conditions

In the present simulation software, inflow, outflow and wall boundary conditions can be set using IB's. The general approach for all of these boundary conditions is the same. The difference between this method and other established ghost-cell approaches is, that the ghost-cells, which are the non-fluid neighbors of fluid cells, are really not being calculated. Within the flow field discretization for an arbitrary variable Φ leads to an equation for each cell p, including coefficient contributions $a_\square$ from the neighboring cells nb and a source term S_ϕ:

$$\Phi_p a_p + \sum \Phi_{nb}\, a_{nb} = S_\Phi$$

As the calculation of Φ neglects all non-fluid cells, contributions from neighboring ghost-cells are gained by interpolation and shifted to the source term:

$$\Phi_p a_p + \sum \Phi_{nb}^{in}\, a_{nb}^{in} = S_\Phi - \sum \Phi_{nb}^{ghost}\, a_{nb}^{ghost}$$

The no-slip wall is the most important boundary condition for complex geometries and its treatment is discussed in the following. Velocities $\boldsymbol{u}$ of the ghost-cells and the adjoining cell face are linearly interpolated in one direction (see fig. 2) to fulfill the no-slip condition on the IB ($\boldsymbol{u}_{IB} = 0$ in the non-moving case):

$$\left.\begin{aligned}
\boldsymbol{u}_{IFA} &= \boldsymbol{u}_{ICL} \cdot \left(1 - \frac{f_R}{f_{IB}}\right) + \boldsymbol{u}_{IB} \cdot \left(\frac{f_R}{f_{IB}}\right) \\
\boldsymbol{u}_{ICR} &= \boldsymbol{u}_{ICL} \cdot \left(1 - \frac{1}{f_{IB}}\right) + \boldsymbol{u}_{IB} \cdot \left(\frac{1}{f_{IB}}\right)
\end{aligned}\right\} \quad f_{IB} > f_R$$

$$\left.\begin{aligned}
\boldsymbol{u}_{IFA} &= \boldsymbol{u}_{ICLL} \cdot \frac{f_{IB} - f_R}{f_{IB} + d_{LL}} + \boldsymbol{u}_{IB} \cdot \left(1 - \frac{f_{IB} - f_R}{f_{IB} + d_{LL}}\right) \\
\boldsymbol{u}_{ICR} &= \boldsymbol{u}_{ICLL} \cdot \left(\frac{f_{IB} - 1}{f_{IB} + d_{LL}}\right) + \boldsymbol{u}_{IB} \cdot \left(1 - \frac{f_{IB} - 1}{f_{IB} + d_{LL}}\right)
\end{aligned}\right\} \quad f_{IB} < f_R$$

The center of the inner cell is named ICL, the outer one ICR, the face neighboring these cells IFA and the position at the immersed surface IB. To avoid the occurrence

of high velocity values at the ghost-cells, which can cause numerical instability, the second interpolation is used if the IB is located very close to the inner cell ICL. The product of velocity and coefficient part of the ghost-cell is then added to the source term. Thereafter the velocity gradient is recalculated, fitting to the appropriate interpolation. The pressure is extrapolated linearly to the IB and the pressure gradient is also recalculated. Finally the mass flux through the involved faces is corrected to be parallel to the IB. The linear interpolation provides first order accuracy at the immersed boundary. To increase accuracy this approach can be replaced by a higher order interpolation.

2.4 Moving Wall Boundary Condition

In most instances a moving boundary condition makes sense only for a no-slip wall. To realize a moving surface, its spatial description has to be known in every time step. Fluid velocities at a moving wall are not zero, they comply with the velocity of the wall itself. This case is considered in the above interpolation: $\boldsymbol{u}_{IB}$ is the velocity vector at the IB, which vanishes in the non-moving case. The velocity of each triangle element of the surface description can be approximated with the displacement $\Delta\boldsymbol{x}_{IB}$ and the time step Δt:

$$\boldsymbol{u}_{IB} \approx \frac{\Delta\boldsymbol{x}_{IB}}{\Delta t}.$$

The identification and marking procedures have to be performed once again, after the IB has changed. Outer cells that become fluid cells during calculation gain their velocity and pressure values with ongoing iteration.

2.5 Solving the Equation System

Discretization and linearization of the governing equations in conjunction with conventionally and IB treated boundary conditions leads to a linear equation system:

$$\mathbf{A} \cdot \boldsymbol{\Phi} = \mathbf{S}_{\boldsymbol{\Phi}}$$

This system comprising of an arbitrary and sparse coefficient matrix $\mathbf{A}$, the variable vector $\boldsymbol{\Phi}$ and a source term $\mathbf{S}_{\boldsymbol{\Phi}}$ is solved using a BiCGSTAB solver. A range of preconditioners like incomplete *LU* or *Cholesky* decomposition are available to improve the convergence behavior. The equations for the velocities and the SIMPLE pressure correction are solved successively.

3 Results

After implementation of the main functions required for IB treatment, an in-depth validation phase follows. Due to the lack of a turbulence model these test cases have to be of incompressible and laminar nature. First simple test cases are used for validation. Afterwards harmonically oscillating IB's are implemented. Finally, the method is applied to cases of increasingly complex geometry, starting with simple 3d pipes and ending with the Weibel lung model.
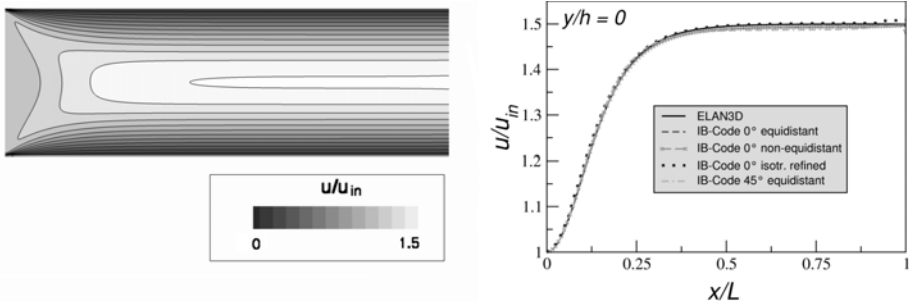
Fig. 3. Developing laminar channel flow at $\mathrm{Re} = 20$. Left: contour plot of u-velocity (only fluid region visible), right: comparison to results of original flow solver
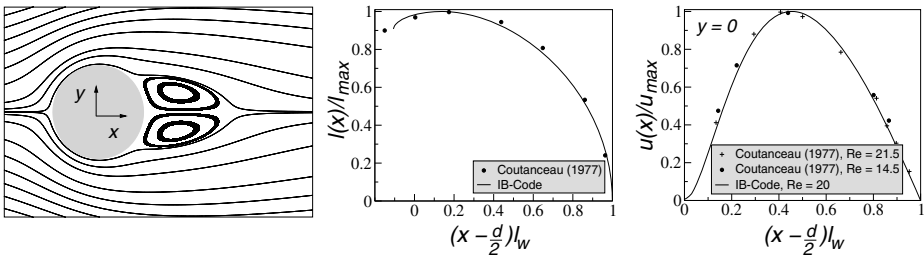
Fig. 4. Laminar cylinder flow at $\mathrm{Re} = 20$ in comparison with experimental data (d: cylinder diameter, l_w: length of the wake, l_{max}: maximum height of the wake)

3.1   Validation Test Cases

Developing flow in a 2d channel is a simple test case to validate IB inflow, outflow and wall boundary conditions. The solution can be directly compared to the results obtained by the original solver. Equidistant, non equidistant and isotropically refined Cartesian grids and the IB under rotation angles of $20\,^{\circ}$ and $45\,^{\circ}$ are tested. The velocity of the fully-developed channel flow near the outlet and the increasing u-velocity in the channel centerline can be compared to the analytical solution and the reference simulation (see fig. 3).

Laminar steady ($\mathrm{Re} = 20$) and unsteady ($\mathrm{Re} = 120$) flow past a 2d circular cylinder are test cases, that use the IB's only at the cylinder surface. The laminar wake regime behind the cylinder and the vortex shedding frequency in the unsteady case are adequate features to be compared with experimental results gathered in [8] (see fig. 4).

Both the channel and cylinder flow yield satisfactory results within the modeling scope.

3.2   Oscillating Rectangular Prism

Flow past an oscillating rectangular prism is an appropriate test case to demonstrate the advantage of the IBM. The new position of the body is calculated every time step,
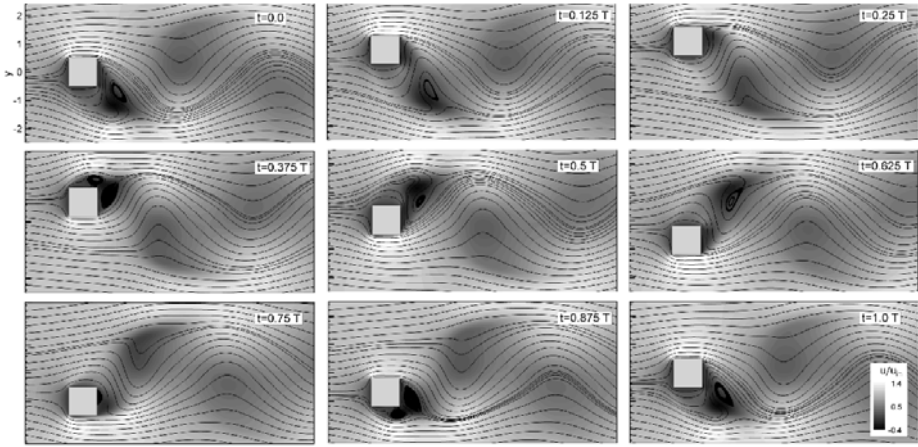
Fig. 5. Flow around an oscillating prism (Re $= 200$, $A/a = 1$, $\omega/\omega_0 = 0.72$)

followed by the identification and marking procedure. As the surface of the prism coating (length a) is representable by only 8 triangles, identifying the domain is relatively time saving (see section 2.2). The deviation in y-direction of the prism is given by:

$$y(t) = A\sin(\omega t)$$

with the angular frequency $\omega = 2\pi f$ and the amplitude of deviation A. The fluid velocities at the IB can be determined analytically by the first derivative. The undisturbed flow past the non oscillating prism has been calculated for Reynolds numbers 170, 200 and 250. The predicted Strouhal number of $\mathrm{St}_0 = 0.138$ of a non oscillating case coincides with experiments from Okajima [9]. The set of pictures (fig. 5) shows the velocity field of one oscillation period (Re $= 200$, amplitude: $A/a = 1.0$, frequency ratio: $\mathrm{St}/\mathrm{St}_0 = 0.72$). It can be seen, that the fluid adheres at the surface and follows the prisms movement. At the maximum deviation separation regions evolve behind the prism (fig. 5: $t = 0.375T$ and $t = 0.875T$), which detach downstream with increasing prism velocity. Spectral analysis of the fluctuating values (e.g. the vertical velocity in a fixed monitoring point) leads to the frequencies contained. The dominant part of the spectrum is the prescribed oscillating frequency whereas the natural frequency St_0 is vanishing.

3.3 More Complex Geometries

Turning from simple validation test cases to more complex geometries, 3d pipes and pipe junctions are investigated. One of the principal aims is the application of the IB-based solver to predict flow physics in the bronchial tree of the upper human lung [10]. The surface, which can be gained by medical CT scans is very complex and intensely curved. The lung model (A) of Weibel [11] is an appropriate first test case for such simulations. It is a 4th generation model consisting of joined pipes with different diameters, branching angles of $\Theta = 60°$ and plane angles of $\Phi = 90°$.
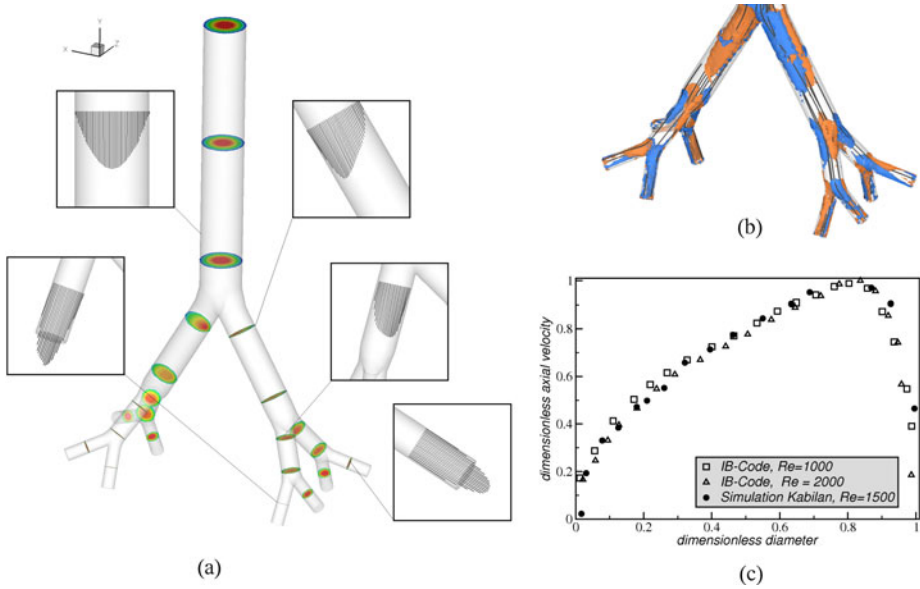
Fig. 6. 4 generation Weibel lung at $Re = 2000$: Velocity profiles and absolute velocity contour levels (a), helicity isosurfaces explaining counterrotating regions (b), comparison of the velocity profile behind 1. bifurcation with results of Kabilan [13]

A laminar velocity profile, which can be obtained by the law of Hagen-Poiseuille, is set to the inlet. Mass flux at the outlets is constant, derived from the respective outlet area. The Reynolds number is determined by the diameter of the first generation tube, kinematic viscosity and the mean inflow velocity. Simulations with increasing Reynolds numbers $Re = 10, 100, 1000$ and 2000 are carried out. Since the whole geometry has a symmetric shape, the flow is also symmetrical. The eight outlet branches can be divided into two groups: four branches that point to the outside and four that point to the inside. Velocity profiles between these two groups of outlet branches differ from each other, which was also found by [12]. Axial velocity profiles and contour plots of the absolute velocity in several stages and planes of interest are shown in figure 6 a. The inlet velocity profile is preserved up to the first bifurcation, where the mean flow is superposed by Dean flow effects, which can be illustrated by helicity contour plots (see fig. 6). The axial velocity profile behind the first bifurcation fits well with the CFD results from Kabilan et al. [13] at Reynolds number of 1500 (see fig. 6 b).

4   Conclusion and Outlook

The IBM was successfully implemented into the established in-house flow solver. All validation studies deliver satisfactory results and coincide well with experiments. The

flow prediction in the Weibel lung model yields promising results in terms of simulating the flow in a realistic CT based lung.

Further work will be carried out to make the solver more applicable to a wider range of problems: turbulence modeling, calculation of integral forces. To improve convergence or to refine the grid at a moving boundary, h-adaptive grid techniques are conceivable.

Acknowledgments

References

[1] Peskin, C.S.: Flow patterns around heart valves: a numerical method. Journal of Computational Physics 10, 252–271 (1972)

[2] Peskin, C.S.: The immersed boundary method. Acta Numerica, pp. 479–512. Cambridge University Press, Cambridge (2002)

[3] Mittal, R., Iaccarino, G.: Immersed boundary methods. Annual Review of Fluid Mechanics 37, 239–261 (2005)

[4] Tseng, Y., Ferziger, J.H.: A ghost-cell immersed boundary method for flow in complex geometry. Journal of Computational Phyics 192(2), 593–623 (2003)

[5] Hylla, E.: Validierung und Erweiterung eines numerischen Verfahrens zur Simulation von inkompressiblen Strömungen mittels der Immersed Boundary Methode. Diploma Thesis, ISTA TU-Berlin (2008)

[6] Xue, L.: Entwicklung eines effizienten parallelen Lösungsalgorithmus zur dreidimensionalen Simulation komplexer turbulenter Strömungen. PhD Thesis, TU-Berlin (1998)

[7] Smailbegovic, F.S., Gaydadjiev, G.N., Vassiliadis, S.: Sparse Matrix Storage Format. In: Proceedings of the 16th Annual Workshop on Circuits, Systems and Signal Processing, pp. 445–448 (2005)

[8] Zdravkovich, M.M.: Flow Around Circular Cylinders. Fundamentals, vol. 1. Oxford Science Publications (1997)

[9] Okajima, A.: Strouhal numbers of rectangular cylinders. Journal of Fluid Mechanics 123, 379–389 (1982)

[10] Frederich, O., Amtsfeld, P., Hylla, E., Thiele, F., Puderbach, M., Kauczor, H.-U., Wegener, I., Meinzer, H.-P.: Numerical Simulation and Analysis of the Flow in Central Airways. In: Proceedings of STAB 2008. NNFM. Springer, Heidelberg (to be published, 2009)

[11] Weibel, E.R.: Morphometry of the Human Lung. Springer, Berlin (1963)

[12] Nowak, N., Kakade, P., Annapragada, A.: Computational Fluid Dynamics Simulation of Airflow and Aerosol Deposition in Human Lungs. Annals of Biomedical Engineering 31, 374–390 (2002)

[13] Kabilan, S., Lin, C., Hoffman, E.: Characteristics of airflow in a CT-based ovine lung: a numerical study. Journal of Applied Physiology 102, 1469–1482 (2007)

Turbulence Modeling and Detached Eddy Simulation with a High-Order Unstructured Discontinuous Galerkin Code

Christian Lübon, Manuel Kessler, and Siegfried Wagner

Universität Stuttgart, Institut für Aerodynamik und Gasdynamik,
Pfaffenwaldring 21, 70569 Stuttgart, Germany
luebon@iag.uni-stuttgart.de

Summary

In the present paper a high-order Discontinuous Galerkin method is presented for the numerical simulation of the separated turbulent flow around complex geometries using unstructured grids. Bassi and Rebay extended the Discontinuous Galerkin method to solve the Navier-Stokes equations for laminar and 3D turbulent flows. Especially, an extension will be provided to calculate unsteady separated flows with a Detached Eddy Simulation, which is a hybrid method between the Unsteady Reynolds averaged Navier-Stokes approach and the Large Eddy Simulation. Some results, like flows over a flat plate and around a sphere, which could not be predicted with an Unsteady Reynolds averaged Navier-Stokes calculation, are calculated with high accuracy and compared with theory and experiments.

1 Introduction

The Discontinuous Galerkin (DG) method combines ideas from the finite element and finite volume methods, the physics of wave propagation, expressed by Riemann problems, and the accuracy obtained by high-order polynomial approximations within elements. It was originally developed for hyperbolic conservation laws in 2D flow [3] and sometimes 3D flow [16], including the Euler equations.

However, in real life applications the flow is in most cases turbulent and 3D. The original development of DG methods was devoted to the Euler equations that contain only derivatives of first order. The breakthrough for solving the Navier-Stokes equations with derivatives of second order was achieved by Bassi and Rebay [2]. Still another big step was to be done, namely to extend the algorithms for the handling of turbulent flows. The unsteady Reynolds averaged Navier-Stokes (URANS) equations had to be solved. Thus, the algorithms

had to be extended to include turbulence models [4, 5]. The present paper is based on our previous experience [9, 10] and extends the algorithms to three-dimensional turbulent flow. This was done by solving the URANS equations and by implementing a Detached Eddy model.

2   Discontinuous Galerkin Schemes

2.1   Basic Equations

The Navier-Stokes equations can be written in the following compact differential form

$$\frac{\partial U}{\partial t} + \nabla \cdot \mathcal{F}_i(U) - \nabla \cdot \mathcal{F}_v(U, \nabla U) = 0 \tag{1}$$

Here U is the vector of conservative variables, $\mathcal{F}_i$ and $\mathcal{F}_v$ are the convective and diffusive flux functions, respectively. The next step is to handle high-order derivatives. According to Bassi and Rebay [2] we first reformulate this equation as a first-order system introducing the gradient of the solution ∇U as a new additional independent unknown Θ and get a second equation

$$\nabla U - \Theta = 0 \tag{2}$$

We now apply the DG approach resulting in the equations for an element E

$$\int_E v_k \Theta dE - \oint_{\partial E} v_k \cdot U_h \cdot \boldsymbol{n} \, d\sigma + \int_E \nabla v_k \cdot U_h dE = 0 \tag{3}$$

$$\int_E \left(v_k \frac{\partial U_h}{\partial t} \right) dE + \oint_{\partial E} v_k \cdot \mathcal{F}_i \cdot \boldsymbol{n} \, d\sigma - \int_E \nabla v_k \cdot \mathcal{F}_i dE$$

$$- \oint_{\partial E} v_k \cdot \mathcal{F}_v \cdot \boldsymbol{n} \, d\sigma + \int_E \nabla v_k \cdot \mathcal{F}_v dE = 0 \tag{4}$$

where $U_h = U(x,t) = \sum_{k=1}^n U_k(t) v_k(x)$ is the approximation for the numerical solution U_k, and the n shape functions v_k are a basis for the polynomial space P^k.

Our scheme can be advanced explicitly as well as implicitly in time. The explicit time integration, used in this paper, is performed with one-step Runge-Kutta type schemes of first to fourth order accuracy.

2.2   Turbulence Modeling

In the present URANS cases the one equation Spalart-Allmaras (SA) model is used [13]. The following equation shows the distribution of the transport variable $\widetilde{\nu}$

$$\frac{\partial \rho \widetilde{\nu}}{\partial t} + \frac{\partial \rho \widetilde{\nu} u_i}{\partial x_i} = \frac{1}{\sigma} \left[\frac{\partial}{\partial x_i} \left((\mu + \rho \widetilde{\nu}) \frac{\partial \widetilde{\nu}}{\partial x_i} \right) + \rho c_{b2} \frac{\partial \widetilde{\nu}}{\partial x_i} \frac{\partial \widetilde{\nu}}{\partial x_i} \right]$$

$$+ c_{b1}(1 - f_{t2}) \rho \widetilde{S} \widetilde{\nu} - \left(c_{w1} f_w - \frac{c_{b1}}{\kappa^2} f_{t2} \right) \frac{1}{\rho} \left(\frac{\rho \widetilde{\nu}}{d} \right)^2 + \rho f_{t1} \Delta U^2 \tag{5}$$

with d as the distance to the closest wall, which represents the turbulent length scale, the vorticity $\widetilde{S}$ and some calibration constants c_i and calibration functions f_i. The main flow equations and the turbulence model equations are solved in a fully coupled manner.

2.3   Turbulence Limiting

From the finite volume method it is well known that the discretization of the transport equations within a turbulence model is a difficult task. High-order methods tend to become unstable when the numerical discretization is inadequate to resolve the true physical solution. It is necessary to stabilize the turbulence model equations to prevent the eddy viscosity, or for the SA model $\widetilde{\nu}$, from becoming negative.

For low order calculations with P^0- or P^1-elements we choose the hard limiting method according to Landmann [7]. In this approach the solution vector u_h should not fall below zero in the elements. For the constant or linear case of the DG polynomial approximation it is easy to determine the global minimum, only the element corners have to be checked. For higher order elements the problem is more difficult because we have to determine the global minimum in every cell. Because of this we use for elements higher than P^1 the approach according to Nguyen et al. [11] where an artificial viscosity term is added to stabilize the turbulence model:

$$\mathcal{F}_{\text{stab}}(U, \nabla U) = \frac{h}{p}\epsilon(\psi(\widetilde{\nu}))\mathcal{F}_v(U, \nabla U), \tag{6}$$

where h and p are the element size and the order of the approximation, $\widetilde{\nu}$ is the sensor variable for the indicator $\psi(\widetilde{\nu})$ which represents the high frequency content in the sensor variable $\widetilde{\nu}$. $\epsilon(\psi)$ is the piecewise element constant viscosity parameter in the model terms.

For calculating the crucial indicator ψ, we first define the total energy E and the energy of the high-order degrees of freedom E_h:

$$E = \widehat{\widetilde{\nu}}^T M \widehat{\widetilde{\nu}}, \tag{7}$$

$$E_h = \widehat{\widetilde{\nu}}^T M_h \widehat{\widetilde{\nu}}. \tag{8}$$

M is the usual mass matrix for the element, but M_h is the mass matrix using only the high-order coefficients. This leads to the calulation of the indicator:

$$\psi(\widetilde{\nu}) = \log \frac{E_h}{E}. \tag{9}$$

If the sensor variable $\widetilde{\nu}$ is determined to be under-resolved and could fall below zero, the corresponding diffusion term is activated with an element piecewise constant value of viscosity.

2.4   Detached Eddy Simulation

The Detached Eddy Simulation (DES) in this study is based on a modification of the S-A model, such that it reduces to RANS close to solid walls and to LES away from the wall [14]. In the S-A turbulence model the turbulent length scale, the distance to the nearest wall d, is replaced by l_{DES}, defined by $l_{DES} = min\left(d, C_{DES}^{SA}\Delta\right)$ where Δ in this case is the largest cell spacing and $C_{DES}^{SA} = 0.65$ is an additional model constant, calibrated for homogeneous turbulence. Near solid boundaries Δ is larger than d and we get a model that acts as a S-A model. Far from walls $d >> \Delta$ a balance between the production and destruction term in the model equation shows that $\widetilde{\nu} \sim S\Delta^2$ like a one-equation subgrid-scale model. Because of the LES part a high-order spatial discretization scheme like the DG scheme with low dissipation is necessary to resolve the large eddies correctly, while the smaller ones are modeled.

3   Results

3.1   Flat Plate Flow

For a detailed validation of the laminar 3D implementation we calculated the flow over a flat plate ($Re = 1 \cdot 10^5$ and $Ma = 0.3$) and compared the velocity and skin friction profiles (Figure 1) with the theoretical solution.
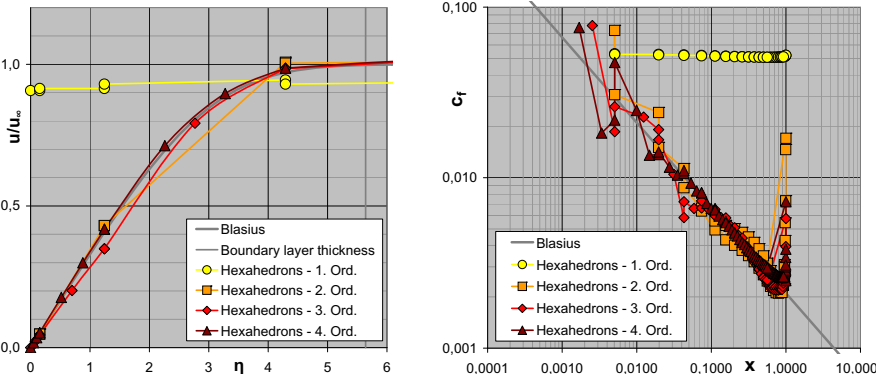
Fig. 1. Velocity and skin friction profile

For the calculations we use really coarse meshes. The results shown are generated on a mesh with 256 cells in total and 8 cell in normal direction. Looking at the first order P^0 solution, it is completely away from the physics, but we get good results for elements higher than P^2. Note that the boundary layer is discretized with only two cells but up to 40 degrees of freedom dependent on the order.

For the validation of the turbulent flow we calculated the fully turbulent flat plate flow with a Reynolds number of $Re = 3 \cdot 10^6$ and a Mach number of

Ma $= 0.3$ using the RANS approach based on the SA model on several grids with different sizes. The results shown in this paper (Figure 2) are calculated on an extremely coarse mesh like in the laminar case with a size of 32 cells in streamwise direction, 1 cell in spanwise direction and only 8 cells in normal direction. The near-wall resolution for elements higher than P^2 is $y^+ \approx 5$.
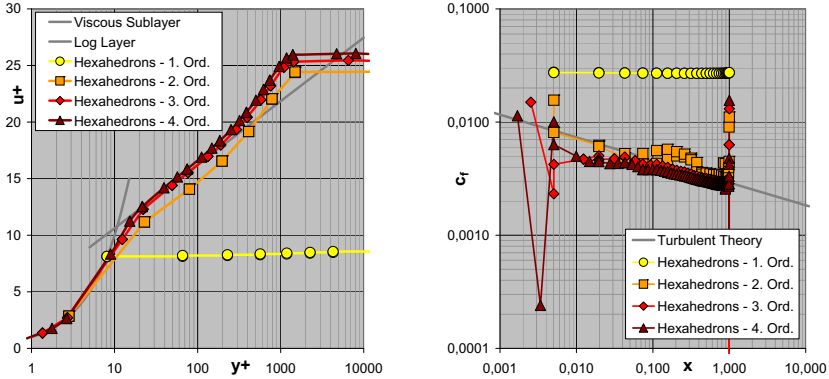
Fig. 2. The law of the wall and skin friction profile

Due to the finite element approach in the DG cells we found a good agreement between the computed and theoretical normalized velocity profiles and are able to reach the law of the wall with this coarse grid as well as the skin friction profile compared with the theory [12]. The third-order hexahedral solution for example works with ten degrees of freedom per cell which is comparable to 4 degrees of freedom in normal direction. For our mesh with only 8 cells in normal direction this means that we use 32 degrees of freedom in this direction.

3.2   Detached Eddy Investigation of the Flow Past a Sphere

The flow past a sphere belongs to the class of separated flows for which the location of flow detachment is not fixed by the geometry and it is not possible to use a classical URANS approach, because of the missing spectral gap between modeled frequencies from the turbulence model and transient frequencies calculated by the simulation. Because of these features it is a good application for DES.

The sphere is known for its drag crisis, which reflects the differences in separation between laminar and turbulent boundary layers. For our investigations we choose a sub-critical case with laminar separation of the boundary layer at $Re = 2 \cdot 10^4$ and a super-critical case with a turbulent boundary layer at $Re = 1.14 \cdot 10^6$.

The DES prediction of the separation point at an azimuthal angle measured from the forward stagnation point of $\Theta \approx 81°$ for $Re = 2 \cdot 10^4$ agrees well with the experiment of Achenbach [1], as well as the separation point for the turbulent calculations of $\Theta \approx 115°$ (Figure 3).
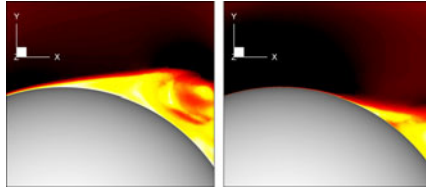
Fig. 3. Instantaneous velocity contours for laminar and turbulent separation

The difficult requirement, that the turbulence model would be suppressed in the laminar regions of the flow is achieved by using the "tripless" approach of Travin et al. [15], so the transition takes place in the wake. Illustrated in Figure 4 we see the velocity distribution for the case with the laminar separation.
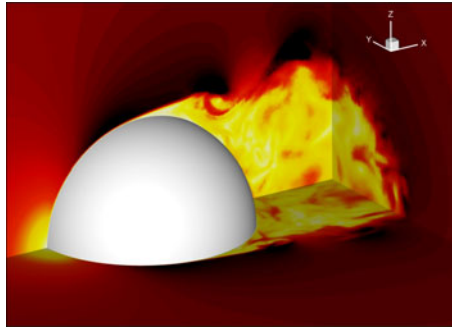
Fig. 4. Instantaneous velocity

A comparison of the pressure distribution with the simulations of Constantinescu et al. [6] and the experiments of Achenbach [1] is given in Figure 5 for both Reynolds numbers.

The mean values are calculated from averaging over $12 \cdot D/U_\infty$ units after an initialization time of $\approx 40 \cdot D/U_\infty$. The prediction of the sub-critical flow at $Re = 2 \cdot 10^4$ is in agreement with the simulation of Constantinescu at $Re = 1 \cdot 10^4$ and the measurements at $Re = 1.62 \cdot 10^4$. The value of c_p is a little bit over predicted. A reason for this could be the different Reynolds number. We found the same behavior for the super-critical case.

For our computations we used several grids and several discretization orders, the results shown are calculated on an unstructured grid with $\approx 1 \cdot 10^6$ cells and an order of four. This means that we get a grid with $\approx 20 \cdot 10^6$ degrees of freedom. Because of the polynomial ansatz functions, which are well-suited to discretize the viscous sublayer, we use a near-wall resolution for elements higher than P^2 of $y^+ \approx 3$ in the fully turbulent case. For time integration we use a fourth-order Runge-Kutta scheme with a time step from $10^{-4} - 10^{-6} \cdot D/U_\infty$ and perform our computation with up to 1020 CPUs on a massively parallel system, the SGI Altix of HLRB II on the Leibniz Supercomputing Centre in munich [8].
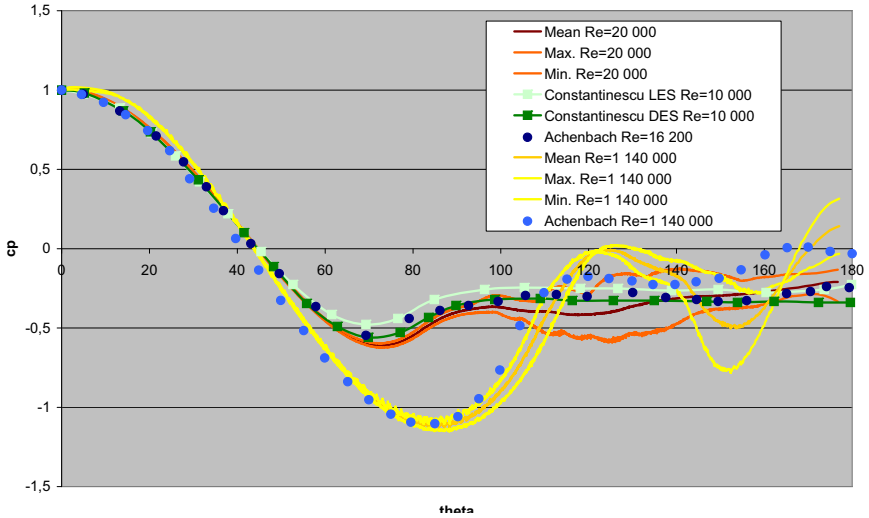
Fig. 5. Pressure distribution
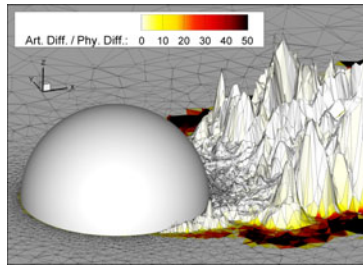
Fig. 6. Artificial diffusion at $Re = 2 \cdot 10^4$ and an order of four with the eddy viscosity on the Z-axis and contour levels of the artificial diffusion

As shown in Figure 6, the diffusion is added primarily along the edge of the turbulent wake so that the eddy viscosity transitions smoothly to free-stream value there. It is important to say that the turbulence model without stabilizing produces a non-smooth transition. For very fine meshes, computing a solution is still possible, but for coarse grids such as those used in this study we are unable to get converged results.

4   Conclusion

We combine advanced numerical methods in an unstructured code for complex geometries with new promising methods in turbulence modeling. It has been shown that it is possible to do a Detached Eddy Simulation, which is a kind of LES with a URANS wall model, within an unstructured code.

The DG discretization with its high accuracy is well-suited for this kind of simulation. It is possible to modify the length scale of other turbulence models like the $k - \omega$ model to get a DES model. This will be the focus of our future research.

References

[1] Achenbach, E.: Experiments on the flow past spheres at very high Reynolds numbers. Journal of Fluid Mechanics 54, 565–575 (1972)

[2] Bassi, F., Rebay, S.: A High-Order Accurate Discontinuous Finite Element Method for the Numerical Solution of the Compressible Navier-Stokes Equations. Journal of Computational Physics 131, 267–279 (1997)

[3] Bassi, F., Rebay, S.: High-Order Accurate Discontinuous Finite Element Solution of the 2D Euler Equations. Journal of Computational Physics 138, 251–285 (1997)

[4] Bassi, F., Rebay, S.: A high order discontinuous Galerkin method for compressible turbulent flows. In: Cockburn, B., Karniadakis, G.E., Shu, C.-W. (eds.) Discontinuous Galerkin Methods, pp. 77–88. Springer, Heidelberg (2000)

[5] Bassi, F., Rebay, S.: Discontinuous Galerkin solution of the Reynolds-averaged Navier-Stokes and k-ω turbulence model equations. Computers & Fluids 34, 507–540 (2005)

[6] Constantinescu, G.S., Squires, K.D.: LES and DES Investigations of Turbulent Flow over a Sphere. In: 38th AIAA Aerospace Sciences Meeting and Exhibit, Reno, AIAA–Paper 2000-0540 (2000)

[7] Landmann, B.: A parallel discontinouous Galerkin code for the Navier-Stokes and Reynolds-averaged Navier-Stockes equations. PhD thesis, University of Stuttgart (2008)

[8] Lübon, C., Keßler, M., Wagner, S.: A Parallel CFD Solver Using the Discontinuous Galerkin Approach. In: High Perfomace Computing in Science and Engineering, pp. 291–302. Springer, Heidelberg (2008)

[9] Lübon, C., Keßler, M., Wagner, S., Krämer, E.: Detached Eddy Simulation of Separated Flow on a High-Lift Device and Noise Propagation. Notes on Numerical Fluid Mechanics and Multidisciplinary Design, vol. 97, pp. 192–201. Springer, Heidelberg (2007)

[10] Lübon, C., Wagner, S.: Three-Dimensional Discontinuous Galerkin Codes to Simulate Viscous Flow by Spatial Discretization of High Order and Curved Elements on Unstructured Grids. Notes on Numerical Fluid Mechanics and Multidisciplinary Design, vol. 96, pp. 145–153. Springer, Heidelberg (2007)

[11] Nguyen, N.C., Persson, P.-O., Peraire, J.: RANS Solutions Using High Order Discontinuous Galerkin Methods. In: 45th AIAA Aerospace Sciences Meeting and Exhibit, Reno, AIAA–Paper 2007-0914 (2007)

[12] Schlichting, H.: Grenzschicht-Theorie. Braun, Karlsruhe (1982)

[13] Spalart, P.R., Allmaras, S.R.: A one-equation turbulence model for aerodynamic flows. La Recherche Aérospatiale 1, 5–21 (1994)

[14] Spalart, P.R., Jou, W.-H., Strelets, M., Allmaras, S.R.: Comments on the feasibility of LES for wings, and on a hybrid RANS/LES approach. In: Advances in DNS/LES (1997)

[15] Travin, A., Shur, M., Strelets, M., Spalart, P.: Detached-eddy simulation past a circular cylinder. Flow, Turbulence and Combustion 63, 293–313 (2000)

[16] van der Vegt, J.J.W., van der Ven, H.: Space-time discontinuous Galerkin finite element method with dynamic grid motion for inviscid compressible flows II. Efficient flux quadrature. Computer Methods in Applied Mechanics and Engineering 191, 4747–4780 (2002)

An Explicit Space-Time Discontinuous Galerkin Scheme with Local Time-Stepping for Unsteady Flows

Christoph Altmann, Gregor Gassner, Frieder Lörcher, Arne Taube,
Jens Utzmann, and C.-D. Munz

IAG - Institut für Aerodynamik und Gasdynamik,
Universität Stuttgart,
Pfaffenwaldring 21
70569 Stuttgart, Germany
taube@iag.uni-stuttgart.de
www.iag.uni-stuttgart.de

Summary

The objective of our project is the development of high-order methods for the unsteady Euler and Navier Stokes equations. For this, we consider an explicit DG scheme formulated in a space-time context called the Space-Time Expansion DG scheme (STE-DG). Our focus lies on the improvement of two main aspects: Increase of efficiency in the temporal and spatial discretization by giving up the assumption that all grid cells run with the same time step and introducing local time-stepping and the shock capturing property, where we have adopted the artificial viscosity approach as described by Persson and Peraire to our STE-DG scheme. Thus, we try to resolve the shock within a few relatively large grid cells forming a narrow viscous profile by locally adding some amount of artificial viscosity.

1 Introduction

Discontinuous Galerkin (DG) schemes may be considered as a combination of finite volume (FV) and finite element (FE) schemes. While the approximate solution is a continuous polynomial in every grid cell, discontinuities at the grid cell interfaces are allowed which enable the resolution of strong gradients. How to calculate the fluxes between the grid cells and to take into account the jumps is well-known from the finite volume community. Due to their interior grid cell resolution with high order polynomials, the DG schemes may use very coarse grids. In this approach, the cumbersome reconstruction step of finite volume schemes is avoided, but for every degree of freedom a variational equation has to be solved. The main advantage of DG schemes is that the high order accuracy is preserved even on distorted and irregular grids. In the following we present a DG scheme based on a space-time expansion (STE-DG), which was proposed in [6] and [4]. Our scheme features *time consistent* local time-stepping. Hence, every grid cell runs with its optimal time step.

An open issue for DG schemes in general is an efficient shock-capturing strategy. The very successful FV shock-capturing consists of a TVD or WENO reconstruction

which is non-oscillatory. In combination with local grid refinement a narrow transition zone at the shock wave is obtained within a few grid cells. This can also be extended to DG schemes in a way such that the trial function is locally replaced by a reconstructed polynomial. As the efficiency of DG schemes relies on the locality of the spatial discretization, the use of this shock-capturing technique is cumbersome, especially for high order. In our approach this would destroy the possibility to introduce local timestepping. Thus, another approach which seems to be more convenient for our DG scheme is to keep the large grid cell and to resolve the shock within the grid cell in a narrow viscous profile by locally adding some sort of artificial viscosity. This was recently proposed by Persson and Peraire [8]. Their approach is quite contradictory to FV shock-capturing, since they keep the order of accuracy high or even increase it locally. Persson and Peraire show that this strategy captures the shock within a transition zone the size of $\delta \sim \frac{h}{p+1}$ where h is a characteristic cell size and p denotes the degree of the polynomial approximation. In this case the shock profile can be sharpened by increasing the degree of the trial function (p-adaptation). While Persson and Peraire applied this shock-capturing by p-refinement within an implicit scheme, we combine it with an explicit scheme which leads to an anisotropic time step distribution due to the stability restriction. But, due to our local time-stepping feature the efficiency is well preserved. Our approach was presented first in [2] and then further developed within the ADIGMA project [1]. This time, we present a refinement especially with regard to the troubled cell indicators used.

2   The STE-DG Scheme for the Euler Equations

2.1   The Equations and the Semi-discrete Variational Formulation

The Euler equations in two space dimensions read as

$$\boldsymbol{U}_t + \boldsymbol{F}\left(\boldsymbol{U}\right)_x + \boldsymbol{G}\left(\boldsymbol{U}\right)_y = \boldsymbol{0} \tag{1}$$

with

$$\boldsymbol{U} = \begin{pmatrix} \rho \\ \rho u \\ \rho v \\ \rho e \end{pmatrix}, \quad \boldsymbol{F} = \begin{pmatrix} \rho u \\ \rho u^2 + p \\ \rho u v \\ \rho u(e + p) \end{pmatrix}, \quad \boldsymbol{G} = \begin{pmatrix} \rho v \\ \rho u v \\ \rho v^2 + p \\ \rho v(e + p) \end{pmatrix}, \tag{2}$$

where ρ, u, v, p, and e denote the density, x- and y-velocity, pressure, and specific total energy, respectively. We consider the equation of state of a perfect gas with

$$p = \rho R T = (\gamma - 1)\, \rho \epsilon \quad \text{and} \quad e = \frac{p}{(\gamma - 1)\, \rho} + \frac{u^2 + v^2}{2}, \tag{3}$$

where ϵ denotes the specific internal energy, γ is the isentropic exponent, and R is the gas constant.

The spatial discretization is based on the weak formulation of equation (1). We multiply the Euler equations with an arbitrary test function $\boldsymbol{\Phi}(\boldsymbol{x})$, integrate over the grid

cell Q_i and use integration by parts for the flux terms to get

$$\int_{Q_i} \boldsymbol{U}_t \cdot \boldsymbol{\Phi} \, dx + \int_{\partial Q_i} \boldsymbol{F}_n \cdot \boldsymbol{\Phi} \, ds - \int_{Q_i} (\boldsymbol{F} \cdot \boldsymbol{\Phi}_x + \boldsymbol{G} \cdot \boldsymbol{\Phi}_y) \, dx = 0, \qquad (4)$$

where ∂Q_i denotes the surface of the grid cell and $\boldsymbol{F}_n$ is normal component of the flux.

To get the semi-discrete DG scheme we introduce a piecewise polynomial approximation $U_h(\boldsymbol{x}, t)$, which is defined in a grid cell Q_i by

$$\boldsymbol{U}_h(\boldsymbol{x}, t) = \boldsymbol{U}_i(\boldsymbol{x}, t) := \sum_{l=1}^{N(p)} \hat{\boldsymbol{U}}_l^i(t) \, \varphi_l(\boldsymbol{x}). \qquad (5)$$

Using a trial space of piecewise polynomials with degree $\leq p$, we can introduce an orthonormal basis $\{\boldsymbol{\varphi}\}_{l=1}^{N(p)}$, where $N(p) = (p+1)(p+2)/2$ in two space dimensions. We choose as test functions the basis functions and get the following $N(p)$ ordinary differential equations for the $N(p)$ unknowns

$$\left(\hat{\boldsymbol{U}}_l^i\right)_t = -\int_{\partial Q_i} \boldsymbol{H} \cdot \varphi_l \, ds + \int_{Q_i} \left(\boldsymbol{F} \cdot (\varphi_l)_x + \boldsymbol{G} \cdot (\varphi_l)_y\right) \, dx = 0, \quad l = 1, ..., N(p).$$
$$(6)$$

As numerical flux we use the HLLC flux (see, e.g., [9]) named $\boldsymbol{H}$. With the use of the dGRP-flux (diffusive Generalized Riemann Problem) as described in [3, 7], this approach has been extended to the Navier-Stokes equations.

2.2 The Space-Time Expansion Approach with Local Time-Stepping

For the STE-approach the semi discrete scheme (6) is simply integrated in time. Due to the local time stepping, we give up the assumption that all grid cells run with the same time step and therefore we do not have any longer a common time level. Let us denote the actual local time level in grid cell Q_i by t_i^n. The degrees of freedom $\hat{U}_l^{i,n}$ represent the solution at t_i^n in this grid cell. Furthermore, each cell may evolve in time with its local time step Δt_i^n which has to satisfy the local stability restriction, which depends on the grid cell diameter, the solution as well as on the order $p+1$, see [6]. With Δt_i^n, the next local time level in Q_i is given as

$$t_i^{n+1} = t_i^n + \Delta t_i^n. \qquad (7)$$

The evolution equations for the degrees of freedom read as

$$\hat{\boldsymbol{U}}_l^{i,n+1} = \hat{\boldsymbol{U}}_l^{i,n} - \int_{t_n}^{t_{n+1}} \int_{\partial Q_i} \boldsymbol{H} \cdot \varphi_l \, ds \, dt \qquad (8)$$

$$+ \int_{t_n}^{t_{n+1}} \int_{Q_i} (\boldsymbol{F} \cdot (\varphi_l)_x + \boldsymbol{G} \cdot (\varphi_l)_y) \, dx \, dt = 0, \ l = 1, ..., N(p).$$

To evaluate the right hand side of the evolution equations the space-time integrals are approximated by proper Gaussian integration rules. The difficulty is, that the values at the space-time Gauss points are not known. In the STE-approach a space-time Taylor expansion of the approximation U_i at the grid cell barycenter $\boldsymbol{x}_i$ at time level t_n

$$\widetilde{\boldsymbol{U}}_i\left(\boldsymbol{x}, t\right) := \sum_{l=0}^{p} \left(\left(t - t_i^n\right) \partial_t + \left(\boldsymbol{x} - \boldsymbol{x}_i\right) \boldsymbol{\nabla}\right)^l \boldsymbol{U}\left(\boldsymbol{x}, t\right)|_{\boldsymbol{x}_i, t_n} \tag{9}$$

is used to get a high order prediction at every space-time Gauss point. While the space derivatives are already available within the DG approach, the mixed space-time derivatives are approximated using the (CK-) Cauchy-Kovalewskaya procedure. To replace the time and mixed space-time derivatives the evolution equation is applied several times, see [6] for more details.

As the evaluation of the fluxes between the grid cells on the right hand side relies on neighbor data as well, the local time-stepping algorithm is based on the following evolve condition: The evolution of the DOF are performed, if

$$t_i^{n+1} \leq \min\left\{t_j^{n+1}\right\}, \forall j : Q_j \cap Q_i \neq \emptyset \tag{10}$$

is satisfied. This means that an element i can only be updated in time, if all neighboring elements' j prospective time level is bigger than the one from element i in concern. This guarantees that the approximate space-time values of the neighbor cells are available. In this manner, the algorithm continues by searching for elements satisfying the evolve condition (10). All elements are evolved in a suitable manner by evaluating the different terms of the right hand side of equation (8) for each element in an effective order. At each time, the interface fluxes are defined uniquely for both adjacent elements, making the scheme exactly conservative, –for more details see [3].

3   Sub-Cell Shock Capturing for DG Methods

3.1   Troubled Cell Indicators

The first step is to detect grid cells in which a strong gradient is approximated and which will lead to spurious oscillations in the approximative piecewise polynomial. The two so-called troubled cell indicators used are the following.

The Spectral Decay Indicator.   In order to determine a suitable sensor for under-resolved parts, we make use of the fact that the solution within each element is represented in terms of an orthogonal basis

$$\boldsymbol{U}_i\left(x, t_n\right) = \sum_{l=1}^{N(p)} \hat{\boldsymbol{U}}_l^i \boldsymbol{\varphi}_l. \tag{11}$$

If the underlying exact solution is smooth, we expect the coefficients of the approximation to decay fast. E.g., using the pressure p from the set of primitive variables we apply a modification of the smoothness sensor proposed in [8] in the form

$$\eta_i^{\text{SDI}}(p) = \log_{10}\left\{\max\left[\left(\frac{\sum\limits_{j=N_i(P_i-1)+1}^{N_i(P_i)}(\hat{p}_{i,j})^2}{\sum\limits_{j=1}^{N_i(P_i)}(\hat{p}_{i,j})^2}\right),\left(\frac{\sum\limits_{j=N_i(P_i-2)+1}^{N_i(P_i-1)}(\hat{p}_{i,j})^2}{\sum\limits_{j=1}^{N_i(P_i-1)}(\hat{p}_{i,j})^2}\right)\right]\right\}.$$
(12)

This spectral decay indicator (SDI) measures the rate of the decay of the magnitude of the last two moments. If this rate is high then we have identified a strong gradient which is not well resolved by the local polynomial, e.g. a shock wave.

The Pressure Gradient Indicator. The previous described modified spectral decay indicator requires, however, quite an amount of fine tuning. Therefore, we use another more robust indicator, as well. The so-called pressure gradient indicator (PGI) is devised in the spirit of [5] for finite volume schemes, and reads as

$$\eta_i^{\text{PGI}}(p) = \frac{|p_{\min} - 2p_i + p_{\max}|}{|p_{\min} + 2p_i + p_{\max}|}.$$
(13)

It estimates the pressure changes from the von Neumann neighbors. Where $p_{\min}$ is set as the minimum pressure of all neighboring cells and $p_{\max}$ the maximum. This η_i^{PGI} is then multiplied with an amplification factor.

3.2 Modified Governing Equation

Once the shock has been sensed, we modify the governing equation locally in this grid cell

$$\boldsymbol{U}_t + \boldsymbol{F}(\boldsymbol{U})_x + \boldsymbol{G}(\boldsymbol{U})_y = \nabla \cdot (\mu \nabla \boldsymbol{U}),$$
(14)

by introducing an artificial viscosity of the form

$$\mu = \mu\left(\eta_i^*, h_i, p_i\right).$$
(15)

The piecewise constant viscosity $\mu\left(\eta_i^*, h_i, p_i\right)$ is chosen as a function of the discontinuity sensor $\eta_i^*(p)$ –where $*$ means either SDI or PGI– and of the available resolution $\sim \frac{h_i}{p_i+1}$ within the grid cell. The discretization of the viscous terms is again based on exact diffusive Riemann solutions for parabolic equations, according to [3,7].

4   Results

This section contains results of two two-dimensional test cases to show the properties of the STE-DG scheme and its shock-capturing technique. The first one is a laminar test case and the second an Euler case.

4.1   Fluid Flow around a NACA0012 Airfoil

This is a numerical simulation of the fluid flow around a NACA0012 airfoil –mandatory test case 3 (MTC 3)– taken from the ADIGMA test case suite. It is set up with the following parameters, angle of attack $\alpha = 2°$, free stream Mach number $Ma_\infty = 0.5$ and the free stream Reynolds number $Re_\infty = 5000$ based on the length of the airfoil $c = 1.0$. It is a laminar but yet unsteady flow computation till $t_{end} = 0.4s$, and we take a mesh with unstructured quads. The simulation was conducted in such a way that for the first half of the time –till $t = 0.2s$– the approximation order was fixed to $\mathcal{O}2$ and after that released to adapt to the optimal or desired value between two and seven. The vortex street formation can be observed in the top part of figure 1, which shows the contour plot of the local Mach number. The bottom plot shows the local polynomial order, which varies between $N = 2$ in the farfield region and $N = 7$ at the tip and in the airfoil's wake.

4.2   Double Mach Reflection of a Strong Shock

The following figures show a zoom on the triple point region of the DMR test problem presented first by Woodward and Colella in [10]. A mach 10 shock in air which initially
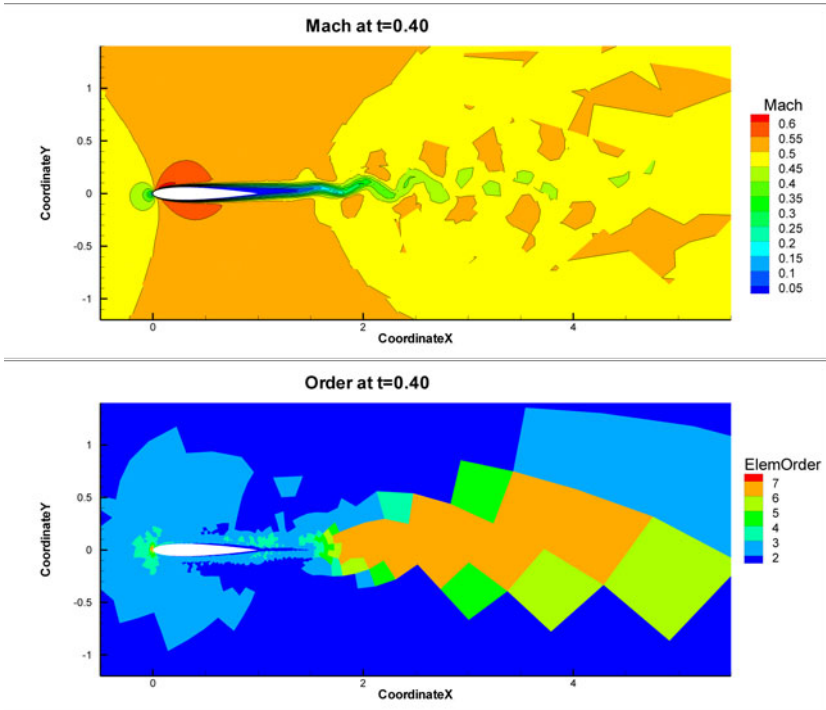
Fig. 1. Fluid flow around NACA0012 with $Re_\infty = 5000$, $Ma_\infty = 0.5$. Local Mach number (top) and computational element order (bottom) at $t = 0.4s$.

makes a $60°$ angle with a reflecting wall. The reflecting wall lies along the bottom of the problem domain. When the Mach 10 shock hits the wall, a triple-point is formed consisting of two shocks and a slightly unstable contact discontinuity that rolls up at the wall boundary. In figure 2, we compare our solution for $t = 0.2$ with a 5th order WENO-FV scheme on the same and on a much finer resolution of $h = 1/480$.
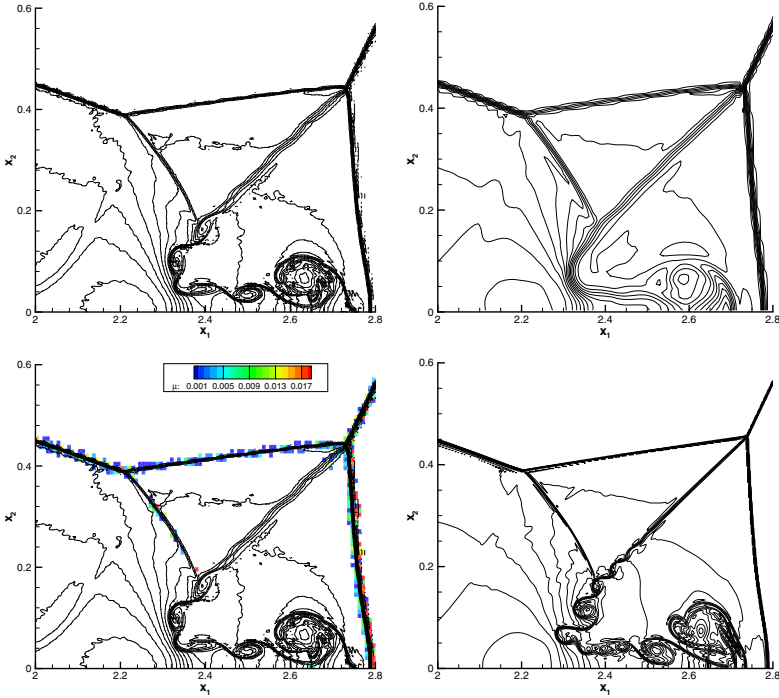
Fig. 2. $Ma = 10$ DMR test problem zoom on the triple point with 30 equally spaced density contour lines from $\rho = 1.5 \ldots 21.5$. Left: DG scheme with $h = 1/120$ and $p = 4$. The cells containing artificial viscosity μ are plotted in the bottom part. Right: 5th order WENO-FV scheme with $h = 1/120$ (top) $h = 1/480$ (bottom).

5   Conclusion

Our STE-DG scheme is able to simulate non stationary problems with high order accuracy. The considered local time stepping algorithm minimizes the total number of time steps and enables us to capture shocks by locally adding artificial viscosity. We even achieve subgrid resolution of the shocks and the local time stepping framework enables us to preserve the efficiency in the explicit unsteady approach.

Acknowledgement

References

[1] Altmann, C., Gassner, G., Lörcher, F., Taube, A., Munz, C.-D.: An explicit space-time discontinuous Galerkin scheme with local time-stepping for unsteady flows. In: 8th World Congress on Computational Mechanics (WCCM8), 5th European Congress on Computational Methods in Applied Sciences and Engineering (ECCOMAS 2008), Venice, Italy (July 2008)

[2] Altmann, C., Taube, A., Gassner, G., Lörcher, F., Munz, C.-D.: Shock detection and limiting strategies for high order discontinuous Galerkin schemes. In: 26th International Symposium on Shock Waves (ISSW 26), Göttingen, Germany (July 2007)

[3] Gassner, G., Lörcher, F., Munz, C.-D.: A contribution to the construction of diffusion fluxes for finite volume and discontinuous Galerkin schemes. J. Comput. Phys. 224(2), 1049–1063 (2007)

[4] Gassner, G., Lörcher, F., Munz, C.-D.: A discontinuous Galerkin scheme based on a spacetime expansion II. Viscous flow equations in multi dimensions. J. Sci. Comput. 34(3), 260–286 (2008)

[5] Jameson, A., Schmidt, W., Turkel, E.: Numerical solution of the Euler equations by finite volume methods using Runge–Kutta time-stepping schemes. In: Proc. of the AIAA 14th Fluid and Plasma Dynamic Conference, AIAA-1981-1259, Paolo Alto, California (June 1981)

[6] Lörcher, F., Gassner, G., Munz, C.-D.: A discontinuous Galerkin scheme based on a spacetime expansion I. Inviscid compressible flow in one space dimension. J. Sci. Comput. 32(2), 175–199 (2007)

[7] Lörcher, F., Gassner, G., Munz, C.-D.: An explicit discontinuous Galerkin scheme with local time-stepping for general unsteady diffusion equations. J. Comput. Phys. 227(11), 5649–5670 (2008)

[8] Persson, P.-O., Peraire, J.: Sub-cell shock capturing for discontinuous Galerkin methods. In: Proc. of the 44th AIAA Aerospace Sciences Meeting and Exhibit, AIAA-2006-1253, Reno, Nevada (January 2006)

[9] Toro, E.F.: Riemann solvers and numerical methods for fluid dynamics, 2nd edn. Springer, Heidelberg (1999)

[10] Woodward, P., Colella, P.: The numerical simulation of two–dimensional fluid flow with strong shocks. J. Comput. Phys. 54, 115–173 (1984)

Numerical Simulation of Upstream Moving Pressure Waves in Transonic Airfoil Flow

Viktor Hermes, Igor Klioutchnikov, Atef Alshabu, and Herbert Olivier

Shock Wave Laboratory, RWTH Aachen University, 52056 Aachen, Germany
hermes@swl.rwth-aachen.de

Summary

Results from a numerical investigation of the unsteady transonic flow around a supercritical BAC 3-11 airfoil will be presented here. The focus of this paper is the phenomenon of upstream moving pressure waves. The used solver is based on the finite difference discretisation of high order accuracy ($N > 5$) and explicit time integration. The mechanisms of pressure wave generation, their development and the influences of the inflow parameter like Mach, Reynolds number and angle of attack are investigated in two-dimensional flow simulations. To analyse the three-dimensional effects simulation of the three-dimensional transonic flow is performed for selected inflow conditions and its preliminary results will be presented.

1 Introduction

Upstream moving pressure waves are observed in the transonic airfoil flows already for several decades [3], [8], [10]. Nevertheless, the phenomenon is not fully understood yet and is still subject of numerous experimental and numerical investigations [1],[4], [7], [9]. Especially, its interaction with the undisturbed flow field and its influence on the transition, turbulence and on the shock/boundary layer interaction are of great interest. For instance, the recent theories about the buffet phenomenon involves the strong pressure wave generation at the trailing edge. The pressure waves are moving upstream, interact with the recompression shock and change the shock strength, its position and the intensity of the shock/boundary layer interaction [7], [9].

In our numerical simulations the vortex/trailing edge interaction that generates pressure waves is observed. The pressure waves are propagating in all direction as a deformed circular shape. The velocity of the upstream moving part of the waves is slower compared to the downstream moving part. The upstream moving parts of neighbour waves are merging to weak shocks while propagating. If a supersonic region is present in the flow, the waves interact with the recompression shock. Weak pressure waves are also observed in the supersonic region. The upstream moving waves are passing outside the supersonic region and introduce small disturbances on the sonic line like Mach lines that are visible inside the supersonic region. The described mechanisms and interactions are observed in the experiment as well [1].

2   Numerical Method

The numerical simulation is performed using a solver, which was developed at RWTH Aachen University based on a finite-difference WENO method of high order accuracy in space and time and shock capturing capability [6]. The transonic flow contains different complex interactions, large gradients like shocks, but also weak pressure waves. For a precise simulation of such a type of flow numerical methods with a small amount of numerical dissipation are essential. The used numerical method meets these demands and will be introduced in the following.

The Navier-Stokes equations in weak conservative form for the compressible flow in general coordinates $\xi = \xi(x,y), \eta = \eta(x,y), \zeta = \zeta(z)$ are employed:

$$U_t + \frac{1}{J}F_\xi + \frac{1}{J}G_\eta + \frac{1}{J}H_\zeta = \frac{1}{J}F_\xi^v + \frac{1}{J}G_\eta^v + \frac{1}{J}H_\zeta^v.$$

Here U is the solution vector of the conservative variables, F, G, H and F^v, G^v, H^v are the inviscid and viscous fluxes respectively. For two-dimensional simulations the fluxes in the third spatial dimension H, H^v are removed. The inviscid fluxes F, G and H are approximated using the WENO scheme formulation according to Jiang and Shu [5]. This scheme is of formally odd order and uses formally an N-point stencil. The actually used WENO stencil is addaptive that is of advantage compared to schemes with fixed stencil. The addaptivity will be described in the following. The formal stencil is subdivided into p sub-stencils ($N = 2p - 1$), that uses p points. The approximation of the fluxes is calculated first for each sub-stencil separately and recombined using non-linear weighting coefficients. The weighting coefficients are determined depending on the smoothness of the approximation. If the approximation of all sub-stencils is smooth, the weighting coefficients are chosen to achieve the formal order of accuracy. In the vicinity of large gradients and discontinuities, such as shocks, smooth flux approximations are weighted heavily and numerical dissipation is added to avoid spurious oscillations of the solution. Thus the scheme is very stable even for very high gradients and aditionally benefit from low dissipation and dispersion error in regions of smooth solution. Beside an adaptive stencil the WENO scheme has some upwind properties and is combined here with a flux-vector splitting technique. The sheme is decomposed into a central and a dissipation term according to Balsara and Shu [2] by applying the fact that the sum of all weighting coefficients is equal to unity. The central term is approximated with an order $M = N - 1$. The dissipation term takes upwinding and the non-linear weighting into account. For details the reader is reffered to [5] and [2].

The viscous fluxes F^v, G^v and H^v are discretised using central difference operators of high even order ($N + 1$). The derivatives of the viscous fluxes contain second derivatives of the velocity vector $(u, v, w)^T$ and temperature T. The approximation of the second derivative of the x-component of the velocity vector u will be explained in detail exemplary for all variables. For the approximation of the second derivative with respect to one spatial direction an approximation operator $M_{i+1/2}()$ is applied. For mixed second derivatives an interpolation operator $L_{i+1/2}()$ is applied to the first and then to the second spatial direction. The operators $L_{i+1/2}()$ and $M_{i+1/2}()$ of even order $N + 1$ are defined as [6]:

$$L_{i+1/2}(u) = \sum_{m=1}^{(N+1)/2} (-1)^{m+1} a_m (u_{i+m} + u_{i-m+1})$$

$$M_{i+1/2}(u) = \sum_{m=1}^{(N+1)/2} (-1)^{m+1} b_m (u_{i+m} - u_{i-m+1}) \Delta\xi^{-1}$$

The coefficients a_m and b_m can be determined analytically for every even order. For details the reader is referred to Klioutchnikov [6].

The time integration is explicit and performed with a third order, low-storage Runge-Kutta-TVD-Scheme [5].

For the presented results the inviscid fluxes are approximated with a ninth order WENO scheme and a tenth order central scheme is used for the approximation of the viscous fluxes. $(N + 1)/2$ fictitious points are added in each direction to maintain the stencil in the vicinity of boundaries. Non-reflecting boundary conditions based on Riemann invariants are used for the subsonic inflow and outflow boundary. No-slip boundary conditions are applied on the airfoil surface. If wind tunnel walls are simulated, than slip wall boundary conditions are applied on them to reduce the otherwise necessary spatial resolution near the wind tunnel walls. This is because the effect of the boundary layer is found negligible on the pressure distribution around the airfoil.

The used numerical method is computational time-consuming, but well parallelisable. Therefore the solver is massively parallelised with means of MPI (Massage Passing Interface). A linear scalability up to 8192 processor cores for a two dimensional test problem with 5120x512 grid points is achieved on the JUGENE supercomputer of Forschungszentrum Jülich.

3   Results

The results of the numerical simulation of two-dimensional transonic flow will be mainly presented here. The simulation of the two-dimensional flow is performed on a 1280 x 130 points grid. The influence of the inflow parameter like Mach Ma_∞, Reynolds number based on chord length Re_c and the angle of attack α are investigated in the following range:

$$Ma_\infty = 0.69 - 0.80, \; Re_c = 0.1 \cdot 10^6 - 3 \cdot 10^6 \text{ and } \alpha = -3° - +4°.$$

The numerical and experimental results are compared for $Ma_\infty = 0.71$, $Re_c = 3 \cdot 10^6$ and $\alpha = 0°$. A qualitative good agreement between the experimental and the numerical instantaneous shadowgraphs can be observed (Fig. 1 a) and b)). Discrepancies between the numerical and experimental shadowgraphs in the boundary layer region of the airfoil rear part have two reasons. On the one hand the vortices observed in the numerical results are growing exponentially towards the trailing edge because the results are based on two-dimensional flow simulation. In three-dimensional flow simulations the size of the vortices is smaller as energy transfer in spannwise direction is possible. On the other hand the experimental shadowgraphs integrate the second derivative of the density in spannwise direction. If flow structures are not two dimensional, they appear smeared
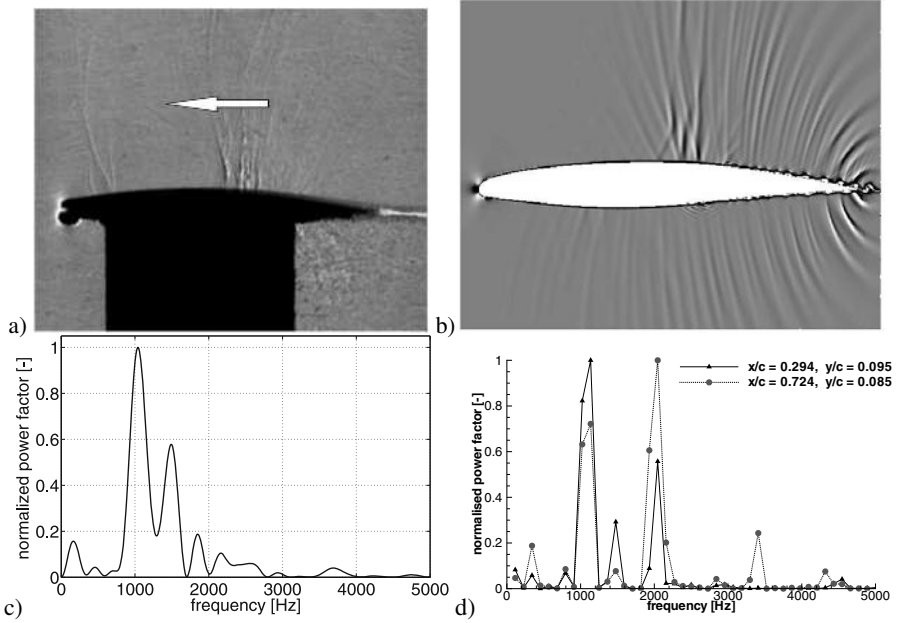
Fig. 1. Experimental a) and numerical b) shadowgraphs. Normalised power factor of the experimental pressure history at x/c = 0.72 and corresponding numerical d) result. Airfoil flow with $Ma_\infty = 0.71$, $Re_c = 3 \cdot 10^6$ and $\alpha = 0°$.

out in the experimental shadowgraphs. Nevertheless, pressure gradients are present in numerical and experimental results in the vicinity of the maximum airfoil thickness, although no local supersonic region is established. Merging of upstream moving pressure waves is observed here, resulting in a shock formation. The shock position is not stable. Shock movement towards the leading edge but also shock desintegration and disappearance is observed.

The statistical properties of the pressure fluctuations are analyzed for characterizing the dynamic behaviour of the wave process. Therefore the pressure histories are first auto-correlated and then Fourier transformed using the FFT (Fast Fourier Transform) method. In comparison to the Fourier spectrum the fraction of periodic signals is amplified in the obtained power density spectrum (PDS). Dominant frequencies in the numerical as well as in the experimental results are found in the range of one to two kHz (Fig. 1c) and d)). In the numerical results a second peak is found at two kHz, whereas the experimental results show a second peak rather at 1.5 kHz. One possible reason for this discrepancy in the results is that the assumption of two-dimensional flow is not fully fulfilled in reality. The wave velocity is estimated by a cross-correlation of the pressure histories at different airfoil positions. A qualitatively good agreement between the numerical and the experimental results is observed here as well.

For the study of the influence of the Mach number, the Reynolds number $Re_c \approx 2 \cdot 10^6$ and the angle of attack $\alpha = 0°$ are kept constant and the wind tunnel slip
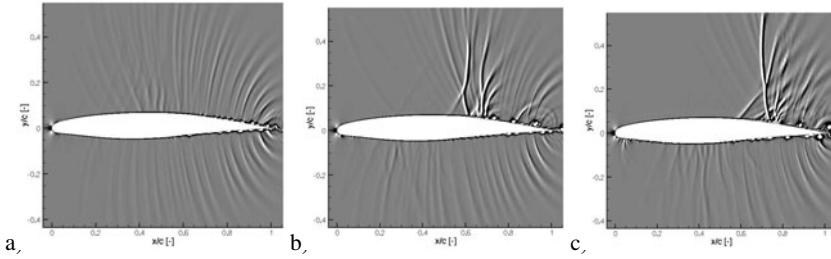
Fig. 2. Numerical shadowgraph visualisation of the flow field for $Re_c = 2 \cdot 10^6$, $\alpha = 0°$ and a) $Ma_\infty = 0.69$, b) $Ma_\infty = 0.73$, c) $Ma_\infty = 0.76$.

wall boundary conditions are applied. Three Mach number regions are identified with different interaction between the upstream moving waves and the flow (Fig. 2). If no supersonic region is present in the flow (low, subcritical Mach numbers) the upstream moving waves pass over the entire airfoil and interact weakly with the flow (Fig. 2 a)). Their velocity decreases first in the region of maximum airfoil thickness and increases than to the leading edge. The highest wave intensity is observed in the region of maximum airfoil thickness. For higher Mach numbers a development of supersonic regions is observed. If the supersonic region is only weakly developed (Fig. 2 b)) the pressure waves are merging with the recompresion shock increasing its strength. The outcome of this is a strong movement of the recompression shock over a part of the airfoil. Shock splitting and merging is observed under this condition as well. For flows with well-developed supersonic regions (Fig. 2 c)) the influence of the pressure waves on the shock position and strength is less. Only the oblique part of the recompression shock is oscillating, whereas the normal part is stable. Strong interaction between downstream moving vortices with the normal part of the shock is observed.

The study of the influence of the angle of attack is performed for a constant Mach and Reynolds number $Ma_\infty = 0.70$ and $Re_c = 1 \cdot 10^6$. For positive angles of attack (Fig. 3 a)) a supersonic region is established in the vicinity of the leading edge on the upper airfoil side and a strong interaction between pressure waves and the recompression shock is observed. The vortices on the upper airfoil side start to develop further upstream in the region of the shock/boundary layer interaction. For negative angles of attack (Fig. 3 b)) the flow over the entire upper airfoil side is subsonic. The flow over the lower airfoil side contains a lot of different pressure waves that are generated by the shock/vortex interaction near the leading edge, the vortex/vortex interaction in the middle part of the airfoil and by the vortex/trailing edge interaction. On the upper airfoil side small vortices are observed far downstream at $x/c \approx 0.75$.

For the study of the influence of the Reynolds number, the Mach number and the angle of attack are chosen constant to $Ma_\infty = 0.73$ and $\alpha = 0°$. The Reynolds number is varied in the range $Re_c = 1 \cdot 10^5 - 2.1 \cdot 10^6$. The results of the simulation with $Re_c = 2.1 \cdot 10^6$ are used to initialise the flow field for the variation. Boundary layer thickening is observed for decreasing Reynolds number. For $Re_c \approx 3 \cdot 10^5$ a boundary layer separation is observed in the time-averaged flow that reattaches upstream the trailing edge. For $Re_c = 1 \cdot 10^5$ the boundary layer separates up to the
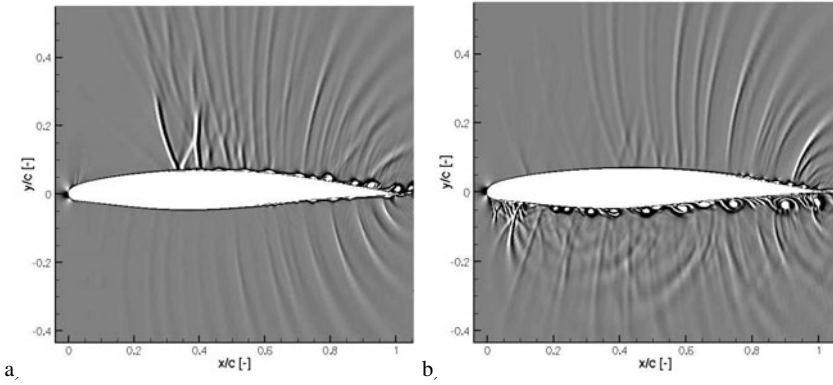
Fig. 3. Numerical shadowgraph visualisation of the flow field for $Ma_\infty = 0.70$, $Re_c = 1 \cdot 10^6$ and a) $\alpha = +3°$, b) $\alpha = -3°$.
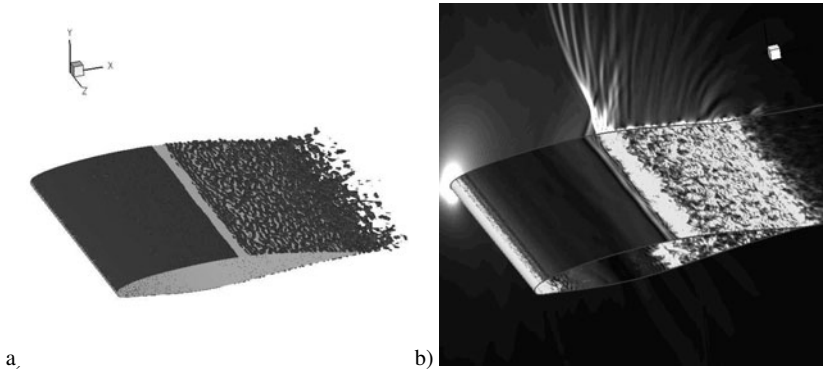
Fig. 4. a) λ_2 visualisation of the vortices in the boundary layer, b) contours of the pressure gradient for $Ma_\infty = 0.71$, $Re_c = 3 \cdot 10^6$ and $\alpha = 0°$.

trailing edge. Vortices with a size of about 10% of the chord length are observed inside the separation bubble that leave the bubble and interact with the trailing edge. The boundary layer separation changes the effective airfoil shape and hence the local flow conditions.

The velocity of the upstream moving pressure waves relative to the airfoil and their Mach number relative to the oncoming flow is calculated by the cross-correlation of pressure histories of two neighbouring positions. The time delay for the largest correlation between the two signals is set as the time difference the wave needs to propagate from one position to the other. In summary the wave velocity is strongly dependent on the local Mach number so that a strong influence is observed in the inflow Mach number and angle of attack variations. The influence of the Reynolds number on the wave velocity is negligible for flows without a pronounced boundary layer separation.

The wave Mach number relative to the flow is found nearly independent of the varied inflow parameter in the investigated range to $Ma_{wave} = 1.03 - 1.05$.

The simulation of the three-dimensional flow is performed on a grid with 1280 x 130 x 120 points to investigate the influence of the third dimension. The results of the experiments [1] show for $Ma_\infty = 0.71$ that the boundary layer becomes turbulent at $x/c \approx 0.6 - 0.65$. This position is in good agreement with the position where vortex formation is observed in the numerical simulation of the two-dimensional flow. Of course the development of the vortices is fundamentally different in two- and three-dimensional flows and therefore affects the pressure wave generation mechanism. In Figure 4 a) the vortices in the boundary layer are visualised by the λ_2 criterion. The vortices in the rear part of the airfoil are complete three-dimensional as expected, but upstream moving pressure waves can still be observed in the simulation results (Fig. 4 b)).

4   Conclusion and Outlook

The used numerical method is found stable and capable to simulate the transonic airfoil flow containing strong shocks as well as weak pressure waves. The upstream moving pressure waves are merging with each other in a non-linear way. The wave velocity relative to the airfoil is strongly dependent on the local flow conditions whereas the Mach number relative to the flow is found nearly independent on the inflow condition in the investigated range. To investigate the influence of the upstream moving waves on the transition and turbulence highly resolved DNS is planned using the JUGENE supercomputer of the Forschungszentrum Jülich.

Acknowledgements

References

[1] Alshabu, A., Olivier, H., Klioutchnikov, I.: Investigation of Upstream Moving Pressure Waves on a Supercritical Airfoil. Aerospace Science and Technology 10, 465–473 (2006)
[2] Balsara, D., Shu, C.W.: Monotonicity Preserving Weighted Essentially Non-Oscillatory Schemes with Increasingly High Order of Accuracy. Journal of Computational Physics 160(2), 405–452 (2000)
[3] Finke, K.: Stoß schwingungen in schallnahen Strömungen. VDI-Forschungsheft Nr. 580, Düsseldorf (1977)
[4] Hermes, V., Klioutchnikov, I., Alshabu, A., Olivier, H.: Investigation of Unsteady Transonic Airfoil Flow. AIAA-Paper 2008 - 0627 (2008)
[5] Jiang, G.S., Shu, C.W.: Efficient Implementation of Weighted ENO Schemes. Journal of Computational Physics 126(1), 202–228 (1996)

[6] Klioutchnikov, I., Ballmann, J.: DNS of Transitional Transsonic Flow about a Supercritical BAC3-11 Airfoil using High-Order Shock Capturing Schemes. In: DLES VI. ERCOFTAC Series, vol. 10, pp. 737–744. Springer, Heidelberg (2006)

[7] Lee, B.H.K.: Self-Sustained Shock Oscillations on Airfoils at Transonic Speeds. Progress in Aerospace Sciences 37, 147–196 (2001)

[8] Srulijes, J., Seiler, F.: A Study on Upstream Moving Pressure Waves Induced by Vortex Separation. In: Proceedings of the 16th International Symposium on Shock Tubes and Waves, pp. 621–628. VCH Publishers, Weinheim (1988)

[9] Soda, A.: Numerical Investigation of Unsteady Transonic Shock/Boundary-Layer Interaction for Aeronautical Application. DLR-Forschungsberichricht 2007-03 (2007)

[10] Tijdeman, H.: Investigation of the Transonic Flow around Oscillating Airfoils. NLR TR 77090, Amsterdam (1977)

Investigation of Resolution Requirements for Wall-Modelled LES of Attached and Massively Separated Flows at High Reynolds Numbers

Xiaoqin Zhang[1], Tobias Knopp[2], Mariafrancesca Valentino[2],
Roland Kessler[2], and Gert Lube[3]

[1] School of Mechanical and Aerospace Engineering, Nanyang Technological University,
50, Nanyang Avenue, 639798, Singapore
xqzhang@ntu.edu.sg
[2] DLR Göttingen, AS-C²A²S²E, Bunsenstr. 10, D-37073 Göttingen, Germany
[3] Institut für Numerische und Angewandte Mathematik, Georg-August-Universität Göttingen,
Lotzestrasse 16-18, D-37083 Göttingen, Germany

Summary

This work is dedicated to the resolution requirements of Large-Eddy Simulation (LES) with near-wall modelling for attached and massively separated flows at high Reynolds numbers using the DLR THETA code. Two sensors are proposed to measure the resolution quality of LES for statistically steady flows. The first sensor is based on the resolved turbulent kinetic energy and the second one considers the resolved turbulent shear stress. These sensors are applied to turbulent channel flow at $Re_\tau = 4800$ and to the flow over a backward-facing step at $Re_h = 37500$ on successively refined meshes, and results are compared with a convergence study of the mean velocity profiles.

1 Introduction

One of the major problems in large-eddy simulation of turbulent flows concerns assessing reliability of the LES results in terms of numerical resolution. Even for fully developed turbulent channel flow, results become poor if the mesh (or the time step) is not fine enough, in particular if using methods that rely on low-order schemes. This issue cannot be overestimated also from an industrial point of view. For industrial applications of LES to flows in complex geometries, grid convergence cannot be reached or ensured by a global mesh refinement study due to extremely large computational costs.

In the present work we focus on the spatial discretisation error for statistically steady flows. As a solution strategy for *statistically steady* flows, this work presents two sensors to measure the resolution quality of the LES in order to ensure that turbulent flow features are properly resolved. These sensors may then be used as a refinement indicator for local mesh adaptation. The final aim is to ensure high quality LES results by providing a tool for automatic grid refinement for LES and thereby reducing the large expertize on proper use of LES demanded from the CFD code user.

The concept of sensor-based mesh adaptation for LES was proposed by [10] with focus on a so-called *adaptive LES*, where $\Delta = \Delta(x)$ is interpreted as a model parameter,

and, if the ratio h/Δ is fixed, Δ is adapted by varying the mesh spacing until a desired turbulence resolution is obtained. In [10], only an abstract formula for turbulence resolution defined by the fraction of resolved to total turbulent kinetic energy is given. An operational formula was proposed in [7] and tested for free-shear layers and regions of separated flow. In the present work, this approach is extended to attached boundary layer flows by investigating a sensor based on the ratio of resolved to total turbulent shear stress. Alternative approaches attempt to separate the influence of the numerical error and the contribution of the subgrid-scale model, see [2], [6].

2   Basic Discretization and Turbulence Modelling

The DLR THETA code is the unstructured solver for flows with small compressibility effects developed at DLR Göttingen based on a finite volume scheme on collocated grids. It uses a projection method to split the calculation of velocity $\boldsymbol{u}$ and pressure p governed by the Navier-Stokes equations

$$\partial_t \boldsymbol{u} - \boldsymbol{\nabla} \cdot (2\nu \mathbb{S}(\boldsymbol{u})) + \boldsymbol{\nabla} \cdot (\boldsymbol{u} \otimes \boldsymbol{u}) + \boldsymbol{\nabla} p = \boldsymbol{f} \quad \text{in } \Omega \times (0, T]$$
$$\boldsymbol{\nabla} \cdot \boldsymbol{u} = 0 \quad \text{in } \Omega \times (0, T]$$

with the rate of strain tensor $\mathbb{S}(\boldsymbol{u}) = \frac{1}{2}(\boldsymbol{\nabla}\boldsymbol{u} + \boldsymbol{\nabla}\boldsymbol{u}^T)$, viscosity ν and source term $\boldsymbol{f}$. The interpolation scheme by Rhie and Chow [11] is applied to avoid spurious pressure oscillations.

The enhancement of the THETA code for LES-type simulations was demonstrated in [12]. Key elements of a proper numerical method are using central difference scheme (CDS) for the convective fluxes in divergence form and a second order time discretisation using the second order backward differencing formula BDF(2). Diffusive fluxes are discretized with the CDS. The classical Smagorinsky model is employed as subgrid scale (SGS) model together with van Driest damping for wall-bounded flows

$$\nu_\text{t} = (C_S \mathcal{D}(y^+) \Delta)^2 |\mathbb{S}| , \qquad \mathcal{D}(y^+) = 1 - \exp(-y^+/A^+) , \quad A^+ = 26$$

with $|\mathbb{S}| = (2\mathbb{S}(\boldsymbol{u}) : \mathbb{S}(\boldsymbol{u}))^{1/2}$ where $\mathbb{A} : \mathbb{B} = \sum_{i,j=1}^{d} A_{ij} B_{ij}$, friction velocity u_τ, and wall-distance in viscous units $y^+ = y u_\tau / \nu$ with viscosity ν.

Alternatively, we use the wall-adapting local eddy-viscosity (WALE) model [9]

$$\nu_t = C_w \Delta^2 \frac{(S_{ij}^d S_{ij}^d)^{3/2}}{(S_{ij} S_{ij})^{5/2} + (S_{ij}^d S_{ij}^d)^{5/4}}$$

with $S_{ij} = (\mathbb{S}(\boldsymbol{u}))_{ij}$ and S_{ij}^d defined by

$$S_{ij}^d = \frac{1}{2}\left(g_{ij}^2 + g_{ji}^2\right) - \frac{1}{3}\delta_{ij} g_{kk}^2 , \quad g_{ij}^2 = g_{ik} g_{kj} , \quad g_{ij} = \frac{\partial u_i}{\partial x_j}$$

where the constant is $C_w = 0.1$ for boundary layer flows.

Results for the low Reynolds number benchmark test cases decaying isotropic turbulence (DIT) and turbulent channel flow at $Re_\tau = 395$ are in very good agreement with
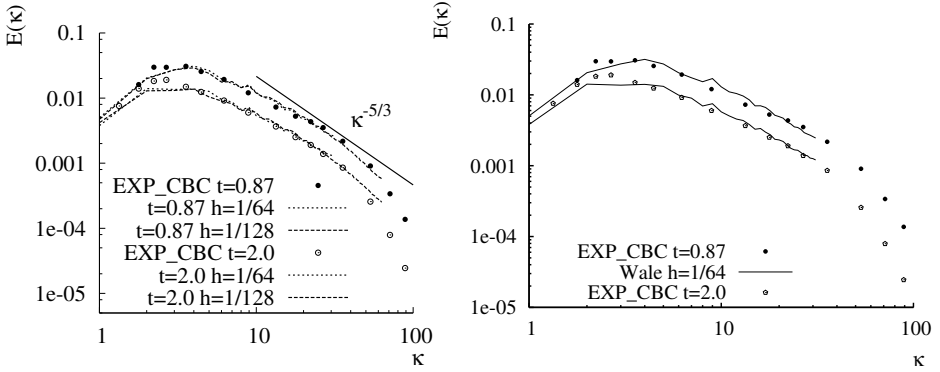
Fig. 1. DIT testcase by Comte-Bellot [3]: Energy spectrum. Standard Smagorinsky model for $N = 64$ with $C_S = 0.1$ and for $N = 128$ with $C_S = 0.094$ (left). WALE model for $N = 64$ with $C_w = 0.55$ (right).
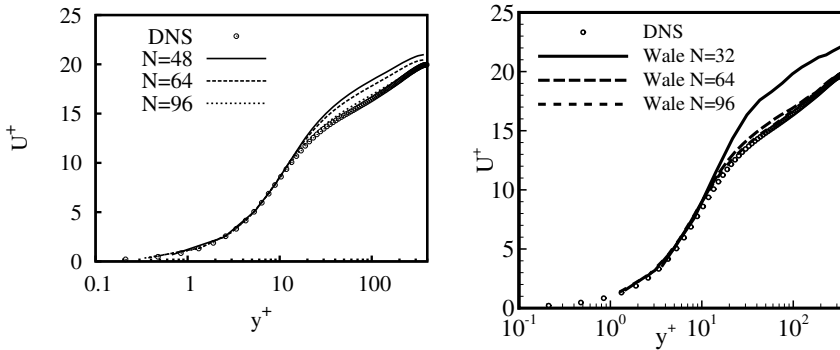
Fig. 2. Channel flow at $Re_\tau = 395$ by [8]: Mean velocity profile for different spatial resolutions. Standard Smagorinsky with $C_S = 0.1$ (left). WALE with $C_w = 0.1$ (right).

results found in literature, see Fig. 1- 2. Interestingly, for channel flow at $Re_\tau = 395$, even on the 64x64x64 mesh, the resolution is not fine enough.

In order to assess the spatial resolution quality of a large-eddy simulation, the aim is to design a sensor S which takes a value in $[0, 1]$ for each control volume of the finite-volume mesh. Moreover we have to specify threshold values s_0, s_1. Then $S > s_1$ indicates that the local mesh resolution is sufficiently fine and $S < s_0$ if the mesh is too coarse.

Recently, an indicator based on the resolved turbulent kinetic energy to measure the resolution quality of statistically steady free-shear layers has been proposed, cf. [7],

$$S_k(\boldsymbol{x}) = \frac{k}{k + k_{\text{sgs}}} \,, \quad k = \frac{1}{2}\langle(\boldsymbol{u} - \langle\boldsymbol{u}\rangle)^2\rangle \,, \quad k_{\text{sgs}} = \frac{1}{2}\langle(\boldsymbol{u} - \overline{\boldsymbol{u}})^2\rangle \tag{1}$$
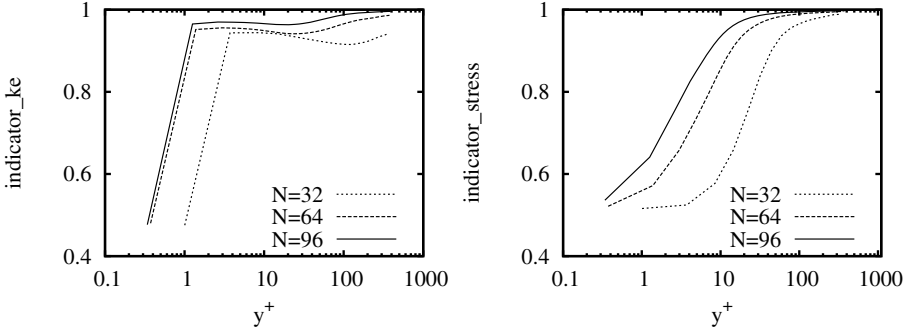
Fig. 3. Channel flow at $Re_\tau = 395$ by [8]: Profile for sensor for LES resolution quality based on resolved turbulent kinetic energy (1) (left) and based on resolved stress (2) (right).

where $\langle \cdot \rangle$ denotes the filtering operator in homogeneous directions and in time and the spatial average $\overline{u}$ is defined by the convolution integral

$$\overline{u}(x,t) \;=\; \int_{\mathbb{R}^d} g_\Delta(\boldsymbol{x} - \boldsymbol{y}) \boldsymbol{u}(\boldsymbol{y},t) \mathrm{d}\boldsymbol{y}$$

with g_Δ being the top hat filter function. The turbulent kinetic energy in the residual or subgrid scale motion cannot be computed from resolved quantities and hence requires modelling. The idea of (1) is to use a scale similarity assumption for the subgrid scale velocity $\boldsymbol{u}_{\mathrm{sgs}} \approx \boldsymbol{u}(\boldsymbol{x},t) - \overline{\boldsymbol{u}}(\boldsymbol{x},t)$.

An alternative indicator considers the ratio of resolved to total shear stress and may be defined by

$$S_s(\boldsymbol{x}) \;=\; \frac{\tau}{\tau + \tau_{\mathrm{sgs}}}\,, \quad \tau = \langle u'v' \rangle\,, \quad \tau_{\mathrm{sgs}} = -\langle \nu_t \rangle \langle \frac{du}{dy} \rangle. \tag{2}$$

For channel flow at $Re_\tau = 395$, these two grid quality indicators (1) and (2) are shown in Fig. 3. Values of indicator (1) are close to 1.0 even on the coarsest mesh. Therefore an improved resolution with decreasing grid spacing can hardly be judged from this sensor for wall-bounded flow. On the other hand, indicator (2) shows a clear trend of improved resolution with decreasing grid spacing. On the 96x96x96 mesh, the indicator for resolved stresses takes values of 0.9 except in the viscous sublayer. This seems to be the minimal required value for wall-resolved LES.

3   Presentation of Results for High Reynolds Number Flows

For flows at higher Reynolds number, wall functions are used to bridge the near-wall region. The wall node is shifted to a user specified position y_δ into the cell adjacent to the wall. Denote $y(1)$ the wall distance of the first node above the wall. Then we use $y_\delta = 0.27y(1)$, which ensures that both y_δ and $y(1)$ are close to the center of their respective control volumes. The universal velocity profile of RANS-type by Reichardt is matched with the instantaneous LES solution at the shifted node y_δ for computing the wall-shear stress, see [7].
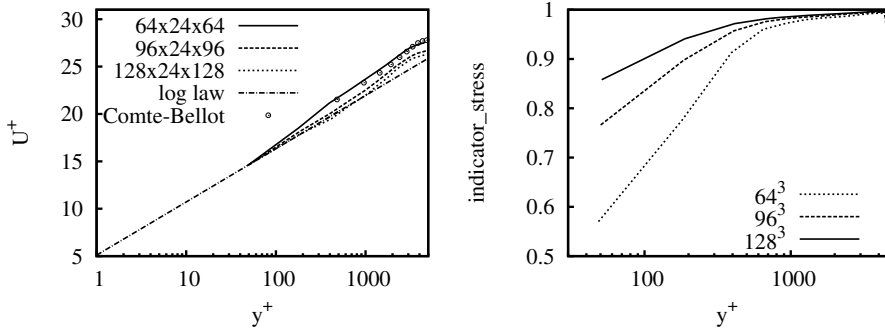
Fig. 4. Turbulent channel flow at $Re_\tau = 4800$. Left: Mean velocity profiles for different spatial resolutions. Right: Sensor based on resolved shear stress (2).

3.1   Turbulent Channel Flow at $Re_\tau = 4800$

We consider turbulent channel flow at $Re_\tau = 4800$. Numerical results are compared also with the data by Comte-Bellot [1]. However, for the three cases considered by Comte-Bellot ($Re_\tau = 2340, 4800, 8160$) the values obtained for slope $1/\kappa$ and constant C of the log law $u^+ = \log(y^+)/\kappa + C$ show a significant spreading and also deviate from the standard values.

The role of the time discretisation error for this flow was studied in [7], showing that $\delta t^+ \equiv \delta t u_\tau^2/\nu = 1.75$ is required to ensure that time discretisation error is sufficiently small. Regarding the spatial discretisation error three meshes are considered with varying mesh size in streamwise and spanwise direction. Meshes of $N_x \times 24 \times N_z$ nodes with $N_x = N_z \in \{64, 96, 128\}$ correspond to $\Delta x^+ = 2\Delta z^+ = 470, 317, 235$. For all meshes $y_\delta^+ = 50$ for the shifted node. The profiles for mean velocity and for the sensor based on resolved stress (2) are plotted in Fig. 4. The log-layer mismatch on the $N_x = 64$-mesh appears in conjunction with a too low resolution of the turbulent shear stress. A resolution of 90% of the turbulent shear stress appears to be necessary to remove the log-layer mismatch, which can be achieved only on the finest mesh. Note that the corresponding spacing $\Delta x^+, \Delta z^+$ is already little coarse compared to existing best practice guidelines for LES with near-wall modelling using wall functions.

3.2   Flow over a Backward-Facing Step at $Re_h = 37500$

Then we consider the turbulent flow over a backward-facing step at Reynolds number $Re_h = U_0 h/\nu = 37500$ based on step height h, studied experimentally by Driver and Seegmiller [4]. Regarding the computational domain used, the length of the inflow part is $4h$ before the step with channel height $8h$ and the channel length after the step is $25h$. At the inlet, the mean velocity profile is prescribed by blending of DNS data in the near-wall region and experimental data [4] in the outer part. The method by [5] is used to generate turbulent structures at the inflow boundary.
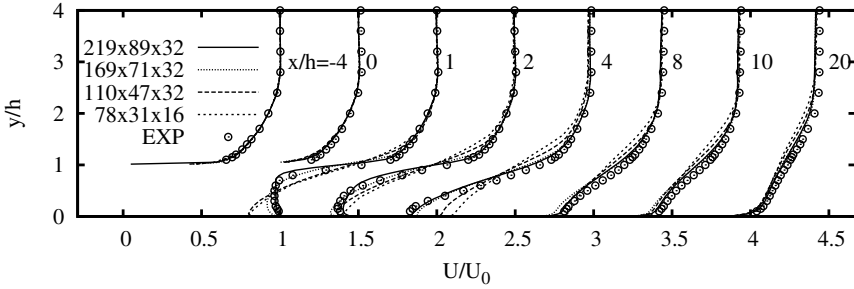
Fig. 5. Flow over backward facing step at $Re_h = 37500$ by [4]: Convergence study of mean velocity profiles at several streamwise positions using different meshes.

The mesh spacing is almost equidistant in $x-$ and $z-$direction and only a small stretching is applied in $x-$direction near the outlet. Wall functions are used on top and bottom wall. The role of the time step size was studied in [7] showing that for $\delta t = 1 \times 10^{-5}[s]$ the time-discretisation error is sufficiently small. After a flow developing time of $348h/U_0$, which is around 12 "flow through" times, the average is computed over a sample time $348h/U_0$, and in spanwise direction.

The aim of a sensor is to assess the mesh resolution without need to perform a global refinement study. Profiles for mean velocity at 8 cross sections and the corresponding experimental data are shown in Fig. 5. The resolution is satisfactory on the finest mesh (219x89x32 nodes), but not on the medium mesh (110x47x32 nodes). Fluctuations, omitted here due to lack of space, are shown in [7]. In order to *develop* such a sensor, we proceed in opposite direction. The first step is to perform a convergence study, and to consider the corresponding distribution of the sensor values. The distributions for the sensors in (1), (2) averaged over time and in spanwise direction, on the medium mesh and on the finest mesh are shown in Fig. 6, 7.

An appropriate sensor has to satisfy the following property: Its values should increase monotonically when refining the mesh. This property may be observed only for special flow regions, e.g., attached boundary layer flows or free-shear layers. Indeed, the two sensors (1) and (2) appear to be suitable for different flow regions.

The sensor values for resolved turbulent kinetic energy (1) increase clearly in the region of the free shear layer and in the recirculation region when refining the mesh. The sensor values also increase inside the boundary layers, but not so obvious as in the other two regions, see also the results for channel flow at $Re_\tau = 395$.

On the other hand, the sensor values for resolved turbulent shear stress (2) are monotonically increasing in the attached boundary layer flow before the step with increasing spatial resolution, confirming results for turbulent channel flow at $Re_\tau = 4800$, see Fig. 4. But the sensor values do not show monotonically increasing behaviour in the free-shear layer and in the entire recirculation region.

The next step is to specify threshold values s_0, s_1. $S > s_1$ indicates that mesh resolution is sufficiently fine and $S < s_0$ if the mesh is too coarse. For the indicator (1) we suggest $s_0 = 0.8$ and $s_1 = 0.9$, see also [7]. Regarding indicator (2), it takes values around 0.875 in the largest part of the boundary layer before the step on the finest mesh.
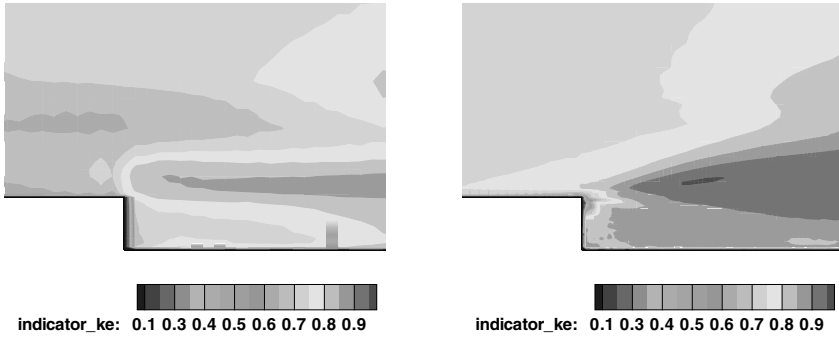
Fig. 6. Flow over a backward-facing step at $Re_h = 37500$ by [4]: Sensor based on the resolved turbulent kinetic energy (1) on medium mesh (left) and on a fine mesh (right) using the Smagorinsky model and wall-functions.
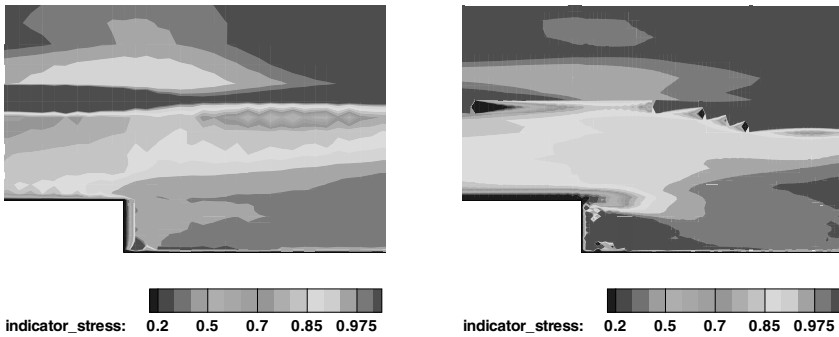
Fig. 7. Flow over a backward-facing step at $Re_h = 37500$ by [4]: Sensor based on the resolved turbulent shear stress (2) on medium mesh (left) and on a fine mesh (right) using the Smagorinsky model and wall-functions.

Little uncertainty in the results may stem from using synthetic turbulence at the inlet. Together with the results for channel flow at $Re_\tau = 4800$, we suggest $s_0 = 0.8$ and $s_1 = 0.9$ which might be little conservative.

4 Conclusion

The resolution requirements of LES for attached and massively separated flows have been considered. For statistically steady flows, two sensors to measure the resolution quality of LES have been presented and compared. A first sensor based on the resolved turbulent kinetic energy appears suitable for free shear layers and regions of separated flow. A second sensor based on the resolved shear stress seems suitable for regions of

attached boundary layer flow. The predictions of the sensors are supported by a mesh convergence study and with existing best-practice guidelines for attached equilibrium boundary layer flows.

Acknowledgements

References

[1] AGARD: A selection of test cases for the validation of large-eddy simulations of turbulent flows. Tech. rep., AGARD-AR-345 (1998)

[2] Celik, I., Cehreli, Z., Yavuz, I.: Index of resolution quality for large eddy simulations. ASME Journal of Fluids Engineering 126, 949–958 (2005)

[3] Comte-Bellot, G., Corrsin, S.: "Simple Eulerian time correlation of full- and narrow-band velocity signals in grid-generated, 'isotropic' turbulence". Journal of Fluid Mechanics 48(2), 273–337 (1971)

[4] Driver, D.M., Seegmiller, H.L.: Features of a reattaching turbulent shear layer in divergent channel flow. AIAA Journal 23, 163–171 (1985)

[5] Klein, M., Sadiki, A., Janicka, J.: A digital filter based generation of inflow data for spatially developing direct numerical or large eddy simulations. Journal of Computational Physics 186, 1652–1665 (2003)

[6] Klein, M.: An attempt to assess the quality of large eddy simulations in the context of implicit filtering. Flow, Turbulence and Combustion 75, 131–147 (2005)

[7] Knopp, T., Zhang, X.Q., Kessler, R., Lube, G.: Enhancement of an Industrial Finite-Volume Code for Large-Eddy-Type Simulation of Incompressible High-Reynolds Number Flow Using Near-Wall Modelling. In: Computer Methods in Applied Mechanics and Engineering (2008) (submitted)

[8] Moser, R.D., Kim, J., Mansour, N.N.: Direct numerical simulation of turbulent channel flow up to $Re_\tau = 590$. Physics of Fluids 11, 943–946 (1999)

[9] Nicoud, F., Ducros, F.: Subgrid-scale stress modelling based on the square of the velocity gradient tensor. Flow, Turbulence and Combustion 62, 183–200 (1999)

[10] Pope, S.B.: Ten questions concerning the large-eddy simulation of turbulent flows. New Journal of Physics 6, 1–24 (2004)

[11] Rhie, C.M., Chow, W.L.: Numerical study of the turbulent flow past an airfoil with trailing edge separation. AIAA Journal 21, 1525–1532 (1983)

[12] Zhang, X.Q.: Identification of model and grid parameters for incompressible turbulent flows. Ph. D. thesis, University Göttingen (2007)

Active Separation Control on the Flap of a Three-Element High-Lift Configuration with Segmented Actuation in Spanwise Direction

Tobias Höll, Bert Günther, Erik Wassen, and Frank Thiele

Berlin Institute of Technology,
Department of Fluid Mechanics and Engineering Acoustics,
Müller-Breslau-Str. 8, 10623 Berlin, Germany
tobias.hoell@cfd.tu-berlin.de
http://www.cfd.tu-berlin.de

Summary

This paper describes numerical investigations of active flow control on the flap of a three-element high-lift configuration at a Reynolds number of $Re = 750\,000$. The flow is perturbed by periodic blowing and suction through slots near the leading edge of the flap. In previous investigations the influence of actuation intensity and frequency, as well as the duty cycle has been assessed. The main focus of this paper is on comparing in what manner the flow field reacts to a segmentation of the actuation in spanwise direction in contrast to a continuous slot. Then a phase shifting of the blowing and suction on the actuation segments is evaluated.

Nomenclature

c, c_k	clean chord length, flap length ($c_k = 0.254c$)
c_L	lift coefficient
C_μ	momentum coefficient $C_\mu = \frac{H}{c}\left(\frac{u_a}{u_\infty}\right)^2$
f, F^+	excitation frequency, non-dimensional excitation freq. $F^+ = f\frac{c_k}{u_\infty}$
H	slot width ($H = 0.00186c_k$)
Re	Reynolds number based on chord length
u_a, u_{exc}	amplitude velocity of excitation in the slot, excitation velocity
u_∞	inflow velocity
$\alpha, \delta_f, \delta_s$	angle of attack, flap deflection angle, slat deflection angle
Δt	time step size
Φ	sweep angle

1   Introduction

The sophisticated high-lift devices of a modern commercial airplane consist of a slat and single or multiple flaps. These elements have to enhance the lift coefficient during take-off in order to reduce take-off speeds and runway lengths. Because of the enormous costs, complexity and weight of these devices, aerodynamic research and development aims at simplification of these whilst maintaining their effectivity. Conventional methods are currently not capable of achieving further significant improvement. However, one promising means to reduce flow separation is offered by active flow control methods. Both numerical and experimental investigations have shown that the effectiveness of high-lift configurations can be significantly improved by delaying flow separation on the flap [10, 6, 7].

This paper describes a numerical investigation of the control of the flow over the flap of a three-element high-lift configuration by means of periodic excitation [4]. An unsteady wall jet emanating from the single slotted flap shoulder close to the leading edge is used to excite the flow and thus provoke either delay of separation or reattachment [9]. The test model consists of a swept wing with an extended slat and a single slotted Fowler flap.

The investigations are mainly focused on a comparison between the use of continuous and segmented excitation slots in spanwise direction [1]. It is investigated whether longitudinal vortices can be induced by segmented excitation slots. Further delay of flow separation is expected to be an effect of them. Hence, it is analyzed if an enhancement in effectivity of active flow control and an extra gain in lift can be achieved by using segmented instead of continuous excitation slots on the flap.

1.1   Active Flow Control

Active flow control methods are characterised by arrangements with an excitation mechanism that inserts external energy into the flow (figure 1).

In the last decades, a large number of experimental and numerical studies have shown the general effectiveness of active flow control for single airfoils. In most investigations, leading edge suction is applied to delay transition [3]. However, most control techniques considered in the past demonstrated low or negative effectiveness.
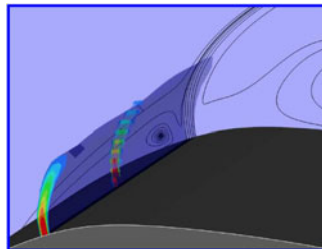
Fig. 1. Periodic wall jet on the upper surface of the flap.
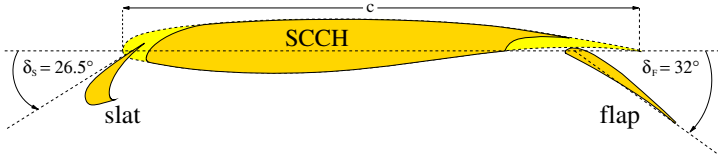
Fig. 2. SCCH high-lift configuration.

In further investigations oscillatory suction and blowing was found to be much more efficient with respect to lift than steady blowing [8, 2]. The process becomes very efficient if the excitation frequencies correspond to the most unstable frequencies of the shear layer, generating arrays of spanwise vortices that are convected downstream and continue to mix across the shear layer.

2   Numerical Simulation Method

2.1   Flow Solver and Turbulence Modeling

As numerical flow solver the in-house code ELAN (**EL**liptic **A**nalysis of the **N**avier-stokes equations) is applied which is based on a fully-implicit three-dimensional finite-volume scheme for solution of the Reynolds-averaged Navier-Stokes equations. The method is of second order accuracy in space and time. Based on the SIMPLE pressure correction algorithm, a co-located storage arrangement for all quantities is applied. Convective fluxes are approximated by a TVD scheme. In previous investigations of unsteady turbulent flows, the LLR k-ω turbulence model by Rung [5] exhibited the best performance. This turbulence model is a two-equation eddy-viscosity model which considers realizability conditions.

2.2   Boundary Conditions

For the numerical computations a level of turbulence of $Tu = 0.1\%$ and the turbulent viscosity ratio of $\frac{\mu_t}{\mu} = 0.1$ is chosen at the inflow. These settings provide free-flight conditions. At the outflow a convective boundary condition is set, therefore unsteady flow structures can be transported outside the domain. The near-wall resolution on the airfoil is fine enough ($y^+ \leq 1$) to use a low-Re formulation.

2.3   Time-Step Size

The unsteady characteristics of the flow are known from previous investigations. Therefore, a time-step size of $\Delta t = 2.1 \cdot 10^{-3} c/u_\infty$ is chosen, because this time-step size proved to resolve the unsteady flow behaviour sufficiently. All calculations which are presented in this paper are carried out using this time-step size. For the excited cases a non-dimensional excitation frequency of $F^+ = 0.6$ is used, which results in a resolution of 200 time steps per oscillation cycle.

(a) Slice through the structured mesh

(b) Surface mesh
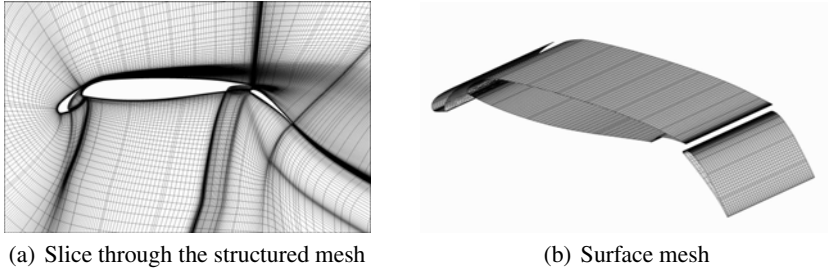
Fig. 3. Block-structured mesh of the SCCH-configuration.

2.4   Method of Excitation

For the actuation, a periodic blowing and suction type boundary condition is used. The perturbation to the flow field is introduced through the inlet flow condition on two small wall sections, arranged in spanwise direction, representing the excitation slots:

$$u_{exc}(\tau, n) = \underbrace{u_a \cdot \sin\left[\frac{n-1}{n_{max}-1} \cdot \pi\right]}_{\text{spatial velocity distribution}} \cdot \underbrace{\sin\left[2\pi \cdot \frac{c}{c_k} \cdot F^+ \cdot \tau\right]}_{\text{time-dependency}}$$

$$\text{with} \quad u_a = u_\infty \sqrt{\frac{c}{H} C_\mu}$$

$$F^+ = f_{per} \cdot \frac{c_k}{u_\infty}$$

$$\tau = t \cdot \frac{u_\infty}{c}$$

$$1 \le n \le n_{max} \quad .$$

where u_a is the velocity amplitude of the perturbation oscillation, F^+ is the non-dimensional perturbation frequency, τ is the dimensionless time given in convective units of the whole configuration, H is the slot width ($H = 0.00186\, c_k$), C_μ is the non-dimensional steady momentum blowing coefficient and n is the actual grid layer of each actuation slot ($1 \le n \le n_{max}$, $n_{max} = 20$ gridlayers per actuation slot). Both intensity and excitation frequency can be chosen differently for each slot, as well as a phase shifting between the actuation on both segments. The oscillating jet is emitted perpendicular to the wall segment of the excitation slot, and is located at 6% chord behind the flap leading edge.

2.5   SCCH High-Lift Configuration

For the numerical investigation the **S**wept **C**onstant **C**hord **H**alf model (SCCH) is used, which represents a generic high-lift configuration consisting of a slat and a flap (relative chord length $c_k = 0.254\, c$) with industrial relevance [1]. The wing has a sweep angle of $\Phi = 30°$ and a constant chord length in the spanwise direction. In order to save

numerical effort, the wing is modeled with infinite span by using periodic boundary conditions. As a consequence, the only considered three-dimensional effect is the one generated by the sweep. Figures 3(a) and 3(b) show the computational mesh, which consists of approximately $4 \cdot 10^6$ cells.

3   Results

3.1   Unexcited Flow

To begin with, it has to be ensured that the unexcited case provides flow conditions which are appropriate for applying active flow control. This means that the flow on the main wing has to be attached whereas maximised flow separation occurs on the upper side of the flap. Therefore, according to Günther et. al. [1], an angle of attack of $\alpha = 6°$, a slat deflection angle of $\delta_s = 26.5°$ and a flap deflection angle of $\delta_f = 37°$ are chosen, because this setting provided the desired flow conditions in preliminary investigations. For all simulations a Reynolds number of $Re = 750\ 000$ is used and fully turbulent flow is assumed.

Apart from that, the unexcited flow shows several characteristics which are suitable for the use of active flow control: Because of the sweep angle of $\Phi = 30°$ and the large extension of the grid in the spanwise direction a strong crossflow is generated. Secondly, large vortex shedding occurs on the flap resulting in interaction with those vortices generated in the shear layer between the recirculation region and the flow passing through the slot between main airfoil and flap [1].

3.2   Excited Flow

Because of these reasons this configuration is suitable for applying active flow control, which then can be used to regulate and delay flow separation. This was proven in earlier investigations on 2D airfoils by Schatz et. al. [8], as well as with continuous excitation
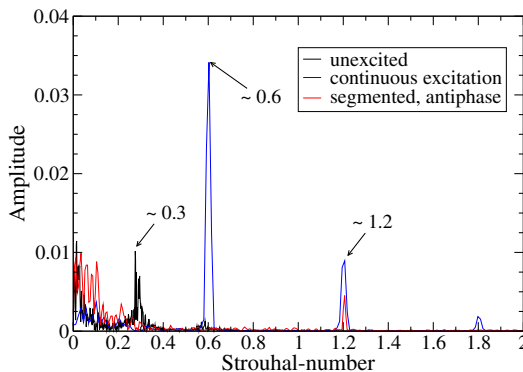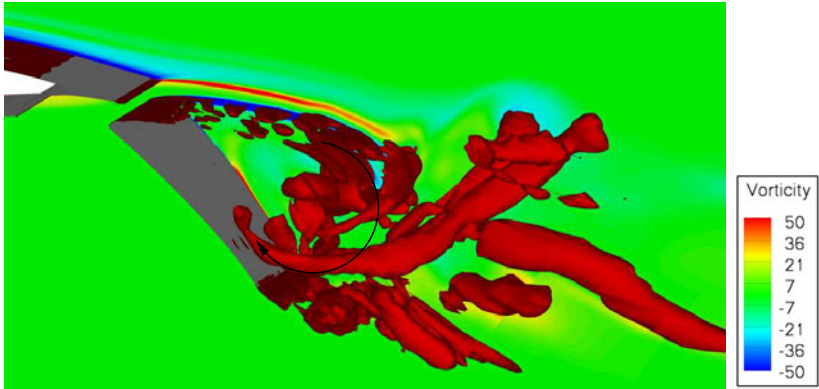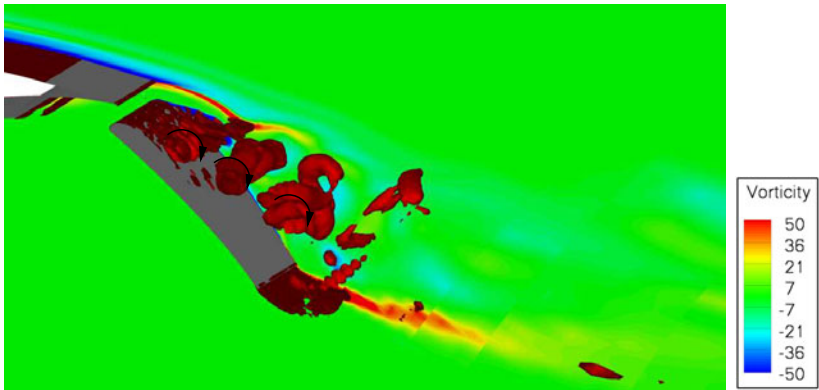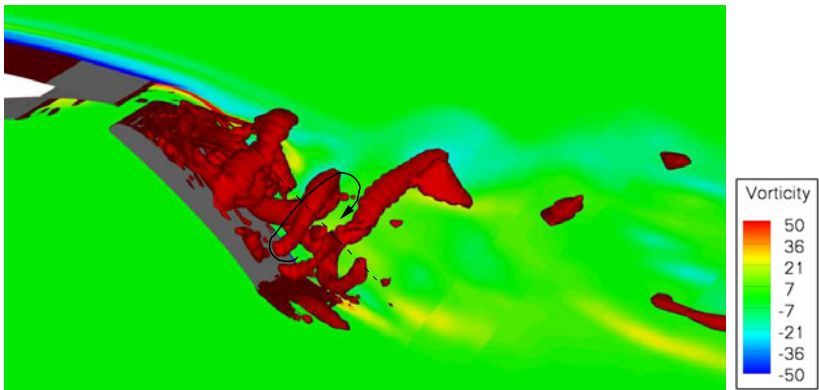

Fig. 4. Frequency analysis of unexcited, continouus and segmented excitation.

(a) Unexcited case

(b) Excited case, continouus slot

(c) Excited case, segmented slot, antiphase excitation

Fig. 5. $\lambda_2 = -200$ isosurface and vorticity contours of excited and unexcited cases.

in spanwise direction on a segment of an infinite swept wing. In contrast to the presented cases, the latter one was conducted at a different Reynolds number and less grid layers in the spanwise direction (16 instead of 40) by Günther et. al. [1]. This paper now presents a comparison of continuous actuation and segmented actuation in the spanwise direction with two actuation segments. These two actuation segments divide the continuous slot in two parts. No strip between both segments is considered, hence one segment has the length of half a spanwidth. For the actuation parameters intensity and frequency $C_\mu = 300 \cdot 10^{-5}$ and $F^+ = 0.6$ are chosen, because they proved to be most effective in previous investigations. At these constant values three different cases of the segmented actuation are compared to the continuous actuation: First of all, an equiphase case, i.e. a case without phase shifting between both actuation segments. In contrast, a case with an antiphased actuation between both actuators. Additionally, one case where only one actuator is used, i.e. only half the spanwise spread is actuated.

The impact of active flow control is clearly depicted in flow visualizations (see figures 5(a) to 5(c)). In contrast to the unexcited case (figure 5(a)), the mixture of the flow is much more enhanced in the perturbed case (continuous slot, see figure 5(b)) just as a smaller recirculation area is observed. Moreover, the detachment is relocated further downstream. The transport of energy from the main flow to the recirculation near the wall is improved and the formation of large coherent vortices is suppressed. As this is already a very promising achievement of active separation control ($\Delta C_L = +19\%$ of the continuous actuator case compared to the unexcited case), the flow conditions can still be improved. As flow visualizations and lift coefficients show, this can be obtained by applying two actuator segments for the infinite wing section instead of the continuous actuation. As visualized in figure 5(c) the three-dimensionality of the flow is increased in all segmented cases compared to the continuous one. This results in an improved mixture of the flow. Furthermore, it can be detected that the flow separation on the upper surface of the flap is a little more displaced in the downstream direction. The most interesting and promising fact however is that longitudinal vortices are induced by the antiphase of the actuation (see sketched arrow in figure 5(c). According to the fact that the inversely phased case provides the largest gain in lift coefficient ($\Delta C_L = +24\%$) it can be concluded that these longitudinal vortices can contribute effectively to the lift enhancement. In contrast, the equiphased case reaches a gain in lift which is a little smaller ($\Delta C_L = +23\%$). Interestingly, actuation on only one slot almost reaches the same level of lift than actuating on the whole spanwidth with a continuous slot ($\Delta C_L = +18\%$), but of course with an energy consumption reduced by half.

All these facts are supported by a frequency analysis of the lift coefficient. Figure 4 shows the frequency spectrum for the unexcited case, the excited case with a continuous slot and the segmented case with antiphase excitation. The fundamental component of the unexcited case can be found at a Strouhal number (formed with the flap chord) of $St_f = f \frac{c_k}{u_\infty} = 0.3$, the first harmonic of the continuous-slot excitation case lies at $St_f = 0.6$ which suits to the dimensionless excitation frequency of $F^+ = 0.6$. For the inversely phased case however, the first harmonic seems to get eliminated. The second harmonic although occurs at $St_f = 1.2$, but is reduced by half in signal strength. Thus,

the segmented actuation not only excites small turbulent structures which generate more mixture of the flow, but also suppresses large coherent structures which are detrimental for the lift gain.

4   Conclusion

To sum up, it can be stated that the segmented actuation in spanwise direction provides a promising means to increase the lift caused by the excitation of smaller structures than with the conventional actuation due to the local profiling of the excitation velocity. These smaller structures offer more interaction among each other which results in quicker dissipation and improved energy transport. Apart from that, longitudinal vortices are generated which apparently are also responsible for a lift gain. This has to be verified by a feature-based analysis of the flow field or by related methods in future work.

Acknowledgements

References

[1] Günther, B., Thiele, F., Petz, R., Nitsche, W., Sahner, J., Weinkauf, T., Hege, H.-C.: Control of Separation on the Flap of a Three-Element High-Lift Configuration. AIAA Paper 2007-265 (2007)

[2] Günther, B., Becker, R., Carnarius, A., Thiele, F., King, R.: Simulation Study of the Robust Closed-Loop Control of a 2D High-Lift Configuration. In: IUTAM Symposium on Unsteady Separated Flows and their Control, Kerkyra (Corfu), Greece (2007)

[3] Maddalon, D.V., Collier, F.S., Montoya, L.C., Land, C.K.: Transition Flight Experiments on a Swept Wing with Suction. AIAA Paper 89-1893 (1989)

[4] Pack Melton, L., Yao, C.-S., Seifert, A.: Active Control of Separation from the Flap of a Supercritical Airfoil. AIAA Journal 44(1), 34–41 (2006)

[5] Rung, T., Thiele, F.: Computational Modelling of Complex Boundary-Layer Flows. In: 9th Int. Symp. on Transport Phenomena in Thermal-Fluid Engineering, Singapore (1996)

[6] Schatz, M., Thiele, F.: Numerical Study of High-Lift Flow with Separation Control by Periodic Excitation. AIAA Paper 2001-0296 (2001)

[7] Schatz, M., Thiele, F., Petz, R., Nitsche, W.: Separation Control by Periodic Excitation and its Application to a High Lift Configuration. AIAA Paper 2004-2507 (2004)

[8] Schatz, M., Günther, B., Thiele, F.: Computational Investigation of Separation Control for High-lift Airfoil Flows. In: Active Flow Control. Notes on Numerical Fluid Mechanics and Multidisciplinary Design, vol. 95. Springer, Heidelberg (2007)

[9] Seifert, A., Darabi, A., Wygnanski, I.: Delay of Airfoil Stall by Periodic Excitation. Journal of Aircraft 33(4), 691–698 (1996)

[10] Tinapp, F.H.: Aktive Kontrolle der Strömungsablösung an einer Hochauftriebskonfiguration. PhD Thesis, Technische Universität Berlin (2001)

Numerical Investigation of Leading Edge Blowing and Optimization of the Slot Geometry for a Circulation Control Airfoil

C. Jensch, K.C. Pfingsten, and R. Radespiel

Technische Universität Braunschweig, Institut für Strömungsmechanik,
Bienroder Weg 3, 38106 Braunschweig, Germany
c.jensch@tu-bs.de

Summary

Numerical simulations for the aerodynamic analysis of a two-dimensional circulation control airfoil at high Reynolds numbers have been carried out. Circulation control systems need a relatively high amount of power to provide the necessary pressurized air. Hence major design paramters as slot height and additional blowing at the nose have been varied to improve the efficiency of the circulation control airfoil. The results show that a significant increase of the efficiency is possible. Additional blowing at the nose protects the leading edge against stalling at lower Mach numbers to enable very high lift coefficients. By variation of the slot height for some configurations the required momentum coefficient of the air jet could be reduced by about 20% at slightly lower lift coefficients.

1 Introduction

In recent years noise emission from aircrafts has become a major problem. Hence the interest in reducing the emitted noise during take off and landing of aircrafts especially at airports located close to urban city centres is large. One contributor of the emitted noise are conventional high-lift systems as slats and slotted flaps [11]. It is presumed that novel gapless high-lift systems without slats have a high potential in reducing the noise. Previous investigations have shown that a high-lift system using circulation control can achieve the same or even higher lift coefficients than conventional high-lift systems [1], [2], [3], [4]. Higher lift coefficients allow a shorter length of the runway for take off and landing and steeper trajectories which would reduce the noise in airport surrounding areas. Additionally it is assumed that the additional weight due to the integration of the circulation control system is counterbalanced by the moderate mechanical complexity of a high-lift system without slats and slottet flaps.

A two-dimensional circulation control airfoil based on the supercritical airfoil of the aircraft of the next generation (Flugzeug der nächsten Generation, FNG) which was provided by the company of Airbus, Germany was recently investigated at the TU Braunschweig [8], [9], [10]. The numerical simulations beared out that high deflection angles without separation and therewith relativley high lift coefficients are

accessible. However, a substantial amount of electric power or bleed air is necessary to provide the needed mass flow at high total pressure for blowing. Hence further investigations have been carried out to increase the efficiency of the circulation control airfoil.

This paper presents some results of the computations done for improving the circulation control airfoil. Different parameters like the slot height h, flap angle η, momentum coefficient of the jet c_μ and angle of attack α were varied. The impact of additional blowing at the leading edge on the performance of the airfoil has been also investigated.

2   Coanda Effect and Momentum Coefficient

2.1   *Coanda* Effect

The *Coanda* effect is named after *Henri Marie Coanda*, who discovered this phenomenon in 1910. He noticed that a tangentially blown air jet stays attached to a convex surface. Due to the turbulent momentum transport the air jet accelerates the air between the jet and the surface. The surface prevents new air to flow in the area between the jet and the surface which reduces the pressure in this area. Thus, the jet is sucked to the curved surface and stays attached to it.

The circulation control technology for airfoils uses the *Coanda* effect to realize flow turning angles without separation of the flow. Therefore a thin air jet of pressurized air is blown tangentially out of a slot directly upstream of a curved surface. This curved surface may be the knuckle shape of a deflected high-lift flap with the *Coanda* radius R. The jet accelerates the boundary layer, so it can bear large adverse pressure gradients along the flap contour. Hence very high flap deflection angles and large effective camber can be achieved which leads to high lift coefficients.

2.2   Dimensionless Momentum Coefficient

A parameter for comparison of circulation control airfoils is the dimensionless momentum coefficient of the air jet c_μ. It is defined by the ratio of introduced jet momentum per time related to the onflow dynamic pressure q_∞ and the wing area S. The following equation for c_μ is calculated by jet velocity v_{jet}, jet massflow $\dot{m}_{jet}$, onflow density ρ_∞ and onflow velocity v_∞:

$$c_\mu = \frac{v_{jet}\ \dot{m}_{jet}}{q_\infty\ S} = \frac{v_{jet}\ \dot{m}_{jet}}{\frac{1}{2}\ \rho_\infty\ v_\infty^2\ S} \tag{1}$$

For lower momentum coefficients the circulation control functions as a boundary layer control. In that case higher momentum coefficients move the point of separation further downstream on the upper surface of the flap until the flow stays attached up to the trailing edge. For a further increase of the momentum coefficient with the point of separation fixed at the trailing edge the circulation control functions as supercirculation. The efficiency of boundary layer control is usually higher than the efficiency of supercirculation. Thus finally airfoil configurations using circulation control should operate

at the edge between boundary layer control and supercirculation for best performance. Hence the momentum coefficient should be just as high as it is necessary to prevent flow separation at the trailing edge.

The efficiency of a circulation control system can be measured by the increase of the maximum lift coefficient over the required momentum coefficient, $\frac{\Delta c_{l,max,clean}}{c_\mu}$. The increase of the maximum lift coefficient is given by the difference between the maximum lift coefficient of the investigated configuration using blowing and the clean configuration. For configurations using blowing at the leading edge and upstream of the flap the sum of both momentum coefficients is used for the calculation of the efficiency. As substantial amounts of electric power or bleed air are needed for circulation control systems, the efficiency of the circulation control airfoils should be enhanced to reduce the needed momentum coefficient for a given lift coefficient.

3 Numerical Airfoil Design

The investigated airfoil was created by the integration of two slots into the FNG airfoil with a large high lift flap with a length of 30% of the chord length. One slot for blowing is located on the upper surface of the airfoil directly upstream of the flap. The slot height is set to values between $h = 0.0063R$ and $h = 0.025R$. For the numerical simulations with additional blowing at the leading edge the second slot is located on the upper surface of the leading edge of the airfoil downstream of the suction peak. Figure 1 shows the shape and the grid of the airfoil and its two slots.

For the steady, two-dimensional numerical simulations a hybrid grid was generated. The structured part for resolving the boundary layer consists of 1500 elements along the surface and 48 layers normal to the surface. The structured part has a height of 150% of the maximum boundary layer thickness. The initial layer thickness was chosen for $y^+ = 1$ even at the stagnation point. The complete grid consists of about 64000 nodes. The numerical solution of the Reynolds-averaged Navier-Stokes equations are done using the TAU flow solver [5]. Techniques like local time stepping, residual smoothing
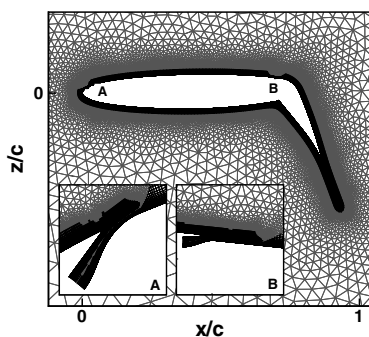

Fig. 1. Grid for the circulation control airfoil, one slot upstream of the flap and one at the leading edge, $\eta = 60°$; *not to scale*
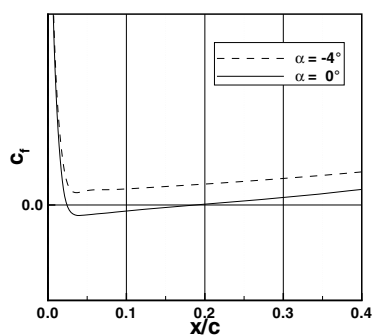
Fig. 2. Skin-friction coefficient on the upper surface, $Ma = 0.125$; $Re = 18 \cdot 10^6$; $\eta = 80°$; $c_\mu = 0.083$

and multi-grid techniques are used for accelerating the convergence to steady state. The boundary layer is assumed to be fully turbulent. The *Spalart-Allmaras* turbulence model for Rotation and/or Curvature effects [12], [13] has been identified to provide reliable predicitions of the flow around circulation control airfoils [8], hence it is used for all computations.

4   Leading Edge Blowing

Early investigations demonstrated the effect of additional blowing out of a second slot at the leading edge of the airfoil [6], [7]. The air jet accelerates the boundary layer which protects the near wall flow from leading edge separation. Hence the angle of attack can be increased and higher lift coefficients can be achieved.

The height of the slot upstream of the flap was set to $h = 0.0125R$. The slot at the leading edge was set to the same height for a momentum coefficient of $c_\mu = 0.043$ and quartered for $c_\mu = 0.011$. The upper surface of the leading edge has been changed along a length of four times the height of the leading edge slot, as seen in Figure 1. The slot is positioned within the surface. Thus, when the slot is closed the original contour of the airfoil is unchanged. Hence there is no significant increase of drag in cruise flight due to the geometry design of the nose slot expected.

For a configuration with blowing only upstream of the flap and a deflection angle of $\eta = 80°$ at a Mach number of the onflow of $Ma = 0.125$ and a Reynolds number of $Re = 18 \cdot 10^6$ the momentum coefficient was set to $c_\mu = 0.083$ to just keep the flow attached to the flap up to the trailing edge. The lift of this configuration can not be increased beyond an angle of attack of $\alpha = -4°$ due to the occurrence of a thin area of reversed flow on the upper surface at the leading edge while the flow stays attached to the flap. The skin-friction coefficient c_f on the upper surface for $\alpha = -4°$ and $\alpha = 0°$ is shown in Figure 2. The negative values of c_f at $\alpha = 0°$ show the area of reversed flow. The graph for the lift coefficient c_l over the angle of attack is shown in Figure 3. The efficiency for this configuration is $\frac{\Delta c_{l,max,clean}}{c_\mu} = 49$. Additional blowing at the leading edge with about the half of the momentum coefficient which was used for the slot upstream of the flap, $c_\mu = 0.043$, protects the leading edge against the area of reversed flow. Due to the additional blowing the circulation of the airfoil is raised and the maximum lift coefficient is increased by $\Delta c_{l,max} = 0.45$ compared to the configuration with blowing upstream of the flap only. Using all the momentum of $c_\mu = 0.126$ combined at the slot upstream of the flap without blowing at the leading edge rises the maximum lift coefficient only by $\Delta c_{l,max} = 0.29$ compared to the configuration blowing with $c_\mu = 0.083$. The graphs for the lift coefficient c_l over the angle of attack α are also shown in Figure 3. It should be mentioned that for some configurations no steady-state solution beyond the angle of attack for maximum lift was available due to unsteady stall behaviour. Anyway, the highest lift coefficients of the steady-state solutions shown in Figure 3 are a good approximation of the maximum lift coefficients. It is seen that by using a second slot at the leading edge higher lift coefficients are achievable for the same overall momentum coefficient. But it should be mentioned that the momentum coeffcient of $c_\mu = 0.126$ leads to supercirculation for the present configuration. Thus,
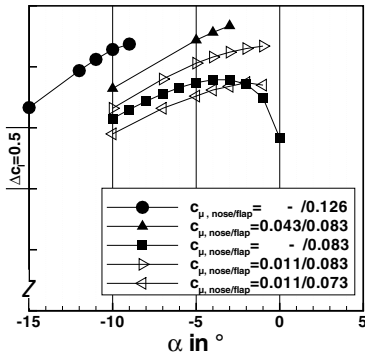
Fig. 3. Lift coefficient over angle of attack for leading edge blowing; $Ma = 0.125$; $Re = 18 \cdot 10^6$; $\eta = 80°$
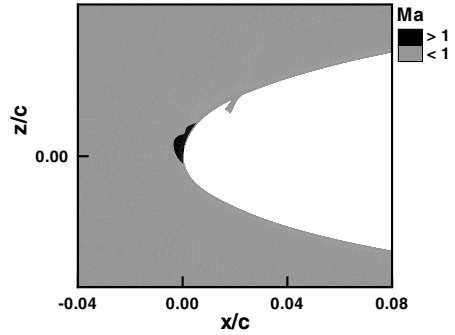
Fig. 4. Transonic flow at the leading edge; $Ma = 0.15$; $Re = 21 \cdot 10^6$; $\eta = 60°$; $\alpha = 7°$; $c_{\mu,nose/flap} = 0.033/0.050$

the efficiency is only about $\frac{\Delta c_{l,max,clean}}{c_\mu} = 37$ for the configuration with leading edge blowing and $\frac{\Delta c_{l,max,clean}}{c_\mu} = 34$ for the configuration with only one slot upstream of the flap.

Additional numerical simulations with smaller overall momentum coefficients at around $c_\mu = 0.083$, where the edge bewteen boundary layer control and supercirculation is expected, were also carried out. In Figure 3 the graphs for the lift coefficient over the angle of attack are shown for configurations using $c_\mu = 0.011$ at the leading edge slot and $c_\mu = 0.073$ and $c_\mu = 0.083$ for the slot upstream of the flap. Splitting the overall momentum coefficient of $c_\mu = 0.083$ to $c_{\mu,nose/flap} = 0.011/0.073$ leads to an efficiency of $\frac{\Delta c_{l,max,clean}}{c_\mu} = 48$ by decreasing the maximum lift coefficient by $\Delta c_{l,max} = 0.02$ compared to the configuration using blowing with $c_\mu = 0.083$ upstream of the flap only. The momentum coefficient combination of $c_{\mu,nose/flap} = 0.011/0.083$ increases the maximum lift coefficient by $\Delta c_{l,max} = 0.28$ with a little higher overall momentum coefficient than the configuration using blowing with $c_\mu = 0.083$ only and an efficiency of $\frac{\Delta c_{l,max,clean}}{c_\mu} = 47$. These results indicate that the edge between boundary layer control and supercirculation is obtained inbetween. Thus leading edge blowing is presumably necessary for achieving maximum lift coefficients higher than those achieved with $c_\mu = 0.083$ at higher efficiency for the investigated configuration.

Further investigations at $Ma = 0.15$ and $\eta = 60°$ were also done. For a configuration using blowing at the flap only the momentum coefficient was set to $c_\mu = 0.050$ to just keep the flow attached to the flap up to the trailing edge. For this configuration a separation bubble at the leading edge appears at an angle of attack three degrees higher than the angle of attack for the maximum lift coefficient. Additional momentum with a coefficient of $c_\mu = 0.033$ is added on the one hand to the slot upstream of the flap, which leads to a momentum coefficient of $c_\mu = 0.083$ and on the other hand to the slot at the leading edge to prevent the separation bubble. In contrast to the previous

mentioned investigations at $Ma = 0.125$ for this deflection angle and Mach number the second variation with blowing at the leading edge is less efficient than using blowing upstream of the flap only. The air jet at the leading edge accelerates the flow. The additional momentum increase the circulation of the airfoil and moves the stagnation point further backwards on the lower surface. This leads to supersonic velocities at the leading edge, shown in Figure 4. For this configuration using blowing at the leading edge is not able to achieve maximum lift coefficients higher than those achieved with blowing upstream of the flap only. This effect counterbalances the improvement due to protection of the leading edge against separation for the investigated configuration.

5   Slot Geometry

The efficiency of the *Coanda* effect depends highly on the slot height [3]. A smaller thickness of the jet is more efficient but if the thickness is too small the jet vanishes before reaching the trailing edge due to strong turbulent momentum transport.

Previous numerical simulations, partly published in [8], were done with a height of the slot upstream of the flap between $h = 0.0125R$ and $h = 0.0251R$ where the slot height of $h = 0.0125R$ was the most efficient. Hence the slot height was reduced further to find the optimum. Slot heights between $h = 0.0063R$ and $h = 0.0125R$ were investigated for different deflection angles of the flap for configurations using blowing upstream of the flap only. The momentum coefficient was set to the minimum value which is required to keep the flow attached to the flap for each configuration. Thus for each slot height the configuration of maximum efficiency was investigated.

The slot height was varied for flap deflections of $\eta = 50°$ and $\eta = 65°$ at $Ma = 0.15$ and $\eta = 80°$ at $Ma = 0.125$. For $\eta = 50°$ the slot height was reduced from $h = 0.0125R$ to $h = 0.0078R$. The graphs for lift coefficient over angle of attack are shown in Figure 5. Due to the reduction of the slot height a slightly smaller maximum lift coefficient is achieved at a much lower momentum coefficient and the efficiency increased from $\frac{\Delta c_{l,max,clean}}{c_\mu} = 58$ to $\frac{\Delta c_{l,max,clean}}{c_\mu} = 72$. By a further decrease of the slot height to $h = 0.0063R$ no higher efficiency is achieved and the minimum momentum coefficient which is required to keep the flow attached to the flap is still about $c_\mu = 0.033$. Hence no further increase of efficiency is expected for slot heights smaller than $h = 0.0078R$. Similar results were observed for $\eta = 65°$. The reduction of the slot height from $h = 0.0125R$ to $h = 0.0078R$ increased the efficiency from $\frac{\Delta c_{l,max,clean}}{c_\mu} = 53$ to $\frac{\Delta c_{l,max,clean}}{c_\mu} = 63$. The slot height of $h = 0.0078R$ was also found to be an optimum for the configuration with $\eta = 80°$ at $Ma = 0.125$. The efficiency was increased from $\frac{\Delta c_{l,max,clean}}{c_\mu} = 49$ to $\frac{\Delta c_{l,max,clean}}{c_\mu} = 52$ by reducing the slot height from $h = 0.0125R$ to $h = 0.0078R$ and decreased again by a further reduction to $h = 0.0063R$.

The numerical simulations demonstrate that the investigated airfoil configurations have an optimum slot height of about $h = 0.0078R$ where a maximum efficiency is reached. For the best performance at each flap deflection a minimum momentum coefficient is needed to prevent flow separation at the trailing edge. Thus for a given maximum lift coefficient a minimum momentum coefficient at an appropriate flap deflection angle is needed for achieving highest efficiency. The needed momentum coefficients for
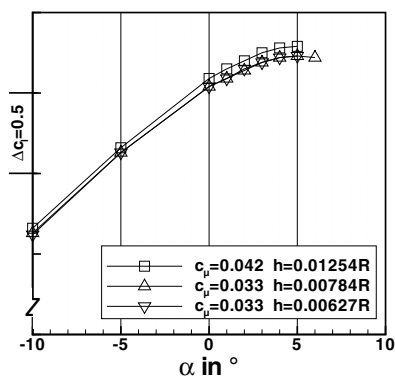
Fig. 5. Lift coefficient over angle of attack for different slot heights; $Ma = 0.15$; $Re = 21 \cdot 10^6$; $\eta = 50°$
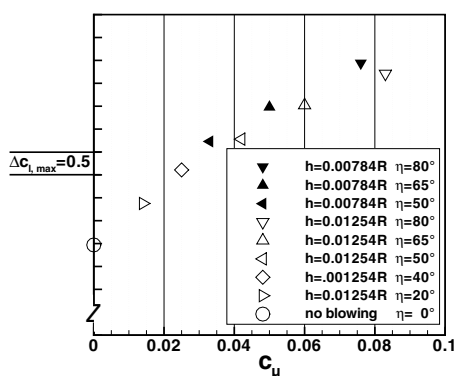
Fig. 6. Minimum momentum coefficients for specific lift coefficients for different configurations

given maximum lift coefficients are plotted in Figure 6 for different configurations. It is seen that the choice of slot height has a significant effect on the needed amount of blowing.

6   Conclusion

Steady-state Reynolds-averaged Navier-Stokes calculations for a two-dimensional airfoil using circulation control have been carried out to increase the efficiency of the circulation control system. Varied slot heights at different flap deflection angles and Mach numbers as well as leading edge blowing have been investigated to optimize the high lift performance of the airfoil.

The numerical simulations for an airfoil using a second slot at the leading edge demonstrate that additional blowing prevents the occurrence of a thin separation bubble near the leading edge. For a configuration at $Ma = 0.125$ with deflection angles of about $\eta = 80°$ it is presumed that additional blowing at the leading edge is necessary to achieve maximum lift coefficients higher than those achieved with $c_\mu = 0.083$ at higher efficiency. But the acceleration of the air at the leading edge at somewhat higher Mach numbers of about $Ma = 0.15$ leads to transonic flow at the leading edge which makes leading edge blowing rather inefficient.

The numerical simulations showed that the variation of the slot height is useful to increase the efficiency of the circulation control airfoil. A slot height of about $h = 0.0078R$ was found to be an optimum where maximum efficiency is achieved.

Acknowledgements

References

[1] Englar, R.J., Huson, G.G.: Development of Advanced Circulation Control Wing High-Lift Airfoils. AIAA Journal of Aircraft 21(7), 476–483 (1984)

[2] Englar, R.J., Smith, M.J., Kelley, S.M., Rover, R.C.: Application of Circulation Control to Advanced Subsonic Transport Aircraft, Part 1 & 2. AIAA Journal of Aircraft 31(5), 1160–1177 (1994)

[3] Englar, R.J., Williams, R.M.: Design of Circulation Controlled Stern Plane for Submarine Applications. David Tayler Naval Ship R&D Center Report NSRDC/AL-200 (AD901-198) (March 1971)

[4] Englar, R.J.: Overview of Circulation Control Pneumatic Aerodynamics: Blown Force and Moment Augmentation and Modification as Applied Primarily to Fixed-Wing Aircraft. In: Applications of Circulation Control Technology, Progress in Astronautics and Aeronautics, AIAA, vol. 214, pp. 23–68 (2006)

[5] Gerhold, T.: Overview of the hybrid RANS code TAU. In: Notes on Numerical Fluid Mechanics and Multidisciplinary Design. MEGAFLOW - Numerical Flow Simulation for Aircraft Design, vol. 89, pp. 81–92 (2005)

[6] Gersten, K., Löhr, R.: Untersuchungen über die Auftriebserhöhung eines Tragflügels bei gleichzeitigem Ausblasen an der Hinterkantenklappe und an der Profilnase. Institutsbericht 62/34, Institut für Strömungsmechanik der Technischen Universität Braunschweig (1962)

[7] Löhr, R., Thomas, F.: Die Auftriebserhöhung eines Rechteckflügels mit Ausblasen an der Profilnase und an der Hinterkantenklappe. Institutsbericht 61/18, Intstitut für Strömungsmechanik der Technischen Universität Braunschweig (1961)

[8] Pfingsten, K.-C., Jensch, C., Körber, K.W., Radespiel, R.: Numerical Simulation of the Flow around Circulation Control Airfoils. In: CEAS-2007-377, First CEAS European Air and Space Conference, Berlin, September 10-13 (2007)

[9] Pfingsten, K.-C., Radespiel, R., Kamruzzaman, M.: Use of Upper Surface Blowing and Circulation Control for Gapless High-Lift Configurations. In: CEAS/KATnet Conference on Key Aerodynamic Technologies, Bremen, June 20-22 (2005)

[10] Pfingsten, K.-C., Radespiel, R.: Numerical Simulation of a Wing with a Gapless High-Lift System Using Circulation Control. In: Notes on Numerical Fluid Mechanics and Multidisciplinary Design, C. Tropea, vol. 96, pp. 71–79. Springer, Berlin (2007)

[11] Pott-Pollenske, M., Alvarez-Gonzalez, J., Dobrynski, W.: Effect of Slat Gap on Farfield Radiated Noise and Correlation with Local Flow Characteristics. In: 9th AIAA/CEAS Aeroacoustics Conference, AIAA 2003-3228, Hilton Head, South Carolina / USA, May 12-14 (2003)

[12] Shur, M.L., Strelets, M.K., Travin, A.K., Spalart, P.R.: Turbulence Modeling in Rotating and Curved Channels: Assessing the Spalart-Shur Correction. AIAA Journal 38(5), 784–792 (2000)

[13] Spalart, P.R., Allmaras, S.R.: A One-Equation Turbulence Model for Aerodynamic Flows. AIAA paper 92-0439 (1992)

Comparison of the Capability of Active and Passive Methods of Boundary Layer Control on a Low Pressure Turbine Cascade

Tom Ludewig[1], Reinhard Niehuis[1], and Matthias Franke[2]

[1] University of the German Armed Forces Munich, Institute for Jet Propulsion,
Werner-Heisenberg-Weg 39, D-85577 Neubiberg, Germany
tom.ludewig@unibw.de
http://www.unibw.de/isa/
[2] MTU Aero Engines GmbH, Dachauer Str. 665,
D-80995 Munich, Germany

Summary

This paper contains results of measurements conducted at the High-Speed Cascade Wind Tunnel of the University of the German Armed Forced in Munich, Germany, on a low pressure turbine cascade provided with several techniques of boundary layer control. Two types of passive turbulators consisting of a roughened surface and a backward facing step are compared with an active blowing on the profile suction side concerning their influences on the profile pressure distribution and the two dimensional losses in the midspan area. Data on the cascade performance are presented for steady and periodically unsteady inflow at various Reynolds numbers with a special focus on the low Reynolds number band.

1 Introduction

The development of jet engines for aircraft propulsion has recently faced a change from pure augmentation of power and thrust to a main focus on economic efficiency and environmental friendliness. In particular the increasing fuel prices are forcing the manufacturers to think about weight reducing measures. The low pressure turbine (LPT) plays a decisive role concerning this task as it provides around one third of the overall mass of a modern engine, [15]. Ways to decrease the weight of a LPT are to diminish the stage count or the number of airfoils a stage consists of. However, if the overall performance of the turbine should be kept constant this inevitably leads to higher aerodynamical stage loading and higher loading of each profile respectively. In general this development is accompanied by increasing profile losses due to thicker boundary layers caused by a stronger deceleration in the rear part of the suction side and enlarged separation zones, [14]. Within the framework of the German national research program "LuFo III - Next Generation Turbine", which is funded by the German Federal Ministry

of Economics and Technology, several techniques to diminish the number of parts and therefore the component weight of LPTs without suffering extensive loss exaltations are investigated. The objective of this survey is to gain an assessment of the relative effectiveness of several tested boundary layer control methods in reducing profile losses of a high-lift low pressure turbine cascade.

Considering the ambient conditions within a turbomachine the rotor-stator-interaction has also to be taken into account as former investigations have shown that wakes from upstream stages have a significant influence on the transition process, [2], [7] and [11]. The stabilizing effect on the boundary layer introduced by the incoming wakes can be used to increase the aerodynamic profile loading especially for those components which are predominantly working at low Reynolds numbers, [6]. The combined impacts of unsteady inflow conditions and boundary layer control mechanisms on the near-wall flow have to be accounted for in the design of these control methods as their capability strongly depends on the transitional status of the boundary layer.

Although a considerable number of investigations on several forms of active and passive boundary layer control methods like transition supporting elements, [12], surface roughness, [10] and [14], vortex generators, [3], or steady blowing, [8] have been conducted on flat plates as well as on turbine profiles, there is less evidence comparing the capabilities of active and passive control mechanisms. For that reason this paper presents experimental data from one active and two types of passive control methods added on the same low pressure turbine profile respectively.

2   Profile Design

The profile, named T161, which was investigated for the purpose of evaluating different boundary layer control methods was designed by MTU Aero Engines GmbH, Munich, as a high-lift-development based on a modern low pressure turbine profile called T160, [4]. To decrease the number of blades the profile lift of T161 has been increased by about 25% compared to the baseline airfoil while leaving the velocity triangles constant, [5]. This leads to a Zweifel coefficient of about 1.2. The acceleration ratio of 1.6 is kept relatively low due to divergent side walls. A cross section of the cascade T161 including the main dimensions and parameters is to be found in Fig. 1. As a consequence of its rear loading design a strong deceleration zone builds up in the rear suction side of this profile. Thus, an extensive laminar separation bubble develops at design inflow conditions and low Reynolds number environments leaving a high achievement potential for boundary layer control measures.

2.1   Passive Turbulators

The first approach to gain a positive effect on the suction side separation is the use of a predefined roughness similar to surface structures resulting from rough machining. Therefore a cartridge with spanwise milled grooves of $0.66‰$ depth (with respect to the axial chord, see Fig. 1) on its surface was built reaching from the acceleration zone on the profile's suction side to the baseline separation point at 78% axial chord.
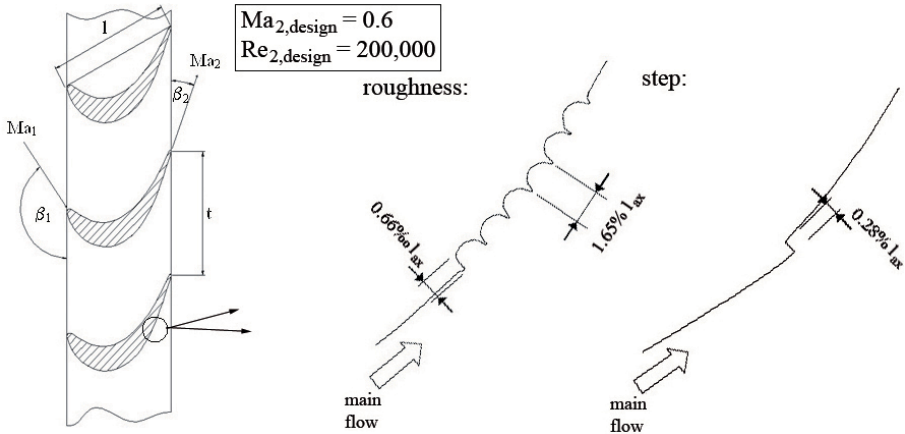
Fig. 1. Cross section of cascade T161 and passive turbulators (not to scale)

Alternatively a second cartridge with a backward facing step was applied. This structure was obtained by adding material to the original contour in a way, that a perpendicular step of 0.28% relative height evolves at 65% axial chord. Upstream of this contour interruption the new profile outline tangentially aligns with the old one. The intention of both passive measures is to generate distortions in the laminar boundary layer to push the transition process on the suction side in order to achieve a stabilization against widespread laminar separation areas. This is either achieved by numerous small bumps (roughness) or a single tough disruption (step).

2.2   Suction Surface Blowing

Avoiding some of the disadvantages of passive control methods like the lack of adjustment possibilities and the missing option to deactivate the system when it is not needed or even disturbing, an active boundary layer control mechanism was investigated as well. For this purpose the airfoil T161 was equipped with two arrays of cylindrical blowing holes at 63% and 69% axial chord respectively. The axes of both hole arrays form an angle of 45° with the local surface tangent without any lateral components. The relative bore diameter is about 2% of the axial chord and the pitch to diameter ratio is 10. Each row is independently supplied with air from an external source through a plenum. The actual blowing ratio is acquired from the measurement of the blowing mass flow and static pressure and temperature in the plenum. It is defined as:

$$B = \frac{(w \cdot \rho)_{blowing}}{(w \cdot \rho)_{mainflow}}. \tag{1}$$

This control method intents to reenergize the laminar boundary layer in order to delay or even inhibit suction side flow separation.

3 Experimental Setup

3.1 High-Speed Cascade Wind Tunnel

The investigations presented in this paper have been performed in the High-Speed Cascade Wind Tunnel of the University of the Federal Armed Forces in Munich which is shown in Fig. 2. The whole open-loop wind tunnel is contained in a cylindrical pressure tank, except for the driving section. Varying the static pressure in the tank, the axial compressor speed, the flow temperature and and the bypass massflow an independent adjustment of Mach and Reynolds number is possible within certain limits, [13]. The turbulence level of the cascade inflow is defined by a passive turbulence grid embedded in the wind tunnel nozzle. For the analyzed measurements it had an order of magnitude of 4%.

3.2 Wake Generator

The periodical rotor-stator-interactions of turbomachines have been simulated by a wake generator using cylindrical bars of 2 mm diameter with a pitch of 80 mm to create a flow characteristic similar to the one downstream of a rotating turbomachine stage, [9]. In the presented experiments these bars had a moving speed of 40 m/s thus resulting in a Strouhal number of about 0.27 referring to design flow conditions.

An unavoidable detriment of the employed wake generator are the gaps needed in the upper and lower wind tunnel wall to pass through the bars. Thus, a massflow defect occurs leading to a variation of the aerodynamic inflow angle. This deflection had to be compensated by accordingly adjusting the geometric inflow angle.

3.3 Measurement Techniques

For the purpose of gaining fundamental experimental data pneumatic measurement techniques were used exclusively. The flow around the airfoils is analyzed by the deployment of numerous static pressure taps in the midspan region of the blades. Furthermore a five-hole-probe has been installed to gather the profile wake along one pitch in
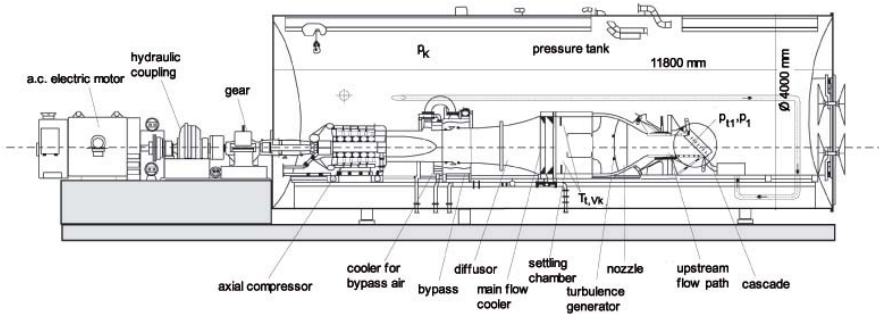
Fig. 2. High-Speed Cascade Wind Tunnel of the University of the Federal Armed Forces Munich

a plane 40% axial chord downstream of the cascade at midspan. The interpretation of the wake traverses follows the assumption of the conversion of the inhomogeneous flow into a corresponding homogeneous one, [1]. All pressure data have been acquired by a Pressure Systems RK98 pressure transducing system.

4   Results

Airfoil pressure distributions and wakes have been gathered at a medium Mach number within a wide range of Reynolds numbers from 50,000 to 400,000. As representative cases the design flow conditions as well as an example of low Reynolds number levels are analyzed for steady and periodically unsteady inflow.

4.1   Steady Inflow

The two most significant parameters for the performance of the flow around an airfoil are the profile pressure coefficient c_p considering the pressure distribution on the blade and the total pressure loss coefficient ζ regarding the profile wake. These two parameters are defined by the inlet and exit total pressures p_{t1} and p_{t2} and the static pressure p_K in the tunnel containment:

$$c_p = \frac{p_x - p_K}{p_{t1} - p_K} \quad \text{and} \quad \zeta = \frac{p_{t1} - p_{t2}}{p_{t1} - p_K}. \tag{2}$$

For the design exit Reynolds number of 200,000 the profile pressure coefficient is shown in the left part of Fig. 3 comparing all investigated boundary layer control methods with the baseline geometry. Concidering the blowing configuration only the most effective version which uses the hole array at 69% axial chord with a blowing ratio of 1.0 is included. The baseline pressure distribution shows a significant separation bubble on the suction side marked by two lines. The backward facing step as well as the blowing configuration achieve a considerable reduction of this phenomenon whereas the surface roughness does not seem to have a far-reaching effect. As expected the profile pressure side is not affected at all. Reducing the Reynolds number to 50,000 (right part of Fig. 3) the differences get even more obvious. Baseline and the roughness geometry produce a strong separation bubble with a trend to a total flow separation indicated by a lower exit pressure coefficient level. Again the blowing is the most effective control method. However it has to be kept in mind that this type of boundary layer control includes the integration of external energy in form of additional massflow.

4.2   Periodically Unsteady Inflow

The respective pressure coefficient distributions at unsteady inflow are depicted in Fig. 4. As a consequence of its insufficient results at steady inflow conditions the surface roughness has not been accounted for any more. By the influence of the periodically impinging wakes the extent of the suction side separation and therefore the capability of all boundary layer control mechanisms is perspicuously reduced. Although a slight effect is still visible, the disruption of the flow indicated by the velocity peaks at the position of
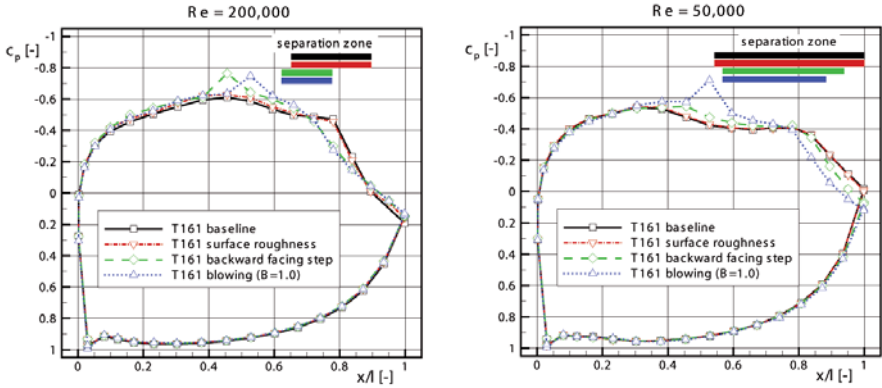
Fig. 3. Distribution of pressure coefficient at Re=200,000 (left figure part) and Re=50,000 (right figure part), steady inflow
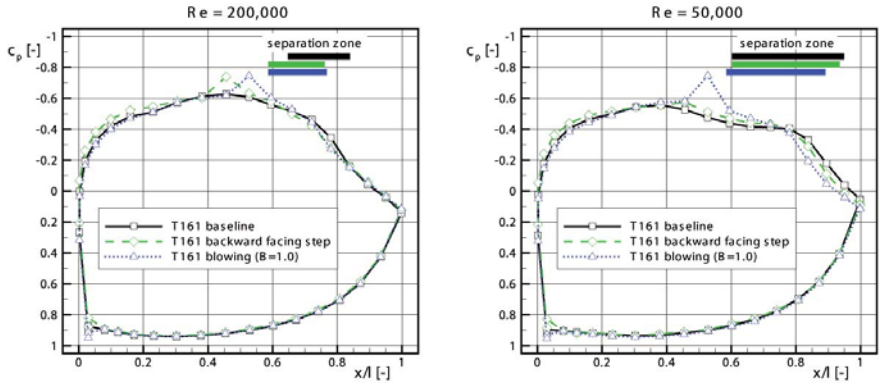
Fig. 4. Distribution of pressure coefficient at Re=200,000 (left figure part) and Re=50,000 (right figure part), unsteady inflow

each geometry variation is likely to be stronger than the impact of the bubble reduction at high Reynolds numbers (left part of Fig. 4). Regarding the lower Reynolds number (right part of Fig. 4) a certain degree of capability of the control methods is regained as the bubble size increases despite the positive effects of the wakes. The comparison between the boundary layer control mechanisms again reveals the blowing as the most capable one.

A validation for the observed results is given regarding the integral total pressure losses plotted against the Reynolds number (see Fig. 5) relating to the value of T161 baseline at design conditions. At steady inflow (left part) this baseline characteristic shows a steep rise of loss for a decreasing Reynolds parameter offering potential for improvement. Although all investigated control methods are able to diminish the losses,
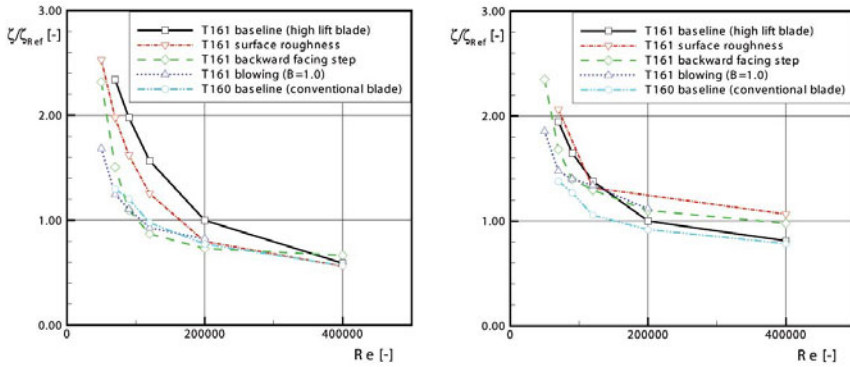
Fig. 5. Relative total pressure losses at steady inflow (left figure part) and unsteady inflow (right figure part)

only blowing and the backward facing step reach the level of the original conventional designed profile T160. Taking the unsteady inflow into account (right part) the loss reduction of all boundary layer control measures is considerably limited or even negated. Only in the Reynolds number band of $Re \leq 120,000$ a significant loss diminishment is achieved by the backward facing step and especially the blowing configuration. However, the loss level of the original profile T160 is obtained by none of them. The development at higher Reynolds numbers reveals an advantage for adjustable and active control methods as to be disengageable when not needed or even disturbing the flow.

5   Conclusions

Two passive and one active form of boundary layer control methods have been investigated on a highly loaded low pressure turbine profile. Blowing and backward facing step achieved significant reductions of loss and separation bubble size whereas the effect of the surface roughness did not meet the expectations. Although the impact of unsteady inflow diminished the effectiveness of the control methods especially the blowing configuration could supply useful results at low Reynolds numbers. The disturbing effects at higher Reynolds parameters revealed the benefits of adjustable and active control methods in comparison to fixed geometries.

Acknowledgements

References

[1] Amecke, J.: Auswertung von Nachlaufmessungen an ebenen Schaufelgittern. Bericht 67 A 49, AVA Göttingen (1967)

[2] Brunner, S., Fottner, L.: Untersuchungen zum Einfluss der Rotor-Stator Interaktion auf die saugseitige Transition eines hochbelasteten ungekühlten Niederdruck-Turbinengitters. DGLR-JT-99-078, UniBwM (1999)

[3] Canepa, E., Lengani, D., Satta, F., Spano, E., Ubaldi, M., Zunino, P.: Boundary Layer Separation Control on a Flat Plate with Adverse Pressure Gradients Using Vortex Generators. ASME Paper No. GT2006-90809 (2006)

[4] Gier, J., Hübner, N.: Design and Analysis of a High Stage Loading Five-Stage LP Turbine Rig Employing Improved Transition Modeling. ASME Paper No. GT2005-68971 (2005)

[5] Gier, J., Franke, M., Hübner, N., Schröder, T.: Designing LP Turbines for Optimized Airfoil Lift. ASME Paper No. GT2008-51101 (2008)

[6] Hourmouziadis, J.: Aerodynamic Design of Low Pressure Turbines. AGARD Lecture Series 167, 8.1–8.40 (1989)

[7] Lee, H., Kang, S.-H.: Flow Characteristics of Transitional Boundary Layers on an Airfoil in Wakes. Journal of Fluids Engineering 122, 522–532 (2000)

[8] McAuliffe, B.R., Sjolander, S.A.: Active Flow Control Using Steady Blowing for a Low-Pressure Turbine Cascade. ASME Paper No. GT2004-53646 (2004)

[9] Pfeil, H., Herbst, R., Schröder, T.: Investigations of the Laminar-Turbulent Transition of Boundary Layers Disturbed by Wakes. Journal of Engineering for Power 105, 130–137 (1983)

[10] Roberts, S.K., Yaras, M.I.: Boundary-Layer Transition Affected by Surface Roughness and Free-Stream Turbulence. Journal of Fluids Engineering 127, 449–457 (2005)

[11] Schobeiri, M.T., Öztürk, B., Ashpis, D.E.: On the Physics of Flow Separation Along a Low Pressure Turbine Blade Under Unsteady Flow Conditions. Journal of Fluids Engineering 127, 503–513 (2005)

[12] Sieverding, C.H., Bagnera, C., Boege, A.C., Cordero Antòn, J.A., Luère, V.: Investigation of the Effectiveness of Various Types of Boundary Layer Transition Elements of Low Reynolds Number Turbine Bladings. ASME Paper No. GT2004-54103 (2004)

[13] Sturm, W., Fottner, L.: The High-Speed Cascade Wind-Tunnel of the German Armed Forces University Munich. Paper presented at the 8th Symposium for Measurement Techniques in Transonic and Supersonic flows in Cascades and Turbomachinery, Genoa, Italy (1995)

[14] Vera, M., Zhang, X.F., Hodson, H.: Separation and Transition Control on an Aft-Loaded Ultra-High-Lift LP Turbine Blade at low Reynolds Numbers: High-Speed Validation. ASME Paper No. GT2005-68893 (2005)

[15] Zhang, X.F., Vera, M., Hodson, H., Harvey, N.: Separation and Transition Control on an Aft-Loaded Ultra-High-Lift LP Turbine Blade at low Reynolds Numbers: Low-Speed Investigation. ASME Paper No. GT2005-68892 (2005)

Active Secondary Flow Control on a Highly Loaded Compressor Cascade by Periodically Pulsating Jets

M. Hecklau[1], V. Zander[1], W. Nitsche[1], A. Huppertz[2], and M. Swoboda[2]

[1] Technische Universität Berlin, Institut für Luft- und Raumfahrt
Marchstraße 12, 10587 Berlin, Germany
martin.hecklau@ilr.tu-berlin.de
[2] Rolls-Royce Deutschland Ltd. & Co. KG
Eschenweg 11, 15827 Dahlewitz, Germany

Summary

The paper describes the impact of active secondary flow control by means of steady and pulsed blowing in a highly loaded compressor cascade. Due to the high loading of the blades, a fully three-dimensional flow field develops. Experimental investigations are undertaken in order to increase the turning by reducing the secondary flow structures in the passage flow field. Results out of oil-flow visualization, profile pressure measurements and stereoscopic Particle Image Velocimetry (PIV) are presented. The corner vortex is moved to the sidewall, resulting in a reduction of the blockage of the passage flow field and an improved turning.

1 Introduction

The axial compressor is one of the main components of a modern aircraft engine. One way to decrease manufacturing and operational costs of axial turbomachinery is the reduction of weight and size of the compressor. For axial compressors this can be achieved by reducing the number of stages. By reaching the same overall pressure ratio of the compressor the pressure ratio has to be increased for the single compressor stage [1]. This leads to very high aerodynamic loaded compressor blades with the risk of stalling and is consequently caused by unstable compressor operation. One way to delay or suppress stalling and boundary layer separation is the use of active flow control (AFC) methods. In external aerodynamics it has been well demonstrated by Wygnanski et al. and Petz & Nitsche [2, 3]. An outline of possible flow control opportunities in turbomachinery is given by Lord et al. [4]. Experimental investigations of an active method for controlling strong secondary flow structures are presented in this work. The measurements were performed at a stator compressor cascade with aerodynamic highly loaded blades. Nerger et al. [5] already analyzed the strong secondary flow structures in a similar test case. He showed the cascade characteristics and described the three-dimensional flow field on the suction surface and the endwalls. The resulting regions of three-dimensional separation contribute greatly to a passage blockage and
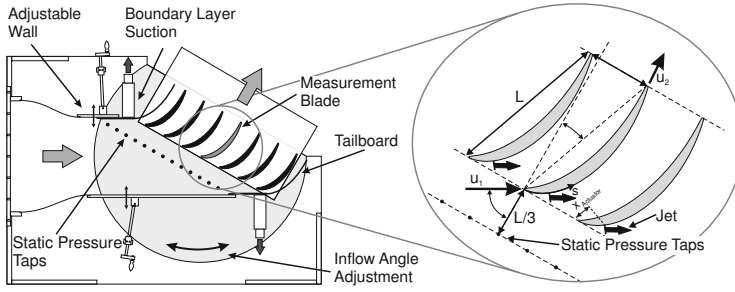
Fig. 1. Cascade Test Rig

limited static pressure rise [6]. Steady and pulsed jets blowing out of the sidewalls of the cascade were used for suppressing the influence of these structures on the passage flow field.

2   Experimental Setup

2.1   Cascade Test Rig

The experimental investigation were performed at a stator compressor cascade in a low-speed cascade test rig. The cascade consisted of seven blades and is shown in Figure 1. A periodical inlet flow is achieved by two additional tailboards and boundary layer suction at the end of the top and bottom endwalls. At each sidewall static pressure tabs are installed for monitoring the inlet flow uniformity. Table 1 summarizes the cascade geometry used in the present study. The cascade test rig is operated in an open wind tunnel. The design inlet flow speed of $u_1 = 34 \frac{m}{s}$ is used for this investigation. Based on the blade chord length the tests were performed at a Reynolds number of $Re_L = 8.4 \cdot 10^5$.

Table 1. Stator blade geometry data

$L = 375\,\text{mm}$	chord length
$S = 420\,\text{mm}$	total length of suction side
$\tau = 150\,\text{mm}$	blade pitch
$h = 300\,\text{mm}$	blade height
$\beta_1 = 60°$	inflow angle
$\gamma = 20°$	stagger angle

Table 2. Actuator parameter

$AR = 50$	slot aspect ratio
$\varphi = 15°$	installed injection angle
$x_{\text{Actuator}}/L = 10.3\%$	slot position at relativ chord length
$u'_j = 37.7 \frac{m}{s}$ (F$^+$=0.28)	RMS value of the
$u'_j = 35.7 \frac{m}{s}$ (F$^+$=1.1)	jet velocity
$u_j = 52.8 \frac{m}{s}$ (F$^+$=0)	mean jet velocity for steady blowing

2.2   Measurement Techniques

The profile pressure distribution measurement is performed with an instrumented blade. It is equipped with fast responding miniature pressure sensors directly below the blade surface. 44 pressure taps are used along the profile, 27 taps placed on the suction side and 17 on the pressure side of the blade. The blade is traversable along the blade height for pressure measurements at different spanwise positions. With a sufficient step size a two-dimensional pressure distribution for the pressure and suction surface can be reconstructed out of time averaged pressure data.

Time resolved stereoscopic PIV was applied in planes normal to the main flow velocity on the suction side of the stator blade. The measurements were performed with a *Quantronix Darwin-Duo* Laser at 527 nm and two *Photron APX-RS* high-speed cameras with a frame rate of 3000 Hz at a resolution of 1024 x 1024 px^2. The resulting time resolution of the PIV measurement was 1500 Hz. The stereoscopic PIV setup is shown in Figure 2. The light sheet is coupled into the passage from the backside of the cascade. The cameras are located on the front side of the cascade and recording light scattered by DEHS droplets as tracer particles in the forward direction. Different chord locations were selected for recording the flow field in a cross plane. *VidPIV* (Intelligent Laser Applications, Germany) was used for evaluation of the stereoscopic PIV measurement. At first the camera images were dewarped with the perspective mapping parameters, corrected by a disparity map. A adaptive crosscorrelation algorithm was used with interrogation window shifting and deforming. Evaluation started with large sized interrogation windows and was reduced to a final size of 16 x 16 px^2 with 50% overlap, resulting in a spatial resolution of 0.88 mm ($M = 9.08 \frac{px}{mm}$). Global and local filters were used for each evaluation step (rate of outliers $< 2\%$) and the filtered vectors were interpolated. The final step is the stereoscopic reconstruction of the vector fields of both cameras to a 3C-velocity field (field of view: 96 mm x 60 mm), using the Tsai parameter out of the perspective mapping node.
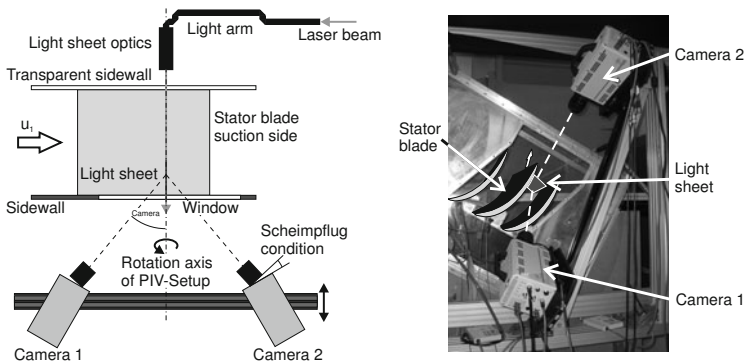
Fig. 2. Stereoscopic PIV Setup

2.3   Sidewall Actuator

Pulsed and steady blowing of compressed air out of the cascade sidewalls was used as an active method for controlling the strong secondary flow structures. The air was blown through rectangular slots, which are aligned perpendicular to the profile contour. A sketch of the used actuator system is shown in Figure 1. In numerical investigations [7] several parameters for steady blowing were studied, such as injection angle, injection mass flow and actuator position. In the experiment the injection angle is $\varphi=15°$ in main flow direction to the sidewall. Table 2 shows the summarized actuator parameters. For symmetrical flow condition while actuating, all passages of the cascade are equipped with actuators on both sidewalls. Furthermore the flow rate of each actuator is monitored and is adjustable. Fast switching valves are used for pulsing the compressed air by variation of the frequency up to 300 Hz.

3   Results

3.1   Base Flow

The base flow is observed for analyzing the flow structures without active flow control. In Figure 3 a) (solid line) the distribution of the pressure coefficient for the suction and pressure side at midspan is shown. The suction peak is located at 10% of the chord and a minor leading edge separation bubble can be observed on the pressure side. As typical for controlled diffused airfoils the suction peak is followed by a separation bubble with laminar-turbulent transition. In the pressure distribution it is indicated by a pressure plateau and a strong positiv pressure gradient. The pressure rise is decreasing in the rear part of the suction side, until it stagnates between 80% chord length and the tailing edge, due to boundary layer separation. Figure 4 (left-hand side) shows a combination of oil-flow visualization and contour lines of the pressure fluctuation. This gives a more detailed view of the three-dimensional separation on the suction surface. The laminar separation bubble width is about 80% of the blade height. Close to the endwalls it
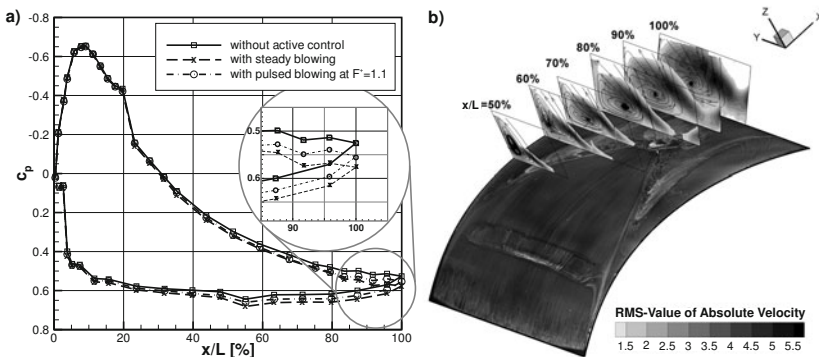
Fig. 3. a) Pressure distribution at midspan for base flow and actuated flow. b) Oil flow visualization with cross planes of the corner vortex.
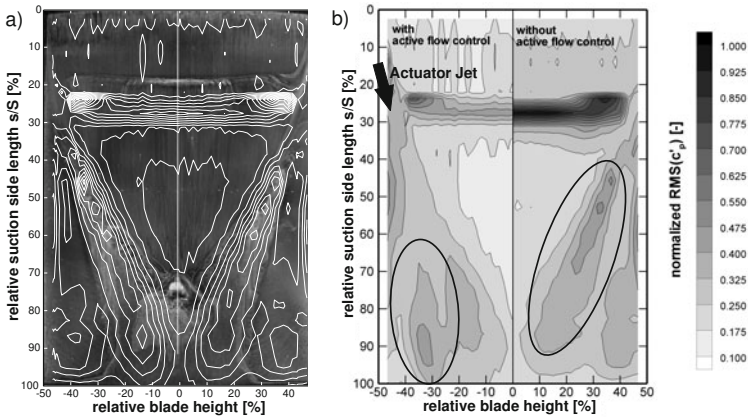
Fig. 4. a) Oil flow visualization and RMS value of the pressure distribution. b) The influence of AFC on the pressure fluctuation, indicated by RMS values.

interacts with the cross flow induced by the secondary flow structures. The bubble is followed by high fluctuation caused by turbulent reattachment. The passage flow is narrowed down to the middle of the blade between 30% and 75% chord length by the corner vortices. The three-dimensional separation line founded by the secondary flow structures, starts at the position of the suction peak. A region of recirculation is indicated by the accumulation of oil paint and high pressure fluctuations. These high RMS values are determined by regions of high shear between the main flow and the corner vortex. Due to the high aerodynamic loading, a pressure induced flow separation accrues. In Figure 3 b) is shown the corner vortex in cross planes at different blade chord positions observed by stereoscopic PIV. The corner vortex is driven by a pitchwise pressure gradient across the passage. The contour level for each cross plane indicates the absolute velocity fluctuation. The position of peak levels is in good agreement with the above shown pressure induced fluctuations on the suction surface. It must be pointed out that the unsteady flow regions have a certain distance vertical to the blade surface, which is growing downstream.

3.2 Active Flow Control

In oder to quantify the effect of steady and pulsed blowing out of the sidewalls, profile pressure measurement and stereoscopic PIV measurements are carried out. The influence of two different excitation frequencies compared to steady blowing are studied at the design parameters of the cascade ($\beta_1 = 60°$, Re $= 8.4 \cdot 10^5$). In Table 2 the actuator parameters are summarized. Forcing frequencies of $F^+ = 0.28$ and $F^+ = 1.1$ are chosen for unsteady actuation, equation (1). The nondimensional blowing momentum coefficient c_μ has a value of $c_\mu = 0.0024$ for unsteady excitation, see equation (2) with the slot width h_{Actuator} and the RMS value of the jet velocity u'_j.

$$F^+ = \frac{f \cdot L}{u_1} \qquad (1)$$

$$c_\mu = 2 \cdot \frac{h_{\text{Actuator}}}{L} \cdot \left(\frac{u'_j}{u_1}\right)^2 \qquad (2)$$

For steady blowing the jet velocity u_j is used instead of the RMS value and results in a momentum coefficient of $c_{\mu,\text{stat}} = 0.0051$. Figure 3 a) shows the pressure distribution at midspan for the actuated passage flow. It can be observed that the laminar separation bubble and the pressure distribution in the front part of the blade is unaffected by AFC. The static pressure is increased at the tailing edge. For steady blowing it has the biggest gain. The static pressure for pulsed blowing at $F^+ = 0.28$ is close to it. In consideration of the momentum coefficient this is bought by two times more injected mass for steady blowing. Due to the excitation of air out of the sidewalls the cascade is enabled to achieve an enhanced pressure rise. Figure 4 b) provides a further look at the three-dimensional flow structures. A comparison is shown of the actuated flow with steady blowing and the base flow. The normalized RMS value is used for highlighting the influence of AFC on the pressure fluctuation. The position of the jet is labeled with an arrowhead at about 15% of the suction side length. In general, the pressure fluctuations are reduced by the sidewall actuators. The footprint of the corner vortex is shaped as a cudgel with enlarged RMS values. The cudgel is blurred and the corner vortex is suppressed by the actuation. The laminar separation bubble is unaffected by the blowing. This leads to the assumption that the corner vortices are directly reduced by the actuators.

Stereoscopic PIV measurements of the secondary flow structures are presented for a detailed view on the spatial movement of the actuated corner vortices. In Figure 5 to 7 are shown cross planes of the corner vortex and different excitation parameters at a chord position of x/L = 70%. In this region the corner vortex is unaffected by boundary layer separation at midspan and is well developed. Only every second velocity vector is shown for the purpose of clarity. The in-plane velocity is indicated by the vector field. The passage flow, measured as an out-of-plane component, is indicated by contour levels. Figure 5 presents the flow field of the corner vortex for base flow condition and
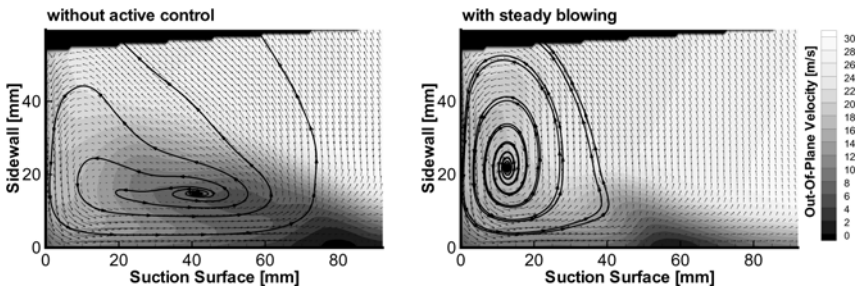
Fig. 5. Flow field of the corner vortex without and with steady blowing at x/L = 70%
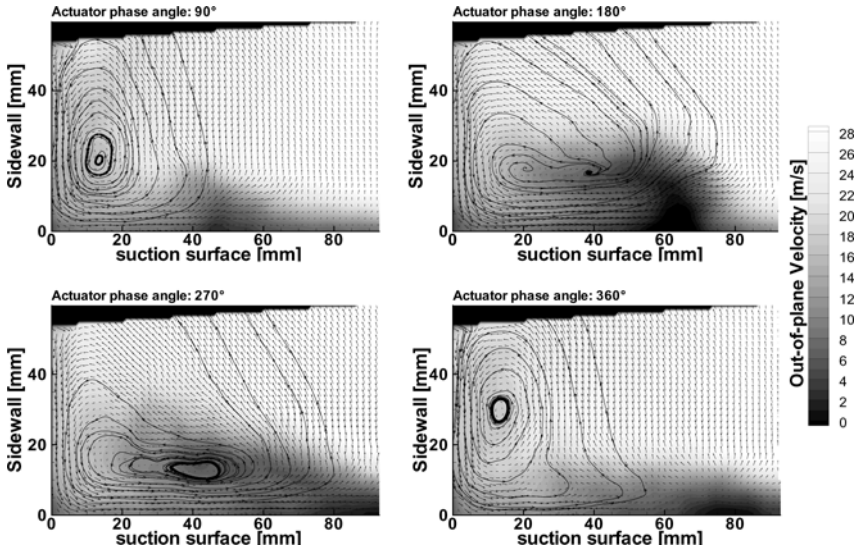
Fig. 6. Phase averaged flow field at x/L = 70% of the corner vortex with pulsed blowing at $F^+ = 0.28$
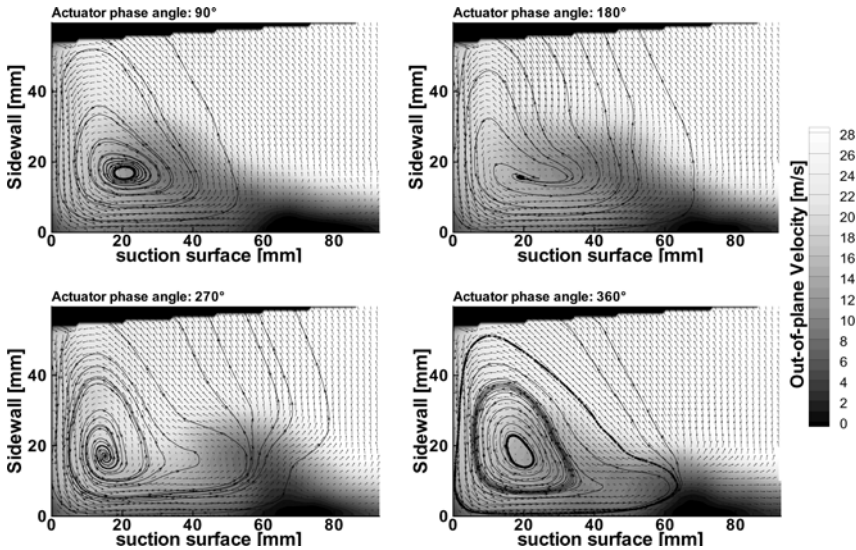
Fig. 7. Phase averaged flow field at x/L = 70% of the corner vortex with pulsed blowing at $F^+ = 1.1$

with steady blowing. The velocity field is time averaged. The vortex indicated by stream lines has changed the position from h = 42 mm to 13 mm towards the sidewall. Also the

region of low wall shear stresses, indicated by small values of the out-of-plane velocity, changes the position. Due to the repositioning of the vortex, the blockage of the passage flow is reduced, which is generated by the secondary flow structures. Figure 6 and 7 are showing the flow field with periodic excitation at two different forcing frequencies. The flow field is phase averaged for four equidistant phase angles. The vortex, forced with the low frequency of $F^+ = 0.28$, is changing between the position of the actuated case and the base flow case, as shown above. While blowing, the vortex is attached to the sidewall and the passage blocking is reduced. During the period without blowing the corner vortex jumps back in the direction of the midspan. The dispersion of the vortex is enlarged which indicates a unsteady movement at this phase angles. By using a higher forcing frequency, as shown in Figure 7, the behavior is different. The position of the vortex does not change that much during the excitation cycle. The regions of small out-of-plane velocity values are stationary at the suction surface of the blade. Only the area with high velocity values of the out-of-plane velocity is deformed.

Summarized, the pulsed blowing is affecting the secondary flow structures. At low forcing frequencies this causes a very unsteady behavior of the passage flow. Using higher frequencies, the corner vortex position is more stationary. This results in almost the same reduction of the passage blockage compared with steady blowing, but requires only half of the momentum coefficient c_μ.

4   Conclusions

Steady and pulsed blowing out of the sidewalls was successfully used for suppression of secondary flow structures on a highly loaded compressor cascade. This could be shown by analyzing the passage flow field by means of oil-flow visualization, profile pressure measurements and stereoscopic PIV. The influence of the strong corner vortex on the flow field was effectively reduced by AFC. The fluctuation of the passage flow could be clearly reduced with steady blowing. Pulsed blowing caused a more unsteady flow field, which was decreasing at higher forcing frequencies. The blockage of the passage flow was reduced by the repositioning of the corner vortex towards the sidewall. This causes a decreased total pressure loss and an increased turning across the passage of the compressor cascade. Compared to steady blowing a distinct reduction of the required momentum coefficient was achieved with pulsed blowing.

Acknowledgements

References

[1] Wennerstrom, A.J.: Highly loaded axial flow compressors: History and current developments. ASME Journal of Turbomachinery 112, 567–578 (1990)

[2] Wygnanski, I.: The variables affecting the control of separation by periodic excitation. AIAA Paper 2004-2505 (2004)

[3] Petz, R., Nitsche, W.: Active separation control on the flap of a two-dimensional generic high-lift configuration. Journal of Aircraft 44, 865–874 (2007)

[4] Lord, W.K., MacMartin, D.G., Tillman, T.G.: Flow control opportunities in gas turbine engines. In: AIAA Conference Proceeding Paper AIAA 2000-2234 (2000)

[5] Nerger, D., Saathoff, H., Radespiel, R.: Experimental and numerical analysis of a highly loaded low aspect ratio compressor stator cascade. In: 7th ETC, Athen (2007)

[6] Gbadebo, S.A., Cumpsty, N.A., Hynes, T.P.: Three-dimensional separations in axial compressors. Journal of Turbomachinery 127, 331–339 (2005)

[7] Mertens, D., Thiele, F., Swoboda, M., Huppertz, A.: Transition modeling effects on the simulation of a stator cascade with active flow control. In: ASME Turbo Expo. (2008)

Simulation of Active Flow Control on the Flap of a 2D High-Lift Configuration

V. Ciobaca

DLR, Lilienthalplatz 7, 38108, Braunschweig, Germany

Summary

The numerical investigations described in the present paper deal with active flow control for a 2D, 2-element high-lift airfoil under low speed wind tunnel conditions. Here, the aim of the flow control application is the transport of fluid-momentum from the outer part of the boundary layer towards the wall to actively reduce or eliminate the large flow separation on the flap. The URANS simulations carried out in this study focus on the variation of the streamwise actuator-slot width and the actuation direction, and their potential to suppress or delay separation. Different slot-exit settings coupled with a constant frequency, duty cycle, and mass flow are discussed regarding their impact on the local flow.

1 Introduction

Flow control technologies have been studied intensively for more than 60 years also due to their potential to make a breakthrough in drag reduction. Active separation control has already been proven to perform well in particular cases for low speed wind tunnel (w/t) conditions by several academic groups. Such recent results are discussed in [1,2,5]. Most of the already existing CFD applications for active time-varying control have been carried out for code validation purposes with variation of the dynamic parameters, such as frequency, velocity ratio or duty cycle with the corresponding geometrical parameters fixed. Classical approaches for performing an evaluation of active flow control, such as first building the experimental model, followed by w/t measurements and afterwards the CFD simulation are no longer sufficient in developing the technology towards industrialization for transport aircrafts.

One of the objectives of the EU-project AVERT (Aerodynamic Validation of Emission Reduction Technologies) is to develop active flow control technologies for low speed applications through complementary numerical simulations and wind tunnel testing. The separation prevention by active devices is investigated in a collaboration of DLR, TUB (TU Berlin), and INCAS (National Institute of Aerospace Research, Romania). TUB focuses on the development and testing of the actuators for
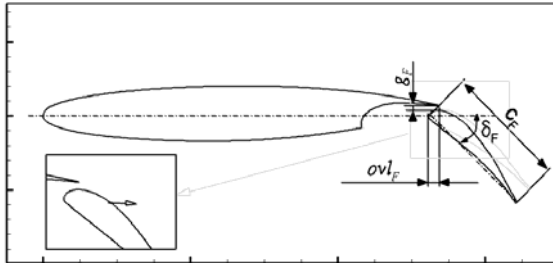
Fig. 1. F15 high-lift configuration

high-lift, while INCAS is responsible for the manufacturing of the w/t model and test campaign. DLR is in charge for the model selection, the variation of geometrical parameters for the actuation under w/t conditions, and the extrapolation to flight Reynolds numbers based on CFD results.

Here, the goal of active control is to reduce or eliminate the large flow separation on the flap, thus reducing the profile drag. The present study explores the variation of the actuation direction and slot width in order to give valuable recommendations for manufacturing the experimental model. The emphasis is laid on the comparison of flow features for different geometrical settings, while the frequency, duty cycle, and mass flow are kept constant for the pulsed blowing application.

2   Geometry and Test Case Definition

The computations were performed for the DLR F15 model using the unstructured DLR-TAU code. Figure 1 shows the F15 airfoil in 2-element configuration with the slat retracted. The reference length for the experimental model is 600 mm based on the actuation system requirements and the w/t test. All computations were carried out in 2D.

The first study started with an analysis of a reference configuration without flow control with the following flap settings: flap -deflection $\delta_F=40.1^\circ$, -gap $g_F/c=0.8\%$ and -overlap $ovl_F/c=2.3\%$. For flow settings it was decided to run for a Mach number of M=0.15, and Reynolds number Re=2.1 million based on the main chord length, representative for a low speed w/t. For this first configuration α_{max} is reached before almost no separation is present on the flap. This trend of having a small or no separation on the flap was actually desired and accomplished in previous experimental and numerical studies for maximizing the performance without flow control [5]. Thus for the study with flow control for the same configuration the flap is further deployed (increasing the flap deflection angle and the gap) to generate a large separation region on the flap. Indeed the numerical studies confirmed this trend. For this the flap was deployed up to $\delta_F=49^\circ$. Figure 2 shows the flow streamlines for the two settings of the flap ($\delta_F=40.1^\circ$ and 49°). In comparison to existing w/t experiments at DLR, the pressure distribution is in good agreement overall, Figure 3. Further on, the setting of the flap by $\delta_F=49^\circ$ was used as reference case without control for the slot-exit geometry variation.
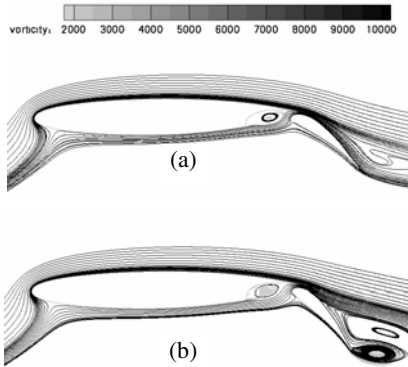
Fig. 2. Flow streamlines for $\alpha=8.5°$, M=0.15. Re=2.1e06 @ (a) $\delta_F=40.1°$ (b) $\delta_F=49°$.
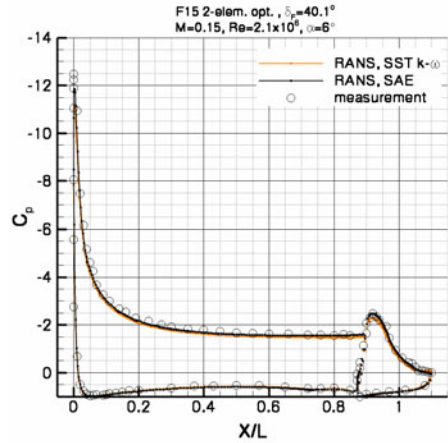
Fig. 3. Pressure coefficient distribution for $\delta_F=40.1°$.

The experimental setup is represented by a 2D model with the actuation system distributed over the complete flap's span. This actuation system consists of about 20 actuators located one next to the other. For the CFD work the actuation was represented as a single actuator, thus only a 2D domain was considered. A flow separation is typically 3D also on 2D geometries. As in 2D high lift state of the art is 2D computations for multi element configurations with moderate separation, only 2D simulations have been carried out with an adequately time request. The actuation was located on the flap suction side, at 20% c_F, in advance of the separation location. The reference flow showed that for large flap deflections the boundary layer already separates on the suction side at 30-35% c_F. The actuation position was chosen to be in the healthy boundary layer (attached flow) and to respect the manufacturing constrains (available space in the flap of the w/t model for the actuators). The two varied geometrical parameters are the width of the slot and the actuation direction. Slot widths of 0.3 and 0.6 mm were considered in the numerical studies, where smaller widths as 0.3 mm for inclined directions are not feasible to manufacture. For the blowing direction, normal ($90°$), inclined –downstream ($45°$) and -upstream ($135°$) were analyzed. The variation of the slot-exit parameters corresponded to the same mass flow, with the duty cycle DC=50%, the frequency f=100Hz (non-dimensional frequency $F^+=f*c_F/V_{inf}=0.32$) and velocity ratio 2 ($\lambda=V_{jet}/V_{inf}$), respective $\lambda=1$ for the large slot width.

3   Computational Strategy

The accuracy of the results obtained with CFD is highly depending on the density and quality of the computational grids. For the TAU reference computations hybrid grids
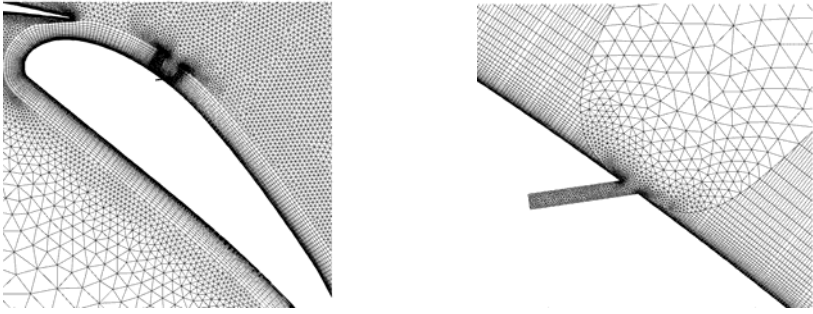
Fig. 4. Unstructured grid in the flap vicinity with a detail view for the actuation slot.

were created using the commercial grid generation software CentaurSoft. For all the evaluation further presented here the unstructured meshes consist of 126, 000 points. In Figure 4 details of the mesh are shown in the vicinity of the actuation slot. The slot is modeled in the CFD work using only triangular cells to discretize it. The prisms stacks are reduced down to zero layers on the flap surface at the junction with the actuator. The simulation of the slot followed the recommendation of Rumsey et al. [3] to include at least some portion of the orifice in the computation for time-varying flow control applications. All the actuation directions were analyzed first for constant blowing by RANS simulations. Later, restarts to URANS with the time varying jets were conducted using a dual time-step approach. For the numerical setting the actuation frequency f=100Hz guided the length of the dual time step, where Δt=2.5e-05 sec. with 500 inner iterations per time step and 400 physical time steps for each actuation cycle. The experimental actuators use a fast switching valve system which leads to a square signal for the mass flow. The boundary condition in the TAU solver allows smoothing the switch from constant blow to no blow, where 10 time steps to run in between are recommended for stability reasons. Concerning the turbulence modeling the 2-equations Menter SST k-ω version was applied. All computations are run fully turbulent.

4   Results

First numerical results show the effects of the excitation direction variation with time-varying flow control (Figure 5). The normal and upstream pulsed blowing on the flap induce for consistent dynamic settings (frequency, velocity ratio, and duty cycle) a reduction in lift coefficient as well as an increase in airfoil drag compared to the downstream blowing. For all three lift curves it is observed that maximum lift is produced at comparable angles of attack, where the airfoil stall is a leading edge-type. Nevertheless, the upstream time varying actuation on the flap induces the airfoil stall for a slightly smaller α as for the other two blowing directions. Thus it is shown that for the settings used here, actuating in the downstream direction is more promising as the other two cases. Figure 6(a) shows the lift curve for α_{jet}=45°, by pulsed and constant blowing in comparison to the reference computation (without flow control).
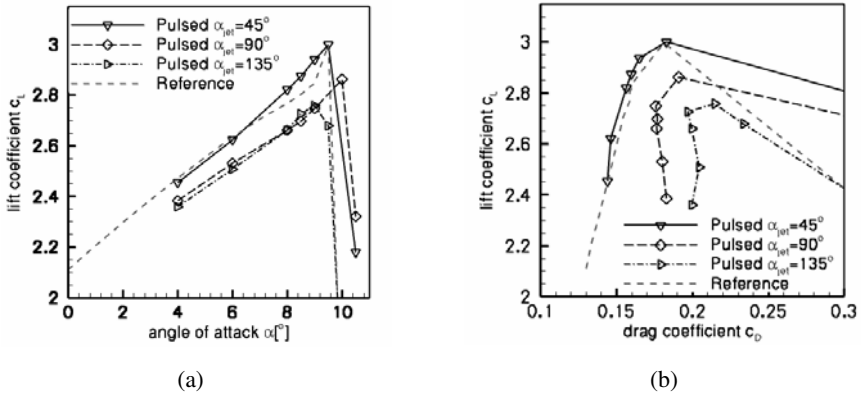
Fig. 5. (a) Lift curve and (b) drag polar for pulsed blowing with $\alpha_{jet}=135°$, $90°$, $45°$.
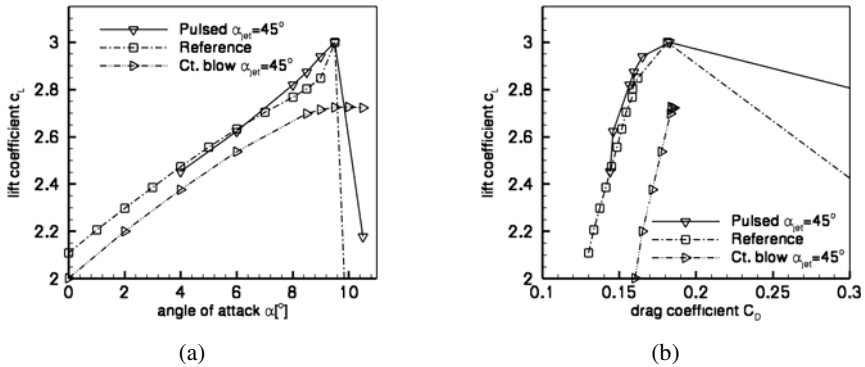
Fig. 6. (a) Lift curve and (b) drag polar for reference and pulsed blowing with $\alpha jet=45o$.

The lift curve with flow control indicates no benefit in the linear region with respect to the reference case, where as close to C_{Lmax} the lift increase is about 0.1 for an $\alpha=9°$. Untypical, for the next computed angle of attack, $\alpha=9.5°$, the flow reattaches on the flap without actuation, and so no further improvement can be realized with flow control. With the next increase of α a leading edge stall occurs on the main element. The drag polar indicates a slight benefit with flow control, Figure 6(b). Constant blowing is obviously weaker for $\alpha_{jet}=45°$ than the oscillatory jet, showing both an increase in drag as a decrease in lift, caused mainly by a larger flow separation on the flap. These results show the same tendency as for previous flat plate computations (not discussed here); an actuation in the flow direction is more promising than upwards or normal excitations.
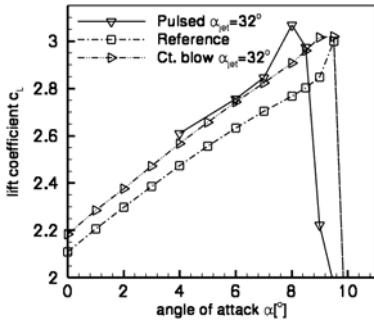
(a)
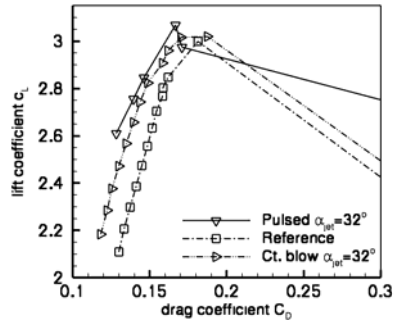
(b)

Fig. 7. (a) Lift curve and (b) drag polar for reference and pulsed blowing with $\alpha_{jet}=32^o$.

(a)

(b)
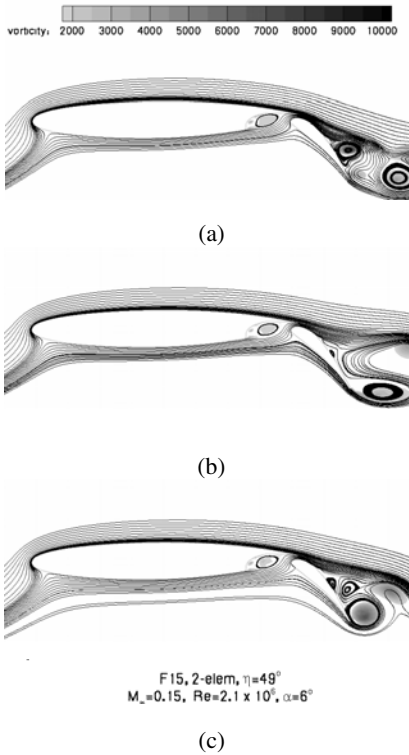
(c)
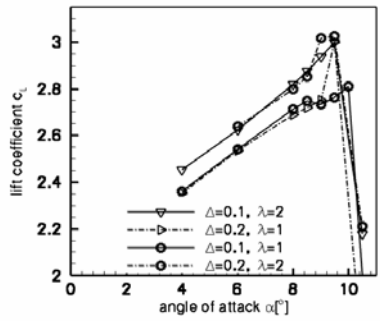
(a)
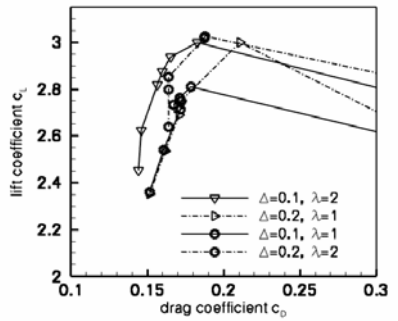
(b)

Fig. 8. Instantaneous flow streamlines and vorticity distribution with control for (a) downstream-, (b) normal-, (c) upstream-blowing.

Fig. 9. (a) Lift curve and (b) drag polar for pulsed blowing with $\alpha_{jet}=45^o$ where $\Delta=0.1$ and $\Delta=0.2$.

Furthermore it was of interest to check the effects of a blowing direction which is more tangential. Thus α_{jet} was reduced to 32°. The same flow conditions, constant and pulsed blowing, applied on the flap showed a further increase in airfoil performance. Figures 7(a) and 7(b) show that flow control results in an increase in lift in the linear region as well as for C_{Lmax} while the drag decreases over the whole envelope. Stall is still caused by leading edge separation on the main element, as for the reference flow. α_{CLmax} decreases by 1.5^o for pulsed blowing caused by an induced increase of circulation on the main wing. In the linear region the constant blowing is almost as beneficial as the time varying actuation mainly as a result of a circulation control effect and not by eliminating the separation.

The instantaneous flow streamlines and the vorticity distribution plotted in Figure 8(a) for an active flow control case (downstream blowing) show that the large flow separation on the flap is reduced by the excitation mechanism, but not eliminated. Here the vortices generated by the actuation are moving downstream on the flap, but do not necessarily follow the entire flap contour. For the other actuation direction analyzed corresponding instantaneous vorticity distributions are plotted in Figures 8(b) and 8(c). The numerical results show that the vortices generated by the pulsed actuation have the tendency to move away from the flap contour for normal and upstream excitations.

Yet, a complete grid and/or turbulence model variation for the URANS computations was not included in the study, and so numerical uncertainties are not addressed. Globally, from actuation direction variation a better performance is observed for a downstream direction, where a more tangential angle (such as 32°) shows the best enhancement in lift mainly due to circulation control, and a slightly increased angle (such as 45°) is promising for an oscillatory blowing mainly and the reduction/elimination of the flap separation.

Next the slot-exit width variation was analyzed. The computations were conducted with the same flow conditions as before with respect to the F15 model, while now the actuation direction was kept constant, $\alpha_{jet}=45^o$. All the results presented above were conducted with a slot width of 0.3 mm. This is equivalent to a ratio of $\Delta=w/\delta=0.1$, where w is the slot width and δ is the boundary layer height. For the width variation study a second value of 0.2 was chosen, leading to a width of 0.6 mm for the slot actuator.

The enlargement of actuator width induces a reduction in lift and an increase in drag in the linear left region, Figure 9, while the stall mechanism is again a leading-edge type for the main wing. Just before the flow separates on the main element, a flow reattachment on the flap is observed, leading to the same maximum lift for the width variation: $C_{Lmax}^{\Delta=0.1,\lambda=2}=C_{Lmax}^{\Delta=0.2,\lambda=1}$. For constant blowing (not illustrated here), the smaller width is also more efficient than the enlarged one, although the differences are reduced compared to the time varying actuation study. In general, from the width variation study the reduced ratio of actuator size to boundary layer height is more promising with a value of $\Delta=0.1$, which is recommended for the experimental model design.

5 Conclusions

URANS simulations concerning local pulsed excitation on a high-lift airfoil were performed focusing on the slot-exit parameters, width and actuation direction. The results show that applying flap gap oscillatory blowing in the flow direction looks more efficient than actuating against the flow or normal to the airfoil surface for a 2D configuration, while by varying the direction towards tangential, the pulsed jet reduces its benefit compared to the constant blowing. Also it was shown that for a constant mass flow a narrower actuator may be more efficient as a larger one. The computations show that an improvement can be achieved up to a threshold, using this preliminary study for the actuation definition. Beyond that further improvements are possible only by using the dynamic excitation parameters. Up to now, all blowing directions were analyzed for a single mass flow and frequency, and it is known that the variation of those two parameters is of great importance for achieving the optimum performance for a configuration.

Acknowledgment

References

[1] Crowther, W.J.: Separation Control on a Trailing Edge Flap Using Air Vortex Generators. Journal of Aircraft 43(5), 1589–1593 (2006)
[2] Petz, R., Nitsche, W.: Active Separation Control on the Flap of a Two-Dimensional Generic High-Lift Configuration. Journal of Aircraft 44(3), 865–874 (2007)
[3] Rumsey, C.L., Schaeffler, N.W., Milanovic, I.M., Zaman, K.B.M.Q.: Time-Accurate Computations of Isolated circular Synthetic Jets in Crossflow. Computers & Fluids 36(6), 1092–1105 (2007)
[4] Scholtz, P., Ortmans, J., Kähler, C. J., Radespiel, R.: Leading Edge Separation Control by Means of Pulsed Jet Actuators, AIAA-2006-2850
[5] Wild, J., Pott-Pollenske, M., Nagel, B.: An Integrated Design Approach for Low Noise Exposing High-Lift Devices, AIAA-2006-2843

Numerical Investigation of a Jet and Vortex Actuator (JaVA)

Muhammad Aqeel Rashad and Ulrich Rist

Universität Stuttgart, I.A.G., Pfaffenwaldring 21, 70550 Stuttgart, Germany
{rashad,rist}@iag.uni-stuttgart.de

Summary

In the present study an active flow control actuator is studied numerically using the CFD package Fluent®. A two-dimensional setup is chosen which corresponds to a cut through a real configuration that was studied experimentally by Lachowicz *et al.* [5] and called "Jet and Vortex Actuator" (JaVA) because of its ability to produce such completely different flow regimes when its actuation frequency and amplitude are changed. Three cases are selected for validation of the simulations. A vortex mode, a vertical-jet and a wall-jet mode. Our simulations yield the *unsteady* flow field, whereas only time-averaged data are available from literature. Thus, our simulations provide extra details of the flows through the gaps intended for a better understanding of the actuator flow. Qualitative and quantitative comparisons of the time-averaged data with the experiments are very encouraging. Especially, the different flow regimes appear for the same parameters as in the experiments.

1 Introduction

Actuator flow control can be of two kinds: passive and active. A passive or conventional flow control actuator has the disadvantage that it is designed only for a specific (flight) condition and also it produces parasitic drag at cruise condition. Active flow control actuators minimize both these disadvantages. These actuators can be used in multiple flight conditions in contrast to passive flow control devices. Furthermore, active flow control actuators produce negligible drag when the system is not actuated.

The current JaVA system evolved from an earlier flow actuator developed by Jacobson & Reynolds [2]. This actuator consists of a cantilevered beam oscillating in a cavity. The plate was placed asymmetrically within the cavity to form wide and narrow gaps when viewed from the top of the plate. A periodically emerging jet, from the narrow slot, generated longitudinal vortical disturbances when interacting with a boundary layer in a water tunnel. In the wake of a small circular cylinder placed in a laminar boundary layer the actuator system delayed transition by about 40 displacement thicknesses. Koumoutsakos [4] conducted a parametric numerical study of an actuator with no external flow. Instead of simulating the motion of a cantilevered beam, piston-type motion was simulated in order to determine the fundamental physical mechanisms
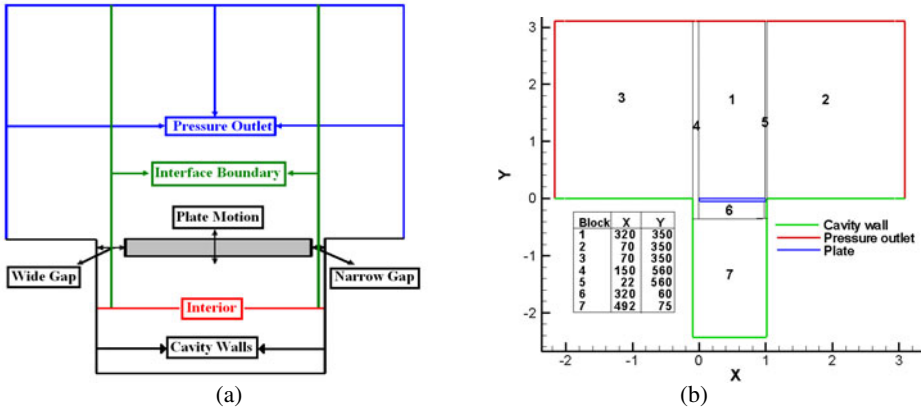
Fig. 1. Basic setup of simulation. (a) Geometry and boundary conditions, (b) Block numbering and number of grid points used in each block.

responsible for disturbance generation from the actuator; note that the motion of the JaVA is also of piston-type. For a given slot width, Koumoutsakos showed that at relatively high frequencies a periodic jet developed from the narrow slot, while at relatively low frequencies, the periodic jet developed from the wide slot. This suggested that the actuator slot flow is Stokes number dependent. However, Saddoughi *et al.* [6] conducted a series of experiments using a cantilevered-beam type actuator with the same Stokes number as Jacobson & Reynolds [2]. It was found that the flow patterns in the two experiments were qualitatively different. Thus, similar to the study of Koumoutsakos, a more basic actuator motion, the piston-type motion, is used in this study to better understand the actuator flow physics.

The active flow control actuator under consideration is from Lachowicz *et al.* [5] and consists of a cavity and a rigid plate that is placed at the top of the cavity such that it forms a narrow and a wide gap on each side of the plate, see Fig. 1. The plate is oscillated in the vertical direction with uniform (but not constant) speed along its length and width, such that the actuator plate acts like a piston pumping air out of the cavity on the downstroke and sucking air into the cavity on the upstroke. This kind of active flow control actuator produces different flow fields (free jet, wall jet, and vortex flow) depending on non-dimensional parameters like scaled amplitude S_a and Reynolds number, see Fig. 2, which are related to the frequency and amplitude of the actuation. Thus, an angled jet is produced at relatively low amplitude and frequency from the wide gap while at relatively high amplitude and low frequency a free jet is produced from the wide gap. As the frequency is increased at low amplitude a wall jet is produced from the wide gap directing towards the narrow gap. The wall jet is primarily horizontal near the narrow gap and is characterized by steady horizontal flow pumping from the wide gap towards the narrow gap end. Such actuators may be used to energize the boundary layer by accelerating the fluid tangentially near the wall surface. As the amplitude is increased from the wall jet regime and at high frequency a vortex is generated at the wide gap. The vortex regime may be used to promote mixing and suppress boundary layer separation.
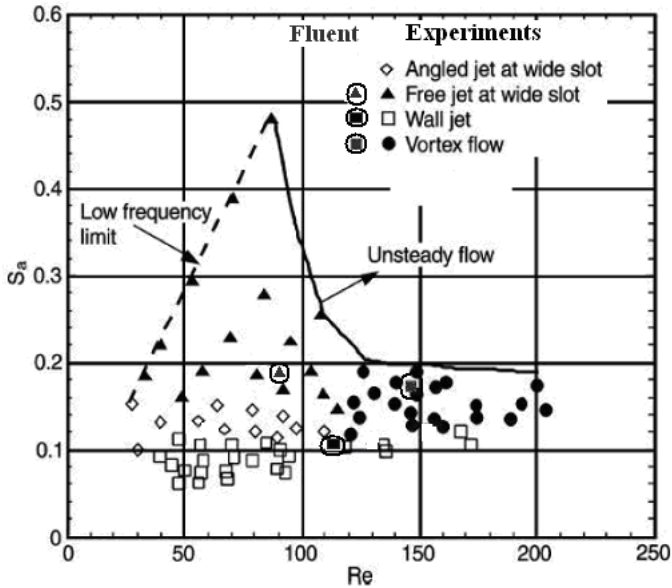
Fig. 2. Comparison with experimentally observed flow regimes [5].

In the present work, different flow fields will be computed and visualized by varying the amplitude and frequency of oscillation.

2 Grid, Boundary Conditions and Numerical Approach

For the flow calculations and visualization use of the general purpose CFD software Fluent® from Fluent Inc. seemed to be the most appropriate, because of the need for simulating rather complex geometries with moving boundaries and grids at different unsteady flow speeds [1]. This software appears to be well-suited because of its versatility to deal with dynamic meshes. We use structured deformable dynamical grids with sliding interfaces between different blocks where necessary, see Fig 1. For the present actuator geometry and boundary conditions the grid generator GAMBIT is used. Grid points are concentrated towards the block boundaries.

For the specification of problem-specific boundary conditions Fluent uses the concept of *"user-defined functions"*, i.e. the user has to specify his/her boundary conditions in a C-like syntax as a function that is bound to the executable upon execution [1]. This is very flexible and general. However, not always free of errors. In some cases it turned out that it is not sufficient to simply specify wall motions (with the idea that this will automatically drive the flow via appropriate boundary conditions). Unexpectedly, it was necessary to specify extra boundary conditions for the fluid on the moving boundaries. This adds extra flexibility, like consideration of permeable walls, for instance, but careful checks are necessary in order to verify use of appropriate boundary conditions for

a given problem. In the present application the blocks attached to the actuator plate (nos. 1 and 6 in Fig 1b) are moving together with the actuator plate. Dispensable grid points are automatically discarded at the interior and at the upper boundary when the block moves towards it and they are regenerated when the movement turns away from the boundaries. Typical grid resolutions of each block are given in the figure.

Since only two-dimensional measurements are available with Lachowicz *et al.* [5] and the flow field in the middle of the actuator is considered to be two-dimensional (if placed in still air, i.e. without a free stream flow in the plane-normal direction), we begin with two-dimensional simulations for comparison but three-dimensional simulations are performed as well.

The motion of the plate is prescribed by the following set of equations

$$\omega = 2\pi f, \qquad T = 1/f,$$
$$x(t) = a\sin(\omega t), \qquad v(t) = \dot{x}(t) = a\omega\cos(\omega t),$$

where f is the actuator-plate vibration frequency, T the oscillation period, a the actuator-plate amplitude, and v the actuator-plate velocity.

3   Results

3.1   Case 1, Vortex Mode

The first simulation is performed for a scaled frequency (Strouhal number) $Sr = fb/v_{max} = b/2\pi a = 5.47$ and a scaled amplitude $S_a = 2\pi a/b = 0.1829$, where b is the plate width. The Reynolds number is defined as $Re = v_{max}b/\nu = 2\pi fab/\nu$. In this case a big vortex is produced above the plate over the wide gap. A secondary weaker vortex is also present towards the narrow gap. In addition, we also observe a small and a large vortex inside the cavity. With many simulations it is observed that the size of the vortex is mesh dependent. So, special care is required to get a mesh-independent vortex. Fig. 3a shows contours of mean velocity magnitude averaged over the last four oscillation periods (22nd to 25th) and these are compared with Joslin *et al.* [3] and Lachowicz *et al.* [5] in subfigures b and c, respectively. The qualitative comparison of the present velocity-magnitude contours with the stream lines provided by these two references indicates a rather excellent comparison with respect to the size of the vortex relative to the width of the actuator plate.

A quantitative comparison of time-averaged velocity profiles along a vertical cut through the vortex center is shown in Fig. 3d. This comparison once again shows that the vortex size in our case is almost equal to the one observed by Lachowicz *et al.*. The quantitative agreement of the positive and negative velocity magnitude maxima agrees much better with the experimental results than the results of the numerical modelling performed by Joslin *et al.* [3].

Fig. 4 shows plots of the instantaneous velocity in the gaps for eight different phases of the oscillation. It can be seen that the flow in the wide gap is very complex. There is flow separation and reversed flow. The reason for this complex flow behaviour is that the wide gap width is very large compared to the plate thickness. In contrast, in the narrow gap in Fig. 4b the flow is more like a mixed *Couette-Poiseuille* flow, simply because

(a)

(b)

(c)

(d)
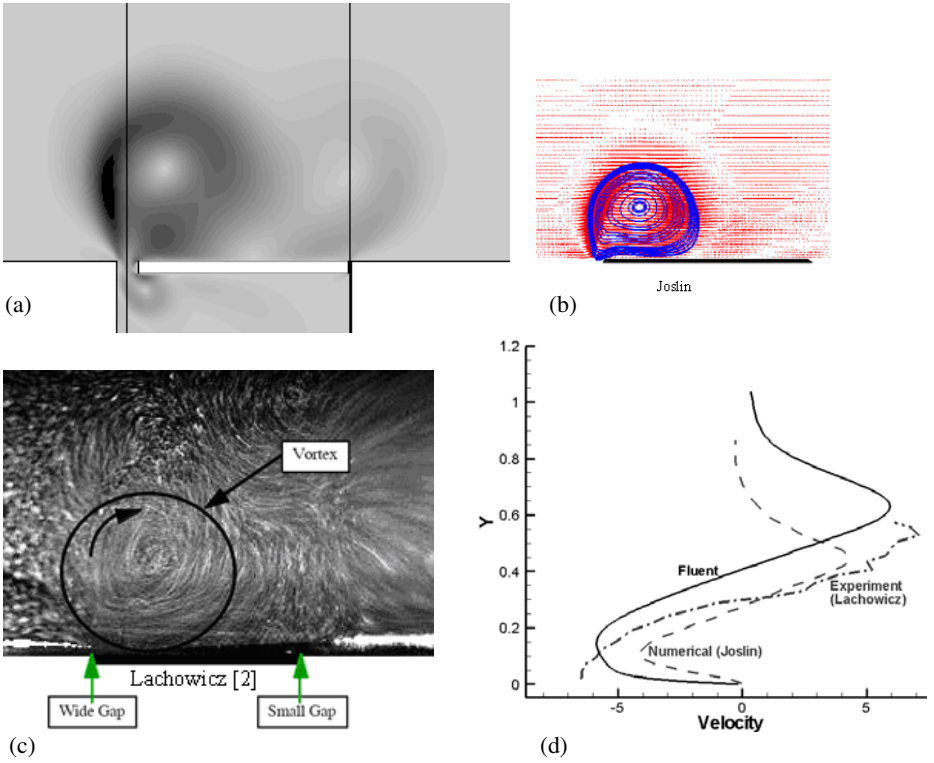
Fig. 3. Comparison of velocity fields. (a) Fluent, (b) Joslin *et al.* [3], (c) Lachowicz *et al.* [5], (d) velocity profiles through the vortex center.

(a)

(b)
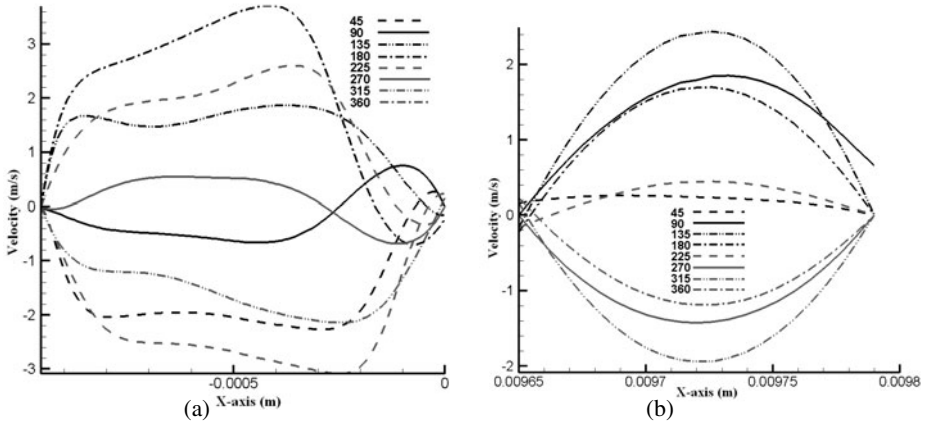
Fig. 4. Comparison of instantaneous velocity profiles (phase angles $45^o - 360^o$) through the gaps. (a) wide gap, (b) narrow gap.

the narrow gap width is very small compared to the plate thickness. Another typical observation (for an oscillating viscous flow) in this figure is that the velocity profiles are not symmetric during outward and inward flow and that the maximal outflow velocity does not occur in phase with the plate oscillation. It occurs about 45° after the plate has reached its upper or lower turning point ($\Theta = 90^o$ or $\Theta = 270^o$). The curve at $\Theta = 90^o$ does not return to zero at the right end. This is simply because for the present set-up, the actuator plate has moved outside the cavity at this time instant and there is no longer a wall at $x > 0.00979$. There is no such phase shift in the wide gap in Fig. 4a.

3.2   Case 2, Free Jet Mode

According to Lachowicz [5] at lower frequency and high scaled amplitude we should expect a free jet at the wide gap. In this case we did simulations for $Sr = 5.30$ and $S_a = 0.19$. With this frequency and scaled amplitude we get a free jet from the wide gap which is slightly tilted towards the narrow gap.

Our quantitative information is presented in Fig. 5 using streamlines and contours of the time-averaged velocity field. Averaging has been performed over the last four time periods. The figure confirms that we get a flow field comparable to the experiment with a free jet from the wide gap which begins in vertical direction before it bends somewhat to the right. Continuing the simulation to later times, straightens the jet further, such
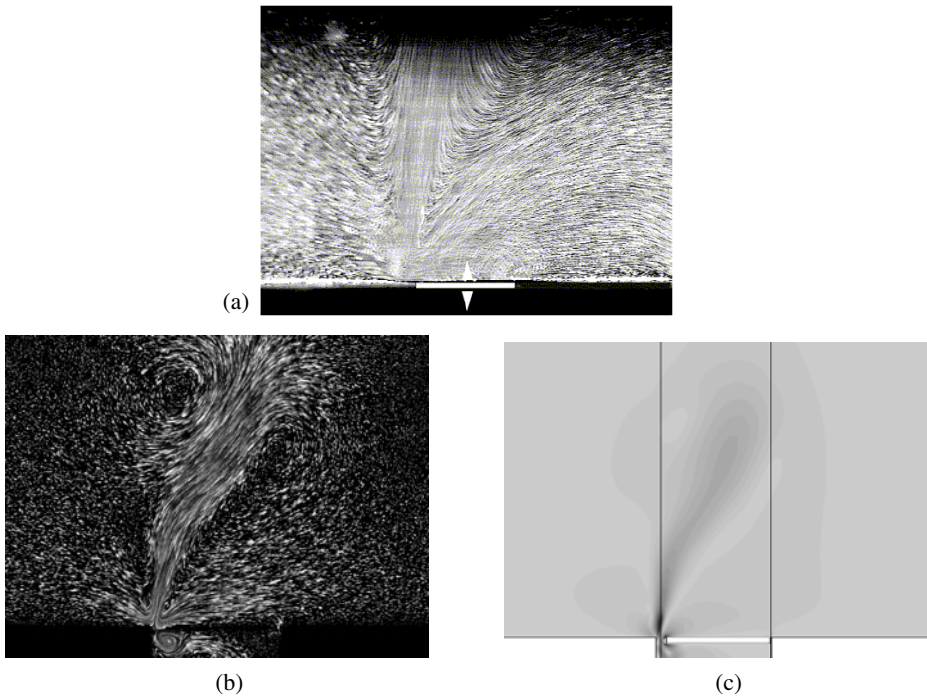
Fig. 5. Comparison of velocity fields. (a) Lachowicz *et al.* [5], (b) and (c) Fluent.
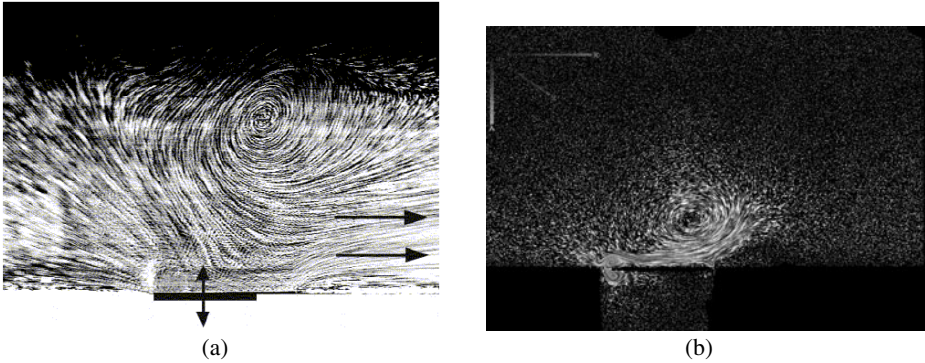
Fig. 6. Comparison of velocity fields. (a) Lachowicz *et al.* [5], (b) Fluent.

that the picture of an inclined jet becomes clearer. Unfortunately, there is no quantitative data available for this mode of actuation to compare the results further.

3.3 Case 3, Wall Jet Mode

According to Lachowicz *et al.* [5] at low scaled amplitude and high frequency we should expect a wall jet pumping fluid from the wide gap to the narrow gap. Therefore, we increased the Strouhal number to $Sr = 9.03$ and reduced the scaled amplitude to $S_a = 0.11$ at the same time. In this case we observe a wall jet from the wide to the narrow gap, i.e., the same qualitative feature as in [5] and this is shown in Fig. 6 where we compare the two averaged flow fields using stream lines. A counter-clockwise rotating vortex sits above the narrow gap. In the experiment the flow towards the actuator on the left of the vortex appears clearer than in the numerical simulation but this is merely an effect of different integration times of the streamline segments. The next difference is that the wall jet continues far beyond the actuator region to the right in the experiment which is less pronounced in the simulation. Here, a continuation of the simulation would extend the jet further to the right. Again, there is no quantitative data available for this mode of actuator to compare with our results.

4   Conclusions

Three different simulations have been performed to show the effects of diverse parameters which influence the flow field. Vertical jet, wall jet, and vortex modes of actuation of the actuator have been detected and compared to available previous results where possible.

In general, it turns out that our simulation methodology is capable of reproducing the observations by Lachowicz *et al.* to full extent. However, discretisation of the computational grid needs some care because the size of the observed vortex can depend on insufficient grid resolution. In other cases it was observed that the jet direction may also depend on resolution. The comparison of the different flow regimes with Lachowicz *et al.* [5] has already been shown in Fig. 2.

For the JaVA design three-dimensional simulations have been started as well. These will be used to study side-wall effects due to the finite extend of the actuator in reality. This is an undocumented feature of the JaVA that deserves attention. Finally, the actuator must be coupled to boundary layer flows in order to assess its efficiency for flow control.

Acknowledgements

References

[1] Fluent Inc.: Fluent 6.2 User's Guide, Fluent Inc., Centerra Resource Park, 10 Cavendish Court, Lebanon, NH 03766 (January 2005)

[2] Jacobson, S.C., Reynolds, W.C.: Active control of streamwise vortices and streaks in boundary layers. J. Fluid Mech. 360, 179–994 (1998)

[3] Joslin, R.D., Lachowicz, J.T., Yao, C.: DNS of flow induced by a multi-flow actuator. In: ASME FEDSM98-5302, ASME Fluid Engineering Meeting (1998)

[4] Koumoutsakos, P.: Simulations of vortex generators. Center for Turbulence Research, Annual Research Briefs, pp. 233–240 (1995)

[5] Lachowicz, J.T., Yao, C., Wlezien, R.W.: Flow field characterization of a jet and vortex actuator. Exp. Fluids 27, 12–20 (1999)

[6] Saddoughi, S.G., Koumoutsakos, P., Bradshaw, P., Mansour, N.N.: Investigation of 'On Demand' vortex generators. Center for Turbulence Research Manuscript No. 171. Stanford University (1998)

Direct Numerical Simulation of Jet Actuators for Boundary Layer Control

Björn Selent and Ulrich Rist

Universität Stuttgart, Institut für Aero- & Gasdynamik,
Pfaffenwaldring 21, 70569 Stuttgart, Germany
selent@iag.uni-stuttgart.de, rist@iag.uni-stuttgart.de
http://www.iag.uni-stuttgart.de

Summary

The paper presents a method to perform direct numerical simulations (DNS) of a jet actuator flow inside a turbulent flat plate boundary layer (TBL). A structured finite difference method is used for the simulations. The numerical scheme is adapted to account for the large scale differences both in geometric and fluid dynamic aspect. Analytical mesh transformations have been implemented to resolve the jet orifice. Suitable boundary conditions are established to model the jet flow. Numerical stability has been added by implementing a compact filter scheme. The TBL baseflow is generated by mimicking experimental approaches and direct simulation of the laminar-turbulent transition process. Simulations of a jet actuator configuration perturbing the turbulent baseflow have been undertaken and the results are evaluated.

1 Introduction

Jet actuators or jet vortex generators (JVG) have been proven to provide a mechanism to positively control boundary layer flows. Experimental work by Johnston et. al. [1] has shown the general ability to suppress separation in flows with adverse pressure gradient. The effect stems from the fact that longitudinal vortices are established inside the boundary layer and a mixing of the BL's faster layers with low-speed layers closer to the wall takes place. The mixing in turn leads to increased skin friction thus enabling the flow to overcome larger pressure gradients downstream. This is a very similar effect observed from passive vortex generators [2]. The advantage of jet vortex generator systems over existing solid generators lies in their flexibility to be applied only when necessary and thus to avoid any parasitic drag. An exhaustive parameter study was undertaken by Godard et. al. [3] covering many aspects of jet actuators such as velocity ratio λ, skew angle β and pitch angle α, hole geometry and direction of rotation. The tested configurations were compared by the increase of skin friction induced by the vortex. From these values the authors deduced an optimum jet configuration. Recent publications also report on the interaction of vortices generated by staggered actuator arrays [4]. For evaluation a momentum integral was used in this case and it was documented that jet arrays were capable of prolonging the positive effect of the vortices further downstream compared to a single line of actuators.

Albeit the outcomes of these experiments yield a very good general idea of the mechanism of active flow control devices there still are a number of open questions involved as no detailed picture of the forming of the vortex and its interaction with the boundary layer could be gained from experiment yet. Therefore, any design suggestions for actuators rely heavily on empirical data and are difficult to transpose to different configurations. Within the AERONEXT research program numerical simulations of jet actuators are to be performed by means of RANS and DNS technique. The regime considered consists of a strong steady jet disturbance in a flat-plate turbulent boundary layer cross flow. Since RANS simulations allow for a faster computation they are well suited to cover numerical parameter studies. The DNS approach on the other hand was chosen for its lack of any model assumptions. Therefore, it is well suited to provide a reference solution for coarser numerical schemes. Furthermore, DNS allows for a computation of the unsteady flow formation especially in the beginning of the vortex generation and detailed analysis of the fluid dynamics involved.

2 Numerical Method

All simulations have been performed using the program *NS3D*, developed at IAG. The method utilizes a hybrid finite difference/spectral scheme for spatial discretization and a standard explicit Runge-Kutte method for time integration. The program is both shared and distributed memory parallelized using MPI and NEC Microtasking programming techniques. Additionally the structured mesh approach allows for strong vectorization on the NEC SX8 platform used.

The program *NS3D* solves the compressible unsteady conservation equations in conservative form on a three dimensional Cartesian mesh. Spatial derivatives in downstream and wall-normal direction are approximated by compact finite differences of order ($O6$) with spectral like resolution [5]. Derivatives on the domain boundaries are approximated by one sided finite differences of order ($O4$). Reduction of order on the boundaries takes place in order to avoid strong numerical damping due to the one-sided stencil. In spanwise direction periodicity is assumed and a spectral method is used to compute spatial derivatives.

Time integration is performed by a standard four-step Runge-Kutta scheme of order ($O4$). In between the RK sub steps as well as in between full time steps the FD stencils are shifted forward and backward alternately thus introducing numerical dissipation and generating a more robust scheme [6].

At the inflow subsonic characteristic boundary conditions are used. At the freestream boundary exponential decay of all disturbances in wall-normal direction is prescribed. At the outflow boundary a relaminarization zone is applied. The wall is assumed to be isothermal and no-slip boundary conditions are used, the wall-normal pressure gradient is assumed to equal zero. Periodic boundary conditions are applied in spanwise direction. Fluctuations are introduced via inhomogeneous wall boundary conditions. In this manner wave like periodic disturbances as well as continuous or cyclic suction and blowing can be realized on the wall.

Initial conditions describe laminar flow on a flat plate with zero pressure gradient.

3   Jet Vortex Generator Simulations

The very nature of jet vortex generator flow simulations poses a number of challenges which need to be addressed.

Firstly, the physical domain size and resolution are determined by the actuator exit geometry and jet dimensions respectively and the downstream development of the induced vortex itself. The resulting scale differences are in the order of magnitude of $L/d = 10^2$. Therefore suitable analytical mesh transformations have been implemented to assure sufficient resolution on both ends of the scale. These transformations allow for mesh compression over the jet orifice and a stretching of the mesh towards the domain boundaries. The actuator is not modelled but the emerging jet is introduced through inhomogeneous boundary conditions. A polynomial of order $(O5)$ is used to prescribe the velocity distribution at the jet exit. The implementation also allows for an arbitrary skew and pitch of the jet.

Secondly, the computational scheme is based on the compressible form of the Navier-Stokes equations. The scheme was chosen in order to be able to model the speed range that is encountered for commercial aircraft. Experimental results agree on the need for a large jet-to-freestream-velocity ratio $\lambda \approx 5$ for efficient vortex generation. In order to avoid transonic effects, the free stream Mach number thus needs to be quite small ($Ma \approx 0.15 - 0.2$). For small Ma the formulation exhibits increasingly singular behaviour which has to be accounted for by decreasing the time step to a level at which dissipation due to forward-backward shifting no longer suffices for stable computations. Thus, a compact filter was implemented to stabilize the computations [5].

3.1   Turbulent Boundary Layer

In order to obtain a turbulent baseflow an approach is chosen which mimics experimental setups. Wavelike disturbances are introduced into a laminar boundary layer and the laminar-turbulent transition is simulated. Suchlike any assumptions of eddy size and frequencies contained in the turbulent spectrum are avoided. The goal is to generate a TBL satisfying the statistical properties of turbulence for a designated Reynolds number based on momentum thickness Re_Θ. It was found that breakdown could be reached fastest using a 2D Tollmien-Schlichting (TS) and a subharmonic 3D wave in combination with a steady homogenous 2D disturbance. The steady disturbance inflicts an inflection point into the laminar profile. A good picture of the effectivity of the tripwire/subharmonic scenario can be gained from figure 1(a). Shown are the maximum amplitudes of the fundamental frequency obtained from FFT analysis of the downstream velocity $u' = u_{turb} - U_0$ with turbulent velocity field u_{turb} and steady laminar velocity field U_0. The graph can be read as description of the baseflow change due to the perturbations. The fully turbulent state is reached farther upstream for the tripwire/subharmonic breakdown compared to the purely subharmonic case. Figure 1(b) depicts a comparison of the displacement and momentum thickness of the boundary layer. The shape factor $H_{12} = \delta_1/\theta$ converges to 1.3 in both cases but at smaller Re_x values for the tripwire case.

The tripwire/subharmonic perturbations have been used to generate a turbulent reference flow of a boundary layer on a flat plate with zero pressure gradient. The physical
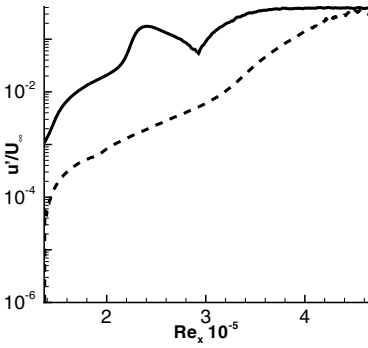
(a) Maximum amplitudes of baseflow change
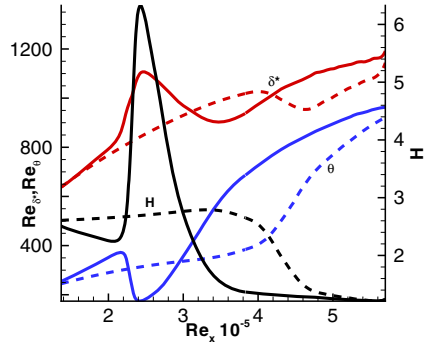
(b) BL thickness, shape factor

Fig. 1. Comparison of transition scenarios, solid lines: tripwire, dashed lines: purely subharmonic
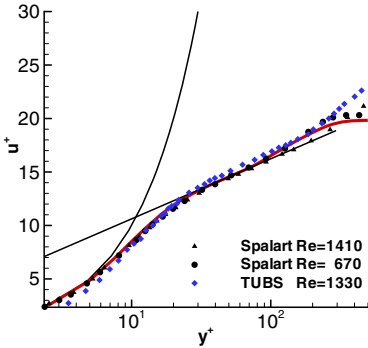
(a) Turbulent mean velocity profile
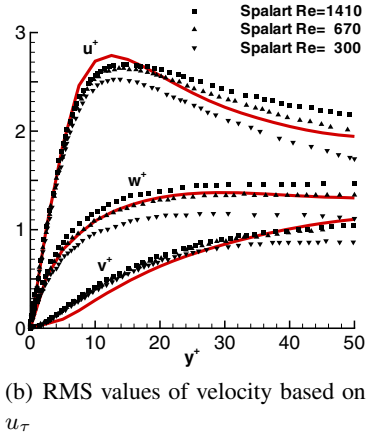
(b) RMS values of velocity based on u_τ

Fig. 2. Turbulent BL, red lines: present computation at $Re_\Theta = 800$

parameters for the computation are as follows: $Re = 100000$, based on freestream velocity $U_\infty = 52 m/s$, kinematic viscosity $\nu = 1.5 \cdot 10^{-5} m^2/s$ and characteristic length $L = 30mm$. The mesh consists of 1200x300x128 nodes in x, y and z directions. Mesh spacings in wall units based on $u_\tau = \sqrt{\frac{\bar{\tau}}{\rho}}$ are $\Delta x^+ \approx 12$, $\Delta y^+ \approx 1$, $\Delta z^+ \approx 6$ and the time step is $\Delta t = 3.9 \cdot 10^{-5}$. The turbulent flow at $Re_\theta = 800$ is compared quantitatively with both numerical and experimental data and the results are shown in figure 2. The turbulent velocity profile is in very good agreement with data taken from Spalart [7] and TU Braunschweig (fig. 2(a)). The rms fluctuations of the spanwise velocity in wall units (fig. 2(b)) is in good agreement with data from Spalart's numerical simulations. Deviations to Spalart's values in downstream and wall-normal direction originate most likely from the compact difference formulation and might be reduced
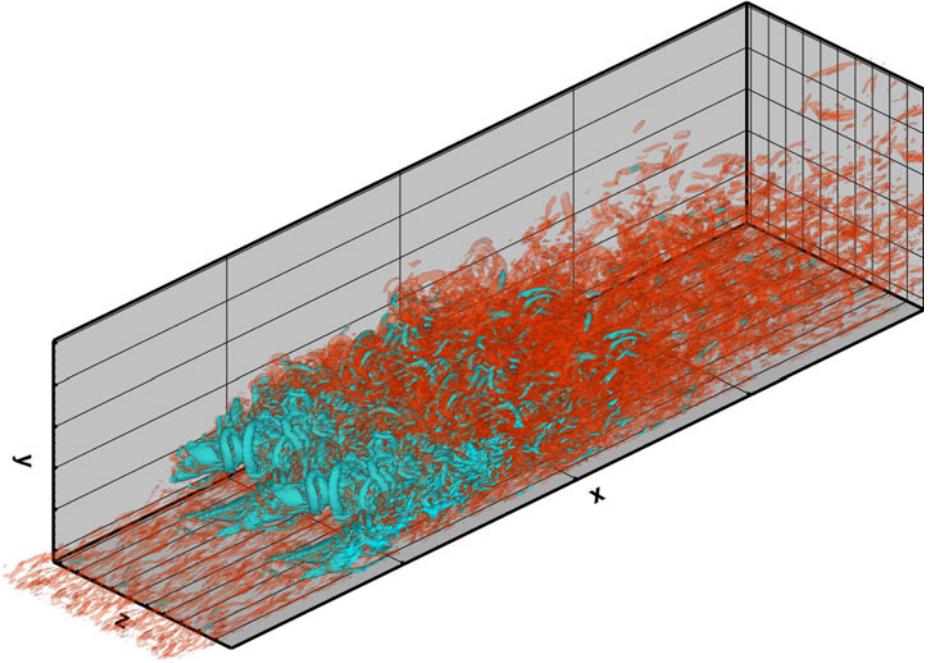
Fig. 3. Jet in TBL, Ma=0.15, $\lambda = 5.2$, blue: isosurface $\lambda_2 = -2000$, red: isosurface $\lambda_2 = -200$

by decreasing Δx and Δy. Within the context of a JVG simulation the TBL deems sufficiently resolved nonetheless and was used as baseflow for following computations.

3.2   Jet Vortex Generator in TBL

Into the TBL baseflow a Jet Vortex Generator was included in subsequent simulations. The jet-to-freestream velocity ratio is $\lambda = 5.2$ and jet exit radius $r = 1mm$. The jet is pitched by $\alpha = 30°$ and skewed to the freestream by $\beta = 80°$. Nozzle distance is set to $2D$ in spanwise direction. The jet centre is positioned at $x = 4.3$. Figure 3 depicts isosurfaces of the vortex identification criterion λ_2 [8] after 144 hrs of computation. It can be seen how a crossflow jet is formed downstream of the nozzle. The jet develops ring-like vortices along its trajectory which interfere with each other. The jet is highly unstable and almost complete breakdown of distinct jet structures takes place over a short distance downstream. A region of increased vorticity develops behind the jet.

Figure 4 depicts time averaged velocity contours of the downstream velocity and velocity vectors in the transverse plane. Shown are four stations in order to obtain an insight in the evolution of the flow due to the jet. The first station at $x = 3.8$ is situated upstream of the jet. It can be seen how the flow already exhibits a wavy structure
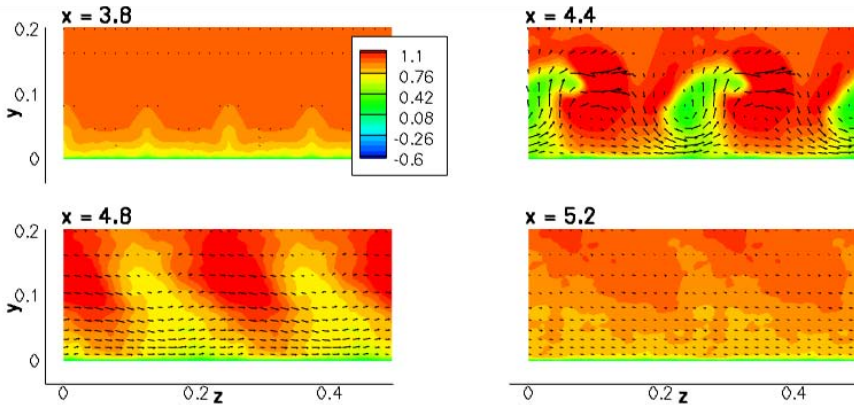
Fig. 4. Vortex and streak development caused by JVG, contours represent mean u velocity. Arrows are velocity vectors in y-z-plane

because of the blockage of the boundary layer before the jets. At $x = 4.4$ a rotational motion can be observed which mixes the layers inside the boundary layer. Low-speed fluid is entrained upwards. On the top outward side of these vortices a high-speed streak is established. Farther downstream at $x = 4.8$ alternating low- and high-speed streak structures are present and the vector field shows a strong spanwise motion. At this station only a small rotational motion is measured. At the last position $x = 5.2$ the flow does not contain distinct structures anymore. The streaks and vortices have almost completely dissipated. For the purpose of separation control, the increase of wall friction is of interest. Figure 5(a) depicts the spanwise mean and time averaged change of wall friction coefficient of the perturbed flow based on the corresponding value for the undisturbed flow over x. In a close distance downstream of the nozzle a negative effect can be seen. The wall friction decreases compared to the baseflow. This is because the jet imposes entrainment on the boundary layer whereas the induced rotational motion is not strong enough to feed high-speed fluid in the near wall regions. Downstream of $x = 4.8$ a region of increased wall friction is visible which corresponds to the streak area described in figure 4. Here the additional momentum of the jet is directed into a crossflow motion. Representative spanwise mean and time averaged velocities are plotted in figure 5(b). Compared to the reference TBL flow the u veloctiy at $x = 4.54$ does not show an increase close to the wall but a strong velocity defect in the overlap region. The u velocity at station $x = 5.2$ on the other hand indicates a transfer of momentum towards the wall whereas the defect in the overlap is diminished. The spanwise velocity at $x = 4.54$ contains strong gradients which might result from taking the mean over regions with alternating strong and weak spanwise motion as seen in figure 4 at $x = 4.4$. Farther downstream the w profile is more uniform which indicates a directed crossflow over the whole span. The maximum value for w is decreasing while travelling downstream due to dissipation. The positive effect of increased friction is lost after a short distance downstream of about $\Delta x = 25D$. The simulated configuration suffers somewhat from the close spanwise distance of the nozzles. Therefore, the anticipated effect of generating a longitudinal vortex in the flow is not reached. The momentum input of
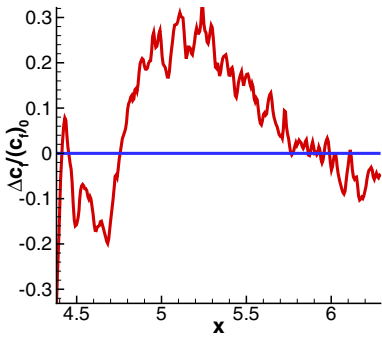
(a) Change of wall friction coefficient, blue line indicates no change.
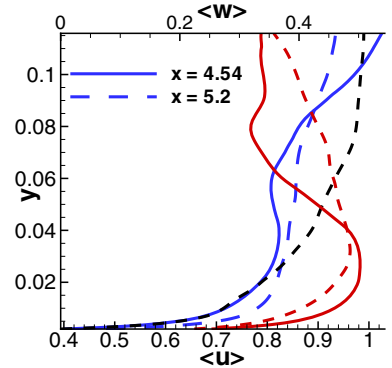
(b) Time averaged mean spanwise velocity, blue line: u, red line: w, black line: u of reference

Fig. 5. Effect of JVG in TBL

the jet is mostly used to deflect the flow in spanwise direction rather than to increase the momentum close to the wall in downstream direction.

4   Conclusions

A numerical scheme is presented for direct numerical simulations of jet vortex generators in turbulent boundary layers. The method is based on the fully compressible form of the conservation equations to allow for simulations of flight conditions. The scheme is capable of resolving the large scale differences involved. A turbulent baseflow was generated by mimicking an experimental setup. A JVG configuration was test by introducing a jet disturbance into the turbulent boundary layer flow and the effect on the boundary layer was evaluated. The simulated case does not show the development of longitudinal vortices but of streak structures and strong spanwise deflection of the mean flow. Further simulations are to be undertaken with increased spanwise jet nozzle distance.

Acknowledgements

References

[1] Johnston, J.P., Nishi, M.: Vortex Generator Jets – a Means for Flow Separation Control. AIAA Journal 28, 989–994 (1990)

[2] Compton, D.A., Johnston, J.P.: Streamwise Vortex Production by Pitched and Skewed Jets in a Turbulent Boundary Layer. AIAA Journal 30, 640–647 (1992)

[3] Godard, G., Foucaut, J.M., Stanislas, M.: Control of a decelerating boundary layer: Parts 1,2,3. Aerospace Science and Technology 10 (2006)

[4] Casper, M., Kähler, C.J., Radespiel, R.: Fundamentals of Boundary Layer Control with Vortex Generator Jet Arrays. In: AIAA Flow Control Conference (2008)

[5] Lele, S.K.: Compact Finite Difference Schemes with Spectral-like Resolution. J. Comp. Phys. 103, 16–42 (1992)

[6] Kloker, M.J.: A robust high-order split-type compact FD scheme for spatial direct numerical simulation of boundary-layer transition. Appl. Sci. Res. 59, 353–377 (1998)

[7] Spalart, P.R.: Direct simulation of a turbulent boundary layer up to $R_\theta = 1410$. J. Fluid Mech. 187 (1988)

[8] Jeong, J., Hussain, F.: On the identification of a vortex. J. Fluid Mech. 285, 69–94 (1995)

Flowfield-Characteristics Generated by DBD Plasma Actuators

Jochen Kriegseis[1], Tobias Dehler[1], Sven Grundmann[2], and Cameron Tropea[1,2]

[1] Fachgebiet Strömungslehre und Aerodynamik
Technische Universität Darmstadt
Flughafenstr. 19, 64347 Griesheim, Germany
`kriegseis@sla.tu-darmstadt.de`
[2] Center of Smart Interfaces
Technische Universität Darmstadt
Flughafenstr. 19, 64347 Griesheim, Germany

Summary

The current study is devoted to investigating velocity fields produced by Dielectric Barrier Discharge (DBD) plasma actuators in quiescent air using a PIV system. The purpose of the study is to determine whether features in the velocity field can be recognized, which already allow direct conclusions about how effective the actuator might be for a particular flow control application. The parameter space investigated in the experiments comprises several electrode sizes, modulation frequencies and actuator voltages. Our interest is focussed at the present time on stabilization of boundary layers or delay of transition. To identify conducive induced velocity fields, we have chosen to examine the proper orthogonal decomposition of the velocity field and show that this representation can have direct physical interpretation of the influence exerted on the boundary layer. Comparing the present results to previous experience with various actuator configurations, we conclude that the following approach is viable and should be persude.

1 Introduction

In 1968 Velkoff and Ketcham [18] demonstrated the effect of electrical fields generated by corona wires placed a small distance from the surface of a flat plate on fluid boundary layers. Roth et al. [16] introduced a wall-mounted plasma actuator as a tool for boundary-layer flow control, a concept which has since been widely investigated for a large number of different applications [12].

The optimization of plasma actuator geometries and operation parameters depends intimately on the application at hand and widely differing optimization strategies are imaginable. For instance, Roth and Dai [17] regarded the power coupled to the neutral gas flow by ion-neutral collisions when optimizing the actuator geometry and materials, modulation frequency and voltage. Direct dependency of actuator-thrust production on the thickness of the exposed electrode was demonstrated by Enloe et al. [5]. Various methods for a velocity augmentation of the ionic wind itself were investigated by Forte et al. [6].

(a) actuator   (b) detail
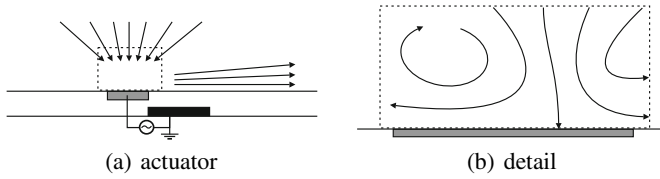
Fig. 1. General (a) and close-up (b) sketch of a DBD plasma actuator and the flow behavior in its vicinity; upper electrode shaded gray, lower electrode filled black.

Experimental investigations by Grundmann and Tropea demonstrated transition delay using continuously operated plasma actuators [7] and active cancelation of Tollmien-Schlichting waves using pulses actuators [8]. The results could be verified numerically by Quadros et al. [14]. Already in these studies, and subsequently confirmed by Duchmann [4], it became clear that the effectiveness of an actuator to successfully influence the boundary layer in the desired manner was very sensitive to the exact actuator geometry, for instance the length of the upper electrode. This was therefore the motivation leading to the present investigation, namely to determine whether such geometry changes are already evident in the velocity field induced by the actuator in a quiescent field. By removing the mean flow in the experiment, actuators of different designs can be directly compared with one another on the basis of their induced velocity field.

The overall flow behavior induced by the actuator is sketched in Figure 1(a), showing a flow directed downwards towards the actuator and a wall jet developing in the downstream direction. Indeed, the fact that an actuator induces a negative vertical velocity in addition to a downstream directed wall jet, is often overlooked. This vertical velocity can be exploited in various manners, for instance to help cancel TS waves (triggered at the correct phase) and delay transition, or to promote transition to turbulence, acting as a simple disturbance. Therefore the magnitude of this velocity may be an important indicator characterizing how effective an actuator will be. A close-up view of the velocity directly above the actuator, as demonstrated by Duchmann [4] or Ramakumar and Jacob [15], reveals that under certain operating conditions a reverse flow can develop, at least in quiescent air (Figure 1(b)). Parameter combinations leading to suppression or minimization of such zones are of particular interest, since they will affect also the magnitude of the resulting wall jet and will also be related to the existence of a vertical velocity component. Therefore, a major objective of the present study is to characterize the velocity fields around an actuator in a systematic manner, identifying for instance translatory or rotational flow patterns as a function of operating parameters. Accompanying studies using the same actuators in various flow fields allow an assessment of which velocity fields are most effective in influencing a boundary layer in a particular manner. Moreover, the present study is restricted to examining the velocity field immediately above the actuator (Fig. 1(b)). On-going work extends the present results to flow regions downstream of the actuator.

2   Experimental Setup

To investigate the velocity field in immediate proximity to the actuator a high resolution PIV system has been employed. The two-velocity component PIV system comprises a Nd:YAG-laser (200 mJ) and double-frame camera (1376×1040 pixels, 1 fps). To capture the flow behavior in the vicinity of the actuator, image sizes of 7×5.3 mm^2 and 18×13.6 mm^2 were chosen. A time delay between images of $\Delta t = 150$ μs was used, appropriate for the expected velocities in the range of 0 to 3 m/s. In order to insure statistical significance of the results, 1000 pairs of images were acquired for each operating condition [13].

The velocity field was computed using the Dantec Dynamics FlowManager software with interrogation areas of 64×64 pixels, i.e. an area of 325×325 μm^2 for the small image size (see Table 1), and an overlap of 75%. Typically, $5-10\,\%$ of the vectors were spurious, due to wall reflections etc. These outliers were eliminated using a range validation. The test section was a closed containment of dimensions $400 \times 280 \times 250$ mm^3.

Table 1. Parameter variations studied: results presented for highlighted conditions .

Variable parameters:	Width of upper electrode [mm]	**1.0, 2.5, 5.0, 7.5**
	Recorded image size [mm^2]	**7 × 5.3**, 18 × 13.6
	Actuator voltage [kV]	7, **8**, 9, 10
	Actuator frequency [kHz]	**6.5**, 9.5
Constant parameters:	Width of lower electrode [mm]	**10**
	Quiescent air [m/s]	$\mathbf{U_\infty = 0}$
Offset:	plane II: Δx_1 [mm]	-10, -8, -6, -4, -2, 0, 3, 6, 9
	plane III: Δx_3 [mm]	1, 3, 5

(a) overview   (b) plane I
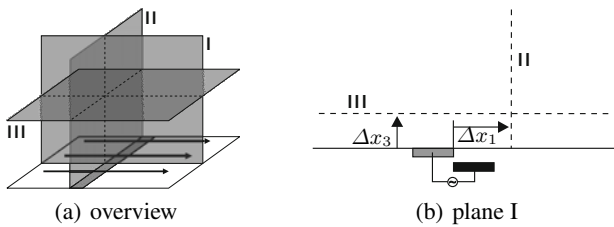
Fig. 2. Measurement planes; upper electrode shaded gray, lower electrode filled black.

All experiments were conducted using a DBD plasma actuator. As sketched in Figure 1(a) these actuators consist of two electrodes that are separated by a dielectric layer. Typically the lower, shielded electrode is grounded, whereas the upper, exposed electrode is driven by a radio-frequency, high-voltage power supply. Although numerous parameters were varied in this study, emphasis was placed on the effect of changing the upper electrode size on the induced velocity field. A complete summary

of all parameters $k \in K$ varied is given in Table 1. Those parameters whose results are displayed in the present work are marked bold. The PIV measurement planes used to study the velocity field are shown in Figure 2, including planes parallel to all coordinate directions, placed in close proximity to the upper electrode (but not presented here).

3   Post Processing

From the outset it was not evident which features of the induced flowfield would be most significant for the present purposes. However, the first step of the analysis is to separate the mean velocity field $\bar{u}$ from the fluctuating parts u'. Exemplarily mean flow and RMS-values are shown in Figure 3 for an electrode width of 2.5 mm. According to Adrian et al. [1], the Reynolds decomposition does a fair job of revealing the small-scale vortices, but it removes large-scale features (mechanisms) that are intimately associated with the mean flow. In order to identify such flow patterns in the PIV data a proper orthogonal decomposition (POD) was therefore used to separate coherent large-scale structures from incoherent small-scale fluctuations like noise, both superimposed on the mean flow $\overline{u}$. A comprehensive overview of this method is given by Aubry [2].

The decomposition utilizes the Reynolds-decomposed fluctuations u' and represents the velocity field in terms of modes; mode zero corresponding to the mean flow $\boldsymbol{\phi}_0 = \overline{u}$ and the higher modes j adding fluctuations about the mean in terms of typical flow patterns $\boldsymbol{\phi}_j$. The ordering of the modes ensures that the kinetic energy contained in the modes decreases with increasing mode number j [11]. Coherent flow structures are generally captured by the first few modes, whereas the main portion of noise and other incoherent fluctuations are found in higher modes. Reconstruction of the velocity field results in coefficients a_j^i, which correspond to the weighting of each mode $\boldsymbol{\phi}_j$ for every single snapshot u^i. However, the mean coefficient $\overline{a_j}$ of each mode must be zero by definition [3].

However this form of the POD analysis is not adequate to quantitatively distinguish differences in velocity fields from different experiments or runs. While similar flows will exhibit a similar distribution of mode coefficient amplitudes, this is at most a qualitative comparison of different velocity fields. For the present purposes therefore, a Common-Base POD (CPOD), as introduced by Kriegseis et al. [9, 10], is more appropriate, providing quantitative comparisons between different input fields. The main difference of this modified method is that after reconstruction for any given experiment

(a) $\bar{u}$ in m/s   (b) $u_{1,\mathrm{RMS}}$ in m/s   (c) $u_{3,\mathrm{RMS}}$ in m/s
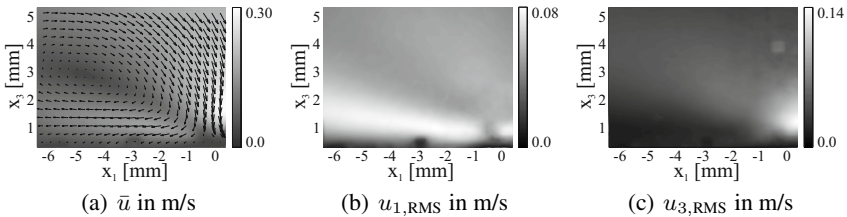
Fig. 3. Mean flow $\bar{u}$, fluctuations $u_{1,\mathrm{RMS}}$ and $u_{3,\mathrm{RMS}}$ (plane I, image size 7×5 mm^2, actuator voltage 8 kV, actuator frequency 6.5 kHz, upper electrode width 2.5 mm).

(a) Mode 0; 1.0 mm   (b) Mode 1; 1.0 mm   (c) Mode 2; 1.0 mm   (d) Mode 3; 1.0 mm

(e) Mode 0; 2.5 mm   (f) Mode 1; 2.5 mm   (g) Mode 2; 2.5 mm   (h) Mode 3; 2.5 mm

(i) Mode 0; 5.0 mm   (j) Mode 1; 5.0 mm   (k) Mode 2; 5.0 mm   (l) Mode 3; 5.0 mm

(m) Mode 0; 7.5 mm   (n) Mode 1; 7.5 mm   (o) Mode 2; 7.5 mm   (p) Mode 3; 7.5 mm
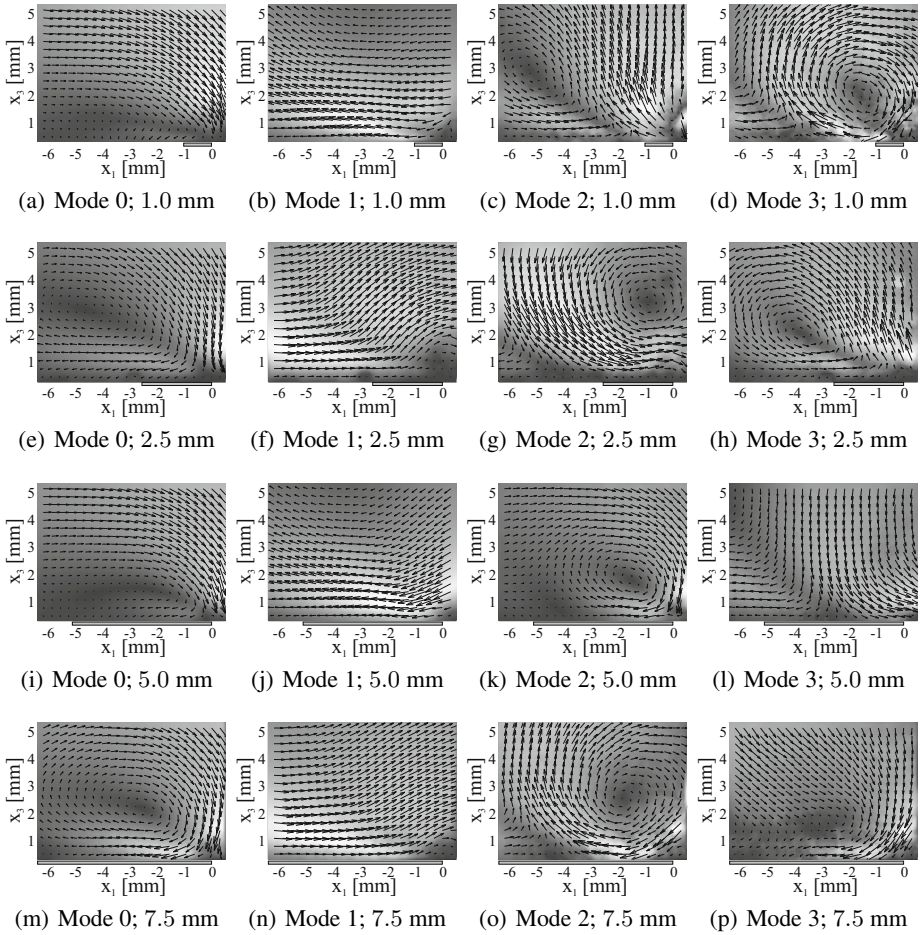
Fig. 4. Standard POD: Mean flows $\boldsymbol{\phi}_{0,k}$ and the three most powerful flow patterns $\boldsymbol{\phi}_{1,k} - \boldsymbol{\phi}_{3,k}$ for varying electrode sizes between 1 mm and 7.5 mm (plane I, image size 7×5 mm^2, actuator voltage 8 kV, actuator frequency 6.5 kHz).

a mean value $\overline{a_{j,k}} \neq 0$ exists for every mode $\boldsymbol{\phi}_j$, which will deviate more or less from the overall mean of zero. The values for $\overline{a_{j,k}}$ represent the mean portion of mode $\boldsymbol{\phi}_j$ in experiment k. Therefore a quantitative evaluation is possible when comparing these mean deviations and corresponding patterns, respectively. The question to be resolved with this study is whether these mean deviations can be associated with optimum (or favorable) parameter settings for a given application, in this case transition delay.

4   Results

The comparison of the POD results processed separately for the particular sizes of the upper electrode (1.0 mm, 2.5 mm, 5.0 mm, 7.5 mm) already yields qualitative insight

Table 2. Coefficient $a_{j,k}$ of each mode j: power portion P_j in %, mean values $\overline{a_{j,k}}$ and standard deviation $\sigma_{j,k}$.

Exp. k		1.0 mm		2.5 mm		5.0 mm		7.5 mm	
Mode j	Power P_j	$\overline{a_{j,k}}$	$\sigma_{j,k}$	$\overline{a_{j,k}}$	$\sigma_{j,k}$	$\overline{a_{j,k}}$	$\sigma_{j,k}$	$\overline{a_{j,k}}$	$\sigma_{j,k}$
1	2.85 %	1.90	2.25	−2.31	1.92	0.71	1.57	−0.59	3.64
2	1.80 %	−0.47	1.32	−1.86	0.86	1.18	0.64	2.30	1.03
3	1.24 %	−0.27	0.77	−0.13	1.42	0.78	0.92	−0.76	1.31
4	0.65 %	−0.59	0.34	0.40	0.58	0.33	0.32	−0.30	0.75

into the flow behavior. Example results obtained with an image size of 7×5 mm^2 in plane I for an actuator voltage of 8 kV and an actuator frequency of 6.5 kHz are pictured in Figure 4. These results reveal the presence of similar flow patterns that describe the flow behavior for all upper electrode sizes. All modes 0, which represent the mean velocity distribution ($\overline{u_k} = \boldsymbol{\phi}_{0,k}$), show the same flow field for the different electrode sizes. The downflow towards the actuator and the associated recirculation zone in the range of the upper electrode is observed in all experiments. The typical flow acceleration of the wall jet starts to the right of the depicted domain. A wall-tangential translatory fluctuation is represented by the first (most powerful) modes $\boldsymbol{\phi}_{1,k}$. The second modes $\boldsymbol{\phi}_{2,k}$ show rotational patterns of different strengths and locations.

Qualitatively, these characteristic patterns occur parameter independent. However, since the modes are derived from different decompositions, their contributions to the different flows are quantitatively incomparable. The method of CPOD [9, 10] sheds light on the strength of these most predominant patterns, allowing quantitative comparison. As the common point of reference to perform the CPOD, the edge between the upper and lower electrodes ($\Delta x_1 = 0$) was chosen.

The results of this common-base analysis are given in Figure 5 and Table 2. Fluctuations of the coefficients of modes 1 and 2 are seen to signify wall-parallel and wall-normal fluctuations of the mean flow. Depending on the sign of the coefficients, mode 3 strengthens or weakens the recirculation zone. Mean values $\overline{a_{j,k}}$ and standard deviations $\sigma_{j,k}$ of the coefficients are given by Table 2. Note that contrary to modes $\boldsymbol{\phi}_{2,k}$ obtained by standard POD, with the CPOD $\boldsymbol{\phi}_3$ represents the rotational mode.

The new mode 2 shows a desirable flow pattern in the sense discussed above, i.e. a rather strong vertical flow can be associated with mode $\boldsymbol{\phi}_2$ (flow from above and acceleration downstream). Hence, one may already speculate that an actuator exhibiting large negative mode 2 coefficients may work quite favorably for transition delay purposes (compare Figure 1(a)). We conclude that $\boldsymbol{\phi}_2$ is a very important mode for the efficiency of the actuator for this application.

Strong fluctuations of any mode can be understood as a disturbance to the mean flow. They will likely weaken the coherent effect of the actuator in a boundary layer or even promote transition. Grundmann and Tropea [7, 8] have already demonstrated that this indeed can be the case, i.e. an improperly chosen actuator geometry may lead to overwhelming disturbances of the boundary layer, promoting transition rather than delaying transition.

The quantitative comparison of the CPOD-modes obtained from different electrode-size ratios demonstrates the effect of parameter variations to the intensity of

(a) Mode 0   (b) Mode 1   (c) Mode 2   (d) Mode 3
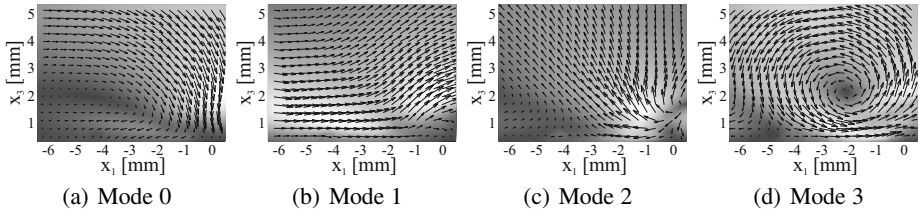
Fig. 5. Common-Base POD: Mean flow $\boldsymbol{\phi}_0$ and the three most powerful flow patterns $\boldsymbol{\phi}_1 - \boldsymbol{\phi}_3$ for $K = 4$ (plane I, image size 7×5 mm^2, actuator voltage 8 kV, actuator frequency 6.5 kHz).

each flow pattern. We conclude that a width of 2.5 mm for the upper electrode is an optimum size (Table 2). For this configuration the mode $\boldsymbol{\phi}_2$ exhibits the highest negative coefficient of magnitude while the rotational mode $\boldsymbol{\phi}_3$ is comparatively small. Moreover, the standard deviation of the mode coefficients, i.e. magnitude of flow disturbances, are rather small for mode 2 and an upper electrode width of 2.5 mm. This conclusion agrees with the findings of Duchmann [4] and Grundmann and Tropea [7, 8], where the configuration with an upper electrode width of 2.5 mm led to the best results in order to delay transition and stabilize the boundary layer.

5   Conclusions and Outlook

The spatial velocity distribution induced in quiescent air by Dielectric Barrier Discharge (DBD) plasma actuators has been measured using a PIV and characterized using a Common-Base POD analysis. The experiments were conducted for several electrode sizes, modulation frequencies and actuator voltages. Coherent structures (modes) of similar character but strongly different mean strength are identified for various operational parameters and actuator geometries.

The results of this study suggest that an actuator with an upper electrode width of 2.5 mm may be the most favorable geometry for achieving stabilizing effects on the boundary layer.

We conclude that the CPOD-based evaluation of the actuator-induced velocity field in quiescent air is a viable means for evaluating the effectiveness of an actuator for a particular purpose. The ultimate goal is to incorporate such an evaluation into the design process of actuators. On the other hand this study is rather preliminary. An obvious extension would be to now investigate also the velocity field downstream of the actuator, capturing also the induced wall jet, and to examine the resulting POD modes. Furthermore, it is necessary to investigate to what extent actuator performance can be characterized using simpler and conventional velocity measures (mean, RMS). A comparison between such measures and the POD analysis presented in this study would then elucidate the benefits of each approach.

References

[1] Adrian, R.J., Christensen, K.T., Liu, Z.C.: Analysis and interpretation of instantaneous turbulent velocity fields. Exp. Fluids 29, 275–290 (2000)

[2] Aubry, N.: On the Hidden Beauty of the Proper Orthogonal Decomposition. Theoret. Comput. Fluid Dynamics 2, 339–352 (1991)

[3] Cordier, L., Bonnet, J.P., Deville, J.: Proper Orthogonal Decomposition: POD. In: Tropea, C., Yarin, A.L., Foss, J.F. (eds.) Springer Handbook of Experimental Fluid Mechanics, pp. 1346–1370. Springer, Heidelberg (2007)

[4] Duchmann, A.: Experimentelle Untersuchung der Transitionsbeeinflussung mit Hilfe von Plasma Aktuatoren, Bachelor's thesis, TU Darmstadt (2007)

[5] Enloe, C.L., McLaughlin, T.E., VanDyken, R.D., Kachner, K.D., Jumper, E.J., Corke, T.C., Post, M., Haddad, O.: Mechanisms and Responses of a Single Dielectric Barrier Plasma Actuator: Geometric Effects. AIAA Journal 42, 595–604 (2004)

[6] Forte, M., Jolibois, J., Pons, J., Moreau, E., Touchard, G., Cazalens, M.: Optimization of a Dielectric Barrier Discharge Actuator by Stationary and Non-Stationary Measurements of the Induced Flow Velocity: Application to Airflow Control. Exp. Fluids 43, 917–928 (2007)

[7] Grundmann, S., Tropea, C.: Experimental Transition Delay Using Glow-Discharge Plasma Actuators. Exp. Fluids 42, 653–657 (2007) ISSN: 0723-4864

[8] Grundmann, S., Tropea, C.: Active Cancellation of Artificially Introduced Tollmien Schlichting Waves Using Plasma Actuators. Exp. Fluids 44, 795–806 (2007)

[9] Kriegseis, J., Dehler, T., Gnirß, M., Tropea, C.: Common-Base Proper Orthogonal Decomposition (CPOD) as a Means of Quantitative Data-Comparison. Meas. Sci. Technol. (submitted)

[10] Kriegseis, J., Dehler, T., Pawlik, M., Tropea, C.: Pattern-Identification Study of the Flow in Proximity of a Plasma Actuator. In: AIAA-2009-1001, 47th AIAA Aerospace Science Meeting, Orlando, Florida, USA (2009)

[11] Meyer, K.E., Pedersen, J.M., Özcan, O.: A Turbulent Jet in Crossflow Analysed with Proper Orthogonal Decomposition. J. Fluid Mech. 583, 199–227 (2007)

[12] Moreau, E.: Airflow Control by Non-Thermal Plasma Actuators. J. Phys. D: Appl. Phys. 40, 605–636 (2007)

[13] Patte-Rouland, B., Lalizel, G., Moreau, J., Rouland, E.: Flow Analysis of an Annular Jet by Particle Image Velocimetry and Proper Orthogonal Decomposition. Meas. Sci. Technol. 12, 1404–1412 (2001)

[14] Quadros, R., Grundmann, S., Tropea, C.: Numerical Simulations of the Transition Delay using Plasma Actuators. In: 7th International ERCOFTAC Symposium on Engineering Turbulence Modelling and Measurements - ETMM7, Limassol, Cyprus (2008)

[15] Ramakumar, K., Jacob, J.D.: Low Pressure Turbine Blade Separation Control Using Plasma Actuators. In: AIAA-2007-371, 45th AIAA Aerospace Science Meeting and Exhibit, Reno, Nevada, USA (2007)

[16] Roth, J.R., Sherman, D., Wilkinson, S.P.: Boundary Layer Flow Control with a One Atmosphere Uniform Glow Discharge Surface Plasma. In: AIAA-1998-0328, 36th AIAA Aerospace Science Meeting and Exhibit, Reno, Nevada, USA (1998)

[17] Roth, J.R., Dai, X.: Optimization of the Aerodynamic Plasma Actuator as an Electrohydrodynamic (EHD) Electrical Device. In: AIAA-2006-1203, 44th AIAA Aerospace Science Meeting and Exhibit, Reno, Nevada, USA (2006)

[18] Velkoff, H.R., Ketcham, J.: Effect of an Electrostatic Field on Boundary-Layer Transition. AIAA Journal 6, 1381–1383 (1968)

Identification and Quantification of Shear Layer Influences on the Generation of Vortex Structures

Kudret Baysal and Ulrich Rist

Institut für Aerodynamik und Gasdynamik, Universität Stuttgart,
Pfaffenwaldring 21, D-70550 Stuttgart, Germany
{baysal,rist}@iag.uni-stuttgart.de
http://www.iag.uni-stuttgart.de

Summary

The analysis of complex flow fields based on the notion of organized motions of flow field features with spatial and temporal coherence, the so-called coherent structures, is one of the principal methods in the development of advanced analysis tools in fluid mechanics. For decades the focus of research was on vortex structures as the only coherent structure of interest, caused by the significant role of these structures in the understanding of the main fluid dynamical events, e.g. turbulence in boundary layers. A new topic is the extension of the flow field analysis by the detection of shear layer structures. The consideration of shear layer structures allows additional insight into dynamic processes, e.g. generation and decay of vortex structures.

1 Introduction

For real-life flow control applications it is desirable to have a better understanding of fundamental fluid dynamical mechanisms and to possess methods for their automatic detection, quantification and monitoring. Traditionally, people use the concept of vortex structures, which are also known as coherent structures in the literature, to describe and generalize a multitude of fluid motions. For a viscous flow, however, shear layers are equally important. This leads to the question of their interactions, i.e., the formation of new vortices either by shear layer roll-up or by the interaction and merging of already existing vortices, and the formation of new shear layers by vortices.

Such problems have already been studied in the past, e.g. in qualitative particle visualisations of flow fields to analyze vortex structures. However, without the availability of a quantitative analysis of fluid dynamics and of numerical methods for an automatic detection of relevant events.

In the present work we first identify shear layers and vortices in a given flow field using numerical implementations of analytical criteria. During their lifetime, criteria, like position, size, vorticity, enstrophy, circulation, etc. of each structure are recorded and tracked, such that a compact graphical representation of the identified dynamics can be shown. We then look for the birth of new vortices, e.g. out of shear layers or

by the merging of two interacting vortices. Once these have been found "by hand" we evaluate and compare the extracted data for these events. Our intent is to find criteria for an automatic identification of events in general configurations using these methods. For clarity and simplification of the discussions the current state of the work will be explained on the basis of a two-dimensional laminar shear layer that has been generated by the merging of two parallel streams behind a flat plate with different velocities in section 3. Consideration of a three-dimensional case would be complicated by ever-changing orientations of local coordinate systems, when the identified structures are twisted.

2   Identification of Coherent Structures

2.1   Vortex Structures

The main vortex identification criteria are derived from the definition of a vortex structure as a finite volume of fluid particles with a rotational motion around a center line. They can be classified according to the following categories:

- The first group contains conventional criteria like vorticity, pressure, as well as the investigation of vortices using streamlines and pathlines. The inadequacies of these criteria and methods were discussed, e.g., by Jeong and Hussain [5].
- The basic concept of the second group of criteria is the eigenvalue analysis of the velocity gradient tensor ∇u in order to detect a vortical motion.
- The widely used Q or Okubo-Weiss criterion, which is described in section 2.2, and the λ_2 [5] criterion are based on the decomposition of the velocity gradient tensor into a rotational motion and shear stress.
- In the last few years the consideration of shear in the identification of vortex structure regions gained the attention of research, as higher shear was identified as a critical factor in the identification of vortex structures.

One of the latest criteria, which is considering the effects of shear in the vortex identification, is the approach of Kolář [6]. His triple decomposition method is an extension of the traditional double decomposition of the velocity-gradient tensor ∇u into a symmetric (Ω) and an antisymmetric (S) part.

The motivation for the triple decomposition is the fact that vorticity cannot distinguish between pure shearing motion and vortical motion, and strain rate cannot distinguish between straining motion and shearing motion. The advantage of a triple decomposition of the velocity-gradient tensor compared to a double decomposition is the inclusion of pure shearing motion as one of the elementary motions of a fluid element.

The outcome of the triple decomposition of the velocity-gradient tensor is $\nabla u = S_{RES} + \Omega_{RES} + (\nabla u)_{SH}$, where the term $(\nabla u)_{SH}$ represents the pure shearing motion, the term S_{RES} represents the new strain-rate tensor which neglects the portion of strain rate effected by shear and the last term Ω_{RES} represents the new vorticity tensor which neglects the portion of vorticity effected by shear.

The new vortex identification criterion based on the outcome of the triple decomposition of the velocity-gradient tensor is related to the vortex identification by vorticity strength in the double decomposition. The newly determined scalar for vortex identification is called ω_{RES} and represents the corrected vorticity. The new criterion is Galilean invariant, it requires no thresholds and the magnitude of the scalar represents the strength of the rotational motion of a fluid element.

Although the influence of high-shear regions in the identification of vortex structure regions is a currently discussed topic in flow field analysis, the understanding of it is still not clear. Hence it is necessary to analyze the effects of shearing on vortex structure identification and vortex dynamics.

2.2   Shear Layer Structures

One of the main characteristics of shear-layer structures is that shear regions are also regions of high vorticity, comparable to vortex structures. Although most studies of flow-field features are based on vortex-structure analysis due to their importance for fluid dynamics, the significance of shear layers on vortex dynamics is not negligible. Shear layers are of interest, for example in vortex generation, vortex-vortex interaction, vortex-shear layer interaction, but also in the understanding of vortex structures and their identification in flow fields.

The main Eulerian shear layer identification criteria are also based on the double decomposition of the velocity gradient tensor ∇u.

As shear layer regions are defined as regions of high strain, the identification of shear layers is based on the strain-rate tensor S, the symmetric part of ∇u. In order to identify a shear layer, it is preferable to compute a scalar value that represents the strength of the strain. One of the most important criteria is the Q criterion, i.e., the second invariant of the velocity gradient tensor, which is typically used for the identification of vortex regions, but can also be used to identify areas of high shear stress. It determines if a point of a flow field is dominated by rotation, i.e., $\|\Omega\| > \|S\| \rightarrow Q > 0$, or by strain, where $\|\Omega\| < \|S\| \rightarrow Q < 0$. Hence it follows that a point is identified as part of a shear layer if $Q < 0$, where the norm stands for the Frobenius norm of Ω and S with $\|\Omega\| = \sqrt{\sum_{i,j=1}^{n} |\Omega_{ij}|^2}$ and $\|S\| = \sqrt{\sum_{i,j=1}^{n} |S_{ij}|^2}$, respectively.

Another method was proposed by Haimes et al. [2], where an eigenvalue analysis of the strain-rate tensor is applied. Since S is symmetric and positive, it has always three real eigenvalues $(\lambda_{S1}, \lambda_{S2}, \lambda_{S3})$. The vector formed by the eigenvalues of S defines the principal axis of deformation and the norm of the second principal invariant is used as a measure of the shear. According to Haimes et al. [2], the rate of shear stress is defined by:

$$S_H = \sqrt{\frac{(\lambda_{S1} - \lambda_{S2})^2 + (\lambda_{S1} - \lambda_{S3})^2 + (\lambda_{S2} - \lambda_{S3})^2}{6}}. \tag{1}$$

In this work, we use the criterion by Haimes et al. [2] since the criterion works directly on the shear stress tensor and the outcome is a measure for the strength of shear stress on a fluid element.

Each of the criteria, Q and S_H, is at least Galilean invariant. Furthermore, the criterion of Haimes et al. [2] is also rotational invariant in contrast to the Q criterion, where the result depends on the orientation of the reference frame (for more detailed information see [3]). Another disadvantage of the Q criterion consists of its exclusive behaviour, i.e., either a region is detected as a vortex or as shear layer. Thus, the criterion decides which of both features, the vortex strength or the strain, dominates at a point inside the flow. In our opinion, this makes the Q criterion actually insufficient for the temporal exploration of shear layers, since they might undergo a roll-up process in order to activate the generation of new vortices. This makes it necessary to know both values, especially at points where both quantities are simultaneously present.

3   Identification of Vortex Generation in a Shear Layer

The present investigations are based on the results of a two-dimensional direct numerical simulation of a subsonic mixing layer behind a flat plate [1]. The analyzed case is isothermal with the Mach numbers $Ma_I = 0.8$ for the upper and $Ma_{II} = 0.2$ for the lower stream. The ratio of the streamwise velocities is $U_I/U_{II} = 4$ and the temperatures of both streams are $T = 280K$. The Reynolds number $Re = 1000$ is based on the inflow velocity of the upper stream U_I and the displacement thickness $\delta_{1,I}$ of the upper stream at the inflow. All quantities are normalized with the displacement thickness at the inflow of the upper stream $\delta_{1,I}$ and the the according inflow velocity U_I.
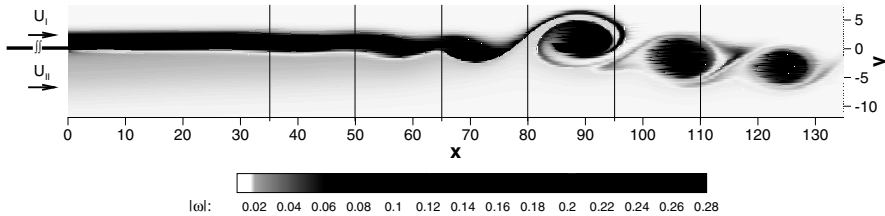
Fig. 1. Snapshot of the vorticity field of the 2D mixing layer behind a flat plate with $\frac{U_I}{U_{II}} = 4$.

The wake of the plate consists of two shear layers of opposite sign, cf. figure 1. The upper one, which is stronger starts to roll-up into vortices at $x \approx 60$. Another observation is the merging of back-to-back vortex structure pairs at $x > 80$. The problem with vorticity, used in figure 1, is that it cannot distinguish between vortices and shear layer.

For that purpose we use the methods introduced above, namely λ_2 for vortex and S_H for shear-layer identification. According results for the snapshot in figure 1 are shown in figures 2a and 2b, respectively.

The shear layer identification in figure 2a shows how the strong upper shear layer disappears further downstream (note the obvious contrast to the vorticity in figure 1).
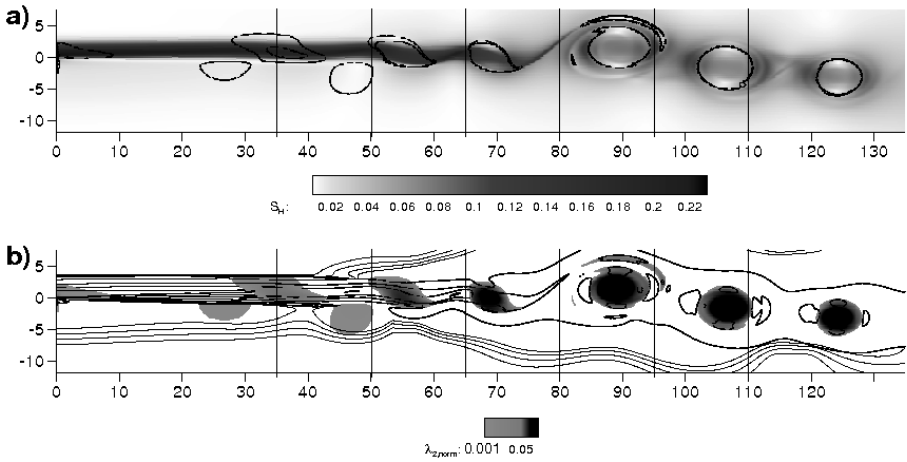
Fig. 2. Visualization of a two-dimensional flow field downstream a flat plate. (a) Shear layer visualisation with the approach of Haimes and display of vortex structures (lines), (b) λ_2 (black regions: $\lambda_2 < 0.05 * (\lambda_2)_{min}$; grey regions: $0.05 * (\lambda_2)_{min} < \lambda_2 < 0.001 * (\lambda_2)_{min}$ and shear layers (black lines: S_H values between 0.03 and 0.27; grey lines: S_H values between 0.006 and 0.012.

Inside the vortices, especially as they grow in strength, the shear develops a local minimum. This has to be expected because a solid-body rotation in the vortex cores should be shear-free. At the same time new shear is generated by friction at the edges of the detected vortices and around them. This kind of behaviour has already been observed earlier in the analysis of isolated vortices [4].

The present example also reveals the dependence of the results on the chosen threshold. To show this, we have considered two different λ_2 thresholds in figure 2b. However, they indicate that the identification of the strong vortices in the downstream part of the domain is independent of the chosen threshold. But the identification of the first occurrence of a vortex is strongly threshold dependent. It may happen directly at $x = 0$ or at any position further downstream, such that an objective definition is not possible.

For the purpose of a better understanding and as a possible parameter for the identification of vortex formation in the present scenario we consider the amplification of the fundamental disturbance and its higher harmonics in figure 3 (obtained from a Fourier analysis of the flow field). This decomposition allows to identify the emergence of the first structures out of very-small-amplitude instabilities. Initially, the fundamental frequency dominates as this one is the most unstable in the upstream boundary layer. As the wake of the flat plate is encountered beyond $x = 0$ the most unstable frequency shifts to a three times higher value, cf. [1]. This is why the second harmonic $(3 \cdot f_0)$ grows faster there. At $x \approx 50$ all modes of the disturbance spectrum finally saturate. This coincides with the formation of the first observable local vorticity maximum within the shear layer in figure 1. The distance of the ensuing individual vortices perfectly agrees with the wave length of the according shear layer instability, i.e. the second higher harmonic.
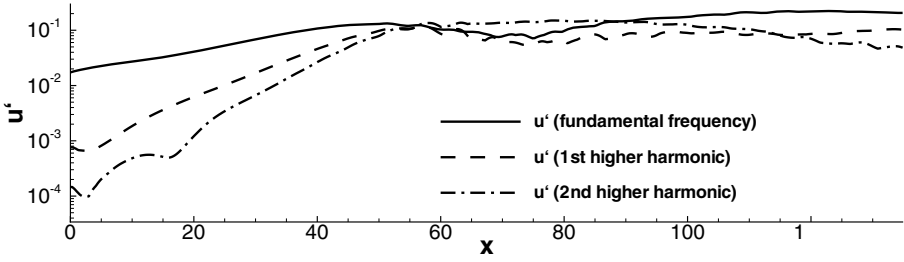
Fig. 3. Maximum amplitude of the streamwise velocity u' downstream of the flat plate. The fundamental frequency and the two higher harmonics of the fundamental frequency are plotted.
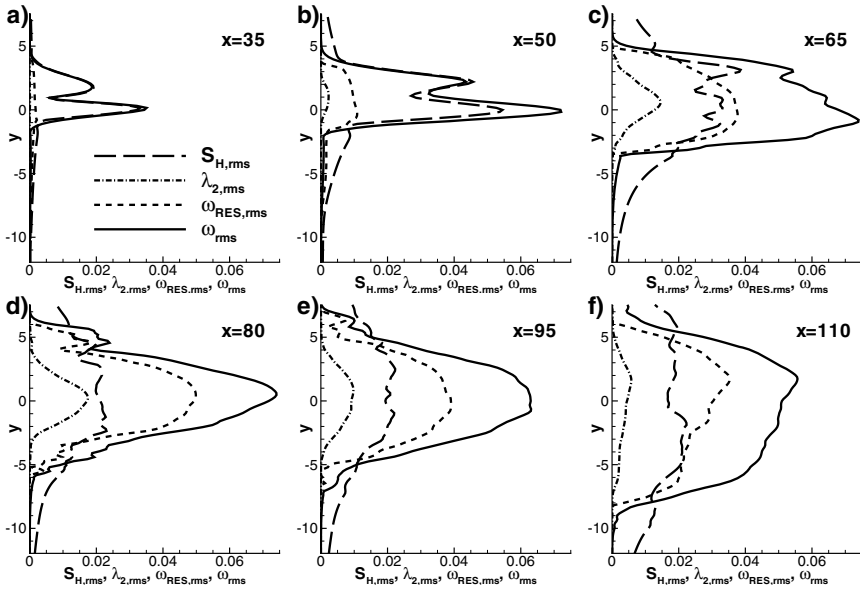
Fig. 4. Visualisation of streamwise evolution of vorticity, shear, residual vorticity and λ_2 based on the amplitudes of ω_{rms}, S_{rms}, $\omega_{RES,rms}$ and $\lambda_{2,rms}$ at different x-positions designated in figures 1, 2 and 5.

A change occurs around $x \approx 87$ where the fundamental frequency supersedes the second harmonic again. This can be associated to the vortex pairing between neighbouring vortices in the instantaneous pictures. Note that the fundamental herewith becomes a subharmonic of the second harmonic. The consideration of figure 3 confirms that the emergence of vortices from the free shear layer is a continuous process that starts at very low amplitudes such that the threshold-sensitivity of the vortex identification scheme is not a failure of the latter but rather a true consequence of the underlying physics.
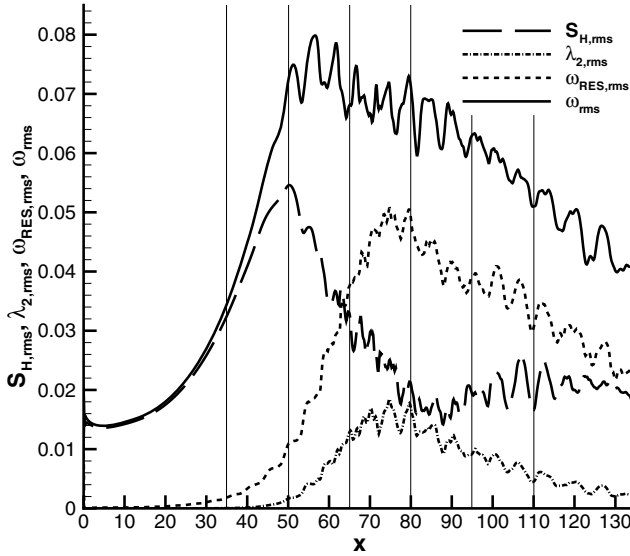
Fig. 5. Visualisation of streamwise evolution of vorticity, shear, residual vorticity and λ_2 based on the amplitudes of ω_{rms}, S_{rms}, $\omega_{RES,rms}$ and $\lambda_{2,rms}$ at $y = 0$

In figures 4 and 5 we discuss the streamwise evolution of vorticity ω, shear S_H, residual vorticity ω_{RES}, and $-\lambda_2$ further. The idea is to show the interplay between vorticity, shear and vortical motion from the initial formation of vortices until the beginning of the pairing stage. For these plots the mean flow has been subtracted and the fluctuation amplitudes are shown as root-mean-square (*rms*) values. A similar analysis could be performed for instantaneous data but here we confine ourselves to the average.

Figure 4 presents vertical cuts through the data at $x = const$ while figure 5 follows the amplitudes at $y = 0$ in streamwise direction. Initially, vorticity and shear are identical and the vortex criteria remain at negligible values, which confirms our statements made further above. The first vertical cut shown in figure 4a clearly depicts the amplitude of a shear-layer instability. At the next station, the shear maximum at $y = 0$ starts to decrease with respect to vorticity. As the vortex criteria start to grow at the same time, we see that the emergence of vortices has started now. At $x = 65$ a changeover takes place: shear S_H and residual vorticity ω_{RES} become equally large. This corresponds to the emergence of a clear vorticity 'blob' in figure 1 and one might think about suggesting this cross-over point as a possible unbiased criterion for the first occurrence of a vortex out of a shear layer. What follows is a dominance of the residual vorticity over shear inside the mixing layer which indicates that the latter has been split into vortices. The widening of the mixing layer in y-direction and the continuous decrease of the maxima further downstream is due to the averaging process when computing the *rms* over many individual vortices. A second increase of the shear maximum after $x \approx 80$

can be attributed to the generation of new shear layers that surround the individual vortices which has already been mentioned in connection with figure 2a. An additional growth occurs in-between neighbouring vortices before they merge because of the high friction there. This contributes to the increase of $S_{H,rms}$ as well.

4 Conclusion

Although the focus of research was on vortex structures for decades, discussions about the importance of shear regions in the identification of vortex structures revealed the relevance of shear in the understanding of the vortex dynamics and flow field analysis. As shown in section 2.2 it is possible to define an additional type of coherent structure, in this case the coherence is based on shear. The example in section 3 shows the importance of shear layer structures in the formation of new vortex structures, hence the mechanism is a roll-up of the shear layers caused by instabilities. Thus, the formation of a vortex structure is a successive process, the additional observation of shear layers and the amplification of shear layer instabilities in the analysis of vortex formation, as shown in figures 4 and 5, is a promising method in the investigation of vortex dynamics and yields deeper insights into the dynamics of vortex formation out of a shear layer and the further development of these vortices, as the observations are based on a threshold independent method. Our next step will be a more detailed analysis of vortex merging using the methods presented here.

Acknowledgments

References

[1] Babucke, A., Kloker, M., Rist, U.: Numerical Investigation of Flow-Induced Noise Generation at the Nozzle End of Jet Engines. Notes on Numerical Fluid Mechanics and Multidisciplinary Design 96, 413–420 (2006)

[2] Haimes, R., Kenwright, D.: On the Velocity Gradient Tensor and Fluid Feature Extraction. In: Proc. AIAA 14th Computational Fluid Dynamics Conference, pp. 3288–3297 (1999)

[3] Haller, G.: An Objective Definition of a Vortex. Journal of Fluid Mechanics 525, 1–26 (2005)

[4] Hauser, M.: Untersuchungen zur Interaktion von Scherschichten und Wirbeln. Diploma Thesis, Universität Stuttgart (2006)

[5] Jeong, J., Hussain, F.: On the Identification of a Vortex. Journal of Fluid Mechanics 285, 69–94 (1995)

[6] Kolář, V.: Vortex Identification: New Requirements and Limitations. International Journal of Heat and Fluid Flow 28, 638–652 (2007)

Global Stability Analysis of Compressible Flow around Swept Wings

Christoph J. Mack[1,2], Peter J. Schmid[1], and Jörn Sesterhenn[2]

[1] Laboratoire d'Hydrodynamique (LadHyX), CNRS-École Polytechnique,
91128 Palaiseau cedex France
[2] Department of Numerical Mathematics (LRT1), Universität der Bundeswehr (UniBw),
Werner-Heisenberg-Weg 39, D-85577 München, Germany

Summary

The global linear stability of compressible flow in the leading-edge region of a swept wing is studied using an iterative eigenvalue method. This method was implemented via a Jacobian-free framework where direct numerical simulations provide computed flow fields as the required input. It has been found that the investigated leading-edge flow is, over a selected range of flow parameters, most unstable to instabilities of the crossflow type. Our results further confirm that convex leading-edge curvature has a stabilizing influence on this flow.

1 Introduction

A thorough understanding of compressible flow around swept wings is essential for the aerodynamic design of high-performance aircraft. In particular, the details of the transition process from laminar to turbulent fluid motion, which causes an increase in drag and a loss of flight performance, play a major role in the description of this flow. Four types of instability mechanisms have been suggested to trigger transition: the amplification of perturbations in the swept attachment-line boundary layer, denoted as *attachment-line* instabilities, the amplification of crossflow vortices in the three-dimensional boundary layer downstream of the attachment line, known as *crossflow* instabilities, *streamwise* instabilities (Tollmien-Schlichting waves) in the boundary layer even further downstream and the amplification of vortices over concave surfaces, denoted as *centrifugal* instabilities (see, e.g., [1, 2]). Above a critical sweep angle, this transition process is dominated by attachment-line and crossflow instabilities in the leading-edge region [3], where convex curvature is known to have a stabilizing effect on the flow [1, 4]. Hence, sweep and leading-edge curvature play an important role for the stability of flow around a swept wing, and it is the focus of this investigation to study the influence of convex leading-edge curvature on the global stability of the flow.

The need for a global stability approach stems from the fact that, owing to the three-dimensional character of swept leading-edge flow, a separation of the wall-normal and the chordwise direction is not possible. Furthermore, attachment-line and crossflow

instabilities are known to coexist in the leading-edge region under realistic conditions and, thus, have to be treated simultaneously. This has been recently confirmed by Mack *et al.* [5] who established a connection between the two instability mechanisms by presenting a combination mode whose amplitude distribution exhibits typical characteristics of both attachment-line and crossflow modes. The necessity of a global approach combined with a rather large computational domain leads to a large-scale stability problem which requires the application of iterative techniques [6, 7]. Among these techniques, Krylov methods have been successfully applied to study the hydrodynamic stability of incompressible (e.g. [7, 8]) as well as compressible flows (e.g. [5]).

1.1 Flow Configuration

Our investigations are based on the flow configuration displayed in Fig. 1b, where the leading-edge region of a wing (see Fig. 1a in dark grey) was modeled by a parabolic body of infinite span. The flow model further consists of a three-dimensional body-fitted grid (in grey) mapped about this parabolic body; the local Cartesian coordinate system is given by the x-direction, the y-direction and the spanwise z-direction pointing along the attachment line, and the local parabolic coordinate system consists of the chordwise ξ-direction and the normal η-direction. The leading-edge radius of the parabolic body is denoted by R. The incoming flow impinges on the body with a velocity q_∞ and sweep angle Λ yielding a sweep velocity w_∞; a zero angle of attack is considered.
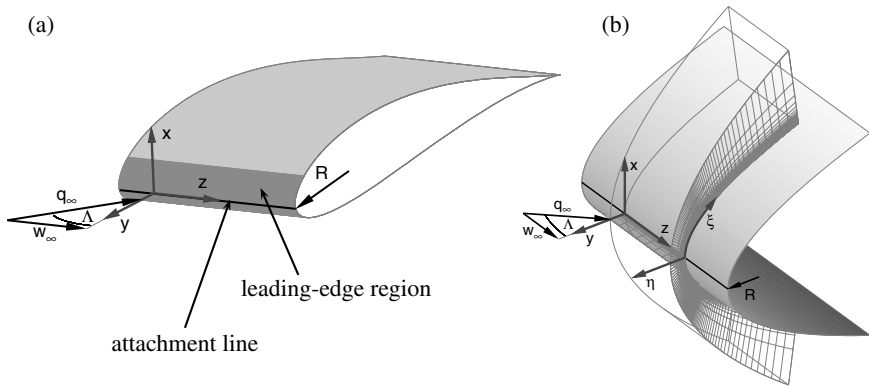
Fig. 1. (a) Sketch of a swept wing showing the attachment line (in black), the leading-edge region (in dark grey), the incoming velocity q_∞ and the sweep angle Λ yielding a sweep velocity w_∞ as well as the local Cartesian coordinate system. (b) Sketch of our three-dimensional flow model displaying the relevant flow parameters, the coordinate systems and the grid-point distribution.

We define a viscous length scale $\delta = (\nu/S)^{1/2}$, a sweep Reynolds number $Re_s = w_\infty \delta/\nu$ and $Ma_s = w_\infty/c_\infty$ with ν, S and c_∞ as the kinematic viscosity, the strain rate at the wall and the speed of sound, respectively. Alternatively, this Reynolds

number Re_s can be reformulated to show an explicit dependence on the leading-edge radius R and the sweep angle Λ

$$Re_s = \left(\frac{v_\infty R}{2\nu}\right)^{1/2} \tan \Lambda, \tag{1}$$

where v_∞ is the wall-normal velocity [4].

1.2   Governing Equations and Numerical Method

The flow is governed by the compressible Navier–Stokes equations, the equation of state for a perfect gas, Fourier's law for the thermal conductivity and Sutherland's law (at ambient conditions) for the viscosity. A constant specific heat ratio $\gamma = 1.4$ and constant Prandtl number $Pr = 0.71$ is considered. The equations are formulated based on pressure p, Cartesian velocities (u, v, w) and entropy s, and are solved on a time-dependent, curvilinear and non-uniformly distributed grid, with a clustering of grid points towards the wall as well as in the leading-edge region, as displayed in Fig. 1b.

In the wall-normal direction, the computational domain is bounded by a detached unsteady bow shock which is incorporated via a shock-fitting mechanism. Along the surface of the body no-slip boundary conditions and adiabatic wall conditions are applied. At the chordwise edges of the computational domain, non-reflecting outflow conditions are imposed, and, under the assumption of infinite span, periodic boundary conditions are used in the z-direction.

Our computations are based on direct numerical simulations (DNS), where the governing equations are solved using a characteristic-type formulation [9]. Within this formulation, the convective terms of the equations are discretized employing a fifth-order compact upwind scheme, and the dissipative and diffusive parts are computed via a sixth-order central compact scheme (see [5, 10] for details on the implementation of the direct numerical simulation).

2   Global Stability Analysis

The complexity of our flow configuration requires us to compute the steady state $\phi_0(x, y, z) = (p_0, u_0, v_0, w_0, s_0)^T$ prior to the subsequent global stability analysis. For this reason, direct numerical simulations are performed to integrate the governing equations in time, and, due to the assumption of periodicity in the spanwise z-direction, a two-dimensional base flow $\phi_0(x, y)$ is sought. Furthermore, since $\phi_0(x, y)$ is stable to two-dimensional perturbations, a simple time-integration based on a Runge-Kutta method can be used to compute it. As an example, the obtained base flow for $Re_s = 800$ as well as selected profiles of the spanwise velocity w, which illustrate the boundary-layer growth in the chordwise ξ-direction, are displayed in Fig. 2.

Applying linear stability theory, a three-dimensional small-amplitude perturbation field $\epsilon\phi' = \epsilon(p', u', v', w', s')^T$ is superimposed onto this base flow.

$$\phi(x, y, z, t) = \phi_0(x, y) + \epsilon\phi'(x, y, z, t) \tag{2}$$
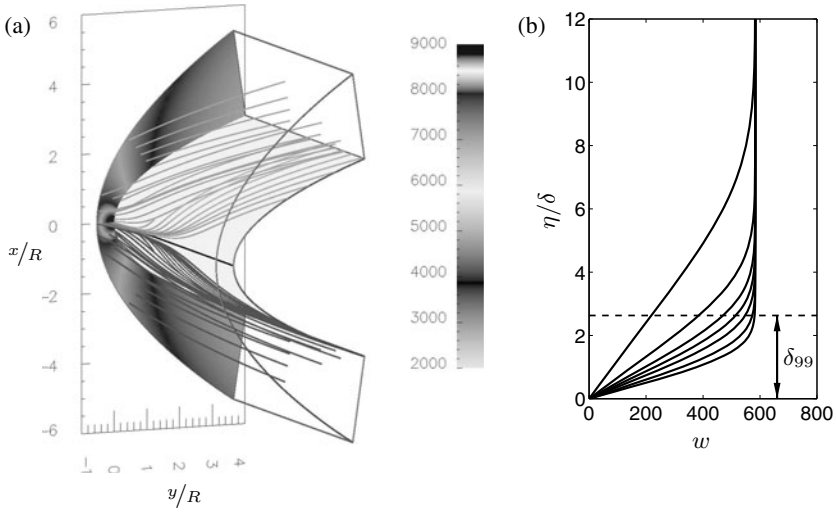
Fig. 2. (a) Streamlines (in grey) and pressure field [in Pa] of the computed steady base flow for $Re_s = 800$ and $Ma_s = 1.25$; a leading-edge radius of $R = 0.1 = 508\delta$ [in m], where $\delta = 1.97 \cdot 10^{-4}$ m, has been used. The resolution is 128×255 points in the normal η-direction and the chordwise ξ-direction, respectively (attachment line in black). (b) Spanwise velocity w at selected positions in the positive ξ-direction; δ_{99} denotes the thickness of the boundary layer along the attachment line.

For the global stability approach, we assume the disturbance field $\phi'(x, y, z, t)$ of the form

$$\phi'(x, y, z, t) = \widetilde{\phi}(x, y)\mathrm{e}^{\mathrm{i}(\beta z - \omega t)}, \tag{3}$$

where $\widetilde{\phi}(x, y)$ and β denote the complex amplitude and the real spanwise wavenumber of the perturbation, respectively, and $\omega = \omega_r + \mathrm{i}\omega_i$ represents its temporal long-term evolution. After an appropriate discretization in space, the discrete global stability problem can then formally be written as

$$\omega \, \widetilde{\phi} = \mathbf{J}(\phi_0) \, \widetilde{\phi}, \tag{4}$$

where $\mathbf{J}(\phi_0)$ represents the $n \times n$ linear stability matrix (the Jacobian matrix), i.e. the discretized Navier–Stokes equations linearized about the (discrete) basic state ϕ_0; $n = 5n_\xi n_\eta$ is the dimension of the eigenvalue problem with n_ξ and n_η as the number of grid points in the chordwise ξ- and the normal η-direction, respectively. For large-scale stability problems, the direct solution of this eigenvalue problem is prohibitively expensive, and iterative solution techniques have to be employed to extract pertinent stability information (see, e.g., [7] for a discussion on the solution of global eigenvalue problems).

2.1 DNS-Based Krylov Technique

The algorithm to accomplish this task is the implicitly restarted Arnoldi method (IRAM), a Krylov subspace technique presented by Sorensen [11]. This method constructs an orthonormal basis $\mathbf{V}_m = [\mathbf{v}_1, \mathbf{v}_2, \ldots, \mathbf{v}_m]$ of the Krylov subspace $\mathcal{K}_m(\phi', \mathbf{J}(\phi_0))$ which is then used to decompose the stability matrix $\mathbf{J}$ in the following way:

$$\mathbf{J}\mathbf{V}_m = \mathbf{V}_m\mathbf{H}_m + \mathbf{f}_m\mathbf{e}_m^T. \tag{5}$$

Herein, $\mathbf{H}_m$ denotes an m-dimensional upper Hessenberg matrix (with $m \ll n$), $\mathbf{f}_m$ is the residual vector orthogonal to the basis $\mathbf{V}_m$, and $\mathbf{e}_m$ represents a unit-vector in the m-th component.

The eigenvalues $\{\theta_j\}$ of the Hessenberg matrix $\mathbf{H}_m$, the so-called Ritz values, are approximations of the eigenvalues $\{\lambda_j\}$ of the matrix $\mathbf{J}$, and the associated eigenvectors $\widetilde{\mathbf{x}}_j$ of $\mathbf{J}$, the so-called Ritz vectors, can be calculated using the orthonormal basis $\mathbf{V}_m$ as

$$\widetilde{\mathbf{x}}_j = \mathbf{V}_m\mathbf{y}_j, \tag{6}$$

where $\mathbf{y}_j$ denotes the eigenvector of $\mathbf{H}_m$ associated with the eigenvalue θ_j. In general, some of the Ritz pairs $(\widetilde{\mathbf{x}}_j, \theta_j)$ closely approximate the eigenpairs $(\widetilde{\phi}_j, \omega_j)$ of $\mathbf{J}$, and the quality of this approximation usually improves as the dimension m of the Krylov subspace sequence $\mathcal{K}_m$ increases. In order to avoid memory problems and numerical errors as m increases, the Arnoldi method is implicitly restarted from the k desired Ritz pairs (see [11] for details).

This class of subspace techniques benefits from the fact that they only require the action of the Jacobian matrix $\mathbf{J}(\phi_0)$ onto a given velocity field ϕ'. These matrix-vector products can readily be obtained from direct numerical simulations via

$$\mathbf{J}(\phi_0)\phi' \approx \frac{\mathbf{F}(\phi_0 + \epsilon\phi') - \mathbf{F}(\phi_0)}{\epsilon}, \tag{7}$$

where ϵ is a user-specified parameter, chosen as $||\epsilon\phi'||/||\phi_0|| = \epsilon_0 = 10^{-8}$, and $\mathbf{F}$ represents the discretized right-hand side of the nonlinear Navier–Stokes equations. This first-order finite-difference approximation allows a Jacobian-free framework where right-hand side evaluations from direct numerical simulations (DNS) provide the input for the iterative stability solver. For a detailed description of this DNS-based Krylov technique including a discussion on the choice of the parameter ϵ_0 see [12].

3   Results

The DNS-based global stability solver was employed to investigate the global stability of computed base flows for selected sweep Reynolds numbers Re_s. The remaining flow parameters are $Ma_s = 1.25$ and $T_w = 728K$ (adiabatic wall), and selected values for the disturbance wave number $\beta = 2\pi/L_z$ were used, with L_z as the fundamental length scale, non-dimensionalized by δ, in the spanwise z-direction; the resolution was 128×255 points in the normal η- and the chordwise ξ-direction, respectively. For the implicitly restarted Arnoldi method $m = 90$, $k = 36$ and a tolerance $tol = 10^{-4}$ have been identified as an efficient choice.

3.1   Spectrum and Global Modes

The investigated flow configuration comprises a multitude of physical processes which will be reflected in the full global spectrum. Mack *et al.* [5] found that shear modes which express the flow characteristics in the three-dimensional boundary layer are most unstable to three-dimensional perturbations for the sweep Reynolds number $Re_s = 800$. Their computed discrete eigenvalues for the disturbance wave numbers $\beta = 0.105$, 0.143, 0.224, 0.262 and 0.314 are shown in Fig. 3b. These eigenvalues appear double, which is a consequence of the symmetry of the flow, and represent the most unstable part of the particular global spectrum. The associated eigenfunctions $v(x, y, z) = \text{Real}\{\widetilde{v}(x, y)\,(\cos \beta z + \mathrm{i}\sin \beta z)\}$ of the three depicted eigenvalues of the $\beta = 0.105$ branch (B1,B2,B3) are displayed in Fig. 3a.
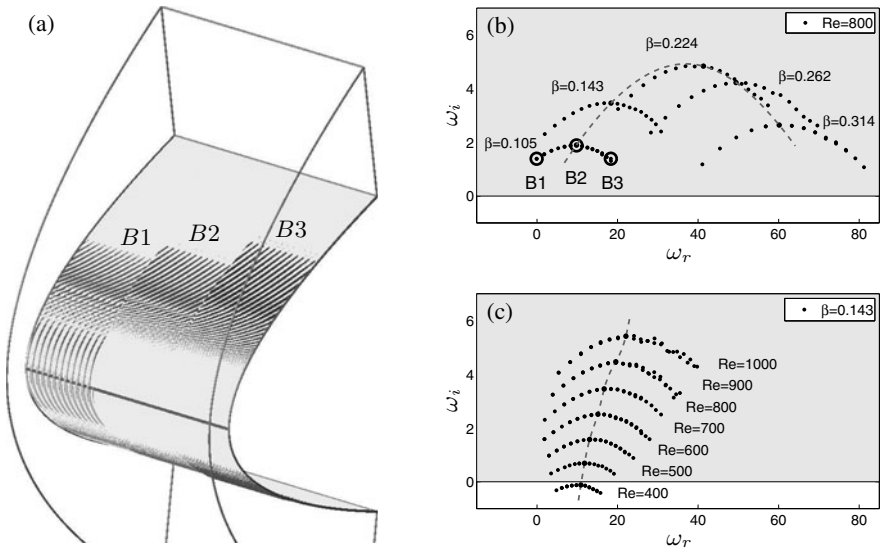
Fig. 3. Results from the global stability analysis: (b) most unstable eigenvalues of the temporal global spectrum for selected values of β (ω_r describes the frequency and ω_i the corresponding growth rate of the perturbation, unstable half-plane in grey); (a) three associated global modes for $\beta = 0.105$ displaying the velocity distribution $v(x, y, z) = \text{Re}\{\widetilde{v}(x, y)\,(\cos \beta z + \mathrm{i}\sin \beta z)\}$ of three eigenvalues depicted in (b). The normalized eigenfunctions are plotted using iso-surfaces with a value of $10^{-2}\, v_{max}$. (c) Temporal spectra for selected values of the sweep Reynolds number Re_s and $\beta = 0.143$. The dashed line in (b) and (c) indicates the evolution of the maximum growth rate.

The slowest-moving global mode (see Fig. 3a, B1) constitutes a combination mode which reveals the same connection between attachment-line instabilities and crossflow vortices as the combination mode (for $\beta = 0.314$) presented in [5]. Its amplitude distribution also exhibits a two-dimensional attachment-line structure while connecting to

the crossflow pattern, known as co-rotating vortices that nearly align with the external streamlines, further downstream from the leading edge of the wing. Fig. 3a additionally displays the most unstable (B2) as well as a fastest-moving global mode (B3). Fig. 3a further shows that faster moving global modes exhibit a more pronounced crossflow component and the dominant part of the global mode lies further downstream from the stagnation line which is in accordance with the findings in [5].

The global boundary-layer modes for $\beta = 0.105$ shown in Fig. 3b feature a disturbance frequency ω_r ranging from -0.091 to 18.3, where the maximum growth rate $\omega_i = 1.90$ is achieved for a frequency $\omega_r = 9.80$. This maximum growth rate increases as β is increased before decaying again, and in their parametric study, Mack *et al.* [5] obtained a maximum modal growth for a spanwise wavenumber of $\beta = 0.213$. In general, the rather large growth rates of the boundary-layer modes can be explained by the inflectional nature of the crossflow instability, since instabilities based on inflectional profiles can be inviscidly unstable.

3.2   Influence of Re_s

The influence of the sweep Reynolds number Re_s on the global stability of the flow is demonstrated in Fig. 3c, and, as expected, a stabilizing effect of convex surface curvature was obtained as Re_s is decreased from 1000 to 400. This observation is in accordance with the experimental findings in [1] and the theoretical studies on the effect of leading-edge curvature in [4]. Our results also indicate that the frequency ω_r of the computed unstable global modes of the crossflow type decreases as Re_s is decreased (see Fig. 3c, dashed line).

4   Conclusions

A DNS-based global stability solver was successfully applied to assess the global spectrum of compressible flow in the leading-edge region of a swept wing modeled by a parabolic body. It was found that, for the investigated parameter choices, boundary-layer modes of the crossflow type characterize the dominant instability mechanism, and convex surface curvature has a stabilizing effect on them. A combination mode displaying the typical features of both local crossflow vortices and local attachment-line instabilities was computed which is in accordance with the findings in [5]. In summary, it was shown that global stability analysis in conjunction with DNS-based Krylov techniques is capable of addressing the global stability of complex flow problems.

Acknowledgments

References

[1] Bippes, H.: Basic experiments on transition in three-dimensional boundary layers dominated by crossflow instability. Prog. Aero. Sci. 35, 363–412 (1999)

[2] Saric, W.S., Reed, H.L., White, E.B.: Stability and transition of three-dimensional boundary layers. Annu. Rev. Fluid Mech. 35, 413–440 (2003)

[3] Schlichting, H., Gersten, K.: Boundary Layer Theory. Springer, Heidelberg (2000)

[4] Lin, R.S., Malik, M.R.: On the stability of attachment-line boundary layers. Part 2. The effect of leading edge curvature. J. Fluid Mech. 333, 125–137 (1997)

[5] Mack, C.J., Schmid, P.J., Sesterhenn, J.L.: Global stability of swept flow around a parabolic body: connecting attachment-line and crossflow modes. J. Fluid Mech. 611, 205–214 (2008)

[6] Theofilis, V., Fedorov, A., Obrist, D., Dallmann, U.C.: The extended Görtler-Hämmerlin model for linear instability in the three-dimensional incompressible swept attachment line boundary layer. J. Fluid Mech. 487, 271–313 (2003)

[7] Theofilis, V.: Advances in global linear instability analysis of nonparallel and three-dimensional flows. Prog. Aero. Sci. 39, 249–315 (2003)

[8] Edwards, W.S., Tuckerman, L.S., Friesner, R.A., Sorensen, D.C.: Krylov Methods for the Incompressible Navier-Stokes Equations. J. Comput. Phys. 110, 82–102 (1994)

[9] Sesterhenn, J.: A characteristic-type formulation of the Navier-Stokes equations for high-order upwind schemes. Comput. Fluids 30, 37–67 (2001)

[10] Le Duc, A., Sesterhenn, J., Friedrich, R.: Instabilities in compressible attachment-line boundary layers. Phys. Fluids 28, 044102 (2006)

[11] Sorensen, D.C.: Numerical methods for large eigenvalue problems. Acta Numer. 11, 519–584 (2002)

[12] Mack, C.J., Schmid, P.J.: A preconditioned Krylov technique for global hydrodynamic stability analysis of large-scale compressible flows. J. Comput. Phys. 3, 541–560 (2010)

Applications of Symmetry Analysis
in Stability Theory

Andreas Nold[1], Martin Oberlack[1], and Alexei F. Cheviakov[2]

[1] Technische Universität Darmstadt, Fachgebiet Strömungsmechanik, Gebäude S1/03,
Hochschulstraße 1, D-64289 Darmstadt, Germany
`office@fdy.tu-darmstadt.de`
`www.fdy.tu-darmstadt.de`
[2] University of Saskatchewan, Department of Mathematics and Statistics,
Room 227 McLean Hall, 106 Wiggins Road, Saskatoon, SK S7N 5E6, Canada

Summary

For decades the stability of nearly parallel shear flows was primarily analyzed employing the Orr-Sommerfeld-Equation (OSE). We show that the OSE is solely based on three symmetries of the linearized Navier-Stokes-Equation for two-dimensional perturbations. In fact, the OSE is a similarity reduction using the latter three symmetries. Though rather successful in boundary layer flows the OSE does not give proper results for the plane channel flow with the classical parabolic flow profile. For this special case we found a new symmetry. It leads to a new ansatz considerably distinct from the OSE with two new similarity variables. We analyzed the scope in which the new ansatz could be used. Finally, we derived a technique to solve the equation via the new ansatz function.

1 Introduction

We consider a parallel base flow $(U(y), 0, 0)^T$ with a two-dimensional perturbation of the form $(u(x, y), v(x, y), 0)^T$. Assume that the Navier-Stokes-Equation holds for the base flow. For the perturbated flow, we get the following set of equations:

$$\frac{\partial u}{\partial t} + U(y) \cdot \frac{\partial u}{\partial x} + v \cdot \frac{dU}{dy} + \left\{ u \cdot \frac{\partial u}{\partial x} + v \cdot \frac{\partial u}{\partial y} \right\} = -\frac{1}{\varrho} \cdot \frac{\partial p}{\partial x} + \nu \Delta u, \quad (1)$$

$$\frac{\partial v}{\partial t} + U(y) \cdot \frac{\partial v}{\partial x} + \left\{ u \cdot \frac{\partial v}{\partial x} + v \cdot \frac{\partial v}{\partial y} \right\} = -\frac{1}{\varrho} \cdot \frac{\partial p}{\partial y} + \nu \Delta v, \quad (2)$$

$$\frac{\partial u}{\partial x} + \frac{\partial v}{\partial y} = 0. \quad (3)$$

Introducing a stream function ψ with $u = \frac{\partial \psi}{\partial y}$ and $v = -\frac{\partial \psi}{\partial x}$ eliminates the continuity equation. Finally, applying the curl gives us equation (4).

$$\frac{\partial}{\partial t} \Delta \psi - \frac{d^2 U}{dy^2} \cdot \frac{\partial \psi}{\partial x} + U \cdot \frac{\partial}{\partial x} \Delta \psi + \nabla \times (\nabla \psi \cdot \Delta \psi) = \nu \Delta \Delta \psi \quad (4)$$

Mostly we will consider the linearized equation for our further considerations.

$$\frac{\partial}{\partial t}\Delta\psi - \frac{d^2 U}{dy^2} \cdot \frac{\partial\psi}{\partial x} + U \cdot \frac{\partial}{\partial x}\Delta\psi = \nu\Delta\Delta\psi \tag{5}$$

We will show how equation (5) systematically leads to the Orr-Sommerfeld-Equation using symmetry analysis. We found one additional symmetry for the parabolic channel flow. This extended set of symmetries leads to a new ansatz function different from the normal mode ansatz. The structure of the new ansatz function has some properties which could be of great interest for the stability theory of channel flows.

2   Symmetry Analysis

Symmetries are an important tool to analyze differential equations. They map the solution manifold of a DE into itself. One point symmetries can be found by means of the Lie-Algorithm [4]. With the help of symmetry analysis, solutions of DE can be found, e.g. using invariant solutions. We say that a solution of a DE is invariant with respect to a symmetry if it is mapped onto itself by this symmetry. For ordinary differential equations, the general solution can be found using symmetry analysis. In the case of partial differential equations we may for the most cases only expect to find special solutions [1, 4].

In the field of fluid mechanics experience has shown that many flows turn out to be invariant under certain symmetries. Also many classical ansatz functions turn out to be invariant under special symmetries. In particular we will show that this is the case of the ansatz leading to the Orr-Sommerfeld-Equation. The present symmetry analysis was done using the GeM package of Cheviakov [3] and the DESOLVE package of Carminati and Vu [2].

2.1   Symmetries Leading to the Orr-Sommerfeld-Equation

For general flow profiles $U(y)$, equation (5) has three symmetries with the following infinitesimals:

$$X_0 = f(x, y, t)\partial_\psi \tag{6}$$
$$X_1 = \partial_x \tag{7}$$
$$X_2 = \partial_t \tag{8}$$
$$X_3 = \psi\partial_\psi \tag{9}$$

(7) and (8) correspond to translation invariances in x-direction and time. (9) is a scaling symmetry in ψ which is a consequence of the linearity of equation (5). The symmetry (6) refers to the superposition principle of any linear DE since f is a solution of the original equation under investigation, here (5). Note that this is also always implied in the OSE. Still it will be always employed subsequently without explicitly mention any more. We formulate a general symmetry as a combination of (7)-(9): $X := \alpha X_1 + X_2 + \gamma X_3$ with $\alpha, \gamma \in \mathbb{C}$. The respective invariant solution is given by

$$\psi = f(y, x - \alpha t)e^{\gamma t} \tag{10}$$

with $f(\xi, \eta) : \mathbb{R}^2 \to \mathbb{R}$. Inserting (10) into (5) gives us

$$(U - \alpha)\frac{\partial}{\partial \eta}\Delta f + \gamma \Delta f - U'' f_\eta = \nu \Delta \Delta f. \tag{11}$$

This equation admits the scaling symmetry $\tilde{X}_1 = f\partial_f$ as well as the translation symmetry $\tilde{X}_2 = \partial_\eta$. We repeat the procedure leading to (10). We choose f to be invariant under the symmetry $\delta\tilde{X}_1 + \tilde{X}_2$ and after renaming the constants, we get an ansatz which we can write as

$$\psi = f(y)e^{i\tilde{\alpha}(x-ct)} \tag{12}$$

with $\tilde{\alpha}, c \in \mathbb{C}$. This ansatz leads directly to the Orr-Sommerfeld-Equation (13) [5, pp.424-429].

$$(U - c)\left(\frac{d^2}{dy^2} - \tilde{\alpha}^2\right) f = \frac{1}{i\tilde{\alpha}Re}\left(\frac{d^2}{dy^2} - \tilde{\alpha}^2\right)^2 f \tag{13}$$

In other words, the OSE is derived from a successive symmetry reduction of the linearized Navier Stokes Equation each time using the full set of admitted symmetries. Note that this holds true for both viscous and inviscid case and is usually referred to as normal mode or modal Ansatz.

2.2 Additional Symmetries for the Channel Flow

For an inviscid parabolic base flow of the form $U(y) = a \cdot (y + b)^2 + d$, we found one additional symmetry:

$$X_4 = (2d \cdot t - x)\partial_x - (y + b)\partial_y + t\partial_t \tag{14}$$

This symmetry does also occur in other formulations of problem (5), e.g. using velocities and pressure (3 equations) or using the stream function and pressure (2 equations).

3   The Channel Flow

3.1   Rescaling

In the present subsection we consider a parabolic channel flow of the form

$$U : [-h/2, h/2] \to \mathbb{R} \qquad y \to U_{max}\left(1 - \left(\frac{2y}{h}\right)^2\right) \tag{15}$$

with $U_{max} = -\frac{\partial p}{\partial x}\frac{h^2}{8\eta}$ where η is the dynamic viscosity (see also [6, p.183]) We define a characteristic velocity and the respective Reynolds number as

$$u_\tau^2 := -\frac{\partial p}{\partial x} \cdot \frac{h}{\varrho} \quad , \quad Re_\tau := \frac{u_\tau h}{\nu}, \tag{16}$$

where ν is the kinematic viscosity. We rescale the variables with

$$\tilde{x}_i := x_i \cdot \frac{2}{h} \qquad , \qquad \tilde{u}_i := u_i \cdot \frac{1}{U_{max}} \tag{17}$$

$$\tilde{p} := p \cdot \frac{1}{\varrho U_{max}^2} \qquad , \qquad \tilde{t} := t \cdot Re_\tau \frac{u_\tau}{4h} \qquad , \qquad \tilde{\psi} := \psi \cdot \frac{2}{U_{max} h}. \tag{18}$$

Then, equation (4) and (5) hold for the dimensionless variables. In place of ν, we then write $1/Re$, where Re is the Reynolds number $Re = \frac{U_{max} \cdot h}{2\nu}$. The base flow transforms to $U : [-1, 1] \to \mathbb{R}$ with

$$\tilde{U}(\tilde{y}) = 1 - \tilde{y}^2. \tag{19}$$

We see that the dimensionless time $\tilde{t}$ is obtained by multiplication of t with the Reynolds number Re_τ. Hence the gradient $\partial/\partial t$ scales with the Reynolds number. Thus for a possibly unstable flow the instability grows faster for high Reynolds numbers.

Henceforth, we will just work with the dimensionless formulation and all tildes will be omitted.

3.2 Invariant Solution

We consider equation (5) in the inviscid case ($\nu = 0$) with the base flow $U : [-1, 1] \to \mathbb{R} : y \to 1 - y^2$. This equation has the Lie-Point-Symmetries X_1, X_2, X_3 and X_4 (see (6)-(9) and (14)). We thus can formulate the following general symmetry

$$X := \alpha \partial_x + \delta \partial_t + \beta \psi \partial_\psi + \gamma((2t - x)\partial_x - y\partial_y + t\partial_t) \tag{20}$$

The case $\gamma = 0$ is not interesting for us as it is treated in the Orr-Sommerfeld-Equation. Hence we rescale X such that $\gamma = 1$. All invariant solutions ψ of (5) with $\nu = 0$ respective to (20) are of the following form:

$$\xi := (t + \delta)(x - t + \delta - \alpha) \tag{21}$$

$$\eta := y(\delta + t) \tag{22}$$

$$\psi := (\delta + t)^\beta f(\xi, \eta) \tag{23}$$

with $f : \mathbb{R}^2 \to \mathbb{R}$. Inserting ansatz (21)-(23) into equation (5) gives us the linear PDE of third order (24)

$$\left((\xi - \eta^2) \frac{\partial}{\partial \xi} + \eta \frac{\partial}{\partial \eta} + (2 + \beta) \right) \Delta f + 2 \frac{\partial f}{\partial \xi} = 0. \tag{24}$$

This equation has no further symmetries except the scaling symmetry in f. In the sequel, we analyze solutions which are invariant under (20) and present ways to find solutions which fulfill the boundary conditions of the channel flow.

3.3 Interpretation of Invariant Solution

Suppose we have a solution ψ which is invariant under symmetry (20). Then, the two velocities u and v can be written as

$$u = \frac{\partial \psi}{\partial y} = (\delta + t)^{\beta+1} \frac{\partial f}{\partial \eta} \tag{25}$$

$$v = -\frac{\partial \psi}{\partial x} = -(\delta + t)^{\beta+1} \frac{\partial f}{\partial \xi} \tag{26}$$

where ξ and η are defined in (21) and (22). We search for paths $(x(t), y(t))$ which satisfy $\xi(x(t), t) = \xi_0$ and $\eta(y(t), t) = \eta_0$, in other words which are constant on ξ and η. These paths are given by

$$\begin{pmatrix} x(t) \\ y(t) \end{pmatrix} = \begin{pmatrix} \frac{\xi_0}{t+\delta} + t - \delta + \alpha \\ \frac{\eta_0}{t+\delta} \end{pmatrix}. \tag{27}$$

The linear component in $x(t)$ suggests a traveling wave solution. Applying the rescaling conditions shows that the travelling wave would have a velocity of U_{max}. The component $\frac{1}{t+\delta}$ suggests a solution with steepening gradients. On the paths given by (27), the amplitude of u, v increases with $(\delta + t)^{\beta+1}$ (see (25) and (26)). Thus, depending on β, on the paths (27) an algebraic growth or decay of the velocities can be observed.

With the steepening of gradients both in x- and y-direction the effect of viscosity increases in time. This is also inherently given in the equation which we get if we insert ansatz (21)-(23) into the dimensionless form of equation (5) with $\nu \neq 0$:

$$((\xi - \eta^2)\frac{\partial}{\partial \xi} + \eta \frac{\partial}{\partial \eta} + (2 + \beta))\Delta f + 2\frac{\partial f}{\partial \xi} = \frac{(\delta + t)^3}{Re}\Delta\Delta f. \tag{28}$$

Thus it seems useful to divide the life of the flow into a period where similarity and thus ansatz (23) holds, i.e. $(\delta + t)^3 \ll Re$, and into a later period where the gradients are too high for the inviscid assumption. Then, the viscous term on the right side of equation (28) equilibrates one or several terms on the left hand side. This is of course not fully valid since t appears as a parameter and similarity is broken in a strict sense. Still, the importance of viscosity becomes apparent.

Further inserting ansatz (21)-(23) into the fully non-linear equation (4) shows that the nonlinear terms decay algebraically with $\beta = -3$. If viscosity is also employed the limits for the temporal validity of the solution hold true as given above.

$$\left((\xi - \eta^2)\frac{\partial}{\partial \xi} + \eta \frac{\partial}{\partial \eta} + (2 + \beta)\right)\Delta f + 2\frac{\partial f}{\partial \xi}$$
$$-(\delta + t)^{\beta+3} \cdot \nabla \times (\nabla f \cdot \Delta f) = \frac{(\delta + t)^3}{Re}\Delta\Delta f \tag{29}$$

It remains to be shown if it is possible to formulate an eigenvalue problem for β for the linear inviscid case. As a result, one could make a statement about the order of the algebraic growth or decay of disturbances.

3.4   Taylor Expansion

In the following section, we will present a possible procedure to solve (24) via Taylor expansion of f in η.

$$f(\xi, \eta) = \sum_{n=0}^{\infty} \eta^n a_n(\xi) \tag{30}$$

We insert this expansion into equation (24). Collecting powers in η gives an infinite system of ordinary differential equations of third order. For $n \in \{0, 1\}$ we get

$$\xi a_n''' + (2 + n + \beta)a_n'' - (n+1)(n-2)a_n'$$
$$+(n+1)(n+2)\xi a_{n+2}' + (n+1)(n+2)(2+n+\beta)a_{n+2} = \qquad 0 \tag{31}$$

and for $n \geq 2$ we get

$$-a_{n-2}''' + \xi a_n''' + (2 + n + \beta)a_n'' - (n+1)(n-2)a_n'$$
$$+(n+1)(n+2)\xi a_{n+2}' + (n+1)(n+2)(2+n+\beta)a_{n+2} = \qquad 0 \tag{32}$$

The system of ODEs (31) and (32) can be splitted into one system of odd and one system of even indices. The systems of ODEs can iteratively be solved if $a_0(\xi)$ and $a_1(\xi)$ are known.

For even indices, we will give a semi-closed solution. Assume that $a_0(\xi) = \xi^m$ and $m + \beta + 1 \geq 1$. Then we get

$$a_2(\xi) := \frac{1}{2!} \left(\frac{m}{m+1+\beta} \cdot \xi^{m-1} - \frac{m(m-1)}{1} \cdot \xi^{m-2} \right) \tag{33}$$

and for $n \geq 2$

$$a_{2n}^m(\xi) := \sum_{k=1}^{n} \left(\left(\prod_{l=0}^{n+k-1} (m-l) \right) \left(\prod_{l=1}^{n-k} \frac{1}{m+\beta+l} \right) b_{n,k} \xi^{m-n-k} \right) \tag{34}$$

with the following iterative scheme for the coefficients $b_{n,k}$

$$b_{n+1,1} := (2n+1)(2n-2)b_{n,1} \tag{35}$$
$$b_{n+1,k} := (2n)(2n-1)b_{n-1,k-1} - b_{n,k-1} + (2n+1)(2n-2)b_{n,k} \tag{36}$$
$$b_{n+1,n+1} := -b_{n,n} \tag{37}$$

The first elements of $b_{n,k}$ are given by

$$b_{2,1} := 4, \qquad b_{2,2} := 1 \tag{38}$$
$$b_{3,1} := 16, \qquad b_{3,2} := -6, \qquad b_{3,4} := -1 \tag{39}$$

It remains to verify under which conditions for β, n and m the resulting series (30) converges uniformly. Furthermore, consistency with the initial conditions has to be investigated.

3.5 Boundary Conditions

For the channel flow with inviscid perturbations we have the boundary conditions $v|_{y=\pm 1} = 0$. Applying these conditions to ansatz (21)-(23) gives us $\frac{\partial f}{\partial \xi} = 0$ for all (ξ, η) (see also (26)). As a consequence, (24) degenerates to

$$\eta \frac{d^3}{d\eta^3} f + (2 + \beta) \frac{d^2}{d\eta^2} f = 0. \tag{40}$$

For $\beta \notin \{-2, -1, 0\}$ (40) has the general solution $f = C_1 \eta^{-\beta} + C_2 \eta + C_3$. The resulting field of perturbations

$$u = -C_1 \beta y^{-\beta-1} + C_2 (\delta + t)^{\beta+1} \tag{41}$$
$$v = 0 \tag{42}$$

does not give any valuable results, as the first term of u is stationary and the second term does not depend on space. Furthermore, all velocities in y-direction vanish. As a consequence, we do not apply boundary conditions directly on ansatz (23), but on the superposition of solutions of (23) for different β.

As (5) is a linear equation, we can apply superposition. We say that our general solution ψ is the sum of invariant solutions ψ_i under the symmetries X_i with the 3-tuples $(\alpha, \beta, \delta)_i$

$$\psi = \sum_i \psi_i. \tag{43}$$

We use the Taylor expansion (30) for f_i

$$\psi_i = (\delta + t)^{\beta_i} \cdot f_i (\xi, \eta) \tag{44}$$
$$= (\delta + t)^{\beta_i} \cdot \sum_{n=0}^{\infty} \eta^n a_{i,n}(\xi). \tag{45}$$

Now, we can formulate conditions for $a_{i,n}(\xi_i)$. Suppose the series (43) converges uniformly. Then the boundary conditions can be rewritten as follows:

$$-v|_{y=1} = \sum_{n=0}^{\infty} \sum_i (\delta_i + t)^{\beta_i+n+1} a'_{in}(\xi_i) = 0 \tag{46}$$

$$-v|_{y=-1} = \sum_{n=0}^{\infty} (-1)^n \sum_i (\delta_i + t)^{\beta_i+n+1} a'_{in}(\xi_i) = 0 \tag{47}$$

Substraction and addition of (46) and (47) allows us to split boundary conditions into one condition for $a_{i,n}$ with even n and one condition for $a_{i,n}$ with odd n:

$$\sum_i \sum_{n=0}^{\infty} (\delta_i + t)^{\beta_i+1+2n} a'_{i,2n}(\xi_i) = 0 \tag{48}$$

$$\sum_i \sum_{n=0}^{\infty} (\delta_i + t)^{\beta_i+2+2n} a'_{i,2n+1}(\xi_i) = 0 \tag{49}$$

We define an equivalence relation $\sim$ by $\beta_i \sim \beta_j \Leftrightarrow (\beta_i - \beta_j) \in 2\mathbb{Z}$. The boundary conditions (48) and (49) act on each equivalence class separately. Assume that $\alpha_i = \alpha = \text{const.}$ and $\delta_i = \delta = \text{const.}$ Collecting powers in (48) and (49) gives us the following boundary conditions for every equivalence class $[\beta_0]$.

$$(\forall m \in \mathbb{Z}) \qquad \sum_{\substack{\beta_i - \beta_0 + 2n = m \\ 2n \geq 0 \\ \beta_i \sim \beta_0}} a'_{i,2n}(\xi) = 0 \tag{50}$$

$$(\forall m \in \mathbb{Z}) \qquad \sum_{\substack{\beta_i - \beta_0 + 2n = m \\ 2n \geq 0 \\ \beta_i \sim \beta_0}} a'_{i,2n+1}(\xi) = 0 \tag{51}$$

Thus, solving the superposition problem with boundary conditions reduces to finding $a_{i,0}(\xi)$ such that (50) and (51) are satisfied with and such that the Taylor expansion converges uniformly with the solution (34).

4   Conclusion

We analyzed the symmetries of the linearized equation for stability theory of parallel flows. We showed that there are three basic symmetries which lead to the Orr-Sommerfeld-Equation. We also showed that for the parabolic channel flow, there is one additional symmetry. This symmetry in combination with the three basic symmetries leads to a completely new Ansatz function. The algebraic growth of the perturbations as well as growth of the viscous terms is inherently given in this Ansatz. We gave one expansion of the invariant function and reformulated the boundary conditions with respect to this expansion.

Acknowledgements

References

[1] Bluman, G.W., Kumei, S.: Symmetries and Differential Equations. Springer, Berlin (1989)
[2] Carminati, J., Vu, K.: Symbolic Computation and Differential Equations: Lie Symmetries. J. Symbolic Computation 29, 95–116 (2000)
[3] Cheviakov, A.F.: GeM software package for computation of symmetries and conservation laws of differential equations. Computer Physics Communications 176, 48–61 (2007)
[4] Frewer, M.: Symmetrie und Selbstähnlichkeit in der Strömungsmechanik (unpublished)
[5] Schlichting, H., Gersten, K.: Boundary Layer Theory, pp. 424–429. Springer, Heidelberg (2000)
[6] Spurk, J., Aksel, N.: Strömungslehre. Springer, Heidelberg (2006)

Investigation on Actuator Arrays for Active Wave Control on a 2D Airfoil

A. Pätzold[1], I. Peltzer[1], W. Nitsche[1], D. Haller[2], and P. Woias[2]

[1] Technische Universität Berlin, Institute for Aeronautics and Astronautics (ILR)
Marchstraße 12, 10587 Berlin, Germany
andreas.paetzold@TU-Berlin.de
[2] University of Freiburg, Department of Microsystems Engineering (IMTEK)
Georges-Koehler-Allee 102, 79110 Freiburg, Germany

Summary

This paper describes different actuators for delaying laminar-turbulent transition by active boundary layer control. Since transition on an unswept 2D wing is initiated by Tollmien-Schlichting instabilities, friction drag can be reduced by attenuation of these waves. The performed experiments are based on earlier investigation with single spanwise as well as streamwise cascaded actuation. As a consequent step and essential part of this work actuator arrays consisting of slots and oscillating surface membranes for spatially distributed actuation were developed. A single spanwise sensor actuator system was applied to a glider, because flow instabilities of free atmosphere can not be simulated in wind tunnel experiments. In this way the method of active TS wave attenuation could successfully be verified under actual flight conditions.

1 Introduction

A delay of laminar-turbulent boundary layer transition on a wing can lead to significant reduction of skin friction drag. The experimental approach is active cancellation of naturally occurring Tollmien-Schlichting (TS) waves. The Active Wave Control (AWC) method is based on the superimposition principle and was already applied in earlier investigation [6, 2]. Streamwise amplification of naturally occurring TS waves is prevented by superimposition of these waves with artificially generated counter waves. Therefore, highly sensitive surface sensors and a fast and powerful actuator are required. The actuation signal is calculated in real time by a closed loop controller out of an upstream acquired reference signal. For effective damping of TS waves the performance of the actuator that introduces counter waves into the flow is crucial. It is required to generate counter waves of a suitable wavelength, frequency range and amplitude. A short actuator response time is necessary for instant reaction to non-periodic instabilities and to minimise the distance between actuator and reference sensor. Different principles
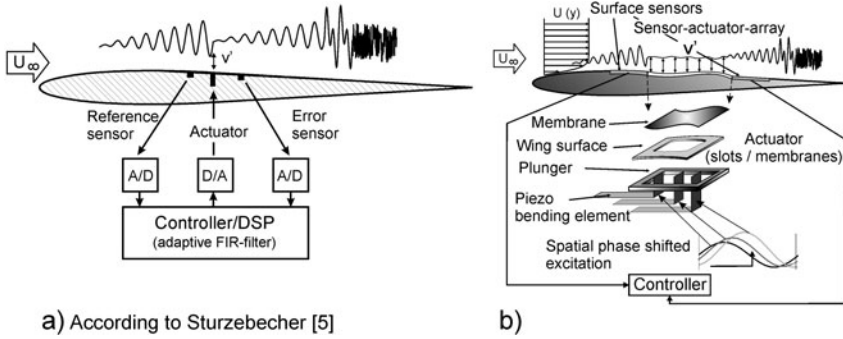
Fig. 1. Actuation Principles: a) Single Spanwise Actuation, b) Spatial Actuation

of actuation were applied: a slot-type suction-blowing system and membrane actuators.

The extension from one sensor-actuator-system to a sequence of streamwise repeated actuator arrays allows for extended transition delay because reamplification of TS waves is retarded [5]. The aim was to perform spatially distributed actuation. This principle requires travelling-wave actuators like a flexible surface membrane which can be deflected at different positions.

2   Experimental Setup and Base Flow

Wind tunnel experiments were conducted with an unswept two-dimensional wing model with a symmetrical NACA0008 airfoil (c=1300mm) in a low turbulence wind tunnel. Different sensors and actuators could be attached to an exchangeable wing module. Base flow investigation at $u_\infty = 20m/s$ ($Re_x = 0.7 \cdot 10^6$) with a single hot-wire probe have shown a boundary layer thickness of 3mm within the range of transition (fig. 2). TS wave packages propagating downstream are most clearly detected at $0.1mm$ normal to the wing's surface, fig. 3a). Fig. 3b) shows the spectrum of the time signal next to the wall ($y = 0.1mm$). It can be seen that actuators have to cope with amplified TS frequencies between 200Hz and 600Hz. From correlation measurements a convection speed of TS waves of approximately 8m/s to 10m/s was determined, depending on the chord position.

For flight experiments a laminar wing glove was mounted on a Grob G103 glider. An actuator and surface sensors were integrated into the wing glove. Flow conditions were monitored by an electronic Prandtl tube, a static pressure transducer and a thermocouple. Basic flight measurements were performed to determine pressure distribution, transition region and TS frequency range [3]. The pre-flight experiments were carried out in the same low turbulence wind tunnel as mentioned above.

Surface mounted hot-wires (SHW) with 5μm in diameter served as sensors for detection of very small velocity fluctuations within the boundary layer in wind
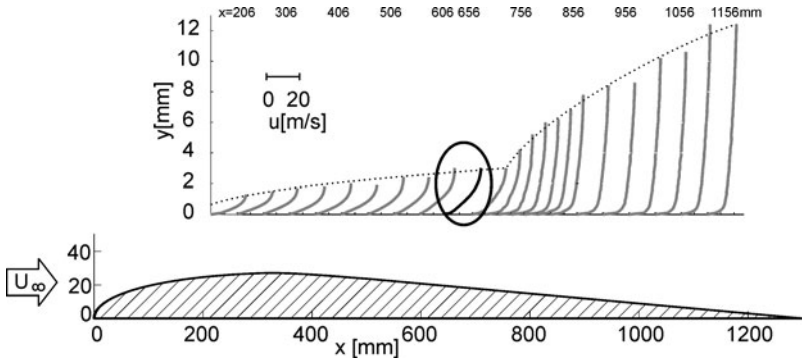
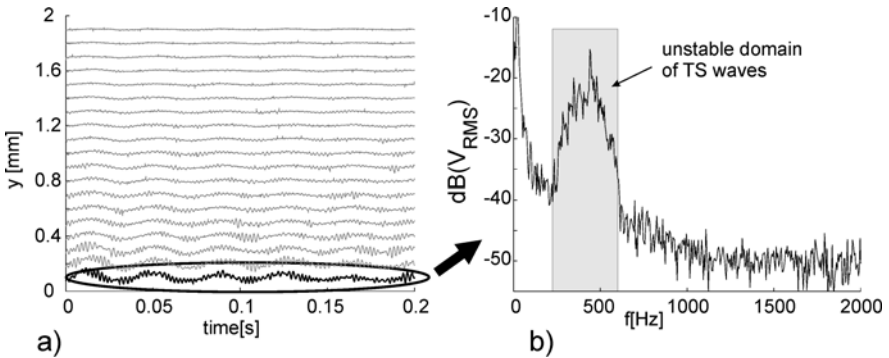**Fig. 2.** Boundary Layer Velocity Profiles at Centerline for $u_\infty = 20m/s$

Fig. 3. Velocity Fluctuations within Transition Region: a)Time Traces (x=656mm, centerline), b) Natural Frequency Spectra for x=656mm; y=0.1mm

tunnel experiments as well as in flight measurements. They generate negligible surface roughness and provide a high signal-to-noise ratio as well as a 30kHz cut-off frequency. For all experiments a multi-channel CTA, a fast dSPACE™digital signal processor and multi-channel amplifier for driving the actuators were used. Additionally, a single hot-wire probe was attached to a traversing unit for investigating the wind tunnel boundary layer flow.

3   Slot and Membrane Actuator Arrays

Conventional actuators only actuated spanwise on a fixed chord position (fig. 1a)). With an extension to a spatially distributed actuation it should now be possible to deflect a certain 'active' surface area for TS wave damping. A slot actuator array for spatial actuation was developed for the NACA0008
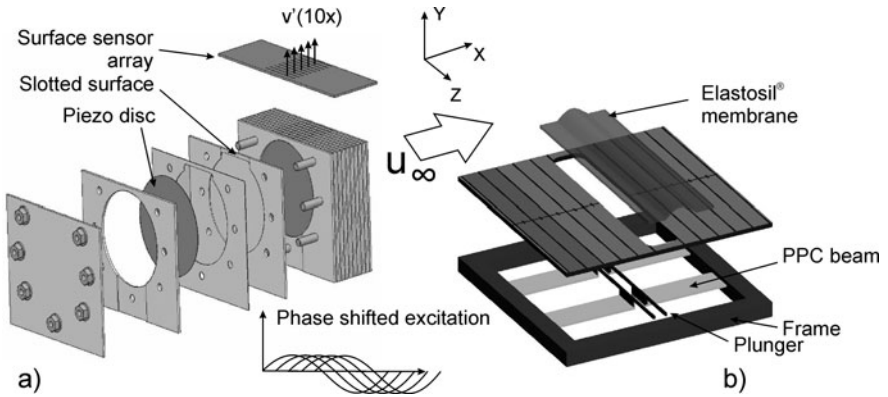
Fig. 4. Travelling Wave Actuators: a) Piezo Slot Actuator, b) Piezo Polymer Actuator [1]

Fig. 5. Generation of Artificial Travelling Waves

airfoil. The compact piezo-driven slot actuator is depicted in fig. 4a). Ten slots were arranged in streamwise direction 3mm from each other, each with a span of 25mm and a width of 0.2mm. Piezo discs produced an oscillating volume of air which leads to a fluctuating jet normal (v) to the wing's surface. With piezo

Fig. 6. Transition Delay With Piezo Polymer Actuator [1]; $u_\infty = 24m/s$

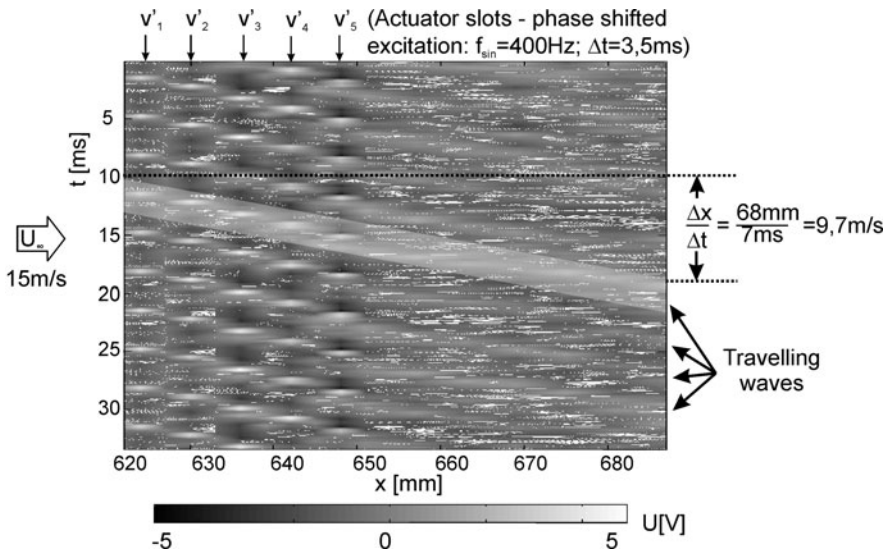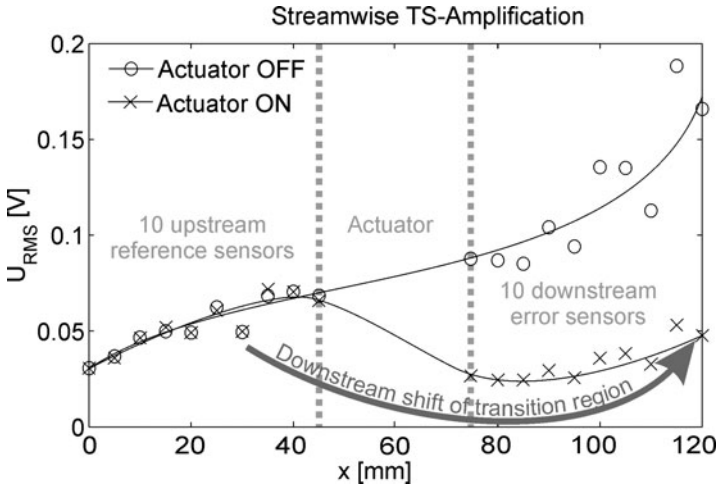discs driven in phaseshifted mode ($f_{sin} = 400Hz; \Delta t = 3, 5ms$) at a flow velocity of 15m/s an artificial travelling wave was generated within the boundary layer. These waves were tracked with SHW sensors between and downstream of the actuation slots (fig. 5). This demonstrates the suitability of piezo slot actuators for spatial TS wave damping.

To reduce surface roughness and to introduce counter waves more smoothly into the boundary layer, progress was made from slot type actuators to flexible spatial membranes. Fig. 1b) illustrates the idea of a flexible surface membrane which is driven by three streamwise cascaded piezo beams. A Piezo Polymer Composite (PPC) actuator was developed in collaboration with "Department of Microsystems Engineering" (IMTEK) at the University of Freiburg [1]. Fig. 4b) shows the PPC actuator that generates travelling bumps on the wing's surface and consists of two plungers which are driven by four piezo polymer beams.

This spatial actuation method needs special control strategies, because several actuation signals have to be calculated out of one global reference sensor. Therefore a Model Predictive Control Algorithm is developed by project partners from the "Department of Plant and Process Technology" (MRT) of Technische Universität Berlin. Together with a PPC actuator and 20 streamwise adjacent surface sensors this control system was applied in wind tunnel experiments. Figure 6 illustrates the effect of active TS wave damping on transition range. TS amplification on the test wing is shifted downstream by approximately 100mm.

4   Membrane Actuator for Flight Experiments

To demonstrate the potential of drag reduction by active TS wave control under real flight conditions a 2D laminar wing glove was used. A single AWC system, consisting of arrays of reference and error sensors and a smooth surface membrane actuator was applied, fig. 8a). The actuator consisted of a flexible Elastosil® membrane (4mm streamwise, 180mm spanwise, $450\mu m$ thickness) which is set into oscillation by six spanwise adjacent magnetic coils, fig. 7a). Spanwise actuator segments worked in-phase and were fed by one common reference signal. The counter wave was calculated in real-time by an adaptive FIR filter algorithm. Filter weights were adapted continuously in order to obtain the least mean square of the remaining error signal downstream of the actuator.

First in-flight measurements at $u_\infty = 23m/s$ have shown a TS amplitude reduction of approximately 68%, which equals a 10dB damping rate at error sensor position, fig. 9a). For further reduction of TS wave amplification the actuator was then optimised. That optimised actuator is capable of higher Reynolds numbers compared to wind tunnel experiments with $15m/s \leq u_\infty \leq 20m/s$. When excited by a 600Hz sine signal, a smooth membrane deformation with a maximum displacement up to $0.05mm$ was observed with a laser vibrometer and plotted in fig. 7b). Increased damping rates could be expected because the improved membrane has shown lower response times in the unstable frequency range around 800Hz [4]. Additionally, a spanwise differentiated actuation provided damping of three-dimensional instabilities. In flight experiments these instabilities already occur in early stages of transition.

With the optimised actuator integrated into the laminar wing glove better damping results were achieved in a wind tunnel pre-flight investigation. The wing glove was mounted in a wind tunnel test section which features an adjustable top wall (fig. 8b) for changing pressure gradient and thereby transition region. According to fig. 9b), the fundamental TS mode was reduced by 15dB which equals 82% of amplitude reduction. These attenuation rates are expected to be demonstrated in flight experiments soon.
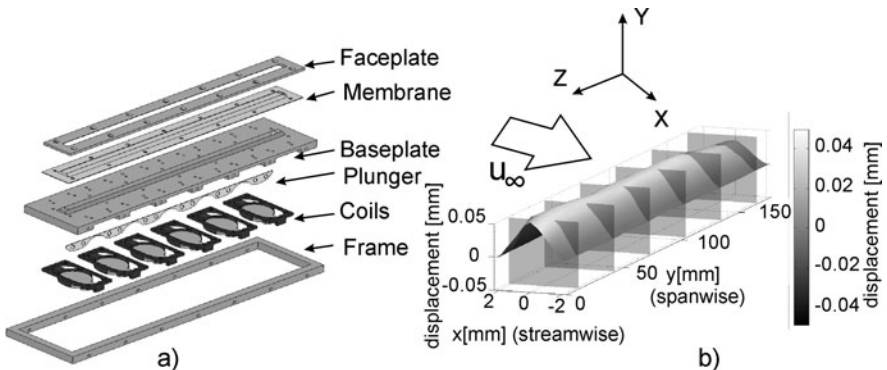

Fig. 7. Membrane Actuator for AWC Flight Experiments: a) Components, b) Membrane Deflection for f=600Hz equiphase
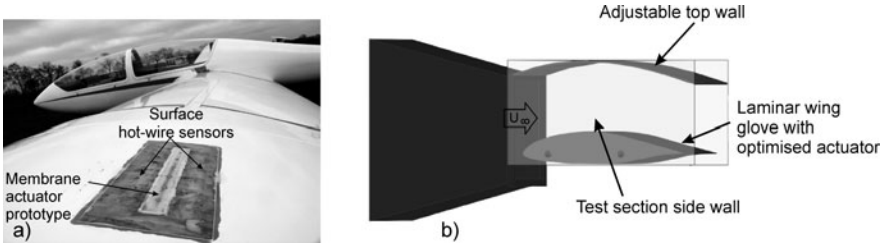
Fig. 8. Flight Test Setup: a) Grob G103 with Laminar Wing Glove and AWC System (Actuator Prototype), b) Wind Tunnel Setup with Laminar Wing Glove (Optimised Actuator)
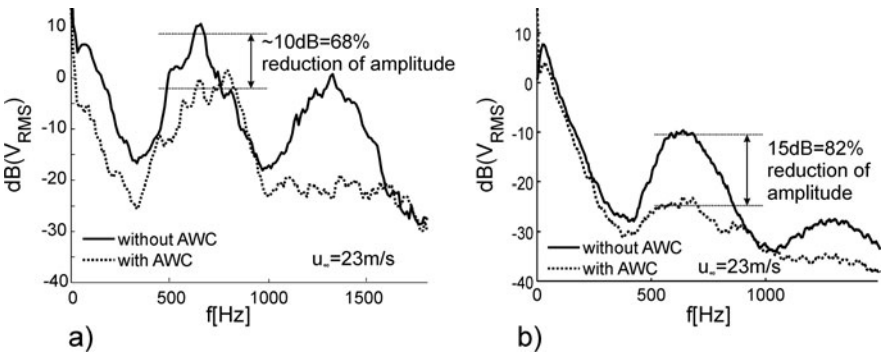
Fig. 9. Error Sensor Power Spectra: a) Flight Experiment (Actuator Prototype), b) Wind Tunnel (Optimised Actuator)

5 Conclusion

Different methods of actuation were developed for active attenuation of TS instabilities within the boundary layer of an unswept wing. A piezo-driven slot actuator and a spatial membrane actuator were employed. Generation of travelling counter waves within the flow was demonstrated successfully with the slot actuator. Together with a new control strategy a spatial attenuation of TS waves will be achieved in further investigation. The method of active TS wave reduction was proved effective under real flight conditions. Improved TS attenuation rates were observed in first wind tunnel tests with an optimised membrane actuator which are expected to be verified in flight experiments.

Acknowledgements

References

[1] Friese, C., Goldschmidtböing, F., Woias, P.: Piezoelectric Microactuators in Polymer-Composite Technology. In: Digest of Technical Papers, Transducers 2003, Boston, USA, June 8-12, pp. 1007–1010 (2003)

[2] Grundmann, S., Tropea, C.: Active cancellation of artificially introduced Tollmien-Schlichting waves using plasma actuators. Experiments in Fluids 44(5), 795–806 (2008)

[3] Peltzer, I.: Comparative in-flight and wind tunnel investigation of the development of natural and controlled disturbances in the laminar boundary layer of an airfoil. Experiments in Fluids 44(6), 961–972 (2008)

[4] Peltzer, I., Pätzold, A., Nitsche, W.: In-flight experiments on active wave control on a two-dimensional laminar wing glove. In: Proc. 7th ETMM, Limassol, Cyprus (June 2008)

[5] Sturzebecher, D., Nitsche, W.: Active cancellation of Tollmien-Schlichting-Instabilities on an unswept wing using multi-channel sensor actuator systems. International Journal of Heat and Fluid Flow 24(4), 572–583 (2003)

[6] Thomas, A.S.W.: The control of boundary-layer transition using a wave superposition principle. Journal of Fluid Mechanics 137, 233–250 (1983)

Experimental Flow Studies on Separation and Reattachment in the Vicinity of Sharp, Wedge Shaped Leading Edges at Low Reynolds Numbers

A.-M. Schreyer[1], W. Würz[1], E. Krämer[1], A. Talamelli[2], and H. Alfredsson[2]

[1] Institut für Aerodynamik und Gasdynamik IAG, Universität Stuttgart, Pfaffenwaldring 21, D-70569 Stuttgart, Germany
Schreyer@iag.uni-stuttgart.de

[2] Kungliga Tekniska Högskolan KTH, Stockholm, Sweden

Summary

The flow field around sharp leading edges in subsonic, low Reynolds number flow is investigated experimentally. Separation occurs already at small angles of attack. Under certain conditions reattachment takes place and a separation bubble develops. As this influences the lift and drag of an airfoil decisively, the conditions leading to reattachment and the formation of a laminar boundary layer are of special interest. The influences of the Reynolds number, angle of attack and leading edge apex angle on the boundary layer properties are studied by means of hot-wire anemometry, flow visualisation techniques and measurements of the pressure distribution over the leading edge. For a small parameter range, laminar separation followed by laminar reattachment is observed.

1 Introduction

The present study focuses on the subsonic flow properties around sharp, wedge shaped leading edges (LE). Due to the strong suction peak followed by a steep pressure rise, the laminar flow separates already at small angles of attack. Under certain conditions reattachment occurs and a separation bubble develops. The separation at the LE can trigger transition from laminar to turbulent flow. A turbulent boundary layer (BL) can overcome higher pressure gradients than a laminar BL, hence BL separation in the rear part of the airfoil and the attending increase in pressure drag are delayed. This can more than compensate the higher skin friction of a turbulent BL [2]. Understanding those mechanisms is essential to reduce the aerodynamic drag of sharp leading edged subsonic airfoils. This is e.g. relevant for small unmanned aerial vehicles (UAV), whose capability to stay in the air as long as possible before needing to refuel is crucial. Sharp LE can also be applied as adjustable turbulators, where the effectiveness depends on the local flow properties at the LE.

The question if there are conditions leading to laminar reattachment of the flow after the LE separation, as first observed by Hamma [8], is of special interest. Due to the strong viscous-nonviscous interaction and pronounced recirculation in the separated flow region, an experimental approach is chosen.

Two-dimensional profile models are investigated in a low speed wind tunnel. To describe the flow field, complementary techniques are applied, including flow visualisation, measurement of pressure distributions at the LE and hot-wire boundary layer measurements (HWA). The influences of the main driving parameters [10][11], the chord based Reynolds number, angle of attack and leading edge apex angle, on the properties of the boundary layer and the separation bubble are studied.

2   Experimental Setup

2.1   Wind Tunnel

The experiments [13] are carried out in the small closed loop low speed wind tunnel of continuous flow type at the Department of Mechanics of KTH, Stockholm. The test section has a width of $400\,mm$, a length of $1100\,mm$ and a height of $500\,mm$.
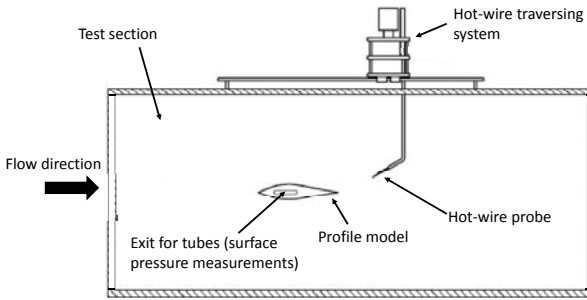

Fig. 1. Schematic of the experimental setup

Fig. 2. Simplified drawing of the profile models: chord length $c = 144\,3\,mm$, max. thickness $t = 19\%$ of c, trailing edge apex angle $\theta_2 = 20°$, the locations of max. thickness are 41% and 39% of c for the profiles with $\theta_1 = 30°$ and $\theta_1 = 45°$, respectively.

The free-stream turbulence level $Tu = 0.3\%$ of this wind tunnel is comparably high. The Laminar Wind Tunnel at the IAG and the Minimum Turbulence Wind Tunnel at KTH Mechanics reach values below 0.02%. At those levels the transition Reynolds number Re_{crit} remains constant in a small region of Tu [14]. With increasing Tu, Re_{crit} decreases and the transition region moves upstream [6][12]. An increase to $Tu \approx 0.3\%$ should only have a small influence on the results [16], but Re_{crit} might still be lower than for quiet wind tunnel experiments. It can be expected that with increasing Tu, the length of the laminar part of the separation

bubble decreases [15][7]. The turbulent BL on the test section walls at the position of the model leading edge was estimated to be 9.7 - $12.8\,mm$ thick, depending on the Reynolds number. To partly balance the static pressure distribution, the test section walls are slightly diverging. The oil visualisation shows disturbances due to interference effects only close to the wall. The flow around the main part of the profile model can be considered two-dimensional [13]. For the test setup see Fig. 1.

2.2   Wedge Profile Models

The 2D models are designed in a way to allow extensive measurements in the vicinity of the wedge shaped LE area which thus is considerably enlarged compared to an actual airfoil. Wedge shaped leading and trailing edge are connected with a rounding to get a steady contour and minimise upstream influences of disturbances (see Fig. 2). The LE angles are chosen based on considerations to reduce radar visibility of a UAV. The overall performance of the airfoil model is not investigated.

The thickness ratio of the models turned out to be a difficult parameter, because of possible flow separation in the rear part. Nevertheless, a certain thickness is needed to obtain a sufficiently large wedge shaped LE part. This also motivates the location of maximum thickness. In addition, blockage effects [1] are considered. The relative size of the model is 0.056. The wingspan is equal to the test section width. The resulting aspect ratio of the models $A_r = 2.8$ is quite low, but successful experiments were performed before with similar experimental setups [12][5]. The models were manufactured from aluminium by CNC milling. The surface of the models was carefully sanded and finally polished. The LE is sharp.

The first pressure tap is located $5\,mm$ downstream of the LE for technical reasons. Thus, the flow behaviour directly at the LE has to be concluded from other measurement techniques. Further taps follow in distances of $2\,mm$ in chordwise direction. To prevent interferences, the taps are slightly shifted in spanwise direction.

2.3   Measurement and Flow Visualisation Techniques

The pressure taps are connected to a Scanivalve DSA3217, an array with 16 temperature compensated piezoresistive pressure sensors, 0 - $0.75\,psi$ pressure range and $\pm 0.05\%$ full scale long term accuracy. Reference is the static pressure at the test section sidewall upstream of the profile. Mean and transient values are acquired at a sampling rate of $200\,Hz$ and time of $10\,s$.

A platinum wire with diameter $d = 5\,\mu m$ and length $l = 1\,mm$ is used for constant temperature anemometry. The wire is driven by an AALabSystems AN-1003 CTA bridge at a resistance ratio $\frac{R_w}{R_0} = 1.5$ [3][4]. The coefficients for the relation between wire voltage drop and flow velocity, the modified King's law eq.(1) [9], and the instantaneous streamwise velocity signal are acquired.

$$U = k_1(E^2 - E_0^2)^{\frac{1}{n}} + k_2(E - E_0)^{\frac{1}{2}} \tag{1}$$

A deviation of maximal 2% of the nominal curve is observed. A sampling rate of $5000\,Hz$ was found to be suitable. Time-averaged quantities up to the fourth order,

i.e. mean wind tunnel speed u, root-mean-square value u_{rms}, skewness factor SU and flatness factor FU, as well as the time derivative of the velocity signal $\frac{du}{dt}$ were computed from the instantaneous data. As a single wire probe was used, the flow direction inside recirculation areas cannot be resolved.

For the oil flow visualisation, a dispersion of oil and UV fluorescent pigments is applied to the model surface. The dispersion is distributed in the local flow direction depending on wall shear stresses. Separation is visualised clearly. Tuft flow visualisation is used to indicate whether the flow is separated or attached. The technique has some limitations for the application in this study. In regions with minor backflow (laminar part of a separation bubble, fully separated flow) tuft movement is barely visible.

3   Results and Discussion of the Results

The influences of the chord based Reynolds number Re, the angle of attack α and the leading edge apex angle Θ on the boundary layer in the vicinity of the leading edge are investigated in a parametric study for $0.5 \cdot 10^5 \leq Re \leq 2 \cdot 10^5$ and $-4° \leq \alpha \leq 10°$. Closer intervals were chosen around the start of the separation bubble formation. Not all measurement techniques were applicable to the whole range of Reynolds numbers. Nevertheless, a detailed evaluation of the flow field was achieved by overlapping results.

3.1   Formation and Size of the Separation Bubble
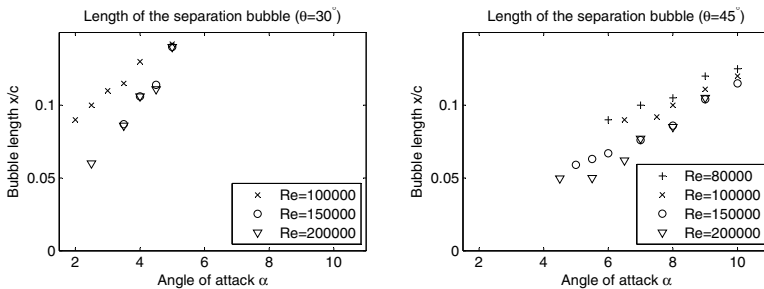
Fig. 3. Separation bubble length versus α (pressure measurements)

Influence of the Angle of Attack. In the wedge shaped LE area, the flow is attached below a critical angle of attack α^*. Above α^* the formation of a separation bubble starts directly downstream of the leading edge. With increasing angle of attack, the bubble length increases (see Fig.3). This trend exists for all Re with similar slope and with different slopes for both Θ. For $\alpha > 10°$ ($\Theta = 45°$) the bubble bursts and the flow is fully separated. BL profiles measured by HWA show the shape and dimensions of the separation bubble in detail. For $Re = 100000$, $\alpha = 6°$ (see Fig.4),

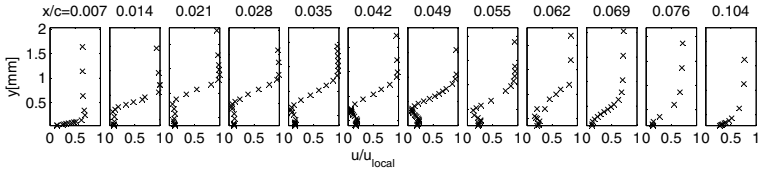**Fig. 4.** Boundary layer velocity profiles scaled with local freestream velocity for $Re = 100000$, $\alpha = 6°$ and $\Theta = 45°$

the bubble has a length between $\frac{x}{c} = 0.08$ and 0.09, which agrees qualitatively with the c_p-measurements, where a length of $\frac{x}{c} = 0.09$ is observed for $\alpha = 6.5°$ (see Fig.5). The offset in angle of attack of $\Delta\alpha = 0.5°$ between the flow states observed by the pressure distributions and HWA results from the non negligible influence of the HWA traversing system on the circulation of the profile model. The pressure coefficient c_p along the LE area is shown exemplarily for $Re = 100000$ and $Re = 200000$ for $-1° \le \alpha \le 10°$ in Fig.5 ($\Theta = 45°$). With increasing α,
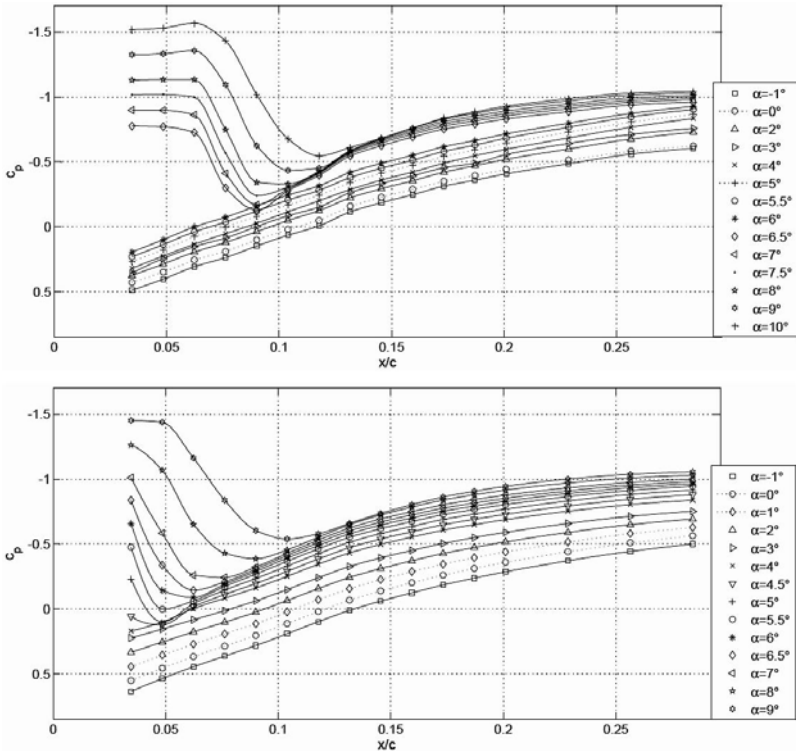

Fig. 5. Pressure distribution over the leading edge of the $\Theta = 45°$ profile, upper picture for $Re = 1.0 \cdot 10^5$, lower picture for $Re = 2.0 \cdot 10^5$

the c_p-curves shift towards lower values at the LE. This causes the LE separation to start at lower Re. For $\alpha = 4.5°$, a bubble develops from $Re = 200000$, for $\alpha = 6°$ already at $Re = 80000$ ($\Theta = 45°$, see Fig.3). For $\Theta = 30°$ this trend is not visible as the lengths of the bubbles are too small to be acquired due to the distance of the first pressure tap from the LE.

Results of the oil flow visualisation confirm those trends but do not show quantitative agreement. In the c_p-measurements, α^* was observed to be slightly larger (not shown). This might be due to the distance of the first pressure tap from the LE: short separation bubbles at small α cannot be acquired. In addition, the oil flow visualisation shows shorter bubbles. This is due to the fact that the exact end is difficult to determine, as the oil flow visualisation only shows the laminar recirculation area clearly, where oil accumulates. In the reattachment area oil can be transported in the main flow direction or reverse, which cannot be optically detected. This turbulent part of the bubble is relatively long (see Fig.5), which thus explains the difference.

Influence of the Reynolds Number. Concluding from the shape of the c_p-curves, no suction peak develops for low α and Re (for $Re \leq 100000$ up to $\alpha \leq 6°$, see Fig.5). For a certain Re (for $\alpha = 6.5°$, $\Theta = 45°$ $Re = 100000$), a laminar separation bubble starts to develop directly downstream of the LE, indicated by a pressure plateau (laminar part of the bubble) followed by an increase in pressure (turbulent part). With increasing Reynolds number, α^* decreases, which is visible for $\Theta = 45°$ in Fig.3. For $\Theta = 30°$ the trend cannot be confirmed due to the position of the first pressure tap. Also the bubble length decreases (e.g. from $\frac{x}{c} = 0.13$ for $Re = 100000$ to $\frac{x}{c} = 0.106$ for $Re = 200000$ at $\alpha = 4°$, $\Theta = 30°$ (see Fig.3)). This influence gets weaker with increasing Re, for $\Theta = 30°$ basically no difference in bubble length is detectable between $Re = 150000$ and $Re = 200000$.

Influence of the Wedge Apex Angle. With increasing wedge apex angle Θ, α^* increases, e.g. from $\alpha^* = 2.5°$ for $\Theta = 30°$ to $\alpha^* = 4.5°$ for $\Theta = 45°$ for $Re = 200000$ (see Fig.3). The influences of α and Re on the pressure coefficient and the bubble length decrease (see Fig.3), the slopes of the curves flatten and they are closer to each other. Also the c_p-x-curves are closer to each other (see [13]). The bubble length decreases for increasing Θ (see Fig.3) and the transition Reynolds number $Re_{c,crit}$ and the angle of attack from which on transition occurs in the free shear layer increase (HWA, not shown). This corresponds in general with the observations of Hamma [8] on the HS 3 airfoil (sharp LE with $\Theta \approx 45°$).

3.2   State of the Boundary Layer

The streamwise velocity u and its rms-value u_{rms} were measured by HWA for different Re and α for both models. The turbulence intensity $\frac{u_{rms}}{U_\infty}$ is used to investigate the status of the flow. The hot-wire probe is positioned at $\frac{x}{c} = 0.2$ downstream the LE at a distance of $x \approx 0.1\,mm$ from the wall. The value $\frac{u_{rms}}{U_\infty} = 0.028$ was marked as transition point according to the observed oscilloscope signal. For a given α, transition is observed at the critical Reynolds number $Re_{c,crit}$, defined here based on the chord length. With increasing α, $Re_{c,crit}$ decreases (see Fig.6).
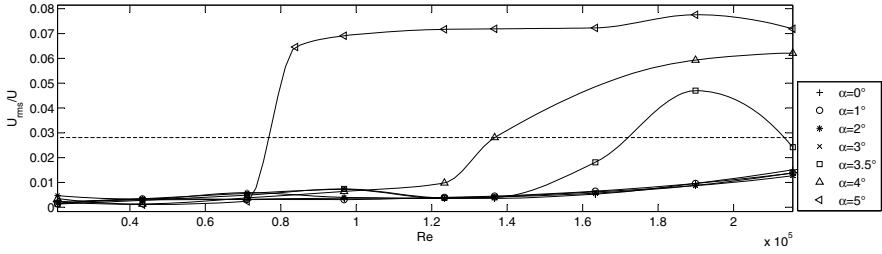
Fig. 6. Plot of $\frac{u_{rms}}{U_\infty}$ versus Re for different α ($\Theta = 30°$)

3.3   Laminar Reattachment

Laminar reattachment was observed for a small parameter range of $114000 \leq Re \leq 163000$ and $3.5° \leq \alpha \leq 4.4°$ for $\Theta = 30°$. This range is visualised as shaded area in Fig. 7. For $\alpha < \alpha_{crit}$ (transition angle of attack, HWA) and $\alpha \geq \alpha^*$ (separation angle of attack, oil visualisation) a separation bubble is observed in c_p-distribution and oil flow visualisation and HWA indicates laminar flow downstream of the reattachment line. Several oil flow visualisation pictures were taken for the same conditions to assure that the effect was not caused by hysteresis effects or disturbances.
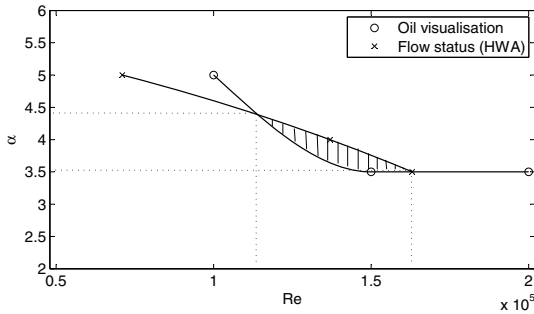

Fig. 7. Range of parameters for which separation and laminar reattachment are observed ($\Theta = 30°$)

4   Conclusion

Separation and reattachment in the vicinity of sharp, wedge shaped leading edges circulated by subsonic flow at Reynolds numbers $Re \leq 200000$ was investigated experimentally. Two cases with apex angles of $30°$ and $45°$ were compared. The influences of the chord based Reynolds number, the angle of attack and the leading edge apex angle on the flow were studied. The conditions for separation bubble development and the bubble length were described, extracted from flow visualisation techniques, hot-wire anemometry and the measured pressure distribution over the leading edge. The flow field depends sensitively on all investigated parameters. With increasing α, separation bubbles start to develop at lower Re and the separation bubble length increases. An increase in Re leads to decreasing α^* and

decreasing bubble length. With increasing Θ, the separation angle of attack α^* increases. The influences of α and Re on the bubble length decrease, as well as the bubble length itself. In a small range of Re and α, laminar reattachment was observed for $\Theta = 30°$. To clarify if this range can be extended, experiments will be performed in a wind tunnel with low turbulence level. To make the results of this study technically applicable, the flow around a model of the actual airfoil has to be studied.

References

[1] Barlow, J.B., Rae, W.H., Pope, A.: Low-Speed Wind Tunnel Testing, 3rd edn. John Wiley & Sons, Chichester (1999)

[2] Batchelor, G.K.: An introduction to fluid dynamics. Cambridge Univ. Press, Cambridge (1967)

[3] Bruun, H.H.: Hot-wire anemometry: Principles and signal analysis. Oxford University Press Inc., New York (1995)

[4] Chew, Y.T., Khoo, B.C., Li, G.L.: An investigation of wall effects on hot-wire measurements using a bent sublayer probe. Meas. Sci. and Tech. 9, 67–85 (1998)

[5] Gleyzes, C., Cousteix, J., Bonnet, J.L.: Theoretical and numerical study of low Reynolds number transitional separation bubbles. In: Proceedings Conference on Low Reynolds Number Airfoil Aerodynamics UNDAS-CP-77B123, pp. 137–152. University of Notre Dame Indiana, USA (1985)

[6] Hall, D.J., Gibbings, J.C.: Influence of stream turbulence and pressure gradient upon boundary layer transition. Mech. Eng. Sci. 14(2), 134–146 (1972)

[7] Häggmark, C.: Investigations of disturbance developing in a laminar separation bubble flow. KTH Stockholm, Department of Mechanics, Diss. (2000)

[8] Hamma, W.: Neu entwickelte Tragflügelprofile für Re<105 mit den zugehörigen Polaren und Ergebnissen aus Grenzschichtbeobachtungen an diesen Profilen, Diplomarbeit (Teil 2), IAG, Technische Hochschule Stuttgart (1963)

[9] Johansson, A.V., Alfredsson, P.H.: On the structure of turbulent channel flow. J. Fluid Mech. 122, 295–314 (1982)

[10] Lutz, T., Würz, W., Wagner, S.: Numerical Optimisation andWind-Tunnel Testing of Low Reynolds-Number Airfoils. In: Conference on Fixed, Flapping and RotaryWing Vehicles at very Low Reynolds Numbers, Notre Dame, Indiana, June 5-7 (2000)

[11] Reichel, V.: Experimentelle Untersuchung zum Einfluss des Nasenradius auf die Eigenschaften von Profilen bei sehr niedrigen Re-Zahlen. Stud. res. proj., IAG (2000)

[12] Schmidt, G.S., O'Meara, M.M., Mueller, T.J.: An analysis of a separation bubble transition criterion at low Reynolds numbers. In: Proceedings Conference on Low Reynolds Number Airfoil Aerodynamics UNDAS-CP-77B123, pp. 125–136. University of Notre Dame Indiana, USA (1985)

[13] Schreyer, A.-M.: Experimental flow studies on separation and reattachment around sharp, wedge shaped leading edges for low Reynolds numbers, Diplomarbeit, KTH Stockholm und IAG, Universität Stuttgart (2007)

[14] Schubauer, G.B., Skramstad, H.K.: Laminar-boundary-layer oscillations and transition on a flat plate, NACA Report No. 909 (1948)

[15] Van Ingen, J.L., Boermans, L.M.M.: Research on laminar separation bubbles at Delft University of Technology in relation to low Reynolds number airfoil aerodynamics. In: Proceedings Conference on Low Reynolds Number Airfoil Aerodynamics UNDASCP-77B123, pp. 89–124. University of Notre Dame Indiana, USA (1985)

[16] Young, A.D.: Some special boundary layer problems. Zeitschrift fuer Flugwissenschaften und Weltraumforschung 1, 401–414 (1977)

Receptivity Considerations for Cascaded Actuators Generating Tollmien-Schlichting Waves

Marcus Zengl and Ulrich Rist

Universität Stuttgart, IAG, Pfaffenwaldring 21, D-70550 Stuttgart, Germany
`http://www.iag.uni-stuttgart.de`

Summary

Different blowing and suction profiles were analyzed for flow control experiments for a generic blowing-and-suction actuator. The aim of this actuator is to dampen Tollmien-Schlichting (TS) waves by superimposing a wave in counterphase. It is essential to dampen only designated waves without introducing other unstable modes. Therefore, the receptivity of the TS waves to the introduced disturbances is an issue. Actuator cascades of multiple actuator elements were investigated for time-periodic forcing. Design parameters and their influence on the ability to generate TS waves without triggering unwanted waves were investigated Hereby, it was assumed that the spatial velocity profile of each actuator element is uniform.

1 Introduction

1.1 Objective

Reducing drag of internal and external flows has always been an issue to improve performance and cost efficiency of vehicles. Delay or even inhibition of laminar-turbulent transition is one possibility to reduce the drag caused by skin friction in wall-bounded non-separating flows. Our objective is to reduce the amplitude of so-called Tollmien-Schlichting waves—responsible for laminar-turbulent transition—by blowing and suction at the wall. Introducing a TS wave of the same amplitude but opposite phase to the wave to be damped results in cancellation of both waves. Applying this technique in the linear regime, before secondary instability sets in, can delay transition considerably [2]. On the other hand, the generation of counterphase waves can unintentionally trigger additional TS waves, promoting the transition process. Applying a time-periodic sinusoidal input signal on a blowing-and-suction actuator does not imply that the slot velocity over time is purely sinusoidal. The output signal contains higher harmonics which are able to trigger higher harmonics of the TS wave to be generated. Our approach is to design the actuator in such a way that it can generate TS waves of multiple frequencies (respectively wavenumbers) while keeping the receptivity of the according higher harmonics as low as possible.

1.2   Previous Investigations

Depending on blowing ratio, spatial distribution, frequency, and spanwise wavenumber the laminar boundary layer reacts differently on excitations by a disturbance strip. Gmelin [1] has found a linear dependence of the effective wave amplitude of a generated TS wave on the Fourier transform of the spatial wall-normal velocity profile at the disturbance strip. Due to the generation of a mixture of modes above the disturbance strip in his direct numerical simulation, he has used a reference simulation with a generated TS wave further upstream. By comparison of both simulations at a control point some wavelengths downstream of the disturbance strip, he determined the effective amplitude of the designated TS wave at the location of the disturbance strip. For a Blasius boundary layer, Gmelin's receptivity constant, i.e. the ratio of the effective wave amplitude to the Fourier-transformed wall-velocity, decreases with increasing frequency.

2   Method

2.1   Wall-Velocity Actuation

At the actuator slot a wall-normal velocity v_{w} is prescribed. We assume spanwise periodicity and time-periodic blowing and suction. Please note that any non-sinusoidal time-periodic actuation with a period of $T = \frac{2\pi}{\omega}$ can be Fourier-transformed such that the wall-normal velocity can be written as

$$v_{\mathrm{w}} = v_{\mathrm{x}}(x) \cos(\beta z) \sum_{h=1}^{\infty} A_h \cos(h\omega t + \phi_h) \ . \tag{1}$$

2.2   Receptivity Considerations

For two-dimensional waves, i.e. $\beta = 0$, we apply a Fourier transform on the spatial amplitude distribution v_{x} with respect to the streamwise wavenumber α

$$V_{\mathrm{x}}(\alpha) = \int_{-\infty}^{\infty} v_{\mathrm{x}}(x) \, e^{-i\alpha x} \, dx \ . \tag{2}$$

Gmelin has shown that the ratio of the effective amplitude of a generated TS wave with the streamwise wavenumber α_{TS} divided by the Fourier integral $V_{\mathrm{x}}(\alpha_{\mathrm{TS}})$ is constant for a given frequency and velocity profile. For oblique-travelling waves the Fourier-transform has to be done in the direction of the wave propagation. However, we will focus on two-dimensional waves in this paper. The influences of different design parameters on oblique travelling waves will head in the same direction. Exemplarily, in Fig. 1 the value of the dimensionless receptivity constant

$$C_{\mathrm{r}} = \frac{\tilde{u}_{\mathrm{TS}}}{|V(\alpha_{\mathrm{TS}})|} \frac{\nu}{U_{\infty}} \tag{3}$$

is plotted versus the dimensionsless frequency

$$F = \frac{\omega\nu}{U_\infty^2} \tag{4}$$

for the Blasius boundary layer. Here, $\tilde{u}_{\text{TS}}$ is the effective amplitude of the generated TS wave defined by its maximum streamwise disturbance velocity. The plot was created using a correlation for the receptivity constant from Marx [3]. Marx fitted the coefficients of his ansatz function to data points obtained by evaluating the receptivity with direct numerical simulation.
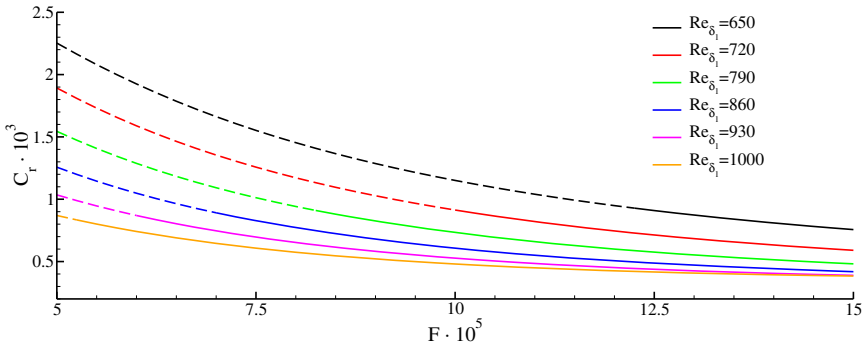

Fig. 1. Receptivity constant C_r versus frequency F for different streamwise positions of the Blasius boundary layer (obtained using correlation from Marx [3]). Dashed lines denote stable waves.

2.3 Actuator Design

In order to optimize the actuator, we try to maximize $\frac{|V_x(\alpha)|}{Q}$ for the designated wavenumber α_{TS}, i.e. the wavenumber of the TS wave to be generated, and minimize it for the TS waves of its higher time harmonics. Here,

$$Q = \int_{-\infty}^{\infty} |v_x(x)| \; dx \tag{5}$$

is the maximum flow rate through the wall. The wavenumbers of the TS wave to be generated and its higher harmonics are given by the dispersion relation

$$D(\alpha, \beta, \omega) = 0 \tag{6}$$

where β is the spanwise wavenumber of the disturbance. Since α is monotonically increasing with increasing ω, we can say that $\frac{|V_x(\alpha)|}{Q}$ is to be minimized for wavenumbers greater than α_{TS}. The value of $|V_x(\alpha)|$ below α_{TS} has no relevance as long as we force with a period of $T = \frac{2\pi}{\omega_{\text{TS}}}$. Since in most cases the wavenumbers of the higher

harmonics with streamwise wavenumbers greater than approximately $6\alpha_{\text{TS}}$ are stable, we focus only on wavenumbers up to this value. Please note that the value of $\frac{|V_x(\alpha)|}{Q}$ can not exceed 1 and is somewhat a measure for efficiency.

In order not to loose generality, the length of the actuator cascade is further scaled to unit length. Each actuator element is then $L_e = \frac{1}{N}$ wide where N is the number of actuator elements. The uniform wall velocity $v_{x,j}$ of an element j is taken to be

$$v_{x,j} = \sin(\alpha_{\text{TS}} x_j + \theta) \tag{7}$$

to achieve a large $V_x(\alpha_{\text{TS}})$ where x_j is the coordinate of the slot center of element j. This leads to the spatial amplitude distribution

$$v_x = \begin{cases} 0 & \text{for } x < 0, \\ \sin\left(\alpha_{\text{TS}} \frac{2\lceil Nx\rceil - 1}{2N} + \theta\right) & \text{for } 0 \le x < 1 \wedge \left|x - \frac{2\lceil Nx\rceil-1}{2N}\right| \le \frac{\Xi}{2N}, \\ 0 & \text{for } 0 \le x < 1 \wedge \left|x - \frac{2\lceil Nx\rceil-1}{2N}\right| > \frac{\Xi}{2N}, \\ 0 & \text{for } 1 \le x \ , \end{cases} \tag{8}$$

with the ratio of the slot width to the element width $\Xi \in (0,1)$, a phase parameter $\theta \in [0, \frac{\pi}{2}]$, and the number of actuator elements N which are to be chosen. Consequently, a descriptive comparison of the amplitude distribution function is that of a continuous sine function $v_x = \sin(\alpha_{\text{TS}} x_j + \theta)$ for $0 \le x < 1$, which is zero for all other values of x. A sketch of an actuator cascade with three elements is drawn in Fig. 2. The walls
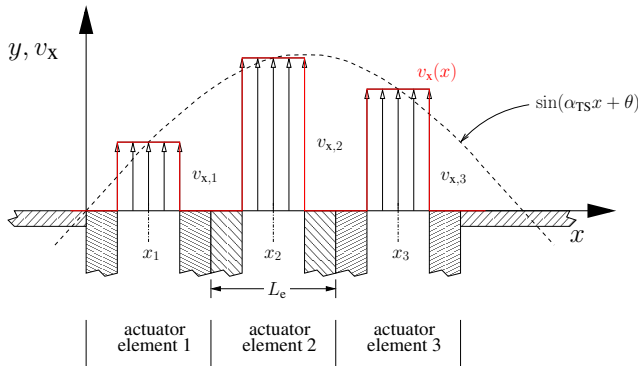

Fig. 2. Sketch of three cascaded actuator elements. Arrows indicate the slot velocity.

of the different actuator elements are shaded, and the velocity vectors are drawn in the slot. The dashed line indicates the function of (7) and the red line indicates the function $v_x(x)$ given by (8).

Please note that the spatial amplitude distribution is adapted to a TS wave of a certain frequency. In the expected case that two or more waves are to be damped the actuation

of the actuators can be superimposed using a particular spatial amplitude distribution for each frequency. Therefore, also wave packets can be damped using the framework of this paper.

3   Discussion of Different Design Parameters

For the design of the actuator cascade a few parameters can be chosen. The ratio Ξ of the slot width to the element width in streamwise direction can be chosen with only few constraints. Please note that in the application a large value of Ξ can affect the baseflow profile due to the lack of the no-slip boundary condition at the wall. Also, the number of elements in the cascade can be more or less arbitrarily chosen keeping the design of the single actuator element. By miniaturization actuator elements with smaller lengths could be used. Also a change in the baseflow to slower free-stream velocities can reduce the element length compared to the wavelength of the relevant TS waves.

3.1   Slot Width Ratio Ξ

In Fig. 3 the velocity profile v_x of an actuator cascade with seven elements is shown for different values of Ξ. Hereby, the amplitude of each actuator element is chosen for a TS
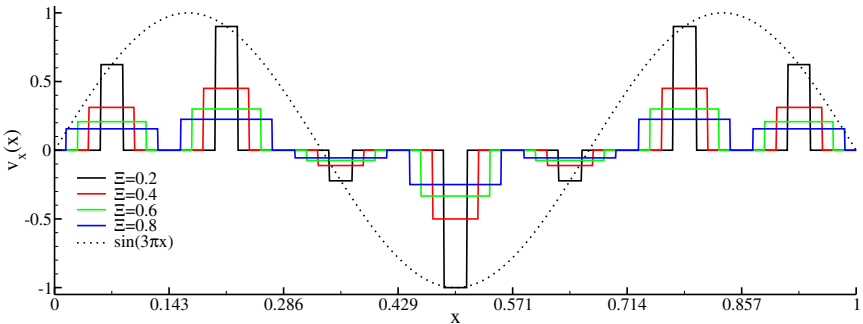

Fig. 3. Comparison of spatial velocity distributions with the same blowing ratio Q for different slot ratios Ξ when a TS wave of the wavenumber $\alpha_{TS} L_e = \frac{3\pi}{7}$ is to be generated. A dashed sine function is shown for comparison. The dotted line indicates the function of (7).

wavelength of $\alpha_{TS} = \frac{3\pi}{7 L_e}$ using (7). The continuous function $v_x(x) = \sin(\alpha_{TS} x + \theta)$ (dotted line)—viable in a numerical simulation—is shown for comparison. The Fourier transforms according to Fig. 3 scaled with the volume flux $\frac{|V_x(\alpha)|}{Q}$ are shown in Fig. 4. All functions have a maximum in the immediate vicinity of α_{TS} and show only slight differences up to a wavenumber of $3\alpha_{TS}$. For higher wavenumbers there are large differences. The higher the slot ratio Ξ, the lower the receptivity for higher harmonics.
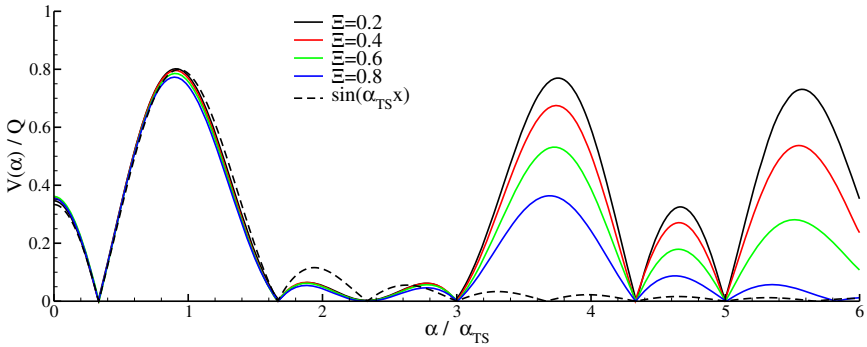
Fig. 4. Comparison of the scaled Fourier transform of the blowing and suction profile for different slot ratios Ξ when a TS wave of the wavenumber $\alpha_{TS} = \frac{3\pi}{7L_e}$ is to be generated. A sine function (dashed line) is shown for comparison.

3.2   Phase Parameter θ

Even though the phase parameter θ is not fixed by the geometry it is a parameter which is to be chosen. Varying the phase parameter θ in (7), for $\alpha_{TS} = \frac{2\pi}{7L_e}$ we obtain the functions $\frac{|V_x(\alpha)|}{Q}$ plotted in Fig. 5. The higher the parameter θ, the higher the wavenumber of the first maximum. All curves exhibit secondary maxima which are, in the plotted region, least distinctive for $\theta = 0$. Therefore, a parameter of $\theta = 0$ is preferable here. However, results for other wavenumbers do not show a clear trend. Therefore, the phase parameter has to be adapted to the specific case depending on the wave to be generated.
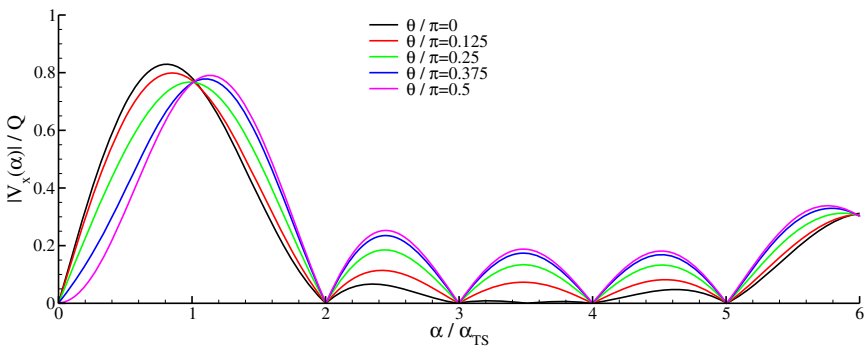

Fig. 5. Comparison of the scaled Fourier transform of the blowing and suction profile for different phase parameters θ when a TS wave of the wavenumber $\alpha_{TS} = \frac{2\pi}{7L_e}$ is to be generated using seven actuators. The slot ratio is $\Xi = 0.8$.

3.3 Number of Actuators

For TS waves which have a wavelength of only a few actuator element lengths, e.g. for $\alpha_{TS} = \frac{\pi}{L_e}$, only a few actuators need to be used to achieve a maximum for $V_x(\alpha_{TS})$. In Fig. 6 the obtained functions $\frac{|V_x(\alpha)|}{Q}$ are plotted for $\alpha_{TS} = \frac{\pi}{L_e}$ and $\Xi = 0.5$ when different numbers of actuator elements are used. All curves exhibit a maximum for $\alpha \approx \alpha_{TS}$. The more elements are used, the narrower are the peaks. However, the size of the peaks cannot be reduced by increasing the number of actuator elements and keeping the same number of elements per wavelength. Comparing the results in Fig. 4 and Fig. 6, we can see that the size of the peaks is smaller in the case with more elements per wavelength. This is due to a better reproduction of a sinusoidal profile. Using more elements gives better results in any case.
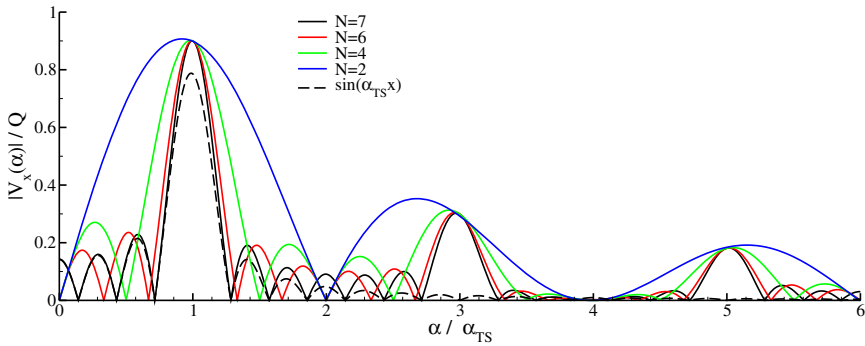

Fig. 6. Comparison of the scaled Fourier transform of the blowing and suction profile for a different number of used actuator elements when a TS wave of the wavenumber $\alpha_{TS} = \frac{\pi}{L_e}$ is to be generated. The slot ratio is $\Xi = 0.5$. The Fourier transform of a sine function (dashed line) is shown for comparison.
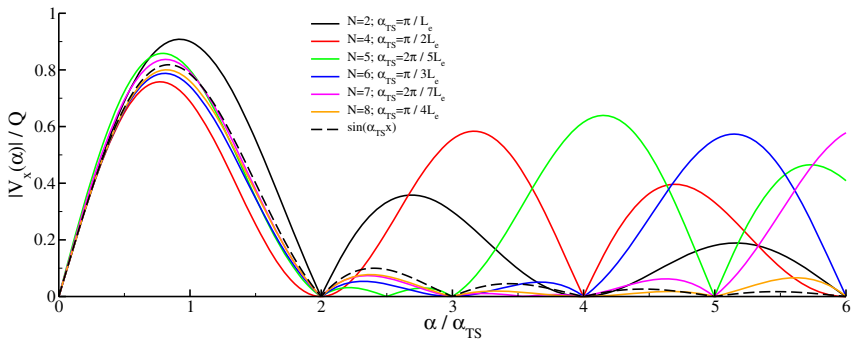

Fig. 7. Comparison of the scaled Fourier transform of the blowing and suction profile for a different number of actuator elements. The TS wavelength is fixed to the length of the actuator cascade. The slot ratio and phase parameter is $\Xi = 0.5$ and $\theta = 0$, respectively. The Fourier transform of a sine function (dashed line) is shown for comparison.

3.4 Length per Actuator Element

In Fig. 7, a comparison of the scaled Fourier transform is shown for different numbers of actuators. The overall length of the actuator cascade is kept at the length of the wave to be generated, i.e. $\alpha_{\mathrm{TS}} L_{\mathrm{e}} = \frac{2\pi}{N}$.

All functions have a maximum at approximately $\alpha = \alpha_{\mathrm{TS}}$. The higher the number of actuators, the higher is the wavenumber of the first secondary maximum. Furthermore, the functions tend to the function of the continuous sine function.

4   Conclusions

It is shown that setting the velocity amplitude of an actuator element j as $v_{\mathrm{x},j} = sin(\alpha_{\mathrm{TS}} x_j + \theta)$ with x_j as the streamwise coordinate of the slot center gives good results in order to generate or dampen TS waves with the wavenumber α_{TS}. Hereby, the parameter θ needs to be optimized for each particular TS wavelength α_{TS}. In order to keep the receptivity of the higher harmonics of the wave to be generated low, it is pointed out that the Fourier transform of the spatial amplitude distribution $V_{\mathrm{x}}(\alpha)$ is to be minimized for the wavenumbers of the higher harmonics. This can be done by the following measures. First, the number of actuator elements per wavelength is recommended to be set to seven or more elements to reduce the receptivity of the first four higher harmonics and might be increased to reduce the receptivity of further higher harmonics. Secondly, a high ratio of the streamwise slot width to the element width can be used to reduce the receptivity of higher harmonics. Thirdly, increasing the number of actuator elements while keeping the actuator length fixed results in narrower peaks in the Fourier transform, and therefore also reduces the receptivity for higher harmonics.

Acknowledgements

References

[1] Gmelin, C.: Numerische Untersuchungen zur aktiven Dämpfung von Störungen im Vorfeld der laminar-turbulenten Transition. Dissertation, Universität Stuttgart (2003)
[2] Laurien, E., Kleiser, L.: Numerical simulation of boundary-layer transition and transition control. J. Fluid Mech. 199, 403–440 (1989)
[3] Marx, M.: Numerische Untersuchungen und Nichtlineare Optimierung zur Aufstellung einer Berechnungsfunktion fr die Rezeptivität der Blasius-Grenzschicht. Studienarbeit (student research project advised by the authors), Universität Stuttgart (2008)

Numerical Investigation of Transition Control by Porous Surfaces in Hypersonic Boundary Layers

Heinrich Lüdeke[1], Neil D. Sandham[2], and Viola Wartemann[1]

[1] Institut für Aerodynamik und Strömungstechnik, DLR Braunschweig
Lilienthalplatz 7, 38108 Braunschweig, Germany
heinrich.luedeke@dlr.de, viola.wartemann@dlr.de
[2] University of Southampton, UK, Southampton SO17 1BJ
n.sandham@soton.ac.uk

Summary

The present numerical investigation of the effect of porous surfaces on transition in hypersonic boundary layers is intended to improve understanding of the physical mechanisms and to provide numerical tools for the prediction of the associated delay in transition. Direct numerical simulations are carried out by a 4th order version of the DLR-Flower code, compared with the results of linear stability theory. Good agreement of both approaches and an accurate prediction of the damping of the Mack-mode instability which is responsible for supersonic transition is demonstrated.

1 Introduction

In contrast to the low speed regime, disturbance evolution in hypersonic boundary layer flows occurs relatively slowly over long length scales. In the case of low level free stream disturbances and negligible surface roughness, the transition process is dominated by exponentially growing Mack modes. For these inviscid modes the boundary layer acts as a wave guide for acoustic noise, where selected frequencies are trapped and amplified, eventually leading to transition. Recently performed stability analysis and experimental studies [2] suggested that this mechanism can be delayed by using an ultrasonically absorptive surface to damp out the Mack mode [1]. Thus the first goal of transition control in high speed boundary layers is to prevent or delay the growth of Mack modes. Numerical studies of different accuracy and effort are possible, starting from stability theory coupled with standard CFD simulations of entire configurations as well as basic studies of single surface pores by DNS. All these techniques have to be verified by analytical solutions and validated by experimental data from literature. Fedorov et al.[2] presented the first linear stability results for porous surfaces, using a one-dimensional model of flow within blind (closed) pores. For the present study direct numerical simulations have been carried out by a fourth order compact finite difference version of the DLR-Flower code implemented by Stephan Enk [3]. We limit the 3D-calculations to rectangular pores so that grids match at the interface, removing

interpolation as a possible source of error. Two- and three-dimensional geometries of the porous surface are investigated. Further simulations of a blunt cone by the second order finite volume version of Flower will be used for comparison with stability theory of the porous surface of such configurations [4].

2   Numerical Approach

2.1   Direct Numerical Simulation

While the basic FLOWer code solves the compressible Reynolds-averaged Navier Stokes equations on block-structured grids with second order finite volume techniques, the high-order version used in the present work [3] uses fourth-order central differencing based on standard compact finite differences. High-order compact filters that are applied at the end of each time step. Sponge-zone boundary conditions are optional to reduce reflections. For the present work we use a 6th order filter and the standard conservative form of the Euler terms. Time advancement is applied by a five-step second order Runge Kutta method. The equations solved are the compressible Navier-Stokes equations for flow of a perfect gas with density ρ, velocity components u_i, pressure p and internal energy e, written in conservation law form as

$$\frac{\partial \rho}{\partial t} + \frac{\partial \rho u_j}{\partial x_j} = 0 \tag{1}$$

$$\frac{\partial \rho u_i}{\partial t} + \frac{\partial \rho u_i u_j}{\partial x_j} + \frac{\partial p}{\partial x_i} = \frac{\partial \tau_{ij}}{\partial x_j} + f_i \tag{2}$$

$$\frac{\partial \rho E}{\partial t} + \frac{\partial (\rho E + p) u_i}{\partial x_i} = -\frac{\partial q_i}{\partial x_i} + \frac{\partial u_i \tau_{ij}}{\partial x_j} + g, \tag{3}$$

where $E = e + u_i u_i / 2$. Forcing terms f_i and g are included in the right hand side of the equations such that a specified parallel base flow $\overline{\rho}(y), \overline{u}_i(y), \overline{E}(y)$ is time independent. In practice these terms are evaluated numerically within the code by computing and storing the initial residual. The equations are closed with the perfect gas law and constitutive relations for q_i and τ_{ij} [6]. This multiblock approach is used in the following without modification for all grids with and without pores.

2.2   Linear Stability Theory

The linear stability code of the University of Southampton, which is used for temporal stability analysis, solves the compressible Orr-Sommerfeld equations for the growth of small disturbances superimposed on a prescribed base flow. Density waves are represented as

$$\rho = \hat{\rho}(y) \exp \left[i \left(\alpha x + \beta z - \omega t \right) \right], \tag{4}$$

and similarly for other variables, where α and β are real wavenumbers in the temporal stability approach and ω as a complex frequency that is the result of the analysis. The imaginary part ω_i gives the disturbance growth rate. A caret over a variable denotes an

eigenfunction. A direct matrix solution method is used, with derivatives computed with a mapped Chebyshev method using a minimum of 150 collocation points. The code was validated by comparison with a number of sources in the literature, including Malik [5]. As shown in [6], the solutions for base flows that do not satisfy the Navier-Stokes equations are not unique and vary slightly depending on the method of derivation. The Orr-Sommerfeld results presented here are based on a derivation from the conservative equations (1-3). For spatial stability investigations of the blunt-cone boundary layer the DLR-NOLOT code is used which will be described in a later chapter.

3   Grids and Initial Solutions

For the grid generation of the study a stretching function is used in all cases that places more points near $y = 0$, including cases with pores. The wall normal grid distribution is given by a $\sinh$ function with an iteratively determined stretching factor. The calculations use periodic boundary conditions in the x and z directions. A no-slip wall with temperature set to the wall temperature of the base flow is applied at $y = 0$ and on the surfaces within the pores. At the outer boundary characteristic conditions are used. The base flow is obtained from a separate solution of the similarity equations for compressible boundary layer flow, solved by a shooting method. We consider here at Mach number $M_\infty = 6$, Reynolds number Re $= 20000$, Prandtl number Pr $= 0.72$, ratio of specific heats $\gamma = 1.4$ and an adiabatic wall boundary condition. Viscosity μ is prescribed by Sutherland's law with a constant of 110.4K and a reference temperature of 216.65K, leading to a wall temperature of 1522.44K. The base profile normal co-ordinate is normalized by the displacement thickness.

4   Results

4.1   Validation for a Smooth Wall

Stability diagrams of the growth rate ω_i against the wavenumber α calculated by the temporal stability code are shown in Fig. 1a). The other part of the figure (Fig. 1b)) shows the spatial growth rate σ against the dimensionless frequency ω, calculated by NOLOT. The most unstable mode is the second (Mack) mode, with a maximum amplification rate near $\alpha = 2.2$ and a dimensionless frequency $\omega = 2.04297$. It has to be noted, that the maxima of the temporal- and spatial growth rates are not identical, but have been compared successfully by previous tests, using a gaster transformation. The first case considered is a smooth wall boundary layer that develops a Mack mode of instability with the base flow as described in the previous section. The two-dimensional Mack mode wavelength is chosen as three times the displacement thickness, giving a streamwise wavenumber of $\alpha = 2\pi/3$. The DNS is initialized with an artifical disturbance at $t = 0$ and the eigenmode is allowed to develop from this. The initial disturbance is given by an exponentially decaying harmonic function for the v-velocity component and the other variables initialized to the base flow condition. From Fig. 1 it can be seen that the chosen wavenumber puts this wave near the peak growth rate of the second mode. The linear stability eigenvalue for this case is $\omega = 2.04297 + i0.03712$.
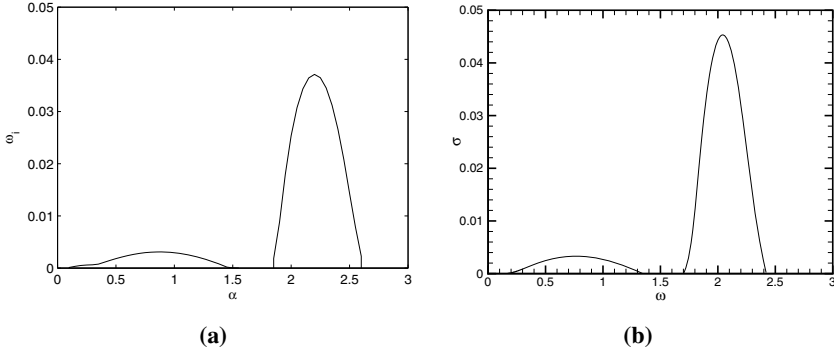
(a)   **(b)**

Fig. 1. Stability diagrams showing the growth rate of two-dimensional disturbances as a function of (a) wavenumber α and (b) dimensionless frequency ω, for the adiabatic wall case

(a)   **(b)**
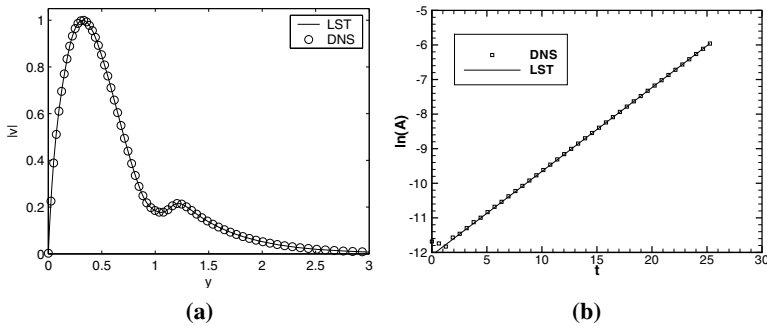
Fig. 2. Smooth wall simulation of a Mack mode in an $M = 6$, $Re = 20000$ boundary layer with $T_w = T_{aw}$, (a) comparison of eigenfunction shape. (b) Direct numerical simulation of disturbance amplitude (symbols) and linear stability theory growth rate (solid line)

The DNS of this case was set up using 32 points in the streamwise x direction and 401 points in the wall-normal direction y. Fig. 2a shows the development of the natural logarithm of the root mean square of the v perturbations (integrated over the y direction) as the simulation proceeds and the developed shape of the Eigenmode by DNS and LST. By $t = 2$ the unstable mode has emerged and grows exponentially over the remainder of the simulation. The slope of the solid line is the growth rate from linear stability theory. The agreement for the growth rate is within 0.5%. The shape of the Mack modes in the field is shown in Fig. 3 by p- and v-contours.

4.2   Mack Mode Stabilisation by Porous Surfaces

Investigating the influence of two dimensional pores on the modes of the previous section results in a reduction of the porosity into spanwise grooves. Two tests are shown here for 8 and 16 pores with a constant porosity of 25% and a pore depth of d=1.0. The grid resolution of the pores in streamwise direction is chosen with 6 cells inside the
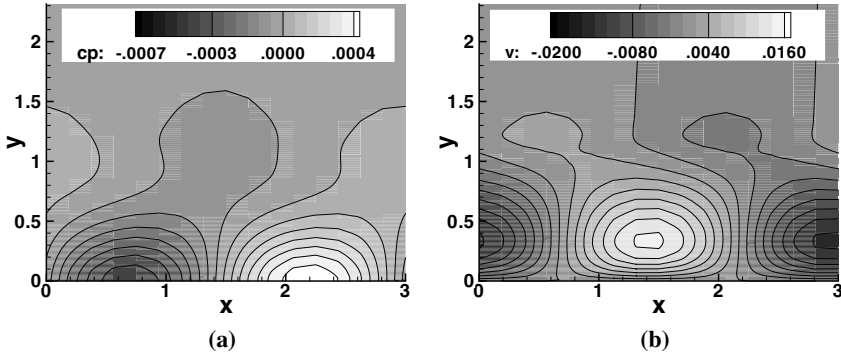
Fig. 3. Mack modes developing inside a Mach 6 boundary layer at re 20000. (a) pressure contours, (b) contours of normal velocity
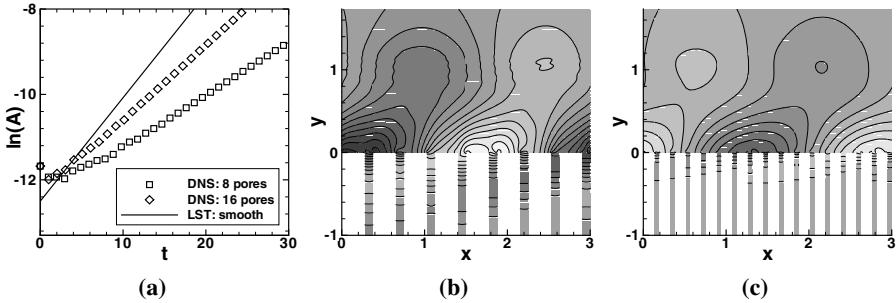

Fig. 4. Mack mode developing above a porous surface with 2D grooves at porosity n=0.25 in a Mach 6 boundary layer at Re 20000. (a) temporal development, (b) contours of p for 8 pores and (c) for 16 pores

grooves which was proven to be sufficient by a grid convergence study with 12 cells inside the pores. In Fig. 4 the Mack mode development for 8 and 16 pores is shown. The growth rate for 8 pores is calculated with 51.0% of the smooth wall case and for 16 pores with 72.2 %. Thus the growth rates are substantially lower compared to the smooth wall case, with higher reductions for fewer grooves. The reasons for this effect are evident from Figure 3 where there is clear flow activity within the grooves. A trailing leg of alternate low and high pressure and positive and negative normal velocity moves within the grooves as the Mack mode passes above. The Mack mode is seen to be superimposed with some high-frequency content, particularly for the 8-groove case (Fig. 4a). This is not a numerical resolution effect, but is caused by sound waves emanating from the groove corners. These waves are of larger amplitude when the grooves are wider.
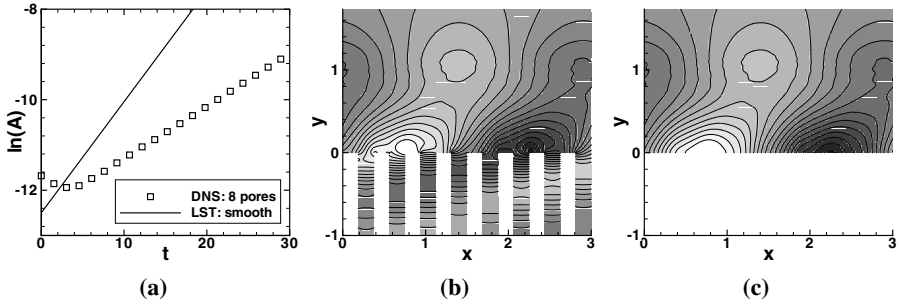
Fig. 5. Mack mode developing above a porous surface with 8 quadratic pores at porosity n=0.25 in a Mach 6 boundary layer at Re 20000. (a) temporal development, (b) contours of p for a plane through the pores and (c) for a plane that avoids pores
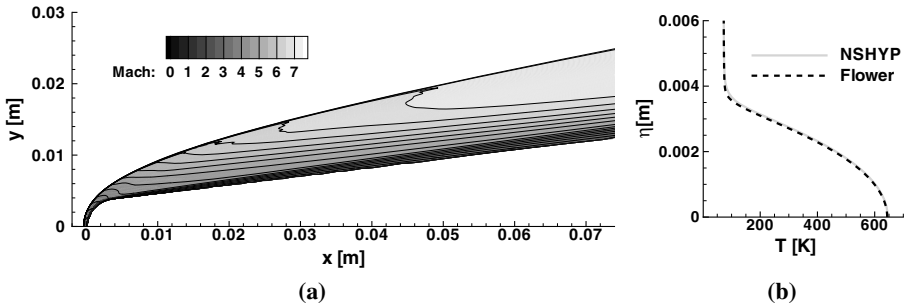

Fig. 6. (a) Mach Number distribution of blunt cone at Mach 8. (b) comparison of temperature boundary layer profiles by different codes for downstream position s=0.8 m

To confirm the assumption that the main influence on the damping is porosity at constant pore depth and not the shape of the pores, a three-dimensional testcase with 8 square pores was set up. Two slices of the flow field are shown in Fig. 5 passing through the pores and the smooth wall part respectively. The damping rate for this case is 48.1 % which is similar to the damping in the two-dimensional case.

4.3   Spatial Linear Stability Theory at a Blunt Cone

For the stability analysis at a blunt cone which is basis for future experiments with porous surfaces, the DLR code NOLOT (NOn-LOcal Transition analysis) [7] is used. For the blunt cone case a spatial local parallel analysis is performed. For this case the NOLOT code used the same wave function as the linear stability code of section 2.2 (see equation 4), but since the NOLOT code is a spatial code the wavenumbers α and β are complex and the frequency ω is real. For the laminar basic-flow calculation, the 2nd order finite volume version of the DLR FLOWer code is used and for the validation
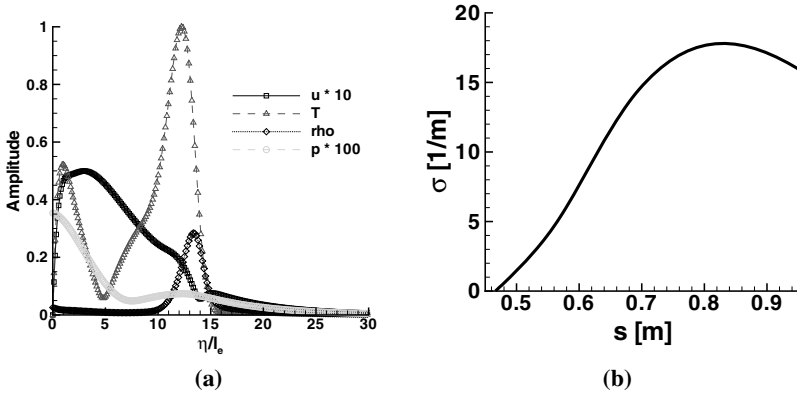
Fig. 7. (a) Amplitude eigen functions of local LST for different quantities by NOLOT, (b) Growth rate σ versus stream position s

the freestream conditions and cone geometries are adapted to the blunt cone numerical investigations of Rosenboom et al. [4] as also used by Stetson et al. [8] for their experiments. The blunt cone has a length of about 1 m, a nose radius of 3.81 mm and a half angle of $7°$. The freestream Mach number is set to $M_\infty = 8$, the freestream unit Reynolds number to $Re_u = 8.202 * 10^6$ 1/m and the freestream static temperature to T_∞ = 54.35 K. Fig. 6a shows the Mach number distribution and 6b the temperature boundary-layer profile in comparison with former CFD results from [4] for the downstream position $s = 0.8$ m. Only small differences can be seen near the edge of the boundary-layer, caused by code differences. Fig. 7 shows NOLOT results for the second mode instability at $s = 0.8$ m and a frequency of 120 kHz which is the detected maximum frequency for the growth rate. In Fig. 7a the amplitude functions $\hat{\rho}(y)$ over the wall-normal coordinate y, normalised with the Blasius length l_e are given. Fig. 7b shows the spatial growth rate σ versus the streamwise position s whereas the maximum spatial growth location is $s \approx 0.8$ m. For further steps of this cone study, porous boundary conditions will be implemented into NOLOT and Flower and comparison of stability and DNS results as well as experimental data is foreseen.

5   Conclusion

A direct numerical simulation approach has been used to study hypersonic flow over a porous surface, in which the individual pores are resolved on the computational grid. The code is validated by a Mack mode in a Mach 6 smooth wall boundary layer with fixed adiabatic wall temperature. Results for spanwise grooves and quadratic pores demonstrate strong stabilization of the Mack mode instability. Except near the region of entry to the pore the flow within the pores is one-dimensional to a good approximation, supporting one of the main assumptions made in the linear stability theory. Pore shape does not seem to be a large factor: different numbers of spanwise grooves and square

pores all give similar growth rates for the same porosity. Finally preliminary investigations of a blunt cone flow by stability analysis for comparison with planned future experiments are carried out.

Acknowledgements

References

[1] Mack, L.M.: Boundary layer linear stability theory. AGARD Special course on stability and transition of laminar flow (1984)
[2] Fedorov, A.V., Malmuth, N.D., Rasheed, A., Hornung, H.G.: Stabilization of hypersonic boundary layers by porous coatings. AIAA Journal 39(4), 605–610 (2001)
[3] Enk, S.: Ein Verfahren höherer Ordnung in FLOWer für LES. DLR IB-124-2007/8, Institut für Aerodynamik und Strömungstechnik, Braunschweig, Germany (2007)
[4] Rosenboom, I., Hein, S., Dallmann, U.: Influence of Nose Bluntness on Boundary Layer Instabilities in Hypersonic Cone Flows. In: AIAA 99-3591, 30th AIAA Fluid Dynamics Conference, Norfolk, Virginia, June 28 -July 1 (1999)
[5] Malik, M.R.: Numerical methods for hypersonic boundary layer stability. Journal of Computational Physics 86(2), 376–413 (1990)
[6] Sandham, N.D., Lüdeke, H.: A numerical study of Mach 6 boundary layer stabilization by means of a porous surface. In: AIAA Aerospace Sciences Meeting 2009, Orlando USA (2009)
[7] Hein, S., Bertolotti, F.P., Simen, M., Hanifi, A., Henningson, D.: Linear nonlocal instability analysis - the linear NOLOT code. DLR-IB 223-94 A56 (1994)
[8] Stetson, K.F., Thompson, E.R., Donaldson, J.C., Siler, L.G.: Laminar boundary layer stability experiments on a cone at Mach 8, Part 2: Blunt cone. In: AIAA Paper 84-0006 (1984)

Investigation of Laser Generated Perturbations for Boundary Layer Stability Experiments

Dirk Heitmann[1], Christian Kähler[2], and Rolf Radespiel[1]

[1] Technische Universität Braunschweig, Institut für Strömungsmechanik,
Bienroder Weg 3, 38106 Braunschweig, Germany
d-h.heitmann@tu-bs.de
[2] Universität der Bundeswehr München, Institut für Strömungsmechanik und Aerodynamik,
Werner-Heisenberg-Weg 39, 85577 Neubiberg, Germany

Summary

This paper describes boundary layer stability experiments with controlled perturbations at hypersonic flow around a flat plate. Laser pulses are used to generate pressure and temperature disturbances. By using multiple laser pulses a wave packet with adjustable amplitude and frequency can be created. The development of such artificial waves is measured with high frequency pressure sensors. The possibility to generate and excite second mode instability waves with this setup is demonstrated.

1   Introduction

The transition on a flat plate at zero angle of attack at hypersonic flows is predicted to result from the growth and final breakdown of instability waves, called the second mode waves [6]. Although this wave was detected in experiments, see e.g. [8], the dominance of this instability at noisy wind tunnel conditions is not reliably assured. Despite of several decades of research the mechanisms leading to and the parameters affecting boundary layer transition are still not completely understood. There are mainly three reasons for the difficulties in the research of this field:

– The instabilities with frequencies in the high kHz-range can hardly be detected. A lot of work has been done using hot-wires, but such measurements are difficult due to the limited mechanical strength of wires with a frequency response high enough. Furthermore this technique suffers from the wake behind the hot-wires support. Recently surface mounted sensors (pressure [1, 2] or heat flux [9]) were found as minimally intrusive measurement techniques, that allow for simultaneous measurements at subsequent positions. This is advantageous for the calculation of amplification rates.
– Nearly all hypersonic wind tunnels have turbulent boundary layers on the nozzle and test section walls. Such boundary layers are known to radiate acoustic disturbances, resulting in noise levels that are much higher than in free flight. In addition these disturbance levels are different for different facilities. Therefore e.g. the transition data on cones scatters by a factor of 4-5, [10].

- For all kind of stability experiments a "wave generator" is desirable, so that waves with well defined amplitude and frequency can be artificially generated or excited. The setup of a disturber for second modes is difficult, as well. The excitation of waves at such high frequencies is mechanically not possible. The so far only successfully operated perturbers are based on an electric glow discharge [5] and are fixed at a certain loction.

In previous works a laser-based perturber was used in subsonic flows [4]. Here such a system is applied to hypersonic flows. A high energy laser pulse can be focussed to generate a plasma, thus generating a thermal and pressure disturbance. By using several laser pulses waves can be created and amplitude and frequency can be adjusted in a very wide range. Another advantage of this setup is, that it is non-intrusive so that the disturbance position can easily be changed, even to the free stream, thus creating only a pressure disturbance that impinges on the boundary layer. Here only disturbances on the surface are treated. The oscillations of natural transition and the artificial disturbances are measured using fast response pressure gauges.

2   Experimental Setup

Facility: The experiments were performed in the Hypersonic Ludwieg Tube Braunschweig (HLB). The HLB is a wind tunnel which runs at a nominal Mach number of 6 for about 80 ms at conventional noise level. The unit Reynolds number regime is $3 - 20 \times 10^6 \, \mathrm{m}^{-1}$. A principal drawing of the HLB is shown in Fig. 1. It consists of a driver tube of 17 m length. The first 3 m upstream of the valve are heated to approximately 480 K. The length of the driver tube determines the tunnel run time. When the valve is opened an expansion wave travels into the storage tube. It is reflected at the end of the tube and reaches the valve section 100 ms after the valve was opened causing a change of pressure and temperature. A fast reacting valve separates the driver tube from the low pressure part. This valve is pneumatically driven and opens within 20 ms, thus reducing the utilizable measurement time to 80 ms. The low pressure part consists of nozzle, test section, diffuser and a 6 m³ dump tank. The nozzle maintains an opening angle of 3°. Hence the flow is still slightly expanding in the test section and the Mach number varies between 5.8 and 5.95 depending on initial driver tube pressure and axial position in the test section. To determine the flow conditions the initial driver tube pressure and the driver tube temperature during the tunnel run are measured. The unit Reynolds number can be calculated with an uncertainty of $\pm 2\%$. A large amount of this uncertainty is due to the temperature stratification (30 K have been measured) inside the storage tube. The noise level by means of pitot pressure fluctuations is between 1% and 1.5% depending on the unit Reynolds number and the position inside the test section [3]. For the experiments described later the position was chosen slightly above the centreline in order to reduce the noise.

Laser: A frequency-doubled Nd:YAG double pulse laser (Quantel Brilliant B) was used for producing the disturbances. The maximum pulse energy is 150 mJ, the pulse duration is approximately 4.2 ns and the repetition rate is 10 Hz, thus only one disturbance
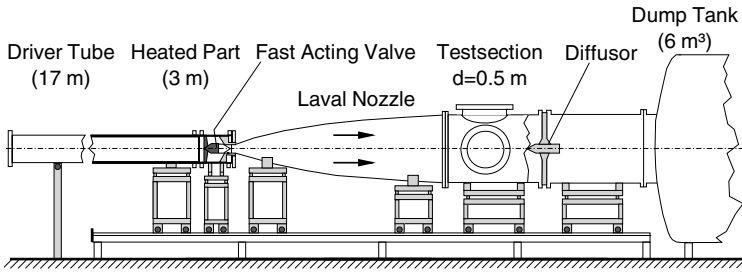
Fig. 1. Cross-sectional view of the Hypersonic Ludwieg Tube Braunschweig (HLB)

can be generated within the tunnel run time. Using the two lasers two peaks, i.e. two oscillations, can be generated. The laser power was measured before the experiments and the power was adjusted by setting the time delay between the optical pumping and the release of the pulse. However, the energy stability is about 5.5% and 7.3% for the two lasers. Therefore the power adjustment yields only in the average equal pulses and the energy of the two pulses during the tunnel run time may differ by 12.8%. The disturbance position for all experiments was at a distance of 260 mm from the leading edge, where the boundary layer is already instable and receptive for disturbances. The laser was focussed on the model surface with a diameter of 2 mm.

Instrumentation and Model: The boundary layer instabilities were measured with four flush mounted pressure sensors of type PCB-M132A31. These sensors measure pressure fluctuations. The natural frequency is specified by the manufacturer as above 1 MHz and the sensitivities are in the range of $0.02\,\mathrm{mV\,Pa}^{-1}$. The power was supplied by an instrument of type PCB-482A22, which at the same time performed signal conditioning. The high-pass filtered data ($>10\,\mathrm{kHz}$) was sampled using a Spectrum

Fig. 2. Sketch of flat plate model

M2i.4652 transient recorder with a sampling rate of 3 MHz. The sensors were mounted in round and rotatable inserts between 284 and 316 mm from the sharp leading edge of the flat plate ($630 \times 198\,\mathrm{mm}^2$), see Fig. 2. Supersonic triangles were mounted on the sides of the model in order to minimize 3-D effects. Due to the free stream disturbances that increase towards the centreline the model was installed 90 mm above this line with a small incidence to compensate for the conical flow.
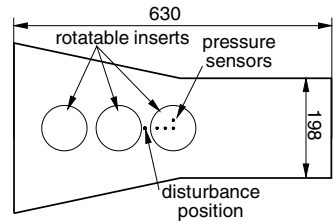
3   Results

3.1   Boundary Layer Instabilities at Natural Transition

Before showing results with artificial disturbances the natural transition is shown. These measurements were already published before and more informations are given in [8]. Figure 3 depicts the spectra of pressure fluctuations for four subsequent pressure gauges.

For the sensor at 192 mm from the leading edge apart from low frequency oscillations (below 50 kHz) no significant peak is visible. The curves of the later sensors show an additional peak slightly above 100 kHz, representing the second mode. The frequency of maximum amplitude decreases towards increasing running length. This is due to the increasing boundary layer thickness, since the second mode waves have wavelengths of approximately twice the boundary layer thickness [6]. The unit Reynolds number ($Re_\infty/l = 6.66 \times 10^6 \, \text{m}^{-1}$) is quite high. This results in a shorter transition length. The second mode is already nea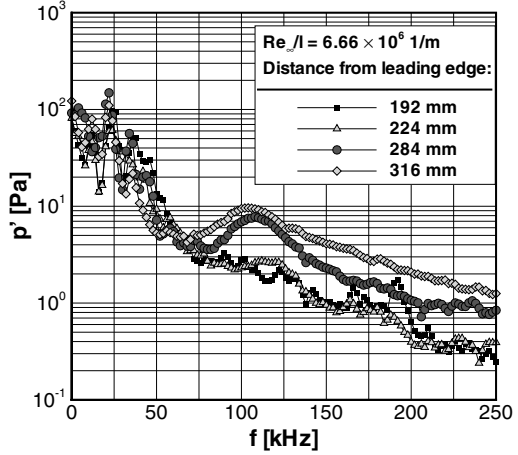r its saturation at $x = 316$ mm. The contour plot in Fig. 4 was obtained from several spectra like those in Fig. 3. Only the sensor

Fig. 3. Spectra of pressure fluctuations at four positions

at $x = 284$ mm was considered and the unit Reynolds number was varied. The second mode is first detectable for a Reynolds number of $Re_x = 1.3 \times 10^6$. With increasing Re_x the most unstable frequency increases slightly.
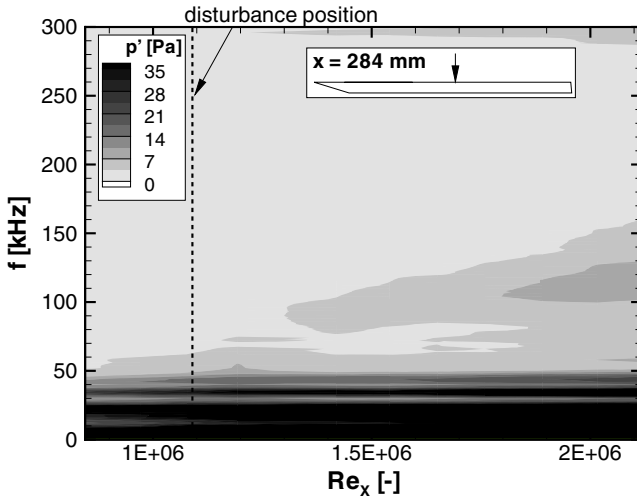

Fig. 4. Spectra of pressure fluctuations at $x = 284$ mm for different unit Reynolds numbers

3.2   Boundary Layer Instabilities with Artificial Disturbances

The disturbances were introduced at a distance of 260 mm from the leading edge. Since the experiments were made at a fixed unit Reynolds number of approximately
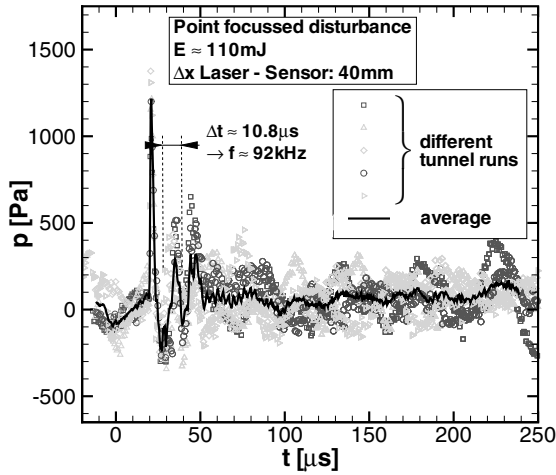
Fig. 5. Time traces of a pressure sensor 40 mm downstrem of a single point shaped disturbance at $E \approx 110$ mJ

$4.19 \times 10^6 \, \text{m}^{-1}$ the Reynolds number, where the disturbance is generated, is fixed at 1.09 Mio. The dashed line in Fig. 4 shows this Reynolds number. Figure 5 shows for five tunnel runs the time traces of a pressure sensor 40 mm downstream of a point shaped single pulse disturbance. In this case the laser was focussed to a diameter of about $\varnothing = 2$ mm and the pulse energy was about 110 mJ. The data shows a lot of scattering for the five runs. However, the average clearly shows three peaks. At this high energy there should be a shock wave propagating from the perturbation position. The first peak represents this shock wave, which reaches the sensor about $20 \, \mu s$ after the laser has fired. With the distance of 40 mm this yields an average velocity of 2000 m s^{-1} for the shock wave plus free stream velocity (≈ 920 m s^{-1}). After this peak two additional peaks appear with 10.8 μs between. This Δt represents a frequency of $f = 92$ kHz, which is in the range where the second mode would be expected. However, the question arises by means of which mechanism a wave can be generated by a single pulse. Possibly the heating of the air causes the boundary layer to get unstable so that a wave is released. This result is quite well repeatable. Masad & Nayfeh, [7] investigated the premature and delayed transition of subsonic boundary layers in dependency of introduced cooling and heating. They found that a cooling strip upstream of the neutral stability point destabilizes the boundary layer, because the wall appears warm to the cooled air that passes over the strip. So the integrated amplification is greater downstream, after a short time where the instability waves were damped. But this is only valid for Tollmien-Schlichting waves in low speed. The theoretical work of Mack [6] indicates a vice versa behaviour for second mode waves, i.e. cooling has a destabilizing effect. In Fig. 6 the time traces of three sensors are shown for three different pulse energies. The curves are averages of five tunnel runs. The upper plot shows an excitation with the highest energy. The shock wave is detected by all three sensors. The foremost sensor 24 mm downstream of the disturbance detects no peaks apart from the shock wave whereas
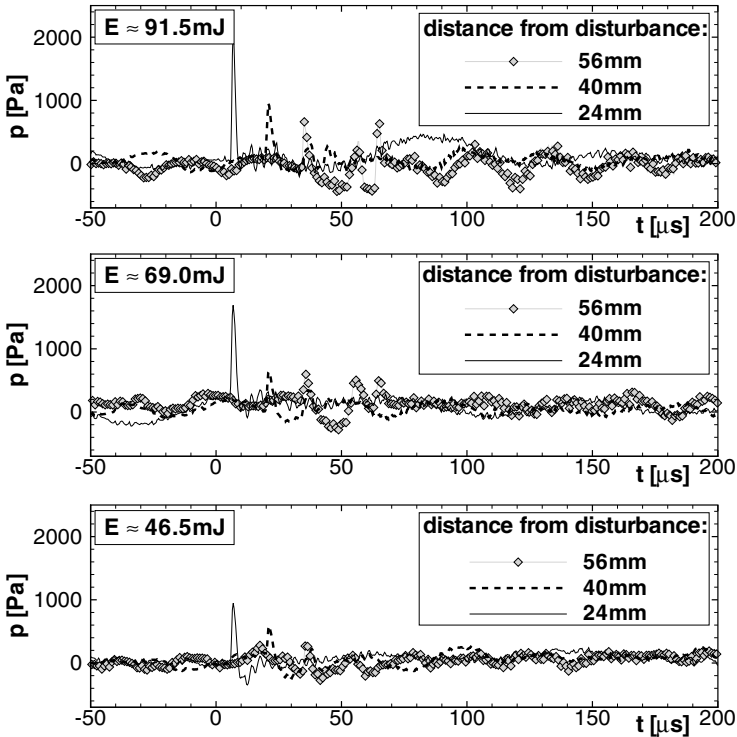
Fig. 6. Time traces of pressure sensors downstream a single point shaped disturbance for pulse energy variation

the sensor at $x = 40$ mm detects two ripples at $t = 30 - 40\,\mu s$ of about the same size and shape. 16 mm downstream these ripples are also visible, while the amplitude is increased, but the amplification of the two peaks is different. For medium pulse energy the shock wave for the foremost sensor shows of course a smaller amplitude. The curve for the sensor at $x = 40$ mm shows one peak apart from the shock wave. But the $x = 56$ mm-curve shows two ripples. I.e. for this less heated air the boundary layer is less destabilized and the formation of a wave happens more slowly. In the lower plot only for the middle and not for the last sensor one additional peak appears. This might be due to a too small heating or it might result from the small signal to noise ratio. It seems that the amplitude of the waves can be adjusted by properly setting the energy of the lasers. In the present case a medium energy was appropriate. For higher energies the growth of the waves took place too fast and for the lower energy the sensors did not detect anything. It must be mentioned that the amplitudes of the artificial waves were already rather large. Note that an amplitude of 700 Pa correlates to the amplitudes of natural wave packets at Reynolds numbers twice as high as in the experiments in Fig. 6 and it must be assumed that non-linear effects influence their growth.
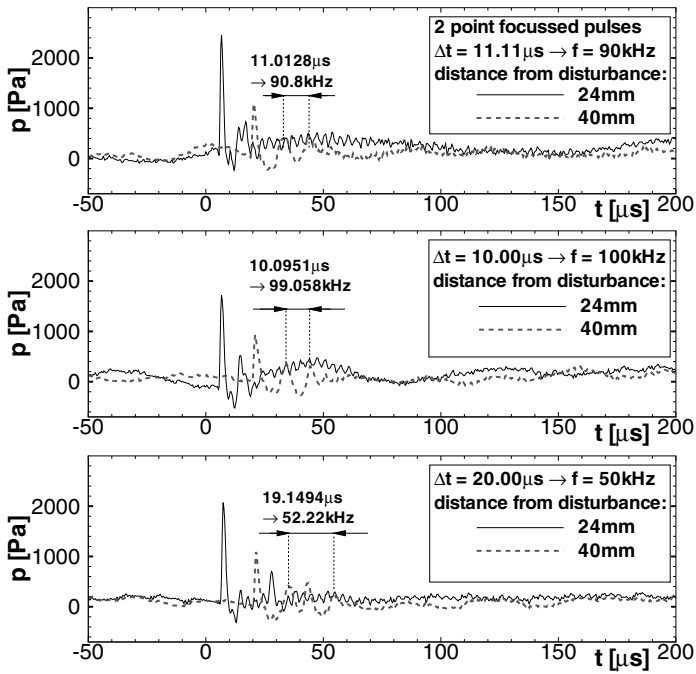
Fig. 7. Time traces of pressure sensors downstream a point shaped double-pulse with different Δt ($E = 91.5\,\mathrm{mJ/pulse}$)

If the instability is generated by a local destabilization of the boundary layer it is questionable if a certain frequency can be prescribed by this approach. In Fig. 7 two laser pulses with different Δt between were used in order to generate waves with different frequencies. The three plots show time traces for $\Delta t = 11.11, 10.0$ and $20.0\,\mu s$ representing the frequencies $f = 90, 100$ and $50\,\mathrm{kHz}$, respectively. In the upper plot (90 kHz) the foremost curve exhibits the peak of the shock wave of the first laser pulse. The shock wave of the second pulse nearly coincides with a released wave. 16 mm further downstream a wave consisting of two ripples is present and the frequency matches the set value very well. The middle plot shows the same good agreement for 100 kHz. This frequencies are very close to the waves released by a single pulse. The good agreement between set and measured time might be a result of mere serendipity. Therefore it is necessary to show the possibility to excite frequencies that are quite different from the unstable ones. This is depicted in the lower plot. Here the forward sensor detects both shock waves more clearly due to the larger Δt, although the first one exhibits a larger amplitude. Although the curves shown here are averages it is assumed that this difference results from deviations in the pulse energies. The curve of the rear sensor shows four peaks, two of them representing the shock waves. However, the adjusted 50-kHz-frequency can still be found in the signal.

4   Conclusion

A laser-based perturber for controlled boundary layer transition experiments was validated for the application in the hypersonic flow regime. The properties of such a perturber are unique concerning the possibility to adjust frequency, amplitude and location of the disturbance. The results of some experiments with point-shaped disturbances on the surface were presented. These results show that by means of such a point source a wave packet can be generated that is extending as it convects downstream. To the author's knowledge this is the first detection of second mode waves, that were generated optically. The wave is presumably generated by the destabilization of the boundary layer due to the thermal disturbance. In this experiments always a combination of pressure and thermal disturbance affected the boundary layer. These two disturbances could be detected separately in the time traces because of their different propagation velocities. It appears that the thermal disturbace mainly drives the forcing since the peaks of the shock wave decreased while the peaks of the thermal disturbance showed growth. In the following experiments with the disturbance above the model are planned in order to separate the effects of thermal and pressure perturbation and clarify this issue.

Acknowledgements

References

[1] Estorf, M., Radespiel, R., Schneider, S.P., Johnson, H.B., Candler, G.V., Hein, S.: Surface-pressure measurements of second-mode instability in quiet hypersonic flow. In: AIAA 2008-1153, AIAA Aerospace Sciences Meeting, Reno, NV (January 2008)

[2] Fujii, K.: Experiment of Two-Dimensional Roughness Effect on Hypersonic Boundary-Layer Transition. J. Spacecraft and Rockets 43, 731–738 (2006)

[3] Heitmann, D., Rödiger, T., Kähler, C.J., Knauss, H., Radespiel, R., Krämer, E.: Disturbance-Level and Transition Measurements in a Conical Boundary Layer at Mach 6. In: AIAA-2008-3951, 26th AIAA Aerodynamic Measurement Technology and Ground Testing Conference, Seattle, Washington, June 23-26 (2008)

[4] Kähler, C.J., Dreyer, M.: Dynamic 3D stereoscopic PIV and schlieren investigation of turbulent flow structures generated by laser induced plasma. In: 12th International Symposium on Applications of Laser Techniques to Fluid Mechanics, Lisbon, Portugal (2004)

[5] Kosinov, A.A., Maslov, A.A., Shevelkov, S.G.: Experiments on the stability of supersonic laminar boundary layers. J. Fluid Mech. 219, 621–633 (1990)

[6] Mack, L.M.: Boundary Layer Linear Stability Theory. Special Course on Stability and Transition of Laminar Flow, AGARD Rept. 709, 379–409 (March 1984)

[7] Masad, J.A., Nayfeh, A.H.: Laminar flow control of subsonic boundary layers by suction and heat-transfer strips. Phys. Fluids A 4(6), 1259–1272 (1992)

[8] Rödiger, T., Heitmann, D., Knauss, H., Smorodsky, B.V., Bountin, D.A., Maslov, A.A., Radespiel, R., Krämer, E.: Hypersonic Instability Waves Measured on a Flat Plate at Mach 6. In: 14th Int. Conf. on Methods of Aerophysical Research, Novosibirsk, Russia (2008)

[9] Rödiger, T., Knauss, H., Krämer, E., Estorf, M., Schneider, S., Smorodsky, B.V.: Hypersonic instability waves measured using fast-response heat-flux gauges. In: AIAA 2008-0638, 46th AIAA Aerospace Sciences Meeting and Exhibit, Reno, Nevada (2008)

[10] Schneider, S.: Hypersonic Laminar-Turbulent Transition on Circular Cones and Scramjet Forebodies. Prog. Aerosp. Sci. 40, 1–50 (2004)

Eulerian and Lagrangian Insights into a Turbulent Boundary Layer Flow Using Time Resolved Tomographic PIV

A. Schröder[1], R. Geisler[1], K. Staack[1], A. Henning[1], B. Wieneke[2], G.E. Elsinga[3], F. Scarano[3], C. Poelma[4], and J. Westerweel[4]

[1] Deutsches Zentrum f. Luft- und Raumfahrt e.V. (DLR), Institut für Aerodynamik und Strömungstechnik Bunsenstrasse 10, 37073 Göttingen, Germany
[2] LaVision GmbH, Anna-Vandenhoeck-Ring 19, 37081 Göttingen, Germany
[3] Delft University of Technology, Department of Aerospace Engineering, Kluyverweg 1, 2629HS, Delft, The Netherlands
[4] Delft University of Technology, Laboratory for Aero- and Hydrodynamics, Leeghwaterstraat 21 2628 CA Delft, The Netherlands
`Andreas.Schroeder@dlr.de`

Summary

Turbulent boundary layer (TBL) flow consists of manifold temporal and spatial scales and is governed by the organization and decay of self-sustaining coherent flow structures driven by entrained high momentum fluid. Generic flow structures such as hairpin-like vortices and spanwise alternating wall bounded low- and high-speed streaks have been observed and extensively analyzed with both experimental and numerical methods. The role of these structures for the wall normal and spanwise fluid exchange has been highlighted mostly within an Eulerian reference frame. But for an understanding of the momentum exchange in turbulent wall flows a step towards a spatially resolved Lagrangian frame of reference would be advantageous. The data achieved from the present application of time-resolved tomographic PIV to a flat plate turbulent boundary layer flow enables for the first time the investigation of the flow structures and related particle motions within a temporally and spatially resolved Lagrangian and Eulerian frame of reference.

1 Introduction

In the turbulence research community two branches can be distinguished either with a more or less application driven focus on shear- and wall bounded turbulence or with a more fundamental research driven interest in so called homogeneous, isotropic turbulence. In the isotropic turbulence branch Lagrangian statistics on temporally highly resolved trajectories of few single spatially independent tracer particles in the flow using different PTV techniques are dominant on the experimental side. While in the shear- and wall bounded turbulence research Eulerian reference frame approaches

using PIV or hot-wire probe techniques became dominant leading to concepts and models of coherent structures as the main carriers of turbulent fluid exchange. This branch development seems to be quite natural as in shear flows the intrinsic turbulent dissipation scale ε and therefore the Kolmogorov scales η and τ$_η$ are depending on the position in space resp. wall distance for TBL, while they are universal in isotropic turbulence making assumptions on highest levels of generality possible relying on high performance DNS data [1][2]. Up to now the experimental Lagrangian turbulence characterization has been performed by statistical analysis over several spatially independent single or groups of particles measured by tracking methods [3][4]. One of the challenges of experimental turbulence research is therefore the combination of both viewpoints in a single experiment.

In the past two decades considerable experimental and numerical work on coherent structures in wall bounded turbulent flows has been carried out. A focus of the present work will be models of coherent flow structures, which have been developed partly by using the PIV techniques [5][6][7][8][9]. In a most recent paper [10] the scaling properties, topologies and distribution functions of vortices in a turbulent boundary layer using conditional averaging and space correlation functions have been described. They found in accordance to earlier PIV measurements [8] that hairpin like vortices are dominantly one sided and cane shaped and play a major role for the spatial organization of wall normal and spanwise flow exchange. They are apparently connected to the turbulence production events, the (instantaneous) negative Reynolds stresses $u'v'$, so called Q2- and Q4- events in the buffer- and log- layer.

The first time results of time-resolved 3D-3C velocity vector fields from turbulent wall bounded air flows gained by using tomographic PIV have been published in [11]. The turbulent mixing due to the Q-2- and Q-4-events, has been found to be connected to a staggered pattern of hairpin-like vortices, see idealized mixer-model of substructure formation inside a turbulent spot [12]. Hairpin vortex forming events have been found in the 3D-3C and time resolved data of [13].

For the first time we achieved flow information with sufficient resolution from both reference frames: Eulerian and Lagrangian. The very high time sampling rate allows to fully resolving the flow for the Kolmogorov time scales. After tomographic reconstruction of a time series of particle image recordings in volumes a PTV algorithm from *LaVision* has been employed enabling to describe the motion of several thousands of particles in a Lagrangian frame of reference within the measurement volume. Time series of instantaneous 3D velocity vector fields have been determined, while 3D-vorticity and swirling strength fields λ$_2$ are represented by iso-surfaces.

2   Test Set-Up and Procedure

The experiments have been conducted in the water tunnel at TU Delft where a turbulent boundary layer flow has been established along a flat acrylic glass plate at a free stream velocity of 0.53 m/s. The plate was employed with an elliptic leading edge, while a nearly zero pressure gradient has been adapted by a trailing edge flap. The flow on the observation side was tripped by a spanwise attached zig-zag band

150 mm downstream of the leading edge resulting in a thickness of the turbulent boundary layer of 38 mm corresponding to $Re_\theta \sim$ 2460 based on momentum thickness. The turbulence level of the free stream was below 0.5 %. For the general characterization of the boundary layer flow a high resolution 2C-PIV experiment with a low-repetition rate system with LaVision Imager PRO-X camera of 4 Mpixels has been performed. One thousand statistically independent particle images in a region of $\sim$ 50 x 50 mm² have been evaluated by 8 x 8 pixels interrogation windows corresponding to a spatial resolution of 4.4 wall units in x- and y-direction in an ensemble correlation mode. The resulting semi-logarithmic boundary layer profile calculated in wall units after applying the Klauser-method for skin friction velocity estimation is given in Figure 1 (bottom-right). The skin friction velocity has been estimated by regression between $y^+ = 44$ and $y^+ = 200$ to $u_\tau = 0.0219$ m/s and the coefficient to $c_f = 0.00345$. Buffer layer, log-layer and bulk region can be distinguished in the single wall distance regions by their characteristic curvatures.
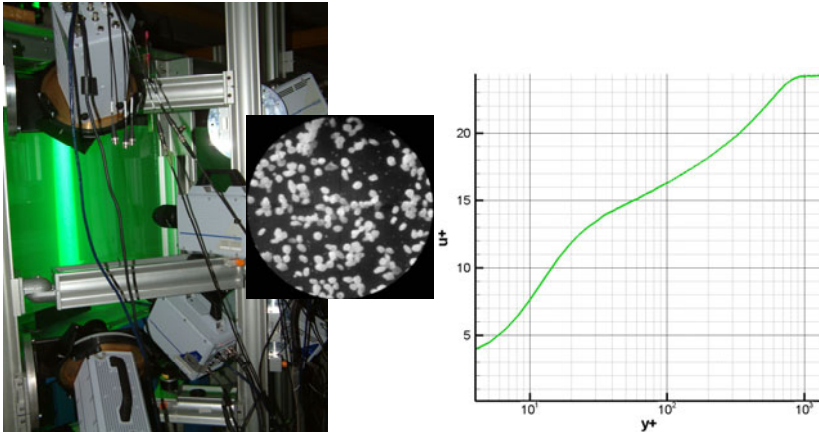

Fig. 1. Six CMOS cameras at 1 kHz framing rate at TU Delft water tunnel. The measurement volume of 63 x 15 x 68 mm³ in TBL at 2.09 m downstream of the leading edge (left). Polyamide seeding particles with ~56 µm diameter (top-right). Profile of TBL at $Re_\theta \sim$ 2460 at measurement position (bottom-right).

In a second step a high-repetition rate tomographic PIV system has been applied by making use of a diode pumped double cavity Nd:YLF high repetition rate laser from *Quantronix* with a pulse energy of 25 mJ at 1 kHz and six *Photron* CMOS cameras in 1024 x 1024 pixels full frame modus (see Figure 1 left). Six cameras have been positioned in an angular viewing geometry adapted in Scheimpflug mounts. The volume illumination in a rectangular shape was realized by guiding the laser beam through two spherical and two cylindrical lenses and a final knife edge frame. As sufficient light was scattered by the polyamide seeding particles with 56 µm average diameter (see Fig 1 top-right) astigmatism effects could be avoided without the use of prisms by reducing the aperture of the four *Zeiss* f = 100 mm and two *Nikkor* f = 105 mm
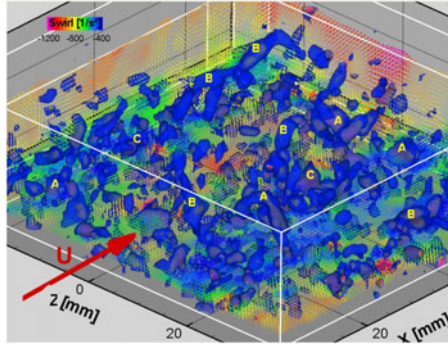
Fig. 2. An instantaneous 3D-velocity volume extracted from a time series depicting flow structures by iso-surfaces of swirl-strength value λ_2 and selected velocity planes at $y^+\sim 75$ ($u-u_{ref}$ color coded, U = 0.53 m/s)

camera lenses down to $f_\# = 11$. A volume of about 63 x 15 x 68 mm³ = 734 x 176 x 793 voxels = 1380 x 328 x 1490 wall units in x-, y- and z direction (x- stream wise and y- wall normal) centred 2090 mm downstream of the leading edge has been illuminated at 1 kHz frequency. Five times 2040 images were captured in a time series of 2 s at 1 kHz each. With the DaVis7.3 software tool the reconstruction of the three-dimensional particle light intensity distributions has been calculated by means of the MART tomographic algorithm optimized for PIV signals [14] returning a 3-D array of voxels where the intensity is digitally stored. Before final reconstruction of the particle image volumes a volume-self-calibration according to [15] has been performed. The particle image volume is analyzed by 3D cross-correlation with an iterative multi-grid volume deformation scheme reaching a final 32³ voxels interrogation box size. For particle image cross-correlation the Δt between two reconstructed volumes has been chosen to be 2 ms in order to enhance the dynamic range of the velocity fluctuations and reduce the number of correlated ghost particles. With a given magnification of 85.9 µm/voxel the final 32³ voxels corresponds to a spatial resolution of ~ 2.75 x 2.75 x 2.75 mm³ and with 75 % overlap a series of instantaneous three-dimensional velocity vector volumes over a grid of 92 x 99 x 22 (200,376) measurement points located every 0.687 mm ~ 15 WU in all directions in space.

3   Results

3.1 Instantaneous 3D-3C(t) Velocity Vector Fields

Processing of 10200 tomographic particle volume reconstructions by MART and local 3D cross-correlations of 5100 (each second pair) has been realized by using DaVis 7.3. Instantaneous velocity vector volumes with a mean particle image shift of ~9 voxels were calculated and after conversion to physical quantities 3D vorticity and swirl strength λ_2 have been determined besides the overall average over all 5100
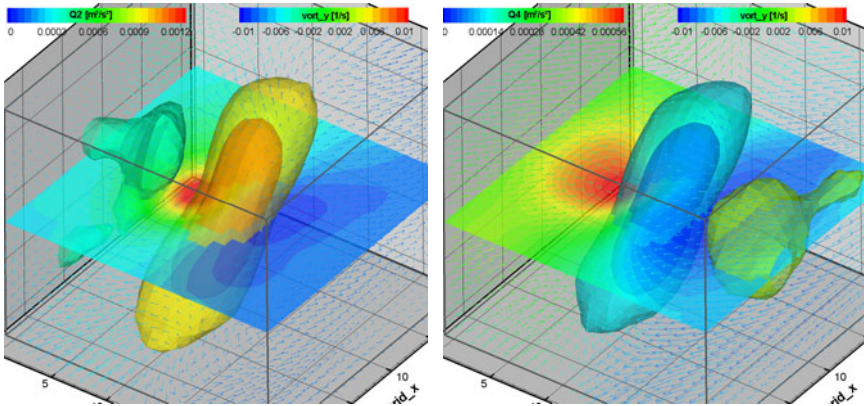
Fig. 3. Generic 3D topology of conditional averaged y-vorticity separated by sign (plus-left and minus-right) represented by iso-surfaces and corresponding Q2- (left) and Q4- (right) events represented by the contour plot with magnitude colour coding in a horizontal plane at $y^+ = 150$

samples. After subtracting the mean from the single instantaneous velocity vector volumes the fields of fluctuation velocities u', v' and w' and the four quadrants of the Reynolds stress Q1 to Q4 have been derived. Examples of the results of global and local statistics are shown in the next chapters.

The number of spurious vectors was less than 1 %. In Figure 2 a snapshot out of the time series of velocity vector volumes shows the distribution of vortical structures formed as arch or hairpin-like (A), cane (B) or arbitrary (C) vortices within the turbulent flow visualized by the iso-surfces of the swirl-strength value λ_2. The colour coding of the vectors represents the $u - u_{ref}$ velocities indicating low and high speed regions. It is visible that low speed regions are closely surrounded by vortical structures of different scales, while the smaller ones are close to the wall. Most of these vortical structures remain stable over longer times while convecting downstream. They are slightly increasing in height while canes induce sometimes a "counter rotating vortex leg" on the opposite side of a low speed streak, but often on a slightly different streamwise position. In some cases very low speed streaks are formed by or connected to packages of successive arch vortices as described in [16]. A topological analysis by space-time-correlations and conditional averaging has been calculated in a next step.

3.2 Conditional Averaging

Two point 3D space-time correlation functions have been calculated and will be presented in another paper due to page limitation. For the vortices and their connection to the turbulence production, namely the Q2 and Q4 events a conditional averaging has been employed over the whole dataset. Therefore a detection and segmentation algorithm has been developed using a threshold and number of neighbours' criteria. A 3D box around that event detected at a distinct wall distance
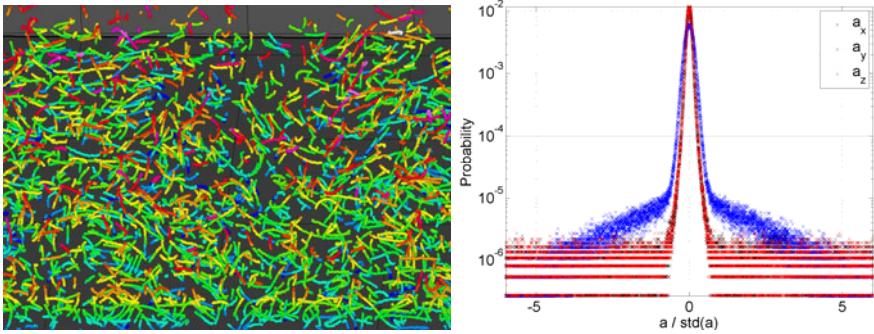
Fig. 4. Relative motion of Lagrangian tracks with more than 40 time steps in a sub-volume (left) and PDFs of the lagrangian acceleration components in the logarithmic layer of the TBL at $Re_\theta \sim 2460$ normalised by the standard deviation in x-direction (right)

(here y = 6.87 mm corresp. to y^+ = 150) has been cut out of the single instantaneous velocity vector volumes. Then all boxes at all found events in 5100 samples have been averaged for gaining a smooth generic topology. Results of the averaged 3D vortex structure for the positive and negative y-vorticity component events with the thresholds +/- 0.05 1/s and the related Q2 and Q4 flow through a horizontal plane is shown in Fig. 3. One can see the vortex structures, connected to both y-vorticity signs, are inclined by an angle of approximately 45°. Q2- and Q4- production events are located directly in the spanwise vicinity of the vortex tube depending on rotation direction, while Q2 possesses ~2 times higher values with less spatial extension. A weak second vortex structure with an opposite sign, but only ~15 % vorticity can be found on the opposite side of the low speed and Q2 event, indicating the low probability of the appearance of *symmetric* hairpin-like or arch vortices. Streamwise shifts of the counter vortex can also contribute to this low probability value.

This confirms the dominant role of vortices for the turbulence production in general. Another calculation for the conditional average of the Q2 event at the same y^+ = 150 position the distance of the averaged neighbouring y-vorticity cores is Δz^+ = 120 and for the Q4 case Δz^+ = 140, which confirms the spanwise spacing of vortices found in literature [9] and supports the idea that the vortex formation at corresponding Reynolds stress events is ruled by near wall streaks even at this wall distance.

3.3 Lagrangian Approach

For the detection of tracer particles in the time series of reconstructed particle image volumes a 3D-PTV algorithm from LaVision has been employed. Sub-pixel 3D-particle locations are fitted within the volume by a 5x5x5 Gaussian fit for all peaks above a certain threshold. Possible particle matches are restricted by several criteria. First velocities must fall within a global possible range, and the change in velocity from one time step to the next must be below an absolute value (here 1 pixel) and also less than an allowed velocity gradient in pixel-displacement / pixel-distance (here 0.5). Finally particles must be visible for several time steps. Only particle tracks

longer than 18 time steps are taken. Next particles are resolved by taking the path where the particle intensity remains the most similar. Figure 4 (left) shows selected 3-D Particle trajectories in a section of the investigated volume with subtracted convection. Note that the figure depicts only a small fraction of the overall identified trajectories. The total number of tracked particles is in the order of 10^5. In order to calculate the Lagrangian accelerations, a moving 3rd order polynomial is used. For each time step, t, and around each point of a measured trajectory a third order polynomial is fitted from t−9 Δt to t+9 Δt for each component, x, y, z.. The acceleration is then derived from the second derivative of the polynomial at the respective time step (see [17] for more details). Figure 4 (right) depicts the PDFs of the acceleration components in the measurement (logarithmic) region normalized by the standard deviation in x-direction. A detailed interpretation of the Lagrangian acceleration goes beyond the scope of this paper. But as a first result, it can be seen that the acceleration distribution has a more intermittent character especially for the y-direction then described by a Gaussian distribution.

4 Conclusions and Outlook

The tomographic PIV technique has been applied to time-resolved particle images for an investigation of the coherent structures in a turbulent boundary layer flow along a flat plate in a water tunnel at $Re_\theta \sim 2460$. Six high speed CMOS cameras are imaging tracer particles which are illuminated by two high repetitive pulse lasers in a volume of 1,66δ x 0.39δ x 1.79δ at 1 kHz. Each of two subsequently acquired and reconstructed particle distributions have been cross-correlated in small interrogation volumes using iterative multi-grid schemes with volume-deformation in order to determine a time series of instantaneous 3D-3C velocity vector fields. Consistent and frequently appearing flow structures can be identified and related to the known models (arch- or hairpin- vortices etc.). Conditional averaging over certain flow events found inside the 3D velocity volumes provides a model of the connection of the turbulence producing Q2- and Q4-events and vortices in a spatial flow topology. Additionally the PDF's of Lagrangian accelerations have been calculated as a first result within the moving reference frame. The aim is to contribute to an enhancement of the understanding of structural self-organization processes, scaling properties and the energy and momentum budgets of wall bounded turbulent flows in the near future.

References

[1] Yeung, P.K.: Lagrangian investigations of turbulence. Annu. Rev. Fluid Mech. 34, 115–142 (2002)
[2] Biferale, L., Boffetta, G., Celani, A., Lanotte, A., Toschi, E.: Lagrangian statistics in fully developed turbulence. Journal of Turbulence 7(6) (2006)
[3] Virant, M., Dracos, T.: 3D PTV and its application on Lagrangian motion. Meas. Sci. Technol. 8, 1539–1552 (1997)
[4] Mordant, N., Lévèque, E., Pinton, J.-F.: Experimental and numerical study of the Lagrangian dynamics of high Reynolds turbulence. New J. Phys. 6, 34 (2004)

[5] Robinson, S.K.: The kinematics of turbulent boundary layer structure. NASA Technical Memorandum, 103859 (1991)

[6] Meinhart, C.D.: Investigation of turbulent boundary-layer structure using Particle-Image Velocimetry Thesis, University of Illinois at Urbana-Champaign (1994)

[7] Schoppa, W., Hussain, F.: Genesis and dynamics of coherent structures in near-wall turbulence. In: Panton, R. (ed.) Self-sustaining Mechanisms of Wall Turbulence, pp. 385–422. Computational Mechanics Publications (1997)

[8] Tomkins, C.D., Adrian, R.J.: Spanwise structure and scale growth in turbulent boundary layers. J. Fluid. Mech. 490, 37–74 (2003)

[9] Kähler, C.J.: The significance of coherent flow structures for the turbulent mixing in wall-bounded flows. Dissertation, DLR Forschungsbericht 2004 -24 (2004) ISSN 1434-8454

[10] Stanislas, M., Perret, L., Foucaut, J.-M.: Vortical structures in the turbulent boundary layer: a possible route to a universal representation. J. Fluid Mech. 602, 327–382 (2008)

[11] Schröder, A., Geisler, R., Elsinga, G.E., Scarano, F., Dierksheide, U.: Investigation of a turbulent spot using time-resolved tomographic PIV., CD-Rom, Paper 1.4. In: Proceedings, 13th International Symposium on Applications of Laser Techniques to Fluid Mechanics, Lisbon (Portugal), June 26-29 (2006)

[12] Schröder, A., Kompenhans, J.: Investigation of a turbulent spot using multi-plane stereo PIV. Experiments in Fluids, Selected issue 36, 82–90 (2004)

[13] Schröder, A., Geisler, R., Elsinga, G.E., Scarano, F., Dierksheide, U.: Investigation of a turbulent spot and a tripped turbulent boundary layer flow using time-resolved tomographic PIV. Experiments in Fluids 44(2), 305–316 (2008)

[14] Elsinga, G.E., Scarano, F., Wieneke, B., van Oudheusden, B.W.: Tomographic particle image velocimetry. Experiments in Fluids 41(15), 933–947 (2006)

[15] Wieneke, B.: Volume self-calibration for Stereo PIV and Tomographic PIV. Experiments in Fluids 45(4), 549–556 (2007)

[16] Ganapathisubramani, B., Longmire, E.K., Marusic, I.: Characteristics of vortex packets in turbulent boundary layers. J. Fluid Mech. 478, 35–46 (2003)

[17] Lüthi, B.: Some Aspects of Strain, Vorticity and Material Element Dynamics as Measured with 3D Particle Tracking Velocimetry in a Turbulent Flow. Dissertation (2002)

An Automated Test Section for the Experimental Optimization of Multi-element High-Lift Systems

S. Blume and W. Nitsche

Technische Universität Berlin, Institut für Luft- und Raumfahrt
Marchstraße 12, 10587 Berlin, Germany
stefan.blume@ilr.tu-berlin.de

Summary

A wind tunnel test section setup is described, which allows an automated analysis and optimization of the aerodynamic performance of two-dimensional three-element high-lift systems by varying the slat and flap settings. The gap, overlap and angle of attack of the high-lift devices are varied by remote by means of side wall integrated flush mounted traverses. The side wall implemented balance system is able to measure lift, drag and pitching moment of each of the high-lift system elements (slat/main section/flap) individually. Finally, results of a systematic analysis of the aerodynamic performance depending on the flap setting as well as an automated flap setting optimization using the Nelder-Mead method [1] are demonstrated.

1 Introduction

The design of high-lift systems is an essential part of the airplane development process. Among structural and system integrative aspects, the aerodynamic performance of the system, which has to fulfill the requirements of the different flight phases, is of major importance. Already during the preliminary phase of the high lift design-process, the definition of the specific high-lift devices for the leading and trailing edge of the wing takes place as well as the determination of the optimum device profiles and their spanwise and chord extension, [2]. In addition, the takeoff and landing performance is optimized depending on the high-lift device settings. The modern CFD-based high-lift design process combines 2D-CFD-methods with optimizer-tools to find the optimum setting, which means the optimum gap, overlap and deflection angle for the high-lift devices, [3]. Multiple flow phenomena affect the flow around a high-lift system; each of them poses a challenge for numerical methods: the laminar-turbulent transition, re-laminarization, geometry as well as pressure-induced separation and the interaction between the wakes and boundary layers. Down to the present day, CFD-methods capture these phenomena occasionally insufficiently due to the complexity of the high-lift flow physics. This paper describes a wind tunnel test section that allows an automated systematic analysis as well as the optimization of the aerodynamic performance of high-lift systems by varying the slat and flap settings. Therefore, this test section is intended to support the numerical preliminary design of high-lift systems.

2   Experimental Set-Up

The experimental optimization of the slat and flap setting of a high-lift system is based on the interaction between the optimizer and the wind tunnel test setup. The optimizer defines the settings of the high-lift devices and evaluates the aerodynamic performance of the high-lift system on the basis of the aerodynamic coefficients delivered by the test setup. Therefore, the wind tunnel test setup has to be able to determine the aerodynamic forces and moments for arbitrary gaps, overlaps and deflection angles of the high-lift devices as well as to transfer this information in terms of aerodynamic coefficients to the optimizer. Subsequently, the specific components of the test setup will be explained in greater detail.

2.1   Balance

The three-element high-lift system contains a slat, main section and flap. The mounting of the three elements between both sides of the test section takes place by means of the side wall integrated balances, shown in Fig. 1. The implemented balance system that determines the aerodynamic forces and moments via strain gauges, which are symmetrically arranged to the balance beams, is based on the idea of [4], which was originally developed for controlling the forces and moments of robot tools. The body of the balance consists of nine solid blocks, connected by symmetrically arranged horizontal and vertical beams. The four corner blocks are fixed mounted to the test section side wall. The other blocks have no contact with the wall and are therefore moveable. The specific high-lift element is mounted to the center block.

   The forces and moments induced by the center mounted element of the high-lift system is determined by twelve strain gauges, applied symmetrically to the connection
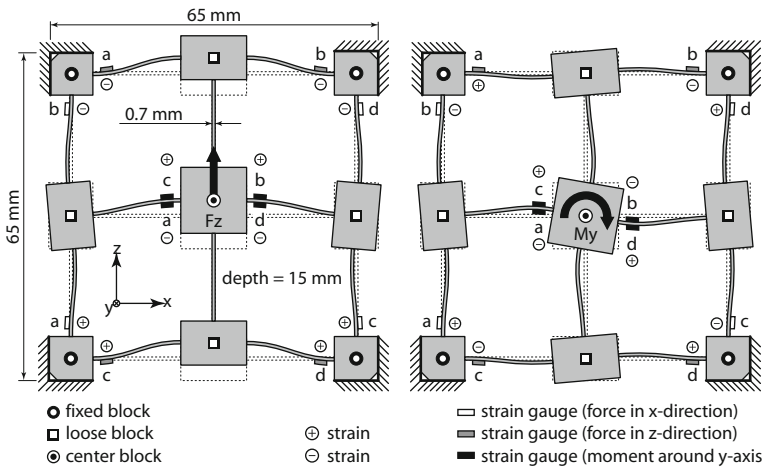

Fig. 1. Deformation of the balance body due to forces F_z (left) and moments M_y (right) induced into the center block
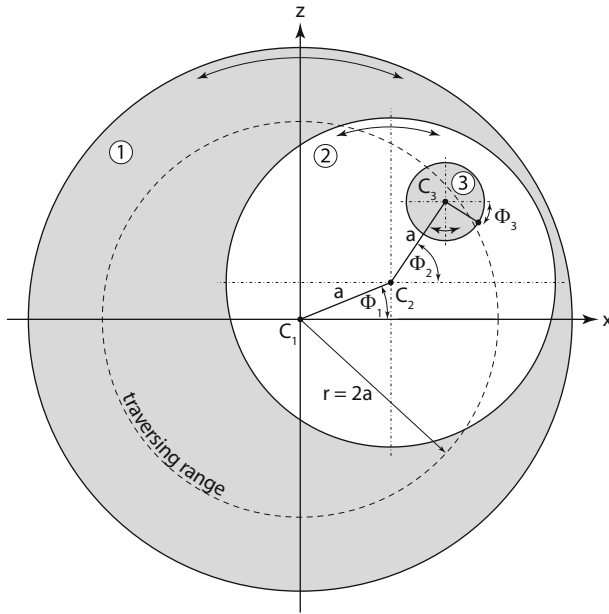
Fig. 2. Arrangement and geometric parameters of the three rotary disks building the eccentric traverse

beams, Fig. 1. The balance is able to detect the forces in x- and z-direction as well as the moment around the y-axis independently. According to [4], the interference errors of a balance of this type are less than 3%. The minimum measurable force is $F_{x,\min} = F_{z,\min} = 0.01\mathrm{N}$, the minimum measurable moment is $M_{y,\min} = 0.001\mathrm{Nm}$. Based on the measured forces and moments and the setting of the high-lift element, the applied lift, drag and pitching moment can be determined.

2.2 Eccentric Traverse

The slat and flap of the high-lift system can be positioned arbitrarily by side wall integrated eccentric traverses. The three necessary degrees of freedom (gap, overlap and deflection angle) are realized by three eccentrically mounted rotary disks, Fig. 2. If the high-lift device is attached to the small rotary disk (3), the rotary angles of the large rotary disk Φ_1 and medium rotary disk Φ_2 define the position of the high-lift device in the x-z-plane. The deflection angle δ is defined by the rotary angle of the small rotary disk Φ_3.

Based on identical distances a between the centers C of the rotary disks, arbitrary settings within a circular traversing range with the radius $r = 4a$ are realizable while retaining closed and smooth test section side walls. Overall, there are four eccentric traverses necessary for moving the slat and flap; one traverse for the slat and one for
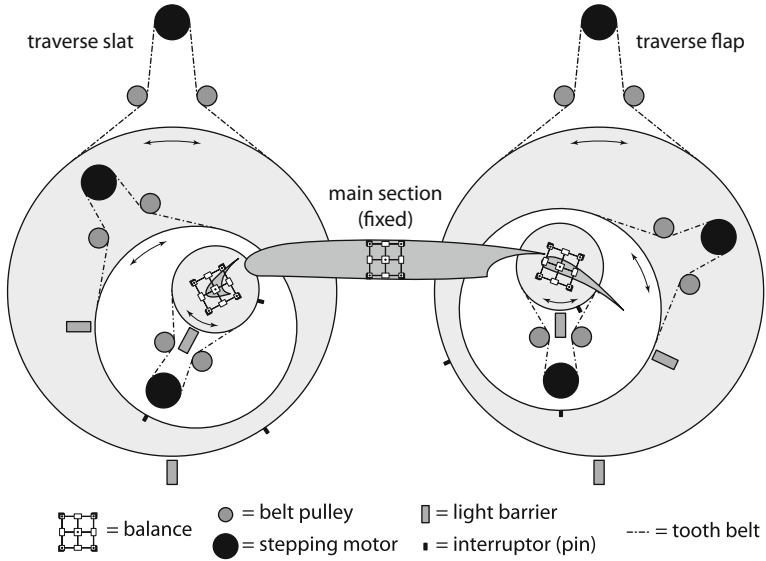
traverse slat

traverse flap

main section
(fixed)

◯= balance   ● = belt pulley   ▯ = light barrier   -·-· = tooth belt
                ● = stepping motor   ▪ = interruptor (pin)

Fig. 3. Schematic set-up of the eccentric traverses within the test section walls

side wall
(**I**)

650 mm

400 mm

400 mm

1   main section
2   slat
3   flap (*not visible*)
4   balance slat
5   balance main wing
6   balance flap
7   stepping motor unit
8   stepping motor unit
9   stepping motor unit
10 light barrier
11 tooth belt
12 traverse rotary disk large
13 traverse rotary disk medium
14 traverse rotary disk small
15 rotary disk (α)

C_∞
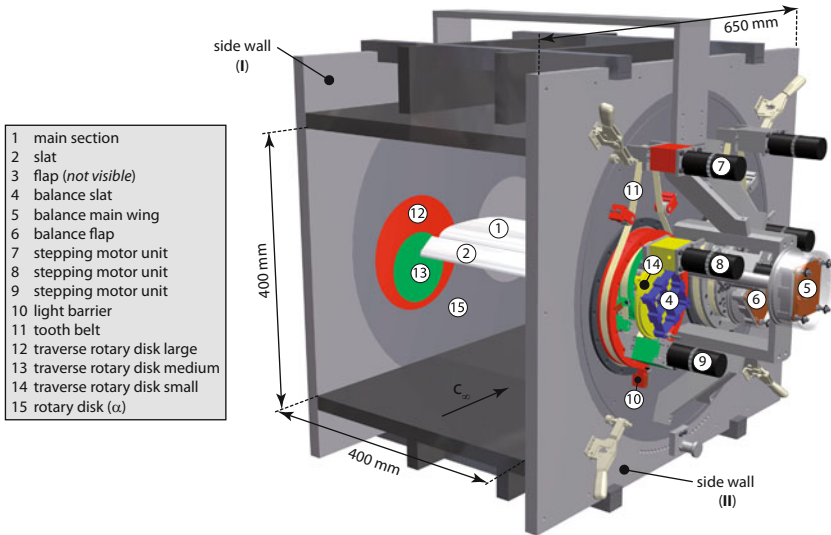
side wall
(**II**)

Fig. 4. Overall view of the test section with the integrated high-lift system

the flap in both side walls of the test section, Fig. 3. The main section of the wing is
mounted directly to the side walls. The rotary disks are driven by stepping motors using

free of play tooth belt drives with a rotation accuracy of $\Delta\Phi_1 \leq 0.02°$, $\Delta\Phi_2 \leq 0.03°$ and $\Delta\Phi_3 \leq 0.05°$. Small pins in the face sides of the rotary disks interrupt the light barrier in a reference position that is used as a basis for the calculation of the high-lift device setting.

2.3 Test Section

Fig. 4 depicts the complete wind tunnel test section. The two-dimensional high-lift system consisting of the main section (1), slat (2) and flap (3) is mounted between the two side walls (I and II). The gap between the side walls and the high lift elements has a width of $d = 0.2$ mm. The mounting of the three elements on both sides of the test section takes place by means of the side wall integrated balances (4-6). The balances and therefore the high-lift devices are positioned by side wall integrated eccentric traverses. These traverses consist of the three rotary discs (12-14), driven by the three stepping motor units (7-9). The angle of attack α of the whole high-lift system can be varied manually by rotating the disk (15).

3 Results

The test setup allows the analysis of the aerodynamic performance of the high-lift system depending on the high-lift device setting as well as the automated optimization of the device gap, overlap and deflection angle. The following pages present some results concentrating on the flap flow obtained at a Reynolds number of $\mathrm{Re} = 2.7 \cdot 10^5$ at an angle of attack of $\alpha = 10°$.

3.1 Systematic Analysis

The individual variation of the parameters gap g_F, overlap o_F and deflection angle δ_F allows an analysis of the influences of the parameters on the aerodynamic performance of the high-lift system. Fig. 5 (left) for example shows the distribution of the lift coefficient c_L of the high-lift system depending on the gap g_F and overlap o_F of the flap for a fixed flap angle $\delta_F = 30°$. Gap g_F and overlap o_F are related to the chord

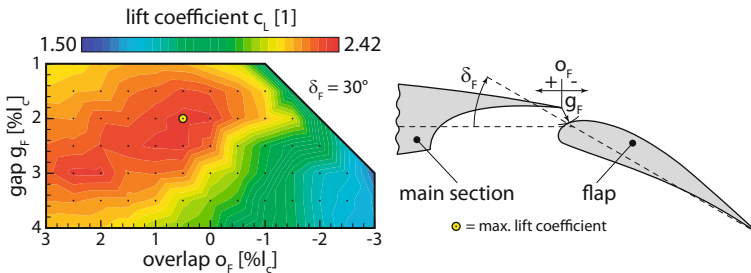**Fig. 5.** Lift distribution for different flap settings, $\delta_F = 30°$

length $l_c = 200$ mm of the cruise wing in clean configuration. The distance between the measuring points is set to $\Delta g_F = \Delta o_F = 0.5\% l_c$. The circular label marks the position of the maximum lift within the flap field. Fig. 5 (right) illustrates the corresponding flap setting that delivers maximum lift for the given flap angle of $\delta_F = 30°$. If the maximum lift coefficients are determined in the exact same manner for several different flap angles δ_F, the optimum flap setting for maximum lift can be found systematically.

During preliminary investigations of different flap settings, the global optimum of the flap setting with respect for maximum lift was determined systematically within the range: $g_{F,\mathrm{opt}} \in [0.5, 1\% l_c]$, $o_{F,\mathrm{opt}} \approx 2\% l_c$ and $\delta_{F,\mathrm{opt}} \in [31°, 36°]$, [5].

3.2   Optimization

More efficient than the systematic search for an optimum flap setting is a targeted optimization possible with the presented test section. In the following, an experimental optimization of the flap setting with respect to the maximization of the lift coefficient c_L of the high-lift system is demonstrated using the gap g_F, overlap o_F and deflection angle δ_F as optimization parameters. The goal function for the maximization of lift is set to $f = 1/c_L^2$. Usually, the angle of attack α is an additional optimization parameter of a high lift system optimization with respect to maximum lift. However, since the adjustment of the angle of attack is not yet automated, the optimization is performed at a fixed angle of attack.

Two different optimization runs with different flap start settings using the Nelder-Mead simplex algorithm [1] will be presented. During preliminary investigations, the simplex algorithm had proven its ability to find good solutions even in a noisy search space using only a moderate number of measurements, [5]. Even if the optimization runs presented here find the global optimum, it has to be considered that the simplex algorithm does not guarantee the detection of the global optimum.

The start setting of the flap for case (a) is set to $g_F = 1.5\% l_c$, $o_F = 1.0\% l_c$ and $\delta_F = 10°$. Case (b) has almost identical start settings, with just a minor change of the
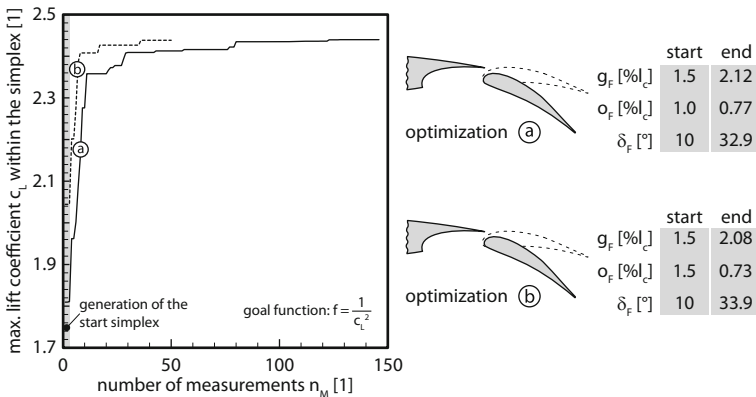

Fig. 6. Optimization: development of the lift coefficient c_L

overlap $o_F = 1.5\%l_c$. The setting of the slat as well as the angle of attack of the high-lift system is fixed.

Fig. 6 depicts the development of the lift coefficient c_L of the high-lift system during the optimization process for the two different start settings of the flap. Although the flap start settings are almost identical, the development of the lift coefficient of the two optimization runs shows a significantly different behavior. While optimization (b) locates a flap setting close to optimum setting within 40 measurements, optimization (a) needs more than twice the number of measurements. This is caused by the established start simplex generation. The start simplex contains the start flap setting as well as three additional flap settings, generated by random modification of the given start parameters. Therefore, the development of the parameters of two optimization runs can differ significantly, even if the Nelder-Mead simplex algorithm is a deterministic method and the start parameters are almost identical.

To clarify the difference between the two optimization runs and to explain the difference of the necessary number of measurements to find a solution close to the global optimum, the development of the parameters gap g_F, overlap o_F and flap angle δ_F is depicted in Fig. 7. Each point describes one analyzed flap setting (g_F, o_F). Based on the start configuration, the line connects the best achieved settings in chronological order. The color of the line expresses the development of the flap angle δ_F. The dotted circle marks the area, where the Nelder-Mead algorithm finally stagnates. While the parameters of optimization (b) move quickly towards the optimum, optimization (a) initially enlarges the gap g_F overshooting the optimum. Therefore, optimization (a) needs a much higher number of measurements to finally stagnate close to the global optimum. The behavior of the high lift system in a certain area around the located optimum is of particular importance for most practical applications. Therefore, a systematic scan around the located optimum is still necessary.

The presented test section features some shortcomings that have to be considered when analyzing and interpreting the optimization results. The small test section height
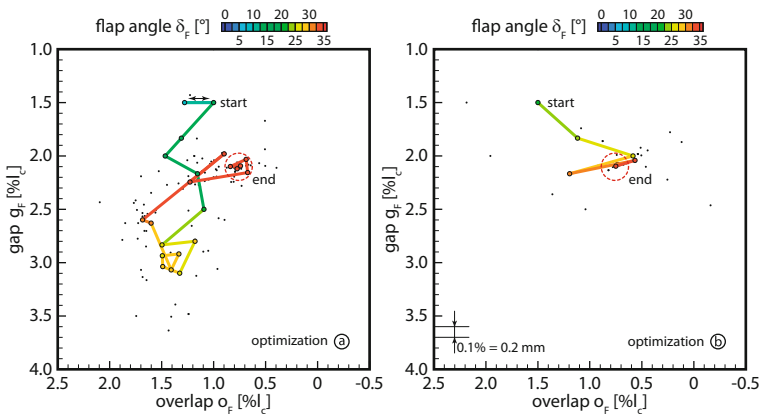

Fig. 7. Optimization: development of gap g_F and overlap o_F

is problematic from the viewpoint of wall interferences. Blockage correction methods have to be applied to the measured aerodynamic forces and moments, [6]. The flow around the high lift system is not really two-dimensional. Wall effects like corner vortices and separation at the intersections of the high lift system elements and the sidewalls affect the flow around the high lift system. These effects and the effects due to the low Reynolds numbers are always included in a 2D-experimental optimum obtained by total force and moment measurements.

4   Conclusion

An automated test section was introduced, which allows the systematic analysis and optimization of the aerodynamic performance of a two-dimensional multi-element high-lift system depending on the slat and flap settings. The gap and overlap of the high-lift devices as well as their deflection angle is varied by remote via stepping motor driven side wall integrated traverses. The aerodynamic forces and moments are determined on each element of the high-lift system individually by means of strain gauge based balances. A successful optimization of the flap setting with respect to the maximization of lift was presented, using the Nelder-Mead simplex method.

The number of checked flap settings that were necessary to find a flap setting close to the optimum setting is in the same range as for the analysis of one flap field shown in Fig. 5. Thus, for the shown examples, the determination of the optimum flap setting based on the Nelder-Mead simplex method is much more efficient than an analytical search that requires the analysis of multiple flap fields for several different flap angles.

References

[1] Nelder, J.A., Mead, R.: A Simplex Method for Function Minimization. The Computer Journal 7(4), 308–313 (1965)
[2] Flaig, A., Hilbig, R.: High-Lift Design for Large Civil Aircraft. In: AGARD Conference Proceedings: High-Lift System Aerodynamics, AGARD-CP-515, pp. 31.1–31.12 (1993)
[3] Reckzeh, D.: Aerodynamic Design of the High-Lift-Wing for a Megaliner Aircraft. Aerospace Science and Technology 7, 107–119 (2003)
[4] Kim, G.-S., Kang, D.-I., Rhee, S.-H., Um, K.-W.: Design and Fabrication of a Three-Component Force / Moment Sensor Using Plate-Beams. Measurements Science and Technology 10, 295–301 (1999)
[5] Blume, S.: Eine experimentelle Methodik zur aerodynamischen Optimierung von Mehrelement-Hochauftriebskonfigurationen. Dissertation, Technische Universität Berlin (2008)
[6] Allen, H.J., Vincenti, W.G.: Wall Interference in a Two-Dimensional-Flow Wind Tunnel with Concideration of the Effect of Compressibility, NACA Report No. 782 (1944)

Application of Pressure-Sensitive Paint for Determination of Dynamic Surface Pressures on a 30 Hz Oscillating 2D Profile in Transonic Flow

C. Klein[1], W.E. Sachs[1], U. Henne[1], Y. Egami[1], H. Mai[1],
V. Ondrus[2], and U. Beifuss[2]

[1] Deutsches Zentrum für Luft- und Raumfahrt e.V. (DLR),
Bunsenstrasse 10, 37073 Göttingen, Germany
[2] Institut für Chemie, Universität Hohenheim
Garbenstr. 30, 70599 Stuttgart, Germany

Summary

Visualization and measurements of aerodynamic effects on a 2D-wing-profile model were conducted using an optical pressure measurement system based on the pressure-sensitive paint (PSP) technique. The PSP technique can be used to obtain absolute pressure distributions on the surface of a model and in addition to evaluate quantitative aerodynamic flow phenomena e.g., shock location, shock-shock interaction, and shock boundary layer interaction, by using scientific grade cameras and image processing techniques. The PSP technique has been used here for investigations of periodic and unsteady flows. In a wind tunnel campaign in the DNW-TWG, a 2D-wing-profile model, which is pitch oscillating at up to 30 Hz, was investigated. The experiment presented here was performed at angles-of-attack $\alpha = 1.12° \pm 0.6°$ at Ma = 0.72. With this work the area of application of PSP to dynamic systems where oscillating pressure changes of the order of 1000 Pa have to be measured at rates of up to 100 Hz is demonstrated.

1 Introduction

Becoming interested by the pressure data measured with PSP for steady cases the aerodynamicists working in the high-speed regime have been asking for a similar technique for investigations of unsteady flow phenomena, such as aeroelastic investigations, turbo machinery, and helicopter rotors. This is the reason why DLR started an internal "Unsteady PSP" project to develop the required hard- and software for industrial unsteady PSP measurements with a time resolution of better than 1 millisecond and with a sampling rate of up to 100 Hz. Application of the PSP technique to unsteady aerodynamic flows requires special measurement instrumentation. The main challenges to obtain PSP results with sufficient accuracy are the development of hardware components, model illumination, and camera observation as well as the pressure-sensitive paint itself. First of all, a dedicated fast

paint has to be designed as pressure sensor in order to reduce the response time of the paint with respect to pressure changes. DLR has developed high porosity paints in which the luminescent dyes are incorporated in a porous polymer. The dynamic calibration of the unsteady paint consists of measuring the phase- and amplitude response of the paint under pressure variations. A dynamic calibration system for measuring the transfer function of the paint has been designed and manufactured. Then, the instrumentation has to be able to acquire images with high framing rates and at low light intensities. Moreover, the software should be able to manage all the necessary synchronization between the PSP system and the wind tunnel in a short time. The industrial aspects of the development are considered in the DLR project as well, which means that the knowledge obtained from the implementation of this measurement techniques for industrial wind tunnels will be used to develop a PSP system that is mobile and fast in both implementation and data processing.

2   Model and Test Facility

The wind tunnel measurements presented in this paper were performed in the Transonic Wind Tunnel DNW-TWG in Göttingen [7]. For the measurements, the wind tunnel was set-up with the "adaptive walls" test section. Since the wind tunnel can be pressurized from 0.3 to 1.5 bar, steady calibration measurements of the pressure-sensitive paint for the complete model could be performed inside the test section itself.

The NLR7301 (DLR-AE4) model [1] is made from carbon fibre material and has a chord length of 300 mm with a span of 1000 mm, see Figure 1. The suction side of the model is equipped with 38 pressure taps (KULITE) along two chordwise lines at mid-span. A spanwise area of 60% of the model surface has been painted with DLR's unsteady PSP and 40% with DLR's temperature-sensitive paint (TSP). Some of the conventional pressure transducer data are used for an offset correction of PSP and others for the comparison between PSP and KULITE data. In addition, the model is equipped with one PT100 thermocouple to measure the model surface temperature during data acquisition.
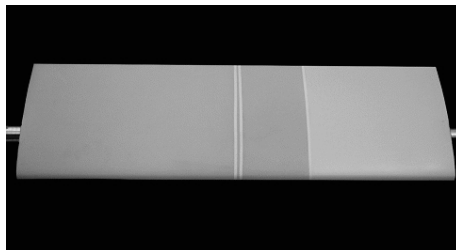

Fig. 1. NLR7301 model painted with unsteady PSP and TSP. Two pressure tap sections are visible in the mid-span area

3   Unsteady Pressure-Sensitive Paint

DLR has been developing pressure-sensitive paints in cooperation with a team from the Organic-Chemistry Institute of the University of Hohenheim.

3.1   Development of Unsteady Pressure-Sensitive Paints

Since the unsteady pressure-sensitive paint should be usable on different model materials (e.g., carbon fibre, steel or aluminium) and should finally also be applicable to large and fully instrumented models, DLR has focused its efforts on pressure-sensitive paint formulations which can be applied by using a spray gun. DLR has developed paints where the luminescent dyes can be incorporated into a highly porous polymer. Other paint formulations such as surface contact paint (anodized-aluminium PSP) [3, 5], where the dye is adsorbed onto a porous alumina layer, can be applied only to aluminium and can not be sprayed. The response time of the high porosity polymer based paint is about 1 ms, while the anodized-aluminium PSP can achieve response times of some 10 µs. The advantage of the DLR paint is that it can be sprayed on any surface. A two-color PSP formulation, based on PtTFPP as the pressure-sensitive luminophore and with a pressure-insensitive reference luminophore, was used for the tests presented here. The radiative lifetimes of the pressure-sensitive dye and the reference dye were measured and do not exceed 0.1 ms. These two dyes were embedded in a fluoric binder. To enlarge the porosity of this polymer TiO_2 material has been added. This paint is applied directly to the model surface, i.e., without an additional screen layer underneath, using a spray gun. A total paint thickness of about 10±2 µm was achieved. Drying time of this paint is about 10 min. Figure 2 shows the emission spectrum of the pressure-sensitive paint when excited at approx. 400 nm. An intensity change of 0.1% with the paint results from a pressure change of approx. 150 Pa. The temperature sensitivity of the paint can be determined from the calibration curves to be approximately -800 Pa/°C.
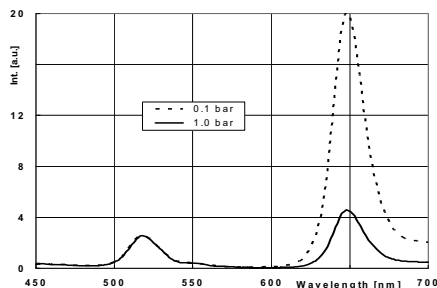

Fig. 2. Emission spectra of the two-color unsteady pressure-sensitive paint at 20°C

3.2   Dynamic Calibration of PSP

The dynamic calibration of the unsteady pressure-sensitive paint consists of measuring the response for amplitude- and phase characteristics of the paint in the presence of pressure variations. An unsteady calibration system for sinusoidal

pressure changes with an amplitude of about ± 5000 Pa between 0 - 100 Hz has been designed and manufactured [6]. For higher frequencies, the amplitude of pressure variations becomes smaller. The maximum frequency of the unsteady calibration system is about 5 kHz. As references for the pressure signal in the unsteady calibration chamber four pressure sensors (ENDEVCO) with high frequency response have been used. Based on this calibration system, the unsteady paint used for the measurements presented here has been calibrated to measure the transfer function of the paint. Figure 3 shows the amplitude and phase characteristics for the paint. At 100 Hz the amplitude of the paint signal shows a decrease of about 5% intensity whereas a phase shift of 12° was measured.
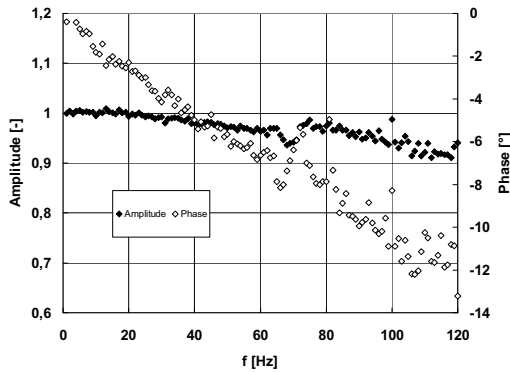
Fig. 3. Amplitude and phase transferfunction for the two color unsteady pressure-sensitive paint

4   Data Acquisition

4.1   Phase Locked Unsteady PSP Data Acquisition

For each observation direction one high power UV flash light source (RAPP-DLR-EP1) is used for excitation of the paint (λ_{ex} = 350 - 400 nm). Each light source consists of three separate high pressure Xenon bulbs with appropriate optical filters and each is connected to optical fibers of 2.0 m length. Therefore, in total, 6 fiber optics illuminated the painted model surface from two directions. For each flashbulb up to 1 J white light in a 100 μs pulse, equivalent to 10 kW peak power, was measured at the exit of each light fiber. Maximum repetition frequency of 0.2 Hz was attained for the high power flashes. It is connected via the internal TCP/IP network with the PSP data acquisition system. The maximal flash duration of the lamps is 180 μs, depending on the actual power settings. A flash monitor output was used to determine the exact time of model illumination. Scientific grade CCD cameras (PCO) with 14-bit resolution were used for image acquisition. The employed optical filters transfer the emitted light as follows: one filter at λ_{em_p} = 630-800 nm for the pressure signal itself and another filter at λ_{em_ref} = 475-590 nm for the reference component (see also the emission spectrum of PSP in Figure 2). Thus, pairs of images were acquired simultaneously by using the twin CCD camera system from each viewing

position. Even though an exposure time of 1 sec for the cameras was used, the effective observation interval was about 300 µs, which is the sum of flash length and fluorescence lifetime of the paint. With this arrangement, just one single flash of 180 µs pulse length of the light sources is sufficient to give a sufficiently large intensity for the CCD camera.

4.2 Unsteady PSP Data Acquisition

In this setup the pressure-sensitive paint was excited by a high power LED (RAPP-DLR-ULD119 with λ_{ex} = 395 - 405 nm). This LED was driven in pulse mode, having up to 15 mJ with pulse durations of about 1 ms. One PhotonMAX: 512B EMCCD (PRINCETON INSTRUMENTS/ACTON) camera was used for image acquisition. PhotonMAX is a 16-bit EMCCD (ElectronMultiplying Charge Coupled Device) camera. This is a new technology on the market today which is able to amplify the charge on-chip (Avalanche Gain technique) before the charge-to-voltage conversion [2]. This makes it extremely light sensitive, being able even to register single photons. As well as the capability of single-photon sensitivity, this camera also allows high framing rates. A 512 x 512-pixel, back illuminated, frame transfer EMCCD and a 10-MHz, 16-bit digitizer provide the performance to measure up to 30 Hz with full pixel resolution. It minimizes dark current by thermoelectrically cooling the detector down to -80 °C.

The employed optical filter in front of the EMCCD camera transmits only the emitted light at λ_{em_p} = 630-800 nm for the pressure signal of the paint.

For the measurements in the wind tunnel the exposure time of the EMCCD was fixed to 1 ms. Depending on data acquisition parameters (ROI, binning, Avalanche Gain) the flash duration of the LED light pulse was adapted between 400 - 800 µs. For the full 512 x 512 pixel resolution of the EMCCD camera a data acquisition frequency of 30 Hz could be realized. Just one single flash of 800 µs pulse length of the LED is sufficient to give enough intensity for the EMCCD camera.

4.3 Triggering the Data Acquisition System

One part of the DLR software "ToPas" (Three dimensional optical Pressure analysis system) controls the automatic data acquisition [4], integrating the PSP system into the wind tunnel data acquisition system. The data acquisition for all systems (wind tunnel parameters, conventional unsteady pressure transducer data, and unsteady pressure-sensitive paint images) is started automatically via computer (using the software SEM_COLLECT in combination with PC-based hardware and software), but the exact triggering mechanism of cameras and excitation light source depends on the data acquisition type (unsteady or phase locked). The software is designed to work with different cameras and light sources using TTL triggers. All monitor output signals from cameras and light sources were measured in parallel by the conventional unsteady data acquisition system (TEDAS).

5   Data Reduction

For data reduction the ToPas Software is used. As a result of the PSP measurement one obtains the pressure distribution on the model surface, which is delivered at each

node of a structured 3D surface grid of the model. Markers are applied at well defined coordinates on the model surface. After detecting the markers in the PSP images, eleven alignment parameters (rotation in x, y and z-direction, translation, perspective, projection, scaling, and lens correction) are calculated by a least square fit of the difference between calculated and measured marker positions. Then, according to these parameters the pixel values can be assigned to the corresponding node of the grid. From this, the pressure on each node can be calculated using the calibration relation. For calculation of absolute pressure values an in-situ calibration is added, which is performed by comparison of conventional pressure sensor values with the PSP results at the location of the corresponding pressure sensors in the wind tunnel model. Data reduction using DLR's software ToPas is performed by scripting methods with a very high degree of automation and reproducibility.

6   Results for the NLR7301 Model

For the pitch oscillating case of the model, oscillations in the intensity of PSP that occurred due to shock oscillations were observed. Using the phase-locked unsteady PSP data acquisition for the 30 Hz oscillating 2D-wing-profile model, 72 images were acquired; this represents a phase resolution of 5°. Although the model is exposed at each phase position only once, the data acquisition for all 72 phase positions of the model takes several minutes due to the limitations imposed by the 0.2 Hz flash frequency and the image readout time. Three typical PSP results using phase-locked unsteady PSP data acquisition, for the 30 Hz pitch oscillating case of the investigated model on the suction side, for Ma = 0.72 at angles of attack (AoA) 0.588, 1.828, 1.564° are shown in Figure 4. In this figure flow is coming from the left for all three different angles-of-attack (AoA) and the pressure coefficient is shown in the area beginning from the centerline of the model in direction to the wind tunnel side wall. Independent of the angle of incidence the non-2-dimensional pressure distribution is clearly visible especially nearby the wind tunnel side wall, caused by the interaction of the flow around the 2D-wing-profil model and the wind tunnel boundary layer. In addition for all different AoA a low pressure area is measured which is caused by a vortex generated at the leading edge of the model close to the wind tunnel side wall. For all different AoA, significant movement of the shock system is also found. For $\alpha = 0.588°$ and $\alpha = 1.828°$ two separate shock positions are found. The first shock is moving downstream into the direction of the second shock whereas the second shock is not moving downstream. The results for the different phase positions for the pitch
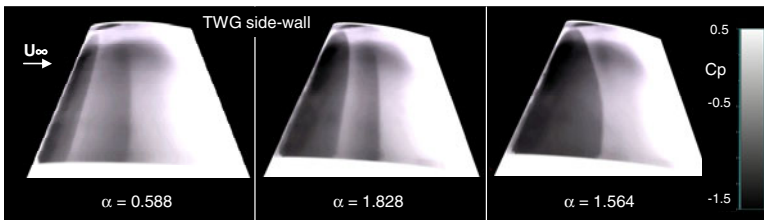

Fig. 4. Cp pressure distribution on the surface of the suction side of the NLR7301 model for Ma = 0.72, pitch oscillating frequency 30 Hz, for three different AoA (phase-locked measured)
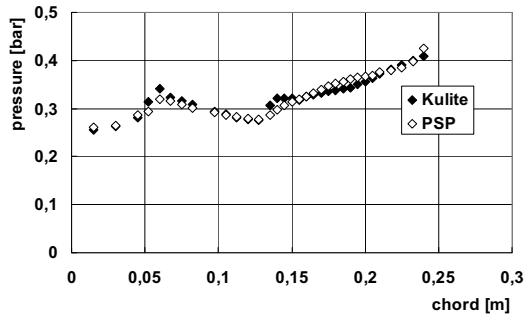
Fig. 5. Comparison of conventional pressure measurement data (KULITE) and PSP on the suction side of the NLR7301 model for Ma = 0.72, pitch oscillating frequency 30 Hz, for AoA = 0.588° (phase-locked measured)

oscillation show significant differences in the position of the shocks. For α = 1.564° only a single shock is measured by means of unsteady PSP. Thus, the response time of the pressure-sensitive paint formulation is sufficiently small to resolve the pressure fluctuations arising from the pitch oscillation of the 2D-wing-profile model in the flow. In order to compare the accuracy of the PSP results they are compared with the conventional pressure measurement (KULITE) data, measured simultaneously. In figure 5 the pressure distribution for α = 0.588° is shown. The agreement is quite good, only nearby the two shock positions a larger discrepancy is obvious. This can be explained by response time of the unsteady paint. To improve the accuracy of the PSP data it is now very interesting to correct the measured PSP data with the information coming from the transfer function of the paint. The evaluation of this data reduction is still ongoing.

With the aid of the unsteady PSP data acquisition technique images have been taken with full pixel resolution (512 x 512 pixels) at an image acquisition rate of about 30 Hz. Since the pitch oscillation of the model was constant at 30 Hz, different timing modes for data acquisition were used:

a) $\Delta\phi$= 5 ° phase-shift mode
images for model at different phase positions: ϕ = 0, 5, 10, 15 …,360, 5, 10, 15…°
b) no-phase-shift mode:
images for model at constant phase position: ϕ = constant

In each mode of operation the complete data acquisition took less than 10 seconds.

In the timing mode a) the shock oscillation is measured by means of unsteady PSP with 5 ° phase resolution. For mode b) relatively small oscillations of the shock position can be resolved by this technique. In this timing mode buffeting effects could in principle also be resolved. By changing the resolution of the EMCCD camera to 128 x 128 pixels by 4 pixel binning, an image acquisition rate of about 100 Hz was achieved. This enables us to get at least 3 images within one period. The complete model could not be measured due to the lower optical resolution of the system. Because of the strong intensity changes arising from the shock oscillation, they could be visualized even in the raw images without requiring any further image processing. This was possible since the EMCCD camera chip was exposed only by one single

LED light pulse for each image. Therefore the result represents the pressure distribution at a well defined time and again no assumptions of periodicity need to be made for averaging reasons.

7   Conclusion

The PSP technique is used for investigations of periodic and unsteady flows. A porous pressure-sensitive paint formulation has been developed. The unsteady PSP formulation has a response time of approx. 1 millisecond with a layer thickness of about 10 µm. The newly developed hardware and synchronization worked well in an industrial wind tunnel environment. Two different experimental set ups have been utilized to investigate periodic and unsteady flows. First, a phase-locked unsteady PSP technique for measurements on periodic processes has been applied. One single flash of less than 200 µs duration was sufficient for paint excitation and delivered enough light for data acquisition by the CCD cameras. There was no need for averaging. The experimental results obtained for the 2D-wing-profile model show that the local pressure can be measured by means of pressure-sensitive paint with an observation time of 1 ms. In addition, real unsteady PSP has been realized by using LED's with one single light pulse in combination with an EMCCD camera. By using this instrumentation the local pressure can be measured in real time. For industrial wind tunnel applications this work extends PSP's useful range to dynamic systems where oscillating pressure changes of the order of 1000 Pa have to be measured at rates of up to 100 Hz.

References

[1] Boerstoel, J.W., van Egmond, J.A.: Design of shock-free, basic airfoils for a supercritical wing, NLR TR 75059 C (1975)
[2] Coates, C.: EMCCD cameras take imaging to a new level. OLE Product Guide, 7–9 (2007)
[3] Kameda, M., Tabei, T., Nakakita, K., Sakaue, H., Asai, K.: Image measurements of unsteady pressure fluctuations by a pressure-sensitive coating on porous anodized aluminium. Meas. Sci. Technol. 16, 2517–2545 (2005)
[4] Klein, C., Engler, R.H., Henne, U., Sachs, W.E.: Application of pressure-sensitive paint for determination of the pressure field and calculation of the forces and moments of models in a wind tunnel. Experiments in Fluids 39, 475–483 (2005)
[5] Merienne, M.C., Le Sant, Y., Ancelle, J., Soulevant, D.: Unsteady pressure measurement instrumentation using anodized-aluminium PSP applied in a transonic wind tunnel. Meas. Sci. Technol. 15, 2349–2360 (2004)
[6] Patent, DE 10 2005 047 623.6-52
[7] http://www.dnw.aero > Wind tunnels >TWG

Simultaneous Measurements of Unsteady Aerodynamic Loads, Flow Velocity Fields, Position and Wing Deformations of MAVs in Plunging Motion

R. Konrath[1], B. Schlager[1], T. Kirmse[1], J. Kompenhans[1],
T.J. Möller[2], R. Wokoeck[2], M. Emge[2], and R. Radespiel[2]

[1] German Aerospace Center (DLR), Institute of Aerodynamics and Flow Technology,
Bunsenstraße 10, 37073 Göttingen, Germany
[2] Technische Universität Braunschweig, Institute of Fluid Mechanics,
Bienroder Weg 3, 38106 Braunschweig, Germany

Summary

A new wind tunnel environment for low Reynolds number testing of Micro Air Vehicles (MAV) is introduced, providing a test rig for plunge and pitch motions and a 6-component force balance. In this study a rigid as well as a flexible version of a typical MAV wing is investigated. Optical measurements techniques are adapted to measure simultaneously the instantaneous model position, orientation, wing deformations and flow fields.

1 Introduction

Micro Air Vehicles (MAVs) operate at very low Reynolds numbers for which existing design methods of conventional aircraft are usually not adequate. The performance of airfoils normally deteriorates rapidly as the Reynolds number decreases below 10^5 [1]. Additionally, the wings of MAVs usually have low aspect ratios, so that the wing tip vortices influence the overall wing behavior significantly which results in non-linear characteristics. Torres and Mueller [2] investigated experimentally different types of wing platforms with aspect ratios in a range of $0.5 - 2$ and found larger nonlinearities in the measured lift data. The application of flapping wing principles used by birds could be a more efficient way to produce lift and thrust for MAVs in comparison to conventional fixed wing designs and propeller propulsion. Jones et al. [3] give an overview over flapping wing propulsion techniques and the kinematics. Another aspect related to the design of MAVs is to introduce some kind of wing flexibility in order to improve the aerodynamic stability (gust response) by damping unsteady forces [4].

The objective of this research is to establish experimental methods allowing a detailed investigation of the behavior of low aspect ratio wings at low Reynolds numbers in plunging or pitching motion. As a test case a rigid as well as a flexible version of

a typical MAV wing consisting a thin cambered-plate airfoil (S5010-TOP24C) of 6% camber with reflex in the trailing edge [5] was fabricated, see Fig. 1. Measurements of the forces and moments are performed on the plunging wings at reduced frequencies of $k = \pi f c / U_\infty = 0.125$ and $k = 0.25$. Optical measurement techniques are applied to get details of the wing behavior and unsteady flow with respect to flexibility effects.
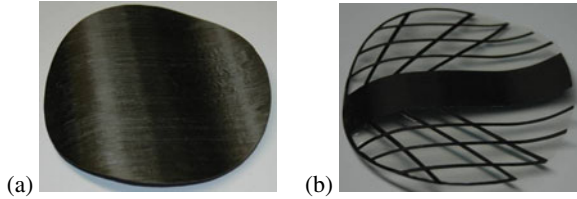

(a)   (b)

Fig. 1. Elliptic wing platforms (b = 15 cm, c = 11.7 cm), leading edge to the left: (a) rigid wing made of carbon fiber (b) flexible version, stiff inner section and battens of carbon fiber with attached thin plastic sheet.

2   Experimental Environment

A low-speed low-turbulence wind tunnel was established at the Institute of Fluid Mechanics (ISM) in Braunschweig, which was especially designed for low Reynolds number testing [6]. The continuously working atmospheric Eiffel-type wind tunnel consists of a 1:16 contraction ratio nozzle. Its rectangular test section of 60 cm height, 40 cm width and 150 cm length incorporates transparent walls. The wind tunnel is driven in suction mode at speeds between 4 and 19 m/s, whereas the maximum turbulence level is Tu < 0.1% at 10 m/s. Motor and fan are decoupled from the wind tunnel circuit to minimize vibrations.

The exchangeable test section consists of a dynamic test rig for 3d wing platforms. The model is connected via a sting to two vertical rods (s. Fig. 2) arranged along the centerline downstream the model. Both can move longitudinally resulting in a pitching and/or plunging motion of the model. The maximum amplitudes for pure pitch and plunge are ±25° and ±200 mm, respectively. The max. frequency for both motion types and their combinations is about 3 Hz. Two additional linear actuators will be provided in near future, allowing also a horizontal movement of the second rod, as indicated in Fig. 2, in order to displace the rotary center of the pitching upstream to the location of the model.
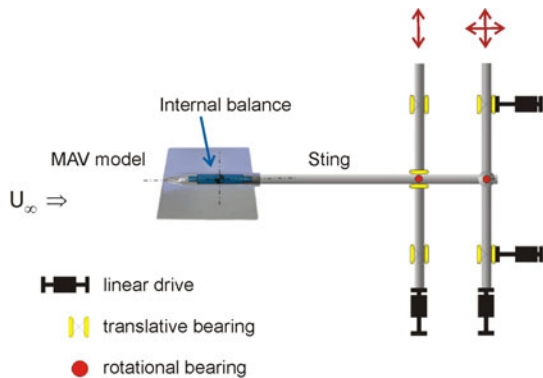

Fig. 2. Actuation principle of dynamic test rig for pitch and plunge.

A very small, especially designed six component internal strain gauge balance is used to determine the aerodynamic forces (107 mm length, 11.2 mm diameter, weight 35 g). The upper limits of the axial and transverse forces are 7 N and 20 N respectively, and the upper limits of the pitch/roll and yawing moments are 0.750 Nm and 0.374 Nm respectively. Using a Hottinger Baldwin Messtechnik MGCplus strain amplifier, the overall accuracy of the balance data is better than 0.025% FS. To eliminate inertial forces, wind-off balance data are taken and subtracted from the wind-on data using the same conditions and after averaging the raw data over 80 periods. Finally, the data is low pass filtered to remove high frequency perturbations from the signals caused by the harmonics of the natural vibration of the system.

3 Optical Measurement Techniques

3.1 MAV Wing Preparation

For the wing position determination point markers and for the 3d shape and deformation measurement a fine dots pattern is needed to be applied to the surface [7]. The markers and patterns should be of high contrast for a good measurement precision. But for PIV the model surface usually should be coated with a suitable black paint to reduce background noise and to avoid laser light flare on the surface [8]. To enable a simultaneous application of these techniques the MAV models are coated using a fluorescent paint and the markers as well as a fine random dots pattern are created with a black paint. The cameras are equipped with optical filters such that the cameras for PIV see only the illumination light (green), while the cameras for wing position detection and deformation see only the emission light of the fluorescent dye (orange). After drying a smooth high-gloss surface appears (Fig. 3) which is elastic enough to avoid its cracking in the case of the flexible wing.
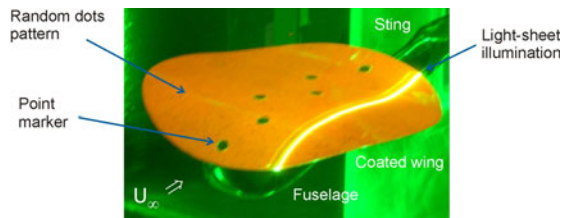

Fig. 3.   Painted MAV model (rigid version) illuminated with green laser light.

3.2 Optical Setups at Test Section

The same optical setup is used for measuring the model position and orientation and to measure the wing shape and deformation (Fig. 4). Two JAI A1 cameras (1392 x 1024 px) are arranged above the top window of the test section symmetrically along the center line of the model. The lenses ($f = 16$ mm) are chosen such that the model is always completely captured from both cameras at viewing angles of $\pm20°$. The upper model surface is homogenously illuminated from above by an extended beam from a 25 mJ Nd:YAG pulse laser.

The PIV setup utilizes two laser light sheets in order to capture the flow field inside a streamwise plane below and above the moving wing at a fixed span position of $b/4$. Two double pulsed Nd:YAG laser heads (Big Skye CFR-400) each providing about 150 mJ light energy per pulse are located behind the top and bottom window of the test section. Two separate PCO-1600 double shutter cameras (1600 x 1200 px) are used to observe the flow field below and above the wing at a right angle to the light sheets.

The optical measurements were performed simultaneously at 10 different phase positions of the sinusoidal movement of the model. The plunging frequency of the models was fixed to 3.14 Hz. To account for the maximum pulse frequency of the used Nd:YAG lasers the sampling rate of the measurements was set to 10.45 Hz, so that a single data set was obtained after three successive cycles. For each run 1050 images were taken by each camera allowing a phase averaging of the results using 105 samples.

3.3 Data Evaluation

For the data evaluations the "Point-Tracker" and "Strain-Master" modules of the Davis software package of LaVision is used. Both techniques [7] use standard algorithms of photogrammetry to determine 3D coordinates of specific targets recorded by a stereo camera system. The point tracking method uses six single point markers, placed in the stiff middle section of the models, to determine the rigid body motion in space.
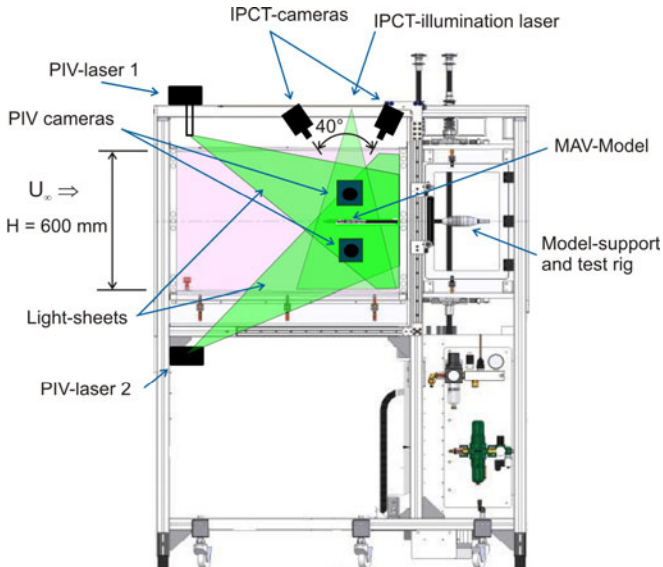
Fig. 4. Side view of optical arrangement at test section.

The image pattern correlation technique (IPCT) uses a random dots pattern on the surface to determine the 3D-deformation of the surface by correlating the obtained images with reference images, e.g. wind-off images. The standard IPCT evaluation process fails if both images are not similar enough. Since in the current case the models exhibit larger movements, this would necessitate one reference image per recorded model position. Here, the results of the position detection technique could be used allowing a deformation analysis with only a single reference image per model. From this a 3d-transformation matrix describing the model movement with respect to position and orientation between the measurement and reference case can be determined which in turn is used to map the measured images into the frame of the reference image. The accuracy of the point tracking and IPCT technique can be estimated to 0.06 mm in physical space.

The moving wing appears in the PIV images of both cameras as a bright line. Such bright areas affect the correlation result and must be masked out before the PIV algorithm can be applied. A small set of masks is manually created for the reference positions of the models. The remaining masks for each run and phase position are automatically generated using the results of the model position detection to shift and rotate the reference mask within the PIV-images. For the evaluation of the PIV images the in-house developed PIV evaluation software package is used applying an iterative multi-grid algorithm [8]. The final interrogation size was 16 x 16 px which corresponds to a spatial resolution of 3.8 mm. Assuming a precision of the determined displacements of better than 0.1 px the uncertainty of the velocity vectors is less than 1% of U_∞. Another systematic error caused by out-of-plane velocities must be considered, which can reach 2% for an out-of-plane velocity magnitude of 0.3 U_∞.

4   Results

4.1   Static Measurements

Figure 5 shows the results of the static force measurements for a chord based Reynolds number of Re = 72 500. Both wings (rigid / flexible) behave similar up to an angle of attack of 20°. The flexible version produces a slightly lower lift ($\Delta c_L \approx 0.1$)
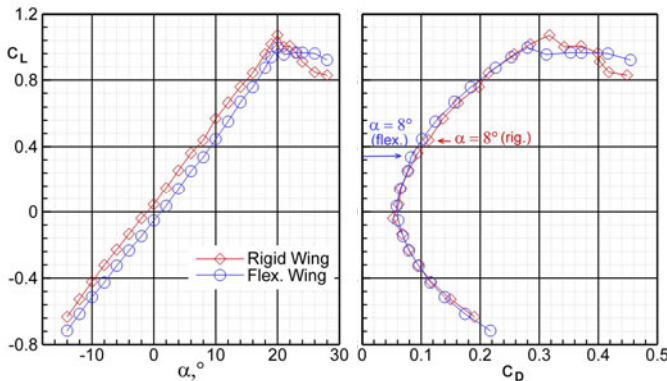

Fig. 5. Static lift and drag coefficients for both wings and Re = 72 500.

for a specific angle of attack, whereas the lift versus drag curves match very well. The abrupt drop of lift at $\alpha = 20°$ indicates that both wings exhibit a leading-edge stall [9] which is less pronounced in the case of the flexible wing.

Figure 6 shows an instantaneous as well as the time averaged flow field above the rigid wing at an angle of attack of 8°. At this spanwise position of $y = b/4$ small vortices shed instantaneously from the wing downstream a chord position of about $x/c_R = 0.4$. A flow separation region can be seen in the time averaged result between $x/c_R \approx 0.5$ and ≈ 0.9.
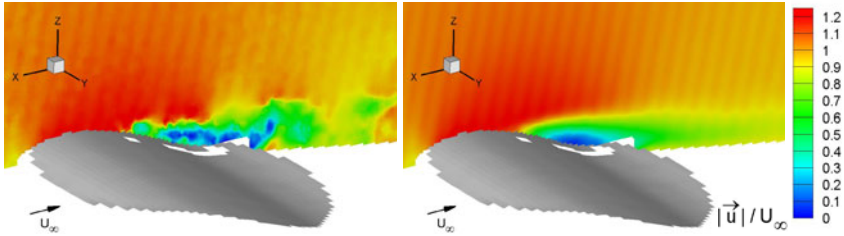
Fig. 6. Instantaneous (top) and time averaged (bottom) flow field above stationary model with rigid wing at a span of b/4 for Re = 72 500 and $\alpha = 8°$.

4.2 Effects of Wing Flexibility and Plunging Motion

In the following results of one investigated dynamic case is described, for which larger differences between the rigid and flexible wings can be seen. Using the maximum possible model frequency of 3.14 Hz and a Reynolds numbers of Re $= c\,U_\infty\,/\,\nu = 72\,500$ ($U_\infty = 9.24$ m/s) a reduced frequency of $k = \pi\,f\,c\,/\,U_\infty = 0.125$ results. The geometric angle of attack is initially set to $\alpha = 8°$, whereas the maximum change of the effective angle of attack is $\Delta\alpha_{eff} = \pm5.88°$ calculated from the model plunge velocity and the free stream velocity. The resulting maximum plunge amplitude related to the wing chord length is $h = l/c = 0.412$. Due to a phase lag between the two servo motors driving the vertical rods of the test rig, the pure plunging motion is actually superimposed by a slight pitching motion. The resulting variation in the geometric angle of attack is resolved by the position detection measurements (s. Fig. 7).

The trace of the dynamic lift coefficient for the flexible wing is plotted in Figure 8 against the sum of geometric and effective angle of attack showing a clear hysteresis reaching higher lift values during the envelope around the bottom dead center (BTC) of plunge with respect to that around the top dead center (TDC).

Figure 9 shows a comparison of the measured velocity fields between the rigid and flexible wing at four different phase positions. The velocity magnitudes vary for both wings according to the change of effective angle of attack. In the case of the flexible wing the extension of the separation region is always smaller in comparison to that of the rigid wing which applies particularly for the midway position of the downward moving wings (Fig. 9c).
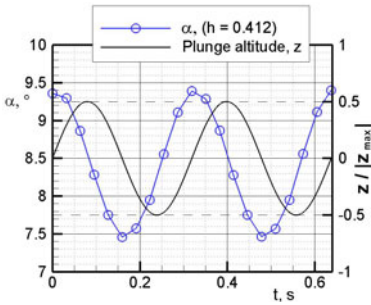
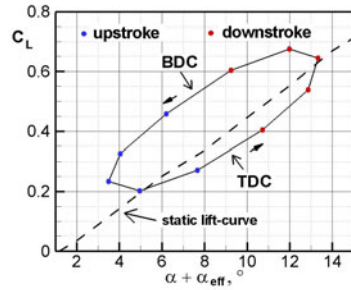**Fig. 7.** Measured variation of the geometric angle of attack α.

Fig. 8. Dynamic lift coefficient for flexible wing, Re = 72 500 and $k = 0.125$.

The corresponding deformation distributions of the flexible wing are shown in Fig. 10. Asymmetric deformations get visible for the cycle average (Fig. 10a) as well as for the deviations from the cycle average (Fig. 10b-d) which are only mentionable high ($\pm$ 0.2 mm) close to the top and bottom dead center. The asymmetrical wing deformations reveal slight inaccuracies of model fabrication.
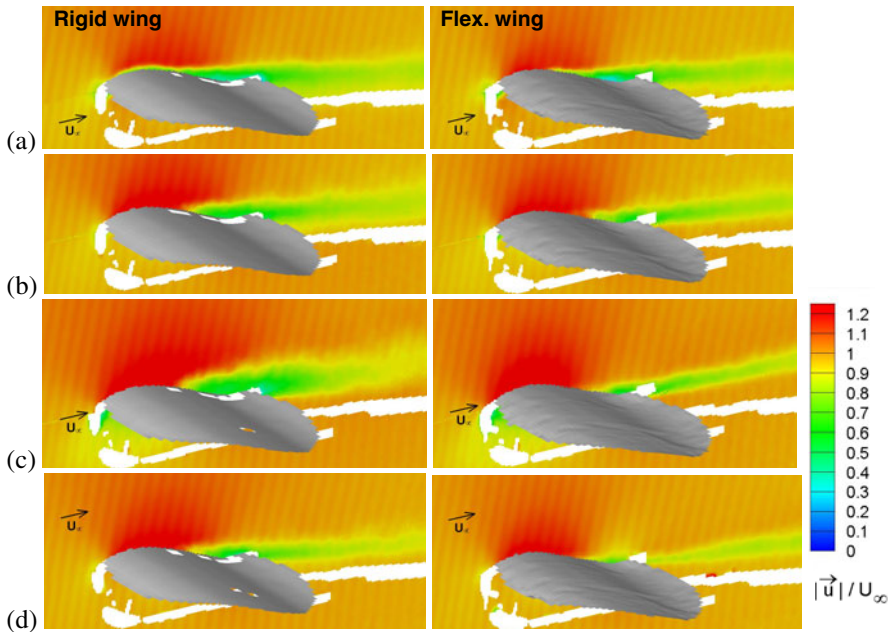
Fig. 9. Phase averaged velocity fields at $b/4$ for Re = 72 500, $k = 0.125$, $h = 0.412$, (left) rigid wing and (right) flexible wing. (a) half way upward, (b) close to top dead center (c) half way downward and (d) close to bottom dead center.
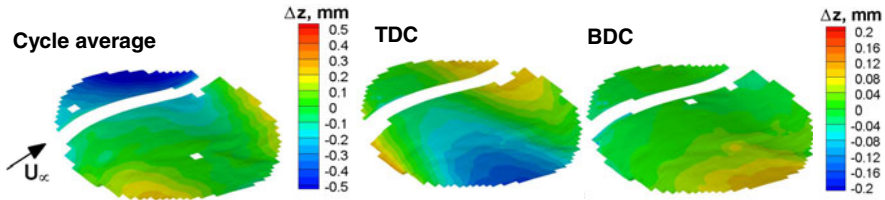
Fig. 10. Deformations Δ*z* (colors) of flexible wing for Re = 72 500, *k* = 0.125.

5   Conclusion

For the first time a simultaneous measurement of forces, model motion, wing deformation as well as flow velocity fields are successfully performed in a wind tunnel. A new dynamic test rig for 3d-MAV models was put into operation along with an especially designed six component balance. A specific painting of the models enabled a parallel application of different optical measurement techniques.

The results allowed a direct comparison between a rigid and flexible MAV wing. A reduced flow separation region could be seen for one dynamic case. More fundamental experiments are necessary to improve the knowledge about the dynamic behavior of MAV wings to improve their aerodynamic performance.

References

[1] Mueller, T.J., de Laurier, J.D.: An Overview of Micro Air Vehicle Aerodynamics. In: Mueller, T.J. (ed.) Fixed and Flapping Wing Aerodynamics for Mirco Air Vehicle Applications, ch. 1, pp. 1–10. AIAA (2001)

[2] Torres, G.E., Mueller, T.J.: Low-Aspect-Ratio Wing Aerodynamics at Low Reynolds Numbers. AIAA Journal 42(5), 865–873 (2004)

[3] Jones, K.D., Lund, T.C., Platzer, M.F.: Experimental and computational investigation of flapping wing propulsion for micro air vehicles. In: Mueller, T.J. (ed.) Fixed and Flapping Wing Aerodynamics for Mirco Air Vehicle Applications, ch. 16, pp. 307–339. AIAA (2001)

[4] Jadhav, G., Massey, K.: The development of a miniature flexible flapping wing mechanism for use in a robotic air vehicle. AIAA Paper 2007-668, vol. 11 (2007)

[5] Shkarayev, S., Null, W., Wagner, M.: Development of micro air vehicle technology with in-flight adaptive-wing structure. NASA/CR-2004-213271, 36 (2004)

[6] Wokoeck, R., Möller, T., Emge, M., Schüssler, J., Radespiel, R.: Experimental Investigation of the Aerodynamic Properties of Mirco Aerial Vehicles in Motion. In: Proc. of European Micro Air Vehicle Conference, Braunschweig, Germany (2008)

[7] Kirmse, T., Wagner, A.: Advanced methods for in-flight flap gap and wing deformation measurements in the project AWIATOR. In: Proc. of 1st CEAS European Air and Space Conference, Berlin (Germany), September 10-13, Paper 206, p. 7 (2007)

[8] Konrath, R., Klein, C., Schröder, A., Kompenhans, J.: Combined application of pressure sensitive paint and particle image velocimetry to the flow above a delta wing. Exp. Fluids 44, 357–366 (2008)

[9] Broeren, A.P., Bragg, M.J.: Unsteady stalling characteristics of thin airfoils at low Reynolds number. In: Mueller), T.J. (ed.) Fixed and Flapping Wing Aerodynamics for Mirco Air Vehicle Applications, ch. 10, pp. 191–213. AIAA (2001)

Development of a Thermo-Optical Sensor for Measurements of Wall Shear Stress Magnitude and Direction

Ilka Rudolph, Matthias Reyer, and Wolfgang Nitsche

Technichal University Berlin, Marchstr. 12, 10587 Berlin, Germany
ilka.rudolph@ilr.tu-berlin.de
http://www.aero.tu-berlin.de

Summary

In recent years, investigations regarding novel thermo-optical techniques for the visualization and quantification of wall shear stress distributions were conducted, [1], [2], [3]. These techniques correlate the temperature field on a structure to the near wall flow. Based on these findings, a new sensor was developed that is capable of measuring skin friction magnitude and direction as well as visualizing the near wall flow. The new thermo-optical sensor presented in this paper was investigated numerically at first, to find suitable correlation parameters. In contrast to existing investigations, a unique correlation parameter was found that produces better and more reliable results than previously proposed parameters. With the help of the numerical results, a sensor was designed, built and tested in wind tunnel experiments.

1 Introduction

The wall shear stress is an important quantity for the evaluation and investigation of flow fields, since a variety of phenomena, such as flow separation or reattachment and transition from laminar to turbulent flow, can be detected from the skin friction distribution. For this reason, in-depth information about the viscous forces is of great interest in fluid mechanics and aerodynamics and a variety of measurement techniques have been developed and tested in the last decades, [4], [5], [6]. Commonly used techniques include skin friction balances, surface hot wires or hot films and pressure probes (i.e. Preston tubes or surface fences). However, many of these techniques require elaborate instrumentation or are restricted to flat surfaces and are only capable of measuring the skin friction magnitude and not the direction (there are some surface hot wire techniques that are able to detect skin friction angles within a $180°$ range, but they require the use of multiple sensors). In addition to those quantitative techniques, a number of qualitative, shear stress visualizing techniques have emerged in recent years, [7], [8]. These techniques exploit that changes in surface temperature are dependent on the state of the flow.

The new sensor that is presented in this paper combines the advantages of the qualitative, visualizing and the quantitative techniques and is able to not only measure the

skin friction magnitude but also its direction. The sensor is based on the so called "thermal tuft" technique which recently has been the focus of studies, [3], [9], [2]. It should be noted that the thermal tuft definition used throughout this paper and in recent literature differs from that used by Eaton, e.g. [10], where a pulsed wall probe consisting of three wires is used to measure the skin friction and the "thermal tuft" or wake of the wires to determine the flow direction. Using the more recent thermal tuft definition, a sensor in its most basic form is a heated spot on a surface. If there is no flow across the sensor, the temperature field will be centered around the sensor. However, if the sensor is subjected to a flow field, the temperature field around the sensor changes and forms what is called a "thermal tuft", which is teardrop shaped and points in the direction of the flow. This characteristic temperature field can be correlated to the wall shear stress and magnitude and direction can be determined. In the present study, numerical simulations were performed to determine possible correlation and design parameters. From these results, a sensor was designed, built and tested in wind tunnel experiments.

2   Numerical and Experimental Setup

The numerical investigations were carried out with the ANSYS CFX software package. A laminar Couette flow (a shear flow between two plates) was simulated, because it allows for a small computational domain and an easy adjustment of the wall shear stress. Since a Couette flow exhibits a linear velocity distribution, the wall shear stress can be calculated from the velocity of the upper wall

$$\tau_w = \mu \left(\frac{\partial u}{\partial y} \right)_w = \mu \, \frac{u_{wall}}{h} \tag{1}$$

where u_{wall} is the wall velocity and h the distance between the lower and upper wall. Therefore, the shear stress on the sensor can be set to a desired value by adjusting the upper wall velocity accordingly. Simulations were carried out for a range of wall shear
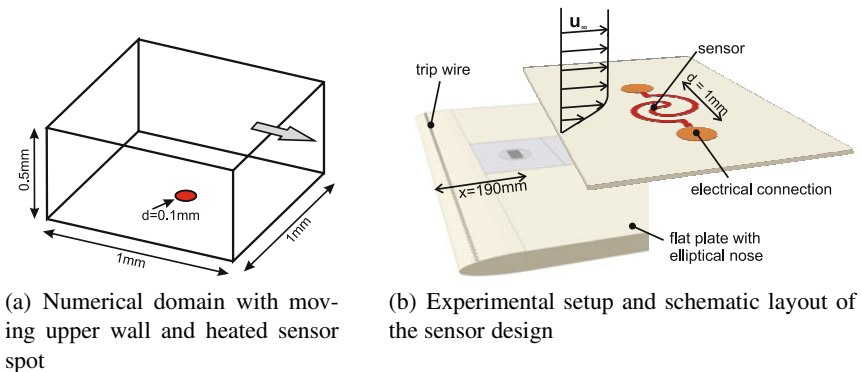

(a) Numerical domain with moving upper wall and heated sensor spot

(b) Experimental setup and schematic layout of the sensor design

Fig. 1. Setup of the numerical simulations and experimental investigations

stress values from $\tau_w = 0.2 - 3\,N/m^2$. The computational domain is illustrated in figure 1(a). The sensor, approximated by a circle, was heated by a constant heat flux boundary condition, while the surrounding structure was assumed to be adiabatic. The ambient temperature was set to $T_\infty = 300\,K$.

Since the experimental investigations were carried out in a turbulent flow, it was unclear if the results from the numerical simulations, where the temperature boundary layer exceeds the thickness of the viscous sublayer, i.e. $y^+(\delta_T) > 5$, could be transferred. In order to clarify the situation, a turbulent flow across a flat plate was simulated as a reference for one shear stress value using the "shear stress transport" (SST) turbulence model. The resulting temperature distribution differed only slightly from the laminar case. Therefore, it was deduced that the Couette flow could be used as a fast and computationally time efficient method to investigate the sensor's temperature field and possible correlation and design parameters.

The experimental investigations were carried out for turbulent flow conditions in an open wind tunnel facility. The setup and the sensor layout are illustrated in figure 1(b). The sensor consists of a copper spiral on a circuit board that is produced in an etching process. The electrical connections are attached from the backside to guarantee a smooth surface. By applying a voltage, the copper heats up due to Joule heating, creating the desired heated spot. The sensor can be inserted into a flat plate with an elliptical nose at a position of $x = 190\,mm$. The sensor insert can be replaced with a skin friction balance which was used for reference measurements. The skin friction balance is a differential head model by Les Industries Fanny Inc. with a floating head diameter of $d = 28.6\,mm$ and an accuracy of $\pm 2\%$. An infrared camera (SC3000 by FLIR Systems) was used to detect the temperature field around the sensor. The camera is calibrated with an accuracy of $\pm 1\%$ and has a closeup lense which is able to resolve $34\,mm \times 25\,mm$ with 320×240 pixel. Measurements were carried out for velocities from $u_\infty = 2.5 - 19\,m/s$, corresponding to Reynolds numbers of $Re_x = 29500 - 225000$ and skin friction values of $\tau_w = 0.04 - 1.5\,N/m^2$.

3   Numerical Results

The numerical simulations were carried out to investigate possible parameters to correlate the temperature field around the sensor with the skin friction and, in a first step, to numerically calibrate the sensor.

Four correlation parameters were investigated and can be found in the schematic drawing of a thermal tuft in figure 2(a):

- tuft length from midpoint: the largest distance from the sensor's center to a point on a temperature isoline (distance $\overline{CE}$)
- tuft length overall: the largest distance between two points on a temperature isoline (distance $\overline{AE}$)
- area: the area contained within a temperature isoline
- integral: the area integral over the whole simulated area or the entire infrared image of the temperature distribution (see figure 2(b)) normalized by the maximum temperature $I = \int\int T/T_{max}\,dx\,dy$.

(a) Sketch of a thermal tuft with points used for the correlation parameters

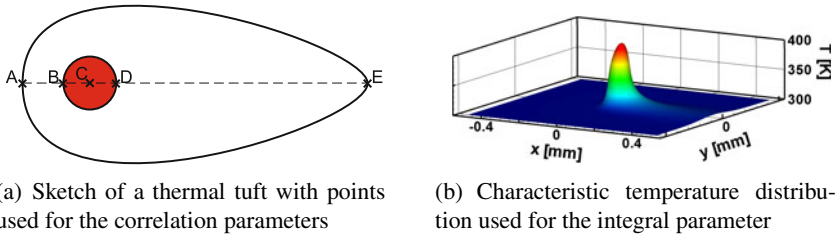(b) Characteristic temperature distribution used for the integral parameter

Fig. 2. Correlation parameters

The area integral differs from the other parameters, because it does not need a temperature isoline to be evaluated. All four parameters produce good calibration curves, but the quality of the length and area parameter calibrations depends very strongly on the choice of evaluation temperature. For this reason, the integral parameter was chosen for the sensor calibration. Figure 3(a) shows numerical sensor calibrations for three different heat flux boundary conditions, where the integral parameter is normalized with the respective maximum for a better comparison. The heat flux influences the calibration curves a great deal. Larger values result in steeper curves, because the changes in the temperature field are comparatively larger.

As mentioned before, the sensor is not only capable of measuring the wall shear stress magnitude but also its direction. The skin friction angle cannot be detected from the integral parameter. However, if the sensor center and an isoline are known, the angle can be directly calculated from the tuft length from the center. Figure 3(b) shows results for one sensor that was operated at three different skin friction angles, $0°, 10°, 50°$.

(a) Comparison of the integral calibration curves for three different heat flux boundary conditions

(b) Deviation of the shear stress angle determined from the numerical results
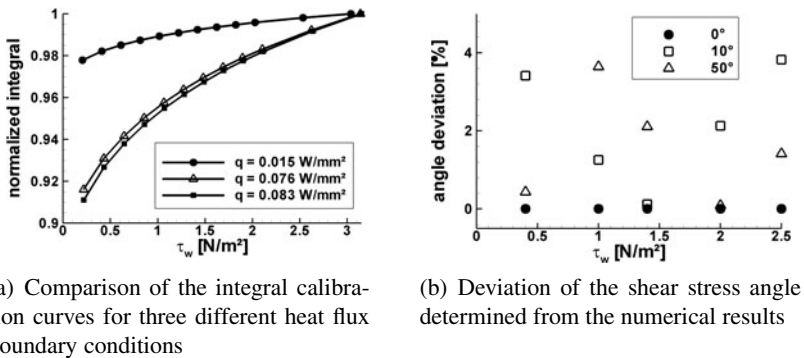
Fig. 3. Results of the numerical investigation

For the $0°$ case, the angles are correctly detected, for the larger angles the accuracy decreases a little. Overall, the method is able to detect the skin friction angle with a deviation of less than four percent.
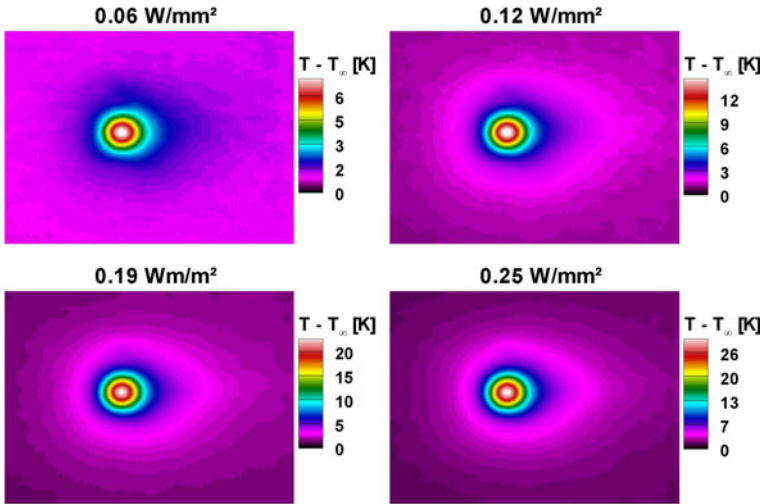
Fig. 4. Infrared images of the temperature distribution around the sensor for four different heat flux values and a wall shear stress of $\tau_w = 0.7 \, N/m^2$

4   Experimental Results

Figure 4 shows infrared images of the temperature distribution around the sensor. The sensor was operated at four different heat flux values which are compared for a wall shear stress of $\tau_w = 0.7N/m^2$. For the lowest heat flux value, the characteristic thermal tufts is hardly noticeable and the temperature field seems noisy. With increasing heat flux, the thermal tuft becomes more pronounced and the overall temperature field less noisy. The electrical contacts, which slightly distort the temperature field, can also be seen in the infrared images (above and below the sensor), although their influence also decreases with increasing heat flux. Even though it seems like a heat flux value as high as possible would be the ideal operating point for the sensor, the influence of the local heating on the boundary layer, and therefore on the quantity to be measured, has to be taken into account. That is why a compromise between good signal to noise ratio with low temperature field distortion and as little influence on the boundary layer due to the heating as possible has to be found.

A direct comparison of numerical and experimental thermal tufts is shown in figure 5 for two wall shear stress values. The characteristic features of the thermal tuft are clearly visible and compare very well. It can be seen in both cases that the temperature field around the sensor contracts with increasing skin friction due to the increased convection. The differences in the temperature fields stem from the assumption of an adiabatic wall for the numerical simulation. Because of that, the wall regions outside of the sensor's direct influence remain at the ambient temperature and do not heat up. Since in reality there are no adiabatic walls, the surface surrounding the experimental sensor clearly allows for a heat flux into the surface. The heating of the sensor does not only create a hot spot but also leads to a slight rise in temperature of the surrounding surface.
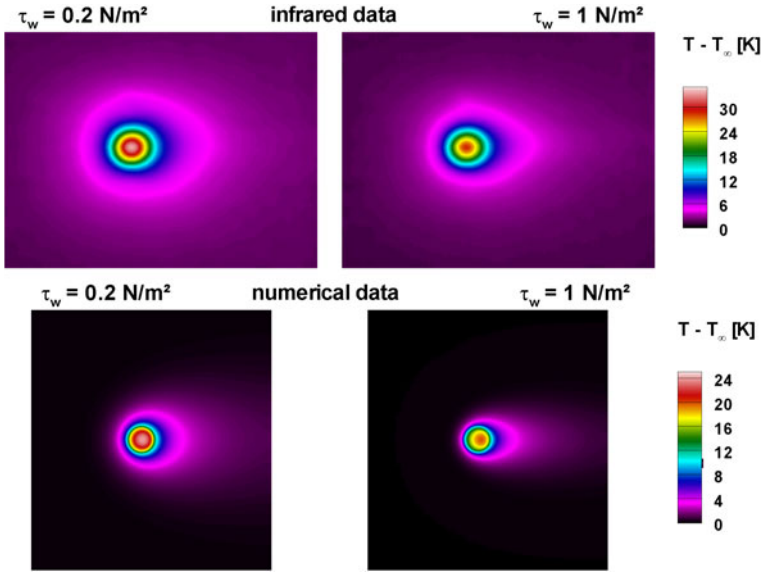
Fig. 5. Comparison of numerical and experimental temperature fields for two wall shear stress values

The influence of the structure and its material properties will be investigated further in new numerical simulations which include the structure underneath and surrounding the sensor.

The integral calibration curves, normalized with the respective maximum, for all four heat flux values are displayed in figure 6(a). The curves compare very well with the numerical calibrations. Higher heat flux values lead to larger changes in the temperature field and therefore to steeper calibration curves, but all values that were examined yield very good results. The influence of the surrounding structure that was described above can be seen here as well. The same heat flux leads to a steeper calibration curve for the numerical sensor than for the experimental sensor. This is caused by the adiabatic wall, which does not account for heat loss into the structure. For this reason, the heat flux in the experiments has to be a lot higher to achieve conditions similar to the numerical simulations.

Figure 6(b) shows the skin friction angles calculated from the infrared images for all four heat flux values. The sensor was not rotated with respect to the flow, so the angle should be zero for all cases. Overall, the angles from the experimental data scatter more than the numerical angles, which is not surprising, considering that the spatial resolution of the numerical data is much higher than the resolution of the infrared images. It can also be seen that the accuracy improves with increasing heat flux. For the largest heat flux value, the angle can be determined with an accuracy of $3°$. One drawback of the current method for the angle detection is the need to pick a temperature isoline. The choice of this isoline largely influences the scatter and accuracy of the angle detection. Therefore, a new method using principal component analysis will be tested in the future.
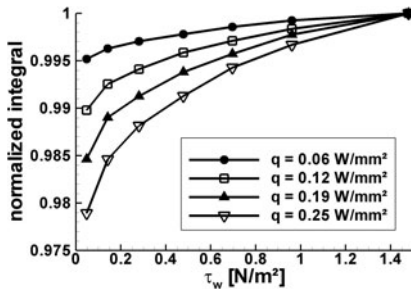
(a) Comparison of the integral calibration curves for four different heat flux values
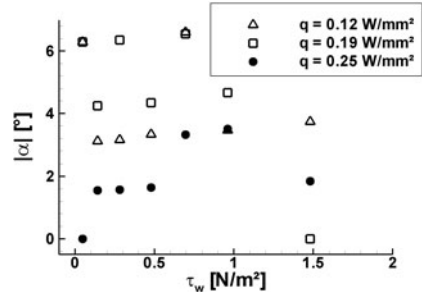
(b) Comparison of the shear stress angle for different heat flux values

Fig. 6. Results of the experimental investigation

5   Conclusion

A new thermo-optical sensor for the measurement of skin friction magnitude and direction is presented. The sensor produces a characteristic, teardrop shaped temperature field ("thermal tuft"), which can be correlated to the wall shear stress. Furthermore, the skin friction angle can be detected from the shape of the thermal tuft. Numerical simulations were performed to identify possible correlation parameters. The area integral of the temperature field was chosen for the skin friction calibration, because it produced the best and most reliable results. This was confirmed for the experimental investigations, where the sensor was successfully calibrated using the integral parameter. The skin friction angle was detected from the tuft length. To evaluate the length, a temperature isoline has to be chosen. The choice of isoline was found to strongly influence the accuracy of the angle detection. From the numerical data the angle could be detected reliably and with a good accuracy. The angles that were calculated from the experimental data showed more scatter due to the lower spatial resolution of the data, but the accuracy improved with increasing heat flux. A new method based on principal component analysis will be tested in future studies.

The numerical and experimental calibration curves compare very well. Higher heat flux values lead to steeper calibration curves because the changes in the temperature fields are comparatively larger. However, the same heat flux leads to a steeper calibration curve for the numerical sensor than for the experimental sensor. This is due to the heat loss through conduction into the surrounding structure in the experiments, which was not accounted for in the numerical simulations. This effect of the assumption of an adiabatic wall could also be seen in a comparison of the temperature distributions around the sensors. In the experiments, the surface surrounding the sensor is heated as well, whereas in the numerical simulations the surrounding structure remains at the ambient temperature. Future numerical studies will account for the heat flux into the walls by including the structure surrounding the sensor in the numerical domain.

References

[1] Reyer, M., Rudolph, I., Nitsche, W.: Investigations into the visualization and quantification of wall shear stress distributions using infrared thermography. In: Proc. of the 25th AIAA Aerodynamic Measurement Technology and Ground Testing Conference (2006), AIAA–2006–3840

[2] Rudolph, I., Reyer, M., Nitsche, W.: A wall shear stress measurement technique using the thermal wakes of small heated spots. In: Proc. of the 26th ICAS Congress (2008)

[3] Baughn, J., Byerley, A., Gregory, J.: An optical method for measuring low wall shear stresses using thermal tufts. In: Proc. of the 44th Aerospace Sciences Meeting and Exhibit (2006), AIAA–2006–647

[4] Nitsche, W., Haberland, C., Thuenker, R.: Comparative investigations on friction drag measuring techniques in experimental aerodynamics. In: Proc. of the 14th ICAS Congress, ICAS-2.4.1, pp. 391–403 (1984)

[5] Naughton, J., Sheplak, M.: Modern developments in shear-stress measurement. Progress in Aerospace Sciences 38, 515–570 (2002)

[6] Fernholz, H.H., Janke, G., Schober, M., Wagner, P.M., Warnack, D.: New developments and applications of skin-friction measuring techniques. Measurement Science and Technology 7, 1396–1409 (1996)

[7] Rudolph, I., Reyer, M., Nitsche, W.: Visualization of time-dependent wall shear stress distributions using infrared thermography. In: Proc. of the 12th International Symposium on Flow Visualization, ISFV12-30.3. (2006)

[8] Ochoa, A.D., Baughn, J.W., Byerley, A.R.: A new technique for dynamics heat transfer measurements and flow visualization using liquid crystal thermography. International Journal of Heat and Fluid Flow 26, 264–275 (2005)

[9] Hunt, E., Pantoya, M.: A laser induced diagnostic technique for velocity measurements using liquid crystal thermography. International Journal of Heat and Mass Transfer 47, 4285–4292 (2004)

[10] Eaton, J., Westphal, R., Johnston, J.: Two new instruments for flow direction and skin-friction measurements in separated flows. ISA Transactions 21, 66–74 (1974)

Flow–Induced Oscillation of a Flat Plate –
A Fluid–Structure–Interaction Study Using
Experiment and LES

J. Gomes[1], M. Münsch[1], M. Breuer[2], and H. Lienhart[1]

[1] Institute of Fluid Mechanics and Erlangen Graduate School
in Advanced Optical Technologies, University of Erlangen–Nürnberg,
Cauerstr. 4, D–91058 Erlangen, Germany
{jgomes,mmuensch,lienhart}@lstm.uni-erlangen.de
[2] Dept. of Fluid Mechanics, Helmut–Schmidt–University Hamburg,
Holstenhofweg 85, D–22043 Hamburg, Germany
breuer@hsu-hh.de
www.lstm.uni-erlangen.de, www.hsu-hh.de/pfs

Summary

The research unit *F*OR 493 tackles the challenging task of fluid-structure interaction (FSI). On the one hand, the objective is to provide reliable experimental reference data for all groups which are developing numerical methodologies to predict such coupled FSI problems. Since measurements on fluid-structure interaction setups using well-defined boundary and operating conditions are rare, the present Particle Image Velocimetry and excitation measurements for a swiveling flat plate support to fill a gap by providing phase-resolved data of this useful test case. On the other hand, the objective is to develop numerical methods for coupled FSI investigations which involve turbulent flows. Thus, an especially designed coupling scheme to be used in combination with the large-eddy simulation technique was set up and applied to study the flow around the hinged flat plate and the development of self-excited periodic processes with rotary oscillation of the flat plate.

1 Introduction

Since FSI plays a dominant role in many fields of engineering such as mechanical engineering (e.g. valves) [1], aerospace engineering (e.g. wings), process engineering (e.g. stirrers), medicine technique (e.g. substitute vocal folds), or civil engineering (e.g. suspension bridges), a strong need for appropriate numerical simulation tools exists. During the development and test phase of these tools reference test cases are required to serve as verification and validation data in order to check the physical models as well as the efficiency of the numerical implementation.

The aim of the present project is twofold. On the one hand, relatively simple but selective and meaningful test cases were established to produce a reference data base
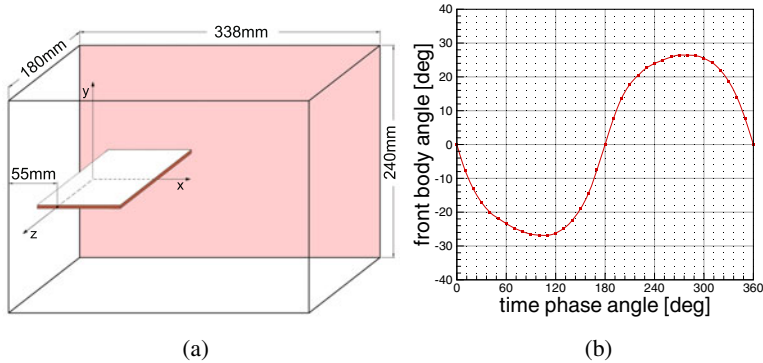
Fig. 1. Test geometry (a) and measured rigid plate angle (b) within a period of motion at Re = 68,000.

of experimental results on fluid-structure interaction [2]. For all test configurations considered, the resulting two-dimensional flow and structural periodic swiveling movement driven by a uniform incoming flow were characterized in detail under well-defined boundary and operating conditions. On the other hand, a numerical methodology was set up which allows to tackle complex turbulent FSI problems by using large-eddy simulation (LES) in connection with an appropriate coupling scheme for FSI.

The experimental and numerical investigations of which the results are presented in this paper were conducted for an uniform incoming flow velocity up to 2 m/s using water as test liquid. The model consisted of a rigid and flat carbon fibre reinforced plate (density equal to 1475 kg/m^3) of 2 mm thickness with a chord length of 64 mm. The model possessed a single rotational degree of freedom around an axle located 20 mm downstream of the leading edge (z-axle in Fig. 1(a)). The spanwise dimension of the plate was chosen to match the dimension of the test section to satisfy approximately the two-dimensionality of the test case.

2   Solution Method

2.1   Experiment

The experimental tests were performed on a vertical closed circuit tunnel specially designed for fluid-structure interaction investigations over a wide range of Reynolds number. The facility not only permits to specify the Reynolds number of the tests by controlling the kinematic viscosity of the working liquid up to 5×10^{-4} m^2/s but also guarantees that the gravity force is aligned with the x-coordinate avoiding the introduction of any asymmetry into the problem. The model was mounted in the 338 mm long test section (cross-section 180 mm × 240 mm) on low-friction ball bearings at 55 mm from the inlet of the test section (see Fig. 1(a)). As far as the measurements are concerned, information of both structure and flow quantities are of capital importance to understand the coupled fluid and structure self-excited movement. Therefore, the measurement techniques were adapted to the present study in a way to measure the

time-phase resolved flow velocity field around the model as well as the unsteady angle of the plate within a period of motion. To measure the flow velocity field, Particle Image Velocimetry (PIV) was the chosen measurement technique [3]. The system consisted of two 1280 pixel $\times$ 1280 pixel synchronized cameras and two laser light sources. Opting for the solution of two parallel cameras and multiple light sources, it was possible to acquire time-dependent composed PIV images at constant frequency of an unobstructed 272 mm $\times$ 170 mm flow field measuring area in the midplane of the test section while keeping the spatial resolution as low as 133 μm $\times$ 133 μm per CCD pixel.

To resolve the measurements in time, the PIV measuring system was operated at constant acquisition rate and both events, the acquisition of a pair of images and the start of a new cycle of the model motion were recorded based upon an absolute clock. Using the recorded events time information, the time-resolved results were reconstructed in a post-processing software introducing the time-phase angle $tpa=t/T \cdot 360°$, where T is the period of the structure swiveling motion cycle in which the measurement was performed and t is the delay of the measurements in respect to the beginning of the cycle. Besides resulting in the minimum acquisition time needed, this solution turned out to be very efficient to cope the small cycle-to-cycle fluctuations of the period time of the plate motion. To record the events time information, a time-phase detector module was designed and integrated into the PIV measuring system. The hardware module works based on a Field Programmable Gate Array and a 1 MHz internal clock. It proved to be capable to monitor up to 250 events/s from 6 different lines with an accuracy better than 2 μs.

The position of the model was monitored using a non-contacting position magnetic sensor on one extremity of the rigid plate axle to measure its angular position. This signal was used to reconstruct the time-phase resolved angular position of the plate as well as to define the beginning of the model swiveling motion cycles. Based on the time-phase angle, the experimental measurements were resolved in the time-phase space with a resolution of 2.5° associated to an uncertainty of 0.5°. Each result corresponded to the average value over 100 measurements.

2.2 Simulation

Since the numerical task is to predict complex turbulent flows around moving (or deforming) structures, which involve large-scale flow phenomena such as separation, reattachment and vortex shedding, the LES technique was chosen as the most appropriate ansatz. In [4] it was shown that RANS is not a suitable approach to compute the flow around an inclined plate. DES is more appropriate if an adjusted version is applied [4]. For the purpose of LES the filtered Navier-Stokes equations for an incompressible fluid are discretized by a finite-volume scheme using blockstructured, curvilinear body-fitted grids with a co-located arrangement of the variables. The integrals are approximated by the mid-point rule and the flow variables are linear interpolated to the cell faces leading to a second-order accurate central scheme. In order to account for the moving/deforming grids, the well-known Arbitrary-Lagrangian-Eulerian (ALE) formulation is applied. It guarantees that besides the mass and momentum conservation also the space conservation law is satisfied.

The turbulent flow field is resolved in time by using small time steps within the LES which leads to a preference of explicit time-marching schemes, i.e., a predictor-corrector scheme of second-order accuracy. The momentum equations are advanced in time based on a three sub-step low-storage Runge-Kutta scheme once per time step (predictor). Afterwards a Poisson equation for the pressure correction is solved based on an incomplete LU decomposition solver until mass conservation is achieved (corrector). Based on this efficient explicit time-marching procedure, a special coupling scheme was designed [5, 6]. It preserves the structure of the predictor-corrector scheme and thus couples the structure to the fluid within the corrector step taking the so-called added-mass effect into account. Consequently, instabilities known from loose coupling schemes and high computational costs of fully implicit schemes (see, e.g., [7]) are avoided.

The LES is performed with the in-house code FASTEST-3D using the Smagorinsky model (C_s=0.1) with Van Driest damping near solid walls. The response of the rigid structure exposed to the fluid flow is described by a spring–mass–model in form of an ordinary differential equation for the plate angle φ, i.e., $I\,\ddot{\varphi}(t) + C\,sin(\varphi(t))=M_z(t)$. This equation is solved by a classical Runge-Kutta scheme where the external moment $M_z(t)$ is determined by the pressure and shear forces acting on the structure. The moment of inertia of the plate and axle is denoted by I=1.624·10^{-5} kg m^2 and C=3.934·10^{-3} Nm is given by the gravitational forces acting on the plate. Thus, the eigenfrequency of the structure is equal to f_e=2.48 Hz. Based on the excitation of the plate which represent boundary nodes of the fluid solver, the entire grid has to be adjusted within each coupling step. Presently, this is conducted by a transfinite interpolation scheme for the movement of the inner grid nodes. For a first prediction of the coupled FSI problem, only an adequate section of one chord length of the experimental setup was taken into account which reduces the computational effort and allows to apply periodic boundary conditions in spanwise direction. Thus the influence of the sidewalls was ignored. At the inlet a constant inflow velocity of 1.07 m/s was set, whereas at the outlet a convective outflow boundary condition was used. No-slip boundary conditions were defined on the upper and lower channel wall and on the swiveling plate itself. The simulation was performed on a rather coarse grid with only 434,176 control volumes. The spanwise direction was resolved with only 4 control volumes. At the trailing edge of the plate the centre of the wall-nearest control volume is placed at y^+=1.51 wall units in wall-normal direction. At the opponent channel walls a wall-normal resolution of y^+=3.02 wall units is chosen. In total 128 control volumes, distributed with a bigeometric mesh law, have been used to resolve the flow field between the plate and each opponent channel wall. The initial wall-normal stretching factor is equal to 1.05 at the trailing edge of the plate.

3   Results

The general character of the self-excited movement of the rigid plate in a uniform turbulent flow up to 2 m/s was registered. For all the flow velocities tested, the resulting swiveling motion has revealed to be very symmetric and reproducible. The RMS of the movement period and of the maximum deflection amplitude was measured to be less than 1.5% and 1°, respectively. Thus the oscillations can be characterized as

limit cycle oscillations (LCO). Increasing the incoming flow velocity, the plate exhibits a reproducible movement for the first time at about 0.25 m/s. From this point on the frequency of the resulting coupled movement increases linearly with the incoming flow speed at a rate of about 0.23 Hz · s/m while the amplitude of the movement presented a local maximum for 1 m/s, approximately. The results shown in the following where obtained for an incoming flow velocity equal to 1.07 m/s and comprehend the time-phase resolved plate angle and velocity field. At this velocity, the Reynolds number, based on the chord length of the plate, was about 68,000. Figure 1(b) represents the evolution of the rigid plate angle within the plate swiveling motion period. During the experiments, the frequency of the motion was measured to be equal to 2.49 Hz associated to a maximum deflection of about ± 27°. As far as the flow field is concerned, in Fig. 2 one can observe the flow field around the plate at four consecutive instants within the swiveling period. The velocity direction is represented by streamlines whereas the scalar map represents the magnitude of the flow velocity non-dimensionalized by the incoming velocity. Concerning the CFD predictions the new coupling scheme adopted for FSI in connection to LES turned out to work quite well for computations of flows around cylindrical structures [5, 6, 8]. First simulations of the swiveling flat plate are carried out, where the effect of the sidewalls in spanwise direction is excluded. The

(a) tpa = 0°

(b) tpa = 60°

(c) tpa = 120°

(d) tpa = 180°
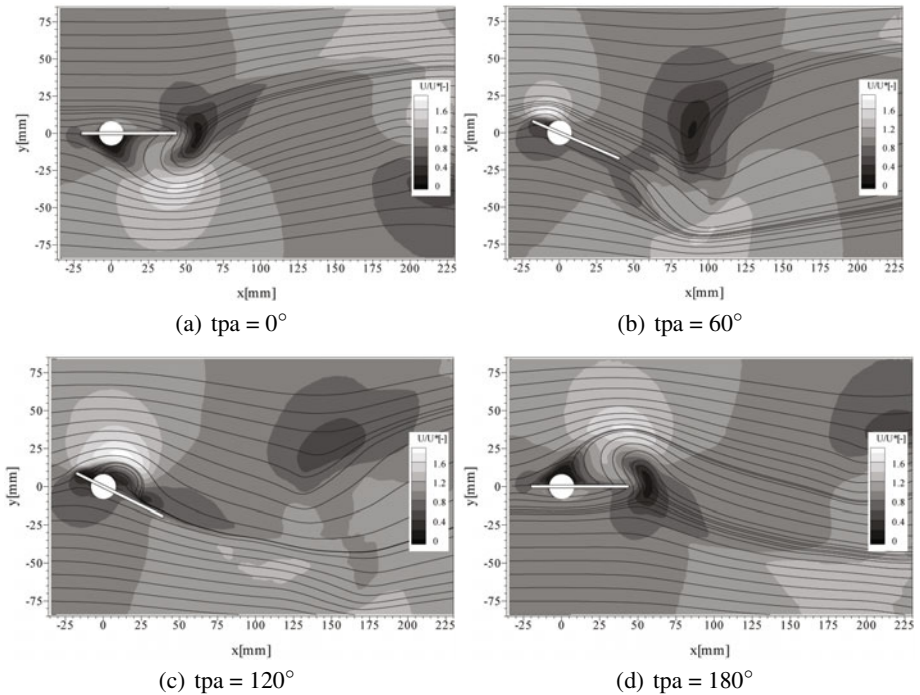
Fig. 2. Measured phase-averaged velocity field (streamlines and total magnitude of velocity) and plate deflection at four different instants of the swiveling motion period at Re = 68,000.

(a)   (b)
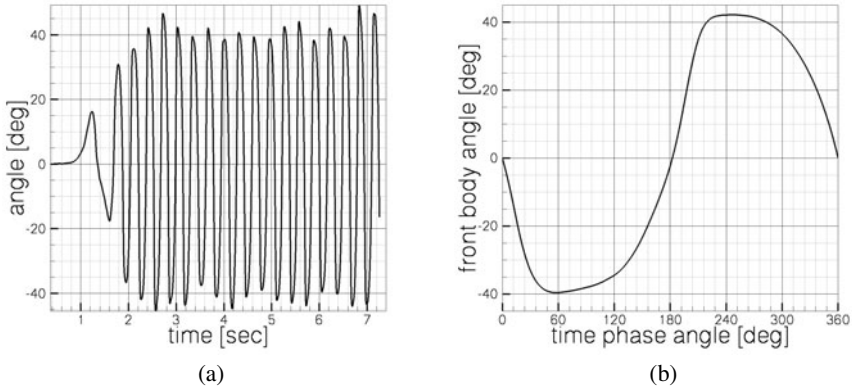
Fig. 3. Computed angular displacements of the plate: (a) as a function of time, (b) for one period as a function of the time phase angle.

(a) tpa = 0°   (b) tpa = 66°

(c) tpa = 122°   (d) tpa = 179°
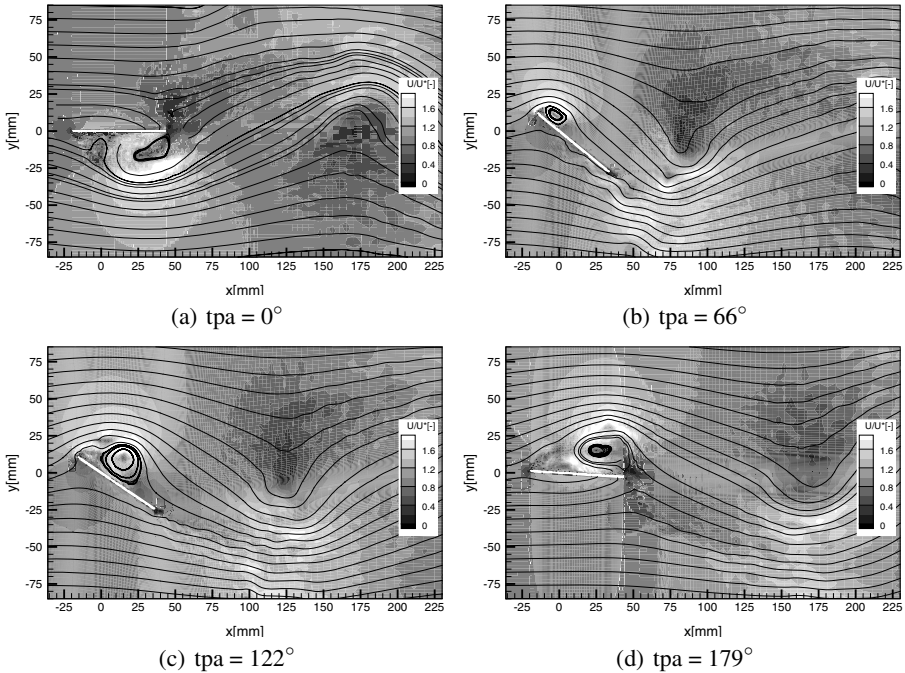
Fig. 4. Computed instantaneous velocity field (streamlines and total magnitude of velocity) and plate deflection at four different instants of the swiveling motion period at Re = 68,000.

resulting external moment $M_z(t)$ is adapted to the original spanwise extension of the plate. Starting the computation with a fixed plate ($\varphi=0°$), the plate is released, i.e. the coupling between fluid and structure is performed at 0.36 s real time. After a settling

time of about 2 s the plate swivels with a frequency of about 3.14 Hz. The amplitudes vary in a range of $\varphi_{min}=-45°$ to $\varphi_{max}=+49°$ (see Fig. 3(a)). In Fig. 3(b) the instantaneous time-phase resolved plate angle for an exemplarily chosen period is shown. Streamlines and contours of the non-dimensionalized velocity magnitude of this period for nearly the same instants in time as for the experiment are plotted in Fig. 4. With increasing deflection angle φ (see Fig. 4(b)) a vortex is generated close to the leading edge of the plate. This vortex grows and is transported in downstream direction, even if the deflection is decreasing again (Figs. 4(c) – 4(d)). Finally, it is convected downstream behind the plate and a similar cycle starts at the opposite side of the plate. Thus the flow field observed can hardly be compared with the flow past an inclined plate at a fixed angle of attack, where a large recirculation region and a trailing-edge vortex shedding process was found [4]. Due to the higher frequency and amplitudes of the predicted motion, the plate angles do not correspond to the experimental plate angles in Fig. 2. Consequently, the predicted and measured flow fields deviate from each other, which can be seen in the different characteristics of the streamlines. For a direct comparison of the simulation and the experiment it has to be taken into account, however, that for the former instantaneous results are depicted in Fig. 4, whereas for the latter Fig. 2 presents phase-averaged data. Nevertheless, computational and experimental results show good qualitative correspondence concerning the spots of high and low velocity magnitude but still differ to some extent regarding the amplitude and frequency of the swiveling motion. Also the limit cycle effect of the oscillation is not fitted as well as in the experimental investigation because of higher cyclical variations of the oscillation amplitudes (see Fig. 3(a)).

4   Conclusions and Outlook

In the experiments, and for the entire flow velocity range tested, the structure reached a oscillating movement with a constant amplitude and a constant frequency very rapidly. After reaching the limit cycle oscillation state, the RMS value of the cycle-to-cycle fluctuation of the period and maximum deflection of the plate was measured to be smaller than 2%. Referring to the simulation, the coupling scheme used was found to be stable for this case, but the maximum deflection angle of the plate obtained in this preliminary simulation turned out to be too large compared to the experiment. Possible reason might be the restriction to a section of the rigid plate. Preliminary tests with an increased grid resolution of 64 an 177 control volumes in spanwise direction have not shown an impact on the computed amplitudes up to now. Thus, in the next step the computational domain has to be extended and the influence of the sidewalls has to be taken into account. Furthermore, the grid resolution has to be increased. As soon as the experimental results and the numerical simulations show a good agreement for the present test case, a similar study is thought to be conducted on more complex geometries. The next object of study will be relatively simple two–dimensional flexible structures. Preliminary experimental tests have shown that a freely rotating cylinder with an attached thin metal membrane satisfies the requirements in terms of reproducibility of the coupled movement within the fluid-structure interaction. Such geometry undergoes large deformations and shows a behavior which justifies its choice for future investigations.

Acknowledgements

References

[1] Naudascher, E., Rockwell, D.: Flow-Induced Vibrations - An Engineering Guide. A. A. Balkema, Rotterdam (1980)

[2] Pereira Gomes, J., Lienhart, H.: Reference Test Cases for Fluid-Structure Interaction Studies. In: Int. Workshop on Fluid-Structure Interaction: Theory, Numerics and Applications, Herrsching am Ammersee, Germany, September 29-October 1 (2008)

[3] Pereira Gomes, J., Lienhart, H.: Experimental Study on a Fluid–Structure Interaction Reference Test Case. LNCSE, vol. 53. Springer, Heidelberg (2006)

[4] Breuer, M., Jovičić, N., Mazaev, K.: Comparison of DES, RANS anf LES for the separated flow around a flat plate at high incidence. Int. J. Numer. Meth. Fluids 41, 357–388 (2003)

[5] Breuer, M., Münsch, M.: Fluid–Structure Interaction Using LES – A Partitioned Coupled Predictor–Corrector Scheme. In: 78th Annual GAMM Meeting, Universität Bremen, Germany, March 31-April 4 (2008)

[6] Breuer, M., Münsch, M.: LES Meets FSI – Important Numerical and Modeling Aspects. In: Seventh Int. ERCOFTAC Workshop on DNS and LES: DLES-7, Trieste, Italy, September 8-10 (2008)

[7] Glück, M., Breuer, M., Durst, F., Halfmann, A., Rank, E.: Computation of Wind–Induced Vibrations of Flexible Shells and Membranous Structures. J. Fluids & Structures 17, 739–765 (2003)

[8] Breuer, M., Münsch, M.: FSI of the Turbulent Flow around a Swiveling Flat Plate Using Large–Eddy Simulation. In: Int. Workshop on Fluid-Structure Interaction: Theory, Numerics and Applications, Herrsching am Ammersee, Germany, September 29-October 1 (2008)

Investigations to the Response Time of a Glued Thermocouple on the Basis of Experimental and Numerical Analyses

Tarik Barth[1], Carl Dankert[2], Günter von Roden[2], and Jan Martinez Schramm[2]

German Aerospace Center (DLR) - Institute of Aerodynamics and Flow Technology
[1] Lilienthalplatz 7, 38108 Braunschweig, Germany
Tarik.Barth@dlr.de
[2] Bunsenstr. 10, 37073 Göttingen, Germany

Summary

This study deals with experimental and numerical investigations of the time response of a mantle thermocouple. Using two different experiments, a clear influence of a glue covering is indicated. The numerical analyses are done using a stand-alone structure and a coupled flow-thermal calculation. Both computational results agree with the experimental data and established a detailed flow investigation of the VxG-experiment. The experimental and numerical investigatons confirm that a thin glue layer of about $1\ mm$ is responsible for a time delay of few seconds.

1 Introduction

There is often a neglected problem with respect to the time response of an applied thermocouple for temperature measurement within a structure or fluid [3]. Mainly, if the temperature is changing within a small time scale, the thermocouple is not able to measure exactly the gradients. An additional delay appears, if the thermocouple is glued together with the object, because the heat conduction of the glue is low. Consequently, there are differences between the measured and the real temperature which have to identify in order to interpret correctly the experimental temperature data. In this study it is shown that a mantle thermocouple with and without a glue covering have a time response of different size. The second objective is to outline the difference between a glued and a pressed thermocouple which are bounded within a ceramic. Both purposes have been analysed using experimental and numerical methods.

2 Experimental Investigations

The experimental studies are based on two different experiments. The first one is a dipping experiment in water of a thermocouple with and without glue. The thermocouple is dip into hot water while the time response will be measured. The second

experiment takes place in the vacuum wind tunnel Göttingen (VxG) of the German Aerospace Center (DLR). It consists of a ceramic body which is loaded by a hypersonic nozzle flow ($Ma \approx 4$). During the heating process the temperature in the middle of the body is measured by a glued thermocouple and by a thermo element which is pressed directly at the ceramic body without lagging. This experiment is complex and quite difficult to simulate. Especially the probe holder affects the flow field and heating process of the probe. Nevertheless, there are different reasons for the choice of this experimental setup and the ceramic probe geometry. The used geometry of the ceramic body should be the same as for the used plane thermal protection panels of a flown re-entry experiment (*SHEFEX*). Furthermore, with respect to save resource, the available experimental equipment should be used. Finally, the flow phenomena in the VxG should be investigated in detail for further experiments.

All measurements are repeated a few times to ensure that repeatability is given. The investigated thermo element is a standard mantle thermocouple (type K) with a diameter of $d = 0.5\ mm$. The measuring point is isolated from the covering. The high temperature glue is often applied and based on a SiO_2 compound. **Table 1** shows the important properties of the used ceramic and glue.

Table 1. Thermal properties of the applied ceramic and glue

Parameter	Unit	Ceramic (C/C-SiC)	Glue (Polytec 905)
Density ρ	kg/m^3	1900	2650
Heat conductivity λ	W/mK	$\perp$ 7.6 − 9.7 $\parallel$ 16.8 − 18.0	1.4
Heat capacity c_p	J/kgK	750-1450	1170

2.1 Dipping-Experiment

This kind of experiment is typical in order to determine the response of thermocouples, because it is inexpensive and quite simple. In few cases the water is flowing with moderate velocities ($v \approx 0.2\ m/s$) in order to increase the heat transfer and enable a faster response. In **Figure 1(a)** the setup of the applied dipping experiment is shown. For this experiment, the water is not flowing and the thermocouples (with and without glue) are dipping into the hot water ($T_{water} = 83\ °C$). The diameter of the glue covering is $d_{glue} = 3\ mm$. In **Figure 1(b)** the results of the measurements are shown. The added line of the diagram corresponds to 90 % of the final temperature which is the reference value for the analysis [6]. It is analysed how much time ($t_{90\%}$) is required in order to reach this temperature level ($T_{90\%}$). For the thermocouple without glue the response time amounts $t_{90\%} = 0.2\ s$ which corresponds to the manufacturer information. In case of a glue covering this time increases to $t_{90\%} = 2.6\ s$. Here, the time constant is in the order of $\tau = 1.4\ s$ and four time constants ($t_{99\%} = 4\tau = 5.6\ s$) are required in order to decrease the measurement error to 1 %. Already this simple experiment shows clearly that an application of a glued thermo element is not recommended for a time accurate measurement. Even a thin glue layer of only $s = 1.25\ mm$ ($s = \frac{d_{\text{glue}} - d_{\text{thermocouple}}}{2}$), as in this case, causes a delay of few seconds. This is a typical problem of high temperature glue and is caused by its small heat conductivity ($\lambda_{glue} = 1.4\ W/mK$).
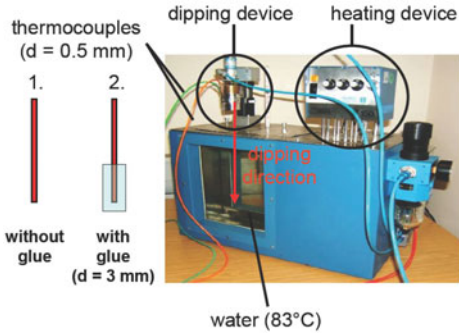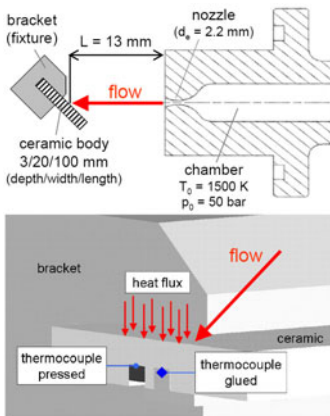
(a) Setup of the dipping experiment
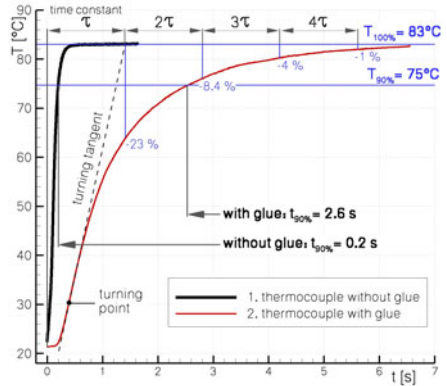
(b) Results of the dipping experiment

Fig. 1. Setup and results of the dipping experiment

2.2 VxG-Experiment

This experiment is done in order to outline the difference between a pressed and glued thermo element. Both elements have to measure the temperature in the middle of the ceramic body. For this purpose two grooves with a depth of $1.5mm$ are included into the sample (depth $3\,mm$), where the thermocouples will be pressed and glued respectively, as it is shown by the lower sketch in **Figure 2(a)**. The sample is fixed by two brackets

(a) Setup of the VxG-Experiment
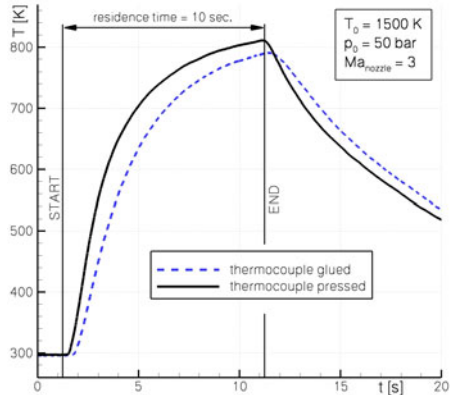
(b) Results of the VxG-Experiment

Fig. 2. Setup and results of the VxG-Experiment

on the left and right side, so that the nozzle flow can flow up along the upper side of the ceramic. In order to avoid a blocking of the nozzle flow, the plate is inclined by

an angle of $45\,°$. The operating gas of the experiment is nitrogen which is compressed and heated in the chamber to $50\ bar$ and $1500\ K$ respectively. The supersonic nozzle accelerates the gas at the exit to $Ma_e \approx 3.1$ where a further expansion to $Ma \approx 4$ is following. This supersonic jet with a mass flow of $\dot{m} = 3.34 \cdot 10^{-3}\ kg/s$ flows on the plate and heats up the structure. The time of the heating process is 10 seconds. After than, the sample is cooled down to ambient temperature. The results of this experiment are shown in **Figure 2(b)**. Although the position of the glued thermocouple is closer to the impact point of the nozzle flow, the measured temperature distribution of this thermo element keeps clearly below the pressed thermocouple. The time delay between both elements at the end of the heating process is $2.65\ s$. The maximum temperature deviation is within the first three seconds and amounts approximately $20\ \%$. This error becomes smaller, because a final steady state will be arrived. In order to understand in detail this experiment, in **section 3.2** numerical simulations for this case are following.

3   Numerical Investigations

The numerical investigations are based on a stand-alone structure calculation and a coupled fluid-thermal computation using the DLR-TAU-Code and the ANSYS-Code. TAU is a three-dimensional parallel hybrid multigrid code. It is a finite volume scheme for solving the Euler and Reynolds-averaged Navier-Stokes (RANS) equations using tetrahedrons and prisms. A validation and description of the unstructured DLR-TAU-Code for hypersonic flows is done in [5]. ANSYS is a commercial development and analysis software which uses the Finite Element Theory to study the physical behaviour of a structure model.

3.1   Sensitivity Analysis

In this subsection the influence of the position of a glued thermocouple (a) and the high of the glue overhang (b) are analysed based on a sensitivity analysis. The dimensions of the ceramic probe are $3 \times 20 \times 100\ mm^3$. It is assumed that the lateral extension of the glue is $10\ mm$.

The parameters (a and b) are illustrated in **Figure 3**. Thereby, two restrictions are included in order to limit the variation range: The maximum overhang of the glue is assumed to 1.5 mm. The second assumption is that the thermocouple is always bounded within the body. So that the maximum distance of the thermo element with respect to the middle of the ceramic is $1.5\ mm$. Each pa-

Fig. 3. Description of a and b

rameter will be changed in $0.5\ mm$-steps. Thus, 12 combinations of a and b are investigated. For the upper surfaces of the probe an adiabatic boundary condition is accepted. The thermal load on the lower side of the ceramic is in the first case, a constant temperature ($900\ K$) which corresponds to a steady heating process. In the second
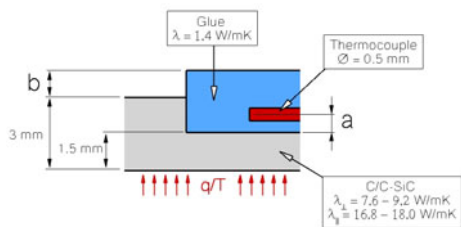
case the thermal load is a exponentially increasing heat flux ($\approx 0 - 1 \ MW/m^2$). The numerical results of the three dimensional computations are summarized in **Figure 4** for three combinations of a and b. Here, the black solid curve corresponds to the temperature in the middle of the sample. Both parameters have a distinct influence on the temperature measurement for both load cases. The analysed temperature decreases with an
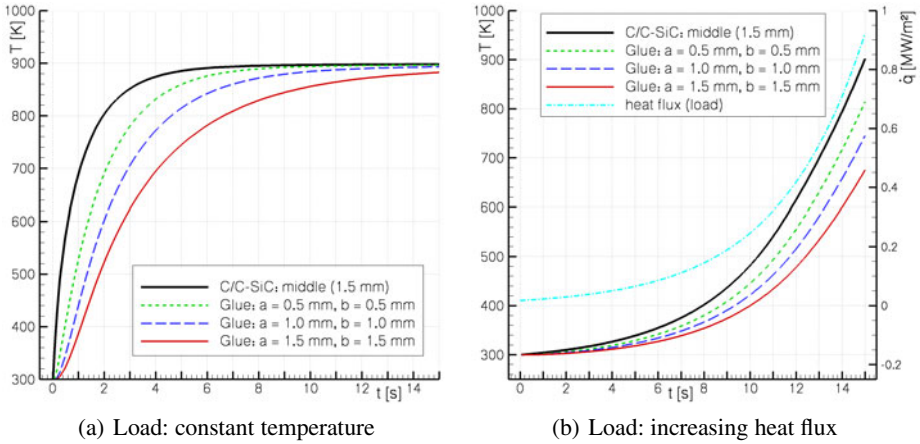

(a) Load: constant temperature   (b) Load: increasing heat flux

Fig. 4. Numerical results of the sensitivity analysis for different load cases

increasing overhang due to the higher heat capacity. The same applies for the sensor position (a), also here the temperature decreases with increasing distance. Finally, this study shows clearly the different core problems depending on the kind of load. If a constant temperature is acting on the body, the largest inaccuracy is in the first seconds. In case of an increasing heat flux, the inaccuracy rises with the proceeding time.

3.2   Coupled Simulation of the VxG-Experiment

In addition to the experimental studies of **section 2.2**, coupled simulations of the VxG-experiment are done. The coupling environment is a loosely coupled approach. The heat flux on the surface is calculated by the flow solver. After then, the solution is interpolated to the boundary grid points of the structure by the commercial MpCCI software of the *Fraunhofer Institut*. These data serve as boundary conditions for the commercial structural solver ANSYS. Finally, the structural solver gives the temperature associated with the applied heat flux, which is then in turn interpolated to the boundary grid points of the flow field and set as boundary condition to the flow solver. A detailed description of this approach is documented in [1].

(a) TAU grid   (b) Ansys grid
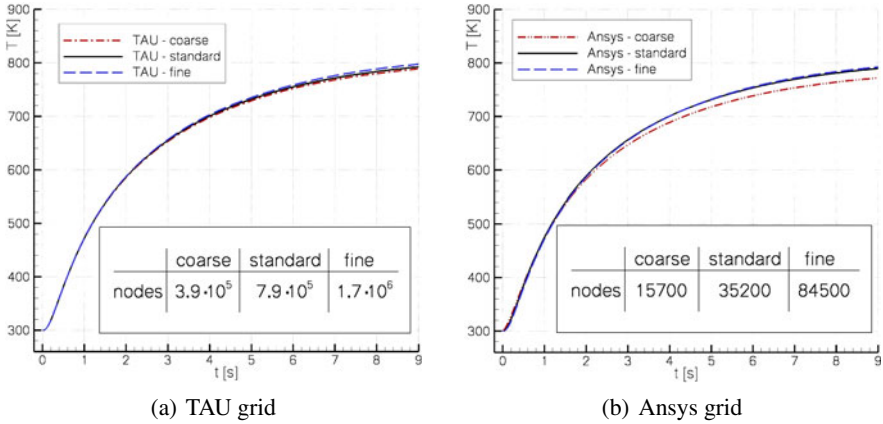
Fig. 5. Mesh sensitivity study: Temperature in the middle of the ceramic
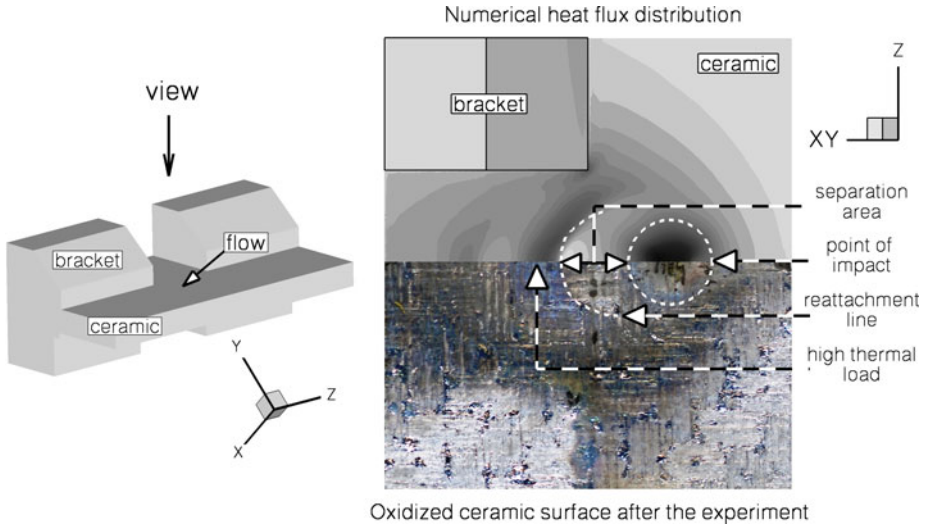

Fig. 6. Numerical heat flux distribution (k-ϵ-model) and photo of the oxidized ceramic

Firstly, a mesh sensitivity study is carried out in order to demonstrate the influence of the mesh fineness. The results of the temperature in the middle of the ceramic are summarized in **Figure 5**.

Based on these results a standard mesh is applied for the structure as well as flow calculations. Using these grids 400,000 iterations are necessary to complete the numerical flow simulation. The computational physical time steps varied between 0.01 second at the beginning and 0.2 second at the end. Finally, nine seconds of the heating process are observed. A convergence of the solution is achieved after 115 fluid-structure coupled iterations. The numerical data of one complete simulation amounts 50 GBytes.

The nozzle flow is not included within the numerical computations in order to reduce the calculation effort. The flow conditions of the nozzle outlet are set as inflow condition of the inlet, see **Figure 8(a)**. Consequently, only the free stream of the flow is computed. The state of the boundary layer within the impact point is assumed to be laminar. Due to the high Reynolds number the state of the remaining boundary layer is set to turbulent. These assumptions are approved by [2] and [4]. In the numerical simulations the turbulent boundary layer is modeled using different turbulence models: Spalart Allmaras (SA), k-ω-model, LEA k-ω-model, and k-ϵ-model. In **Figure 6** the numerical heat flux distribution is compared with the oxidized sample surface.

Due to high thermal loads the surface color of the ceramic is changed (oxidized) and reflects the characteristics marks like: impact point, separation area, reattachment line, and area of high thermal load. Based on this comparison, a first interpretation to the applicable turbulence model can be done as follows. The k-ϵ- and LEA-k-ω-models offer the best agreements with experimental results. In case of the other both models (SA and k-ω) the thermal loads are too low and the reattachment position differs respectively. This assessment will be confirmed by the results of the coupled numerical calculations which are shown in **Figure 7**. Also here, the best agreement with the measurement for

(a) Temperature at the pressed position   (b) Temperature at the glued position
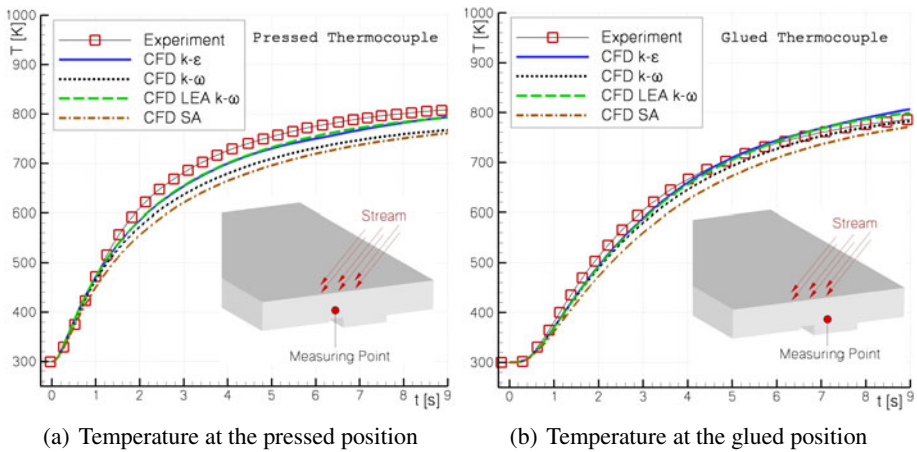
**Fig. 7.** Comparison of experimental and numerical results

the glued and pressed thermocouples is obtained using the k-ϵ- and LEA-k-ω-models. The reasons for the higher variation of the pressed thermo element may be see in the neglected roughness of the ceramic and the modeled thermal conductivity of the brackets. Nevertheless, in consideration of this very complex hypersonic flow case, the numerical results are very satisfying in comparison with the experiment.

Finally, in **Figure 8** a detailed overview about the complete flow topology is given. Here, the Mach number (flow field) and heat flux (surface) distributions are shown at the beginning of the experiment ($t = 0\,s$ and $T_{\text{wall}} = 300\,K$). The nozzle flow is expanded to $Ma \approx 4$. Behind the point of impact a separated flow is following, see **Figure 8(b)**. In this range a weak thermal load can be detected. There after the flow is reattached and
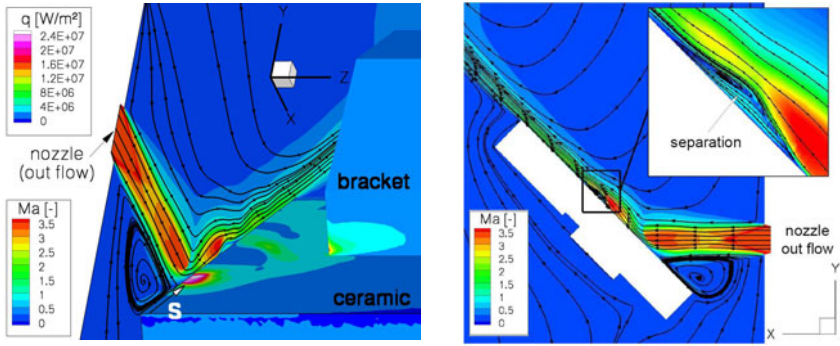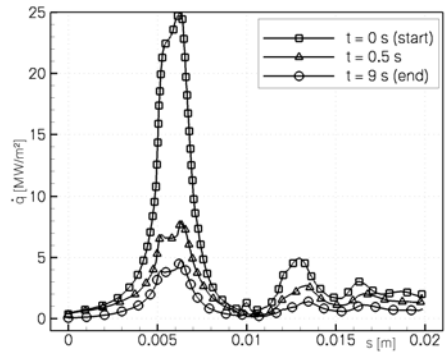
(a) Mach number and heatflux distributions

(b) Separation of the flow, x-y-plane
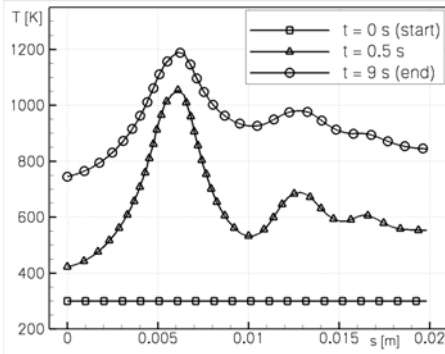
(c) Temperature along s

(d) Heat flux along s

Fig. 8. Numerical results for the VxG-experiment

causes a high heat flux on the structure. In the diagrams of **8(c)** and **Figure 8(d)** the heat flux and temperature distributions are analysed along a cross line (*s*) over the sample for three time steps ($t_{\text{start}} = 0\ s$, $t = 0.5\ s$ and $t_{\text{end}} = 9\ s$). Considering these curves it can be summarized that already after 0.5 second the maximum surface temperature in the impact point is nearly reached and the heat flux decreases clearly.

4   Conclusions

The dipping experiment shows that the response in time of a glued thermocouple amounts to 2.6 seconds in order to reach 90 % of the final temperature. Even a standard mantle thermocouple has a time delay of 0.2 seconds which has to be taken into account for a measurement analysis. The VxG-experiment shows clearly the influence of the glue on the measurement in comparison to a pressed thermo element. The difference between a pressed and glued thermocouple is at the end of the heating process in the order of 2.5 seconds. These results have been confirmed by coupled flow-thermal calculations. Consequently, a glued thermocouple should be avoided for a time accurate temperature measurement.

References

[1] Barth, T.: Advanced Aerothermodynamic Analysis of SHEFEX I. In: 1st European Air and Space Conference (CEAS), Berlin (2007)

[2] Hofmann, H., Martin, H., Kind, M.: Numerische Simulation des Wärmeübergangs vom stationären Prallstrahl an eine Wand. Chemie Ingenieur Technik (74) (2002)

[3] Huhnke, D.: Temperaturmesstechnik. Oldenbourg Industrieverlag München (2006)

[4] Kadem, N., et al.: Numerical Simulation of Heat Transfer in an Axisymmetric Turbulent Jet Impinging on a Flat Plate. AIAA Paper 2006-8115 (2006)

[5] Mack, A., Hannemann, V.: Validation of the unstructured DLR-TAU-Code for Hypersonic Flows. AIAA 2002-3111 (2002)

[6] VDI/VDE 3522: Zeitverhalten von Berührungsthermometern. VDI/VDE-Handbuch Messtechnik I (April 2001)

Shock Tunnel Experiments and CFD Simulation of Lateral Jet Interaction in Hypersonic Flows

M. Havermann[1,*], F. Seiler[1], and P. Hennig[2]

[1] French-German Research Institute of Saint-Louis (ISL)
5 rue du Général Cassagnou, F-68301 Saint-Louis, France
[2] LFK Lenkflugkörpersysteme GmbH
Landshuter Str. 26, D-85716 Unterschleißheim, Germany
seiler@isl.tm.fr

Summary

An experimental and numerical study of lateral jet interference with hypersonic cross flows was performed at ISL. The experiments were conducted with a generic high-velocity missile model in the ISL high-energy shock tunnel STA at Mach numbers of 4.5 and 6. For each Mach number two duplicated atmospheric altitude conditions, three angles of attack and three side jet pressure ratios were studied. The flow was visualized using differential interferometry and the surface pressure was measured with fast response pressure gauges. In parallel, a numerical simulation with a CFD code was done and the calculations were validated by the experiments. The CFD simulation allowed calculating the jet interaction amplification for the different experimental flow parameters.

1 Introduction

Lateral jets can be effectively used for aerodynamic flight control at low stagnation pressures, which means either a low-pressure flow to be found at high altitudes or a low-velocity flow. At higher, super- or hypersonic flight velocities in the lower atmosphere, however, the interaction between lateral jet and the super- or hypersonic cross flow leads to a complex flow pattern, which was already discovered more than 40 years ago [1]. The main aspects of this pattern are shown schematically in Fig. 1 with the separation shock in front of the bow shock and the wake region downstream. In addition to the jet thrust a considerable pressure force acting on the body is generated by jet/cross-flow interference resulting from shock wave/boundary layer interaction and boundary layer separation. To design a flight control system it is important to know the effectively exerted force at the actual flight condition. This force is generally redefined as an interaction amplification factor, which is the ratio of the total normal force, including the jet thrust, divided by the pure jet thrust. Such
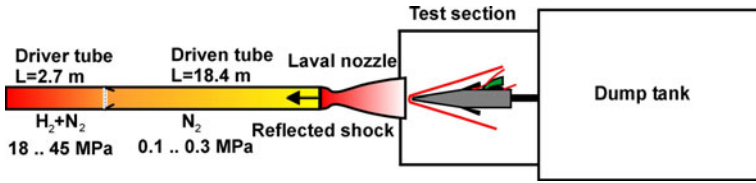

Fig. 1. ISL shock tunnel STA

amplification factors were measured in an experimental wind tunnel study for a generic axisymmetric missile by Brandeis and Gill [2]. In addition to flow visualization they measured forces, moments, and surface pressures in three different wind tunnels for a Mach number range between 2 and 10. However, for Mach numbers above 4.8 the Reynolds numbers of the wind tunnels were too low to produce fully turbulent boundary layer flow. In a more recent study, Havermann and Seiler [3] used a shock tunnel facility to generate both laminar and turbulent boundary layers. They found that depending on the boundary layer state in front of the side jet the separation shock extension changed. An appropriate experimental duplication of real flight conditions is therefore essential.

2   Experimental Tools

2.1   Shock Tunnel STA of ISL

The side jet experiments were carried out in the ISL high energy shock tunnel facility STA, which now allows to reproduce real atmospheric flight conditions at Mach numbers of 3, 4.5, 6, 8 and 10. The facility consists of a conventional shock tube with an inner diameter of 100 mm, which is equipped with a supersonic nozzle and a 10-m³-dump-tank (Fig. 2), forming a so-called shock tunnel. The shock tunnel is operated with hydrogen as driving gas and nitrogen as driven gas in the shock-reflection mode with tailored interface conditions yielding a stationary testing time of about 2 milliseconds for the Mach numbers in this study. The Mach number 4.5 and 6 flows were produced by different parallel-flow Laval nozzles that expanded the flow into the test section. Experiments for two atmospheric flight conditions with altitudes of 15 and 21 km are discussed herein with the correct density, pressure and ambient temperature as they are in these heights, see Table 1 for the flow conditions.

Table 1. Shock tunnel flow conditions used for experiments and CFD simulation

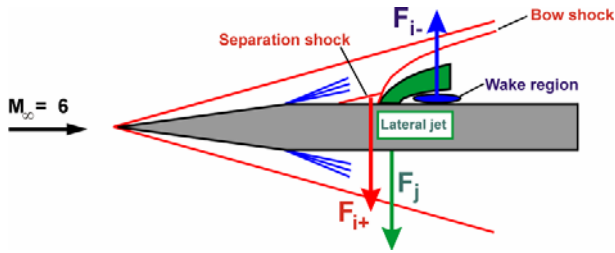| Altitude [km]	M_∞ [−]	u_∞ [m/s]	p_∞ [kPa]	T_∞ [K]	ρ_∞ [kg/m³]	Re_∞ [m⁻¹]
15	4.53	1354	11.8	215	0.185	17.9×10^6
15	5.94	1782	11.9	217	0.185	23.5×10^6
21	4.53	1354	4.9	215	0.077	7.2×10^6
21	5.94	1782	4.8	217	0.075	9.5×10^6

Fig. 2. Flow field created by side-jet interference and force components (F_i: interaction force, F_j: jet thrust)

2.2 Missile Mock-Up

A generic missile model was designed for the shock tunnel experiments (Fig. 3). The model geometry is a cone-cylinder configuration with a cone half-angle of 7.125 deg, a length of 507 mm, and a diameter of 50 mm, corresponding approximately to LFK's hypersonic demonstration missile HFK-L2 scaled down by a factor of 4. The supersonic side jet was generated by expanding pressurized nitrogen gas from an external gas supply through a conical Laval nozzle that was mounted in the model. The nozzle exit diameter was 5 mm and the exit Mach number 2.5. The jet stagnation pressure was varied between 10 and 30 bar to obtain always underexpanded jets with pressure ratios between 70 and 220. The experiments were carried out for three different angles of attack (AOA): 0 deg, +5 deg, and -5 deg.
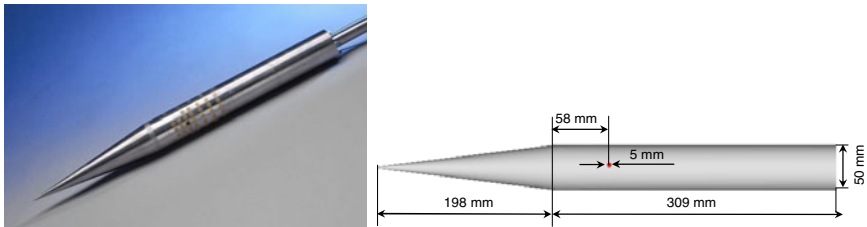
Fig. 3. Generic shock-tunnel HFK-missile model

2.3 Measurement Techniques

Two measurement methods were applied: a) flow visualization and b) pressure measurements. The variation of the density gradient in the compressible flow around the model was visualized by a differential interferometer (DI), which uses polarized light and a Wollaston prism to generate two light beams with a very small spatial beam separation (Fig. 4). The two beams are collected by a second Wollaston prism and analyzed by a second polarizer allowing interference of the two beams, which usually gives interference fringes. In the setup used here, the interferometer was adjusted to an infinite fringe spacing so that the interferograms look similar to schlieren pictures [4]. The images were captured with a single-frame PCO Pixelfly CCD camera at a resolution of 1280 x 1024 pixels. Light illumination was provided by a continuous light source and the camera's shutter

time was 100 µs. The surface pressure on the model around the lateral jet was measured by means of fast-response piezo-resistive pressure transducers (Kulite XCL 80). An array of 24 sensors mounted flush to the wall was grouped around the jet exit (Fig. 5). From calibration measurements the measurement uncertainty is estimated to be ± 10 %.
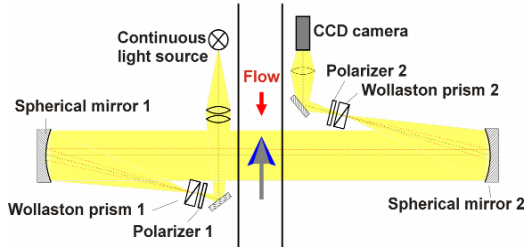

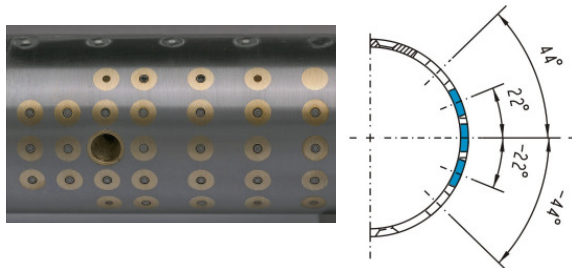**Fig. 4.** The differential interferometer as used at the ISL Shock Tube

Fig. 5. Array of pressure ports and angular positions

3   Experimental Results

Because of the limited number of pressure transducers the experimental data can only give a first indication on the effects of the different parameters on the interaction amplification. The boundary layer influence (related to this is the flight altitude) was already discussed in a previous publication [3]. For the three angles of attack the measured pressure distribution is plotted together with the theoretical pressure for the jet-off case on the centreline axis; the corresponding interferograms are also shown (Fig. 6). The pressure rise in front of the side jet caused by the separation shock (cf. Fig. 1) is clearly visible. It can be estimated that the 0-deg and the +5-deg case have higher relative pressures p(jet_on)/p(jet_ off) both upstream and downstream of the jet compared to the -5-deg case, which indicates higher interaction amplification.

Similar figures with centreline pressure distributions and interferograms are plotted for the two Mach numbers and the different pressure ratios of the lateral jet (Figures 7 and 8). The pressure ratio of the lateral jet seems to have a great influence on the relative pressure distribution. Comparing the Mach numbers, some higher pressures upstream can be recognized for Mach 4.5, whereas downstream of the jet the Mach 6 case has higher pressures. However, for a comprehensive quantification of the effects of the different parameters a CFD simulation is necessary.
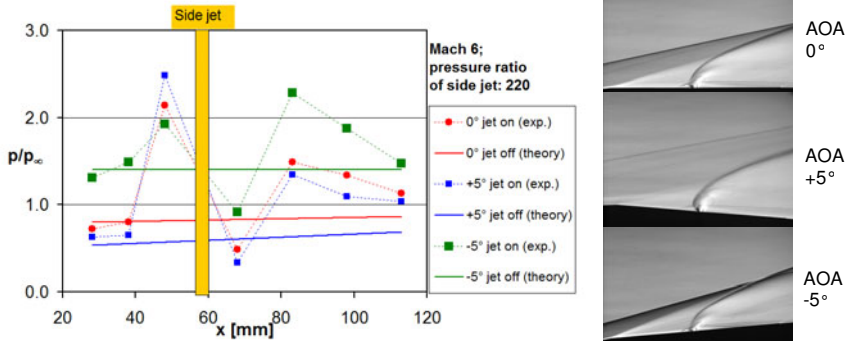
Fig. 6. Wall pressure measurements on centreline axis at Mach 6 for 0/+5/-5-deg AOA and corresponding differential interferograms
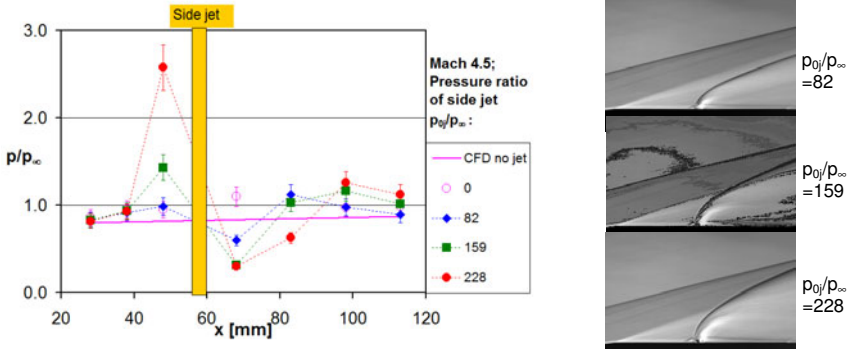

Fig. 7. Wall pressure measurements on centreline axis at Mach 4.5 (AOA: 0 deg) and corresponding differential interferograms
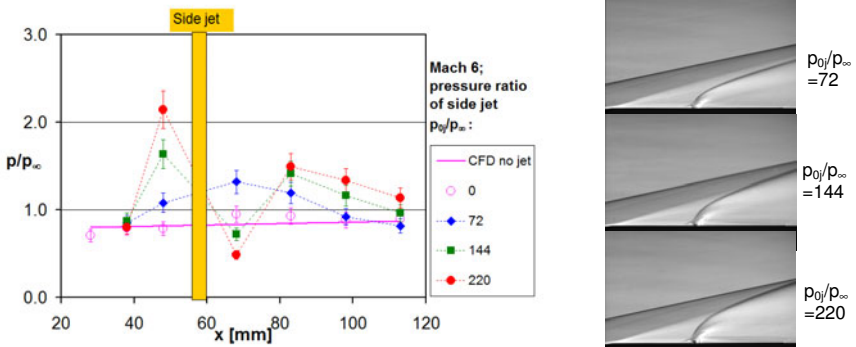

Fig. 8. Wall pressure measurements on centreline axis at Mach 6 (AOA: 0 deg) and corresponding differential interferograms

4   CFD Simulation

4.1   CFD Code

A steady-state, 3D-CFD simulation was done using the code CFD++ by Metacomp Technologies [5]. This code solves the conservation equations in a density-based formulation and is therefore well-suited for highly compressible fluid flows. Both laminar and turbulent flows can be simulated; for the high-temperature effects real gas models are available. In the turbulent flow simulation the realizable k-ε-model was used to close the turbulent RANS equations. The side jet itself was not modelled, instead a one dimensional outflow at Mach 2.5 with defined conditions was assumed, which is justified considering the small jet half-angle of about 10 deg. A half-cylindrical hybrid 3D-grid with 1.57 million cells (Fig. 9) was generated with the MIME grid generator, also from Metacomp Technologies. For the boundary layer simulation a structured grid with 20 layers from the body surface up to a height of 3 mm was created. The first grid layer had a distance of 2.5 µm from the wall so that a correct wall boundary layer simulation with y+<1 was assured. The rest of the grid was modelled with unstructured elements, which were refined in the side jet area down to 0.6 mm of cell size. The calculation was stopped when the normalized residuum fell below 10^{-5}, which occurred at less than 500 iterations. A CPU time of about 7 h was required running two Pentium 4 processors in parallel at 3 GHz.
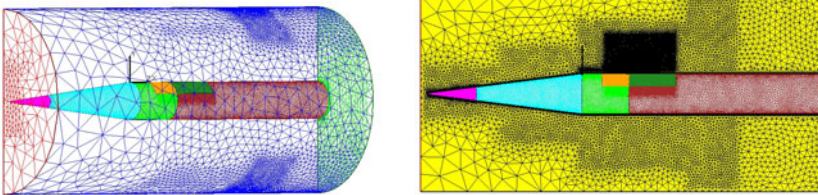

Fig. 9. Half-cylindrical hybrid grid with mesh refinements around the jet area

One example for CFD validation by the experiments is shown for Mach 4.5, AOA=0 deg and a side jet pressure ratio of 228: Figure 10 compares the calculated density gradient to the experimental interferogram and Figure 11 the calculated pressure distribution at the angular positions of the pressure ports (cf. Fig. 5) to the pressure measurements. Considering the measurement uncertainties, simulation and experiments agree reasonably well.
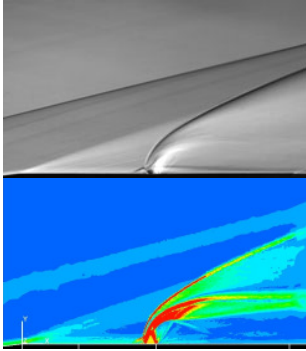
Fig. 10. Comparison of experimental and numerical density gradient (Mach 4.5; AOA=0°; p_{0j}/p_{∞}=228)
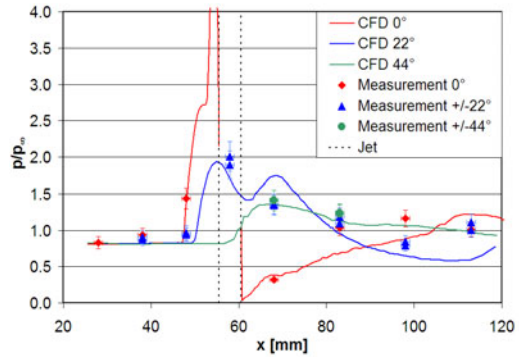
Fig. 11. Comparison of experimental and numerical pressures at angular positions of pressure ports (Mach 4.5; AOA=0°; p_{0j}/p_{∞}=228

4.2 Calculated Interaction Amplification Factors

Each experimental condition was simulated and the interaction amplification factor was determined in the following way: the pressure distribution on the body surface excluding the jet exit area was integrated and the resulting force in the jet axis was calculated. The jet thrust F_J was obtained in the same way considering only the jet area (compared to the 1D theory this gave nearly the same results). For the flow cases with an angle of attack the pressure force due the asymmetrical shock and expansion fan pattern also had to be taken into account (F_I(jet off)). The amplification interaction factor therefore reads:

$$K=\frac{F_j+F_I(\text{jet on})-F_I(\text{jet off})}{F_j} \qquad (1)$$

A factor of K > 1 indicates that the jet thrust is amplified, K =1 that the pure jet thrust is available and 0 < K < 1 means that the jet thrust is reduced by a pressure force in the opposite direction of the jet thrust vector.

The results for all calculated conditions are summarized in Fig. 12. The Mach number of 6 exhibits nearly 50% more interaction amplification than the Mach 4.5 flow, which is mainly due to the higher pressures downstream of the jet. Furthermore it can be seen that compared to the 0-deg AOA, a positive AOA increases and a negative AOA decreases the interaction amplification. A laminar calculation also showed a reduced interaction amplification. The dependence on the jet pressure ratio was found to be small for both Mach numbers.
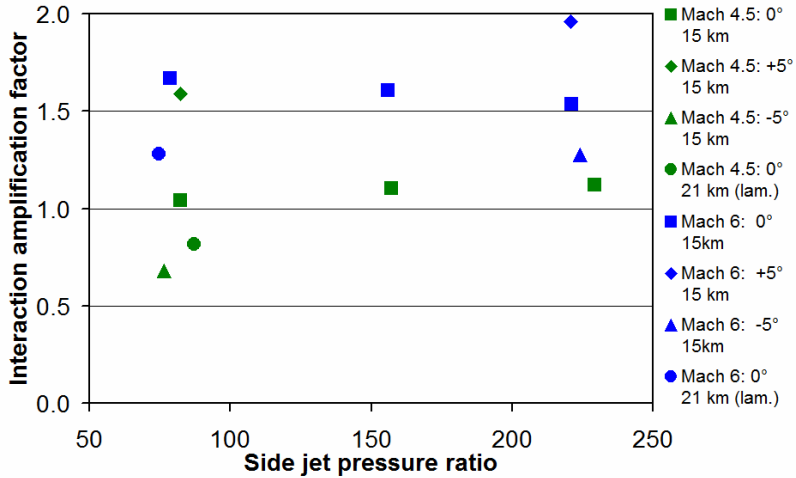
Fig. 12. Interaction amplification factors obtained from CFD simulation for different flow and side jet conditions

5   Conclusions

The interaction of a supersonic side jet with a hypersonic cross-flow was studied experimentally and numerically for a generic high-velocity missile model. The experiments were conducted in the ISL shock-tunnel facility at Mach numbers of 4.5 and 6 for real flight conditions, which means that both turbulent and laminar boundary layers could be correctly simulated. Several other parameters were varied during the experiments: the flight altitude, the angle of attack, and the side jet pressure ratio. The experimental results gave a first indication of the influence of these parameters and they were further used for validating the CFD simulation. The CFD data allowed to quantify the influence of the different flow and side jet parameters on the interaction amplification. The highest influence had the angle of attack and the flight Mach number. The boundary layer state (laminar or turbulent) also showed some effect, whereas the side jet pressure ratio influence was found to be low for the range of studied pressure ratios.

References

[1] Zukoski, E.E., Spaid, F.W.: Secondary Injection of Gases into a Supersonic Flow. AIAA Journal 2(10), 1689–1696 (1964)
[2] Brandeis, J., Gill, J.: Experimental Investigation of Side-Jet Steering for Supersonic and Hypersonic Missiles. Journal of Spacecraft and Rockets 33(3), 346–352 (1996)
[3] Havermann, M., Seiler, F.: Boundary Layer Influence on Supersonic Jet/Cross-Flow Interaction in Hypersonic Flow. In: New Results in Numerical and Experimental Fluid Mechanics V: Contributions to the 14th STAB/DGLR Symposium Bremen, Germany 2004, pp. 281–288. Springer, Heidelberg (2006)
[4] Oertel sen, H., Oertel jun, H.: Optische Strömungsmesstechnik, Braun Verlag (1989)
[5] http://www.metacomptech.com

Heat Transfer at the Nose of a High-Speed Missile

J. Srulijes[1], F. Seiler[1], P. Hennig[2], and P. Gleich[2]

[1] French-German Research Institute of Saint-Louis (ISL)
5 rue du Général Cassagnou, F-68301 Saint-Louis, France
[2] LFK-Lenkflugkörpersysteme GmbH
Landshuterstr. 26, 85716 Unterschleißheim, Germany
srulijes@isl.tm.fr

Summary

The heat loads during high-speed missile flight have to be considered in the design process by selecting appropriate geometries, structures and materials. To model these loads, especially at the nose, it is necessary to know the heat flux data in dependence of the time-dependent flow conditions. Therefore, great interest is focused on heat flux data gained from ISL shock tunnel experiments. These were done for Mach number between 3.5 and 10 for flight altitude conditions ranging from sea level up to 60 km. On the nose surface of a blunt and a sharp cone heat fluxes were measured with special, fast-reacting thin film temperature gauges. The results are compared with theoretical calculations based on the classical boundary layer theory for the laminar as well as for the turbulent boundary layer formation at a conical missile nose. Best agreement exists between the heat fluxes measured and the analytical solutions for a sharp cone.

1 Introduction

The flow around a hypervelocity missile is strongly influenced by the bow wave at the head of the missile. Especially the front part of such a missile experiences extremely high heat fluxes. As a consequence, the temperature of the nose can increase during flight. Parameters influencing the heating are: the flight altitude, i.e. the atmospheric density, the flight speed and the flight time. Additionally, the geometry, material and dimensions of a missile and especially the nose's cone angle and the contour of the nose tip are also significant parameters influencing the heating rate on the front part of the missile. Very high heat loads can destroy the surface. Therefore, the design procedure of all high-speed and hypersonic missiles has to consider, by selecting appropriate geometries structures and materials, the heat loads which missiles have to withstand. Since the heat transfer rate depends on flow conditions and on missile design characteristics, it is essential to measure reliable heat fluxes to correctly predict the heat loads on missile surfaces and structures.

The analytical method of Seiler et al. [2] for calculating the surface heat flux as applied in this paper is shown to be accurate enough to be used as a fast prediction tool in early design phases. In later development phases CFD (Computational Fluid Dynamics) codes have to be used to model geometrical details of the missile and to reach higher precision in local temperature predictions.

To predict the structural load capacity of a high-speed missile and to protect the surface, especially the nose, with suitable materials, comprehensive information on the heating scales present in flight must be provided. A generic design of a missile nose has been selected to carry out experiments and theoretical studies for realistic flow conditions. In this way we are confident to get a better insight into the heating processes and to obtain reliable data also for other less critical parts of the missile.

Surface temperature measurements in flight are very difficult to carry out. For that reason, the ISL's shock tubes were used. In this test facility the conical missile head is fixed in front of a shock tunnel nozzle inside a measuring chamber. The measurements and the corresponding calculations were carried out for Mach numbers 3.5, 4.5, 6, 8 and 10 for flight altitude conditions from sea level up to 60 km. Two geometries were tested, i.e. a sharp cone and a blunt cone. A boundary layer develops at the surface of the cone. For moderate flight altitudes the Reynolds number ranges from zero at the nose tip to more than $R_e \approx 6 \cdot 10^6$ at the end of the cone. Therefore, transition from laminar to turbulent boundary layer occurs in these flight scenarios somewhere downstream the tip of the missile predicted at $Re_{TR} \approx 3 \cdot 10^6$. At very high altitude flights, i.e. at low atmospheric densities, only laminar boundary layer formation may occur along the surface of the cones. For this study fast running calculation procedures were developed to find solutions for the boundary layer formation at the surface of a missile's front part in flight, modelled as sharp tipped conical nose. This is done for both, the laminar and the turbulent case. For this purpose, the boundary layer approximations of Prandtl are applied to obtain solutions in terms of quasi-analytical relations, see Schlichting [1], Seiler et al. [2] and Srulijes et al. [3].

2   Experiments

2.1   Shock Tunnel Facilities

Two high energy shock tubes, having 100 mm inner diameter and a total length of about 22 m, are located in the shock tube laboratory of ISL. Test flows with Mach numbers ranging from 3 up to 10 can be duplicated using nozzles having exit diameters from 200 mm up to 400 mm. The atmospheric conditions can be varied in these shock tunnels in order to simulate the flight conditions at altitudes from sea level up to more than 60 km. Test times up to 3 ms are obtained when the facilities are operated as a shock tunnels in reflected mode. The facilities are driven under tailored interface conditions. The shock tunnel experiments are able to fully duplicate the real atmospheric flight conditions [9].

The scope of this paper does not allow discussing all the measurements and calculations done in the frame of the joint ISL / LFK project. Therefore, and just as an

example, we restrict ourselves to present in detail two flight altitudes for one Mach number only. For these experiments the flow is accelerated inside of a contoured nozzle of 218.7 mm exit diameter, designed for M = 6. The two flight altitudes discussed are: a) 15 km and b) 21 km, respectively. The average measured flow conditions at the nozzle exit are:

a) p = 12.2 kPa, ρ = 0.186 kg/m^3, T = 222 K, u = 1800 m/s,   M = 5.93.
b) p = 4.7 kPa, ρ = 0.074 kg/m^3, T = 215 K, u = 1778 m/s,   M = 5.95.

The free stream unit Reynolds number has been calculated for condition a) $23.5 \cdot 10^6$ m^{-1} and for condition b) $9.6 \cdot 10^6$ m^{-1}. A sharp conical body of 7.125° half angle and length L of 210 mm, measured along the cone's surface, as well as a blunt cone having a nose radius of 4.5 mm were used. The unit Reynolds number at the cone surface has been calculated to be $33.9 \cdot 10^6$ m^{-1} for condition a) and $13.0 \cdot 10^6$ m^{-1} for condition b).

Figure 1 shows the blunt shock tunnel model and a Pitot probe arranged in front of the contoured Mach-6-nozzle used.

Fig. 1. Blunt nose cone model and Pitot probe in front of the Mach-6-nozzle

2.2   Heat Flux Measurement

Special thin film gauges for fast heat transfer measurement, bought from the "Stoßwellenlabor" of the RWTH Aachen in Germany were used to measure the surface heat flux [4]. In Fig. 2 left two sensor photos are shown with the cylindrical gauge body and the thin film covering the front part. The body is made from Zirconium oxide and the thin layer is of Nickel.
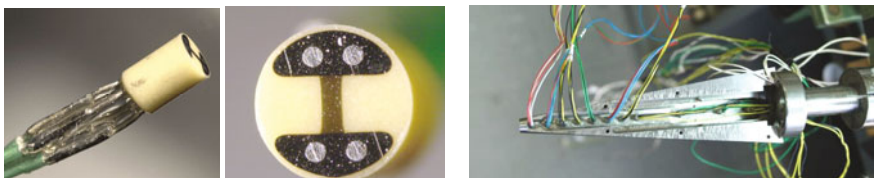

Fig. 2. Thin film gauge (left) and opened missile head model (right)

At eleven measuring stations along the cone's surface the thin film gauges are mounted flush with the outer contour. The implementation procedure is seen in Fig. 2, right hand side. The heat flux transferred from the gas flow to the gauge's thin film heats the gauge body and the thin film layer temperature rises by the same amount. By measuring the film layer temperature increase ΔT as a voltage change using an electrical circuit, the temperature rise of the gauge body is measured. The variation ΔR of the film resistance R_0 is detected and related to the temperature change as follows: $\Delta R = \alpha R_0 \Delta T$ (α = temperature coefficient). Applying a one-dimensional solution of the heat conduction equation, see Oertel [5, 6], the heat flux at the gauge surface at $y = 0$ is calculated as a function of time:

$$\dot{q}(y=0,t) = \sqrt{\frac{\rho c \lambda}{\pi}} \cdot \frac{d}{dt} \int_0^t \frac{\Delta T(0,t)}{\sqrt{t-\tau}} d\tau \tag{1}$$

The variables ρ, c and λ used in this relation are the density, the heat capacity and the heat conduction of the body of the thin film gauge. With the calibration factor $E = \sqrt{\pi \rho c \lambda}/2\alpha$ for each gauge the heat flux $\dot{q}$ is calculated from the recorded temperature change ΔT.

2.3 Experimental Results for M = 6

The heat flux measured along the surface of the cones for 15 km flight altitude is shown in Fig. 3. It can be seen that for $x < 90$ mm, i.e. for $x/L = 0.43$, the measured heat flux matches quite well the laminar boundary layer solution. For $x > 90$ mm transition to turbulent boundary layer starts for both the sharp and the blunt cones, finally reaching for the sharp cone a heat flux about three times the amount of the laminar one and for the blunt one, as expected, a lower value.
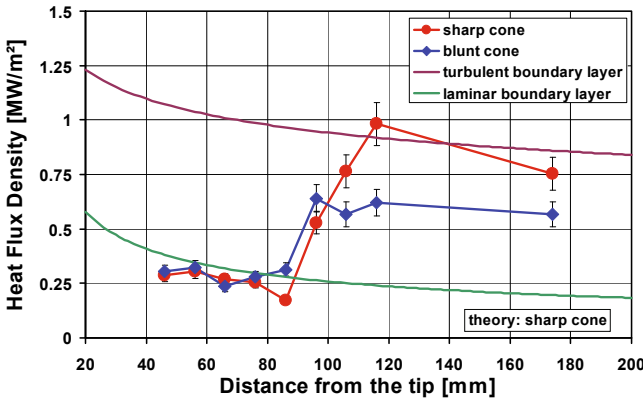

Fig. 3. Heat flux density in 15 km flight altitude for the 7.125° cone at Mach 6

The transition Reynolds number range at the cone's surface is for both cases $3.05 \cdot 10^6 \leq Re_{TR} \leq 3.73 \cdot 10^6$. The agreement of the measured values with the turbulent

boundary layer solution for the sharp cone is quite good within the given error bars of about ±10%. A temperature overshoot at transition near the edge of the boundary layer was not found, probably due to an insufficient resolution of the experiments in length direction, see Schneider [7].

For the 21 km altitude flight condition the experimental and theoretical heat flux results are given in Fig. 4. The calculation is just done for a laminar boundary layer formation. Looking at the measured data points, there are only small deviations between the two. The boundary layer is fully laminar along the projectile surface. No transition occurs.
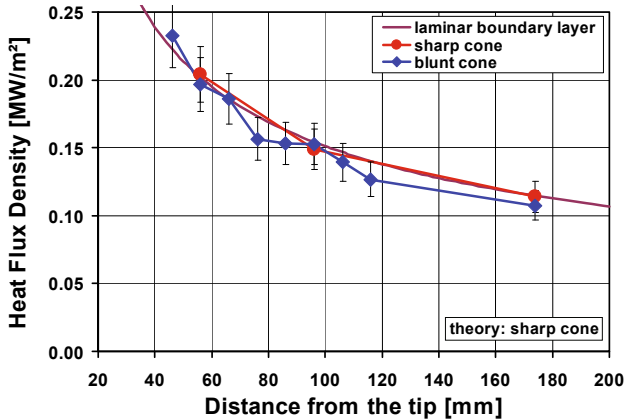
Fig. 4. Heat flux density in 21 km flight altitude for the 7.125° cone at Mach 6

The heat fluxes obtained at the blunt cone contour in case of experiments with models inclined by ±2.5° angle of attack (AoA) are drawn in the Fig. 5 diagram compared to the case with no AoA. The windward (-2.5°) and leeward (+2.5°) heat fluxes are about ±30% compared to the zero AoA ones.
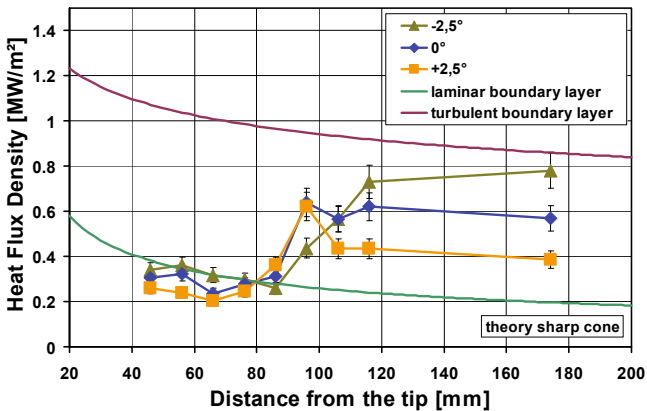

Fig. 5. Heat flux density in 15 km flight altitude at Mach 6 with angle of attack

For the 21 km altitude flight condition the experimental and theoretical heat flux results with AoA are given in Fig. 6.
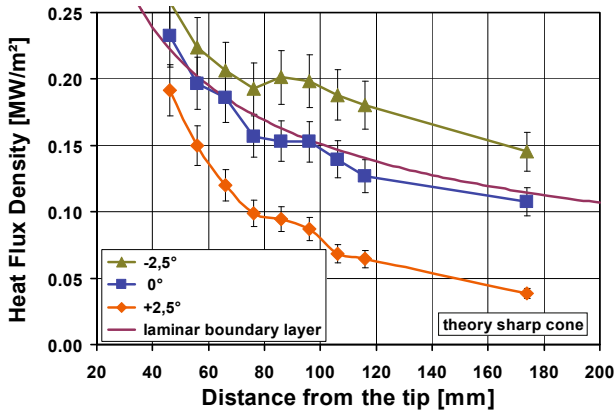

Fig. 6. Heat flux density in 21 km flight altitude at Mach 6 with angle of attack

The calculation is just done for the laminar boundary layer formation for the case without AoA. A comparison with the measured data points only shows small deviations between the two for the zero AoA experiment with regard to the measuring error of ±10%. The agreement is well established showing the applicability of the solution obtained for laminar boundary formation. In this case the boundary layer is fully laminar along the missile's nose surface. No transition occurs along the surface of the cone's nose. In the case of a laminar boundary layer, with ±2.5° AoA, the windward (-2.5°) and leeward (+2.5°) heat fluxes are increased, respectively lowered, compared to the heat flux data theoretically and experimentally determined with no AoA.

2.4   Summary of the Experimental Results for M = 3.5 up to M = 10

Figure 7 shows a summary of heat flux measurements with the generic missile blunt nose for all flight altitudes and Mach numbers studied. The heat flux values shown are measured at a distance of 50 mm from the (sharp) cone's nose. It can be seen that considerably high heat flux values were measured up to a flight altitude of about 15 km ($\dot{q} \geq 0.6\,\mathrm{MW/m^2}$). For higher flight altitudes the measured heat flux values are much lower than 0.6 MW/m². Depending on the flight time duration these heat fluxes may still represent a significant threat to the structure of the flying missile.

As an example of the mentioned threat, Fig. 8 shows the surface temperature as a function of flight duration for the nose of a generic missile flying at Mach 10 in a flight altitude of about 25 km. The conical nose is hollow with a 2 mm CrMoVa-Steel shell. The calculation is done using a stepwise in time quasi-stationary algorithm

without considering radiation thoroughly described in Seiler et al. [8]. Four positions from the cone's tip, i.e. 65 mm, 70 mm, 75 mm and 80mm are plotted. After flight duration of about 35 s the melting temperature is reached and due to the ablation of the surface material the temperature remains constant at about 1800 K.
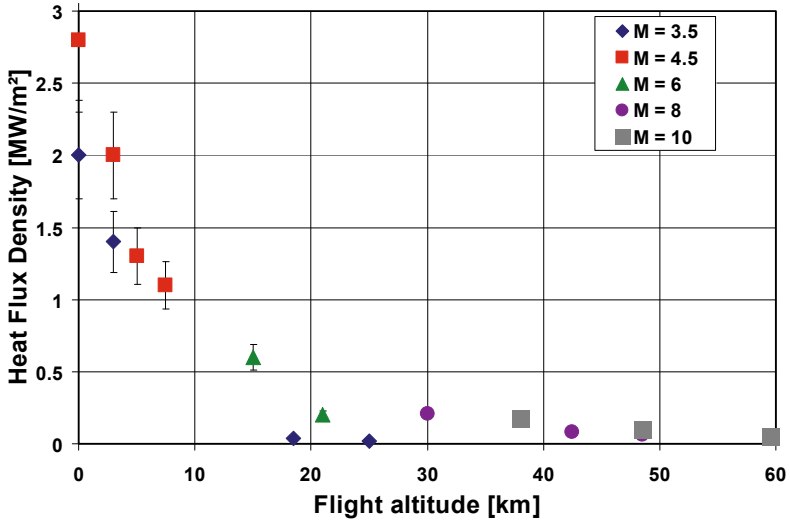

Fig. 7. Heat flux density measurements on a blunt nose for 3.5, 4.5, 6, 8 and 10 Mach numbers and flight altitudes up to 60 km
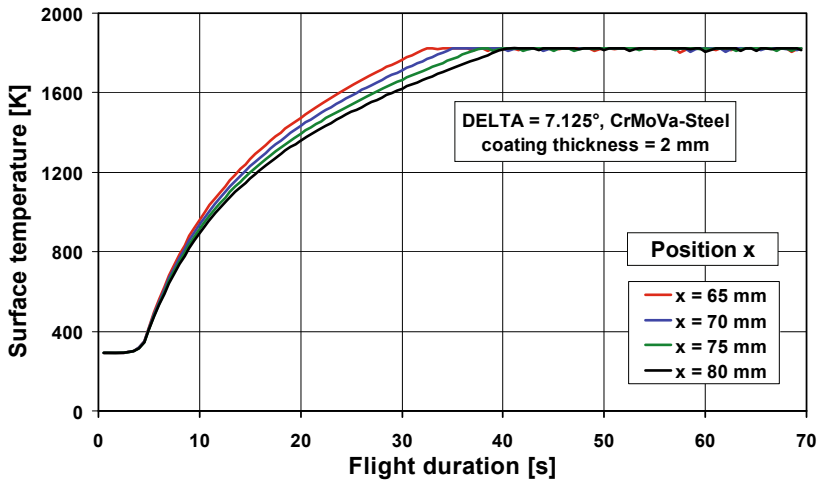

Fig. 8. Cone surface temperature vs. flight duration for a CrMoVa-Steel nose

3   Conclusions

The heat flux at the surface of a 7.125° nose cone of a missile flying in earth atmosphere at Mach numbers ranging from 3.5 up to 10 and at flight altitudes up to 60 km was simulated with the high energy shock tunnels of ISL. For comparison, theoretical data for the surface heat flux on a sharp cone model have been calculated using relations given by solutions for the laminar and turbulent boundary layer formations. The scope of this paper does not allow discussing all the measurements and calculations done. Therefore, as an example, we restrict ourselves to present only two flight altitudes for Mach number 6 with ±2.5° and without AoA. The 15 km altitude flight duplication shows boundary layer transition from laminar to turbulent for a Reynolds number greater than $3.05 \cdot 10^6$ at about a distance of 90 mm from the cone tip. At 21 km altitude the boundary layer develops fully laminar. A summary plot of the ISL / LFK study for the whole range between Mach number 3.5 and 10 from ground level up to 60 km flight altitude is presented as well. The theoretically determined heat fluxes and the experimental results are, within the given error bars, in good agreement.

References

[1]   Schlichting, H.: Boundary-Layer Theory. McGraw-Hill, New York (1960)
[2]   Seiler, F., Werner, U., Patz, G.: Theoretical and experimental modelling of real Projectile Flight Heating. J. of Sp. and Rockets 38(4), 497–503 (2001)
[3]   Srulijes, J., Seiler, F.: Analytically obtained data compared with shock tunnel heat flux measurements at a conical body at M = 6". ISL-report PU 662/2004 (2004)
[4]   Olivier, H. (2009),
      `http://www.swl.rwth-aachen.de/en/industry-solutions/thin-films/`
[5]   Oertel, H.: Stoßrohre. Springer, Wien-New York (1966)
[6]   Oertel, H.: Wärmeübergangsmessungen. In: Kurzzeitphysik. Springer, Wien-New York (1967)
[7]   Schneider, S.P.: Hypersonic Laminar-Turbulent Transition on Circular Cones and Scramjet Forebodies. Aerospace Sciences 40(1-2), 1–50 (2004)
[8]   Seiler, F., Peter, H., Zettler, G., Mathieu, G.: Heat transfer behaviour in gun tubes. In: 22nd International Symposium Innenballistik der Rohrwaffen, BAKWVT Mannheim, Mannheim, ISL-report PU 631/2001 (2001)
[9]   Seiler, F., Gnemmi, P., Ende, H., Havermann, M., Schwenzer, M.: Study on lateral jet/cross flow interaction in the high energy ISL shock tunnel. In: 23rd Int. Symp. On Shock Waves, Forth-Worth, Texas, USA, ISL-Report PU 628/2001, July 22-27 (2001)

Analysis of Jet Thruster Control Effectiveness and the Interaction with Aerodynamic Surfaces for a Slender Cylindrical Missile

K. Weinand[1], K.-J. Dahlem[1], R. Höld[1], D. Stern[1],
B. Sauerwein[2], and F. Seiler[2]

[1] MBDA LFK-Lenkflugkörpersysteme GmbH,
Landshuter Str.26, D – 85716 Unterschleißheim, Germany
[2] Deutsch-Französisches Forschungsinstitut Saint-Louis
5, Rue due General Cassagnou, F-68301 Saint-Louis, France

Summary

An experimental and computational study of a supersonic missile with a slender cylindrical airframe and a divert jet thruster system for attitude control was a cooperation of the French-German Research Institute of Saint-Louis and MBDA LFK. The aerodynamic of a defined missile model with lateral jet was calculated with Computational Fluid Dynamics (CFD) methods and the same configuration was measured in a shock tube for validation of the numerical procedure. The verified CFD flow field solutions allow an extensive analysis of the jet thruster control effectiveness, the complex fluid interactions of freestream and thruster crossflow and their physical effects on the airframe. It is possible to analyze the change of the pressure contours on the complete airframe or dedicated aerodynamic surfaces of the missile and therefore the deviations of the missile aerodynamic caused by the lateral jet.

1 Introduction

Modern air defense missiles (see example in figure 1) designed to intercept very fast and/or maneuvering targets have to provide a high amount of surpassing agility and speed. Especially if the system requirements demand an effective hit to kill ability, as necessary for the defense against ballistic missiles reentry vehicles. Therefore the effect on the intruder's warhead is primarily realized by the kinetic energy of the high speed approach of the interceptor and the target. To ensure the safety of the defended area it is mandatory to maintain a specified keep out altitude, but with increasing altitude air defense interceptors suffer from decreasing effectiveness of standard aerodynamic control surfaces. The dynamic pressure at the fins is, in spite of the high missile velocity, insufficient to change the missile attitude with the necessary speed and agility. It is possible to advance the control command response times

considerably by additional use of lateral jet thrusters for attitude control (figure 1). The divert thrusters induce additional aerodynamic moments for a fast change of the missile attitude also at high intercept altitudes. The attitude control system provides a high amount of additional agility over the complete mission envelope.
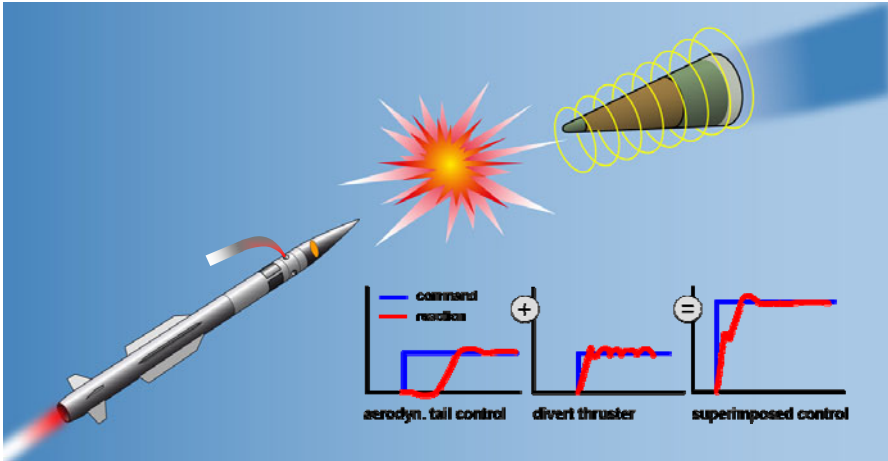

Fig. 1. Hit-to-Kill missile, attitude control lateral reaction force interaction characteristics.

For that reason defense systems with an effective lateral thrust technology are characterized by improved hit performance. The divert thruster delivers not only lateral thrust, the jet also alters the complete missile flow field and the pressure contours of the airframe. The strong and complex flow interactions of the missile freestream and the crossflow depend on the fluid parameters Mach number, altitude, attitude, missile airframe design and the magnitude of the jet and it is not practicable to specify these fluid interactions with a simple mathematical model.

2   Geometry

Most air defense interceptors are similarly designed: Ogival supersonic nose, high aspect ratio fuselage, cruciform fins and high chord wings. All examined operational missile systems use solid propellant rocked motors, so air intakes and the aerodynamic interactions with the air intake flow are not regarded for the analysis of fluid dynamic effects on aerodynamic surfaces of a generic air defense missile configuration. The attitude control system thruster is located right behind the nose (to ensure the best turning moment) and upstream, in front of the wings. Looking forward from behind the missile, for this study the radial orientation of the thruster nozzle centerline and outflow direction lies aligned with the vertical body fixed axis (z-axis). The wing and fin panel roll angle Φ is 45° (x-roll attitude) to the jet flow symmetry

surface. Due to the upstream position of the jet right in front of the wings it was expected that the altered missile flowfield changes not only the pressure contours on the fuselage close to the thruster nozzle, but also the effectiveness of the wings and to some amount also of the far downstream installed fins or stabilizers. To prove or discord these assumptions a complete missile design with all aerodynamic relevant surfaces had to be considered.
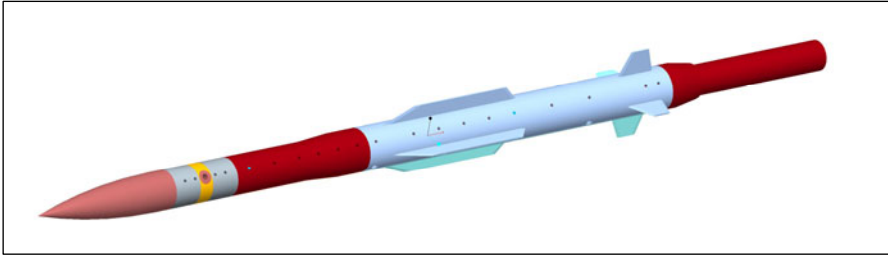

Fig. 2. CAD drawing of the lateral thrust missile

Figure 2 shows the selected missile geometry in conformation to the described air defense missile design characteristics. For the shock tube tests the missile model had to be scaled 1:10. The computer-aided-design (CAD) drawing in figure 2 illustrates also the sub components of the shock tube missile model design: The missile frontend with the nozzle for the jet, the wing section and the control fins without deflection angle. The drawings show also the positions of the piezo-resistive miniature pressure transducers to measure the missile surface pressures. Twenty sensors are aligned with the nozzle at irregular distances. As apparent in the model pictures the pressure measurement positions are closer together in the vicinity of the nozzle and wings. This array of sensors was selected to capture the crossflow effects for the complete air defense missile configuration. Extensive measurements close by and around the outflow nozzle were subject of a preceding study [1].

The scaled model is well suited for the ISL's shock tube measurement chamber but the miniaturization made the integration of the gas supply pipe, nozzle and additional twenty sensors complex. Figure 3 illustrates the solution for the gas jet of the shock tube reference model. The position of the gas supply pipes ensures enough installation space for the sensors and cabling. The gas flows into a stagnation chamber before it is accelerated by

Fig. 3. Jet nozzle drawing

a conical divergent supersonic nozzle to the crossflow jet. The outflow nozzle component of the model is a cylindrical exchangeable part of the missile model and it is possible to mount it in different radial positions. That makes the model more flexible, because it is possible to vary the outblow direction relative to the aerodynamic surfaces. Another advantage is that the nozzle part is easily
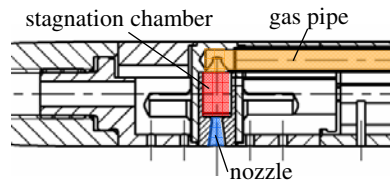
exchangeable to realize different jet Mach numbers with additional supersonic nozzles (for this study a Mach 2.5 nozzle was used). The boundary conditions for the lateral thrust nozzle of the shock tube model are summarized in table 1.

Parallel to the shock tube model a CFD volume mesh for the same missile configuration was generated. The used volume mesh is a hybrid unstructured grid. The boundary layer at the missile surfaces is discretized with multiple structured layers of prisms. To advance the accuracy of the flow simulation the very dense boundary layer mesh has a moderate grid growth rate normal to the wall and fulfills the 'non-dimensional wall distance' y+ criterion without the use of wall functions. Unstructured tetrahedrons are used to build the freestream volume mesh close to the

Table 1. Boundary conditions for the lateral thrust nozzle

MISSILE MODEL GEOMETRY	
ref. caliber	~ 25 mm
jet position / missile length	0.0236
nose geometry	ogive
FREE STREAM CONDITIONS	
Mach number	4.5
incidence angle	0°, ±5°
roll angle	0° (x-attitude)
Rollrate	none
Altitude	15 km
NOZZLE EXIT GEOMETRY	
quantity of simulated nozzles	1
exit slice plane	circle (on cylinder)
centerline (outflow direction)	rectangular to the missile fuselage surface
NOZZLE EXIT FLOW CONDITIONS	
Mach number	2.5
velocity profile	homogenous
pressure ratio	~ 150
total temperature	~ ambient temperature
chemical composition	nitrogen (N2)

missile. This grid of tetrahedron elements is much more compact in the vicinity of the thruster nozzle outflow and in the area of the jet. The number of grid points is also increased where structural features of the missile change, like at the wing-fuselage intersection line. This selective mesh refinement ensures the solution independency of the grid with application oriented use of computing resources. Computing power is focused on flow areas with high gradients of the solution vector. The mesh gets rapidly coarser in direction to the far field boundaries of the computation volume. With this meshing strategy it was possible to realize close to twenty million 3D cells (up to 14 million tetrahedrons and 6 million prisms).

3   Test Campaign

All measurement runs for this study were realized at the ISL shock tube wind tunnel STB (see photo in figure 4). STB is a high energy shock tube and it enables to simulate flow conditions similar to the free flight environment for a real missile. The measurement range of the ISL shock tubes goes up to Mach number 10 and altitudes of 60 kilometers complying with the realistic static pressure
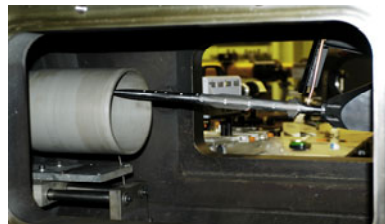

Fig. 4. STB test chamber interaction

according to the standard atmosphere model. That is only feasible with these kinds of wind tunnels and therefore shock tubes are a well suited test facility for aerodynamic data validation of supersonic missiles at high altitudes. To perform supersonic flight velocities a special Mach number adapted expansion nozzle is necessary to ensure a parallel free stream flow within the wind tunnel measurement volume.

4   Numerical Solution

For the step to validate the numerical method and the procedures to compute the aerodynamic coefficients the same configuration, under the same boundary conditions (table 1) as for the experiment, was calculated with CFD. Special comparison runs with the DLR TAU-solver were computed for the previously defined missile configuration. Figure 5 shows in the top picture Mach number contours in the vertical symmetry plane for angle of attack of 0° and Mach 4.5 for the complete missile. The contour picture shows already how asymmetric the flowfield becomes because of the interaction with the jet flow. The bottom left picture shows the crossflow area. This numerical contour solution is the exact complement to the corresponding shock tube test. The match of the schlieren photo and the numerical contour plot shows a good conformity of all flow interaction characteristics. From left to right, the boundary layer, increase of boundary layer thickness in the front of the nozzle, recirculation area, separation shock and bow shock in front of the crossflow are all well captured. Further to the right the shocks in the jet, the jet flow mixing and the recompression shocks in the low pressure wake of the jet are also very well reproduced by the numerical solution. Of course a sole visible check of the solutions is not usable to prove the method.
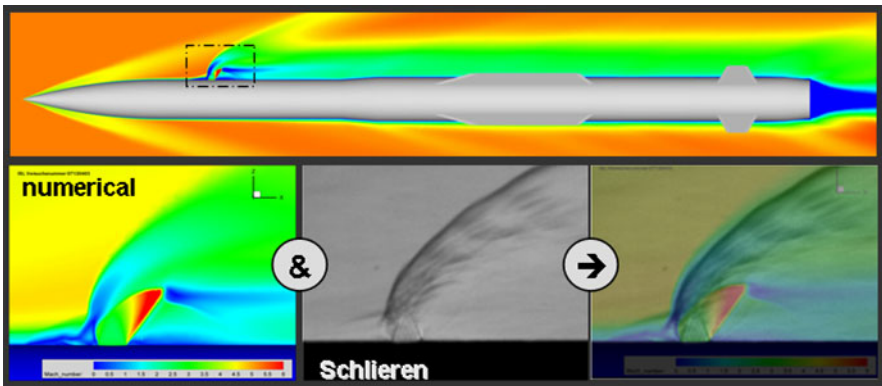

Fig. 5. Comparison of experimental and numerical solution

In a next step the fuselage surface pressure values of the CFD solutions were, for the same 20 transducer installation points, extracted. Figure 6 shows the comparison of experimental and numerical data (pressure is referenced to farfield pressure) for

angle of attack 0° and Mach 4.54. The topview of the missile shows the CFD calculated surface pressure contours. The blue line represents the CFD data slice collinear with the jet nozzle and the transducer measuring points (orange dots). In the comparison plot the numerical data (blue) is plotted with 4% error bars and the experimental data (orange) is plotted with 10% error bars. In the upper right corner of figure 10 an enlargement shows the solution data in front of the jet. For the 0° angle of attack comparison the experimental and numerical data matches very well, including the high pressure area in front of the jet. The comparison data and the missile topview picture show that due to the lateral thruster crossflow the missile surface pressure contours are significantly altered. The resulting surface forces and therefore aerodynamic coefficients are validly reproduced by the numeric method.
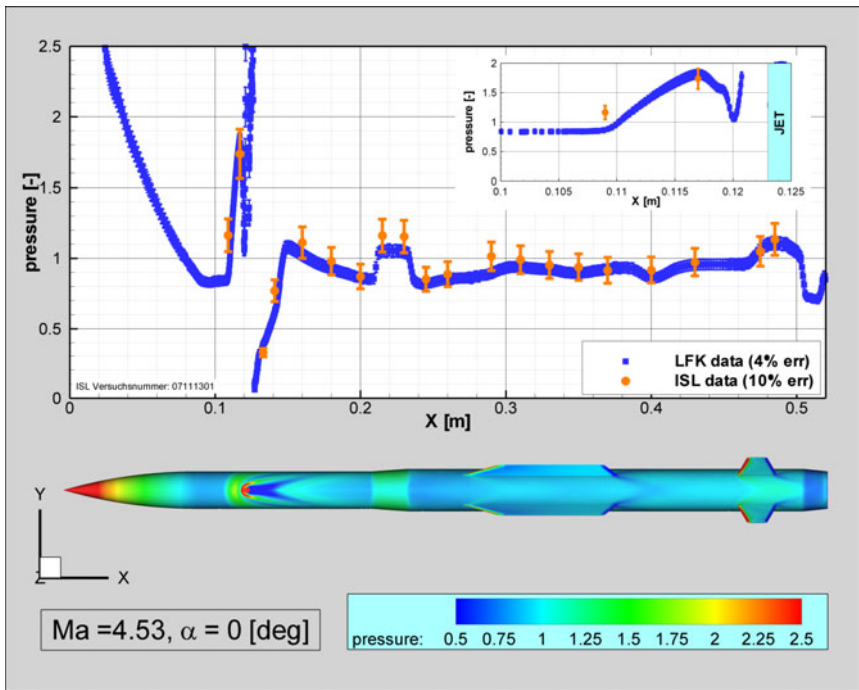

Fig. 6. Validation - Pressure Comparison [α= 0°]

5   Analysis

It was now, with the validated numerical method and procedure, possible to calculate a complete aerodynamic data field for a slender cylindrical missile with jet thruster attitude control. The missile aerodynamic was computed and analyzed under consideration of the flow interactions with the aerodynamic surfaces (here fuselage and wings) of the missile. The complete aerodynamic data field was generated with

realistic hot gas crossflow of a thruster (with layout design massflow) and without the thruster. The ranges of the aerodynamic data field are summarized in table 2.

Table 2. Aerodynamic data field ranges

velocity range (Mach) [-]	[1.2, 5.0]
incidence angle range [°]	[-20, +20]
altitude range [km]	[0, 30]

It was assumed that the interaction of the jet crossflow with the fins has a minor effect on the missile aerodynamic compared with the effects on fuselage and wings. For an example case at Mach 2 and 15 km altitude the missile CFD surface was partitioned to compare the lift forces of the wings (upper and lower) with the lift forces of the fins (upper and lower) if the jet is switched on or off. In this case, only the upper wings show a mentionable difference between lift for jet on and off. For negative angles of attack the change of lift on the upper wings is even more obvious. Between -10° and 0° angle of attack the lift of the upper wings is more or less neutralized by the jet interaction. So this test case is evidence for the effect of jet flow interaction on aerodynamic forces and also for the assumption that the effect is negligible on the fins of the defined slender missile geometry (depending on the distance between thruster and fins).
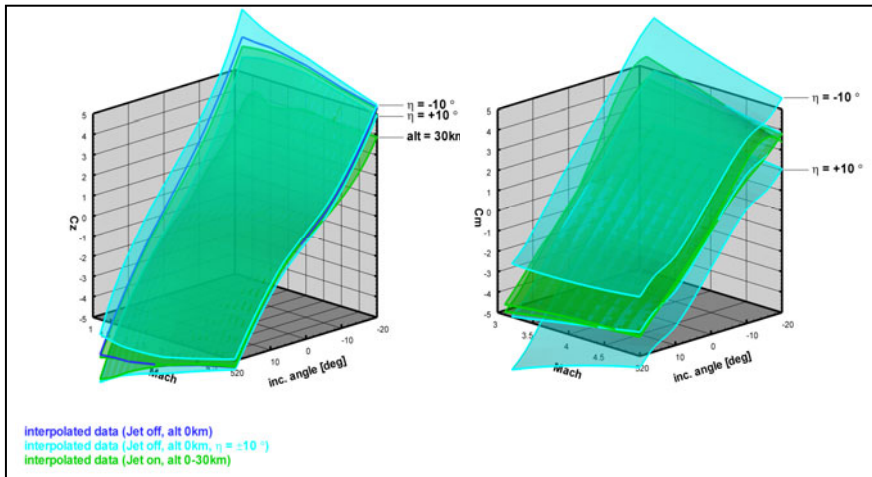

Fig. 7. Normal force coefficient [left] and Pitch moment coefficient [right] at different altitudes (jet on) compared to pitch elevator deflections (jet off)

With generating a complete missile aerodynamic with lateral thrust effects we were able to analyze that the crossflow of lateral thruster alters the aerodynamic coefficients of a missile aerodynamic and that this effect is increasing with the

altitude of the missile (see green carpets in figure 7). The question is how to evaluate the changes of the missile aerodynamic. Figure 7 (left side) shows that the deviations of the normal force coefficient are in order of a ±10° fin deflection (blue carpets in figure 7), for negative incidence angles in the transonic range even more. Quantitative the deviations are not negligible. This has to be considered for missile designs with direct lateral thrust control. But for the presented missile design with attitude control system we have to consider other conditions as well:

1) The thruster is used for attitude control => deviations of the moment coefficients and therefore the distributions of changed pressure areas (w.r.t. the moment reference point) are dominant.
2) The major flight Mach number range of air defense missiles with attitude control systems is supersonic. Effects in the transonic range are not crucial.
3) Depending on the short jet runtime (short pulses instead of continuous flow); deviations of the normal force may have no considerably effect on the missile performance (like the lateral acceleration ability) but they are certainly additional impulses to be handled by the autopilot.

We see in figure 7 (right side) that the effect on the pitching moment of the presented missile design is quite small and negligible in the supersonic Mach range. For the normal force coefficient (figure 7, left side) the effect was in order of a ±10° fin deflection but not for the pitching moment coefficient. There is only one considerable difference between sea level and 30km altitude around incidence angel of -10° and as before the effect is increasing with decreasing speed.

Summarizing, the effect of jet thrusters on aerodynamic surfaces is generally significant and has always to be considered and understood in aerodynamic modeling. For the analyzed missile configuration the deviation effect is small for the effectiveness of the attitude control systems.

References

[1] Seiler, F., Sauerwein, B., Schacherer, M.: Untersuchungen zur Seitenstrahlsteuerung einer aktuellen Flugkörperkonfiguration im Stoßrohr-Windkanal bei realen Konditionen, ISL-Bericht CR/RV 432/2007 (2007)
[2] Seiler, F., Sauerwein, B., Bastide, M., Schacherer, M., Weinand, K., Hennig, P.: Untersuchungen zur Seitenstrahlsteuerung einer aktuellen generischen Flugkörperkonfigurationen im Stoßrohr-Windkanal bei realen Flugkonditionen, Schlussbericht, E/T43 X/7 A031/7 F 860 [21], VE-Nr. 07021 (2007)

New Explanation of Noise Production by Supersonic Jets with Gas Dredging

H. Oertel Sen[1], F. Seiler[2], and J. Srulijes[2]

[1] Retired from the French-German Research Institute of Saint-Louis (ISL)
[2] French-German Research Institute of Saint-Louis (ISL)
5 rue du Général Cassagnou, F-68301 Saint-Louis, France

Summary

Supersonic jets emit Mach waves producing noise in their environment. Various experimental techniques have been used in the past for investigating the behaviour of structures present in the supersonic jet boundary layer. These structures are accompanied by long, almost straight and nearly parallel Mach waves. These Mach waves appear both outside and inside the jet. It was experimentally found that these Mach waves move at three preferred speeds: w, w' and w''. They depend simply and exclusively on the jet Mach number M_i and the speed of sound ratio between inside (a_i) and outside (a_a) of the jet. Quite simple empiric formulae for w, w' and w'' have been established by Oertel sen. but no satisfying explanation could be found at that time. Recently, however Oertel sen. proposed a new idea based on the growth of long living pairs of vortices formed inside of the jet boundary layer. Vortices move with the velocities w' and w'' respectively, whereas the centre of the pair moves with w. The w'- and w''-vortices move supersonically with respect to a_a, therefore produce the so-called w'-Mach waves outside of the jet. The w'' - vortices move with $u_i - w'' > a_i$, therefore produce the so-called w''-Mach waves inside of the jet. This theory suggests a new method of jet noise reduction.

Nomenclature

flow velocity
u^* speed in jet boundary layer
u_i inside the jet

progagation velocity
w center of vortex pair
w' front vortex
w'' rear vortex

speed of sound
a general
a_i, a_a jet inside, gas outside

Mach numbers
$M_i = u_i / a_i$ inside the jet
w / a_a of the w-Mach wave outside
w' / a_a of the w'-Mach wave outside
$(u_i - w)/a_i$ of the w-Mach wave inside
$(u_i - w'')/a_i$ of the w''-Mach wave inside

Mach angles
α w - Mach wave inside and outside
α' w'- Mach wave outside
α'' w''- Mach wave inside

1   Introduction

A supersonic jet is known to be the source of tremendous noise which can become intolerable in the neighbourhood of jet engines, cutting torches and other supersonic jet producing devices. Most of the noise is emitted in form of Mach waves. Many Mach waves are long, almost straight and nearly parallel. They appear inside and outside of the jet and are quite regular. It is clear that a certain order must exist inside of the jet boundary layer, the mixing layer, separating the moving jet inner part from the outside gas at rest. The practically ideally expanded supersonic free jets in Fig. 1 at $M_i = 2$ shows the outside and inside produced Mach waves visualized by Oertel [1] using a differential interferometer.
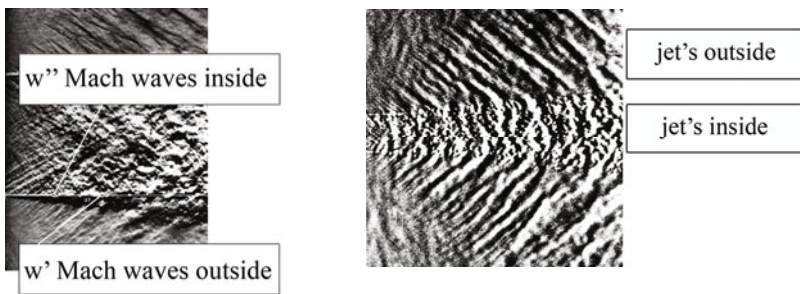

Fig. 1. Mach waves inside and outside of a supersonic correctly-expanded free jet

In the past, the origin of the noise produced by Mach waves was attributed to a multitude of different phenomena. They have been assumed to originate from turbulence [2] as well as from coherent structures of different nature [3, 4, 5]. Experimental investigations using shadow visualization technique [6] did not answer the question definitely and none of the above assumptions corresponds to reality. This is why various investigations were conducted at ISL. The kinetics of the Mach waves was investigated extensively by Oertel [7-11] using high speed movies, double exposure streak records and immobilizations on a film moving at the searched wave speed. Recent descriptions on supersonic jet noise produced by fine- and large-scale turbulent structures are given by Tam [12] and Bailly et al. [13], which are in fact quite different built compared to the explanations herein. For example D. Papamoschou and A. Bunyajitradulya [14], D. Papamoschou and M. Debiasi [15] as well as A. Bassetti [16] investigate the jet noise production too, but on a basis which not compares to the mechanisms described in this.

The experiments of Oertel [7-11] were performed with the ISL high energy shock tubes as extensively described by Oertel in some of the referenced reports. The reflected shock method as well as the non-reflected shock method had been used for producing pressure adapted jets, most of them having Mach numbers M_i about 2. The experimental results can be represented by simple formulae empirically predicted by means of the experimental outcomes. Two strong different Mach waves (w and w′) exist outside the jet as well as two different inside (w and w″). They were found to

be produced by "jet boundary layer structures" propagating downstream at the three mentioned speeds. The 327 experimental points in Fig. 2 were fitted given the following Mach number equations:

$$\frac{u_i - w}{a_i} = \frac{w}{a_a} \ (1), \qquad \frac{u_i - w'}{a_i} = \frac{w'}{a_a} - 1 \ (2), \qquad \frac{u_i - w''}{a_i} = \frac{w''}{a_a} + 1 \ . \ (3)$$

The w'-Mach waves outside of the jet are the most easily recognizable and were those which have also been visualized by [6]. They appear at $w' \geq a_a$, that means at supersonic speed of the coherent structures compared to the speed of sound a_a outside of the jet. The w''-Mach waves appear at $u_i - w'' > a_i$ because for this the velocity difference $u_i - w''$ must exceed the sound speed a_i inside. The w-Mach waves exist in the range of $w \geq a_a$ (outside) or $(u_i - w)/a_i \geq 1$ (inside). They are much shorter than the other two because their angle is much larger The w

Fig. 2. Mach numbers

- w' - w''-Mach waves only depend on the jet speed u_i and the speed of sound inside, a_i, and outside, a_a, and do not depend on the gas viscosities. An explanation for the w -Mach waves near the jet exit had easily been found. It supposes that the thin jet boundary layer is seen as a shear layer with some inner deformations moving with the w-velocity but w -waves may also be seen downstream. Their contribution to the jet noise is small.
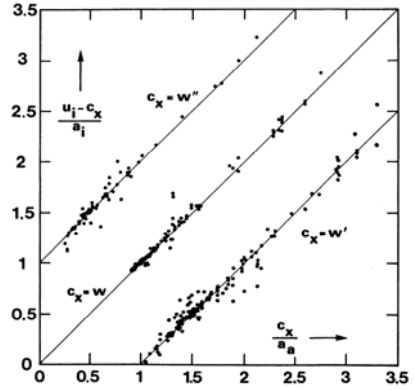
2 w - Mach Waves

In the experiments of Oertel [e. g. 10] a very thin jet boundary layer developed for a short distance after the jet's exit. In this case the jet boundary layer could be considered as a shear layer in which deformations are present as shown in Figure 3. Long-living deformations will subsist in case the gas pressures are equal at both sides. The point-symmetric deformation of the shear surface subsists at the condition of pressures at both sides of the surface being point-symmetric too. They are point-symmetric at equal relative Mach numbers in the frame moving with the speed w of the point of symmetry. For the speed w of the deformed shear layer this is the case if:

$$\frac{w}{a_a} = \frac{u_i - w}{a_i} \ . \ (4)$$

Using $M_i = u_i/a_i$ it follows:

$$\frac{w}{a_a} = \frac{M_i}{1+a_a/a_i} \quad . \text{(5)}$$

The w-wave Mach numbers w/a_a outside and $(u_i-w)/a_i$ inside are required to be ≥ 1 for a Mach wave formation. The Mach angle can be calculated by: $\sin\alpha = a_a/w$ (6).
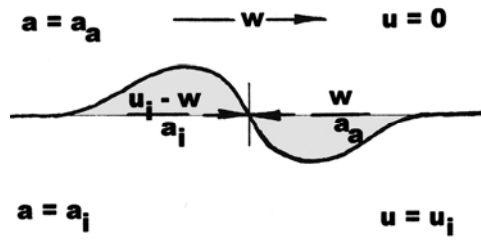
Fig. 3. Deformation of the shear layer

3   New Approach to the Jet Boundary Layer Structures

3.1   General Considerations

With growing distance from the jet exit the jet boundary layer thickens more and more. The jet boundary layer deformations develop into coherent structures which form pairs of vortices moving downstream, one behind the other, see Fig. 4.
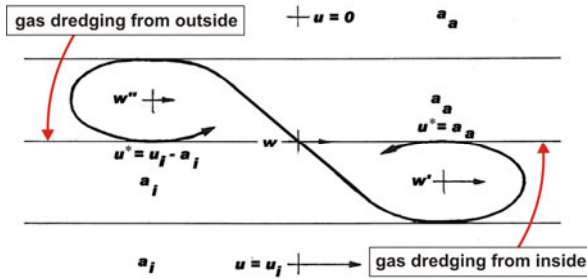
Fig. 4. Pair of vortices

Its centre is still moving with the w-speed, but the axes of the vortices move with $w' > w$ (front vortex) and $w'' < w$ (rear vortex). The front vortex produces a Mach wave outside and the rear one inside the jet, comparable to the bow wave around a supersonically flying projectile. The w' and w'' vortices grow downstream. Their lengths are proportional to the velocity differences $w'-w$ and $w-w''$, their lateral extend proportional to the following conditions for coexistence:

- The front and rear vortices must remain in different separated zones,
- It this does not occur, the front vortices destroy the rear vortices of the foregoing pairs,
- Both zones touch each other in a plane moving with velocity w .

Additional requirements are:

- The rear vortices move with $w'' \geq 0$ for producing at $u_i - w'' > a_i$ Mach waves inside the jet,
- The front vortices velocities are $w' \geq a_a$ for producing Mach waves outside of the jet,
- Equal local under pressures at both sides of a vortex exist at the condition of equal subsonic relative Mach numbers in the frame moving with the speed of the centre of the vortex. In this frame the vortex is a virtual stationary one. Its outer streamline as a convex one forces the passing flows to temporarily contraction,
- The front vortices "dredge gas" from the jets inside with a_i and the rear vortices "dredge gas" from outside with a_a towards the jet boundary layer, i. e., the plane where the two vortices touch each other, see Fig. 4,
- The condition of touching at velocity $u = w$ is quite important. Only with this assumption the theory validates the empirical results.

This new approach provides a totally different profile of the sound speed present inside the jet boundary layer as compared to the former theories for turbulent jet boundary layer formation.

3.2 The w'-Mach Waves

The w'-Mach waves outside are created by the front waves which move with the w'-velocity (blue coloured zone). Lets begin by considering the special case $u_i = a_i + a_a$ with $a_a = a_i$ as shown in Fig. 5. For producing Mach waves in the region outside of the jet, the flow velocity in this zone must be in the range given by $u_i > u > a_a$.

By the above mentioned "gas dredging", gas from outside is transported into the jet boundary layer and therefore the speed of sound a_a can be used for calculating the relative Mach number at the upper layer of the blue w'-zone: $(w' - a_a)/a_a$. Using the relative Mach number at the lower layer of this zone in Fig. 5, $(u_i - w')/a_i$, the

Fig. 5. Front vortex: case w

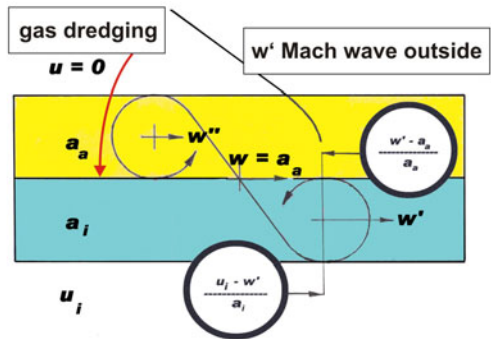following equations (7 and 8) can be established. The Mach angle is: $\sin \alpha' = a_a / w'$.

$$\frac{u_i - w'}{a_i} = \frac{w' - a_a}{a_a} \quad (7) \quad \text{or} \quad \frac{w'}{a_a} = \frac{M_i + 1}{1 + a_a / a_i} . \, (8)$$

In the general case $w'/a = 1 + a_a / a_i$ the requirement of equal relative Mach numbers writes

$$\frac{u_i - w'}{a_i} = \frac{w' - w}{a_a} . \, (9)$$

With w calculated by equation 5 the following equations come:

$$\frac{w'}{a_a} = \frac{M_i + w / a_a}{1 + a_a / a_i} \quad (10) \quad \text{or} \quad \frac{w'}{a_a} = M_i \frac{2 + a_a / a_i}{(1 + a_a / a_i)^2} . \, (11)$$

In the special case $w / a_a = 1$ this equations 10 and 11 becomes exactly equal to equation 8. The Mach angle α' can be calculated by: $\sin \alpha' = a_a / w'$ (12)

3.3 The w''-Mach Waves

Similar considerations can be taken into account for the w''-Mach waves inside the jet. They are produced by the rear vortices. They move downstream with the velocity w'' and are only able to form Mach waves if the velocity difference $u_i - w''$ is larger than a_i. This is valid for vortices moving in a layer with the velocity $u_i - a_i > u > 0$. The relative Mach numbers can be deduced from Fig. 6.

$$\frac{u_i - a_i - w''}{a_i} = \frac{w''}{a_a} \quad (13) \quad \text{or} \quad \frac{w''}{a_a} = \frac{M_i - 1}{1 + a_a / a_i} \quad (14) \quad \text{or} \quad \frac{u_i - w''}{a_i} = \frac{M_i + a_a / a_i}{1 + a_a / a_i} . \, (15)$$

In the general case $w / a_a = 1$ the requirement of equal relative Mach numbers writes:

$$\frac{w - w''}{a_i} = \frac{w''}{a_a} , \, (16)$$

as shown in Fig. 6.

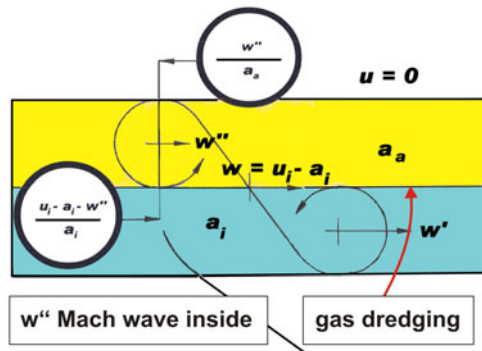With w calculated by equation 5 the following equations result:

Fig. 6. Rear vortex: case $u = u_i - a_i$

$$\frac{w''}{a_a} = \frac{M_i - w/a_a}{1 + a_a/a_i} \quad (17) \quad \text{or} \quad \frac{w''}{a_a} = \frac{M_i - a_a/a_i}{\left(1 + a_a/a_i\right)^2} . (18)$$

In the special cases $w/a_a = 1$ the equation 17 reduces exactly compared to equation 10. Of interest is the resulting equation for $(u_i - w'')/a_i$:

$$\frac{u_i - w''}{a_i} = \frac{M_i + \dfrac{a_a}{a_i}\dfrac{w}{a_a}}{1 + a_a/a_i} . (19)$$

For the special case: $\dfrac{u_i - w''}{a_i} = \dfrac{M_i + a_a/a_i}{1 + a_a/a_i} . (20)$

For the general case: $\dfrac{u_i - w''}{a_i} = M_i \dfrac{1 + 2(a_a/a_i)}{(1 + a_a/a_i)^2} . (21)$

The Mach angle α'' can be calculated by:

$$\sin \alpha'' = \frac{a_i}{u_i - w''} > \sin \alpha_i = \frac{1}{M_i} \text{ at } w'' = 0 . (22)$$

4   Conclusions

The central point of the theory presented herein is the new concept of "gas dredging" where rear vortices transport gas from outside and front vortices jet gas into the jet boundary layer. Consequently, the sound speed profile is totally different to the profiles assumed up to now by existing theories. The well-known formulae from previous research work for the w'- and w''-Mach waves are explained straightforwardly by these new theoretical assumptions. Combining the formulae 8 and 14 or 10 and 17 furnishes the result: $w = (w'+w'')/2$. This is true for all values of w/a, i. e., w/a = 1 in the special cases as well as w/a > 1 or w/a < 1 in the general cases. Some observed occurrence of w-Mach waves all over the length of the jet may be due to the fact that the contact surface moving with w in reality is a weak shear layer producing Mach waves too. Its contribution to the jet noise is small. Such production of Mach waves must not be confused with the transformation of long w-Mach waves to short w-Mach waves out of the transition zone at the end of the supersonic jet. They must be due to vortex interactions. The equations for the special cases feed exactly the empirical values. Those for the general cases are somewhat more complicated. Within a wide range of M_i and a_a/a_i the special formulae are satisfying approximations. It is exclusively in the special case $a_a = a_i$ that the Mach angles α' and α'' are equal ones. At other sound speeds their difference could easily be measured. This fact supports the theory. Remember that $\sin \alpha''$ goes to $1/M_i$ for w'' going to zero.

A direct experimental verification of the theory could be done by light sheet experiments with coloured gases and particles to see if the "dredging" is as efficient as assumed. Further results could be provided by experiments with relative Mach numbers exceeding one which cause the vortices to collapse because in this case the gas pressures acting from both sides change from suction to pressing. The relative Mach numbers have been assumed to be subsonic ones. Only in this case they produce the suction which is necessary for the widening of the vortices up to the coexistence limit. For to high M_i the relative Mach numbers would become supersonic ones. The under-pressure transforms into over-pressure. The formation of the regular vortex pairs must become suppressed. This does not mean the disappearing of all Mach waves. Also in this case w'- and w''-Mach waves have been observed. But they were rare and random ones. The jet noise might become diminished. The relative Mach numbers become supersonic at the following limits:

$$\frac{w''}{a_a} > 1 \text{ for } M_i > \frac{a_i}{a_a}\left(1 + \frac{a_a}{a_i}\right)^2 \quad (23) \quad , \quad \frac{u_i - w'}{a_i} > 1 \text{ for } M_i > \left(1 + \frac{a_a}{a_i}\right)^2 . \ (24)$$

References

[1] Oertel, H.: Coherent structures producing Mach waves inside and outside of the supersonic jet. ISL report CO 82/218 (1982)

[2] Ffowcs Williams, J.E., Maidanik, G.: The Mach wave field radiated by supersonic turbulent shear flows. J. Fluid Mech. 21(4), 641–657 (1965)

[3] Tam, C.K.W.: Directional acoustic radiation from a supersonic jet generated by shear layer instability. J. Fluid Mech. 461(4), 757–768 (1971)

[4] Michalke, H.: A note on the spatial jet-instability of the compressible cylindrical vortex sheet, DLR report, DLR-FB-70-51 (1970)

[5] Gropengießer, H.: Beitrag zur Stabilität freier Grenzschichten in kompressiblen Medien, DLR report, DLR-FB-69-25 (1969)

[6] Laufer, J., Schlinker, R., Kaplan, R.E.: Experiments on supersonic jet noise. AIAA J. 14(4), 489–497 (1976)

[7] Oertel, H.: Jet noise research by means of shock tubes. In: Proceedings of the 10th International Shock Tube Symposium, Japan, Kamimoto (1975)

[8] Oertel, H.: Mach wave radiation of hot supersonic jets investigated by means of a shock tube and new optical technics. In: Proceedings of the 12th International Symposium on Shock-Tubes and Waves, Israel, Jerusalem (1980)

[9] Oertel, H.: Measured velocity fluctuations inside the jet boundary layer of a Supersonic jet. In: Recent contributions to fluid mechanics. Springer, Berlin (1982)

[10] Oertel, H.: Coherent structures producing Mach waves inside and outside of the supersonic jet. In: IUTAM Symposium on complex structures in turbulent flow, IMST-Univerity d'Aix-Marseille, France (1982)

[11] Oertel, H.: 33 years of research by means of shock tubes. In: 14th International Symposium on Shock Tubes, Australia, Sydney (1983)

[12] Tam, C.K.W.: Supersonic jet noise. Ann. Rev. Fluid Mech. 27 (1995)

[13] Bailly, C., Candel, S., Lafon, P.: Prediction of supersonic jet noise from a statistical acoustic model and a compressible turbulence closure. Journal of Sound and Vibration 194(2) (1996)

[14] Papamoschou, D., Bunyajitradulya, A.: Evolution of large eddies in compressible shear layers. Phys. Fluids 9(3) (1997)
[15] Papamoschou, D., Debiasi, M.: Noise measurements in supersonic jets treated with the Mach wave elimination method. AIAA J. 37(2) (1999)
[16] Bassetti, A.: A statistical jet-noise model based on the acoustic analogy and a RANS solution, University of Southampton, Institute of Sound and Vibration Research, Doctoral thesis (2009)

Pattern Recognition in High Speed Schlieren Visualization at the High Enthalpy Shock Tunnel Göttingen (HEG)

J. Wolfram and J. Martinez Schramm

German Aerospace Center (DLR), Institute of Aerodynamics and Flow Technology,
Spacecraft Section, Bunsenstraße 10, Göttingen, 37073, Germany
Jeremy.Wolfram@dlr.de

Summary

Time resolved digital high speed image recordings of flow properties using schlieren and shadowgraph methods have become standard tools in today's investigations of hypersonic flows. Postprocessing is often necessary to enhance image quality, followed by quantitative image analysis to measure important flow features. Therefore, a software has been developed allowing flexible design of evaluation workflows and a high degree of automation. Evaluation of shock stand-off distance and shock angle in experimental visualization series at HEG can be carried out. Even force prediction based on analysis of model displacement has been realized. The tool and design considerations based on typical problems of hypersonic flow visualization are discussed. Flow image analysis processes and results using a pattern recognition approach known as "Hough transformation" are presented.

1 Introduction

Since more than 140 years [6] optical diagnostics utilizing schlieren and shadowgraph methods are applied to evaluate gaseous flow topologies in general and later on in hypersonic flows. The emerging digitalization of high speed kinematics enables observations of flow processes at small time scale in order of milliseconds or below. At transient working facilities like the High Enthalpy Shock Tunnel Göttingen (HEG) with typical measurement times in the order of few milliseconds, such diagnostics also support the measurement of time dependent flow behavior. Modern digital image based approaches can provide important support for automatic evaluation of such time resolved data. Important information such as shock shapes, shock-shock interactions and mixing layers should preferably be extracted fully automated by pattern recognition methods. This allows drawing conclusions considering the time development of flows.

1.1   Experimental Conditions

The High Enthalpy Shock Tunnel Göttingen, HEG, of the German Aerospace Center, DLR, is one of the major European ground based test facilities for the investigation of hypersonic and re-entry flows. More information about the HEG is given in Hannemann et al. [2].

While data for physical values such as pressure and heat flux is obtained at model surface, optical measurements like schlieren and shadowgraph methods are utilized to measure gas phenomena in the test section flow field. Typical test times in HEG are in the order of few milliseconds. In this duration high speed time resolved recordings of optical flow visualization techniques are applied during experiments in HEG. The optical layout for schlieren or shadowgraph measurement at the HEG follows a Z-path arrangement [5]. Two types of cameras are used for image acquisition, an analog Cordin drum camera model 318 and a Shimadzu HPV-1, which is a digital high speed video camera with frame rates of up to 1 million frames per seconds. Typical image sequence lengths are about 50 pictures using the Cordin and 100 pictures using the Shimadzu camera. As light sources a Nd:YAG laser or spark gap lights are used.

1.2   Measurements in Visualizations

After acquiring time resolved image sequences of flow conditions a postprocessing stage is useful to enhance image quality dependent on evaluation process goals. First of all there are properties of the measured flow itself. Objects of investigation in hypersonic flows typically are the flow around the model under test and local flow properties as shock waves or mixing layers which can be resolved by the here mentioned flow visualization methods.

The first step of postprocessing digital images achieved by optical measurements is to enhance the quality of the images. Dependent on the purpose this step may vary. For example preparing image sequences for movie animations of the recorded flow needs other processing chains than preparation for mathematical image analysis to extract aggregated information. A lot of impairments must be addressed. The most important ones are contrast enhancement to better turn out wanted features, correction of changing or inhomogeneous illumination, noise reduction and image registration, if necessary. For each of these tasks numerous algorithms and methods are known. Each of them having advantages and disadvantages, an elaborate selection by the evaluating scientists is necessary. Following such mainly low level image processing, the goal is to automatically extract application dependent information of the visualized flow properties. For example to extract a shock stand-off distance at a tunnel model a detection of the shock shape and also the model in the image is necessary. While the tasks mentioned before are often carried out partially in an automatic manner, these problems are often solved by manual measures in images. Even if this generates often fine results in practice this process is very time consuming. Further on results are hard to reconstruct or to repeat, because of implicit subjective influence by the evaluating person and not having a documented process from origin data to results. An appropriate software tool could solve such shortcomings.

2   Visual Data Manipulator

A visual programming environment [4] called "Visual Data Manipulator (VDM)" is used as base platform for in-house software development of flow visualization analysis software. The software is still under development but already allows building and execution of workflows to analyze image sequences measured in HEG experiments. Up to date more than 100 building blocks are available for designing a goal-oriented automatic digital image evaluation [7]. These building blocks cover a broad range from low level to high level based image processing methods, like contrast enhancement, edge extraction, noise removal, transformations, feature detection and the measurement of geometric forms.

The platform is realized as a distributed system using the Java programming language. The data exchange between the building blocks uses OMG's CORBA technology as middleware approach. This allows the building blocks to be developed and provided in most of the popular programming languages and operating systems. By now, most building blocks are implemented in Java using the built-in multithreading capabilities to achieve high calculation throughput on modern multicore computer systems.

Batch processing for image sequences is provided by looping capabilities. Parts of processes could also be used as a building block on their own to reduce complexity and provide additional modularity. Even though most building blocks are designed for automatic use, user interaction for semi-automatic evaluation processes is also supported. Furthermore the user is able to track the evaluation progress and to examine the results
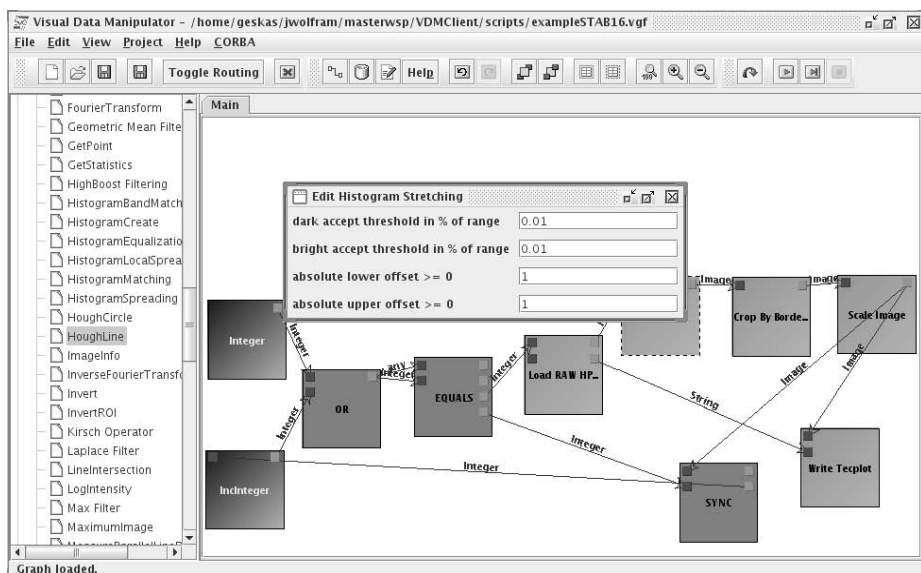

Fig. 1. Screenshot of "Visual Data Manipulator" with example process chain represented as graph of building blocks at the right, an opened property editor for one of the used building blocks at the center, and the list of available building blocks on the left.

of every execution step during the execution phase in order to adapt the process to suit needs better.

To get an impression of the visual programming environment used, Fig. 1 shows the software's user interface containing an example image processing graph and an opened property editor of one building block.

3   Results and Discussion

In many cases in hypersonic flow visualizations shock waves play an important role. The first two examples of flow image analysis below cover such cases. The third example is dedicated to object tracking. All image series of these cases were automatically processed by the VDM with therefore optimized process chains consisting of up to about 30 combined building blocks. Every example makes in some way use of a pattern recognition method developed by Hough [3]. In short, the idea is to create a search space for parameterized image object definitions. For every candidate point in an image, which could be part of the object searched for, a process is triggered. Several specific calculations are performed increasing a vote value for suitable parameter combinations in the search space. If all candidate points are processed, the parameter combination with the highest vote count is accepted as result. This technique is used here for line and circle detections. But this method is not limited to the mentioned shapes. An approach for arbitrary complex shapes has been published as "Generalized Hough Transformation" by Ballard [1]. The method of Hough provides better results than e.g. fitting models with least square minimization under noisy circumstances. The main drawback of the method is its high computational complexity.

3.1   Shock Stand-Off Distance Measurement for Cylinder Model

An important case is the extraction of shock stand-off distance at an object, here a cylinder, in hypersonic flow. In Fig. 2 selected steps from image evaluation are presented. Starting from the original image after some manipulations a circle detection matching the cylinder is performed. The circle center is located on the stagnation point line. In parallel a shock wave fit is performed using a region growing approach. Then
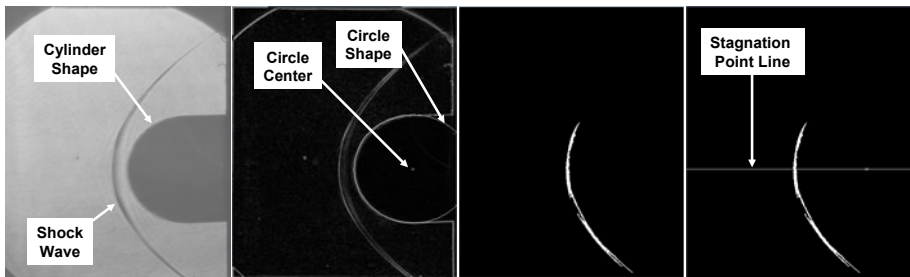

Fig. 2. Processing stages of shock stand-off distance measurement. From left to right: original image; gradient image with detected circle as cylinder shape; partial shock wave fitting; stagnation point line intersecting circle center and shock shape.
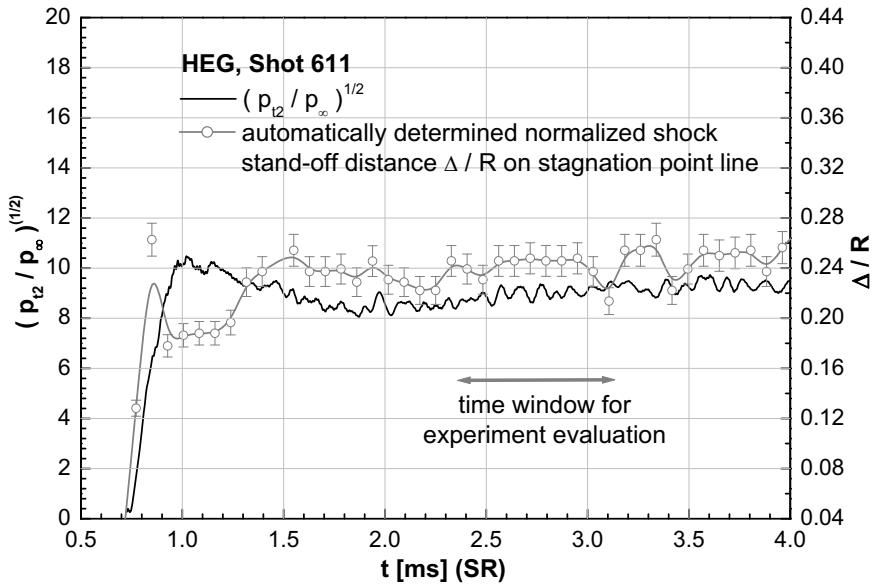
Fig. 3. Comparison of development of free stream conditions to automatically detected shock stand-off distance in front of a cylinder over time. With Δ = shock stand of distance, R = cylinder radius and $(p_{t2}/p_\infty)^{1/2}$ ratio beeing approx. proportional to the flow Mach number. Measurement time starts after shock reflection (SR).

these results are combined. The distance between intersections of the stagnation point line with the matched circle and the shock wave fit is measured. This shock stand-off distance is evaluated for the whole image series recorded at HEG. Fig. 3 shows the normalized measured shock stand-off distance over time (zero indicates the start of the tunnel) along with the measured pressure ratio of the stagnation point pressure of the cylinder to the free stream static pressure. This ratio is proportional to the freestream Mach number of the flow. The development of both quantities can be used to monitor the flow. Especially in facilities like the HEG a sudden increase of these quantities can be an indication of the arrival of driver gas from the tunnel, which is usually different from the test gas used.

3.2   Shock Angle Measurement in Scramjet Combustion Chamber

In the second case a shock angle is measured in a scramjet combustion chamber. With the knowledge of this angle it is possible to draw conclusions on the flow Mach number in the combustion chamber spatially shortly before fuel injection. Fig. 4 presents steps of this image analysis. Starting from the original recording denoising and calculation of gradient image is performed. Because of strong noise additional context sensitive filtering is necessary to match lines in the image afterwards. A linear approximation of
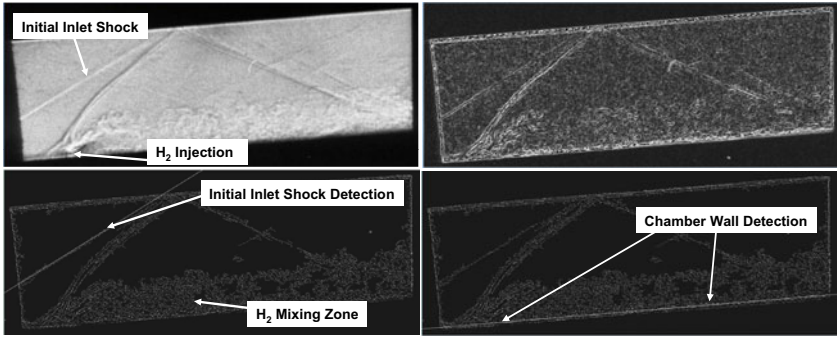
Fig. 4. Processing stages of combustion chamber shock angle measurements. From left to right, first row: original and gradient image; second row: detected initial inlet shock approximated by a straight line and detection of lower chamber wall.
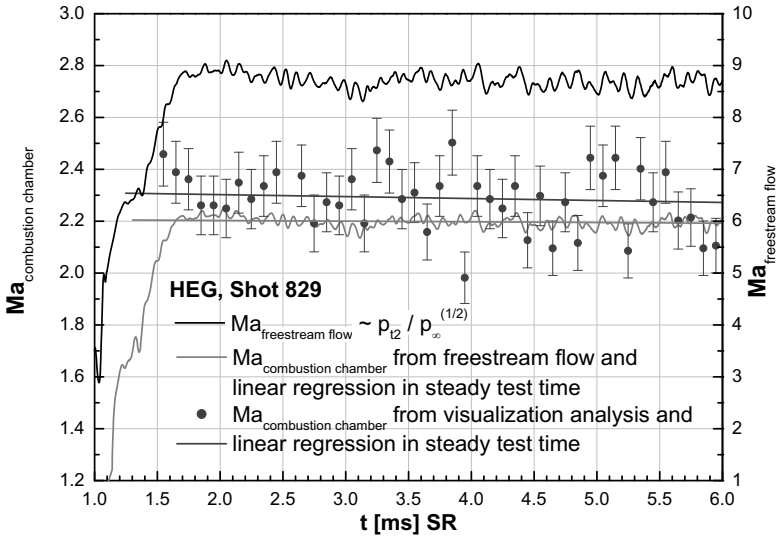

Fig. 5. Comparison of Mach number in scramjet combustion chamber determined by freestream flow condition and by automatic measurement of shock angle (Mach angle) in flow visualizations. Recording time starts after shock reflection (SR).

the selected shock wave and the chamber wall is extracted. The angle between these two lines is measured for all images of the shot. Treating this angle as Mach angle one can determine the flow Mach number at the combustion chamber inlet. Additionally a prediction of the Mach number in the combustion chamber is given. The determination of this Mach number is based on the free stream Mach number of the flow calculated from the pressure ratio described above. After the application of oblique shock theory considering the geometry of the combustor, the Mach number in the combustion chamber can be calculated. A comparison over time is given in Fig. 5. It is obvious that the steadiness in the combustion chamber is not as good as the assumption based on the

free stream proposes. Here it is demonstrated that image analysis techniques deliver additional important information about flow characteristics.

3.3   Model Displacement Tracking for Force Prediction in HEG Flow

In this proof of concept study the approach of predicting total forces applying on a model by displacement tracking using pattern recognition techniques is investigated. In future this is going to be applied to high speed visualizations of HEG flow. In this study no flow was present. A sphere with diameter $d = 0.04$ m and mass $m = 0.2864$ kg was fastened at the end of a several meters long suspension to represent a pendulum. With a momentum measuring hammer a force is exerted resulting in a spatial sphere displacement. By considering small deflection angles the harmonic motion can be reduced to a linear motion in drag direction. Images of a high speed visualization recording of such an experiment are shown in Fig. 6. By using the VDM the location trajectory of the sphere was determined over time fully automatically using once again a "Hough approach". The trajectory provides the displacement velocity of the sphere. Moreover from the time resolved hammer force recordings a momentum can be calculated by integrating this force signal. This allows a calculation of the model displacement velocity under assumption that the momentum transfers without losses into displacement. The comparison of these with both methods determined displacement velocities is promising. The average deviation between results of these two measurement methods is about 4%. But especially applying lower momentums led to increasing differences between both measurement methods mainly caused by limited spatial resolution of the visualization processing. Therefore for future applications at HEG with low spatial model movement the pattern recognition methods for model tracking have to be improved to provide trajectories with several times higher accuracy as the camera resolution.
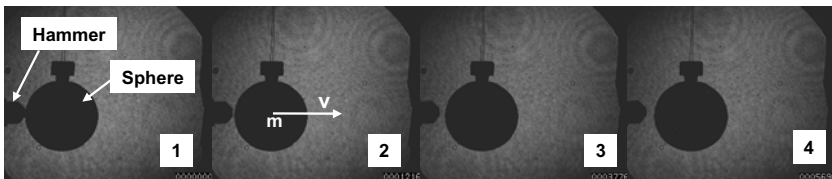

Fig. 6. Time resolved displacement of a sphere after transfer of momentum from a hammer strike. Time after strike increases from left to right image.

4   Conclusions

The presented image processing software based on the VDM is well suited for at least semi-automatic evaluation of image series of high speed flow visualizations. This technique offers a fast, reproducible and self describing analysis of important flow features. Because of flexible and extensible design this tool can be adapted to future hypersonic flow field investigations.

In future existing building blocks for high level object recognition should be improved to deliver accuracy above camera resolution first. Additional methods are going to be developed which will deal with the description and tracking of complex geometries. This requires as another future task, to improve performance of algorithms respectively their implementations. Last but not least the field of force prediction should be developed to higher maturity.

Acknowledgements

References

[1] Ballard, D.H.: Generalizing the Hough Transform to Detect Arbitrary Shapes. Pattern Recognition 13, 111–122 (1981)

[2] Hannemann, K., Schnieder, M., Reimann, B., Martinez Schramm, J.: The Influence and the Delay of Driver Gas Contamination in HEG. In: 21st AIAA Aerodynamic Measurement Technology and Ground Testing Conference, Nr. AIAA 2000-2593, Denver, CO (2000)

[3] Hough, P.: Method and Means for Recognizing Complex Patterns, U.S. Patent (1962)

[4] Kolleck, M.: Konzeption und Implementierung eines Werkzeuges zur Auswertung von Messdaten mit Hilfe von "visual programming", Thesis, University of Cooperative Education Mannheim (2005)

[5] Martinez Schramm, J., Karl, S., Hannemann, K.: High Speed Flow Visualization at HEG, New Results in Numerical and Experimental Fluid Mechanics IV. Notes on numerical fluid mechanics and multidisciplinary design, vol. 87, pp. 229–235. Springer, Heidelberg (2004)

[6] Toepler, C.: Beobachtungen nach einer neuen optischen Methode - Ein Beitrag zur Experimentalphysik, Max Cohen und Sohn, Bonn (1864)

[7] Wolfram, J.: Bildanalyse zeitlich aufgelster Sichtbarmachungen von Hochenthalpieströmungen in einer verteilten "Visual Programming"-Umgebung, Master Thesis, University of Göttingen (2008)

Preliminary Design of a Mach 6 Configuration Using MDO

Robert Dittrich and José M.A. Longo

German Aerospace Center (DLR) - Institute of Aerodynamics and Flow Technology

Lilienthalplatz 7, 38108 Braunschweig, Germany

robert.dittrich@dlr.de

Summary

The paper presents a multidisciplinary optimization (MDO) process for the analysis of configurations with engines strongly integrated into the airframe. The coupled treatment of several physical disciplines like aerodynamics, flight mechanics, propulsion and structure is discussed taking into account the major steps of a flight envelope of a hypersonic transport aircraft like transonic acceleration, hypersonic cruise and subsonic landing. The technique is successfully applied optimizing a Mach 6 transport aircraft considering a single as well as multiple flight conditions. In both cases the optimization technique allows to improve the cruise range of the vehicle.

1 Introduction

In the frame of the EU ATLLAS Project (Aerodynamic and Thermal Load Interactions with Lightweight Advanced Materials for High Speed Flight) the appropriate requirements for the airframe and propulsion materials of future high speed transport airplanes are derived from two configurations, a Mach 3 supersonic and a Mach 6 hypersonic transport. For the Mach 6 configuration is not the aim of the ATLLAS project to design a specific vehicle but to explore todays state of the art technology limits to realize such kind of concept.

Hypersonic atmospheric vehicles are propelled either by ram- or scramjet type of engines, i.e. a kind of propulsion system which requires a successful integration into the airframe in order to avoid major propulsion-efficiency losses. Such propulsion-integration has received considerable attention during the eighties. While it was recognized the need of use massively CFD in order to achieve a successful design, CFD was at that time almost in its infancy. However, today a multidisciplinary optimization technique could provide the right platform for the realization of such kind of vehicle as is the aim to demonstrate in the present work.

2   Reference Design Configuration

In order to carry out a MDO process, the definition of the vehicle to be optimized shall be done in a way that sufficient information about engine performance and structure layout are available. Since EU projects are strongly limited in time and resources to perform a completely new design, it was here decided to select from open literature of past studies a baseline configuration. Only configurations which match the reference ATLLAS mission, i.e. transportation of 200 passengers over a distance of 7000 km at a cruise Mach number 6 and an altitude about 30km, while providing the major amount of technical data have been considered. In view these criteria, the HYCAT-1A [1] [2] has been selected as baseline for a future MDO process. The availability of a huge database including wind tunnel tests and the promising compromise between hypersonic and subsonic performance as well as good trim capabilities, both major requirements for a realistic hypersonic aircrafts, favor the HYCAT-1A. This vehicle has a classical horizontal tail, characteristic sharp forebody leading edge which merges to the wing leading edge and it is driven by a combined turbojet-ramjet engine based on hydrogen fuel. The fuselage is 105 meter long with a spanwidth of 28 meters.

Being rigorous, the baseline vehicle for the MDO process, namely the ATLLAS Mach 6 reference configuration, is not equal to the HYCAT-1A but similar. Also corresponding mass budget estimation, turbo-ramjet performances, mission profile, aerodynamic database, structure analysis and trim capabilities have been specifically generated for the baseline configuration while those of the HYCAT-1A are used for crosscheck purpose. In such a way, the most critical issues of the configuration can be indicated and hence major objectives and important system requirements and constraints for the MDO can be formulated. In particular here the major issues that have to be considered during the MDO process are (1) the mandatory integration of the engine due to the lift increase, (2) the identification of the end of cruise phase with worst trim conditions and (3) the low frequency lateral and vertical bending of the configuration due to the large dimensions.

3   MDO Tool

The MDO tool consists of several modules for different subtasks which are added to a function chain where at the end a defined objective function is updated. The workflow for a 3-point MDO process is demonstrated in Figure 1 and is generally defined by parameterized geometry generation, mass modelling for component masses and centre of gravity computation, CFD grid generation, numerical aerodynamic flow solving, thrust and trim capability determination, FEM grid generation and dynamic structure analysis, constraints check and objective function update. Most of the modules are also depending on the flight regime e.g. transonic or cruise conditions. Concerning the MDO this has mainly a big impact on the propulsion system integration. Hence geometrical and physical differences of the engine in different mission points are considered.

The MDO tool includes both, hypersonic critical issues as well as general MDO relevant aspects. The propulsion system is integrated in the MDO in a form that intake and nozzle flow is directly computed in the CFD and the combustion chamber is covered as
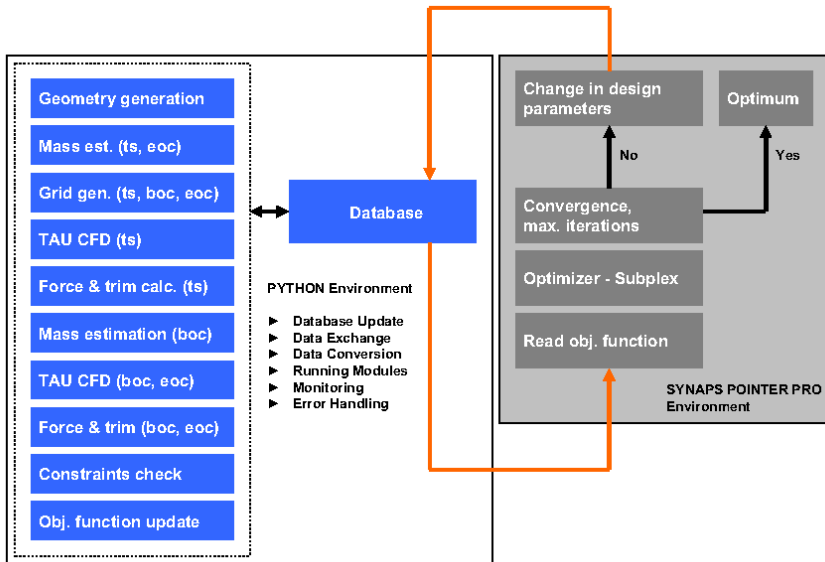
Fig. 1. Flow chart for 3-point MDO process

a black box with given properties so that the gross thrust can be determined. To speed up the MDO process special methods are developed like a modular mesh generation procedure which strongly reduces meshing time. The MDO tool is built up using some commercial software but also using own developed source codes. All modules are embedded in a new and fully automated PYTHON environment taking over running and monitoring of modules, data exchange and conversion, machine communication and database update. The modular concept of the MDO process allows simple removing, adding and modifying of modules.

The MDO tool is linked to the commercial software SYNAPS POINTER PRO [7] which offers several types of optimizers. In the presented MDO the Subplex optimizer, a function ranking method, is favoured. Below the basic modules of the MDO tool are shortly presented.

3.1 Geometry Generation

The geometry generation is one of the major modules of the MDO tool because most of the engaged modules are depending on the geometry. For the geometry generation an own tool is developed based on NURBS curves [3] by defining control points. A certain number of NURBS curves are arranged in 3D-space resulting in a surface. The geometry is divided in several surfaces and changing NURBS attributes offers different kinds of surface interfaces from complete smooth to kinked ones. The geometry description is completely parameterized, so that the airframe is controlled by about 100 parameters and the engine by 40 parameters. Figure 2 shows the generated geometry of the reference design. The tool allows global and local geometry changes modifying

NURBS control points and guarantees water closed geometry. Additionally inner surfaces for tanks and passenger cabin are created. Furthermore the geometry tool can be used directly for node creation needed for structure models.
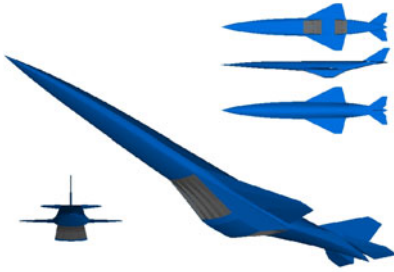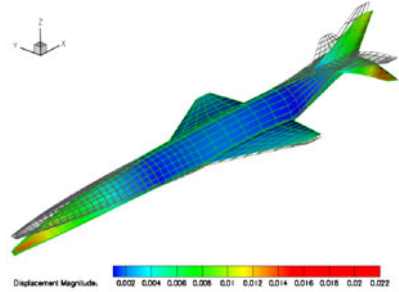

Fig. 2. Reference design geometry

Fig. 3. FEM: vertical bending mode

3.2   FEM Calculation

An initial FEM model provided by ATLLAS partner FOI is adapted to the MDO process including automated mesh generation connected to the geometry procedure. The model consists of 4 nodes shell elements for cover plates, bar elements simulating frame stations, spars and stringers and rigid body elements for component connections. For FEM computations the numerical structure solver NASTRAN is used with concentration on dynamic eigenvalue analysis [6] to consider critical bending modes of the configuration as demonstrated in Figure 3.

3.3   Mass Estimation

For the mass estimation the initial mass budget is splitted into constant and geometry depending masses in form of mass distributions. Applying a new configuration geometry now surface areas and geometrical centre of gravity of these surfaces are determined. Every surface is then loaded with a constant mass and a mass distribution given by the splitted mass budget. In combination with the new calculated tank volumes component masses, fuel masses and centre of gravity depending on fuel charging can be updated, see Figure 4.

3.4   CFD Grid Generation

Allowing large geometry changes during the MDO re-meshing of the CFD grid within every optimization loop is needed. Therefore the commercial unstructured grid generator CENTAUR [5] is used. For higher accuracy grids with about 1.8 million nodes are used where almost half of the nodes reside inside the engine zone. Suitable source placement guarantees constant mesh refinement for certain local geometry parts like wing leading edges. For an optimization procedure covering 3 flight conditions it is necessary to use 3 different meshes due to (1) the different engine modes, (2) the
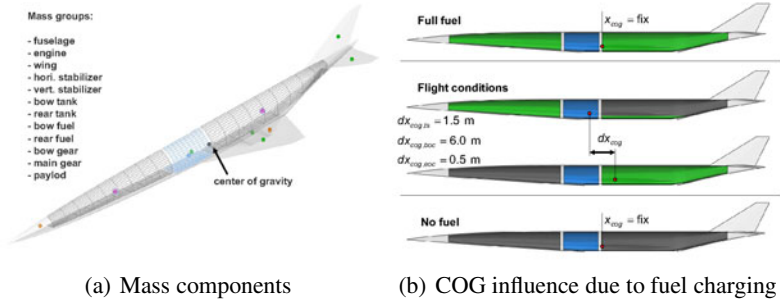
(a) Mass components   (b) COG influence due to fuel charging

Fig. 4. Mass and centre of gravity modelling

different deflections of the horizontal stabilizer and (3) the CFD requirements in far field for each flight conditions. It turns out grid generation is one of the main driver for the overall loop time. So a special modular grid generation procedure is developed by splitting the 3D-field around the configuration into several zones which can be re-meshed independently, see Figure 5(a). Only zones where the geometry changes have to be re-meshed and then grids for different flight conditions are created by grid uniting of main, engine and horizontal stabilizer zone. Hence the overall meshing time during one loop is strongly reduced.

(a) Grid zones of modular CFD grid   (b) Mach number plot for M = 6.0
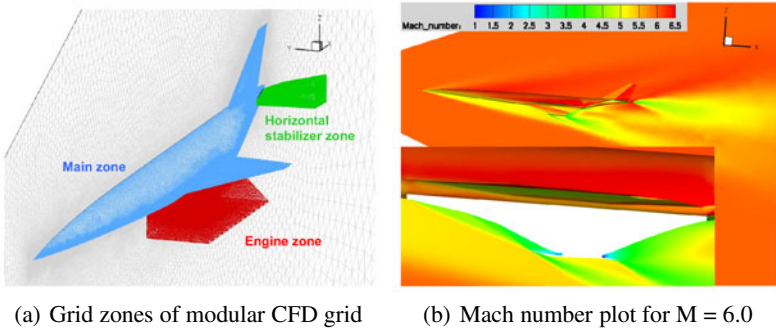
Fig. 5. TAU CFD calculation

3.5 CFD TAU Calculation

The CFD calculations are performed using the DLR TAU code [8], a Reynolds-averaged Navier-Stokes flow solver applicable for subsonic as well as hypersonic cases. For reducing flow solver time TAU is running in Euler mode in addition with large parallel computing. The drag due to skin friction is taken into account after CFD calculation by a turbulent flat plate model. Fast convergence is reached using three level multigrid, 2nd order AUSMDV upwind scheme for flux discretization and three step Runge-Kutta method for relaxation solving. The targeted lift is provided by the mass estimation hence
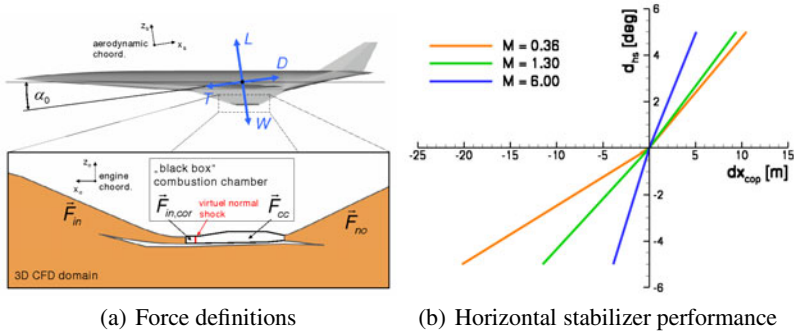
(a) Force definitions   (b) Horizontal stabilizer performance

Fig. 6. System forces and horizontal stabilizer performance

the resulting angle of attack and flow field is numerically computed. Figure 5(b) shows a Mach number plot for cruise conditions including a zoom to the engine where the outer engine walls are set to invisible to show intake compression and nozzle expansion.

3.6 Force and Trim Calculation

The force balance is calculated from the CFD results plus a force model for the black box combustion chamber presented in Figure 6(a) including the gross thrust and small intake corrections. Forces for intake and nozzle are already included in the CFD calculation. Thus the main force coefficients for lift, drag, thrust and pitch moment are computed. To determine the trim capability, the location of the pressure point is computed based on the above information and compared with the centre of gravity. Here plays an important role the effectiveness of the horizontal-stabilizer deflection, which as Figure 6(b) brings out decreases as the Mach number increases. On the other side the specific fuel consumption is calculated from the net thrust given by intake, combustion chamber and nozzle force and fuel mass flow for the current engine mode.

3.7 Objective Function and Constraints Handling

As objective function for the MDO process it is chosen the range due to linkage of aerodynamic and engine performance as well as fuel and operating empty mass.

For an optimization considering only one flight condition, the Breguet range is used. For a multiple flight-condition optimization, a new expression for the range is evaluated by integrating the basic range equation for un-accelerated horizontal flight.

The configuration constraints which can not be found in the range equation are added to the objective function in form of a penalty function which gives the final objective function. Hence the constrained optimization problem is changed to an unconstrained optimization problem. As disadvantage of this method a noisy objective function characteristic is expected. Main constraints are: (i) the intake air mass flow for begin of

cruise, (ii) the distance between centre of gravity and pressure point for all calculated mission points, (iii) the gross lift off weight and (iv) the resulting force in flight direction for all cruise points.

3.8 Optimizer

As mentioned in the beginning the Subplex optimizer is applied for the MDO process. The Subplex optimizer is based on the Nelder-Mead simplex (NMS) method which is often recommended as best optimizer for noisy function due to a function value ranking system which is not depending on absolute objective function values. Furthermore no parameter sensitivity study is necessary, but NMS is limited to low dimensional problems ($n < 6$). The Subplex optimizer now makes the NMS feasible for high dimensional problems by determining subspaces of the parameter space where the NMS can be applied, a so called subplex cycle is evaluated. Convergence can be observed after three till five subplex cycles [4].

4 MDO Applications

The structural module is not included in MDO processes below. A first MDO considering only one flight condition, begin of cruise, has been performed to validate the functionality of the MDO tool. In every loop the targeted lift is determined by the configuration gross lift off weight calculated by the mass module minus a constant fuel mass for acceleration and climb. The targeted lift is then given as input for the CFD calculations. Overall 13 geometrical design parameters, 4 for wing, 4 for horizontal stabilizer and 5 for fuselage have been chosen. The result of the optimization for a single flight condition is shown in figure 7(a). There the initial configuration is compared against the optimized one. The cruise range is increased by 10 percent due to increase of L/D and tank volume without losing aerodynamic performance.
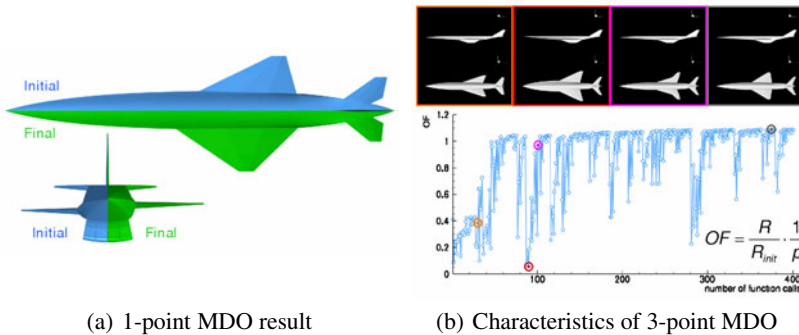

(a) 1-point MDO result   (b) Characteristics of 3-point MDO

Fig. 7. MDO applications

Then an optimization considering 3 flight conditions has been realized as described in Figure 1 by adding the transonic acceleration phase (M = 1.3) and the end of cruise phase (this last due to the critical trim condition mentioned above). The configuration mass at begin of cruise is now depending on the transonic performance which determines fuel consumption during acceleration and climb. The number of design parameters has increased up to 22. Assuming lift is proportional to mass, constant cruise velocity and flight height the basic range equation is integrated in a form that the aerodynamic performance at end of cruise is included in the cruise range calculation. Figure 7(b) presents the current results for the multiple flight conditions optimization. The objective function (OF) is defined by the range to initial range ratio $\frac{R}{R_{init}}$ divided by the penalty function p. The Figure shows the evolution of the configuration along the MDO process. The optimization process leads out a system with an increased objective function by 9 percent.

5   Conclusions

A new MDO tool with application to a Mach 6 hypersonic configuration has been presented. The initial design, major requirements and important constraint formulations for the MDO process are discussed followed by the description of the automated modules for the different subtasks. Three of four targeted disciplines are considered while a structural modeling concerning dynamic eigenvalue analyses is prepared for its implementation in the MDO tool. The modular build-up of the MDO tool allows modifying several modules for future improvements. The functionality of the MDO tool is demonstrated for a single as well as for a multiple flight conditions resulting in all the cases in an increase of the cruise range.

Acknowledgment

References

[1] Brewer, G.D., Morris, R.E.: Hypersonic Cruise Aircraft Propulsion Integration Study Volume I/II, NASA Contractor Report, CR-158926-1 (1979)
[2] Ellison, J.C.: Investigation of the Aerodynamic Characteristics of a Hypersonic Transport Model at Mach Numbers to 6, NASA Technical Note D-6191 (1971)
[3] Piegl, L.: The NURBS Book, 2nd edn. Springer, Heidelberg (1997)
[4] Rowan, T.: Functional Stability Analysis of Numerical Algorithms, Thesis, Department of Computer Sciences, University of Texas at Austin, USA (1990)
[5] CENTAUR Version 7.5 B1, CentaurSoft (2007), http://www.centaursoft.com
[6] MSC NASTRAN 2007 r1 Quick Reference Guide, MSC. Software Corporation, Santa Ana, USA (2007)
[7] SynapsPointer Pro 2, Synaps Ingenieur-Gesellschaft mbH, Bremen, Germany (2003)
[8] TAU Technical Report, DLR, Institute of Aerodynamics and Flow Technology, Braunschweig, Germany (2007)

Numerical Investigation of the Isolator Flow Field of a SCRAMJET Engine with Elevated Wall Temperatures

C. Fischer, T. Neuenhahn, and H. Olivier

RWTH Aachen University, Shock Wave Laboratory,
Aachen 52056, Germany

Summary

The flow field in an isolator of a scramjet configuration has been investigated at elevated wall temperatures for different free stream conditions in the hypersonic test facility TH2. The influence of wall temperature and total temperature has been investigated. It has been found that the separation phenomena grow with higher wall temperatures and lower total temperatures.

1   Introduction

At the Shock Wave Laboratory heated ramp models have been investigated in the hypersonic wind tunnel TH2 for many years. The stagnation temperature of the facility reaches from 1500 K to 7400 K and the Mach number from 6.8 to 12. For the Graduiertenkolleg 1095/1 "Aero-Thermodynamic Design of a Scramjet Propulsion System for Future Space Transportation Systems" an inlet model with isolator has been manufactured. The surfaces of that model (ramps and lips) can be heated up to 1000 K. In the first phase of the project the external compression was investigated experimentally and numerically [6], [7]. This is now followed by the investigation of the isolator flow field.

The flow field in the isolator is strongly influenced by the boundary layers on the wetted walls and their possible separation regions. Existing investigations of the isolator flow [1], [2], [8] show the strong influence of the boundary layer profiles on the flow field. In [2] the thickness of the boundary layer profile was experimentally simulated with a foreplate leading to a decreased achievable pressure rise with a thicker boundary layer profile. In [1] and [8] the flow field in constant area ducts with backpressure was investigated with variations in the boundary layer profiles. In [1] the shock train length was reduced with wall cooling. In [8] an empirical correlation was obtained for the shock train length. It was found to be growing for increased values of momentum layer thickness and therefore for bigger boundary layers.

During hypersonic flight the aerodynamic surfaces do heat up influencing the boundary layer profile. This has to be considered for the design of a SCRAMJET engine intake. As far as known by the authors for flight conditions the effect of elevated wall temperatures on the flow field has not been investigated experimentally in previous studies of the isolator. Therefore as first attempt this effect is studied numerically. Within the Graduiertenkolleg experiments with SCRAMJET-models

with heated inlets and isolators are planned for the near future. The goal of the described research is the numerical characterization of the influence of wall and free stream temperature on the shock wave boundary layer interaction at the lip shock induced separation bubble and the shock train created by the pressure rise in the combustion chamber.

2   Numerical Tool

The commercial CFD code CFX has been employed for the numerical study of the outer compression flow because it easily allows to simulate boundary layer transition with a well validated transition model. Experimental data has indicated transitional behavior of the ramp flow. CFX can solve the steady or unsteady Navier-Stokes equations implicitly using a finite volume method and a second order advection scheme. The employed mesh generator ICEM Hexa 11.0 allows the generation of high quality hexahedral grids. For all computated cases a grid convergence study has been performed showing the grid independence. At the wall the criteria $y+$ less than 1 was ensured. All the results shown in the following have been obtained for a grid converged solution. The code was validated for hypersonic flow by Neuenhahn [5] and successfully used to simulate double wedge [5] and scramjet inlet flow [7]. To simulate the whole system of inlet and isolator the method of mesh splitting was used. The simulation of the whole system was splitted into three spatial regions. First the whole inlet was calculated to obtain the inflow profile for the isolator. Two domains were used to calculate the isolator. One in the front for the expected huge separation bubble [3], [4] caused by the shock wave boundary layer interaction induced by the lip shock. The second domain covers the rear part of the isolator to catch the buildup of the shock train.
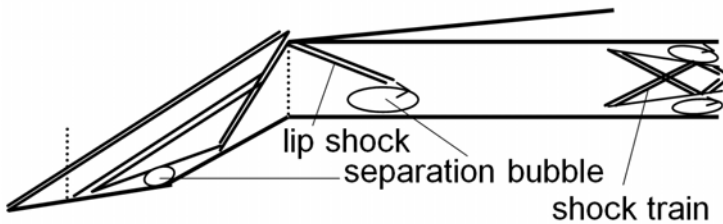

Fig. 1. Scheme of SCRAMJET inlet flow

3   Free Stream Conditions

Conditions I and II as listed in Table 1 were used as free stream conditions for the calculations. Both sets of free stream conditions are characterized by the same Mach and Reynolds number, which allows to study total and wall temperature effects on the flow field separately.

Table 1. Free stream conditions for simulations

Cond.	T_0 [K]	p_∞ [Pa]	T_∞ [K]	U_∞ [m/s]	Ma_∞ [-]	$Re_{\infty,1}$ [10^6/m]
I	1680	570	120	1770	8.1	4.6
II	3360	1910	240	2490	8.1	4.6

4   Model Geometry and Outer Compression

In Figure 2 the geometry of the model is shown together with a schlieren image of the ramp flow, numerical Cond. I Tw= 300K. It shows that in this case the ramp shocks intersect at the leading edge of the intake lip. The separation bubble in front of the compression corner is also visible. The model can be divided into five sections, the first two ramps add to an outer compression angle of 20.5° (l_1 and l_2). Downstream of the first part of the isolator where the lower wall (l_3) and the lip (l_5) are parallel and have no angle of attack the lower wall (l_4) gets an slightly negative angle of attack to counteract the buildup of the boundary layer. The parallel part of the isolator has a height of 15.5 mm. At the end of the isolator a movable symmetric double wedge simulates the pressure rise in the combustion chamber to initiate a shock train.
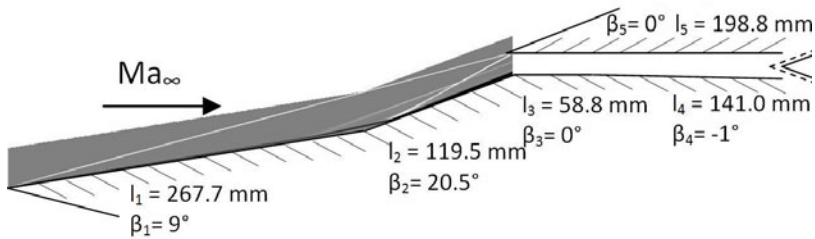

Fig. 2. Model geometry and numerical schlieren for the inlet flow (T_w = 300 K, Cond. I)

5   Inflow Profiles at the Isolator Entrance

Figures 3 and 4 show temperature and velocity profiles for the boundary layer on the inlet. The profiles in Figure 3 were taken in front of the separation bubble on the inlet ramps (left dotted line Figure 1). They show a laminar boundary layer which is thicker for higher wall temperatures and lower total temperatures (Cond. I). For the same total temperature the boundary layer is thicker for higher values of T_w/T_0 while the comparison of the two conditions shows different profiles for cases with constant T_w/T_0 with different values of the two. Cond. II 800K has a thinner boundary layer compared to Cond. I, 300K even so it features a higher T_w/T_0.
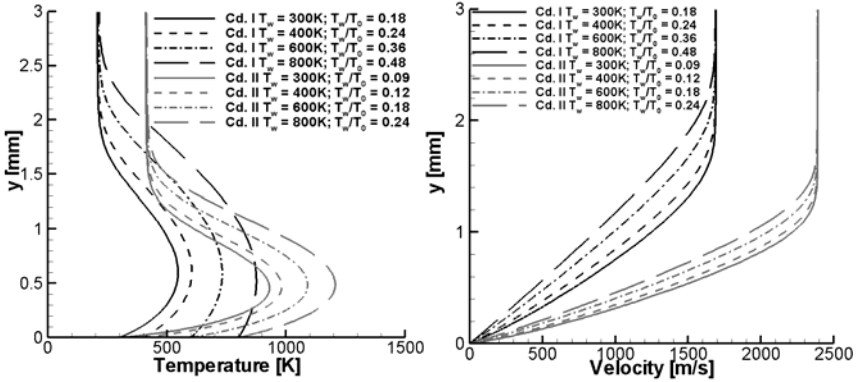
Fig. 3. Temperature (left) and velocity profiles (right) in the boundary layer in front of separation bubble on inlet ramp
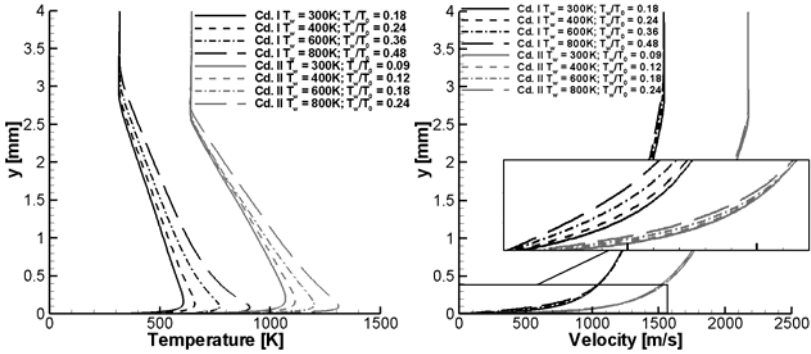

Fig. 4. Temperature (left) and velocity profiles (right) in the boundary layer at isolator entrance

This increased thickness reduces the velocity gradient at the wall and with it the shear stress. Due to the force balance of the upstream acting pressure of the second ramp shock and the shear stress the separation point travels upstream and increases the separation size [6]. For higher total temperatures the boundary layer is thinner for the investigated wall temperatures including those cases with constant T_w/T_0. This together with the higher velocity gradient due to the higher free stream velocity increases the velocity gradient at the wall leading to a decrease in separation size. So the effect is influenced by the wall and total temperature and the temperature ratio T_w/T_0.

The profiles in Figure 4 were taken on the ramp at the position of the isolator lip (right dotted line Figure 1). At this point the boundary layer profiles are fuller indicating turbulent flow. As before the boundary layer thickness is also thicker for higher wall temperatures and lower total temperatures.

6 Isolator Flow Field

In Figure 5 the flow field in the first part of the isolator is shown. The lip shock induces a big separation bubble filling about 60% of the height of the duct. The incoming shocks from the ramps also induce a small separation bubble on the lip near its leading edge. Experimental investigations of a similar inlet isolator configuration with a continuous passage between inlet ramp and isolator at Mach 7 [2] show a similar but smaller separation bubble filling about 30% of the duct. Numerical computations of the same setup [3] resulted in a separation bubble filling about 50% of the duct. The computations were performed for a wall temperature of 300 K.
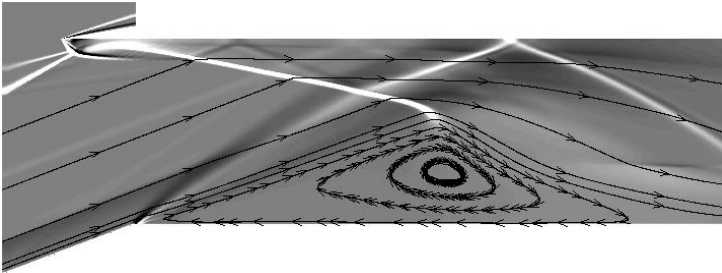
Fig. 5. Schlieren image of the SWBI at the beginning of the isolator (Cond. I, T_w=300K)

In Table 2 the separation length for the separation bubble is listed for different wall temperatures and different total temperatures (Cond. I and II). The length of the separation bubble has been determined by the classical criterion of negative skin friction. The separation length is increasing for higher wall and lower total temperatures. In summary as it is obvious from Table 2 there is a separate influence of the wall and total temperature on the length of the separation bubble as well as of the wall to total temperature ratio. The effect is also consistent with the boundary layer profiles shown in Figure 4. There are higher gradients in the profiles for higher wall and lower total temperatures and higher values of T_w/T_0. Especially the velocity profiles do not differ as much as for the laminar boundary layer on the inlet ramps. Therefore the relative change of the separation size in the isolator is consistent but smaller than the change of the separation size on the inlet as discussed before and in [6].

Table 2. Separation length for lip shock induced separation bubble for different wall and total temperatures

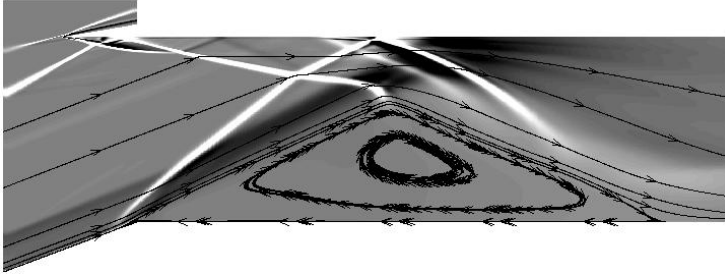| T_w [K]	Sep. length Cond. I [mm]	Sep. length Cond. II [mm]
300	44.3	43.4
400	45.0	43.6
600	46.2	43.7
800	46.5	44.9

Fig. 6. Schlieren image of the SWBI at the beginning of the isolator (Cond. I, Tw=800K)
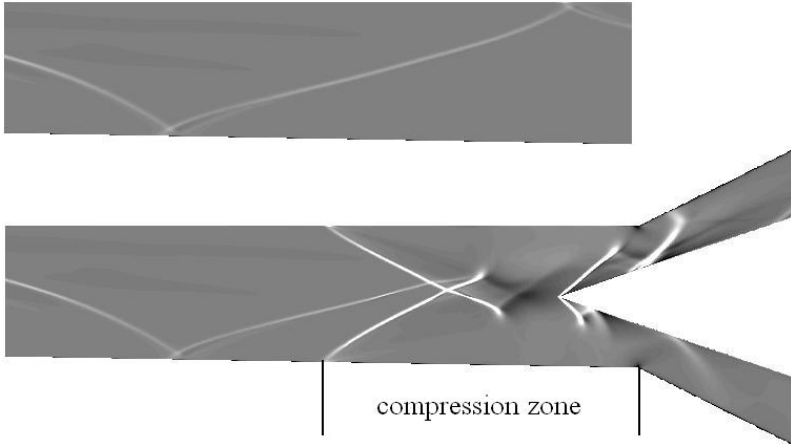

compression zone

Fig. 7. Schlieren images of the rear section of the isolator without (top) and with compression zone (bottom), (Cond. I, Tw = 300K)
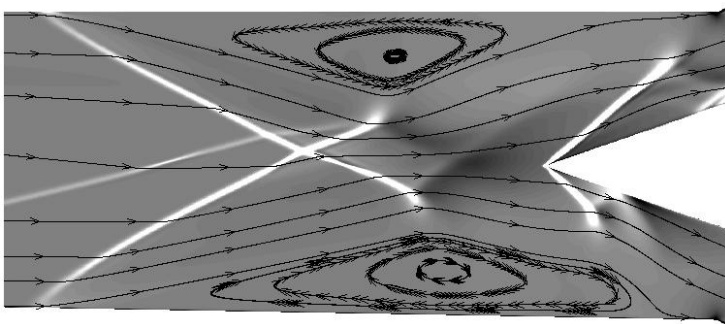

Fig. 8. Detail of the compression zone with streamlines (Cond. I, T_w = 300K)

For the higher wall temperatures (600 K and 800 K at Cond. I;   800 K at Cond. II) the separation bubble does grow upstream beyond the kink and therefore first there is a shock, followed by the expansion changing the flow field in the whole isolator (Figure 6).

Figures 7 and 8 show schlieren images of the rear part of the isolator. In the picture at the top the flow field in the isolator is undisturbed while in the picture below a shock train is initialized by a double wedge. The shock system induced by the double wedge generates a pressure rise as the combustion chamber does. The leading edge of the wedge is placed 10 mm upstream of the isolators end leading to a throttle degree of 40.6 %.

The length of the shock train for different wall and total temperatures is listed in Table 3. The length of the compression zone was defined as the distance between the rear end of the isolator and the most upstream separation point. As for the separation bubble the trend shows growing length for higher wall temperatures and lower total temperatures.

Table 3. Compression zone length

Condition	length [mm]
Cond. I, T_w = 300K	39.1
Cond. II, T_w = 300K	37.9
Cond. II, T_w = 600K	41.3

7   Conclusion

A series of numerical calculations was conducted to investigate the influence of elevated wall temperatures and total temperatures on the flow field of a scramjet isolator. Both the separation bubble and the compression zone do grow with increasing wall and decreasing total temperatures and different values of the two with the same ratio does not lead to a similar flow field. In future simulations will be conducted with higher throttle degrees and higher wall temperatures.

Acknowledgements

References

[1] Cuffel, R., Back, L.: Flow and heat transfer measurement in a pseudo shock region with surface cooling. AIAA Journal 14(12) (1976)
[2] Emami, S., Trexler, C.A., Auslender, A.H., Weidner, J.P.: Experimental investigation of inlet-combustor isolators for a dual-mode scramjet at a Mach number of 4. NASA Technical Paper 3502 (1995)

[3] Häberle, J., Gülhan, A.: Investigation of two-dimensional scramjet inlet flowfield at Mach 7. Journal of Propulsion and Power 24(3), 446–458 (2008)

[4] Krause, M., Reinartz, B., Ballmann, J.: Numerical computations for designing a scramjet intake. In: ICAS 2006, Hamburg (2006)

[5] Neuenhahn, T., Olivier, H.: Numerical study of wall temperature and entropy layer effects on transitional double wedge shock wave/boundary layer interactions. In: 26th International Symposium on Shock Waves, Göttingen (2007)

[6] Neuenhahn, T., Olivier, H.: Influence of temperature effects on the shock wave/boundary layer interaction of a SCRAMJET-inlet. In: DLRK 2008, Darmstadt (2008)

[7] Peters, A.: Numerische Untersuchung der Wandtemperatur- und Entropy-Layer-Einflüsse auf transitionelle Stoß/Grenzschicht-Wechselwirkungen an der Doppelrampe im Hyperschall. Diplomarbeit, Shock Wave Laboratory, RWTH Aachen University (2007)

[8] Waltrup, P.J., Billig, F.S.: Structure of shock waves in cylindrical ducts. AIAA J. 11(10), 1404–1408 (1973)

Numerical Simulation of Nozzle Flow into High Vacuum Using Kinetic and Continuum Approaches

Martin Grabe[1], Rolf-D. Boettcher[1], Stefanos Fasoulas[2], and Klaus Hannemann[1]

[1] DLR, Bunsenstraße 10, D-37073 Göttingen, Germany
martin.grabe@dlr.de
[2] ILR, Technische Universität Dresden, D-01062 Dresden, Germany

Summary

Laminar nitrogen flow expanding through a conical nozzle into high vacuum is numerically reproduced and compared to available experimental data. As the gas density varies quickly by several orders of magnitude, leading to high rarefaction and thermal non-equilibrium, standard (continuum) CFD tools are not sufficient to accurately model the expanding flow. In the work presented here, the efficiency of Navier-Stokes solvers is to be exploited where applicable, supplying the boundary conditions for a kinetic Direct Simulation Monte Carlo (DSMC) solver to handle the domain of rarefaction and non-equilibrium. The hypersonic character of the flow suggests to attempt a pure downstream coupling. The validity of this approach is to be verified.

1 Introduction

The experimental investigation of small satellite thruster plumes is an important area of research in the Spacecraft Section of the DLR Institute of Aerodynamics and Flow Technology, and the unique DLR High-Vacuum Plume Test Facility (STG) allows for investigation of plume expansion under space-like conditions. STG is a large cryo-pumped vacuum chamber of about $10\,m^3$ expansion volume that is capable of maintaining a background pressure of $p_b < 10^{-8}\,bar$ while the thruster is in operation. Suitable numerical methods to support the experiments are however not readily available, as the common Navier-Stokes solvers may only be applied to the dense, near-isentropic core of the flow, while the non-equilibrium regime of the plume expansion has to be treated by kinetic methods such as Direct Simulation Monte Carlo (DSMC). Solving the whole of the nozzle flow with the DSMC method is however prohibitively inefficient.

In order to support and complement the experimental investigation of thruster plumes in the STG, possible ways of combining the DLR's own continuum flow solver TAU [1] with a particle method [2] are to be investigated. To this aim, a well documented reference case of pure nitrogen gas expanding through a conical thruster nozzle into high vacuum is selected to be numerically reproduced and compared to measurements.

To obtain a solution of the whole nozzle flow field, the efficiency of the continuum solver is to be exploited where applicable, supplying the boundary conditions for the kinetic solver. The hypersonic character of the flow suggests to attempt a pure downstream coupling. The validity of this approach is to be verified.

2   Nozzle Expansion

Gas flow expanding from a reservoir into a high vacuum is characterized by a hypersonic radial expansion from the exit plane. Figure 1 schematically shows the main features of such a flow. The gas is assumed to be nearly at rest at the nozzle reservoir at a pressure p_0 and temperature T_0. The rapid expansion downstream the nozzle throat and hence the decrease in density also decreases the number of intermolecular collisions, thus hindering instant energy exchange among the molecules and leading to thermal non-equilibrium. The rarefaction and the subsequent establishment of non-equilibrium lead to a breakdown of the continuum assumption as the gas continues to expand.
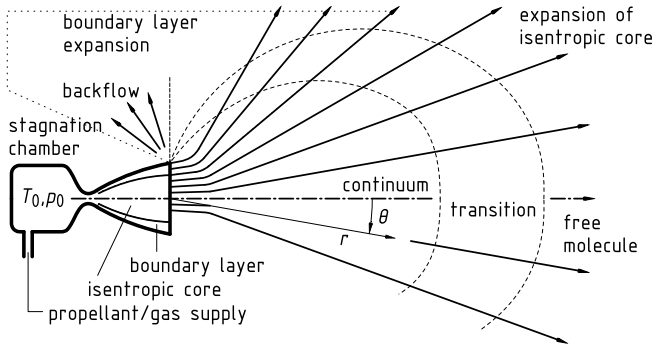

Fig. 1. Schematic view of a nozzle flow expanding into vacuum

When T_0 is of similar order or less than the temperature of the nozzle wall, the effective flow heating leads to the formation of thick boundary layers with strong gradients that may again be responsible for the formation of thermal non-equilibrium, and thus are subject to treatment by a kinetic approach.

3   Numerical Methods and Problem Approach

It is well known that the conservation equations of mass, momentum and energy in a small spatial fluid element can be derived macroscopically by assuming the gas to be sufficiently dense to be approximated as a continuum, or microscopically from the

Boltzmann equation by allowing only a small deviation from local thermal equilibrium. This implies that typical length- and time scales of a particular problem are large compared to the molecular mean free path or mean time between intermolecular collisions. If either assumption fails, more general descriptions need to be resorted to.

The tool used in this work to treat this so-called continuum domain is the DLR TAU code, an implementation of the finite volume method to solve the conservation equations [1].

The numerical treatment of rarefied and strongly non-equilibrium flows requires methods that recognize the particulate nature of the gas. The most efficient, robust and most popular numerical method today for treating rarefied gas flows is termed Direct Simulation Monte Carlo (DSMC) [3]. The algorithm employs simulator molecules, each representing a large ensemble of real particles, and decouples their motion and collisions within a timestep: first, the position of the particles is updated according to their velocities, regardless of wether the trajectories might intersect. Then collisions between nearby molecules are carried out on a stochastical basis. To obtain macroscopic quantities like density, bulk velocity and temperature, the properties of the particles are sampled over many timesteps. The actual number of timesteps used for sampling determines the degree of statistical scatter in the solution.

As physically accurate simulations rely on a spatial resolution of the order of a particle's mean free path (i. e. the average distance between two subsequent intermolecular collisions) and a meaningful number of particles within a cell is required to keep statistical scatter low, the DSMC method gets computationally more expensive as the gas density increases. It is thus limited by economic, not by physical constraints.

3.1 Determination of Interface Conditions

The two fundamental questions associated with combining two simulation methods is *where* to couple them and *how* the coupling is to be done. In this work the codes are to be combined along a physically significant boundary, and hence the first question associated with the location of the flow interface requires the definition of a criterion that signals the domain of validity for the CFD method.

The number of concurrently employed continuum breakdown parameters in recent literature suggests difficulties in singling out one universally applicable criterion. Several proposed formulations have been trialed in the course of this work.

A well known parameter characterizing the degree of rarefaction in a flow is the Knudsen number Kn, relating the mean free path λ to a characteristic dimension. It is frequently suggested to employ a gradient length based on some flow parameter Q, such as density ρ, speed u or temperature T [4]:

$$\text{Kn}_Q = \lambda \frac{|\nabla Q|}{Q}, \text{ where } Q \in \{\rho, u, T\} \ . \tag{1}$$

These can be shown to be not independent of each other, and the Knudsen number based on density is most frequently used.

The Navier-Stokes equations of continuum gas dynamics can be derived from kinetic theory by assuming only small deviation from local thermal equilibrium. This

small deviation introduces terms associated with heat flux q and shear stress τ. It is thus reasonable to assume, that the magnitude of these non-equilibrium terms may indicate the degree of deviation from local thermal equilibrium. One such parameter has been put forth by Garcia et al. [5], it compares the suitably normalized values of the non-dimensional heat flux and shear stress:

$$B = \max(|\hat{q}|, |\hat{\tau}|) \ . \tag{2}$$

The parameter B can be shown to slightly over-predict continuum breakdown if compared to more rigorous mathematical derivations, and thus lends itself well as a breakdown parameter.

Of the different breakdown criteria investigated in this work, the Knudsen number based on the density gradient length, Kn_ρ, and the parameter B seemed most promising to detect the continuum limit where it would be expected from experimental observations. Figure 2 compares Kn_ρ and B when applied to the flow under investigation in this work. Two important conclusions can be drawn from Fig. 2: first, both parameters (and in fact all others investigated) clearly signal non-equilibrium in the boundary layer, up to the nozzle throat. Second, the anticipated pear-shaped structure of the continuum domain (cf. Fig. 1) is only reproduced by parameter B. Separate investigations carried out in the course of this work indicated that a value around $B = 0.03$ would result in an acceptable trade-off between best-possible physical accuracy and a smallest possible DSMC domain.

The second question posed at the beginning of this subsection was concerned with how to couple the two solvers along the interface detected by the continuum breakdown parameter. As a two-way communication between a DSMC solver and a classical CFD code poses significant challenges due to the scatter inherent in results of the DSMC simulation, it was decided to follow a most simple approach: the whole flow field is initially computed with the CFD solver with as low a background density as possible and disregarding physical appropriateness. Then a continuum breakdown parameter is applied to the solution and a coupling interface is determined. This interface line acts as an inflow boundary for the DSMC domain and the corresponding boundary conditions are extracted from the CFD solution. This essentially corresponds to a one-way
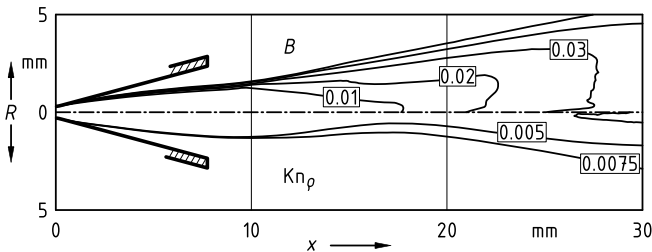

Fig. 2. Comparison of continuum breakdown in the flow investigated here (see Sec. 4) predicted by the Knudsen number based on the density gradient (bottom) and parameter B based on non-equilibrium terms in the Navier-Stokes equations

transport of information from the CFD into the DSMC domain, labeled "downstream coupling" in this text. It is expected that this simplification is justifiable in the case of hypersonic flows.

4   Reference Case

A small conical thruster nozzle (cf. Fig. 3) is selected for which there are numerous experimental results available [6]. One of the best documented sets of data for the nozzle under investigation is available at DLR for pure nitrogen flow at $p_0 = 0.5$ bar and $T_0 = 300$ K. The nozzle wall may be approximated as isothermal at a temperature of $T_W = 300$ K.
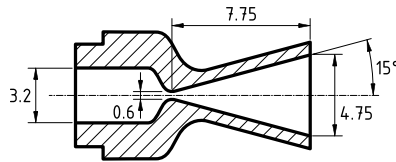
Fig. 3. Geometric dimensions of the DASA 0.5N conical nozzle (values given in mm)

5   Results

Two aspects need to be verified to judge the applicability of the pursued detached downstream coupling approach. One is concerned with the vicinity of the coupling interface (near field), which needs to exhibit physically reasonable (i. e. smooth) state transition from the continuum to the kinetic domain, the other is of more pragmatic nature, namely to determine how well the numerical results can reproduce the experimental data in the far field.

5.1   Near Field Results

A successful coupling of two solvers along an interface is characterized by not displaying discontinuities of flow variables across the interface. Figure 4 shows plots of normalized number density n and temperature T in two representative planes A and B perpendicular to the coupling interface. It immediately becomes apparent that the temperature transitions smoothly from one domain into the other, while the number density shows unnatural behavior in both planes. In plane A, the density in the DSMC domain, right at the coupling interface, is noticeably smaller than the value at the continuum side of the same location. Recall that DSMC is treating the flow as composed of a large number of particles, each having a random thermal velocity component superimposed on the macroscopic, observable bulk flow velocity. The ratio of the flow speed u to the most probable thermal speed $\tilde{c}$ of the random molecular motion (approximately equal to the sound speed) is called molecular Mach number S. If the normal component of
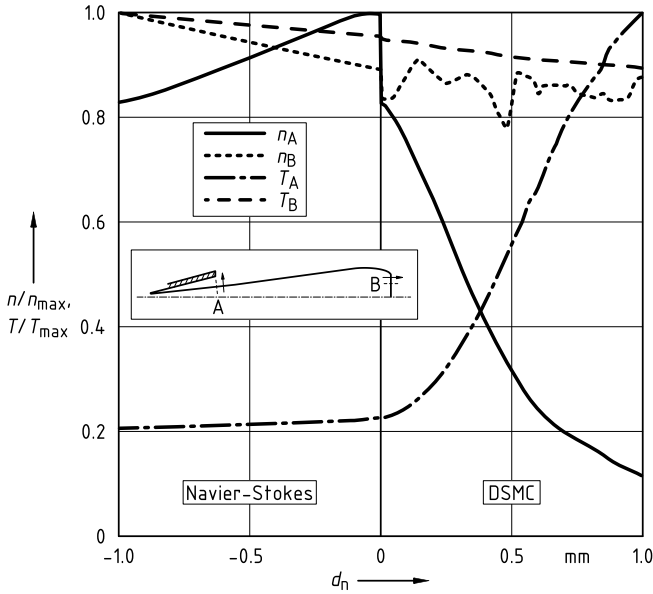
Fig. 4. Density (n) and temperature (T) variation across the coupling interface

the flow velocity is in the order of the most probable thermal speed or smaller, i. e. if $S_n \lesssim 1$, a significant number of molecules actually cross the interface in the opposite direction of u_n.

The coupling interface was chosen in this work on a purely physical basis and it was stated in subsection 3.1, that large gradients in the boundary layer caused breakdown of the continuum assumption in the shear layer between the near-isentropic core of the nozzle flow and the boundary layer. The interface thus determined on physical reasoning is however nearly parallel to the flow streamlines for the most part of the identified continuum limit, and hence the normal component of the velocity is mostly very small. This explains the discontinuity of the density profile A in Fig. 4. Though density profile B exhibits large amplitudes of scatter, which is a well known problem in axisymmetric DSMC simulations, the general trend does not indicate a density jump. This is expected, as $S_n \gg 1$ at this position of the interface.

5.2   Far Field Results

Particle flux measurements at various positions in the flow field for the setup investigated here were already available as angular and radial profiles at distance r measured from the nozzle exit plane and angle θ measured from the axis of symmetry. A representative angular profile at $r = 0.5\,\text{m}$ comparing the measured values of particle flux (crosses) and the results of the DSMC calculation (solid line) is displayed in Figure 5.

Despite the problems at the DSMC inflow boundary, discussed in the previous subsection, the far field results agree quite well. There are two discrepancies to be noted,
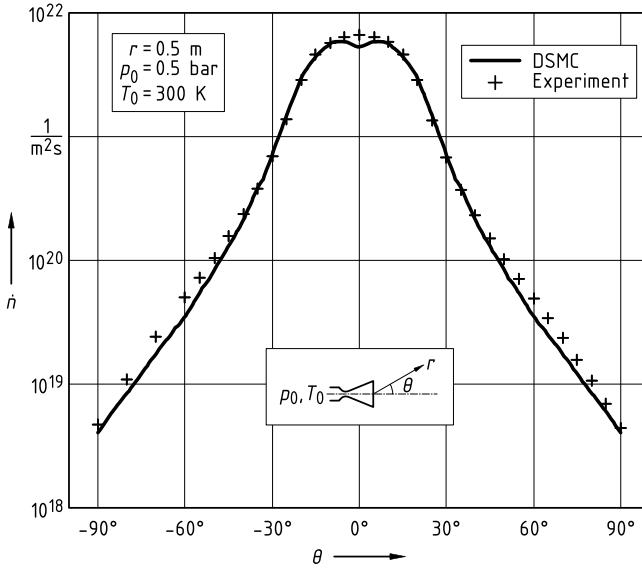
Fig. 5. Angular profile of particle flux $\dot{n}$ at $r = 500\,\text{mm}$ from the nozzle exit plane

the most obvious being the "dent" in the numerical results at $\theta = 0^\circ$. This unphysical result has to be attributed to general problems of less sophisticated axisymmetric DSMC procedures near the axis of symmetry. Apart from that the measurements yield a notice-ably higher particle flux in the region of $45^\circ < |\theta| < 90^\circ$. This may be explained by again resorting to a description of the gas at a molecular level. For simplicity, the noz-zle wall was assumed to be of uniform temperature in the simulation, while in reality it will be cooler at the nozzle lip than near the nozzle throat. Since particles colliding with the wall are assumed to be reemitted diffusively, i. e. assuming a random thermal velocity depending on the wall temperature, a warmer wall will result in a more pro-nounced thermal motion, which in turn leads to a larger number of particles in the back flow ($\theta > 90^\circ$) and a smaller fraction of molecules reaching areas further downstream. Also the observed lower density in the boundary layer due to the suboptimal coupling conditions may contribute to the lower particle flux.

6 Conclusion

Large gradients in the shear layer cause the continuum breakdown parameters to signal non-equilibrium in the whole (thick) boundary layer, up to the nozzle throat. More than 80% of the coupling interface is thus nearly parallel to the flow direction. In a molecular picture, this means significant backflow of particles into the continuum domain, hence the assumption of uni-directional transport of information is violated, which becomes manifest in an unphysical density jump across the coupling interface.

A pure downstream coupling is thus not applicable to this kind of flow. This deficiency however appears not to have a significant impact on the flowfield far

downstream of the nozzle exit plane. The downstream coupling approach may thus be sufficient for an engineering estimation of flow field conditions distant from the nozzle.

The development of hybrid continuum/DSMC methods remains an active field of research, since (upstream) coupling to Navier-Stokes solvers poses difficulties mostly due to the stochastic nature of the employed DSMC algorithm. A flexible 3D, state-of-the-art DSMC solver is currently being developed, bearing in mind possible coupling approaches to the DLR TAU code to allow for a numerical treatment of flow interaction with realistic spacecraft geometries.

References

[1] Anonymus: Technical documentation of the DLR Tau-code. Technical Report IB 123-2004/00, DLR Institut für Aerodynamik und Strömungstechnik Braunschweig, Göttingen (2004)

[2] Laux, M.: Direkte Simulation verdünnter, reagierender Strömungen. PhD thesis, Institut für Raumfahrtsysteme, Universität Stuttgart (1996)

[3] Bird, G.A.: Molecular Gas Dynamics and the Direct Simulation of Gas Flows. Oxford University Press, Oxford (1994)

[4] Boyd, I.D.: Predicting breakdown of the continuum equations under rarefied flow conditions. In: Ketsdever, A.D., Muntz, E.P. (eds.) Rarefied Gas Dynamics: 23rd International Symposium, pp. 899–906. American Institute of Physics (2003)

[5] Garcia, A.L., Alder, B.J.: Generation of the chapman–enskog distribution. Journal of Computational Physics 140, 66–80 (1998)

[6] Plähn, K.: Experimentelle Untersuchung und Modellierung von Abgasstrahlen aus Kleintriebwerken in der Kryo-Vakuum-Anlage STG. PhD thesis, Universität Hannover, Forschungsbericht 1999-39 (1999)

Advanced Flight Analysis of SHEFEX-I

Tarik Barth and José M.A. Longo

German Aerospace Center (DLR) - Institute of Aerodynamics and Flow Technology
Lilienthalplatz 7, 38108 Braunschweig, Germany
Tarik.Barth@dlr.de

Summary

The first **SH**arp **E**dge **F**light **EX**periment of DLR has been established to demonstrate the feasibility of space vehicles with facetted Thermal Protection System (TPS). This study presents the thermodynamic behaviour of SHEFEX-I during the re-entry flight range of $60\ km$ down to $20\ km$ using a multidisciplinary simulation. Major effects like influence of the thermocouple position, overhang of the glue, and contact condition between the heat flux sensor and the TPS are analysed. The results of numerical calculations agree well with the experimental data.

1   Introduction

Hypersonic systems are complex, difficult to design and expensive to develop due to a lack in the physical understanding of the involved flow regimes and a lack of data for design. In order to improve the reliability of the access to space, problems related to vehicle operations and refurbishing for instance, must be highly simplified. SHEFEX-I was started from northern Norway Andøya Rocket Range on 27. October 2005. The project is a low cost flight experiment, which should demonstrate the feasibility of space vehicles with facetted TPS by keeping or improving aerodynamic properties. The TPS consists of simple flat panels with sharp edges and without any constraints in the system compatibility and reliability of space vehicles, see **Figure** 1. The main purpose was to enable the time accurate investigation of the flow effects and the associated structural answer during the hypersonic flight. An additional goal of the experiment was to verify the potential of multidisciplinary design tools [3]. Data of 47 sensors distributed on the surface of the

Fig. 1. View of SHEFEX-I

forebody like pressure transducers (8), thermocouples (34), and heat flux sensors (5) have been recorded for analysis [4]. A complete description of the experiment is published in [2].

2   General Comments

In this study the thermodynamic behaviour of SHEFEX-I during the re-entry flight is studied using a coupled fluid-thermal calculation. For this the energy balance between convection, radiation, conduction, and ablation is essential. Only the term of ablation is neglected, the other components will be taken into account by the numerical computation. In **Figure 2(a)** the sensor positions on the upper site of SHEFEX-I are shown. The sensor denotation conforms to the following definition: "Sensor"-"panel number"-

(a) Sensor positions   (b) Thermal model
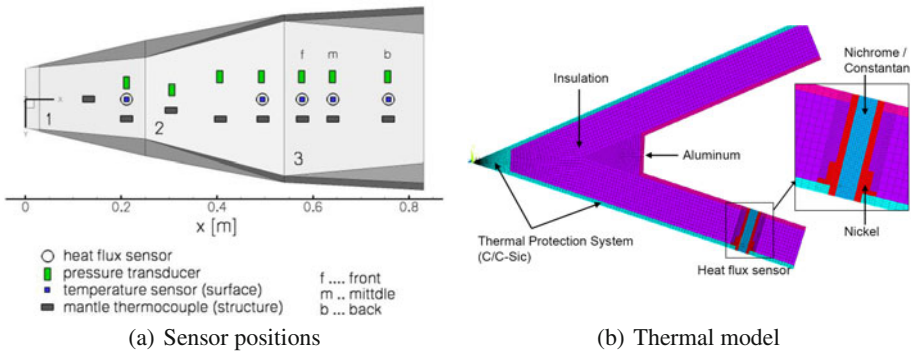
Fig. 2. Sensor positions and thermal model of SHEFEX-I

"positon", for example: "HFS-3-b" corresponds to the heat flux sensor on panel 3 at the back position. The TPS, with a thickness of $3\ mm$, consists of the DLR's Carbon Reinforced Silicon Carbide (*C/C-SiC*) material. The heat flux sensor consists of a combination of Nickel (housing) and Nichrome/Constantan (thermopile). Because of that the thermal properties of the TPS and the sensor are different. Therefore, both materials will be heated-up at different speed and their wall temperatures have to be considered separately for the thermal model. The inside of the vehicle is isolated by an Aluminium oxide (Al_2O_3) fibre with a thickness of $27\ mm$. The complete thermal model is shown in **Figure 2(b)**.

3   Numerical Investigations

For the numerical flow simulations Navier-Stokes calculations are performed using the flow solver TAU of the DLR. TAU is a three-dimensional parallel hybrid multigrid code and is validated by [7] for hypersonic flows. It is a finite volume scheme for solving the Euler and Reynolds-averaged Navier-Stokes (RANS) equations using tetrahedrons and prisms. Prismatic elements were used for boundary layer regions while the

tetrahedral elements are used primarily in inviscid flow layer regions. A second order upwind scheme is used for the inviscid fluxes. For time discretization, including local time stepping, a three stage Runge-Kutta method is implemented. The TAU code includes different turbulence models. In the present case, the two-equation k-ω-model was used, because other studies, for instance [8], pointed out that satisfactory results can be obtained using this turbulence model. The coupling environment is a loosely coupled approach and is validated by [6]. Firstly, the heat flux on the surface is calculated by the flow solver. Secondly, the solution is interpolated to the boundary grid points of the structure by the commercial MpCCI software of the *Fraunhofer Institut*. Thirdly, these data serve as boundary conditions for the commercial structural solver ANSYS. Finally, the structural solver gives the temperature associated with the applied heat flux, which is then in turn interpolated to the boundary grid points of the flow field and set as boundary condition to the flow solver. Then, as the beginning of the next iteration step, the heat fluxes are again computed by the flow solver.
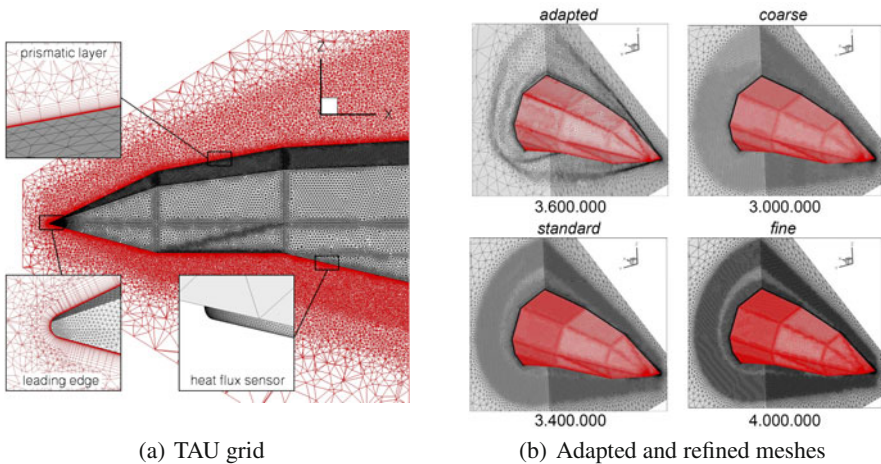

(a) TAU grid   (b) Adapted and refined meshes

Fig. 3. Numerical grids for flow calculations

To generate the grids from the CAD data, the commercial CENTAUR mesh generator was used. The Navier-Stokes mesh has 30 prismatic layers at the wall. The height of the first cell is selected in such a way, that $y^+ < 1$ for all simulations. The mesh for each altitude range consists of approximately 3.400.000 points. **Figure 3(a)** shows the grid with the prismatic layer and detailed views on the leading edge and at the location of a heat flux sensor. The leading edge has a small radius ($R = 0.2\ mm$), because an absolute sharp edge is not feasible with respect to manufacture tolerances. Also, during the re-entry flight a change of the geometry as a result of high temperature (ablation) would be possible. In previous studies [1] the influence of the rounding radius was analysed with the result that a radius smaller than $0.2\ mm$ has no impact on the shock position. The heat flux sensors have a small projection length (obstruction height) of $0.5\ mm$, because the installation condition within the TPS was not absolutely smooth.

In order to use the same grid within a defined altitude range for different time steps with different flow conditions (for instance: angle of attack, angle of yaw, velocity) the grid is refined within the whole shock area (all occurring shock positions included) so that an adaptation of the grid is not needed. Otherwise for every time step an adapted grid has to be created and loaded for the post-processing. To ensure that the refined mesh is fine enough to solve correctly the regions where high gradients are presented, three different refinement levels are investigated for the critical free-stream condition ($H = 20\,km$ and $Ma = 6.2$). For these calculations a steady-state coupled algorithm is applied. **Figure 3(b)** shows the analysed grids. The first one is an adapted mesh with three adaptations. The total number of nodes for all grids amounts between 3 and 4 million points. The comparison of the heat flux for all four grids along the lower side of SHEFEX, see **Figure 4(a)**, shows that the discretization of a standard mesh fulfils the criteria of mesh independence and can be used instead of the adapted grid. Furthermore, the influence of

(a) Flow   (b) Structure
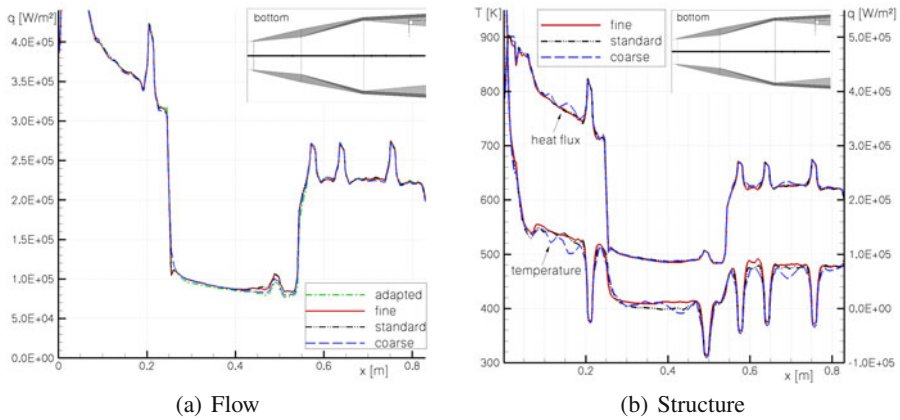
Fig. 4. Heat flux and temperature along the windward side for different meshes.

the structure's mesh is evaluated on the basis of three grids of different sizes. In **Figure 4(b)** the results of the mesh sensitivity study are shown. The results pointed out that the differences between the investigated meshes are mainly on the order of 1-2 %. Only the coarse grid delivers a clear deviation in comparison to the other meshes. Consequently, the application of the standard grid is recommended for a global thermal analysis.

4 Sensitivity Analysis

In order to interpret correctly the comparison of the experimental and numerical temperature data, in this section a sensitivity analysis is done. **Figure 5** shows a sketch of the mounting condition for the mantel thermocouple within the TPS. The thermo element was glued in a slot with a depth of $1.5\,mm$. For the post-flight analysis of SHEFEX-I, the mantle thermocouple position within the structure (a) and the overhang of the glue (b) are two important parameters and source of errors during the analysis. Unfortunately, both parameters (a and b) are unknown and as documented by

pictures, these parameters were not equal to zero. In order to outline the influence of the sensor position, **Figure 6(a)** shows the computed distribution of the temperature within the TPS and isolation normal to the wall. The results pointed out that the sensor position affects enormously the temperature measurement, because the gradients are very high.
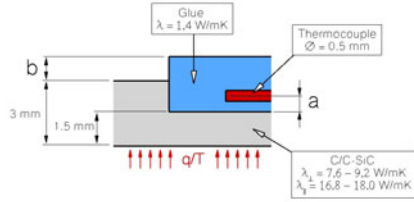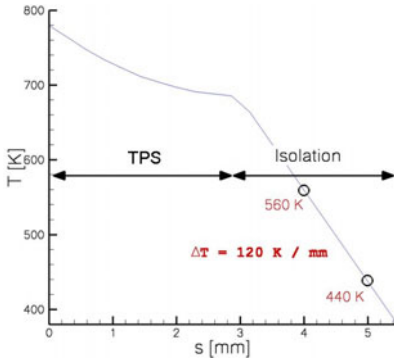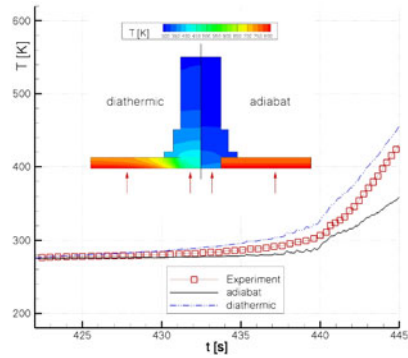

Fig. 5. Description of a and b

(a) Temperature normal to the wall   (b) Diathermic and adiabatic condition

Fig. 6. Results of the sensitivity analysis.

In addition, the modelling state between the heat flux sensor and the TPS is analysed on the basis of two different boundary conditions. In the first case a free heat exchange (diathermic condition) between both is applied. In opposite to that, for the second case no heat transfer (adiabatic condition) over the contact area is possible. The results, see **Figure 6(b)**, with respect to the temperature distribution at the probe center for both variants differ clearly, but enclose as expected the experimentally observed data. At the end of the heating process the surface temperature of the heat flux sensor using the diathermic boundary condition heats up $100\ K$ more than for the adiabatic case. In summary it can be noted, that the temperature analysis is subject to a relative large source of error and respective uncertainties in comparison to the numerical simulations.

5   Numerical Results of the Re-entry

In this section comparisons of numerical and experimental data for the re-entry flight within the altitude range of $60\ km$ ($t_{\text{re-entry}} = 422\ s$) down to $20\ km$ ($t_{\text{re-entry}} = 445\ s$) are carried out. The investigated re-entry flight comprises 23 seconds represented with 460 computations of $\triangle t = 0.05\ s$, for the flow solution while convergence of the solution has been achieved after approx. 1000 fluid-structure coupled iterations. All

in all approx. $1.5 \cdot 10^6$ iterations have been necessary to complete the numerical flow simulation, generating almost 4.000 GB numerical data.

At first, the surface pressure of PS-1-h is discussed in **Figure 7**. A previous study [1] pointed out that a maximum uncertainty of 14 % in pressure may be expected depending on the applied atmospheric model (CIRA86, US Standard 1976, and GRAM90).

Measurements obtained for the mesosphere and upper stratosphere $(95 - 35 \ km)$ in north Norway between April and September 1999 by the German "Physikalisches Institut der Universität Bonn" [5] indicate, CIRA86 is the best model for the SHEFEX-I conditions. The experimental pressure values of SHEFEX-I are well captured by the numerical results for the whole investigated altitude range. The pressure increases from $20 \ Pa \ (H = 60 \ km)$ to $40.000 \ Pa \ (H = 20 \ km)$ and reflects clearly the changing of the angle of attack.
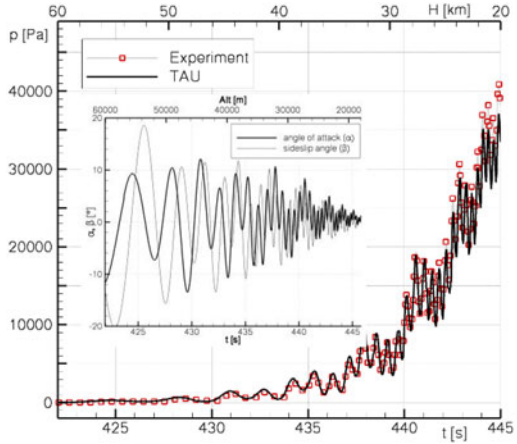

Fig. 7. Pressure distribution of PS-1-b

For the comparison of the HFS-1-b heat flux sensor, see **Figure 8(a)**, a well agreement with the experimental data has been achieved. The flow solver does not model transition from laminar to turbulent flow. Consequently, the user has to define the state of the boundary layer. Here three ranges have been considered: the first one is laminar and has been assumed between 60 and $28 \ km$. After that $(28 - 26 \ km)$, a transition region is followed, where depending on the AoA a change between laminar and turbulent flow takes place. Finally, the boundary layer becomes fully turbulent.

Figure 8(b) shows the heat flux of the sensor (HFS-3-b). Here it is evident that the transition from laminar to turbulent takes place earlier, namely already beginning at approx. $34 \ km$. Furthermore, there is no transition like for the first heat flux sensor (HFS-1-b). The change between the laminar and turbulent status of the boundary layers occurs suddenly. In **Figure 8(c)** the results of the surface temperature (RST-1-b) of the first heat flux sensor are presented. The behaviour and gradients of both curves are concordant. The deviations observed in the range between 36 and $25 \ km$ are related to corresponding differences in heat fluxes. The same applies for the surface temperature (RST-3-b) of **Figure 8(d)**. Also here, the temperature distribution reflects the heating process and heat flux behaviour, respectively. The calculated heat flux distribution of the HFS-3-b sensor is a little low. Because of that, also the temperatures are below the measured values. Nevertheless, a reasonable agreement between numerical and experimental data with respect to the temperature of the heat flux sensors is given.

As explained in **section 4**, the temperature measurement of the TPS using thermocouples is subject to relatively large uncertainties, because the exact position of the mantel thermocouple (a) and the overhang of the glue (b) are unknown. Consequently,
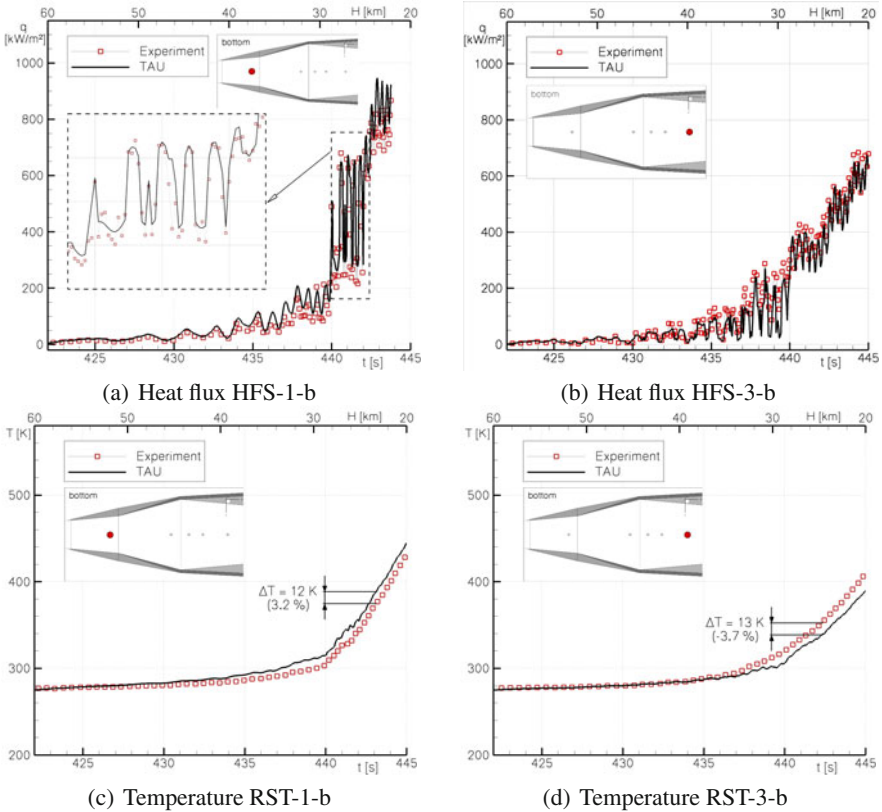
(a) Heat flux HFS-1-b

(b) Heat flux HFS-3-b

(c) Temperature RST-1-b

(d) Temperature RST-3-b

Fig. 8. Results of the coupled simulation.

for the following comparison a variation of a and b is useful in order to include all possible combinations. Thereby, two restrictions have been included in order to limit the variation range. The first one is that the maximum overhang (b) of the glue amounts to $1.5\ mm$. The second assumption is that the thermocouple was always bounded with glue. So that the maximum distance (a) of the thermo element is $2.5\ mm$. **Figure 9(a)** shows the temperature distribution of TS-1-b. Here, the black dash-dot-line presented the temperature in the middle of the TPS. The remaining curves include the influence of a and b. The measurement (symbols) is within the possible combination range and agrees with three combinations which appear probably. Finally, **Figure 9(b)** shows the numerical surface temperature distribution of SHEFEX-I for $H = 20\ km$, where the post-flight analysis is finished. From this picture it is clearly identifiable that mainly the leading edge heats up. Here, temperatures of the order of $1500\ K$ are predicted. The remaining panels keep quite cold. Thus, the experiment has shown that a vehicle, only consisting of flat panels and sharp edges, can be practicable for a re-entry flight.
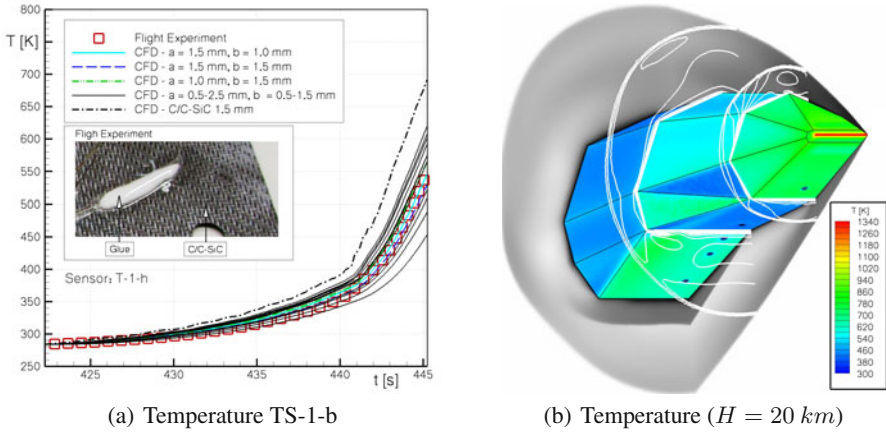
(a) Temperature TS-1-b   (b) Temperature ($H = 20\ km$)

Fig. 9. Results of the sensitivity analysis.

6   Conclusions

In this study an advanced aerothermodynamic analysis for SHEFEX-I has been performed. Careful investigations of the influence of the thermo sensor position, the overhang height of the glue, and the heat transfer between the heat flux sensor and the TPS are carried out in order to identify the source of errors of the thermal analysis. A coupled fluid-thermal calculation within the re-entry flight range of $60\ km$ down to $20\ km$ has been performed. This extensive calculation delivers the aerothermodynamic behaviour during the re-entry flight. The investigation of the structure's temperature shows clearly the problem of a glued mantel thermocouple and the uncertainties with respect to a post-analysis. Considering all investigated sources of errors the numerical results for the pressure, the heat flux, and the surface temperature distributions of the analysed re-entry flight range offer a very reasonable agreement in comparison with experimental data. Finally, this study pointed out that a faceted vehicle with sharp edges can be a feasible concept for re-entry flight.

Acknowledgements

References

[1] Barth, T.: Aero- and Thermodynamic Analysis to SHEFEX I. Engineering Applications of Computational Fluid Mechanics 1(1) (2007)
[2] Barth, T., Eggers, T.: SHEFEX - A First Aerodynamic Post-Flight Analysis. In: 15. DGLR-Fach-Symposium AG STAB, Darmstadt, de (2007)

[3] Eggers, T., Longo, J.M.A., et al.: The SHEFEX Flight Experiment Pathfinder Experiment for a Sky Based Test Facility. AIAA Paper 2006-7921 (2006)

[4] Gülhan, A., Requardt, G., Siebe, F., Koch, U., Esser, B.: Instrumentation and In-Flight Data of the SHEFEX Flight Experiment. In: Proceedings of the 1st International ARA Days on Atmospheric Re-Entry Systems, Missions and Vehicles, Arcachon, France (June 2006)

[5] Lübken, F.-J.: Thermal structure of the Artic summer mesosphere. Journal of Geophysical Research 104(D8), 9135–9149 (1999)

[6] Mack, A.: Analyse von heißen Hyperschallströmungen um Steuerklappen mit Fluid-Struktur Wechselwirkung, DLR-Forschungsbericht 2005-23 (2005)

[7] Mack, A., Hannemann, V.: Validation of the unstructured DLR-TAU-Code for Hypersonic Flows. AIAA 2002-3111 (2002)

[8] Schramm Martinez, J., Reimann, B.: Aerothermodynamic Investigation of the Pre-X Configuration in HEG. In: 15. DGLR-Fach-Symposium AG STAB, Darmstadt, de (2007)

Analysis of the Heat Transfer in Liquid Rocket Engine Cooling Channels

J. Bartolome Calvo[1] and K. Hannemann[2]

[1] DLR, Institute of Aerodynamics and Flow Technology, Lilienthalplatz 7,
38114 Braunschweig, Germany
Javier.BartolomeCalvo@dlr.de

[2] DLR, Institute of Aerodynamics and Flow Technology, Bunsenstr. 10,
37073 Göttingen, Germany
Klaus.Hannemann@dlr.de

Summary

Simulations of supercritical nitrogen flow in cooling channels are compared with experimental results provided by EADS-Astrium Ottobrunn. The objective is to extend and validate the DLR-Tau code to compute and predict the heat transfer in cooling channels of liquid rocket engines. To simulate the flow accurately, the roughness of the surface, the thermophysical properties of the supercritical fluid, as well as the conduction in the structure are modeled.

1 Introduction

The reliable design of a rocket combustion chamber, such as the one of the Ariane 5 liquid rocket engine, has to be based on accurate predictions of heat transfer for both the cooling channel and the combustion chamber. The most loaded part is the throat of the nozzle, where the high heat fluxes and the pressure difference cause the so-called dog-house effect which limits the lifetime of the structure [14]. The design of the channels so far relied mostly on Nusselt number correlations combined with the experience of the designer. With the development of Computational Fluid Dynamics (CFD) and the increase in computational power, there is a need to use these techniques to reduce the uncertainties in the design process. Moreover, other effects can be analyzed, such as the stratification in the cross section and thus providing a complete characterization of the flow entering the combustion chamber. This article is focused on the heat transfer in cooling channels and on heat conduction across the wall. Heat transfer on the hot-side including combustion and injection in the chamber is not taken into account. Up to now, an approch which includes the full physics of the flow in cooling channels is not available in the open literature. For example, Fröhlich et al. [5] describe the challenges in designing a liquid rocket engine at high pressures. Concerning the cooling

channels, they characterize the flow as being turbulent with a Reynolds number between 2.5 and $4.0 \cdot 10^6$, and a Prandtl number between 0.7 and 1.1. To design the engine, one-dimensional heat transfer correlations are used. The correlations have to be adjusted, for example, near the throat to take into account the curvature of the channel, the boundary layer development, and other effects. It is also emphasized that the evolution of CFD methods allows the cross-check with one-dimensional tools, and the evaluation of the thermal stratification which can affect the mixture ratio in the chamber. Naraghi et al. [12] use a similar approach. Woschnak et al. [18] extend the one-dimensional approach by considering the diffusion in the cross section. It is a quasi two-dimensional approach which permits the prediction of the thermal stratification. Fröhlich et al. [4] investigate the flow in the cooling channels with the k-ϵ turbulence model and wall functions with a parabolic marching procedure. Liu et al. [10] consider the two-dimensional thermal conduction across the structure between chamber and cooling channels; take into account the effects of the roughness but with a simplified one-dimensional approach. Wang et al. [17] investigate a standard high pressure engine case and optimize the aspect ratio and the number of channels using the commercial code Fluent and the k-ϵ turbulence model. Kuhl et al. [8] develop a tool to analyze the thermomechanical problem in cooling channels, which covers the elasto-plastic response of the material. However, they treat the flow as incompressible with constant viscosity and thermal conductivity as a function of the temperature. Immich et al. [6] investigate the main technologies for future combustion chambers. They point out, that there is a need to characterize the flow in the cooling channels and to evaluate the uncertainties resulting from the temperature distribution, thermal stratification, and turbulence.

2   Numerical Methods

The DLR-Tau Code is used to solve the Navier-Stokes equations and the commercial Finite Element Method (FEM) solver Ansys is applied for the heat conduction in the structure. Flow variables are discretised using a central scheme, and the advancement in time is done by a multi-stage Runge-Kutta time stepping solution algorithm. To improve the convergence and accuracy, the preconditioning technique already implemented in the code [15], was extended to a generic fluid. Both computational codes are coupled using a tool which was developed and validated within the DLR IMENS-3C and its precursor projects [11]. The simulation of the cooling channels takes into account both the roughness of the wall and the thermophysical properties of the fluid.

2.1   Roughness Modelling

There are mainly three ways to simulate the roughness effects of a surface: (1) the models which rely on the idealized sandgrain roughness, (2) discrete element methods which take into account the pressure blockage of the rough elements, and (3) meshing of the complete rough surface. The sandgrain approach seems to be the most appropriate, since the interest is focused on the general effects of a rough surface in the mean flow, not on the flow between the roughness elements. The sandgrain roughness of the surface is modeled by changes in the turbulence models. For the one equation Spalart-Allmaras model (SAO), the so-called Boeing extension of Aupoix and Spalart [1] is

used. For two equation models, Wilcox k-ω and k-ω Shear Stress Transport (SST), a new roughness extension [7] was recently developed and validated. This new model overcomes the necessity of finer meshes by increasing the roughness Reynolds number k_r^+. For internal flows, the models were validated with the experiments of Nikuradse [13] in the transitional ($5 < k_r^+ < 70$) and fully rough regimes ($k_r^+ \geq 70$). The roughness of the surface increases the pressure drop in the channels causing a higher friction velocity and the velocity profiles become sharper. The other main effect is the change in the thermal boundary layer. The heat transfer is higher than on a smooth surface, and the Reynolds analogy valid for smooth surfaces does not apply anymore [3]. The increase in momentum is caused by pressure forces acting on the rough elements, while the only mechanism of heat transfer is the molecular thermal conductivity. The current models slightly overpredict the heat transfer [1].

2.2   Dense Gas Properties

The properties of the hydrogen which flows through the cooling channels of a liquid rocket engine are given by the cryogenic state in the tank. It is heated along the length of the channels and becomes supercritical. The pressure is higher than the critical pressure and the temperature increases causing a change from liquid to supercritical, and exhibit large variations. Therefore, the properties of nitrogen - considered here - are calculated using a state-of-the-art multiparameter equation of state of Span et al. [16], and the transport properties of Lemmon and Jacobsen [9]. Instead of computing the thermodynamic properties starting from the equation of state, a table containing all the variables is provided to the flow solver. The table contains the thermodynamic variables as a function of the conservative variables, density, and energy. During the iterations, the solver looks up the variables in the table. This procedure is robust and computational efficient. The implementation of the thermophysical properties was verified comparing
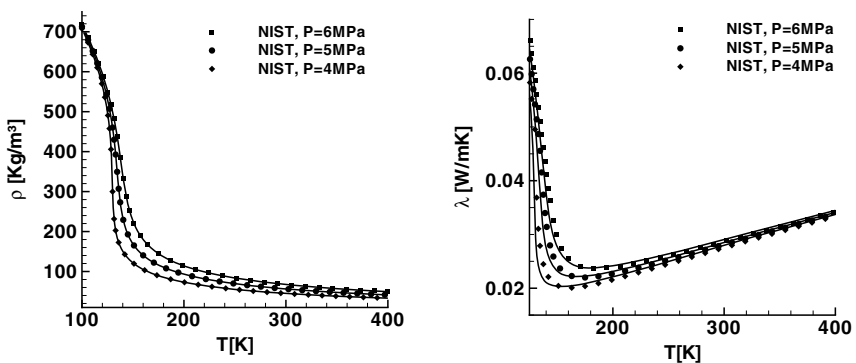

Fig. 1. Density (left) and thermal conductivity (right) as a function of pressure and temperature. Lines: thermophysical properties obtained with [16] and [9], symbols: data of the NIST (National Institute of Standards and Technology).

the results with the data base of the National Institute of Standards and Technology (NIST). Figure 1 shows the comparison of the density and the thermal conductivity as a function of pressure and temperature.

2.3   Coupling of Computational Codes

The DLR-Tau code is coupled with Ansys using a coupling environment developed within the DLR IMENS-3C project. Ansys is only used to solve the conduction problem across the structure. The physical quantities of the thermal problem, heat flux and temperature, are exchanged using the MpCCI (Multi parallel Coupled Computational Interface) interpolation routine. An equilibrium solution is achieved using a loose coupling approach until convergence is achieved [2].

3   Results

A generic thermo-mechanical fatigue experiment to test life and fatigue processes in rocket engines is considered here. As can be seen schematically in Figure 2, the experiment consists of five straight cooling channels with an inlet and an outlet manifolds. The boundary conditions set to solve the problem are temperature and mass flux at the inlet, pressure at the outlet. The channels are heated by two lasers in the center of the panel. It was observed that during the experiments the channels begin to deform changing both the pressure drop and the mass flux across each channel. Therefore, in order to simplify the problem, a test case without deformation was defined and provided by EADS-Astrium Ottobrunn. The boundary conditions were chosen to be an average of the two experimental runs SN07 and SN20. The outlet pressure is 45 bar, the inlet temperature is 160 K, and the ratio between hydraulic diameter and roughness height is $D_h/k_r = 1000$. The material of the channels is the alloy Inconel 600.

The flow in the channels is turbulent and weakly compressible with high heat transfer rates. The heat addition accelerates the flow and the density decreases. Further, the thermal stratification effects are remarkable at the outlet section. Three different meshes are used to solve the problem, consisting of approximately 0.3, 0.6 and 1.2 millon points for a half channel with a first spacing of 0.1 micrometers at the wall. The complete grid including the inlet and outlet manifolds consists of 5.5 million points.
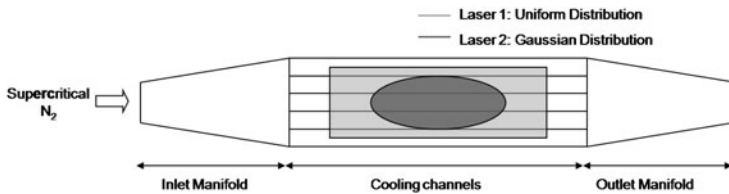

Fig. 2.   Schematic representation of the experiment, main parts: inlet manifold, five cooling channels, and outlet manifold. Two lasers radiate the center of the cooling channels.

3.1 Panel Test Case Results

The symmetrical, thermally coupled problem is solved iteratively for different turbulence models. The temperature distribution along the central channel is shown in Figure 3 (left). The agreement with the experimental runs is satisfactory. The high differences in the temperature originate in the turbulent heat flux vector of the energy equation, and may be caused by the nonlinear evolution of the thermophysical properties. The validation of the roughness models has shown that the differences in the temperature are small when the fluid behaves like a perfect gas, and become higher as the critical temperature is approached. The thermal field in the fluid is shown in Figure 3 (right). The pressure drop increases in the heated region due to the changes in the thermophysical properties, see Figure 4 (left). As a result of the heat addition, the density decreases near the wall, the flow is accelerated and the maximal velocity occurs near the upper wall of the channel. This effect increases with higher heat flux and heated length.
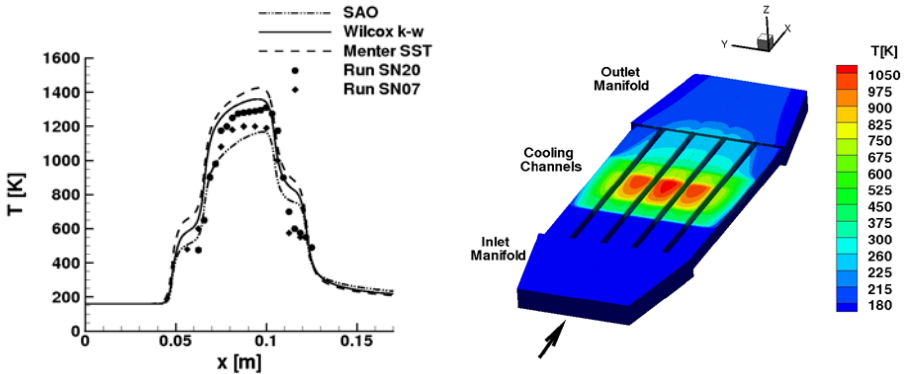
Fig. 3. Calculated temperature profiles along the symmetry axis of the five cooling channels using different turbulence models compared with two measured profiles (left); Equilibrium temperature field on the fluid side obtained with SAO (right).

3.2 Sensitivity Analysis

To analyze the sensitivity of the solution, only the central channel of the panel is considered. The hypothesis is that the mass flux is uniformly distributed among the five channels being one fifth of the total mass flux at the manifold inlet. A grid refinement study for the SAO model shows that the medium mesh is appropriate to analyze the problem, see Figure 4 (left). Results, not shown here, with two-equation turbulence models show nearly grid independent results. A refinement of the FEM mesh has no influence on the solution of the coupled problem. Computations with different roughness levels show almost no difference between a rough and a smooth wall. The evolution of the roughness Reynolds number along the center line of the channel is shown in Figure 4 (right). It starts in the transitional rough regime ($5 < k_r^+ < 70$), and as the heat

is added to the flow it decreases to a value below 5, i.e. the surface is hydraulically smooth. Although the roughness does not play an important role in this test case, in a real application, it is necessary to predict the pressure drop to be able to dimension the pumps which feed the channels. Furthermore, the Reynolds number computed with the hydraulic diameter of the channel is higher than in the present test case. Thus, the viscous length is smaller, and it is expected that the roughness of the surface would have more influence on the results.
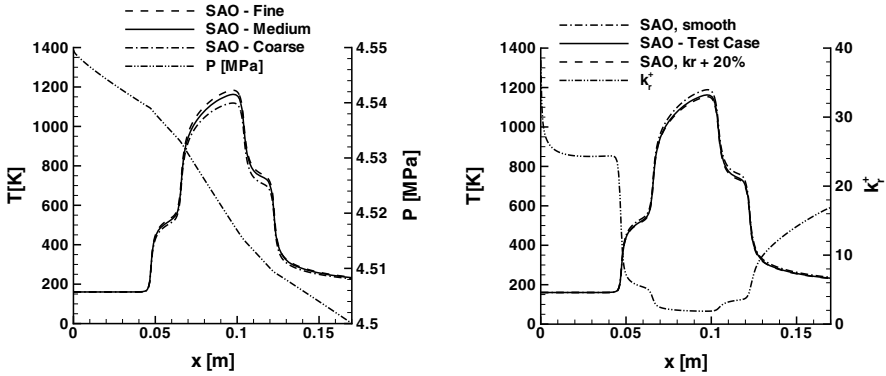
Fig. 4. Temperature along the symmetry of the channels with different meshes (left) and different roughness levels (right) with SAO. Pressure drop (left) and k_r^+ evolution (right).

The results are sensitive regarding the inlet temperature. This is a consequence of the large variation of the thermal conductivity and viscosity near the critical temperature. If the inlet temperature is decreased, for example to 150 K at the inlet, the thermal conductivity of the fluid decreases considerably as shown in Figure 1. The maximal temperature in the central channel increases by 5%. If the temperature at the inlet is 170 K, the maximal temperature decreases by approximately 4%. Also, the pressure at the outlet was varied in the study showing no influence on the maximal temperature. During the experimental runs, the mass flux is kept constant although the channels undergo a deformation. To analyze this effect, four computations were performed with different mass fluxes. The results show that a change in the mass flux of 5% causes the maximal temperature to change 3%. Finally, the uncertainties regarding the lasers which heat the panel are analyzed by changing the heat flux. The results show that changes in heat flux are nearly proportional to changes in temperature. The variation of the heat flux also covers the uncertainties involved in the estimation of the absorption coefficients of the surface.

4   Summary

To compute the flow in cooling channels of liquid rocket engines, modifications of eddy-viscosity turbulence models to model rough surfaces, and the thermophysical

properties of supercritical nitrogen were separately implemented and validated in the DLR-Tau code. Both modules were subsequently used to compute a generic cooling channel test case with temperature levels similar to those expected in flight. The capability to simulate the flow in cooling channels of liquid rocket engines could be demonstrated. The analysis was completed by sensitivity studies of the input parameter and satisfactory agreement with the experimental results were obtained.

Acknowledgements

References

[1] Aupoix, B., Spalart, P.R.: Extensions of the Spalart-Allmaras turbulence model to account for wall roughness. International Journal of Heat and Fluid Flow 24, 454–462 (2003)

[2] Bartolome Calvo, J., Mack, A.: Study of the Heating of a Hypersonic Vehicle launched by a Lorentz Rail Accelerator. International Review of Aerospace Engineering 1, 269–277 (2008)

[3] Dipprey, D.F., Sabersky, R.H.: Heat and Momentum Transfer in ssmooth and rough tubes at various Pradntl numbers. International Journal of Heat and Mass Transfer 6, 329–332 (1963)

[4] Fröhlich, A., Immich, H., LeBail, F., Popp, M.: Three-Dimensional Flow Analysis in a Rocket Engine Coolant Channel of High Depth/Width Ratio. In: AIAA 91-2183 (1991)

[5] Fröhlich, A., Popp, M., Schmidt, G., Thelemann, D.: Heat Transfer Characteristics of H2/O2 Combustion Chambers. AIAA 93-1826 (1993)

[6] Immich, H., Altling, J., Kretschmer, J., Preclick, D.: Technology Developments for Thrust Chambers of Future Launch Vehicle Liquid Rocket Engines. Acta Astronautica 53, 597–605 (2003)

[7] Knopp, T., Eisfeld, B., Bartolome Calvo, J.: A new extension for k-omega turbulence models to account for wall roughness. International Journal of Heat and Fluid Flow (2009) (to appear)

[8] Kuhl, D., Riccius, J., Haidn, O.J.: Thermomechanical Analysis and Optimization of Cryogenic Liquid Rocket Engines. Journal of Propulsion and Power 18, 835–846 (2002)

[9] Lemmon, E.W., Jacobsen, R.T.: Viscosity and Thermal Conductivity Equations for Nitrogen, Oxygen, Argon, and Air. International Journal of Thermophysics 25, 21–69 (2004)

[10] Liu, Q.Y., Like, E.A., Cinnella, P.: Coupling Heat Transfer and Fluid Flow Solvers for Multidisciplinary Simulation. Journal of Thermophysics and Heat Transfer 19, 417–427 (2005)

[11] Mack, A., Schäfer, R.: Fluid Structure Interaction on a Generic Body-Flap Model in Hypersonic Flow. Journal of Spacecraft and Rockets 42, 769–779 (2005)

[12] Naraghi, M.H., Dunn, S., Coats, D.: A Model for Design and Analysis of Regeneratively Cooled Rocket Engines. AIAA 2004-03852 (2004)

[13] Nikuradse, J.: Strömungsgesetze in rauhen Rohren. VDI-Forschungsheft 361 (1933)

[14] Quentmeyer, R.J.: Experimental Fatigue Life Investigation of Cylindrical Thrust Chambers. NASA TM X-73665 (1977)

[15] Radespiel, R., Turkel, E., Kroll, N.: Assesment of Preconditioning Methods. DLR-Forschungsbericht 95-29 (1995)

[16] Span, R., Lemmon, E.W., Jacobsen, R.T., Wagner, W.: A Reference Quality Equation of State for Nitrogen. International Journal of Thermophysics 19, 1121–1132 (1998)

[17] Wang, Q., Wu, F., Zeng, M., Luo, L., Sun, J.: Numerical simulation and optimization on heat transfer and fluid flow in cooling channel of liquid rocket engine thrust chamber. International Journal for computer aided Engineering and Software 23, 907–921 (2006)

[18] Woschnak, A., Suslov, D., Oschwald, M.: Experimental and Numerical Investigation of thermal Stratification Effects. AIAA 2003-3214 (2003)

Analysis of High-Lift Generated Noise via a Hybrid LES/CAA Method

D. König[1], S.R. Koh[1], M. Meinke[1], A. Birkefeld[2], J. Utzmann[2],
C.D. Munz[2], and W. Schröder[1]

[1] Institute of Aerodynamics, RWTH Aachen University,
Wüllnerstraße 5a, 52062 Aachen, Germany
[2] Institute of Aerodynamics and Gasdynamics, University of Stuttgart,
Pfaffenwaldring 21, 70550 Stuttgart, Germany

Summary

The flow field and the acoustic field of a high-lift configuration consisting of a slat and a main wing are numerically investigated by an efficient hybrid LES/CAA method. The flow parameters are $Ma = 0.16$, $Re = 1.4*10^6$, and $\alpha = 13$ deg. The simulated flow is in good agreement with experimental findings. The turbulent flow structures especially in the slat cove shear layer reveal patterns similar to those observed in a plane shear layer and an impinging jet, respectively. The acoustic analyses identify the slat gap as the origin of tonal and broadband noise ranging from 1 to 3 kHz.

1 Introduction

Due to the increasing air traffic during the next decade the development of larger aircraft and a higher take-off and landing frequency are expected. Both imply a significantly higher noise exposure to the people living or working near airports whereas the sensitivity concerning noise rises. Therefore, stricter regulations for airplane licenses and night flying restrictions are required. Hence, it is essential for the aviation industry to consider a low-noise design during the aircraft development process.

The generated noise can roughly be divided in engine and airframe noise. Since quite some progress has been made in the reduction of jet noise, airframe noise has become more and more important. Especially during landing, when engines run almost in idle condition, airframe noise is an essential part of the emitted sound. The major contributors of airframe noise are high-lift devices, e.g. slats and flaps, and landing gears. For a low-noise design of these airplane parts a detailed understanding of the underlying sound generating turbulent flow field is required.

In the current work the noise generated by the flow over a high-lift configuration consisting of a slat and a main wing is numerically investigated using an efficient hybrid LES/CAA method. That is, in the first step, a three-dimensional compressible large-eddy simulation is performed to study the unsteady turbulent flow field and to sample data, which is required for the further acoustic analyses. Then, in the second step, the acoustic simulations are based on solutions of the acoustic perturbation equations (APE) [3, 4]. The simulations are done for a flow at a Mach number of M=0.16

and a Reynolds number, based on the freestream velocity and the clean chord length, of Re=$1.4 \cdot 10^6$. The angle of attack is α=13 deg. These flow parameters are related to the experiments of Kolb et al. [9].

The paper is organized as follows. In section 2, the numerical methods and the computational setups of the flow field and the acoustic field are described. Subsequently, in section 3 the results are shown. First, the flow field is analyzed starting with the mean flow properties followed by the evaluation of the turbulent flow structures. Then, the results of the acoustic simulation and the associated post-processed data are discussed.

2   Numerical Methods and Computational Setup

2.1   Large-Eddy Simulation

The three-dimensional unsteady compressible Navier-Stokes equations are solved based on a large-eddy simulation (LES) using a MILES (monotone integrated LES) approach [1]. The vertex-centered finite-volume flow solver is block-structured. A modified AUSM method is used for the formulation of the inviscid terms [10] which are discretized to second-order accuracy by an upwind-biased approximation. For the viscous terms a centered approximation of second-order is used. The temporal integration from time level n to $n + 1$ is done by a second-order accurate explicit 5-stage Runge-Kutta method, the coefficients of which are optimized for maximum stability. For a detailed description of the flow solver the reader is referred to Meinke et al. [11].

The computational mesh used for the LES consists of 32 blocks with approximately 55 million grid points. The extent in the spanwise direction amounts to 2.1% of the clean chord length and is resolved by 65 points. Roughly 3000 and 280 cells are distributed in the streamwise and normal extension of the computational domain. Using the friction velocity $u_* = \sqrt{\tau_w/\rho}$ to define the non-dimensional inner coordinates $\Delta h_i^+ = \Delta h u_*/\nu$ the mesh resolution near the surface is $\Delta x^+ \approx 100$, $\Delta y^+ \approx 1$, and $\Delta z^+ \approx 22$. These values are approximated by the analytical solution of a flat plate during the grid generation process.

On the far-field boundaries of the computational domain boundary conditions based on the theory of characteristics are applied. A sponge layer [7] is imposed on these boundaries to avoid spurious reflections, which would affect the acoustic analyses. On the walls, an adiabatic no-slip boundary condition is applied with a zero pressure gradient normal to the wall. In the spanwise direction periodic boundary conditions are used.

2.2   Acoustic Simulation

The acoustic analyses are done by solving the acoustic perturbation equations (APE) in the APE-4 formulation [3]. This system of equations possesses the same wave operator as the basic acoustic perturbation equations which have been derived by filtering the linearized conservation equations in the Fourier/Laplace space [3]. The left-hand side of the APE-4 formulation constitutes a linear system describing linear wave propagation in mean flows with convection and refraction effects. The right-hand side represents the acoustic source terms. In this work only the perturbed Lamb vector $(\omega \times u)'$ is considered. That is, it is conjectured that vortex sound is the major contribution.

The numerical algorithm to solve the APE-4 system is based on a 7-point finite-difference scheme using the dispersion-relation preserving scheme (DRP) [16] for the spatial discretization including the metric terms on curvilinear grids. This scheme accurately resolves waves longer than 5.4 points per wave length (PPW). For the time integration an alternating 5-6 stage low-dispersion low-dissipation Runge-Kutta scheme [6] is implemented.

To eliminate spurious oscillations the solution is filtered using a 6th-order explicit commutative filter [15, 17] at every tenth iteration step. Since the APE system does not contain convection of entropy and vorticity perturbations [3] the asymptotic radiation boundary condition by Tam and Webb [16] is sufficient to minimize reflections on the outer boundaries. On the inner boundaries between the differently resolved LES and acoustic domains, where the transition of the inhomogeneous to the homogeneous acoustic equations takes place, a damping zone is formulated to suppress artificial noise generated by a possible discontinuity in the vorticity distribution [14].

The two-dimensional acoustic mesh for the APE solution has a total number of 1.8 million grid points. This 2D-formulation is due to the fact that especially at low Mach number flows the turbulent length scales are significantly smaller than the acoustic length scales and as such the noise sources can be considered compact. This treatment tends to result in somewhat overpredicted sound pressure levels which can be corrected following the method described by Ewert et al. [5].

3   Results

The discussion of the results starts by presenting time and spanwise averaged flow data and by comparing numerical and experimental findings. Subsequently, a discussion of the instantaneous turbulent flow structures follows. Then, the distribution of the major noise source, i.e., the distribution of the Lamb vector is shown. Finally, the results of the acoustic simulation and the obtained post-processed data are shown.

The Mach number distribution and some selected streamlines of the time and spanwise averaged flow field are depicted in Fig. 1. Two stagnation points are visible, one
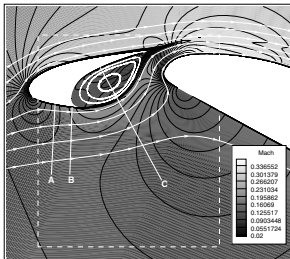

Fig. 1. Streamlines and Mach number contours of the time and spanwise averaged LES flow field data. The dashed box marks the section shown in Fig. 2.
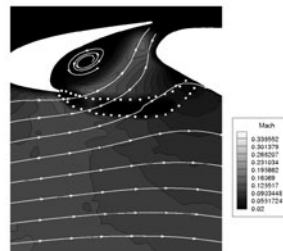
Fig. 2. Streamlines and Mach number distribution of the PIV measurement. The dotted area marks the position of the slat support used in the measurements.

near the nose of the slat and the other one on the lower side of the main airfoil. It is evident that the slat cove region is an area of very low Mach number, which is characterized by a strong recirculation being illustrated by the streamlines. This recirculation area is separated from the flow passing the slat gap by a shear layer which emanates from the slat cusp. Shortly downstream of the slat gap the Mach number distribution reaches its peak value in the suction area above the main wing. In Fig. 2 the result from a particle-image velocity (PIV) measurement is shown. The laser for the light section was positioned beneath the high-lift configuration such that no data for the flow on the suction side is available. However, by juxtaposing Figs. 1 and 2 it is obvious that the computational and experimental findings on the pressure side are in very good agreement. The distribution between the slat cusp and the main wing stagnation point is caused by some diffuse reflections due to the test arrangement. Figure 3 shows the LES and experimental velocity distribution on the lines A, B, and C, defined in Fig. 1, as a function of the non-dimensional coordinate s. Except for the near wall regions, where slight differences are visible, the numerical and experimental results match very well. Figure 3c shows that both, the large-eddy simulation and the PIV measurement to determine approximately likewise recirculation zones in the slat cove.

The distribution of the turbulent kinetic energy $k = \frac{1}{2}\left(u'^2 + v'^2 + w'^2\right)$ is depicted in Fig. 4. High k values occur in the shear layer, the recirculation area, and in the wake of the trailing edge of the slat. The peak value of k is produced in the reattaching shear layer where the flow impinges upon the lower surface near the trailing edge of the slat. This corresponds to the results presented in [2].

We turn now to discussing the unsteady turbulent structures in the slat region. The the vortical structures are visualized by λ_2 contours [8]. Figure 5 reveals vortical structures in the boundary layers of the slat and main airfoil, downstream of the slat trailing edge, and in the slat cove region. The turbulent flow in the slat cove is bounded by a turbulent shear layer which develops from the slat cusp and reattaches near the slat trailing edge. The grey scales mapped onto the λ_2 contours visualize the Mach number distribution. Right downstream of the cusp the shear layer forms predominantly two-dimensional, spanwise vortex structures in the following referred to as rollers which result from of the velocity profile in the shear layer and the associated Kelvin-Helmholtz instability [12]. The vortical structures from the slat cove recirculation area penetrate into the shear layer and distort the rollers. The mixing and interaction of shear layer structures
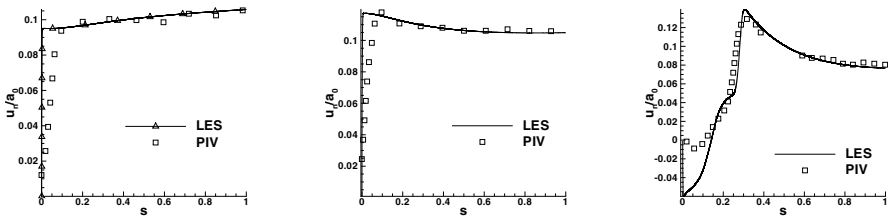

Fig. 3. Distribution of the velocity on line A (a), line B (b), and line C (c), which are defined in Fig. 1, as a function of the coordinate s along this line; comparison of LES and PIV data.
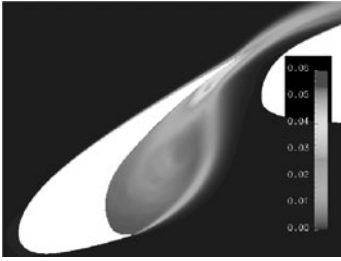
Fig. 4. Turbulent kinetic energy k non-dimensionalized by u_∞^2 in the slat region .

Fig. 5. Vortical structures in the slat area visualized by λ_2 contours with mapped on Mach number distribution.
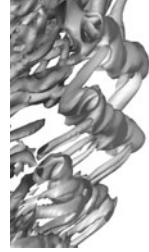

Fig. 6. Rollers and streamwise rib vortices in the shear layer visualized by λ_2 contours.

Fig. 7. Vortical structures in the reattachment area of the slat cove shear layer visualized by λ_2 contours.

Fig. 8. Y-component of the perturbed Lamb vector.

with structures from the recirculation area seem to lead to instabilities, which enhance the development of streamwise orientated vortical structures between two rollers. Similar structures, which are termed rib vortices, have been described e.g. in [12] and [13]. Figure 6 shows some rollers and rib vortices shortly before the shear layer reattaches. Note the sinusoidal appearance of the rollers. It seems that the rollers develop a slightly curved or wavy shape due to their interaction with the rib vortices.

Figure 7 illustrates some more pronounced vortices in the reattachment region, whose axes are aligned with the streamwise direction. These structures seem to be generated by sinusoidal form of the spanwise rollers and by the convection of the rib vortices which are highly stretched by the accelerated slat gap flow. It is obvious that the parts of the rollers pointing in the direction of the slat gap undergo a stronger
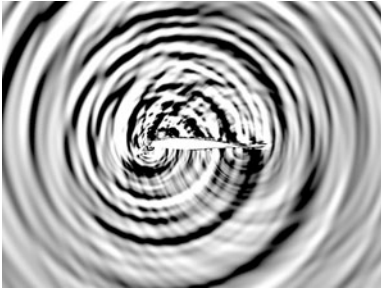
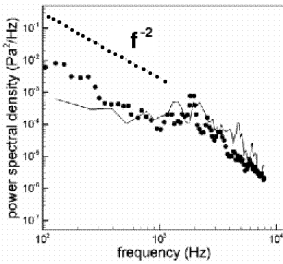**Fig. 9.** Acoustic pressure contours based on the CAA solution.

Fig. 10. Power spectral density for an observer point located at $r = 3.53c$, $\theta = 305°$; experimental (symbols) and numerical (solid line) results.
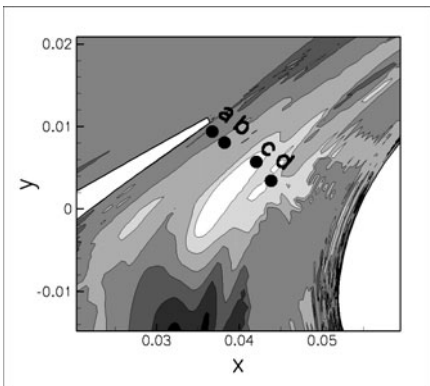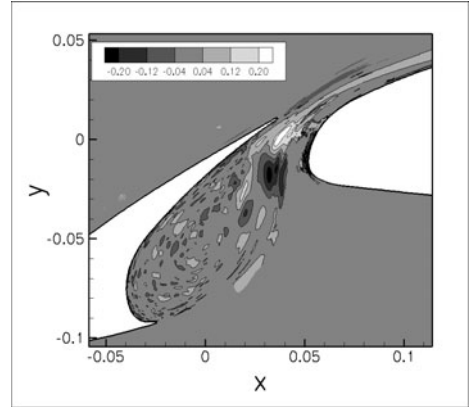

Fig. 11. Results of a space correlation between the acoustic pressure at $r = 3.53c$, $\theta = 305°$ and the perturbed Lamb vector.
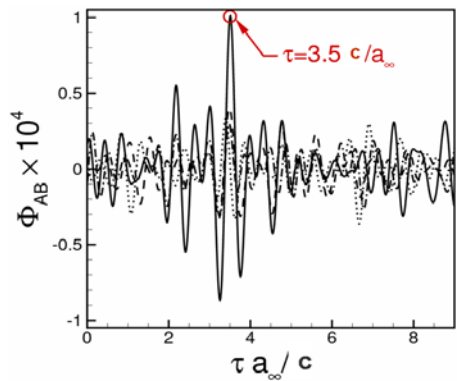

Fig. 12. Zoom of Fig. 11. Points a, b, c, and d define the position where a cross correlation has been performed.

Fig. 13. Results of the cross correlation for the points a, b, c, and d (Fig. 12). Maximum correlation at a time shift of $t = 3.5c/a_\infty$.

acceleration leading to a pronounced distortion of the rollers such that they finally collapse. The remaining structures are predominantly aligned with the streamwise direction.

The major noise source, the perturbed Lamb vector, is shown in Fig. 8. High Lamb vector values are located in the turbulent boundary layers, the wakes of the slat and the main wing, and in the slat cove shear layer. The resulting acoustic field is shown in Fig. 9. The pressure fluctuations are mainly generated in the slat region and at the trailing edge of the main wing. It is obvious that the waves generated in the slat region dominate. Likewise results were computed by a discontinuous Galerkin method.

The frequency spectrum for a far-field location of a radial distance $r = 3.53c$ and an angle $\theta = 305$ deg, where c is the clean chord length and θ is defined counter-clockwise, is shown in Fig. 10. Except for some tonal components at 5 kHz which are not captured in the measurements [9] the magnitude and the decay of the simulation is in good agreement with the experimental findings. To analyze the acoustic field in more detail the distribution of a filtered acoustic signal is investigated. Therefore, a 2 kHz band-pass filter at the center frequency of 2 kHz is applied to the frequency domain and the filtered time signal is reconstructed by an inverse Fourier transformation. A spatial correlation $RS_{AB} = \frac{<A(\boldsymbol{x},t)B(\boldsymbol{x}+\Delta\boldsymbol{x},t_{ret})>}{\sqrt{<A((\boldsymbol{x},t)^2><B(\boldsymbol{x}+\Delta\boldsymbol{x},t_{ret})^2>}}$, where $<>$ denotes the time aver-age and t_{ret} is a retarded time, between the acoustic signal A and the perturbed Lamb vector B is shown in Fig. 11. It is evident that the maximum correlation occurs in the slat gap region. Furthermore, a cross correlation $RC_{AB} = \frac{<A(\boldsymbol{x},t)B(\boldsymbol{x}+\Delta\boldsymbol{x},t+\Delta t)>}{\sqrt{<A((\boldsymbol{x},t)^2><B(\boldsymbol{x}+\Delta\boldsymbol{x},t+\Delta t)^2>}}$ between the acoustic pressure and the Lamb vector is performed. The results for the points a, b, c, and d, defined in Fig. 12, are shown in Fig. 13. All four points have their highest correlation at a phase shift of $t = 3.5c/a_\infty$. Especially the correlation for point c, which is located in an area of high spatial correlation, is extremely pronounced. The observed phase shift of $t = 3.5c/a_\infty$ is nearly exactly the time a signal traveling at the speed of sound a_∞ needs to cover the distance $\Delta\boldsymbol{x}$ between points A and B. Hence, both correlations reveal the slat gap as a major contributor to the mixed tonal and broadband noise in the frequency range of 1 kHz to 3 kHz. It can be concluded that the coupling between the pressure waves generated by the periodically impinging turbu-lent structures of the slat cove shear layer on the slat surface and the reflection of these waves at the main wing surface leads to some resonance effects causing the tonal noise components. In other words, the geometry of the slat gap and the nature of the shear layer are responsible for the pronounced tonal components between 1 and 3kHz. From this analysis it seems to be useful to use active flow control to suppress the macroscopic shear layer oscillations to obtain a low noise slat design.

References

[1] Boris, J.P., Grinstein, F.F., Oran, E.S., Kolbe, R.L.: New insights into large eddy simulation. Fluid Dynamics Research 10, 199–228 (1992)
[2] Choudhari, M.M., Khorrami, M.R.: Slat cove unsteadiness: Effect of 3d flow structures. In: 44th AIAA Aerospace Sciences Meeting and Exhibit, AIAA Paper 2006-0211 (2006)
[3] Ewert, R., Schröder, W.: Acoustic perturbation equations based on flow decomposition via source filtering. Journal of Computational Physics 188, 365–398 (2003)

[4] Ewert, R., Schröder, W.: On the simulation of trailing edge noise with a hybrid LES/RANS method. Journal of Sound and Vibration 270, 509–524 (2004)

[5] Ewert, R., Zhang, Q., Schröder, W., Delfs, J.: Computation of trailing edge noise of a 3d lifting airfoil in turbulent subsonic flow. AIAA Paper 2003-3114 (2003)

[6] Hu, F.Q., Hussaini, M.Y., Manthey, J.L.: Low-dissipation and low-dispersion Runge-Kutta schemes for computational acoustics. Journal of Computational Physics 124(1), 177–191 (1996)

[7] Israeli, M., Orszag, S.A.: Approximation of radiation boundary conditions. Journal of Computational Physics 41, 115–135 (1981)

[8] Jeong, J., Hussain, F.: On the identification of a vortex. J. Fluid Mech. 285, 69–94 (1995)

[9] Kolb, A., Faulhaber, P., Drobietz, R., Grünewald, M.: Aeroacoustic wind tunnel measurements on a 2d high-lift configuration. In: 13th AIAA/CEAS Aeroacoustics Conference (28th AIAA Aeroacoustics Conference), AIAA 2007-3447 (May 2007)

[10] Liou, M.-S., Steffen, C.J.: A new flux splitting scheme. Journal of Computational Physics 107, 23–39 (1993)

[11] Meinke, M., Schröder, W., Krause, E., Rister, T.: A comparison of second- and sixth-order methods for large-eddy simulations. Computers and Fluids 31, 695–718 (2002)

[12] Rogers, M.M., Moser, R.D.: The three-dimensional evolution of a plane mixing layer: the Kelvin-Helmholtz rollup. Journal of Fluid Mechanics 243, 183–226 (1992)

[13] Sakakibara, J., Hishida, K., Phillips, W.R.C.: On the vortical structure in an plane impinging jet. Journal of Fluid Mechanics 434, 273–300 (2001)

[14] Schröder, W., Ewert, R.: LES-CAA Coupling. In: LES for Acoustics, Cambridge University Press, Cambridge (2005)

[15] Shang, J.S.: High-order compact-difference schemes for time dependent maxwell equations. Journal of Computational Physics 153, 312–333 (1999)

[16] Tam, C.K.W., Webb, J.C.: Dispersion-relation-preserving finite difference schemes for computational acoustics. Journal of Computational Physics 107(2), 262–281 (1993)

[17] Vasilyev, O.V., Lund, T.S., Moin, P.: A general class of commutative filters for LES in complex geometries. Journal of Computational Physics 146, 82–104 (1998)

Acoustics and Turbulence Related to the Flow over a Flexible Plate Structure behind an Obstacle

S. Müller[1], S. Becker[1], T. Uffinger[1], F. Schäfer[1],
J. Grabinger[2], and M. Kaltenbacher[2]

[1] Institute of Process Machinery and Systems Engineering (iPAT),
Friedrich-Alexander-University Erlangen-Nuremberg, D-91058 Erlangen, Germany
mue@ipat.uni-erlangen.de
http://www.ipat.uni-erlangen.de/
[2] Department of Sensor Technology (LSE), Friedrich-Alexander-University
Erlangen-Nuremberg, D-91052 Erlangen, Germany

Summary

Experimental and numerical investigations of the fluid-structure interaction and the radiated sound induced by the turbulent flow over a thin flexible plate structure are presented. Various inflow conditions are generated by placing obstacles of different size, shape, position and material in front of a flexible plate. The flow-induced vibration of the plate structure is measured using a laser-scanning vibrometer. Based on the measurement of the vibration of the flexible plate, the sound radiation to the far field is computed employing a finite-element acoustics solver. The flow is investigated in detail using three-component hot-wire anemometry. Microphone measurements are carried out to generate a basis of comparison. The experiments are performed in an acoustic wind tunnel.

1 Introduction

In many technical applications one can find a constellation where a fluid is flowing over a flexible plate structure. Due to turbulent fluctuations in the fluid, the structure is loaded irregularly with pressure and shear stress forces causing a vibration of the plate. On the other hand, the vibration influences the flow field so that one has a two-sided coupling between fluid and structural mechanics. In this situation, two mechanisms of sound generation arise. Vibrational sound is generated by the structural movement of the plate. Additionally, the turbulent flow fluctuations lead to the production of flow-induced sound.

The emission of noise due to flow-induced vibrations of a flexible plate has received much attention in the literature. One of the early investigations in this direction was the work of Davies [1], where the excitation of a thin flexible panel by wall-pressure fluctuations of a turbulent boundary layer was studied using modal analysis. The boundary layer excitation of flexible plates and the resulting emission of noise has also been investigated by, e.g., Howe and Shah [2]. In most of the studies, the influence of the fluid on the flexible plate is modeled based on spectra of the turbulent wall-pressure fluctuations in the boundary layer. A more explicit treatment of the flow over

the plate was performed by Zolotarev [3]. Up to now there is very little work towards a comprehensive investigation of the fluid flow, the structural mechanics and the acoustics as well as the interaction of the different fields (see, e.g., Vergne et al. [4]).

In the present work, the interaction of a fluid flow with a thin flexible plate structure and the resulting acoustic field was studied in detail. For this purpose, a test case was developed which represents a simplified model of a car underbody. A description of the test case is given in the following section. Both experimental and numerical investigations of the test case were carried out. The experiments were performed in a low-noise wind tunnel. Further details of the numerical and the experimental methods are given below. Finally, the results of the study concerning the flow field, the vibration of the flexible plate and the generated sound are presented.

2   Model Setup

The basic setup consists of a flexible plate structure which is part of an otherwise rigid wall. The streamwise and spanwise extension of the whole setup amounts to 1000 mm $\times$ 660 mm, respectively. The flexible plate is made of stainless steel with a thickness of h = 40 μm. The density is ρ = 7855 kg/m^3, the modulus of elasticity is E = 2 $\times$ 10^{11} N/m^2, and the Poisson number is ν = 0.3. The plate is pre-stressed in the main flow direction at a value of σ = 7 $\times$ 10^6 N/m^2. The streamwise and spanwise extension of the flexible part of the plate amounts to 130 mm $\times$ 660 mm, respectively. To modify turbulence characteristics of the inflow, different obstacles were mounted in front of the flexible plate. A sketch of the setup and the investigated obstacle shapes are depicted in Figure 1 and Figure 2, respectively.
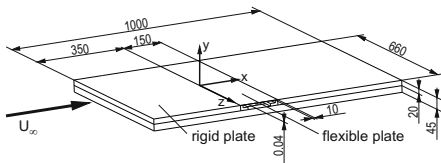

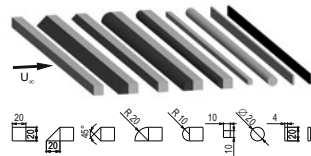**Fig. 1.** Schematic drawing of the setup (units in mm)

Fig. 2. Investigated obstacle shapes (units in mm).

In this paper, the results of three different configurations are presented. One case with a square cylinder obstacle in front of the flexible plate, the other with a rubber strap and the last without an obstacle. The edge length of the square cylinder is D = 20 mm and the cross-section area of the rubber strap 20 mm $\times$ 4 mm, respectively. The obstacles were positioned spanwise in 0 mm horizontal distance to the thin steel plate and just on top of the rigid aluminum plate. In the present investigation, free-stream velocities of U$_\infty$ = 20 m/s and U$_\infty$ = 40 m/s were studied, corresponding to a Reynolds number of Re = 26 000 and Re = 52 000, respectively, based on U$_\infty$ and D.

3   Experimental Method

The measurements were performed in the acoustics wind tunnel of the University of Erlangen-Nuremberg, which is equipped with sound absorbers (unechoic chamber condition).

A 1/2" free field condenser microphone (B&K 4189) at a 1 m distance perpendicular to the overflown side of the flexible plate is employed for the sound measurements.

Phase-resolved scanning vibrometer measurements are carried out to identify the vibration modes of the flexible plate. For this purpose, a Polytec single-point Laser-Doppler velocimeter (OFV-303) is used together with a Polytec scanning vibrometer (OFV-056). The single-point vibrometer constantly detects the vibrations of the centre point of the plate, where the highest amplitudes are expected, while the surface of the plate is scanned with the scanning vibrometer. This measurement yields the amplitude and the phase of the plate vibration at each node of the measurement grid (15×19 points).

To investigate the structure-acoustic interaction, correlation measurements with the single-point velocimeter and the microphone are carried out. Simultaneous recording of the radiated sound in the far-field and the velocity of the plate surface is guaranteed by the data acquisition card employed (NI 4472).

For the measurement of turbulent velocity fluctuations at high sampling rates, hot-wire anemometry (HWA) is applied using a three-component hot-wire probe (Dantec 55P91). A state-of-the-art StreamLine system by Dantec is employed. The measurements are made at different positions in main flow direction along two lines 10 mm and 20 mm above the flexible plate. At each location, a measurement time of 55 s is used at a sampling rate of 20 kHz.

4   Numerical Method

For the acoustics computations, the in-house finite-element multi-physics solver CFS++ [5] is applied. This program is based on a finite-element discretization of the wave equation which describes the propagation of sound to the far field. Thereby, the acoustic fluid is at rest, i.e., the mean flow is not taken into account. Structure-acoustic coupling is incorporated by applying appropriate boundary conditions to the wave equation.

The phase-resolved vibrometer measurements result in information on amplitude and phase of the plate displacement at discrete frequencies. Applying these results to the plate (Dirichlet boundary condition), the velocity field of the plate surface is computed in the frequency domain by use of the Finite Element Method. The normal component of the acoustic particle velocity at the interface between structure and acoustic fluid is set to the velocity of the plate surface in normal direction. Based on this, the time-harmonic sound pressure at the microphone position is computed in the frequency domain at certain frequencies. The results comprise the superpositon of different modes without performing a modal analysis.

5   Results

5.1   Measured Sound Radiation

Figure 3 and 4 show frequency spectra of the measured sound pressure level for U_∞ = 20 m/s and 40 m/s. For U_∞ = 20 m/s, the spectrum of the case without obstacle shows several peaks in the range between 100 and 200 Hz, which corresponds approximately to the first eigenfrequency of the plate obtained by modal analysis. In the higher frequency range, there is only a small difference from the reference case with the empty test section. The spectra obtained for the cases with obstacle are very similar. In comparison with the empty test section, the sound radiation of the flexible plate with obstacle shows a prominent peak at about 115 Hz, which corresponds exactly to the first eigenfrequency of the plate. Additionally, at higher frequencies a large increase in broadband noise is observed.
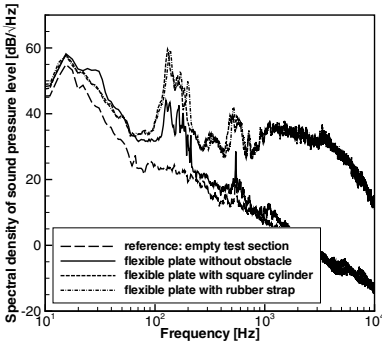
Fig. 3. Sound pressure level at a 1 m distance perpendicular to the plate (U_∞ = 20 m/s)
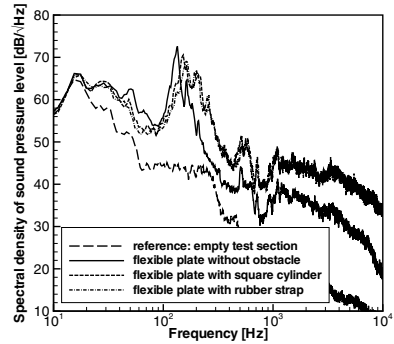
Fig. 4. Sound pressure level at a 1 m distance perpendicular to the plate (U_∞ = 40 m/s)

The sound pressure level of the tonal noise component at 115 Hz in Figure 3 is much lower in the case without obstacle than in the cases with obstacle. However, this finding cannot be generalized. In the mesurements a strong influence of the free-stream velocity U_∞ on the acoustic field was observed. Overall, the sound pressure levels for U_∞ = 40 m/s (see Figure 4) are significantly higher than for U_∞ = 20 m/s, which is in accordance with expectation. However, in this case the presence of an obstacle leads to a peak between 100 and 200 Hz which is lower and wider than without obstacle while the broadband noise over 1 kHz is higher than in the case without obstacle. The rubber strap as obstacle leads to a stronger reduction of the height of the tonal peak at around 115 Hz than the square cylinder obstacle. To understand this phenomenon and to separate vibrational sound from flow-induced sound, detailed investigations of the structural movement and the turbulent flow field were conducted.
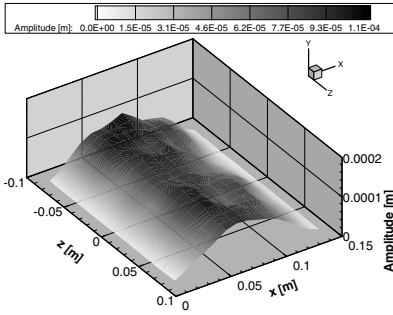
Fig. 5. Distribution of the vibrational amplitude of the flexible plate without obstacle at 115 Hz ($U_\infty = 40$ m/s)
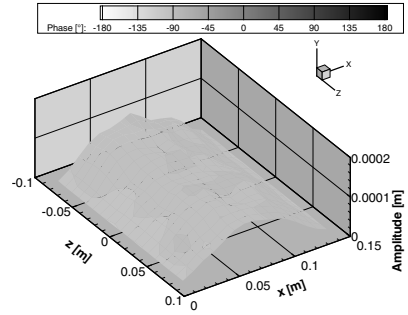

Fig. 6. Distribution of the vibrational phase of the flexible plate without obstacle at 115 Hz ($U_\infty = 40$ m/s)
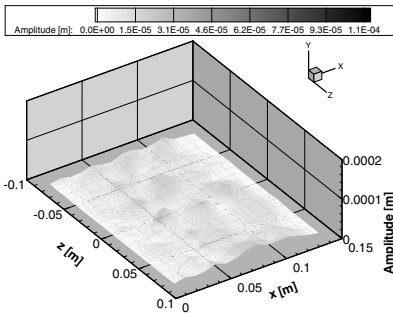

Fig. 7. Distribution of the vibrational amplitude of the flexible plate with square cylinder at 115 Hz ($U_\infty = 40$ m/s)
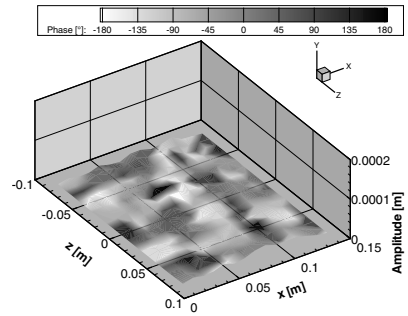

Fig. 8. Distribution of the vibrational phase of the flexible plate with square cylinder at 115 Hz ($U_\infty = 40$ m/s)

5.2   Fluid-Structure Interaction

The distributions of amplitude and phase of the plate vibration at 115 Hz for the case without obstacle and the case with square cylinder are depicted in Figures 5 and 6 and in Figures 7 and 8, respectively. The displacements were measured with the scanning vibrometer at $U_\infty = 40$ m/s. One can clearly identify the first eigenmode of the flexural vibration of the plate in the case without obstacle. Contrary, the case with obstacle shows a diffuse excitation of the surface of the flexible plate.

Figure 9 shows frequency spectra of the measured vibration amplitude of the plate which are averaged over the 285 points of the measurement grid. The spectrum for the setup without obstacle shows a prominent peak at about 115 Hz, which corresponds to the first eigenfrequency of the plate. In agreement with Figure 7, the spectra for the cases with obstacle show significantly smaller vibration amplitudes without any sharp peak.
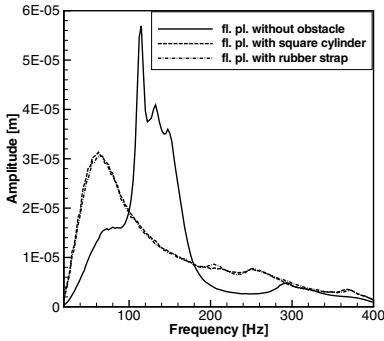
Fig. 9. Frequency spectra of the measured vibration amplitude, averaged over plate area ($U_\infty = 40$ m/s)
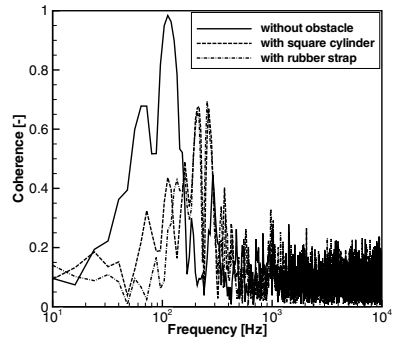

Fig. 10. Spectra of the coherence between sound pressure signal and plate velocity signal ($U_\infty = 40$ m/s)
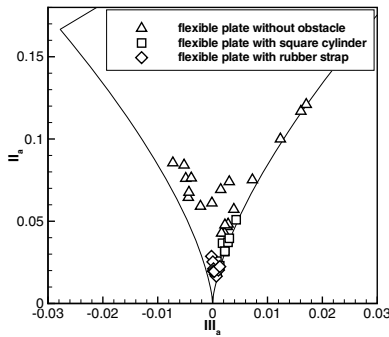

Fig. 11. Invariant map with three-component hot-wire measurement data ($U_\infty = 40$ m/s)

To identify the contribution of the plate vibration to the sound in certain frequency ranges, measurements of the correlation between the acoustic pressure at the microphone position and the velocity in the center point of the vibrating plate were conducted. The corresponding coherence spectra are provided in Figure 10. In the case without obstacle a strong correlation is found around 115 Hz, which is in accordance with expectation in view of the measured sound pressure level and the measured plate vibration. In agreement with the spectra of the sound pressure level in Figure 4, the cases with obstacle show similar results with a lower and wider peak in the coherence spectra. The results of the correlation measurements indicate that the tonal low-frequency noise is due to the structural vibration of the flexible plate, whereas the high-frequency broadband noise is due to flow-induced sound.

The data of the three-component hot-wire measurements plotted in an anisotropy invariant map [6] are shown in Figure 11. In contrast to the case without obstacle, the cases with obstacle can be found in the lower middle of the invariant map. This means that the turbulence generated by the obstacles close to the plate is much more

isotropic than in the turbulent boundary layer in the flow without obstacle. A property of isotropic turbulent flows is a short correlation length of the turbulent patterns. This leads to an uncorrelated excitation of the plate (see Figure 7) and consequently to a reduction in the peak of the tonal frequency and to more broadband noise than in the better correlated flow without obstacle (see Figure 4). Moreover, the rubber strap leads to a stronger isotropic turbulence than the square cylinder obstacle, which can be seen as explanation for the stronger reduction of the height of the tonal peak in Figure 4. It seems that additional vibrations of the flexible rubber strap are the reason for the stronger isotropy of the turbulent fluctuations in comparison to the case with the rigid square cylinder.

5.3   Simulated Sound Radiation

Figures 12 and 13 show a comparison of the measured and the simulated sound pressure level at 1 m distance perpendicular to the overflown side of the flexible plate for U_∞ = 20 m/s and U_∞ = 40 m/s, respectively. Results of the phase-resolved scanning vibrometer measurements acted as input for the calculation of the sound propagation to the far field with CFS++.
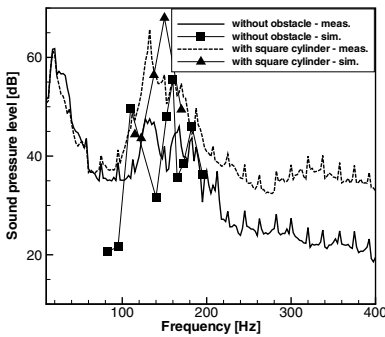

Fig. 12. Measured and simulated sound pressure level at a 1 m distance perpendicular to the plate (U_∞ = 20 m/s)
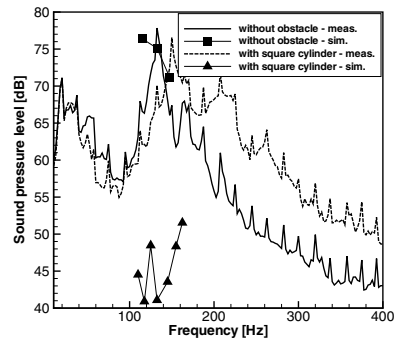
Fig. 13. Measured and simulated sound pressure level at a 1 m distance perpendicular to the plate (U_∞ = 40 m/s)

For U_∞ = 20 m/s, both cases without obstacle and with square cylinder show a good agreement between measurement and simulation. The tendency is predicted correctly by the computational method with higher amplitudes in the case with obstacle in front of the plate structure. The good result of the computation of the sound pressure level based on the measured velocity field of the plate surface indicates that the sound generation at these discrete frequencies is dominated by the vibration of the flexible structure and not by the flow-induced noise due to turbulent fluctuations.

For U_∞ = 40 m/s, one can observe a nearly in-phase movement of the plate surface in the case without obstacle which corresponds to an acoustic monopole (see Figure 6).

In this case the simulated sound pressure level agrees very well with the measurement (see Figure 13). Contrary, in the case with square cylinder no correlation of the phase is observable in Figure 8. The difference of around 30 dB between measurement and simulation indicates that the noise induced by the structural vibration contributes significantly less to the detected sound in the far-field than the noise induced by the turbulent fluctuations in the wake of the obstacle.

6   Conclusion

Experimental and numerical investigations of the fluid-structure interaction and the radiated sound induced by the turbulent flow over a flexible plate structure were conducted. Based on the scanning vibrometer measurements of the plate vibration, the sound radiation to the far field was computed employing the finite-element multi-physics solver CFS++. Three-component hot-wire measurements provided detailed information concerning the distribution of the turbulent velocity fluctuations in space. Microphone measurements were performed to generate a basis of comparison. For $U_\infty = 40$ m/s, the presence of an obstacle right in front of the flexible plate led to a reduction of tonal low-frequency vibrational noise due to an uncorrelated excitation of the plate by strong isotropic turbulence. Simultaneously, the stronger turbulence resulted in more high-frequency broadband noise than in the case without obstacle. For a conveyance this means that less noise is radiated into the passenger cabin.

Acknowledgements

References

[1] Davies, H.G.: Sound from Turbulent-Boundary-Layer-Excited Panels. Journal of the Acoustical Society of America 49(3), Part 2, 878–889 (1971)

[2] Howe, M.S., Shah, P.L.: Influence of Mean Flow on Boundary Layer Generated Interior Noise. Journal of the Acoustical Society of America 99(6), 3401–3411 (1996)

[3] Zolotarev, I.: Fluid-Structural-Acoustical Interactions of a Thin Plate in a Channel with Flowing Fluid. American Society of Mechnical Engineers 1, 403–410 (1997)

[4] Vergne, S., Auger, J.-M., Périé, F., Jacques, A., Nicolopoulos, D.: 'Aeroelastic Noise. In: Wagner, C., Hüttl, T., Sagaut, P. (eds.) Large-Eddy Simulation for Acoustics, pp. 272–293. Cambridge University Press, Cambridge (2007)

[5] Kaltenbacher, M., Hauck, A., Triebenbacher, S., Link, G., Bahr, L.: CFS++: Coupled Field Simulation. Tech. Rep., Department of Sensor Technology, University of Erlangen-Nuremberg (2007)

[6] Lumley, J.L.: Computational Modelling of Turbulent Flows. Advances in Applied Mechanics 18, 123–176 (1978)

Large–Eddy Simulation of
Three–Dimensional Cavity Flow Using a
Time–Conservative Finite–Volume Method

Orhan Aybay[1], Michael Breuer[1], and Li He[2]

[1] Institute of Fluid Mechanics, Friedrich–Alexander University Erlangen–Nuremberg,
Cauerstr. 4, 91058 Erlangen, Germany
`orhan.aybay@lstm.uni-erlangen.de`
[2] Department of Engineering Science, Oxford University, Oxford, UK

Summary

A three–dimensional time–conservative finite–volume method is employed for the numerical analysis of the compressible flow and sound generation of an open rectangular cavity with a length–to–depth (L/D) ratio of 5 and a width–to–depth (W/D) ratio of 1. A Mach number of 0.85 and a Reynolds number of 6.8 million based on the cavity length are used as flow conditions. The large–eddy simulation (LES) technique is used in order to predict the turbulent flow field and the near–field cavity noise directly. Numerical results are compared with experimental data and results of high–order numerical schemes for sound pressure level (SPL) along the cavity floor. The computed near–field results using the present second–order scheme show high accuracy and high resolution comparable to those of high–order numerical schemes.

1 Introduction

Compressible flows over open cavities have significant industrial applications, such as car sunroof, aircraft weapon bay, and landing gear wheel well. The flow over cavities generates very complex flow fields and involves shear layer instabilities, turbulence, aeroacoustics, flow separation, and reattachment. Open cavity flows are governed by a feedback mechanism. Instability waves are generated in the free shear layer and convected from the cavity leading edge to the cavity rear wall along the shear layer. Due to the interaction between the vortices and the back wall of the cavity, strong pressure variations and acoustic waves are generated in the vicinity of the cavity rear wall. Part of the acoustic waves radiate into the far–field and the other part of the acoustic waves (i.e. pressure waves) propagate inside the cavity in the upstream direction. When the pressure waves reach the cavity leading edge they further excite vortical disturbances in the shear layer and cause the shedding of new vortices. Since these vortical structures are convected again in the streamwise direction along the shear layer, a feedback loop results. Self–sustained oscillations inside the cavity generate intense density and pressure fluctuations that may lead to strong vibrations up to structural damage as well as aerodynamic and acoustic problems. Initial investigations to understand the physics of

the flow over rectangular cavities were conducted by Rossiter [1] in 1964. Furthermore, a well–known semi–empirical relation to predict the frequency of the cavity tones was first proposed by him.

The modeling requirements of aeroacoustics problems are substantially different from traditional fluid dynamics problems. Even loud flows radiate a small fraction of their total energy as sound [2]. The acoustic signals are typically much smaller than those of the mean flow variables. The sound intensity is five to six orders smaller [3]. The numerical schemes should resolve acoustic waves with low dissipation and dispersion errors in order to obtain accurate sound prediction. Thus high–order numerical schemes [3,4] have been widely used to investigate the cavity noise [5,6,7,8]. However, they attend to have difficulties in simulating regions with high gradients or discontinuities, e.g., shock waves. The major drawbacks of high–order schemes are the lack of a shock capturing property and the difficulty to deal with complex geometries.

In this study, the objectives were twofold. On the one hand, to develop an advanced high resolution, low dissipation second–order accurate scheme based on a time–conservative finite–volume approach to be able to simulate complex unsteady aerodynamic and aeroacoustic problems similar to high–order schemes. On the other hand, to couple this numerical methodology with the LES technique, since LES is well suited to predict the near–field aerodynamic noise directly as well as to simulate the turbulent flow field.

This paper compares the present second–order scheme with the results of high–order numerical schemes [7, 8] as well as experimental data [9, 10] for the flow over a rectangular cavity. The specific case was provided by AGARD [10] as a benchmark problem and experiments were carried out by QinetiQ as part of the project on Turbulence Modeling for Military Application Challenges [9].

2   Numerical Methodology

Numerical analysis of cavity noise prediction is carried out using a high–resolution three–dimensional time–conservative finite–volume method. The flow solver was developed at the School of Engineering, Durham University in UK [12]. The method is based on the space–time conservation element and solution element (CE/SE) method originally proposed by Chang [11] at NASA Glenn Research Center. The original CE/SE method was extended for structured grid by Zhang *et al.* [14].

2.1   Subgrid–Scale Modeling for Compressible Turbulent Flows

The time–conservative finite–volume method is combined with a top–hat filter where the smallest filter width Δ is chosen as equal to the grid spacing. Thus an explicit filtering operation of the velocity distribution assumed to be cell–wise constant leads to the initial distribution again. Hence the governing equations are not *explicitly* filtered and the filtering operation is *implicitly* given by the numerical method used. The full set of governing equations can be found in [12].

In this study due to its simplicity the classical Smagorinsky subgrid–scale (SGS) model [13] is employed. The subgrid–scale stress tensor is modeled as

$$\tau_{ij}^{SGS} = -2C_R \overline{\rho} \Delta^2 \tilde{S}_M (\tilde{S}_{ij} - \frac{1}{3} \tilde{S}_{kk} \delta_{ij}) + \frac{2}{3} C_I \overline{\rho} \Delta^2 \tilde{S}_M^2 \delta_{ij} \tag{1}$$

where $\tilde{S}_M = (2\tilde{S}_{ij}\tilde{S}_{ij})^2$ and $\tilde{S}_{ij} = 1/2 \cdot (\partial\tilde{u}_j/\partial x_i + \partial\tilde{u}_i/\partial x_j)$, $C_R = 0.0324$ and $C_I = 0.00575$ are the Smagorinsky model constants. The filter width Δ is defined as $(\Delta x \cdot \Delta y \cdot \Delta z)^{1/3}$. The first term appearing on the right–hand side of eq. (1) is the incompressible term in Smagorinsky's model and the second term is the compressible correction known as Yoshizawa's expression [12].

The subgrid–scale heat flux is modeled as follows

$$q_i^{SGS} = -C_p \frac{C_R \rho \Delta^2 \tilde{S}_M}{Pr_t} \frac{\partial\tilde{T}}{\partial x_i} \tag{2}$$

where C_p and $Pr_t = 0.9$ are the specific heat and turbulent Prandtl number, respectively. Expressions defining the resolved shear stress τ_{ij} and the resolved heat flux q_i can be found in [12].

2.2 Time–Conservative Finite–Volume Method

The time–conservative finite–volume method employed in this study is based on a multiblock structured grid in three–dimensional space, which was extended from the numerical scheme given by Zhang *et al.* [14] with some modifications [12]. In this method, spatial and temporal discretizations are unified. The conservation of space–time fluxes is enforced over the surface of the control volume. The conservation form of the three–dimensional unsteady Navier–Stokes equations with respect to a stationary reference frame, with no external body force and heat generation can be expressed as:

$$\frac{\partial \mathbf{U}}{\partial t} + \frac{\partial \mathbf{F}}{\partial x} + \frac{\partial \mathbf{G}}{\partial y} + \frac{\partial \mathbf{H}}{\partial z} = \frac{\partial \mathbf{F_v}}{\partial x} + \frac{\partial \mathbf{G_v}}{\partial y} + \frac{\partial \mathbf{H_v}}{\partial z} \tag{3}$$

where $\mathbf{U}$ is the vector of conservative variables, $\mathbf{F}$, $\mathbf{G}$ and $\mathbf{H}$ are the convective flux vectors and $\mathbf{F_v}$, $\mathbf{G_v}$ and $\mathbf{H_v}$ are the viscous flux vectors in the x, y and z directions, respectively.

Let $x_1 = x$, $x_2 = y$, $x_3 = z$ and $x_4 = t$ be the coordinates of a four–dimensional space–time Euclidean space E_4. By using Gauss' divergence theorem the integral form of eq. (3) can be expressed as follows

$$\oint_{S(V)} \mathbf{h} \cdot d\mathbf{s} = 0 \tag{4}$$

where $\mathbf{h} = (\mathbf{F} - \mathbf{F}_v, \mathbf{G} - \mathbf{G}_v, \mathbf{H} - \mathbf{H}_v, \mathbf{U})$ are the flux vectors in space–time of mass, x–momentum, y–momentum, z–momentum, energy and the vector of conservative variables. $S(V)$ is the surface of an arbitrary space–time region V in E_4 and $d\mathbf{s} = \mathbf{n}d\sigma$ where $\mathbf{n}$ is the outward unit normal vector and $d\sigma$ is the area of a surface element on $S(V)$. The time–conservative finite–volume method integrates eq. (4) in E_4 to evaluate the flow variables. The equation states that the total space–time flux $\mathbf{h}$, leaving the volume V through $S(V)$ vanishes. The discretized conservative variables and the convective fluxes are assumed to be continuous and linearly distributed inside the control volume and they are approximated by the first–order Taylor series expansion whereas the viscous fluxes are assumed to be constant. For any space–time solution point $\mathbf{U}(x, y, z, t)$, $\mathbf{F}(x, y, z, t)$, $\mathbf{G}(x, y, z, t)$, $\mathbf{H}(x, y, z, t)$, $\mathbf{F}_v(x, y, z, t)$,

$\mathbf{G}_v\,(x,y,z,t)$ and $\mathbf{H}_v\,(x,y,z,t)$ are approximated with the help of $\mathbf{U}^*$, $\mathbf{F}^*$, $\mathbf{G}^*$, $\mathbf{H}^*$, $\mathbf{F}_v^*$, $\mathbf{G}_v^*$ and $\mathbf{H}_v^*$, respectively.

The conservative variables ($\mathbf{U}$) are approximated by the first–order Taylor series expansion as follows

$$\mathbf{U}^*\,(x,y,z,t) = (\mathbf{U})_{Q^*} + (\mathbf{U}_x)_{Q^*}\,(x - x_{Q^*}) + (\mathbf{U}_y)_{Q^*}\,(y - y_{Q^*})$$
$$+ (\mathbf{U}_z)_{Q^*}\,(z - z_{Q^*}) + (\mathbf{U}_t)_{Q^*}\left(t^n - t^{n-\frac{1}{2}}\right) \tag{5}$$

where Q^* stands for the solution point. The approximated convective fluxes ($\mathbf{F}$, $\mathbf{G}$, $\mathbf{H}$) are expressed similarly by using the first–order Taylor series expansion. Then, the diffusive fluxes ($\mathbf{F}_v$, $\mathbf{G}_v$, $\mathbf{H}_v$) are assumed to be constant inside the control volume (i.e, $\mathbf{F}_v^*\,(x,y,z,t) = (\mathbf{F}_v)_{Q^*}$).

$(\mathbf{U})_{Q^*}$, $(\mathbf{U}_x)_{Q^*}$, $(\mathbf{U}_y)_{Q^*}$, $(\mathbf{U}_z)_{Q^*}$ and $(\mathbf{U}_t)_{Q^*}$, are the coefficients of the Taylor series expansion in eq. (5) and they are the numerical analogues of the values of $\mathbf{U}$, $\partial\mathbf{U}/\partial x$, $\partial\mathbf{U}/\partial y$, $\partial\mathbf{U}/\partial z$ and $\partial\mathbf{U}/\partial t$ at point Q^*, respectively. Let $(F_{m,l})_{Q^*}$, $(G_{m,l})_{Q^*}$ and $(H_{m,l})_{Q^*}$ are the components of the Jacobian matrices of $\mathbf{F}$, $\mathbf{G}$ and $\mathbf{H}$ associated with the solution point Q^*, respectively. The components of the Jacobian matrices can be defined as

$$(F_{m,l})_{Q^*} = \frac{\partial\mathbf{F}}{\partial\mathbf{U}}, \qquad (G_{m,l})_{Q^*} = \frac{\partial\mathbf{G}}{\partial\mathbf{U}}, \qquad \text{and} \quad (H_{m,l})_{Q^*} = \frac{\partial\mathbf{H}}{\partial\mathbf{U}}. \tag{6}$$

for $m = 1, 2, \ldots, 5$ and $l = 1, 2, \ldots, 5$. The spatial derivatives of $\mathbf{F}$, $\mathbf{G}$ and $\mathbf{H}$ can be expressed by using the chain rule. Here only the spatial derivative of $\mathbf{F}$ in x direction is given and the other spatial derivatives can be expressed similarly

$$(\mathbf{F}_x)_{Q^*} = \sum_{l=1}^{5} (F_{m,l})_{Q^*}\left(\frac{\partial\mathbf{U}}{\partial x}\right)_{Q^*} \tag{7}$$

In order to define the temporal coefficient $(\mathbf{U}_t)_{Q^*}$ of the Taylor series expansion in the eq. (5), eq. (3) can be considered without the viscous flux vectors and the following expression can be obtained

$$(\mathbf{U}_t)_{Q^*} = -\sum_{l=1}^{5}[(F_{m,l})_{Q^*}\,(\mathbf{U}_x)_{Q^*} + (G_{m,l})_{Q^*}\,(\mathbf{U}_y)_{Q^*} + (H_{m,l})_{Q^*}\,(\mathbf{U}_z)_{Q^*}] \tag{8}$$

The viscous diffusion terms have no influence on the distribution of $(\mathbf{U}_t)_{Q^*}$ in each control volume. However, the viscous terms ($(\mathbf{F}_v)_{Q^*}$, $(\mathbf{G}_v)_{Q^*}$ and $(\mathbf{H}_v)_{Q^*}$) will have their contributions on the integral equations. Furthermore, the viscous fluxes can be evaluated as functions of $\mathbf{U}$, $\mathbf{U}_x$, $\mathbf{U}_y$ and $\mathbf{U}_z$.

Consequently, the only independent discrete variables to be solved simultaneously at each grid points are the components of the conservative variables ($\mathbf{U}$) and their spatial gradients ($\mathbf{U}_x$, $\mathbf{U}_y$ and $\mathbf{U}_z$). Although the convective fluxes and the diffusive fluxes can be completely determined inside the control volume as functions of the conservative variables ($\mathbf{U}$) and their gradients ($\mathbf{U}_x$, $\mathbf{U}_y$ and $\mathbf{U}_z$) one should note that the temporal coefficients $(\mathbf{F}_t)_{Q^*}$, $(\mathbf{G}_t)_{Q^*}$ and $(\mathbf{H}_t)_{Q^*}$ of the Taylor series expansions will appear

Table 1. Comparison of modal frequencies at K29

$Mode$	I	II	III	IV
Rossiter's Formula	159 Hz	371 Hz	582 Hz	794 Hz
Experiment [9, 10]	151 Hz	370 Hz	605 Hz	773 Hz
4th–order Scheme [7]	131 Hz	332 Hz	553 Hz	794 Hz
Present 2nd–order Scheme	154 Hz	367 Hz	580 Hz	823 Hz

with additional time terms to evaluate the total space–time flux over the control volume. Hence the flux conservation is not only enforced in space but also in time. Contrarily, traditional methods focus only on the conservation of the spatial fluxes and employ a separate discretization in space and time.

2.3   Test Case: Rectangular Cavity Flow

The cavity geometry with a length–to–depth (L/D) ratio of 5 and a width–to–depth (W/D) ratio of 1 is taken from the M219 cavity configurations [9]. Its length L is 508 mm, the width W and the depth D are equal to 101.6 mm. The dimensions of the computational domain are: $11D$ (streamwise)$\times 4D$ (wall–normal) $\times 2D$ (spanwise). The domain is decomposed into 64 subdomains for parallel computations. The grid consists of $415 \times 130 \times 60 \approx 3.24 \times 10^6$ CVs above the cavity and $260 \times 80 \times 30 \approx 0.625 \times 10^6$ CVs inside the cavity. The flow conditions correspond to a free–stream Mach number of 0.85 and a Reynolds number of 6.8 million based on the cavity length. The stagnation pressure and temperature are set to 99,600 Pa and 305 K, respectively. These flow conditions were imposed as inflow boundary condition and the spatial derivatives of the flow variables were set to zero. The inflow boundary was set to 2 times the cavity depth upstream of the cavity whereas the outflow boundary was set to 4 times the cavity depth downstream of the cavity. A steady turbulent boundary layer profile was implemented at the inflow to achieve the boundary layer thickness of 10.16 mm at the leading edge of the cavity according to estimation of $0.37 \times Re_x^{-0.2}$. Hence the resulting boundary layer thickness at the cavity leading edge was found to be similar to the experimental value. In order to trigger cavity flow oscillations, random velocity fluctuations were added to the mean velocity in the inflow profile. When the self–sustained oscillations inside the cavity started, the perturbations were turned off again. Periodic boundary condition in spanwise and no–slip boundary condition at the walls were imposed. Non–reflecting boundary conditions were applied to the outflow and farfield boundaries. The flux–based nature of the method leads to the use of simple but effective non–reflecting boundary conditions which allow fluxes remain continuous across the boundary surfaces. For example, at the outflow boundary, where there are substantial gradients in y direction, the non-reflecting boundary condition requires that

$$U_i^n = U_{i'}^{n-1}, \qquad (U_x)_i^n = 0, \qquad (U_y)_i^n = (U_y)_{i'}^{n-1}, \qquad \text{and} \quad (U_z)_i^n = 0. \quad (9)$$

where n is the time level and i' is the index of an interior node closest to this boundary.

3   Results and Discussion

Fig. 1 (left) shows a snapshot of the magnitude of the vorticity on the central plane. After the development of the shear layer, vortices break down before the middle of the cavity and grow larger in size whereas they propagate in the streamwise direction. Furthermore, the intensity of the resolved turbulent kinetic energy distribution increases after the vortices broke down as expected and can be seen in Fig. 1 (right).

Numerical results are compared with experimental data [9, 10] as well as the results of high–order numerical schemes by Chen *et al.* [7] and Nayyar *et al.* [8]. A comparison of modal frequencies, i.e. low frequency tones, at K29 ($x/L = 0.95$) is given in Table 1. The computed 1th mode frequency is slightly over–predicted compared to the experimental data with an error of about $+2\%$ whereas the 2nd and 3rd mode frequencies are under–predicted by about -1% and -4%, respectively. Lastly, the 4th mode frequency is over–predicted with an error of about $+6.5\%$. Consequently, all modal frequencies are well predicted and within the 7% error limit with respect to the experimental data as well as Rossiter's semi–empirical predictions of the modal frequencies [1] given by $f_n = U_\infty/L \cdot (n - \gamma)/(M_\infty + 1/\kappa)$ where U_∞ and M_∞ are the free–stream velocity and the Mach number, respectively. L is the length of the cavity and n is the mode number. $\kappa = 0.57$ and $\gamma = 0.25$ are empirical constants corresponding to the average convection speed of the vortical perturbations in the shear layer and a phase delay, respectively.

Fig. 2 (left) represents the history of pressure fluctuations for a time interval of $0.2\ s$ at the K29 position. The simulation is carried out with a time step of $5.0 \times 10^{-7} s$ and the pressure signals were sampled every 330 time steps corresponding to a sampling rate of ≈ 6 kHz which is in accordance with the experimentally used value. After the initial transients exited the domain, the simulation was carried out for $0.25 s$ and the first $0.05 s$ of the pressure signals are truncated. The numerically sampled data is presented in terms of sound pressure level (SPL). The SPLs are related to the energy carried by the sound wave, defined by $SPL(dB) = 20 \log_{10} P_{rms}/P_{ref}$ where the P_{rms} is the root–mean–square pressure fluctuation and $P_{ref} = 2.0 \times 10^{-5} Pa$. The computed pressure spectrum decomposed into Rossiter modes (low frequency tones) and broadband noise up to $3\ kHz$ is depicted in Fig. 2 (right) since the peak human hearing range is 1 to $3\ kHz$.
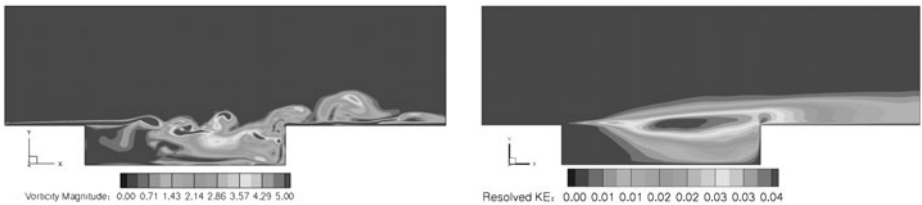

Vorticity Magnitude: 0.00 0.71 1.43 2.14 2.86 3.57 4.29 5.00   Resolved KE: 0.00 0.01 0.01 0.02 0.02 0.03 0.03 0.04

Fig. 1. Snapshot of the magnitude of the vorticity on the central plane of the cavity *(left)* and resolved turbulent kinetic energy *(right)*

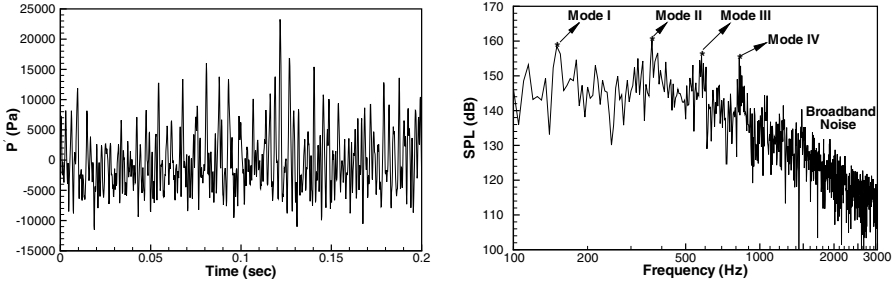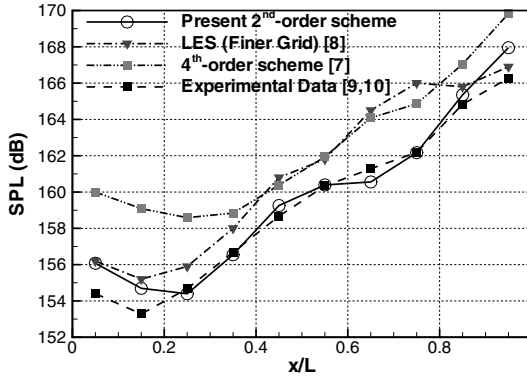**Fig. 2.** History of pressure fluctuations *(left)* and SPL spectrum at K29 *(right)*

Fig. 3. Comparison of SPL along the cavity floor

The intensity of the noise generation inside the cavity can be seen from the comparison of SPL along the cavity floor with experimental data as well as results of other numerical schemes available in the literature [7, 8]. The results obtained by Chen *et al.* [7] is based on a 4th–order central finite–difference scheme whereas the numerical method used by Nayyar *et al.* [8] is a cell–centered finite–volume method where MUSCL interpolation is used to provide 3rd–order accuracy. Fig. 3 clearly shows that the SPL curve increases in streamwise direction in the cavity due to the spreading of the energy from the shear layer after it breaks down. The SPLs computed by the present time conservative scheme along the cavity floor are in very good agreement with the experimental data [9, 10]. Compared to other numerical results using either an LES on a finer grid ($\approx 8.4 \times 10^6$ CVs) [8] or a fourth–order accurate scheme [7] the deviations to the measurements are much smaller.

4   Conclusions

Numerical analysis of the compressible flow and sound generation of an open rectangular cavity have been carried out by a three–dimensional modern flow simulation

technique, namely time–conservative finite–volume method. Instantaneous iso–surfaces of the vorticity demonstrate the highly unsteady and three–dimensional nature of the cavity flow. The cavity is dominated by the low frequency tones and they are well predicted with respect to the experimental data as well as Rossiter's relation. Near–field spectral results are also in very good agreement with the experimental data. The results computed by the second–order time–conservative finite–volume method show high accuracy and high resolution comparable to those of high–order numerical schemes.

References

[1] Rossiter, J.E.: Wind Tunnel Experiments on the Flow Over Rectangular Cavities at Subsonic and Transonic Speeds. Reports and Memoranda. Aeronautical Research Council 3438 (1964)

[2] Colonius, T., Lele, K.S.: Computational Aeroacoustics: Progress on Nonlinear Problems of Sound Generation. Progress in Aerospace Sciences 40, 345–416 (2004)

[3] Tam, C.K.: Computational Aeroacoustics: An Overview of Computational Challanges and Applications. J. of Comp. Fluid Dynamics 18(6), 547–567 (2004)

[4] Lele, S.K.: Compact Finite Difference Schemes with Spectral–Like Resolution. J. of Comp. Physics 103(1), 16–42 (1992)

[5] Lai, H., Luo, K.H.: A Three–Dimensional Hybrid LES–Acoustic Analogy Method for Predicting Open–Cavity Noise. J. of Flow Turbulence and Combustion 79, 55–82 (2007)

[6] Gloerfelt, X., Bogey, C., Bailly, C.: Large–Eddy Simulation for Acoustics. In: Wagner, C., Hüttl, T., Sagaut, P. (eds.), ch. 6.3. Cambridge University Press, Cambridge (2007)

[7] Chen, X., Sandham, N.D., Zhang, X.: Cavity Flow Noise Predictions. University of Southampton, Report No. AFM–07/05, pp. 1–51 (2007)

[8] Nayyar, P., Barakos, G.N., Badcock, K.J.: Analysis and Control of Weapon Bay Flows. RTO–MP–AVT–123, NATO–RTO (2005)

[9] Peshkin, D.A.: TurMMAC Application Challenge Test Case Specification: M219 Cavity. QINETIQ/FST/CAT/WP020905 (2002)

[10] de Henshaw, M.J.C.: M219 Cavity Case. Verification and Validation Data for Computational Unsteady Aerodynamics, RTO-TR-26, AC/323(AVT)TP/19, 473–480 (2000)

[11] Chang, S.C.W.: The Method of Space–Time Conservation and Solution Element – A New Approach for Solving the Navier–Stokes and Euler Equations. J. of Comp. Physics 119, 295–324 (1995)

[12] Aybay, O., He, L.: Development of a High–Resolution Time Conservative Finite Volume Method for Large–Eddy Simulation. Engineering Letters 16(1), 96–103 (2008)

[13] Smagorinsky, J.S.: General Circulation Experiments with the Primitive Equations. Monthly Weather Review 91(3), 99–165 (1963)

[14] Zhang, Z.C., Yu, S.T., Chang, S.C.: A Space–Time Conservation Element and Solution Element Method for Solving the Two and Three–Dimensional Unsteady Euler Equations using Quadrilateral and Hexahedral Meshes. J. of Comp. Physics 175, 168–199 (2002)

A Hybrid Method for CAA

Andreas Birkefeld and Claus-Dieter Munz

Institute of Aerodynamics and Gasdynamics, Universität Stuttgart, Germany
`birkefeld@iag.uni-stuttgart.de`
`http://www.iag.uni-stuttgart.de`

Summary

A scheme for computational aeroacoustic calculations on coupled structured and unstructured meshes for industrial applications is presented. Based on two sophisticated CAA solvers, one finite difference code for structured grids and one discontinuous Galerkin solver for unstructured grids, the described framework is able to combine the advantages of both grid types and thereby reduce the effort for simulations of aeroacoustics in complex structures. In this paper the underlying coupling mechanisms and the process management are described. Finally the operability and the ability to preserve the convergence order of the single schemes are shown.

1 Introduction

For the simulation of aeroacoustical phenomena in complex structures, e.g. high lift wing configurations or tube flows with obstacles the generation of a structured grid is very complicated or even impossible and consequently, the application of unstructured grids is advantageous. However, in the far field which very often covers the larger part of the computational domain the generation of structured grids is really straightforward, so one can benefit from their advantages in terms of memory demand, grid handling effort and visualization. This leads to the idea of coupling schemes that work on those different types of grids. Former work has been done in this field by Utzmann [1], who worked on the coupling of different solver types, equations, orders, grid types and grid spacing, delivering an expert-system-like solver framework. This project is based on this work and aims at the development of a user friendly framework for industrial application. Hence, the bandwidth of included solvers and coupling mechanisms has been reduced drastically and more aspects of the preprocessing and initialization have been automated.

2 The Used Codes

2.1 PIANO

PIANO (Perturbation Investigation of Aerodynamic Noise) has been developed by the Institute of Aerodynamics and Flow Technology (IAS) at the German Aerospace Center

(DLR) in Braunschweig. It is a finite difference solver for linearized acoustic equations (Linearized Euler Equations and Acoustic Perturbation Equations) on block structured, boundary-fitted grids.

PIANO applies a Dispersion-Relation-Preserving (DRP) discretization of 4th order in space, the time integration is done either with a standard Runge-Kutta scheme of 4th or 6th order or with a Low-dissipation and Low-dispersion Runge-Kutta scheme (LDDRK). PIANO is parallelized using the Message Passing Interface (MPI). The decomposition of the computational domain depends on the block structure. For more information about PIANO's mode of operation refer to [2].

At the moment further development of PIANO is ongoing which includes the grid coupling described in this paper. These improvements are referred to as PIANO+. In this paper that name is used as a short term for the coupled framework consisting of NoisSol and PIANO.

2.2   NoisSol

NoisSol has been developed by the Institute of Aerodynamics and Gasdynamics at Universität Stuttgart. It uses an ADER-DG scheme (Arbitrary High Order Scheme using Derivatives Discontinuous Galerkin) of high order to solve the linearized acoustic equations on unstructured grids. The element types used are triangles and tetrahedrons. It applies global or local timestepping. For details of the numerical scheme refer to [3]. NoisSol is parallelized with MPI as well.

3   Grid Coupling

The decomposition of the computational domain will be done such that both programs work on non overlapping grids with straight coupling interfaces. The information of the coupling partner will be included using ghost cells (NoisSol) or ghost points (PIANO). The ghost points and cells will be generated by mirroring the last cells / nodes inside the computational domain at the interface. Due to the size of PIANO's finite difference stencil three rows of ghost points are needed. NoisSol only needs ghost cells for those elements, which share one edge (2D) or surface (3D) with the coupling interface.

Former work on the coupling between FD and DG showed that continuity of the primitive variables rather than continuity of the fluxes is very suitable to prevent artificial reflections at the interface. Thus, in PIANO+ this method is used for the coupling.

3.1   Setting of the Ghost Points

PIANO applies different multi-step Runge-Kutta-schemes for the time integration. It is necessary to update the ghost points after each Runge-Kutta step. For transient boundary conditions it is known that setting the boundary values of the intermediate, unphysical time levels with physical values will degrade the scheme to 2nd order. Carpenter et.al. [4] suggest a method to avoid this effect using the value and the time derivatives of the ghost point at the initial, physical Runge-Kutta level of each time step.

To determine the necessary time derivatives of the state at the ghost point position one can benefit from the Cauchy-Kovalevskaja (CK) procedure, which is the key feature

of the ADER-DG scheme. This operation calculates the time derivatives of the degrees of freedom $\hat{\mathbf{u}}_i$ at the beginning of the current time step τ. The data is represented in a modal basis, i.e. as a linear combination of hierarchic basis functions ϕ_i:

$$\mathbf{u}(\mathbf{x}(\xi), t) = \sum_{i=1}^{n_{DegFr}} \hat{\mathbf{u}}_i(t)\, \phi_i(\xi)$$

where n_{DegFr} is the number of degrees of freedom $\hat{\mathbf{u}}_i$, which adds up to $n_{DegFr} = n_{Poly}\,(n_{Poly}+1)\,(n_{Poly}+2)$. n_{Poly} is the maximum polynomial degree of the basis functions. ξ is the position of the ghost point in the DG reference element which can be determined with the inverse of the linear transformation $\mathbf{x} = \mathbf{x}_1\,(1-\xi_1-\xi_2)+\mathbf{x}_2\xi_1+\mathbf{x}_3\,\xi_2$.

Thus, the state within the whole timestep can be developed in a Taylor series at the beginning of the timestep:

$$\mathbf{u}(\mathbf{x}(\xi), t) = \sum_{i=1}^{n_{DegFr}} \sum_{j=0}^{n_{Poly}} \frac{(t-\tau)^j}{j!} \left(\frac{\partial}{\partial t}\right)^j \hat{\mathbf{u}}_i(\tau)\, \phi_i(\xi) \tag{1}$$

Equation (1) allows the calculation of the time derivatives of $\mathbf{u}$ at any time level within the time step:

$$\left(\frac{\partial}{\partial t}\right)^k \mathbf{u}(\mathbf{x}(\xi), t) = \sum_{i=1}^{n_{DegFr}} \sum_{j=k}^{n_{Poly}} \frac{(t-\tau)^{j-k}}{(j-k)!} \left(\frac{\partial}{\partial t}\right)^j \hat{\mathbf{u}}_i(\tau)\, \phi_i(\xi) \tag{2}$$

The coupling information for several timelevels within the next time step can be computed at its beginning. Thus, in case of a larger DG timestep only one data exchange per timestep is necessary, which reduces the communication effort significantly.

3.2   Setting of the Ghost Cells

In the applied ADER-DG scheme information is represented in a modal basis, as described above. Thus, the state in the DG ghost cell needs to be transformed from node based information into the degrees of freedom $\hat{u}_i$ using a L2-projection:

$$\hat{u}_i = \frac{\int_T \Phi_i\, u\, dV}{\int_T \Phi_i\, \Phi_i\, dV}$$

While the denominator can be precalculated analytically, the numerator is calculated by Gauss quadrature after each data exchange. Therefore, the state in the ghost cell has to be known at the Gauss points.

To determine these values in the PIANO domain a polynomial interpolation with an odd maximum order n_{Poly} is used. This allows the use of a symmetric stencil around the cell, in which the point is located. Where required the stencil is shifted away from the interface (figure 2). To allow a fast calculation of the interpolated values at each exchange time level it is convenient to calculate coefficients for each grid point in the

stencil using a Lagrange interpolation scheme. For a point within the cell $[\tilde{i}, \tilde{i} + 1] \times [\tilde{j}, \tilde{j} + 1]$ with known ξ the Lagrange coefficients would be (in case of a non shifted stencil):

$$L_i = \prod_{a=\tilde{i}-n}^{i-1} \frac{\xi_1 - a}{i - a} \prod_{a=\tilde{i}+1}^{\tilde{i}+n+1} \frac{\xi_1 - a}{i - a} \qquad \forall\, i = \tilde{i} - n \ldots \tilde{i} + n + 1$$

$$L_j = \prod_{b=\tilde{j}-n}^{j-1} \frac{\xi_2 - b}{j - b} \prod_{b=j+1}^{\tilde{j}+n+1} \frac{\xi_2 - b}{j - b} \qquad \forall\, j = \tilde{j} - n \ldots \tilde{j} + n + 1$$

where $n = 0.5\,(n_{Poly} - 1)$. These L_i and L_j can be calculated at the beginning of the simulation for each Gauss point and stored. The value of f at the location ξ then would be:

$$f(\xi) = \sum_{i=\tilde{i}-n}^{\tilde{i}+n+1} \sum_{j=\tilde{j}-n}^{\tilde{j}+n+1} f_{i,j}\, L_i\, L_j$$

This calculation needs to be done for each ghost Gauss point at a coupling interface before the data exchange is done.

The in-cell-position ξ of a point has to satisfy the equation

$$\mathbf{x}(\xi) = \sum_{i=0}^{n_{Poly}} \sum_{j=0}^{n_{Poly}} \mathbf{a}_{ij}\, \xi_1^i\, \xi_2^j \tag{3}$$

The factors $\mathbf{a}_{ij}$ are unique for each cell and depend on the values of $\mathbf{x}$ at the grid points in the stencil and can be calculated by solving (3) for each grid point in the stencil.

If the structured grid is non curved and equidistant in the area of the interpolation stencil (which is not implausible for a far field mesh), ξ can be calculated directly from the coordinates of the nearest grid points, which leads to an enormous speedup. Otherwise it has to be determined as solution of the nonlinear equation system (3).

The whole initialization and interpolation process described in parts 3.1 and 3.2 has been presented in 2D only for lack of space but has been developed and implemented for 3D almost identically.
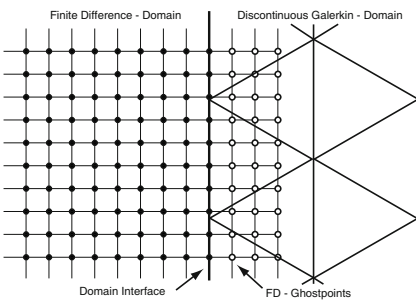
Fig. 1. FD-Ghostpoints
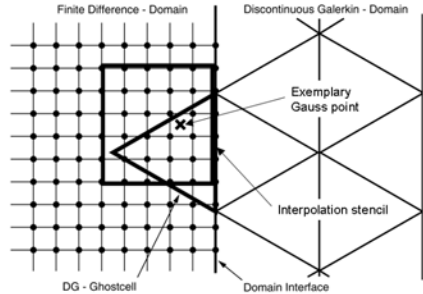
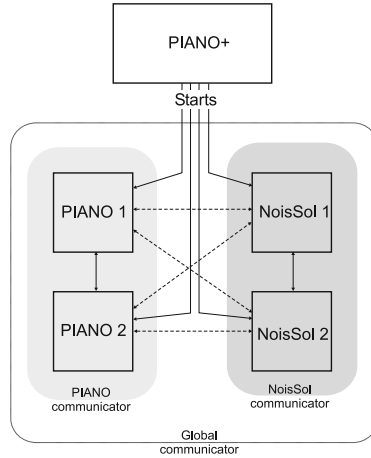**Fig. 2.** DG-Ghostcells

Fig. 3. Communication structure

4   Time Step Coordination

Since the acoustic equation are of hyperbolic type, the timestep of an explicit solver has to be limited by the Courant-Friedrichs-Levy (CFL) condition. Thus, the time step depends on the local cell size and, especially when meshing complex structures, the cell size and consequently the time step may vary noticeably. Hence, the use of local time steps decreases the computation time without any loss in accuracy or stability.

As mentioned before NoisSol applies global or local time stepping. PIANO uses a global time step for all blocks. For the coupling a subcycling is used. That means during every NoisSol time step several PIANO time steps can be done, where this is possible due to larger DG cells.

This subcycling ensures that no temporal interpolation is necessary for the determination of the coupling information in PIANO.

The NoisSol cells at the interface will all use the same time step which is calculated as the minimum of the time steps of all cells involved. The time steps are then adapted to ensure that the NoisSol timestep is a multiple of the PIANO time step and to fit the end and output time levels.

5   Process Management

The coupling is developed such that both included programs are conserved as stand-alone programs. This allows the transfer of new features from the single codes to the coupled version, which thereby benefits from the ongoing improvement work done at the codes.

Since the coupling bases on an information transfer between the two solvers, a common communication infrastructure is necessary. This can be provided by the MPI framework, which is used for both NoisSol's and PIANO's parallelization. The MPI
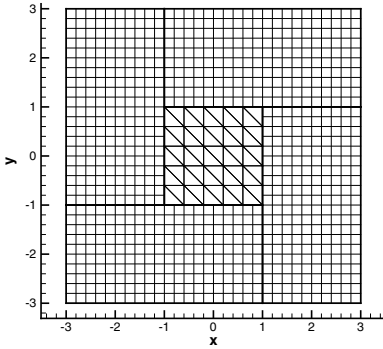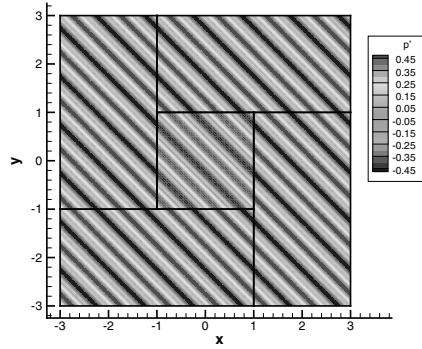
Fig. 4. Mesh

Fig. 5. Initial condition, pressure

2.0 standard defines a feature called *MPI_COMM_SPAWN_MULTIPLE*, which starts arbitrary numbers of instances of different external programs and links them with one global communicator. The processes of each program are additionally linked by another communicator for their internal data exchange.

After their start-up the solvers initialize the coupling automatically. The coupling interfaces are marked as own boundary type during grid generation. The matching interfaces in both grids and the processes hosting them are determined without user interaction.

6   Convergence Test

To proof that the coupling is able to maintain the order of accuracy over the whole domain a convergence test was performed. PIANO has a theoretical convergence order of 4 in space and time, NoisSol will be adjusted to 4th order as well. For this test a simple square shaped domain is chosen in which a small square with an unstructured grid is surrounded by 4 structured blocks which leads to 4 coupling interfaces (Figure 4). The domain is confined by periodic boundaries.

The initial condition is a planar sinusoidal wave, shaped proportional to one of the eigenvectors of the linearized Euler equations. Hence, the initial state represents an acoustical wave which will be transported with the speed of sound. This allows the simple calculation of the local error due to the known analytical solution:

$$(\rho \ u \ v \ p)^T = \mathbf{b} \ sin \left(k_1 x + k_2 y - \omega t \right)$$

where $\mathbf{b} = 0.5 \left(\frac{\rho_0}{c_0} \ -\frac{1}{\sqrt{2}} \ -\frac{1}{\sqrt{2}} \ \rho_0 c_0 \right)^T$ is one of the eigenvectors of the linearized Euler equations with the corresponding eigenvalue $u_0 - c_0$; $k_i = \frac{2\pi}{\lambda_i}$ are the wave numbers in x- and y-direction and $\omega = (-c_0)\sqrt{k_1^2 + k_2^2}$ is the wave speed in normal direction.

The meanflow values are initialized as $\rho_0 = 1.0$, $u_0 = 0$, $v_0 = 0$ and $p_0 = 0.714285714$, which leads to $c_o = 1.0$.

The case presented here was initialized with $\lambda_1 = \lambda_2 = 1$, which results in a wave travelling diagonally through the computational domain in negative x- and y-direction (Figure 5). The total simulated time was $t = 5$, which means that the waves have done about half a cycle through the domain. The convergence rates were calculated with the L_1, L_2 and L_∞ norms of the local error of the acoustic pressure p', evaluated at $t = 5$.

Table 1. Convergence rates

	h	$L_1(p')$	$L_2(p')$	$L_\infty(p')$	$\mathcal{O}_{L_1}$	$\mathcal{O}_{L_2}$	$\mathcal{O}_{L_\infty}$	$\mathcal{O}_{L_1}$	$\mathcal{O}_{L_2}$	$\mathcal{O}_{L_\infty}$
PIANO	0.0500	9,23E-4	1,04E-3	1,77E-3						
	0.0250	6,30E-5	7,09E-5	1,21E-4	3,87	3,87	3,87	(3.83)	(3.83)	(3.81)
	0.0125	4,02E-6	4,52E-6	7,75E-6	3,97	3,97	3,97	(3.96)	(3.96)	(3.96)
NoisSol	7,07E-2	8,03E-4	9,04E-4	1,61E-3						
	3,54E-2	5,58E-5	6,28E-5	1,10E-4	3,85	3,85	3,86	-	-	-
	1,77E-2	3,62E-6	4,07E-6	7,13E-6	3,95	3,95	3,95	-	-	-

In table 1 the values in parentheses show the convergence rates for an identical calculation with a completely structured domain. The table shows that the achieved order of accuracy captures the theoretical value very well and is almost identical to the value of the uncoupled scheme. Figure 6 shows that there is no error caused by the coupling. In fact there is a lower local error in the wake of the coupling area which results from the lower local error of the calculation in the unstructured area and which is not disturbed by the coupling interface. The low error magnitude and the design of the test case imply that the final pressure distribution is very similar to figure 5 with a shifted position of the wavefronts and hence is not shown here for lack of space.
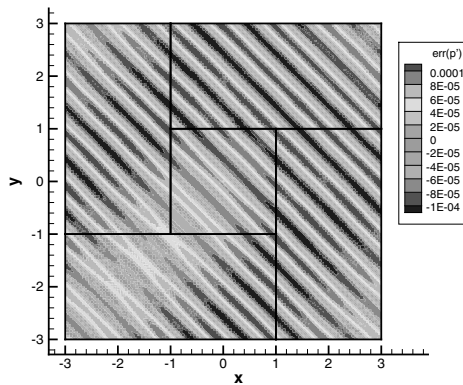

Fig. 6. Local pressure error, t=5

7   Conclusions

A technique for the coupling of structured grids for a finite differences scheme and unstructured grids for a Discontinuous Galerkin scheme was presented. The results indicate the ability of the framework to initialize and operate the coupling completely automated and the operability of the implemented process management. Furthermore, it was shown that the coupling is able to maintain the order of accuracy of the single solvers.

Acknowledgments

References

[1] Babucke, A., Dumbser, M., Utzmann, J.: A coupling scheme for direct numerical simulations with an acoustic solver. In: ESAIM: proceedings (2006)

[2] Delfs, J., Bauer, M., Ewert, R., Grogger, H., Lummer, M., Lauke, T.: Numerical Simulation of Aerodynamic Noise with DLR's aeroacoustic code PIANO. Manual, IAS DLR Braunschweig (2007)

[3] Dumbser, M.: Arbitrary High Order Schemes for the Solution of Hyperbolic Conservation Laws in Complex Domains. PhD thesis, Universität Stuttgart (2005)

[4] Carpenter, M.H., Gottlieb, D., Abarbanel, S., Don, W.S.: The theoretical accuracy of Runge-Kutta time discretizations for the initial boundary value problem: A careful study of the boundary error. ICASE report No.93-83, 78 (1993)

Aerodynamic and Aeroacoustic Analysis of Contra-Rotating Open Rotor Propulsion Systems at Low-Speed Flight Conditions

Arne Stuermer and Jianping Yin

DLR Institute of Aerodynamics and Flow Technology
Lilienthalplatz 7, 38108 Braunschweig, Germany

Summary

Contra Rotating Open Rotor (CROR) propulsion systems have come back into focus as a possible economic and environmentally friendly powerplant for future transport aircraft. Having been widely applied to the simulations of single rotation propellers, the DLR CFD code TAU and the aeroacoustic analysis tool APSIM have been employed for the analysis of the complex aerodynamics and aeroacoustics of this type of propulsion system. In order to demonstrate the codes applicability to these simulations a generic 8x8 pusher CROR powerplant was designed and uRANS computations at typical sea-level take-off conditions of $M = 0.2$ were performed for two angles of attack. The results allow for a detailed analysis of the aerodynamic interactions between the two rotors as well as the noise generation mechanisms.

1 Introduction

Increasing environmental and economic pressures have renewed interest in Contra-Rotating Open Rotor propulsion systems as a powerplant for commercial transport aircraft, as they promise a step change in efficiency due to their ultra-high bypass ratio. These engines were the focus of a large research undertaking led by NASA and US industry in the late 1970s and 1980s, motivated by the high fuel costs arising from the 1973 oil crisis [1]. This project included experimental investigations both in the wind tunnel and in flight test as well as inviscid simulations of CROR configurations [2]. However, primarily due to the decrease in oil prices, interest in bringing these engines to market waned and further research was essentially abandoned. In todays context of heightened focus on fuel efficiency and environmental impact the primary challenges for the realization of a commercially viable CROR engine relate to the issues of noise emissions and installation effects with the airframe. The former is an important aspect during the low-speed take-off and approach phases of flight, where the impact on community noise needs to be addressed. The rapid improvement of numerical tools in aerodynamics and aeroacoustics such as the DLR TAU and APSIM-Codes allow these methods to play a vital role in enhancing understanding and developing solutions for these issues [3, 4]. In this paper, the results of a numerical investigation of a generic 8x8 CROR are discussed. Unsteady Reynolds-Averaged Navier-Stokes (uRANS) simulations for the isolated powerplant at typical low-speed conditions were performed for

two angles of attack and the noise emissions were computed using a method based on the Ffowcs-Williams/Hawkings (FW-H) equations. A detailed analysis of the results is presented, highlighting the complex aerodynamic and aeroacoustic phenomena of CROR propulsion systems.

2   Geometry and Test Case Definition

A generic CROR powerplant was designed as a numerical test rig to allow for the study of relevant parameters that affect the aerodynamic and aeroacoustic performance. The engine was aimed at a take-off thrust requirement of 88kN at sea level conditions and cruise thrust of 19kN for flight at $M = 0.75$, making it representative of a powerplant for typical single-aisle aircraft. The initial baseline CROR version under study is an 8x8 bladed pusher configuration with a rotor diameter of $D = 4.2672$m. The general layout of the powerplant is shown in figure 1. A generic blade for use in both rotors was designed using blade element theory and CFD-computations, with the focus on obtaining a representative blade shape in terms of the aerodynamic performance [5]. The simulations are performed for the two angles of attack of $\alpha = 0°$ and $4°$ at sea level conditions with a Mach number of $M = 0.2$. The rotational speeds of both rotors are set identically to 1029rpm, while the blade pitch settings leading to a power balance between the two rotors are $36.35°$ and $35°$ for the front and aft rotors respectively. The core engine inlet and exhaust flow fields are simulated using a boundary condition available in the DLR TAU-Code.
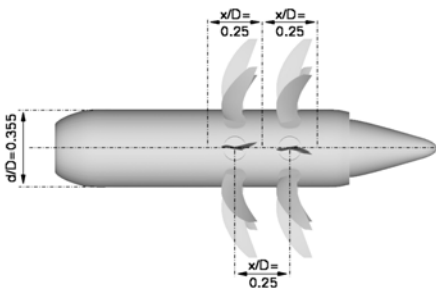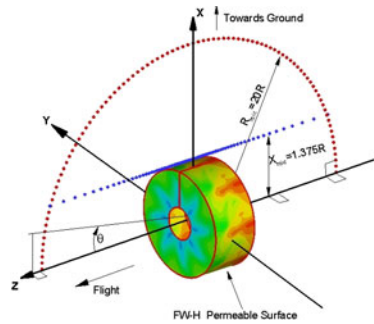

Fig. 1. CROR geometric layout

Fig. 2. Microphone definitions

3   Simulation Approach

A coupled simulation utilizing the DLR TAU-Code for the uRANS CFD computations and the DLR APSIM-Code for a subsequent computation of the noise emissions was performed, a process chain that has already been successfully applied to a number of

propeller and helicopter investigations [4, 6]. The DLR TAU-Code is an unstructured finite-volume vertex-based CFD solver. For the simulation described here, spatial discretization of the convective fluxes is done using a second order central differencing scheme with matrix dissipation while the viscous fluxes are discretized with central differences. Turbulence is modeled with the 1-equation model of Spalart-Allmaras as modified by Edwards [7, 8]. The well-established dual time approach is used in the DLR TAU-code to compute unsteady flows with a temporal resolution set to equate to a rotor rotation of $\Delta\Psi = 0.5°$ per physical time-step [9]. In order to simulate the relative motion of the rotors use is made of the codes Chimera capability as well as the implemented motion libraries [10].

The meshes for the isolated CROR configuration were generated using either the CentaurSoft Centaur or the ANSYS ICEM CFD mesh generation software and drew on grid resolution requirement experienced gained in past work on propeller and open rotor simulations. Special care was taken to ensure an adequate boundary layer resolution, with the spacing of the initial cell layer on the surfaces set to yield values of the non-dimensional wall-distance of $y+ = 1$ to allow for a good resolution of the viscous sublayer. The complete 20-block Chimera mesh which was used for the uRANS computations consists of $40.858.867$ nodes.

The simulations were run using 320 processors of the DLR $C^2A^2S^2E$-cluster in Braunschweig. A total of 6 full propeller revolutions were computed in order to obtain a fully periodic solution, which resulted in a runtime of 15 days for each case.

The Aeroacoustic Prediction System based on Integral Method (APSIM) was developed at the DLR Institute of Aerodynamics and Flow Techniques for the prediction of rotor or propeller noise radiated in the free far-field. The methodology of APSIM is based on both Ffowcs-Williams/Hawkings (FW-H) and Kirchhoff formulations and only linear sound propagation is taken into account. APSIM is designed to calculate wave propagation over large distances in uniform flows. The sound propagation is computed employing a permeable surface approach by using the unsteady CFD data on the nacelle Chimera boundary as input, as shown in figure 2. The calculations, performed in the time domain, deliver a pressure time history at any desired observer location. This is Fourier analyzed to arrive at the acoustic spectrum.

4   Aerodynamic Analysis

The unsteady simulations allow for a detailed analysis of the forces and moments acting on both individual blades as well as the rotors as a whole during the course of one rotation. Figure 3(a) compares the development of a reference blades thrust for the two low-speed cases investigated, with the axial flow case shown in black while the blade force for the powerplant at $\alpha = 4°$ angle of attack are shown in red. Forward rotor forces are shown as solid lines, while the aft rotor is represented by dash-dotted lines. At axial flow the blades of both the front and aft rotor show a 32- or 16-period sinusoidal oscillation of the thrust coefficient around a constant mean value respectively. This oscillation is due to the mutual interactions between the blades of the two rotors. The aft rotors blades shows notably larger amplitudes in the fluctuations, caused by the interactions with the forward rotors blade wakes and tip vortices. The influence of the
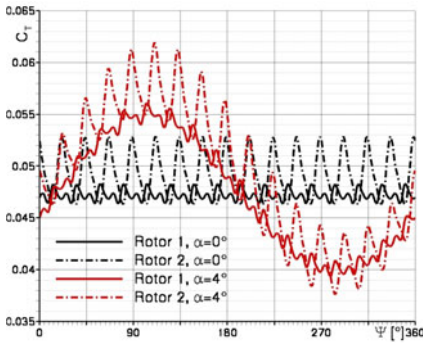
(a) Blade thrust coefficient for $\alpha = 0°/4°$
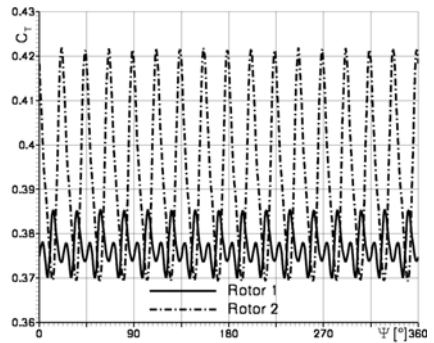
(b) Rotor thrust coefficient at $\alpha = 0°$

Fig. 3. CROR blade and rotor thrust coefficient development during one rotation

angle of attack on the blade force development during a rotation becomes apparent when comparing the black and red lines in figure 3(a). The differences are due to a component of the freestream velocity being aligned with the plane of propeller rotation for non-axial flow. This component is dependent on the angle of attack and the azimuthal position of the blade, leading to a cyclic variation of the local incidence angle and relative velocity for a blade as it rotates. This effect is most pronounced when comparing the local flow conditions for an airfoil section of a blade on its downward sweep to those of a diametrically opposed blade on the upward sweep. In the former case the relative velocity is larger and at a greater local incidence angle than it is for the latter. This results in larger blade forces being produced on the downward than on the upward sweep. The forward and aft blade thrust forces, plotted as the solid and dash-dotted red lines in figure 3(a), both show the angle of attack influence in the form of a 1-cycle sinusoidal oscillation, which is overlapped by a similar 32- or 16-cycle interaction-driven oscillation seen for the axial flow case. The increased blade loading during the downward sweep is reflected in the increasing blade thrust, with the maximum value being attained by both blades for an azimuthal position of approximately 110°. On the upward sweep, blade thrust forces are seen to decrease, resulting in a minimum blade thrust occurring around 300°.

The unsteady oscillations are also found for the complete rotor loads, as shown for the example of the thrust coefficient of the axial flow case in figure 3(b). Again, a 32-or 16-cycle oscillation around a constant mean value during a rotor revolution is evident. As for this 8x8 CROR all blades of the two rotors are either aligned or not, the blade-blade interactions seen in figure 3(a) add up for the rotor loads. For reference, table 1 lists the mean rotor performance for both of the low-speed cases. For the axial flow case the total rotor thrust is 87.588kN, split at a ratio of 48.93 : 51.07 in favor of the aft rotor. Thus the take-off thrust requirement is met by the generic CROR powerplant for the selected blade pitch settings, as is the aim of obtaining a power balance between the rotors, with a split of 49.97 : 50.03 achieved. The rotor efficiencies are 57.17% for the front and 59.59% for the aft rotor. At angle of attack, the efficiencies degrade slightly,

Table 1. Mean rotor efficiency η, thrust C_T and power C_P coefficients

	α	Rotor 1			Rotor 2		
		C_T	C_P	η	C_T	C_P	η
Take-Off at sea level and $M = 0.2$							
Case 1	$0°$	0.377046	0.628816	57.17%	0.393507	0.62962	59.59%
Case 2	$4°$	0.378082	0.630793	57.15%	0.393311	0.62975	59.55%

while overall rotor thrust increases to 87.683kN. As identical blade pitches were used, the rotor thrust balance naturally shifts a bit to $49.01 : 50.99$, and the power ratio to $50.04 : 49.96$.

Figure 4(a) shows an image of the vortex system for this type of propulsion system at low-speed flight conditions. The contours of vorticity highlight the complex interaction of the forward rotors blade wakes and tip vortices with the aft rotor. Due to the equal diameter of the two rotors, the vortex generated at the first rotors tip is seen to directly interact with the aft rotors blades, which leads to periodic unsteady oscillations in that blades loading. The upstream rotors blade wakes also play a dominant role in the interaction with the aft rotor and the figure shows that the TAU-simulations are able to resolve and sustain these viscous flow phenomena quite well. These wakes are then ingested by the second rotor, and also lead to periodic fluctuations in the blade forces. The impact of these interactions, already seen in the discussion of the blade and rotor forces, is further detailed in the plot of the blade thrust distribution for the axial flow case in figure 4(b). Shown in blue and red lines are the mean blade thrust distribution and two selected time-accurate snapshots for the front rotor and aft rotors respectively. As expected when recalling the vortex system shown in figure 4(a), the aft blades thrust distribution show large oscillations. The amplitude of the fluctuations are seen to be quite important near the hub due to the interaction with the strong upstream blades viscous wakes. The oscillations are even more pronounced near the tip, caused by the impingement of the front rotors tip vortices. This dominant interaction phenomenon is of great significance for the aeroacoustics of this type of propulsion system. It can also be seen that the front rotor is affected by the blade-blade interactions, with thrust fluctuations evident along the entire span, albeit of a lesser magnitude than seen for the aft blade. These fluctuations are cause by the upstream impact of the aft rotors potential field, which has a very notable impact on the pressure side of the front rotor blades in particular. The importance of this aft rotor impact on the front rotor for interaction noise emissions was not fully understood in the past, highlighting the benefits of employing modern high-fidelity simulations for the analysis of these types of flows [11].

5   Aeroacoustic Analysis

Figure 2 shows the locations of the virtual microphones used for the acoustic evaluation with the DLR APSIM-Code. The coordinate system origin is centered on the front rotor. Farfield polar directivities were computed for a microphone array at a distance of 20 rotor radii from the propeller center, while a near-field noise radiation evaluation
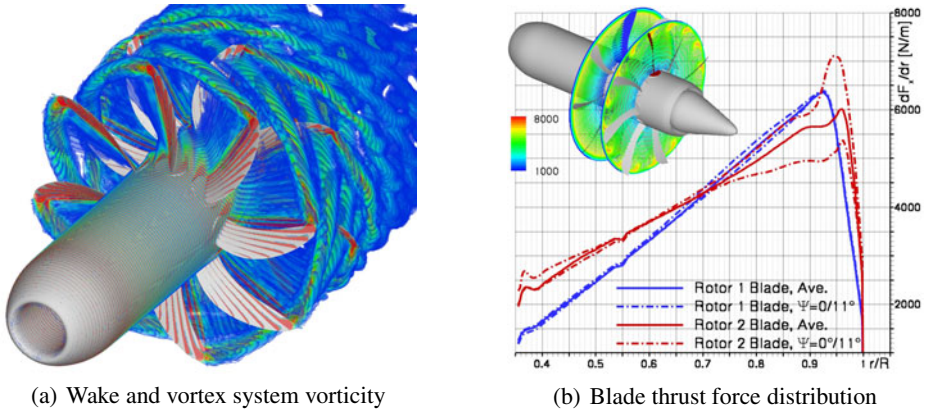
(a) Wake and vortex system vorticity

(b) Blade thrust force distribution

Fig. 4. Blade wake and tip vortex interactions for CROR at $\alpha = 0°$

(a) Nearfield sound pressure levels

(b) Farfield sound pressure levels

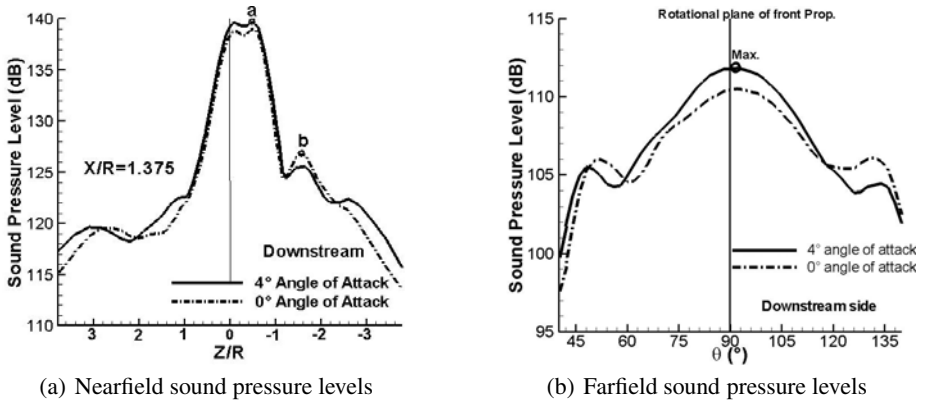**Fig. 5.** Comparison of CROR ground noise directivities for $\alpha = 0°/4°$

was done for an axial line of microphones parallel to the engine axis at a distance of 1.375 rotor radii. The FW-H permeable surface on which the noise source terms are described coincide with the nacelle Chimera boundary used in the CFD simulation. In order to avoid the contamination of the acoustic signal by the strong gradients in the rotor wake, some of the flow data on the downstream Chimera boundary was omitted in the aeroacoustic analysis.

The sound pressure level (SPL) directivities for the near field microphone array are plotted in figure 5(a). Peak noise levels are found in the vicinity of the rotor planes. Noise levels here are slightly increased for the CROR at non-axial flow conditions. The saddle type peaks near the rotors are a clear indication of the front and aft rotor thickness and loading noise radiation. The aft rotor peak noise levels, marked as "a", are marginally higher than those of the front rotor, due to the slightly higher loading of the aft rotor as well as the interactions with the front rotor blade wakes and

(a) Tonal spectrum in vicinity of rotor plane

(b) Tonal spectrum aft of rotor plane
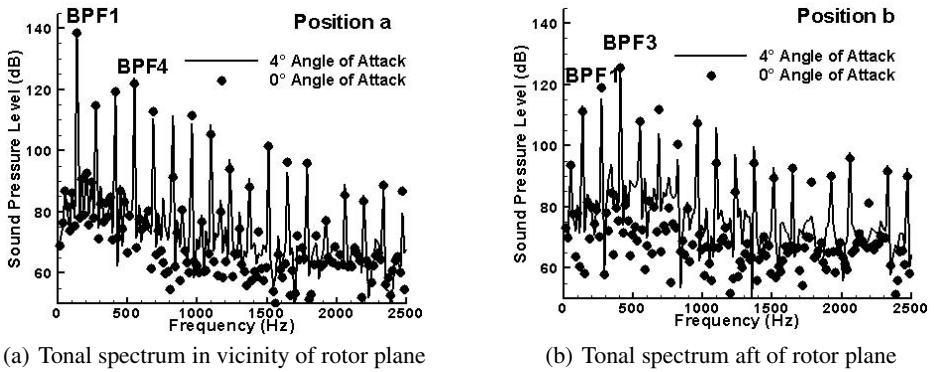
Fig. 6. Ground microphone nearfield acoustic spectra

tip vortices. The level drops sharply for microphone locations up- and downstream. Interaction driven noise is a major contributor to the notable SPL increase downstream of the aft rotor, marked as "b". An indication of this can be derived from figure 6, which shows the sound spectra for the two positions identified as "a" and "b" in figure 5(a). At position "a", plotted in figure 6(a), the tones at the blade passing frequency (BPF) dominate the overall level of the spectrum. Interaction tones are also seen to be important, as evidenced by the increases in sound pressure levels for the first three harmonics of the rotor tones. The relatively high level of the BPF4 tone at four times the blade passing frequency correlates well with the 32-cycle oscillations seen in the front rotor blade loadings in figure 3(a), indicating the notable contribution of the front rotor to the interaction noise emissions. At the downstream position "b" shown in figure 6(b), the higher harmonic tones, in particular the BPF3-tone at three times the blade passing frequency, are seen to be the most significant in the noise spectrum. This tone is caused primarily by the rotor-rotor interactions. The BPF3-tone could be driven by the interaction tones that occur at the frequency combinations of 2BPF1(front)+BPF2(aft) or BPF1(front)+2BPF2(aft).

The farfield polar directivity for the two flight conditions, of particular interest for the flyover noise emissions, are compared in figure 5(b). Maximum levels are seen to occur at a location between the two rotors, while interaction tone noise is greatest toward the rotor rotation axis in the polar angle ranges between $0° < \theta < 60°$ upstream and from $130° < \theta < 180°$ downstream.

6 Conclusion and Outlook

A coupled aerodynamic and aeroacoustic analysis of a generic 8x8 CROR powerplant at low speed flight conditions using high-fidelity CFD simulations with the DLR TAU-Code and a noise propagation computation with DLR APSIM-Code was presented. The CFD results revealed strong mutual interactions between the front and aft rotor, leading

to strong periodic fluctuation of the blade loads. The dominant interaction phenomena were found to be the front rotor blade wakes and particularly the tip vortices as they interact with the aft rotor. The noise emissions are characterized by dominant rotor-alone tones in the vicinity of the planes of rotation and interaction tones radiated towards the front and rear. The results indicated a notable influence of the rear rotors potential flow-field on the forward blades leading to an important contribution of the front rotor to the interaction tone noise generation.

In order to further enhance the understanding of CROR aerodynamics and aeroacoustics future studies will focus on the performance and noise impact of a reduced diameter aft rotor, increased rotor-rotor spacing as well as an increased blade number forward rotor. Additionally the impact of aspects of the simulation approach such as mesh densities will be studied in detail.

References

[1] Hager, R.D., Vrabel, D.: Advanced Turboprop Project, NASA SP-495 (1988)
[2] Nallasamy, M., Podboy, G.G.: Effects of a Forward-Swept Front Rotor on the Flowfield of a Counterrotation Propeller. In: AIAA-94-2694, 30th AIAA/ASME/SAE/ASEE Joint Propulsion Conference, Indianapolis, IN, USA (1994)
[3] Kroll, N., Fassbender, J.K.: MEGAFLOW - Numerical Flow Simulation for Aircraft Design. Notes on Numerical Fluid Dynamics and Multidisciplinary Design, vol. 89, pp. 81–92. Springer, Heidelberg (2005)
[4] Yin, J., Delfs, J.: Improvement of DLR Rotor Aeroacoustic Code (APSIM) and its Validation with Analytic Solution. In: 29th European Rotorcraft Forum, Friedrichshafen (2003)
[5] Stuermer, A.: Unsteady CFD Simulations of Contra-Rotating Propeller Propulsion Systems. In: AIAA 2008-5218, 44th Joint Propulsion Conference, Hartford, CT, USA (2008)
[6] Stuermer, A.: CFD Validation of Unsteady Installed Propeller Flows using the DLR TAU-Code. In: CEAS-2007-104, 1st European Air and Space Conference, Berlin (2007)
[7] Spalart, P.R., Allmaras, S.R.: A One-Equation Turbulence Model for Aerodynamic Flows. AIAA 1992-0439 (1992)
[8] Edwards, J., Chandra, S.: Comparison of Eddy-Viscosity-Transport Turbulence Models for Three-Dimensional, Shock-Separated Flows. AIAA Journal 34(4), 756–763 (1996)
[9] Jameson, A.: Time Dependent Calculations Using Multigrid, with Applications to Unsteady Flows Past Airfoils and Wings. In: 10th AIAA Computational Fluid Dynamics Conference, Honolulu, HI, USA (1991)
[10] Madrane, A., Raichle, A., Stuermer, A.: Parallel Implementation of a Dynamic Unstructured Chimera Method in the DLR Finite Volume TAU-Code. In: 12th Annual Conference of the CFD Society of Canada, Ottawa, Ontario, Canada, pp. 524–534 (2004)
[11] Woodward, R.P., Hughes, C.E.: Aeroacoustic Effects of Reduced Aft Tip Speed at Constant Thrust for a Model Counterrotation Turboprop at Takeoff Conditions. In: AIAA-90-3933, 13th Aeroacoustics Conference, Tallahassee, FL, USA (1990)

Computation of Trailing Edge Noise with a Discontinuous Galerkin Method

M. Bauer

DLR (German Aerospace Center), Institute of Aerodynamics and Flow
Technology, Lilienthalplatz 7, 38108 Braunschweig, Germany
marcus.bauer@dlr.de

Summary

Trailing edge noise of a semi-infinite, thin, flat plate situated in low Mach number flow is computed in two spatial dimensions. The Acoustic Perturbation Equations (APE), which are employed as governing equations, are discretized via a Discontinuous Galerkin Method (DGM). Results are compared with theory and Finite Difference (FD) computations. Next to the radiated sound field, special attention is paid to the conditions very close to the trailing edge (TE).

1 Introduction

Airframe noise is generated by the transformation of turbulent energy into acoustic energy in the vicinity of edges, such as the TE of an airfoil or of a deployed slat. Considering the low noise engines of modern airliners, it is an important noise source during the approach phase. Unstructured grids greatly ease the mesh generation process when airframe noise of complex geometries is of interest. The DGM [1, 2, 6, 7, 11] provides a robust, high-order accurate discretization even on this type of grid and offers excellent wave propagation characteristics. However, the fidelity of the computed airframe noise field also depends on the fidelity of the computed aeroacoustic source mechanism: the aforementioned transformation of turbulent energy into acoustic energy at edges.

References [6, 11] investigate the reliability of the DGM to compute the acoustic response of various two-dimensional (2D) objects to incident vortical gusts. An infinitely thin, flat plate and a non-lifting as well as a lifting airfoil served as test objects, and the nonlinear Euler equations as well as the linearized Euler equations were considered as governing equations. Results are in good or very good agreement with semi-analytical and numerical reference data.

In the present work, TE noise of a semi-infinite, thin, flat plate is computed with a DGM on an unstructured, triangular grid (2D). The APE [8, 9] are employed as governing equations. To simplify matters, the flow has low Mach number, and the turbulent source term of the APE is computed from a simple,

analytical velocity field. DG-APE results are compared to theoretical solutions and to FD computations.

The goal of this work was to figure out, how reliably the employed DGM captures aeroacoustic noise generation at a TE.

2   Theory

2.1   Particularly Employed Form of APE

The APE [8, 9] for constant sound speed c_0 read in matrix-vector notation:

$$\frac{\partial \boldsymbol{U}}{\partial t} + \frac{\partial \boldsymbol{F}^x}{\partial x} + \frac{\partial \boldsymbol{F}^y}{\partial y} - \boldsymbol{S} = \boldsymbol{0}. \tag{1}$$

In (1), t denotes time, and x and y are the two-dimensional Cartesian spatial coordinates. $\boldsymbol{U}$ is the vector of unknowns and $\boldsymbol{F}^x = \boldsymbol{AU}$ and $\boldsymbol{F}^y = \boldsymbol{BU}$ are the flux vectors with

$$\boldsymbol{U} = \begin{pmatrix} p' \\ u' \\ v' \end{pmatrix}, \qquad \boldsymbol{A} = \begin{pmatrix} u_0 & \varrho_0 c_0^2 & 0 \\ \frac{1}{\varrho_0} & u_0 & v_0 \\ 0 & 0 & 0 \end{pmatrix}, \qquad \boldsymbol{B} = \begin{pmatrix} v_0 & 0 & \varrho_0 c_0^2 \\ 0 & 0 & 0 \\ \frac{1}{\varrho_0} & u_0 & v_0 \end{pmatrix}, \tag{2}$$

where p denotes pressure, ϱ density, and u and v the x- and y-directed velocity component, respectively. A prime marks unknown time- and space-dependent perturbation variables, whereas an index 0 indicates time-averaged, i.e. steady, mean flow quantities known in advance. The computations presented in this article are based on a simple, spatially constant mean flow field, see section 3.1 for details.

$\boldsymbol{S}$ is the APE source vector. For vortex sound problems like airframe noise, its first component can be assumed to be zero, and its second and third component are given by the linear perturbed Lamb-vector [8, 9]. In 2D Cartesian coordinates, the employed source vector thus reads

$$\boldsymbol{S} = - \begin{pmatrix} 0 \\ -\omega_3' \cdot v_0 - \omega_{30} \cdot v' \\ \omega_3' \cdot u_0 + \omega_{30} \cdot u' \end{pmatrix}, \tag{3}$$

where $\omega_3 = \frac{\partial v}{\partial x} - \frac{\partial u}{\partial y}$ is the z-component of the vorticity vector.

2.2   Discretization of APE via DGM

The 2D computational domain is partitioned into non-overlapping triangular elements $E^{(m)}$. The entries of the vectors $\boldsymbol{U}, \boldsymbol{F}^x, \boldsymbol{F}^y$, and $\boldsymbol{S}$ are approximated by an expansion of type

$$f^{(m)} \approx \tilde{f}^{(m)} = \sum_{l=1}^{N} \hat{f}_l^{(m)}(t) \cdot \Phi_l^{(m)}(x, y) \tag{4}$$

in each element. As the approximation $\tilde{f}^{(m)}$ is supposed to be a full 2D polynomial of degree three in this work, the number N of expansion terms according to the Pascal triangle is $N = 10$ [14]. The symbols $\hat{f}_l^{(m)}$ denote the expansion coefficients and $\varPhi_l^{(m)}$ are given spatial shape functions. The overall approximate solution $\tilde{U}$ may be *discontinuous* along the edges between neighboring elements in the framework of the DGM. A detailed description of the particularly employed DGM may be found in Ref. [2].

It was implemented in the programming language FORTRAN 90/95, using as reference shape-functions Lagrange polynomials of degree three with standard distribution of the so-called nodes [2, 14]. Consistently, time integration is performed by a standard explicit fourth order Runge-Kutta scheme, and the overall order of accuracy of the code is four, which was verified by convergence tests.

3   Computations

3.1   Test Setup

Dimensionless quantities were used. They were computed from dimensional quantities, marked by superscript * or subscript ∞, like

$$t = t^* \frac{c_\infty}{L^*}, \quad \boldsymbol{x} = \frac{\boldsymbol{x}^*}{L^*}, \quad \varrho = \frac{\varrho^*}{\varrho_\infty}, \quad \boldsymbol{v} = \frac{\boldsymbol{v}^*}{c_\infty}, \quad p = \frac{p^*}{\varrho_\infty c_\infty^2}, \tag{5}$$

where $\boldsymbol{x} = [x, y]^\mathrm{T}$ is the coordinate vector and $\boldsymbol{v} = [u, v]^\mathrm{T}$ the velocity vector. The dimensional reference quantities are a length of $L^* = 1\,\mathrm{m}$ as well as the density and sound speed at infinity.

Actually, TE noise of an infinitely thin, flat plate with a finite length of $0.2\,\mathrm{m}$ was calculated. Conditions of a semi-infinite plate were emulated by the fact, that the computational domain only comprised the plate's rear part, see figure 1.

To approximate low Mach number flow, the entries of the APE mean flow matrices $\boldsymbol{A}$ and $\boldsymbol{B}$ were set to $u_0 = v_0 = 0$ and $\varrho_0 = c_0 = 1$.

A simple, analytical, turbulent velocity field $\boldsymbol{v}_t = [0, \cos(\alpha x - \alpha v_c t)]^\mathrm{T}$ with wave number $\alpha = 1571.0$ and convection velocity $v_c = 0.05$ was substituted for the velocity perturbations of the source vector $\boldsymbol{S}$ from Eq. (3). This velocity field is a simplified form of the synthetic turbulent velocity field as proposed in the framework of the SNGR (Stochastic Noise Generation and Radiation) method [3, 4], where it is calculated as the sum of some ten or hundred discrete, random Fourier modes. Note, that $\boldsymbol{v}_t$ is frozen and incompressible, $\nabla \cdot \boldsymbol{v}_t = 0$. The source was computed in a single source patch with extension $-0.036 \leq x \leq 0.036$, $0.0 \leq y \leq 0.004$ above the TE, see also figure 1. The final source vector $\boldsymbol{S}$ follows from Eq. (3) by furthermore assuming $u_0 = v_c \neq 0$, $v_0 = 0$ and by introducing additional weighting functions W_i:

$$\boldsymbol{S} = -W_a(x) \cdot W_b(y) \cdot W_t(t) \cdot \begin{pmatrix} 0 \\ 0 \\ v_c \frac{\partial v_{t_y}}{\partial x} \end{pmatrix}. \tag{6}$$
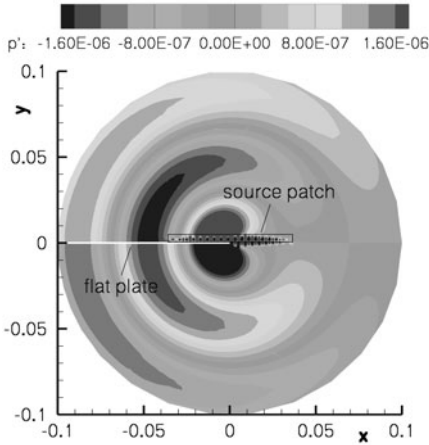
Fig. 1. Snapshot of pressure perturbations p' from DG-APE code on coarse triangular grid.
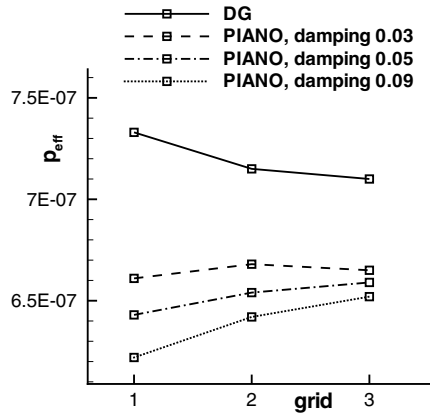
Fig. 2. Root mean square values of sound pressure at $(x, y) = (0, 0.08)$; grid numbers 1, 2 and 3 denote coarse, medium and fine grid, respectively.

The weighting functions all ranged between zero and one. To reduce spurious noise [3, 8], $W_a(x)$ smoothly faded the source term in and out in x-direction, i.e., the direction of convection of v_t. $W_b(y)$ modeled the generic y-distribution of the turbulent kinetic energy at the TE of a flat plate [3]. The source was faded in temporally at the beginning of a computation by $W_t(t)$ to attenuate spurious steady contributions to the perturbation quantities in the source patch. Such steady contributions actually do not cause any spurious noise, but they corrupt contour plots.

Comparative computations were performed with DLR's CAA[1] code PIANO[2] [5], which employs the fourth order accurate Dispersion Relation Preserving (DRP) FD scheme [12] for the spatial discretization. Artificial selective damping (ASD) [13] damped spurious short waves. The standard fourth order explicit Runge Kutta scheme was used for time integration in PIANO, too, just like in the DG-APE code.

Tables 1 and 2 list important parameters of the block-structured PIANO grids and of the unstructured, triangular DG grids. In both cases, there was a coarse, a medium, and a fine mesh, and all meshes were refined in the source patch area. The triangular grids cover a circular domain with radius $r = 0.1$ around the TE, whereas the block-structured grid domains are squares with $-0.1 \leq x, y \leq 0.1$.

3.2   Results

Figure 1 shows a snapshot of the pressure perturbations computed with the DG-APE code on the coarse grid. Small scale, large amplitude turbulent structures

---

[1] Computational Aero Acoustics.

[2] Perturbation Investigation of Aerodynamic Noise.

Table 1. Parameters (dimensionless) of block-structured grids; Δ denotes distance between grid points; $\Delta_{\min} = \Delta x_{\min} = \Delta y_{\min}$, and $\Delta_{\max} = \Delta x_{\max} = \Delta y_{\max}$

	coarse	medium	fine
$\Delta_{\min} \cdot 1000$	0.12	0.08	0.06
$\Delta_{\max} \cdot 1000$	5.00	3.33	2.50
no. of pts.	161.102	355.810	630.872

Table 2. Parameters (dimensionless) of unstructured grids; L denotes triangle edge length, $N = 10$ is the number of shape functions per element according to (4), and E the overall number of elements.

	coarse	medium	fine
$L_{\min} \cdot 1000$	≈ 0.500	≈ 0.375	≈ 0.300
$L_{\max} \cdot 1000$	≈ 13.33	≈ 10.00	≈ 8.00
$N \cdot E$	94.600	174.880	268.720

are induced in the source patch, and sound waves are radiated from the TE. They are perfectly symmetric (with opposite sign) along $y = 0$, although there is only a source patch above the flat plate. Contour plots from the other computations are very similar.

Figure 2 displays root mean square values $\tilde{p}$ of the sound pressure at receiving point $(x, y) = (0, 0.08)$ above the TE. Considering PIANO, the amplitude increases when the ASD damping coefficient is reduced. The DG amplitudes exceed those from PIANO, but the difference decreases towards finer grids. On the finest grids, $\tilde{p}$ from DG exceeds $\tilde{p}$ from PIANO (damping 0.03) by about 7 % or 0.6 dB. The amplitude differences between the various simulations do not develop on the way of the sound waves from the TE to the receiving point $(x, y) = (0, 0.08)$. They are almost identical at e.g. a receiving point $(x, y) = (0, 0.01)$ much closer to the TE. Thus, they must be due to a different strength of the aeroacoustic noise generation mechanism at the TE.

The exact solution very close to the TE can be calculated analytically. Since $\boldsymbol{v}_0 = \boldsymbol{0}$, $\varrho_0 = \text{const}$, and $\lim_{y \to 0} W_b(y) = 0$, i.e., $\lim_{y \to 0} \boldsymbol{S} = \boldsymbol{0}$, the APE transform into the simple homogeneous acoustic wave equation, where the velocity potential Φ' may be substituted for the pressure perturbations p' yielding $\frac{1}{c_0^2} \frac{\partial^2 \Phi'}{\partial t^2} - \Delta \Phi' = 0$. This further reduces to the potential equation $\Delta \Phi' = 0$ in the vicinity of edges. The respective solution for a semi-infinite, thin, flat plate can thus be found via conformal mapping:

$$\Phi' = r^{0.5} \cos(\gamma/2), \qquad r \neq 0, \tag{7}$$

with $r = \sqrt{x^2 + y^2}$ and $\gamma = 180° - \theta$, see figure 3 (top left). Finally, one can calculate $\boldsymbol{v}' = \nabla \Phi'$, and e.g. end up with:

$$v' = 0.5 \, r^{-1.5} (y \cos(\gamma/2) + x \sin(\gamma/2)), \qquad r \neq 0, \tag{8}$$

as illustrated qualitatively in figure 3, too. Solution (8) is not defined at the TE, i.e., at $r = 0$. Furthermore, if an observer, who is initially located right at the TE, moves an infinitesimal distance into any direction, then $v' \to \infty$, except along the surface of the plate, where $v' = 0$. Also note that $\nabla \cdot \boldsymbol{v}' = \nabla \cdot \nabla \Phi' = \Delta \Phi' = 0$, i.e., theoretically no noise is generated right at the TE.

Figure 3 also shows snapshots of computational results for the v' field at the TE. The big shape on top of the respective pictures was induced by the source.
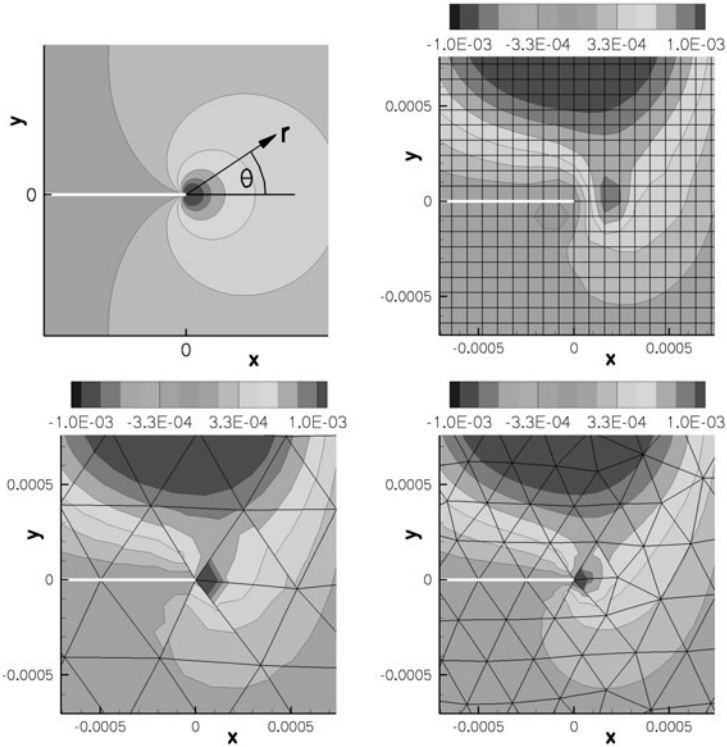
Fig. 3. Solutions of v' field in vicinity of flat plate trailing edge; top left: theory; top right: PIANO with damping 0.05 on medium grid; bottom left: DG on coarse grid; bottom right: DG on fine grid.
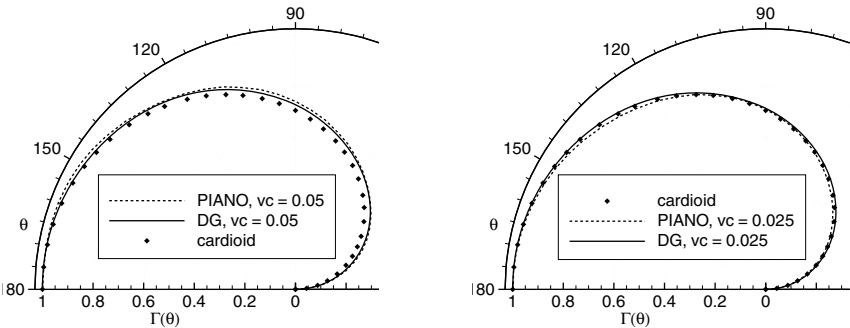

Fig. 4. Sound pressure directivities along circle with dimensionless radius $r = 0.08$ around flat plate trailing edge using medium grids and damping 0.03 within PIANO.

The amplitude differences from figure 2 can be explained by way of figure 3 in terms of the structure which developed around the TE. It was always stronger in DG than in PIANO. Focusing on the DG solutions, its extension decreased

the finer the grid (although its maximum amplitude increased). In the PIANO computations, the structure grew with reduced damping and towards finer grids. It may also be worth noting, that the DG solutions are closer to the difficult theoretical solution at the TE than the PIANO results, because -like in theory- the maximum occurred right at the TE in DG. It always occured somewhat downstream in PIANO, though, where a coarser grid and increased damping moved it further downstream.

Finally, figure 4 presents sound pressure directivities $\Gamma(\theta) = \frac{\tilde{p}(\theta)}{\tilde{p}(\theta)_{\max}}$. In spite of the difficult situation right at the TE, there are hardly any differences between the solutions from DG and PIANO. Furthermore, for a halved convection velocity of $v_c = 0.025$, the theoretically expected cardioid curve $\Gamma(\theta) = \sin(\theta/2)$ [10] is met very well.

4   Conclusions

The employed DG scheme seems capable of capturing aeroacoustic noise generation at the TE of a semi-infinite, thin, flat plate situated in low Mach number flow: the computed sound pressure field looks very reasonable, and there is excellent agreement of the sound pressure directivities from DG, FD, and theory. But, on the other hand, the sound pressure amplitudes slightly differ among the various computations. This is explained by the conditions very close to the TE, where the computations deviate from each other and also from the tough theoretical solution.

To judge the computed amplitudes, the exact solution for the whole domain may be calculated via the respective tailored Green's function. The influence of a non-zero, non-uniform mean-flow velocity field may be another point of future interest.

References

[1] Atkins, H.L., Shu, C.-W.: Quadrature-Free Implementation of Discontinuous Galerkin Method for Hyperbolic Equations. AIAA Journal 36(5), 775–782 (1998)
[2] Bauer, M., Dierke, J., Ewert, R.: Application of a Discontinuous Galerkin Method to Predict Airframe Noise. AIAA-paper 2009-3175, American Institute for Aeronautics and Astronautics (2009)
[3] Bauer, M., Zeibig, A., Költzsch, P.: Application of the SNGR-Model to Compute Trailing Edge Noise. Research Report, Institute of Acoustics and Speech Communication, Dresden University of Technology, Germany (2006),
http://www.ias.et.tu-dresden.de/akustik/Publikationen/
Stroemungsakustik/Publikationen_STAK.htm
[4] Béchara, W., Bailly, C., Lafon, P., Candel, S.: Stochastic Approach to Noise Modeling for Free Turbulent Flows. AIAA Journal 32(3), 455–463 (1994)
[5] Delfs, J.W., Bauer, M., Ewert, R., Grogger, H.A., Lummer, M., Lauke, T.G.W.: Numerical Simulation of Aerodynamic Noise with DLR's Aeroacoustic Code PI-ANO (Version 5.1). Manual, Deutsches Zentrum für Luft- und Raumfahrt e.V. Institute of Aerodynamics and Flow Technology (2007)

[6] Dumbser, M.: Arbitrary High Order Schemes for the Solution of Hyperbolic Conservation Laws in Complex Domains. PhD thesis, University of Stuttgart, Germany (2005)

[7] Ehrenfried, K., Meyer, C., Dillmann, A.: Simulation of Sound Propagation in Boundary Layers based on Möhring's Acoustic Analogy. AIAA-paper 2003-3272, American Institute for Aeronautics and Astronautics (2003)

[8] Ewert, R., Meinke, M., Schröder, W.: Computation of Trailing Edge Noise via LES and Acoustic Perturbation Equations. AIAA-paper 2002-2467, American Institute for Aeronautics and Astronautics (2002)

[9] Ewert, R., Schröder, W.: Acoustic Perturbation Equations based on Flow Decomposition via Source Filtering. Journal of Computational Physics 188(2), 365–398 (2003)

[10] Ffowcs Williams, J.E., Hall, L.H.: Aerodynamic Sound Generation by Turbulent Flow in the Vicinity of a Scattering Half Plane. Journal of Fluid Mechanics 40(4), 657–670 (1970)

[11] Rasetarinera, P., Kopriva, D.A., Hussaini, M.Y.: Discontinuous Spectral Element Solution of Acoustic Radiation from Thin Airfoils. AIAA Journal 39(11), 2070–2075 (2001)

[12] Tam, C.K.W., Webb, J.C.: Dispersion-Relation-Preserving Finite Difference Schemes for Computational Acoustics. Journal of Computational Physics 107, 262–281 (1993)

[13] Tam, C.K.W., Webb, J.C., Dong, Z.: A Study of the Short Wave Components in Computational Acoustics. Journal of Computational Acoustics 1, 1–30 (1993)

[14] Zienkiewicz, O.C., Taylor, R.L., Zhu, J.Z.: The Finite Element Method - Its Basis and Fundamentals, 6th edn. Elsevier Butterworth-Heinemann (2005)

Towards Numerical Simulation and Analysis of the Flow in Central Airways

Octavian Frederich[1], Phillip Amtsfeld[1], Eike Hylla[1], Frank Thiele[1], Michael Puderbach[2], Hans-Ulrich Kauczor[3], Ingmar Wegner[4], and Hans-Peter Meinzer[4]

[1] Berlin Institute of Technology, Institute of Fluid Mechanics and Engineering Acoustics, Müller-Breslau-Str. 8, 10623 Berlin, Germany
[2] German Cancer Research Center, Department of Radiology, Im Neuenheimer Feld 280, 69120 Heidelberg, Germany
[3] University Hospital Heidelberg, Department of Diagnostic Radiology, Im Neuenheimer Feld 400, 69120 Heidelberg, Germany
[4] German Cancer Research Center, Department of Medical and Biological Informatics, Im Neuenheimer Feld 280, 69120 Heidelberg, Germany
Octavian.Frederich@TU-Berlin.DE

Summary

To analyse the flow in natural geometries of central airways an interdisciplinary project by medical and engineering partners has been created. The work presented summarises necessary developments, preliminary investigations and new insights into the unsteady flow with a focus on numerical fluid mechanics. The objective of the investigations is the analysis and physical understanding of the dynamic flow in central airways, which should later allow to improve artificial ventilation towards a more lung protective approach than actual strategies.

1 Initial Situation and Objectives

The flow physics inside the central airways of human (and also animal) lungs up to this point are unknown. Understanding the flow physics is imperative for artificial ventilation, which is the only known life-sustaining therapy in case of an acute lung injury. Since parameters used for ventilation are primarily based on empirical models, this therapy is accompanied by serious side effects and high mortality of patients. Although modern ventilation strategies have been adapted towards lung protection, e.g. by using lower tidal volumes and positive end-expiratory pressure to avoid lung collapse, often the lung is seriously damaged or suffers from inflamation. In order that artificial ventilation relies on physiology and physical phenomena a variety of interdisciplinary projects funded by the German Research Foundation (DFG) have been launched. The combined work of medical and engineering scientists in this framework is intended to overcome serious side effects and reduce the limitations of artificial respiration, and

therewith optimise the artificial respiration for the patient to ameliorate the present dissatisfying clinical situation. Deepening the understanding of fluid and structural physics and describing quantitatively the functional relevance of temporary and fixed deformations will allow to develop protective ventilation strategies or at least to provide an efficient parameter set based on observed physics. Numerical simulation enables the physical analysis of variations in the complex system of patient and respirator, and the integration of realistic models for uncaptured effects like lung impedance.

The aim of the authors' project is the numerical prediction and evaluation of the convective flow in dynamically changing geometries of the central airways. To achieve this an automated workflow had to be developed, which allows to investigate the flow in several different geometries and to extract the differences and functional relevance due to geometry changes. The work presented here comprises a description of the developments required for the workflow and the analysis of influencing parameters as well as of changing flow direction in steady geometries.

In the following the developed workflow and the geometries are described in section 2. An overview of the numerical method and parameters for the simulations is given in section 3. Thereafter the results of parameter variations and flow analysis are presented in section 4 and discussed before conclusions and outlook.

2   Workflow and Configurations

Dynamic geometries of the central airways (human or animal) are gathered using state-of-the-art radiologic imaging modalities, ranging from time-resolved Magnetic resonance imaging (MRI) to Computed tomography (CT). Thereafter image segmentation algorithms employing extended adaptive region growing [1] are utilised to segment the anatomic volume of the airways with as many bifurcation levels as possible. Dependant on the image quality, the current method achieves up to five levels, whereas optical inspection allows more levels. Based on the segmented voxels the bronchial surface is generated by smoothing, refinement and magnification such that the anatomy is represented realistically. The segmentation procedure is integrated in a powerful graphical environment, which directly allows parameter variations and optical inspection of the segmented geometry w.r.t. the image stack. In the case of acquired dynamic data surface displacements fields are generated between different temporal surface representations. Finally, the surface skeleton is extracted and used to trim the surface axis-normal using point and airway direction in order to generate planar end-faces for the application of numerical boundary conditions. The surface representation and for dynamics the deformation fields are the base for fluid-dynamical analysis over the entire respiration cycle. Additional temporal surfaces required for the dynamic simulations due to the necessary temporal resolution are calculated by interpolation between two successive displacements fields. A sketch of the highly automated workflow is shown in figure 1.

The focus of the work presented is to examine the influence of several simulation parameters in order to obtain a set of parameters adequate for a realistic prediction of the flow. Therefore, the numerical experiments have been conducted using one timestep (inspiration) of the dynamic dataset, which has been acquired by CT in a human lung (depicted in figure 1).
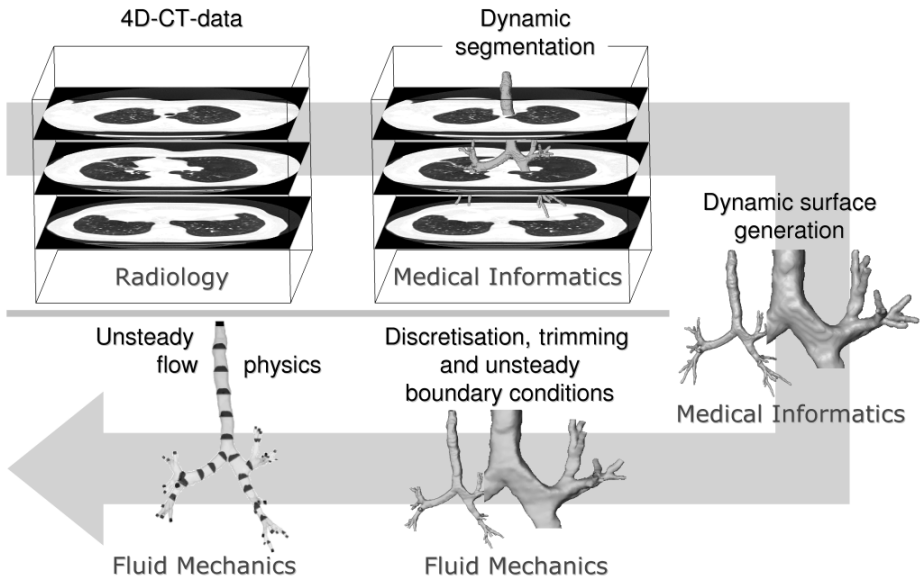
Fig. 1. Workflow realised for dynamic simulations.

3   Numerical Approach and Parameters

The flow prediction in dynamically changing natural geometries requires somehow the adaption of the computational grid or domain. Since the deformations or geometry changes in central airways can be of the same order as the diameter of the bronchi, grid deformation algorithms are not suitable. On the other hand the regeneration of the grid in each timestep and subsequent interpolation of the field values requires too much resources. A method developed exactly for problems with natural changing geometries is the Immersed Boundary method (IB) described by PESKIN for the first time [2].

The IB method together with a proper computational infrastructure has been implemented in a variant of the in-house flow solver ELAN at TU Berlin [3]. The original code employing the Finite-Volume method has been adapted for unstructured Cartesian meshes with local refinement, which allows to use the advantages of the IB method to full capacity. The validated implementation of Immersed Boundaries is based on a variant of the "ghost-cell" approach with an immersed surface represented by triangles [4]. For the parameter varying simulations in a steady geometry unstructured tetrahedral grids with the commercial package StarCD are employed. This two-fold strategy allows to use the advantages of both techniques as well as to validate the flow prediction utilising immersed boundaries.

The spatial discretisation of the fluid region within the human lung geometry involves 730 000 tetrahedrons or 6 200 000 hexahedrons for StarCD and the IB code, respectively. The comparably higher resolution of the IB grid is due to the appropriate resolution of small tubes at high bifurcation levels, which has not been considered for the tetrahedral grid. Based on different assumptions three volume fluxes of 125, 243

and 333 ml/s, three different shaped inlet profiles (block, laminar, double-peak) and two different methods for distributing the flux fraction at the numerous outlet boundaries have been investigated in a steady geometry. On the one hand the volume flux on the separated outlet faces has been distributed explicitly based on the fraction of the total outlet area. On the other hand the distribution is realised implicitly with an additional lung-shaped volume (cf. figure 2 top-left) and a pressure boundary condition applied on its surface. In addition, the changing flow direction during the respiration cycle has been modelled in a first step by a sinusoidal curve for the temporal volume flux, whereas the average volume flux is prescribed by the steady ones. The varied parameters are summarised in table 1.

Table 1. Varied Parameters.

volume flux	inlet profile	flux distribution
125 ml/s (calm)	block	area fraction (tree)
243 ml/s (normal)	laminar	volume with pressure-bc (lung)
333 ml/s (fast)	double-peak	

4   Results

The highest Reynolds number considered is prescribed with approx. $Re = 3155$ for fast breathing with a volume flux of 333 ml/s. All simulations performed up to this Reynolds number revealed that the flow in the geometry investigated remains laminar, such that no high-grade turbulence modelling is necessary. Although turbulent content has been prescribed in the field and on the inlet, the turbulent kinetic energy reaches near zero levels shortly behind the inlet. For this reason, fully turbulent and laminar simulations with StarCD predicted an almost identical flow field.

In figure 2 the pressure coefficient and the vertical velocity component along a volume line are summarised for a single parameter variation each with all other parameters fixed. The variation of the volume flux has obviously hardly any influence to the normalised velocity field, but the pressure load in the lower airways increases with increasing flux. The influence of the inlet profile used is only moderate with the largest differences for the laminar profile due to the doubled velocity magnitude in the bronchus centre compared to the constant profile.

To distribute the volume flux to the separated outlets based on the area fractions means each outlet is applied by the same velocity magnitude directed towards the local face normal. This approach represents a strong constraint to the velocity field, which has to be avoided. A more realistic distribution has been determined by adding some large volumes, those boundaries (insert in sketch of figure 2) in the steady case are applied with zero pressure boundary conditions. In this way differences in particular fractions of $\pm 40\%$ are observed, which results in an increased pressure load for the more realistic lung model (figure 2 right).
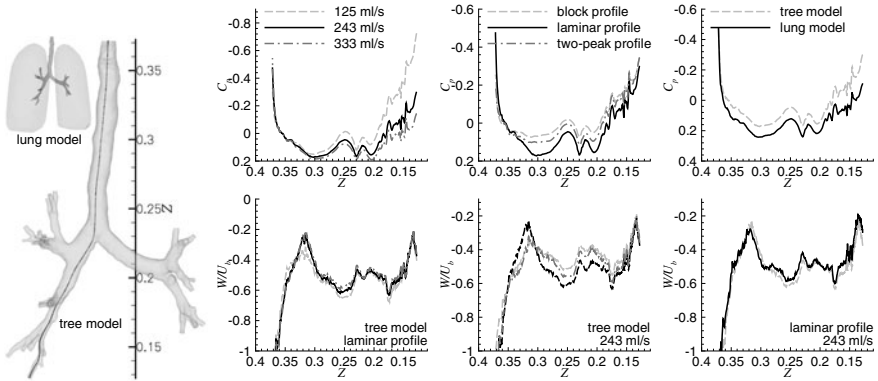
Fig. 2. Pressure coefficient C_p and vertical velocity W/U_b in a volume line (sketch) with varying volume flux (left), inlet profile (middle) and flux distribution (right); additional volumes required for modelling the volume flux distribution (insert in sketch);
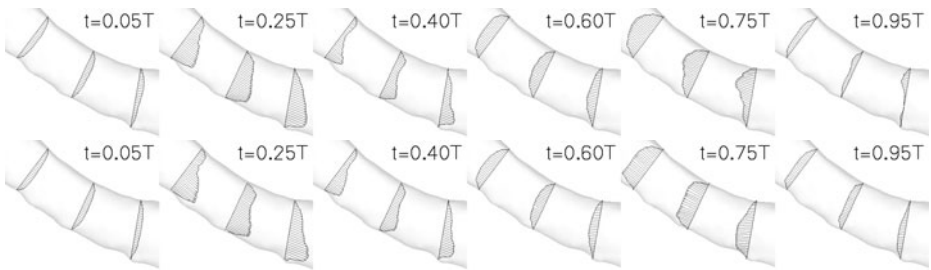

Fig. 3. Velocity profiles for several stages of an oscillatory flow in steady (top) and dynamically deformed geometry (bottom) behind first bifurcation.

As a result of the unsteady simulation for the flow with sinusoidally changing direction velocity profiles are predicted with a double-peak shape (projected to a plane), which have been measured previously [5]. These profiles, exemplarily depicted in figure 3 (top), are significantly different to the results obtained for the steady case, and therefore emphasise the importance of unsteady and even more dynamic simulations. A generic double-peak shaped velocity profile has also been used as inlet profile in order to refine the boundary conditions in steady case, but with moderate success (cf. figure 2 middle).

Right from the simulations in steady geometries the understanding of the flow topology is deepened. Irrespective of the configuration investigated or parameters used, the simulations predict counter-rotating vortex rolls (Dean vortices). The effect of these rotating structures has been interpreted as a natural "wash-out" of the central airways (figure 4). In addition the laminar character of the flow observed seems to be conserved by these vortex rolls. A hypothesis for the interpretation in the medical sense is that
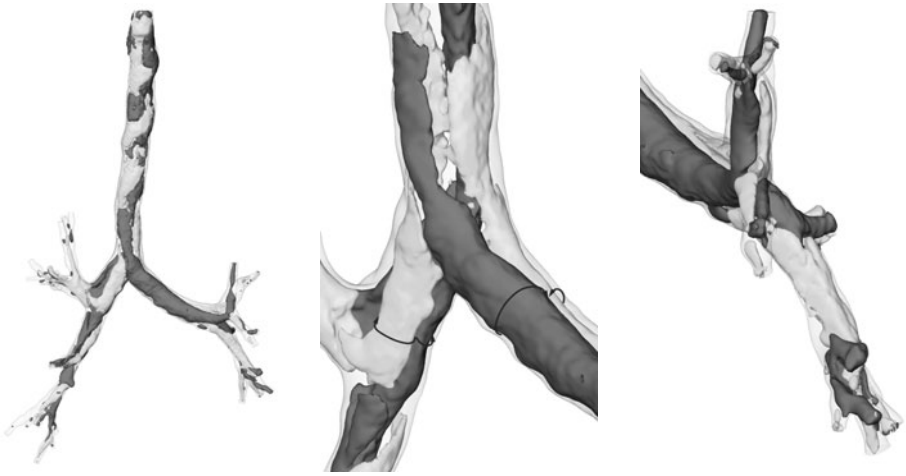
Fig. 4. Counter-rotating vortex rolls represented by iso-surfaces of positive (light) and negative (dark) helicity: overview (left), first bifurcation (middle), further bifurcations (right).

any disturbance of these vortical structures affects the self-purification of the airways. Therefore it might be an important component for temporal or chronical obstructions.

The unsteady simulations with sinusoidally varied flux showed, that although the helicity magnitude of the vortex rolls changes also sinusoidally, the rotational direction of each single structure is conserved. This observation is consistent with the principle of angular momentum conservation in fluid mechanics. Furthermore, the unsteady simulations revealed the absence of perceptible separation regions with respect to the flow direction throughout the entire respiration period as often observed in two-dimensional (numerical) experiments, e.g. [6].

In the framework of an unsteady flow simulation with dynamically changing geometry, the enlargement of the computational domain by an additional lung volume is unsuitable. Thus, a calibration method for the unsteady distribution of the volume fluxes has been established. Therefore, a steady geometry of the bronchial tree has been connected to the lung volume sketched in figure 2, a slip condition is applied to the volume boundaries and these are translated sinusoidally towards the local normal direction in order to achieve an unsteady flux in the central airways. During the unsteady simulation the temporal volume flux at each of the boundaries ("inlet" and "outlet") is recorded and finally used as prescribed flux for the dynamic simulations without the lung volumes. The flux fraction could possibly be adapted by correction factors taking into account the dynamically changing surface, which has not been tested so far.

First results of preliminary tests of the newly implemented Immersed Boundary method show that the flow quantities and fluxes follow the segmented geometry [4], although the spatial discretisation is similar to a stepwise approximation (figure 5 a,b). This behaviour could be achieved by the combination of IB and the flux-based Finite Volume method [3]. Especially for the dynamic simulations this approach is best suited. A quantitative comparison between the commercial StarCD and the in-house IB code is given in figure 5 c for the volume line already used in figure 2. The results demonstrate

(a) surface of fluid domain and pressure distribution

(b) streamlines with original surface

(c) comparison of IB code and StarCD
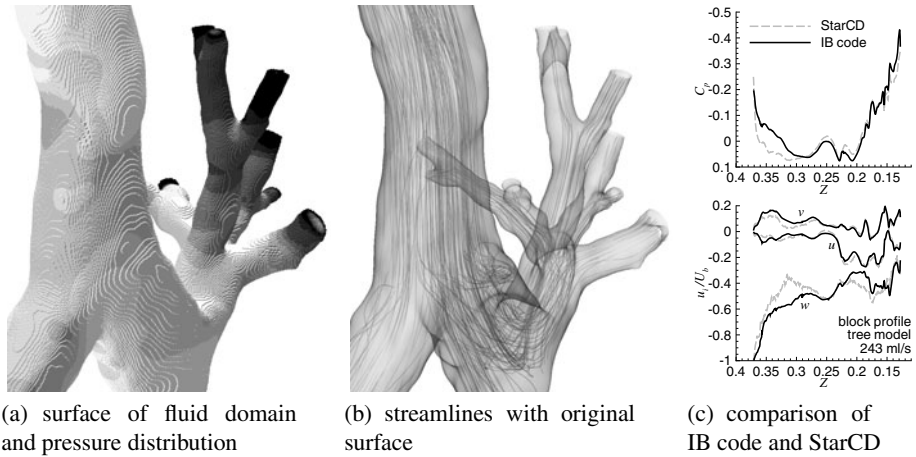
Fig. 5. Results of steady simulation with the developed Immersed Boundary code.

acceptable agreement, whereas the differences are attributed to the considerably higher resolution in the IB grid, as well as to slightly different numerics and outflow boundary conditions.

In a next step the oscillatory flow was investigated in a sinusoidally varied geometry with constant generic deformations towards the surface normals. The physics of this flow has not been examined in all details, but the velocity profiles predicted tend to flatten under expiration compared to the flow in a steady geometry, whereas the peaks are strengthened in inspiration (cf. figure 3). In addition, the global unsteady flow topology differs only slightly compared to that in a steady geometry, but some local flow features are strongly affected.

5   Conclusion and Outlook

Steady, unsteady and dynamic flow simulations have been performed successfully in natural geometries of central human airways. To enable the simulation in dynamically changing geometries an automated workflow has been established, which allows to investigate different pathologic lung diseases in series. Important parameters of influence have been identified using steady simulations, such that a volume flux appropriate for tidal breathing, a laminar inlet profile and calibrated flux fractions can now be used as reasonable boundary conditions. The results of the unsteady, oscillatory flow reveal the necessity of the dynamic simulation, and the methods utilised can cover these simulations in dynamic geometries. So far generic deformations were applied, thus the affect of dynamically changing geometry on the flow physics can not be concluded yet.

The methods developed are currently applied to dynamic geometries acquired during artificial ventilation of porcine airways. The results will allow to demonstrate the

concept and to investigate the influence of natural geometry changes. Although, workflow and IB code reached a robust state, continuous improvement is conducted in order to account for further physiological effects, e.g. lung impedance.

Acknowledgements

References

[1] Wolber, P., Wegner, I., Heimann, T., Wolf, I., Meinzer, H.-P.: Tracking und Segmentierung baumförmiger, tubulärer Strukturen mit einem hybriden Verfahren. Bildverarbeitung für die Medizin (BVM), 242–246 (2008)

[2] Peskin, C.S.: Flow patterns around heart valves: a numerical method. J. Comput. Phys. 10, 252–271 (1972)

[3] Hylla, E.: Validierung und Erweiterung eines numerischen Verfahrens zur Simulation von inkompressiblen Strömungen mittels der Immersed Boundary Methode. Diploma thesis, ISTA TU Berlin (2008)

[4] Hylla, E., Frederich, O., Mauß, J., Thiele, F.: Application of the immersed boundary method for the simulation of incompressible flows in complex and moving geometries. In: Proceedings of STAB 2008. NNFM. Springer, Heidelberg (2009) (to be published)

[5] Riethmuller, M.L.: Biological fluid dynamics. VKI research report (2000)

[6] Wilquem, F., Degrez, G.: Numerical modelling of steady inspiratory airflow through a three-generation model of the human central airways. J. Biomech. Eng. 119, 59–65

Protective Artificial Lung Ventilation: Impact of an Endotracheal Tube on the Flow in a Generic Trachea

L. Krenkel[1], C. Wagner[1], U. Wolf[2], A. Scholz[2], M. Terekhov[2], J. Rivoire[2], and W. Schreiber[2]

[1] Deutsches Zentrum für Luft- und Raumfahrt, Institut für Aerodynamik und Strömungstechnik, Bunsenstr. 10, 37073 Göttingen, Germany
Lars.Krenkel@DLR.de
[2] Universitätsklinikum Mainz, Langenbeckstr. 1, 55131 Mainz, Germany

Summary

Computational Fluid Dynamics (CFD) and experimental investigations on a generic model of the trachea have been carried out focusing on the impact of an endotracheal tube (ETT) on the resulting flow regime. It could be shown that detailed modelling of the airway management devices is essential for proper flow prediction, but secondary details as Murphy Eyes can be neglected. Models with bending and connector promote the formation of stronger secondary flows and disturbances which persist for a longer time.

1 Introduction

Since a large number of patients admitted to the intensive care unit require artificial ventilation support, it is essential to improve the understanding of the ventilation and oxygenation mechanisms in the human respiratory system. Of major interest is also the understanding of the impact of airway management devices, as e.g. endotracheal tubes, and different protective ventilation strategies on the governing flow regime in the central airways.

For patients suffering from adult respiratory distress syndrome (ARDS), acute lung injury or, at the worst, from acute lung failure, mechanical ventilation is the fundamental life saving therapy but even after years of practical experience and research the mortality rate is still high. This is related to inspiratory lung epithelia overstretching and repeated collapse and re-expansion of alveoli, which results in adverse shear forces. These shear forces tend to aggravate the aetiopathology, finally leading to ventilator associated lung injury (VALI).

Protective ventilation strategies aim at sufficient gas exchange and oxygenation while reducing ventilation associated injuries. A promising lung protective ventilation strategy is the "High Frequency Oscillation Ventilation (HFOV)" which is investigated numerically and experimentally within the framework of an interdisciplinary research project focusing on protective artificial ventilation. The

main objective of the research group, consisting of physicians, physicists, and engineers of the University Hospital Mainz and the DLR Göttingen is the optimisation of the protective HFOV. Therefore it is necessary to investigate and to understand the complex gas transport mechanisms in the lung and, furthermore, to identify the governing influencing parameters, and finally to optimise the boundary conditions and the settings of the HFOV. A set-up has been developed which allows for numerical and experimental cross-validation and for stepwise increase in complexity of the investigated upper central airways models. This paper focuses on the impact of the modelling of endotracheal tubes on the resulting flow field in a generic model of the trachea, as ETTs are an important influencing parameter in artificial ventilation.

2   Experimental and Numerical Setup

The effect of artificial ventilation in general and HFOV in particular on the air flow in the central human airways is investigated, using simulation and measurement techniques commonly associated with aeronautical engineering together with medical imaging and reconstruction techniques. Based on medical computer tomography (CT) imaging and reconstruction algorithms numerical CFD simulations are conducted using the unstructured incompressible DLR code THETA. Special emphasis is placed on the analysis of the governing transport mechanisms during steady and unsteady flow through the upper central airways. Experimental investigations with non-invasive measurement techniques (i.e. Particle Image Velocimetry, Laser Doppler Anemometry, and magnetic resonance -MR- based velocity measurements) are conducted using similar geometries/models with regard to the CFD simulations. In a first step, numerical simulations and experimental investigations of simple generic models of the trachea and the first bifurcation have been carried out. Furthermore, investigations on the effect of different gas species and their mixture on the air flow, as well as on the effect of an endotracheal tube on the governing flow regime have been undertaken. Finally, numerical simulations of steady state flow through a model of the upper central airways have also been conducted.

2.1   Generic Model of the Trachea and the First Bifurcation

Results presented in this paper have been obtained with a simplified model of the trachea and the first lung bifurcation. The model consists of a long straight tube, a detachable symmetric (α=30/30°) or asymmetric (α=25/45°) bifurcation with an inlet-to-outlet area ratio of ½ with two short tube endings. The set-up can be either connected to a closed loop steady blowing ventilator system or to the oscillatory HFV apparatus with additionally attached elastic endings (balloons). The tubes as well as the bifurcations and all connectors are made from Plexiglas® to allow for the application of non-invasive optical measurement techniques. For connecting the ventilation systems to the long straight pipe, a 9 mm endotracheal tube with cuff is used. The generic trachea is based on a pipe with a diameter of 20 mm which has been cut into two halves and which has been extended in cross stream direction by a flat 10 mm top and bottom plate. These two parallel plates reduce the diffusive

reflections which usually appear in pipes where optical measurement techniques are applied. Details of the model geometry are illustrated in Figure 3.

2.2 Numerical Methods: DLR THETA Code

The numerical simulations have been carried out using the 3D-DLR-CFD code THETA which solves the Reynolds averaged incompressible Navier-Stokes equations [4]. For steady simulations, the SIMPLE method and for time resolved simulations, the Projection method for the pressure velocity coupling was applied. For the momentum and the turbulence equation solver the quadratic upstream difference scheme (QUDS) was used. For additional convergence acceleration, a V3 multi grid cycle was applied for solving the Poisson equation together with a least square gradient reconstruction algorithm. Furthermore, the domain decomposition approach was used for efficient parallel computing. In terms of turbulence modelling, the standard k-ω (low Reynolds) turbulence model with near wall resolution and optional wall function treatment has been applied. Simulations are carried out on fully unstructured tetrahedral grids or on hybrid grids consisting of pseudo-structured prism layers in the vicinity of solid walls and unstructured tetrahedral cells in the remaining domain. The application of thin, in main flow direction stretched prism cells, allows for a finer resolution of boundary layers and thus for improved gradient evaluation at a reduced number of nodes.

3   Endotracheal Tube and Its Impact on the Flow Field

The concept of lung protective HFOV is based on the limitation of the inspiratory pressure and the reduction of the tidal volume by applying a continuously high mean airway pressure and superimposing a high frequency pressure oscillation (up to 15 Hz) with low tidal volume application in the order of the lung's anatomical dead space. As many research groups ([1], [2], [5], [7]) have ascertained, the gas transport under HFOV is highly complex, not well understood, and superposed of different transport mechanisms (i.e. convection, diffusion, Taylor dispersion). The governing flow is mostly laminar but, for higher frequencies, also turbulent flow regimes, especially in the vicinity of bifurcations and the ETT, are observed.

Numerical simulations with the THETA code of a constant flow in a 3rd generation lung model revealed a highly complex flow field dominated by secondary flow phenomena and vortical structures at the bifurcations (see Figure 1). Experimental data from HFOV animal experiments and experiments focusing on the flow field in a generic trachea with endotracheal tube in the magnetic resonance tomograph in Mainz (see Figure 2), as well as results from other research groups ([3], [6]) revealed that the endotracheal tube has a strong impact on the predicted flow field. One major reason for this is the ETT induced change in cross section area. Due to different length scales and change in the total cross section area in the airways including the airway management devices (tube, connector, etc.), the Reynolds number varies from below 1000 in the upper central airways and in the airways deeper down to 4000, or even higher, in the endotracheal tube (for physiological gas, e.g. air, but even higher for

Fig. 1. Isosurfaces of normalised helicity (left) and vortical structures (right) of the constant flow in a 3rd generation lung model
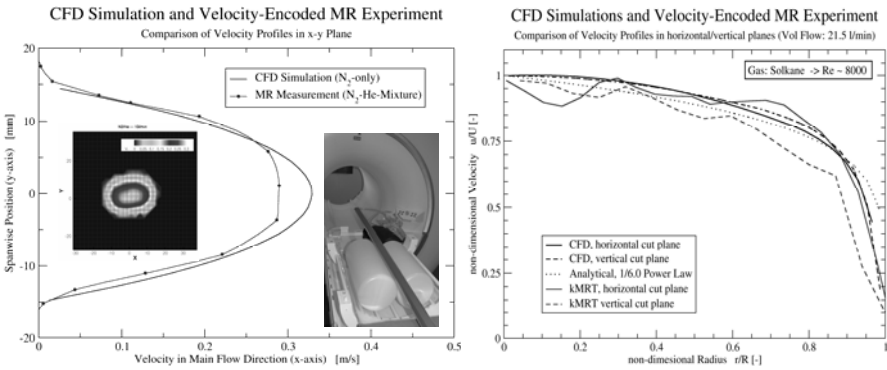
Fig. 2. Comparison of numerical, experimental and analytical data of the flow in a generic trachea with 9 mm ETT (Gas: He/N_2 and C_3HF_7)

dense medical gases, e.g. Solkane®). In addition, vortical structures develop at discontinuous changes in cross section area or at rough edges, i.e. at the connector or the Murphy eye of the tube. At increased Reynolds numbers, disturbances formed at discontinuous area alterations and a free shear layer developing at the outlet of the ETT (free stream jet) may alter the generally in airways expected laminar flow towards turbulence. Finally, secondary flow structures develop as a result from the tube bending in accordance with the Dean number. In the following subsections, at first, experimental data of the flow in a generic trachea is compared to CFD simulations. Secondly, the impact of a 9 mm endotracheal tube model geometry on the flow field is investigated.

3.1 Comparison of Experimental and Numerical Results

Figure 2 shows two comparisons of experimental magnetic resonance (MR) based velocity measurements in a generic trachea using two gases with different properties (helium and C_3HF_7 - Solkane®) with corresponding CFD simulations. The velocity was measured approx. 50 diameters downstream of the inlet, where the flow could be assumed to be fully developed. For the helium case, the bulk inlet velocity was adjusted for a mean tracheal Reynolds number, based on the mean pipe velocity, of 1500, resulting in a maximal Reynolds number of 3330 in the endotracheal tube,

whereas for the second (C_3HF_7) set-up, the mean tracheal Reynolds number was adjusted to approx. 8000. Since no ETT was used for the second set-up, there was no region with a higher Reynolds number. The experimental and numerical geometry used was identical for the second case, but for the first set-up, the geometry differed slightly since in the CFD simulations the inflow consisted only of a rudimentary modelled tube, i.e. only the straight ending and not the complete 90° bending of the tube was shaped.

In general, the experimental and numerical results agree well in the side band of the velocity profiles but show differences in the centre axis area of the flow. For both, the low and the high Reynolds number case, the experimental data show an unexpected plateau instead of a properly developed peak velocity. The velocity profile of the higher Reynolds number set-up is shown in a non-dimensional plot with an additional analytical velocity distribution derived from the "1/6 power law" $u/U = (1 - r/R)^{1/6}$. The power law gives a good approximation of a turbulent pipe flow velocity profile with limitations in the near wall and centre line region. Comparing the analytical with the experimental data it becomes apparent that the MR based velocity encoding technique seems to cut off the peak velocities while gaining good results in the high gradient boundary region. As most recent results revealed, this phenomenon only appears at low mean flow velocities (less than 1.5 m/s) and is most likely related to necessary signal averaging and smoothing during evaluation as a result of signal inconsistency in the centre of the MR coil. The slight variations in the area with strong gradients are mostly related to a coarse resolution of the experimental data (voxel size ~(2 mm)³, Figure 2) in comparison to CFD (cell size ~(0.5 mm)³). Furthermore, there is a small but noticeable deviation with respect to the velocity profile (slightly stronger curvature into positive y direction). This might be a result of the simplified tube geometry which prevents the development of secondary flows as induced by the 90° tube bending.

3.2 Impact of Tube Model Geometry on the Resulting Flow Field

As a result of the latter finding, various numerical simulations have been carried out, focusing on the impact of the tube model geometry, respectively the level of detail, on the resulting flow field. Figure 3 illustrates the investigated geometries ranging from a simple straight tube ending, over a tube with bending, and finally a tube with bending and connector. Besides, the effect of the so-called Murphy Eye, which is a hole in the side wall of the tube close to the exit, was investigated.
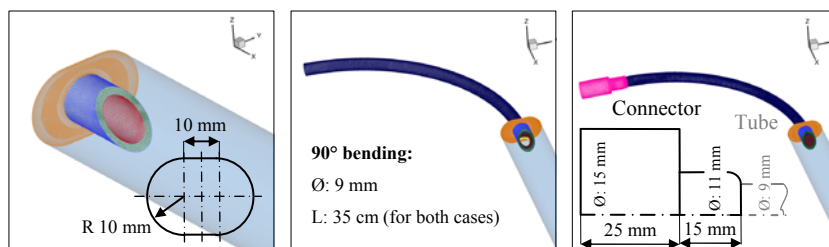
Fig. 3. Geometries: straight tube ending (left), tube with bending and Murphy eye (middle), and tube with bending and connector (right)

Prior to the numerical investigation, a grid convergence study for the case with connector had been conducted. Different resolutions and grid topologies (unstructured and hybrid meshes with varying number of prism layers) had been compared in terms of convergence history and solution independency. The best compromise in terms of grid size and solution quality was chosen. All grids have a similar hybrid grid topology and the cases with bending consist of approx. 2.6 to 3.4 million nodes (with/without connector and/or Murphy eye). The single tube ending mesh consists of only 2.1 million nodes. The first cell height was adjusted to a y^+ value of unity. For a better near wall resolution and gradient evaluation, 10 prism layers were used. Bulk velocity profiles adjusted with respect to a constant volume flow rate have been applied at the inlets. Turbulence quantities have been set to default values for all cases (turb. intensity=1%, turb. length scale=0.01m).

Figure 4 depicts the results of the CFD simulations using the "standard k-ω" turbulence model in terms of produced turbulent kinetic energy and by visualising isosurfaces of swirl $(\cup \hbar \omega)/(\rho \cdot \|u\|)$ for a constant value of "s=-300". The swirl
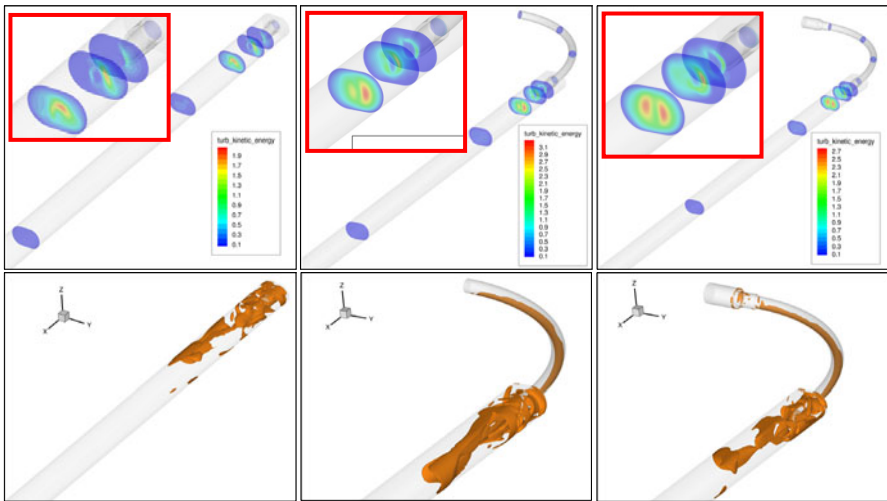
Fig. 4. Comparison of CFD data: distribution of turbulent kinetic energy (upper row) and isosurface visualisation of swirl (lower row)

visualisation can be interpreted as a visualisation of the three-dimensionality of the flow. The higher the value or the higher the amount of isosurfaces, the stronger the helical/rotational motions of the flow (velocity vector parallel to vorticity vector). It is obvious that the simple straight tube ending does not produce so many strong secondary flow structures in contrast to the bended tubes. The visible small amount of swirl is related to a jet flow regime at the outlet of the straight ETT ending. Comparison of both cases with bending reveals only slight differences in swirl and turbulent kinetic energy distribution. As expected, the discontinuous change in cross
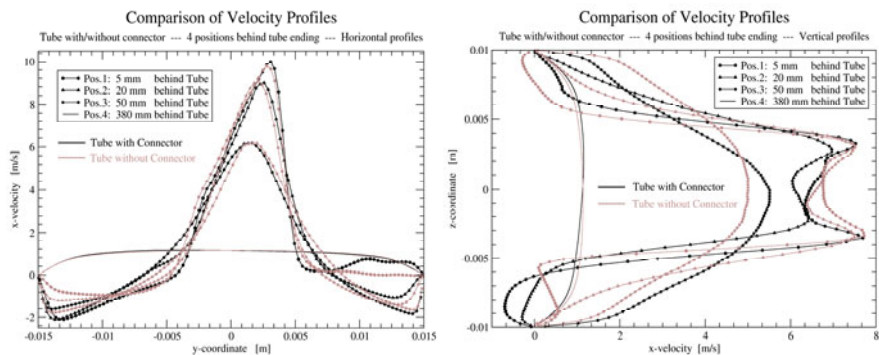
Fig. 5. Velocity profile comparison: model with/without connector in a horizontal and vertical cut plane at different positions behind ETT

section area seems to result in production of more turbulent kinetic energy. Figure 5 compares the resulting velocity profiles at different distances downstream of the tube in a horizontal (right) and a vertical (left) cut plane. The model with connector leads, in vertical direction, to a more asymmetrical velocity distribution in comparison to the model without connector, at least close to the ETT. Further downstream, both cases show similar profiles with a peak shifted slightly away from the centre line for the case with connector in the vertical plane. An explanation for this may be the generation of stronger vortical structures which decay slower for the case with connector.

Not shown is the impact of the Murphy Eye on the flow field, which is almost negligible. The strongest effect can be observed in the vicinity of the "eye" where a local re-circulation area develops with a slight effect on the jet formation at the main outlet of the tube. Therefore, it can be concluded from the steady numerical flow through simulations that for high quality calculations it is indispensable to model the bending of the endotracheal tube. The difference between the geometry with and without connector is smaller but the set-up with connector seems to generate more and stronger disturbances which persist for a longer time. 20 tracheal diameter downstream of the tube are most of the disturbances decayed and only the case with connector still shows a slight distortion of the flow field, which can also be seen, in general, in the most recent experimental kMRT (contrast gas MRT) data. Since the difference in mesh point numbers is almost negligible, it is recommended to use the detailed geometry model with connector.

4   Conclusion

Numerical and experimental investigations of the impact of endotracheal tubes on the flow revealed that endotracheal tubes have an important impact within the trachea and accordingly in the central airways of the lung. A numerical parametric study on the effect of the tube's level of detail on the resulting flow regime showed that it is necessary to model not only the tube ending but also the bending which is essential

for the development of secondary flows. A symmetrical flow regime 20 diameters downstream of the tube was achieved with a fully resolved tube with bending, whereas the tube with bending and connector generates stronger vortical structures resulting in a slightly asymmetric velocity field. A final validation with further experimental data and additional DNS is due to come.

Further numerical and experimental investigations focusing on more complex configurations, using a 4th generation cast model, are in preparation.

Acknowledgements

References

[1] Chang, H.K.: Mechanisms of Gas Transport during Ventilation by High Frequency Oscillation. J. of Applied Physiology 56, 553–563 (1984)

[2] Fort, P., Farmer, C., Westerman, J., et al.: High Frequency Oscillatory Ventilation for Adult Respiratory distress Syndrome – A Pilot study. Crit.Care.Med. 25 (1997)

[3] Haberthür, C., Mehlig, A., Stover, J.F., et al.: Expiratory endotracheal tube compensation reduces dynamic hyperinflation in a physical lung model. Critical Care 13(1) (2009)

[4] Knopp, T., Zhang, X., Kessler, R., et al.: Enhancement of an industrial finite-volume code for large-eddy-type simulation of incompressible high Reynolds number flow using near-wall modelling. In: Comput. Methods Appl. Mech. Engrg. (2009) (in press)

[5] Pillow, J.J.: High-Frequency Oscillatory Ventilation: Mechanisms of Gas Exchange and Lung Mechanics. Crit. Care. Med. 33, 135–141 (2005)

[6] Rocco, P.R.M., Zin, W.A.: Modelling the Mechanical Effects of Tracheal Tubes in Normal Subjects. Eur. Respir. J 8, 121–126 (1995)

[7] Slutsky, A.S., Drazen, J.M.: Ventilation with Small Tidal Volumes. N. Engl. J. Med. 347, 630–631 (2002)

Numerical Simulation of Nasal Cavity Flow Based on a Lattice-Boltzmann Method

Georg Eitel, Rainhill K. Freitas, Andreas Lintermann, Matthias Meinke,
and Wolfgang Schröder

Institute of Aerodynamics, RWTH Aachen University,
Wüllnerstrasse 5a, 52062 Aachen, Germany
g.eitel@aia.rwth-aachen.de

Summary

The flow in a real human nose is numerically simulated at steady inspiration and expiration. The analysis uses a Lattice Boltzmann method (LBM) which is particularly suited for flows in extremely intricate geometries. The nasal geometry is extracted from computer tomography (CT) data using a so-called reconstruction pipeline. Thus, for any nose the surface geometry can be defined and a numerical mesh can be generated. The focus of this investigation is on the analysis of the flow field at steady inspiration and expiration with respect to secondary flow structures. It is evidenced that strong vortical structures appear near the throat at inspiration forming a pair of counter-rotating vortices which disappear at expiration. Overall, at exhalation less vorticity is generated in the flow than at inhalation.

1 Introduction

The human nose is a complex respiratory organ and serves for tempering, moistening, and cleaning of respired air. The study of nasal flow plays an important role in medicine and biomedical engineering. Major fields of investigation in otorhinolaryngology are correlations between breathing comfort and nasal geometry, aerosolized drug delivery, and olfactory mechanisms [18, 19]. The fundamental understanding of the impact of the geometry of the nasal cavity on the flow field is important for a successful nose surgery [1]. Up to now surgical modifications are primarily based on simple empirical values. Due to the high geometric intricacy of the nasal cavity, there is still a considerable amount of uncertainty concerning the details of the flow field. Numerical and experimental results for realistic models are rare and certain phenomena cannot be reproduced with simplified geometries.

Consequently, the objective of this study is the detailed simulation of nasal flow in a realistic geometry. Therefore, the nasal geometry is reconstructed from magnetic-resonance imaging (MRI) or computer tomography (CT) data and the respiratory flow field is simulated via a Lattice-Boltzmann method (LBM) [3]. Unlike former numerical and experimental investigations [6, 7, 11, 12, 13, 14], in which a simplified nose

geometry was used, the present method can be efficiently applied to variable, realistic airway geometries. This is essential for the development of computer assisted surgery. Since the LBM is capable to capture small scale features of a nasal cavity flow the results serve to fundamentally understand respiratory mechanisms.

In this work the nasal flow has been simulated at steady inspiration and expiration. The obtained velocity distributions are illustrated in streamline patterns and coronal cross sections showing the strongly asymmetric geometry to cause a complex flow structure to develop. Furthermore, particular characteristics for each respiratory phase are evidenced.

In the following sections, first the reconstruction of the nose geometry and the numerical method are briefly described. Then, the results for steady inspiration and expiration are discussed and finally, some conclusions are drawn.

2   Geometry Reconstruction

To generate the mesh, a stereo-lithography (STL) model of the nasal cavity has to be reconstructed from CT or MRI data. In the following, the reconstruction procedure applied for CT data is described in detail. The first step consists of a preprocessing of the provided image data, which is necessary for an easier extraction of the region of interest (ROI), i.e., the nasal cavity. To highlight the boundaries of the nasal cavity surface, a 3 by 3 convolution filter is applied, which increases the sharpness of the image.

Then, bounding planes are inserted at the nostrils and the throat to prevent the segmentation algorithm to reach into the mouth, lungs and outer cranium volume. The segmentation is performed using seeded region growing as described in [2]. This algorithm recursively selects neighboring voxels to determine the ROI using an upper and a lower threshold defining an interval in Hounsfield space. That is, the air is represented by an interval in the lower region of the Hounsfield scale. The output is a binary three-dimensional image which serves as input to the Marching Cubes algorithm presented in [15]. This algorithm generates the associated triangle surface in the surface reconstruction step based on bilinear interpolation and a triangle look-up table. Unfortunately, this representation is not smooth enough and contains aliasing effects due to the cubic structure of the constituting voxels of the ROI. Therefore, the surface is smoothed using Laplacian [16] or windowed sinc function smoothing [17], where the former applies a smoothing kernel based on the weighted sum of the neighborhood distance for each surface vertex and the latter applies a transfer function to the discrete Fourier space of the graph signal. Both algorithms were tested and evaluated by an error measurement. While the Laplacian smoother shrinked the surface and therefore continuously increased the error in each iteration, the windowed sinc-function smoother avoided such a behavior, which is why the latter was preferred.

The resulting STL surface data depicted in Fig. 1 is the basis to generate the computational grid by an in-house automatic Cartesian-grid generator, which is described in detail in [10]. Generating a computational mesh with a typical resolution of 5 million cells takes only several minutes on a standard PC. The complete conversion from raw CT data to a Cartesian grid is performed in less than one hour. Compared to standard approaches the convenient geometry processing is a clear benefit of the present method.
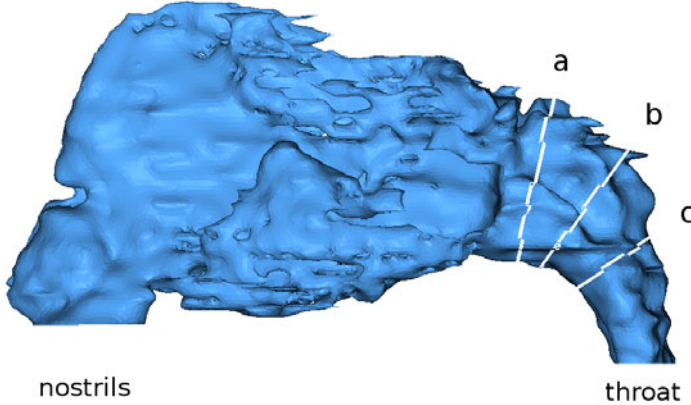
Fig. 1. STL-surface data; the white lines indicate the position of the cross sections shown in Figs. 2 and 3.

3   The Lattice-Boltzmann Method

Next, a brief description of the Lattice-Boltzmann Method (LBM) using the BHATNAGAR, GROSS AND KROOK (BGK) [4] approximation will be given. A detailed derivation of the LBM and an extensive discussion can be found in [3]. The BGK approximation uses a simplified collision term for the Boltzmann equation leading to the so-called BGK equation without external forcing

$$\frac{\partial f}{\partial t} + \xi_i \cdot \frac{\partial f}{\partial x_i} = \omega(f^{eq} - f). \tag{1}$$

The quantitiy ω represents the collision frequency, f^{eq} is the Maxwell equilibrium distribution function, f is the particle distribution function, and ξ_i is the i-th component of the molecular velocity vector. That is, the left-hand side of Eq. 1 contains the temporal change and the propagation term, whereas the right-hand side describes molecular collisions. The corresponding algorithm is based on the iterative computation of propagation and collision processes for each cell of the computational grid and is highly adapted for parallelization. Another advantage of the LBM algorithm is its efficient boundary treatment for fixed walls. The macroscopic flow variables are determined by summation over the base moments of the distribution function f. The standard LBM describes weakly compressible flows and it has been shown in the literature [9] that the LBM solves indeed the Navier-Stokes equations. All results presented in this study were obtained by the incompressible lattice-BGK (LBGK) method. This numerical scheme has been applied recently to a simplified model of the human nasal cavity [7] and the results showed to be in good agreement with those obtained from a Finite-Volume method. More details on the numerical approach can be found in [8].
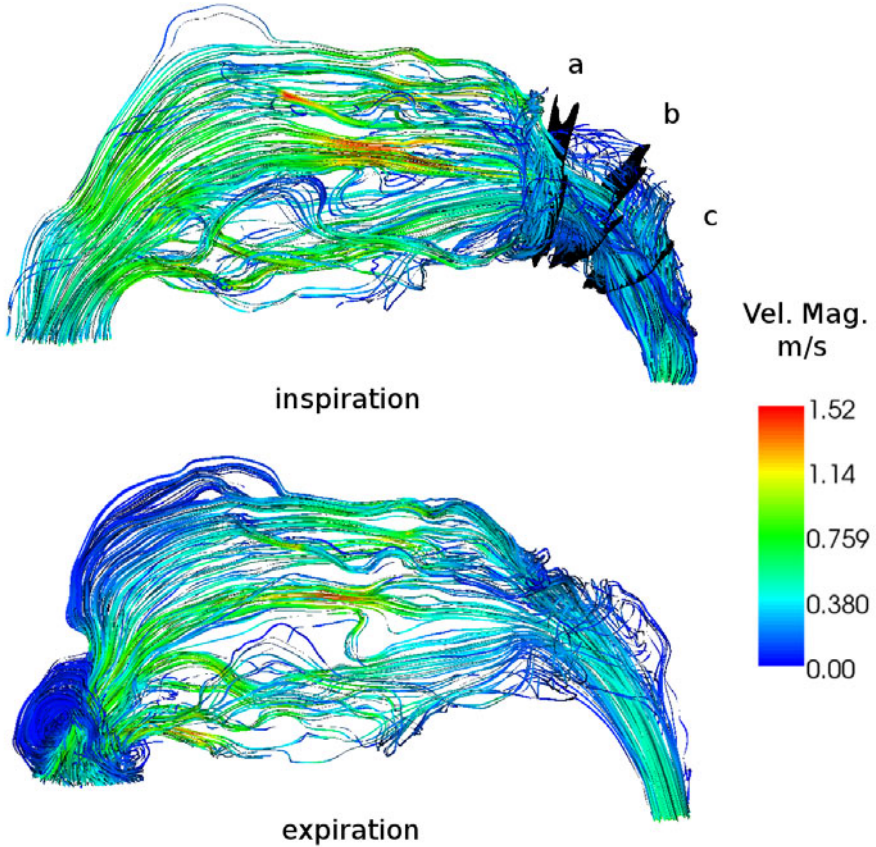
Fig. 2. Streamlines for the right nasal cavity; inspiration (top), expiration (bottom).

4   Results

It has been shown in a sequel of papers by I. HÖRSCHLER ET AL. [11, 12, 13, 14] that the flow in a nasal cavity can be assumed laminar and steady. The present work focuses on the comparison of the steady flow field at inspiration and expiration. Based on the findings in [11] the simulations were performed without any turbulence model. To investigate the structure of the flow field in a real nasal cavity, first simulations were conducted for the geometry shown in Fig. 1.

At the inlet cross section the velocity and the pressure distribution are prescribed, whereas a zero-gradient formulation of the macroscopic flow variables is implemented for the outlet. The boundary conditions are prescribed such that a constant flow rate of $96\,\mathrm{ml/s}$ for inspiration and expiration, i.e. a Reynolds number of $Re = 600$ based on the hydraulic diameter of the throat, is achieved. The no-slip boundary condition at solid walls is implemented by an interpolated bounce-back scheme [5]. The simulation
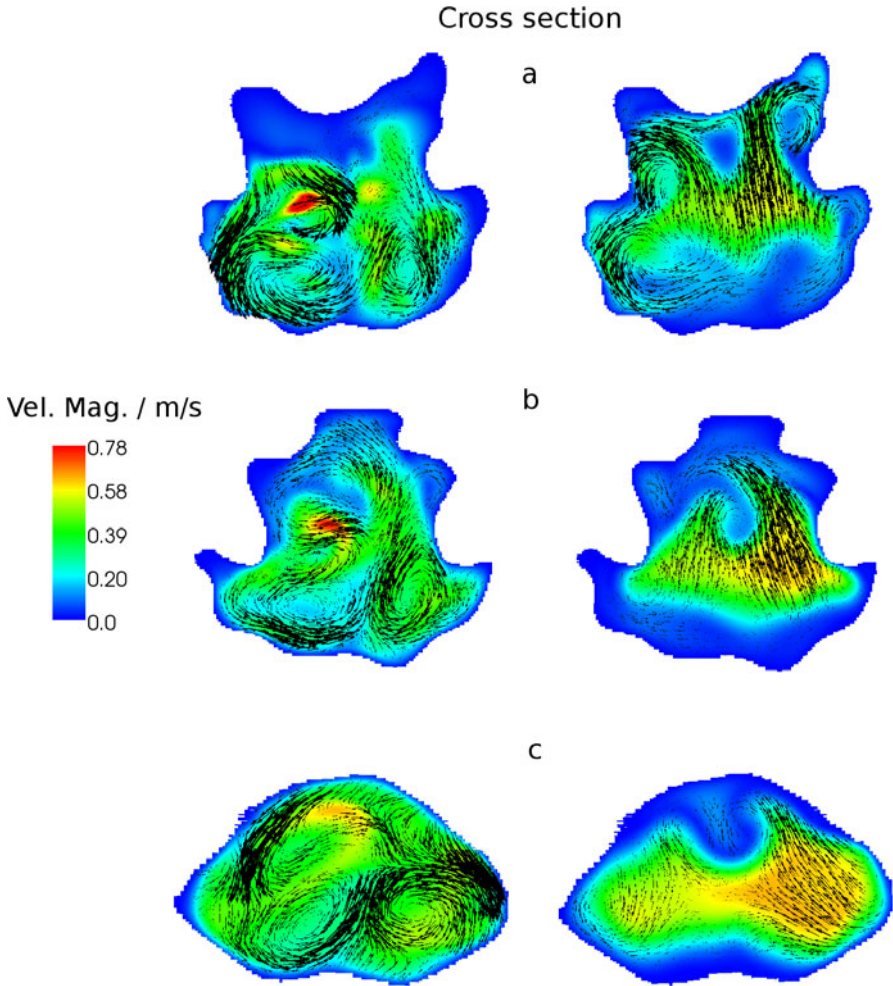
Cross section

Fig. 3. Velocity distributions in three coronal cross sections; inspiration (left), expiration (right); the velocity magnitude is given by the color and the vectors evidence the velocity distribution in the respective cross section.

for inspiration and expiration has been performed on a mesh consisting of 5 million cells and each computation took approximately 5 hours running on 32 Power6 SMT processors with 4.7 GHz.

The three-dimensional character of the flow field is evidenced by the streamlines for the right nasal cavity (dorsal view) presented in Fig. 2. Although both flow fields have similar main pathways, several differences are apparent. At inspiration the velocity increases, since the turbinates form a converging inner cavity. Moreover, these turbinates divide the flow into a multiple-channel geometry with several nozzle-like channels above the inferior turbinate which enhance the velocity maxima denoted by

red streamlines. Downstream of the septum the decomposed flow merges again causing strong vortical structures to develop.

At expiration the air flows from the throat over the turbinates towards the nostrils. The flow reaches further into the forehead region than at inspiration. A recirculation region is formed above the nostrils and hardly any vortical structures are observed near the throat. Note, however, that the flow field in the throat is strongly determined by the imposed boundary condition.

To gain insight into the secondary flow structures in the region between the turbinates and the throat, three cross sections *(a,b,c)* were defined in Fig. 1. The corresponding velocity distributions for steady inspiration and expiration are depicted in Fig. 3. At inspiration one observes a pronounced asymmetric flow downstream of the septum forming a pair of counter-rotating vortices. This flow structure is initiated by a vertically deflected mass coming from the upper regions. These jets are guided along the outer wall and impinge upon each other on the bottom of the throat. The observed flow structures are likely to be essential for moistening and cleaning inhaled air. During expiration the flow near the throat has bearly any velocity components perpendicular to the mainstream direction. Nevertheless, two counter-rotating vortices form in the upper region of the geometry just upstream of the turbinates.

These results evidence the highly intricate flow structure in a nasal cavity. In agreement with studies for a simplified nose model [13, 14] it can be concluded that the flow field at expiration possesses less vorticity than that at inspiration.

5   Conclusions

A realistic geometry of a human nasal cavity has been reproduced from tomography data and the flow field has been numerically simulated using an LBGK algorithm. This method has been proven to be an efficient tool to simulate flows through highly intricate geometries and it possesses a structure being well suited for massively parallel simulations due to its good parallel scalability. Another interesting feature of the applied numerical method is the automated grid generation for arbitrary geometries.

The flow field has been analyzed at steady inspiration and expiration for a constant flow rate of 96 ml/s. The visualization has evidenced the intricate three-dimensional character of the flow field. At inspiration strong vortical structures have been observed resulting in counter-rotating vortices along the throat. At expiration a recirculation region has occured near the nostrils, whereas the flow in the throat has been characterized by only a slight vortical flow.

The complete process of CT-data acquisition, geometry reconstruction, and numerical flow simulation can be performed in one day for one patient. Thus, the application of the presented method for computer assisted surgery will be feasible in the near future. By means of a virtual reality environment a surgeon will gain insight into the complete three-dimensional geometry of the nasal cavity. Furthermore, the flow field simulation will show regions of separations, high shear, etc. In a second step the consequences of surgical modifications could be analyzed with respect to fluid dynamic criteria such that it might be possible to determine a clearly improved shape of certain regions of the nasal cavity with respect to, e.g., inhalation and exhalation requirements.

Acknowledgement

References

[1] Adams, L., Krybus, W., Meyer-Ebrecht, D., Rueger, R., Gilsbach, J., Mösges, R., Schlöndorff, G.: Computer assisted surgery. IEEE, Computer Graphics and Applications 10, 43–51 (1990)

[2] Adams, R., Bischof, L.: Seeded region growing. IEEE Transactions on Pattern Analysis and Machine Intelligence 16(6), 641–647 (1994)

[3] Benzi, R., Succi, S., Vergassola, M.: The Lattice Boltzmann Equation: Theory and Applications. Physics Reports 222(3), 145–197 (1992)

[4] Bhatnagar, P.L., Gross, E.P., Krook, M.: A Model for Collision Processes in Gases. I. Small Amplitude Processes in Charged and Neutral One-Component Systems. Phys. Rev. 94(3), 511–525 (1954)

[5] Bouzidi, M., Firdaouss, M., Lallemand, P.: Momentum transfer of a Boltzmann-lattice fluid with boundaries. Physics of Fluids 13(11), 3452–3459 (2001)

[6] Brücker, C., Park, K.I.: Experimental study of velocity fields in a model of the human nasal cavity done by DPIV. In: Proc. 1st Int. Symp. Turbulence and Shear Flow Phenomena, Santa Barbara, California, September 1999, pp. 831–836 (1999)

[7] Finck, M., Hänel, D., Wlokas, I.: Simulation of nasal flow by lattice Boltzmann methods. Computers in Biology and Medicine 37, 739–749 (2007)

[8] Freitas, R.K., Meinke, M., Schröder, W.: Investigation of Wall-Bounded Turbulent Flow using Lattice Boltzmann Methods (2008) (submitted to Computers & Fluids)

[9] Hänel, D.: Molekulare Gasdynamik. Springer, Berlin (2004)

[10] Hartmann, D., Meinke, M., Schröder, W.: An adaptive multilevel multigrid formulation for Cartesian hierarchical grid methods. Comput. Fluids 37, 1103–1125 (2008)

[11] Hörschler, I., Brücker, C., Schröder, W., Meinke, M.: Investigation of the Impact of the Geometry on the Nose Flow. European Journal of Mechanics B/Fluids 25(4), 471–490 (2006)

[12] Hörschler, I., Schröder, W., Meinke, M.: Comparison of steady and unsteady nasal cavity flow solutions for the complete respiration cycle. Computational Fluid Dynamics JOURNAL 15(3), 354–377 (2006)

[13] Hörschler, I., Schröder, W., Meinke, M.: Numerical Analysis of the Impact of the Nose Geometry on the Flow Structure. Part I: Septum spurs. Computational Fluid Dynamics JOURNAL 16(2), 219–234 (2008)

[14] Hörschler, I., Schröder, W., Meinke, M.: Numerical Analysis of the Impact of the Nose Geometry on the Flow Structure. Part II: Nasal valve and lower turbinate. Computational Fluid Dynamics JOURNAL 16(3), 243–260 (2008)

[15] Lorensen, W.E., Cline, H.E.: Marching cubes: A high resolution 3D surface construction algorithm. In: SIGGRAPH 1987: Proceedings of the 14th annual conference on Computer graphics and interactive techniques, pp. 163–169. ACM, New York (1987)

[16] Taubin, G.: A signal processing approach to fair surface design. In: SIGGRAPH 1995: Proceedings of the 22nd annual conference on computer graphics and interactive techniques, pp. 351–358. ACM, New York (1995)

[17] Taubin, G., Dudhia, J., Zhang, A.P.K.T., Golub2, G.: Optimal surface smoothing as filter design. In: Buxton, B.F., Cipolla, R. (eds.) ECCV 1996. LNCS, vol. 1064, pp. 283–292. Springer, Heidelberg (1996)

[18] Weinhold, I., Mlynski, G.: Numerical simulation of airflow in the human nose. European Archives of Oto-Rhino-Laryngology 261, 452–455 (2004)

[19] Zhao, K., Scherer, P.W., Hajiloo, S.A., Dalton, P.: Effects of Anatomy on Human Nasal Air Flow and Odorant Transport Patterns: Implications for Olifaction. Chem. Senses 29(5), 365–379 (2004)

Simulation of the Flow in a Human Nose

Roland Kessler[1], Markus Rütten[1], and Julien Pennecot[2]

[1] DLR Göttingen, Institute for Aerodynamics and Flow Technology,
Bunsenstraße 10, D-37073 Göttingen, Germany
[2] CIMNE Barcelona, Edifici C-1, Campus Nord UPC,
Gran Capit, 08034 Barcelona, Spain

Summary

The human nose is a very complex organ. The main airways together with a multiplicity of nasal cavities and sinuses are involved in the various functions of the nose. It warms and humidifies the inspired air, filters out small particles and supports the olfaction process by transporting odor-bearing particles to the muscous membranes. The flow simulations presented in this paper are based on the geometry of a real human nose. Based on a series of CT images, a body-fitted, hybrid numerical grid was built up. The DLR THETA code is used to simulate the unsteady flow inside the nose. The transport of a marker gas is simulated to visualise the entrainment of air from the sinuses to the inspired air.

1 Introduction

The analysis of fluid mechanical phenomena is a key for a better understanding of many complex biological processes. Especially in the field of respiration, numerical simulations of fluid flows has become a valuable tool for the study and explanation of complex physical and biological processes. While simplified simulation models are often used in the past, high resolution computer tomography (CT) in connection with modern reconstruction algorithms allow the setup of very complex grids for advanced numerical simulations.

Two different concepts are proposed for numerical fluid simulations in highly complex geometries: cartesian grids and unstructured body fitted grids. The former approach allows a very simple and efficient numerical method in the inner flow regime [1]. However, the boundary treatment is complicated and may affect the overall accuracy of the simulation. The second approach requires a more elaborate numerical scheme for the inner part of the simulation domain, but allows a simpler implementation of the boundary conditions.

With the use of the DLR THETA code, which is an extension of the TAU code for low Mach number flows, we choose the body-fitted approach for the studies in the present paper. The simulation of the flow in a human nose is an excellent example for evaluating the accuracy and the performance of our simulation tools. Besides the quality of the initial grid, the adaptation of the grid is essential for an accuracte and efficient numerical solution on unstructured, hybrid grids.

From the physical point of view, we are interested in the temporal behaviour of the flow. The Reynolds numbers of typical flows through the nose are in a transition range and both, steady and unsteady results are possible. The role of the fluid in the paranasal sinuses is not well known. Although these cavities may not be important for the main flow, we are interested in the mass exchange between the meatuses and the adjacent paranasal sinuses.

2   Numerical Method

We use the DLR THETA code for solving the incompressible Navier-Stokes equations. This code is a finite volume method based on the well known DLR-TAU code. The dual grid approach is applied to unstructured, hybrid grids and all variables are stored at the same location (colocated or non-staggered approach). An efficient coupling of the velocity and the pressure fields is ensured by the projection method or the SIMPLE alogorithm. The well-known chequerboard instability of the pressure is eliminated by a 4th order stabilisation term, which is added to the left and the right hand side of the Poisson equation.

The discretisation of the convective terms is done using upwind methods of 1st or 3rd order as well as central 2nd order schemes. A 2nd order implicit time integration scheme allows stable simulations even for large time-steps. A matrix-free formulation is used for solving the linear equations. This formulation reduces considerable the memory requirements of the code. The multi grid method ensures efficient solutions of the linear equations even on fine grids. More details of the numerical method and its validation can be found in [3] The domain decomposition is used as a parallelisation concept. The parallel efficiency is high on desctop computers with only a few cpus as well as on massive parallel systems with hundreds of cpus.

3   Results

3.1   Grid Generation and Adaptation

In this study, we start from a high fidelity CFD mesh of the complete nasal cavity based on a set of CT images. The surface mesh was generated by a tool which uses the following techniques: blurring, edge detection, thresholding, advancing front and marching cube method, non-shrinking smoothing and polygon reduction methods [2]. Once the surface grid is built, we used the grid generator NETGEN to generate the volume grid. Up to three prism layer are positioned near the wall and the remaining volume is filled with tetrahedrons. As the flow is expected to be laminar, a clustering of cells near the walls is not required. However, the near wall structured layers lead to better overall accuracy of the simulations.

The initial grid generated by the algorithm described above consist of about 2 Mio primary elements (prisms and tetraeders). The number of unknowns for the related dual grid is 790.569. A first adaptation step was performed using the magnitude of the velocity as a simple indicator. The resolution remains unchanged in most of the paranasal sinuses, where the velocity is found to be very small. In regions with a high magnitude
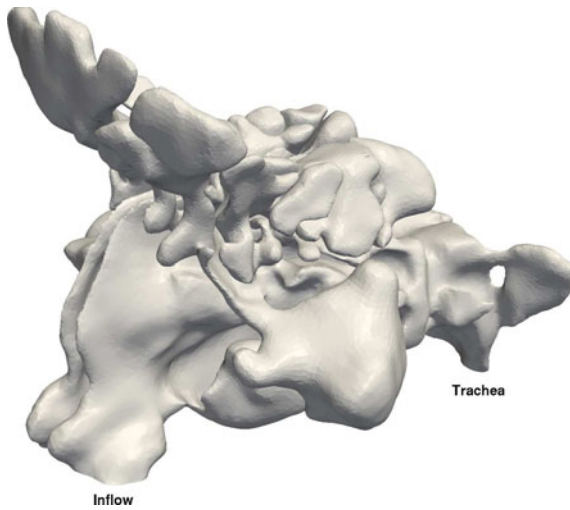
Fig. 1. Surface of the reconstructed human nose

of the velocity, the resolution is increased by a subdivision of the primary elements of the grid. The total number of points increases to 2.6 Mio points for the finer grid. As the coarse and fine grid solutions differ by less than 10%, no further adaptation step is performed. All results shown below are performed using the adapted grid and the 3rd oder scheme for the convective terms.

3.2   Unsteady Simulation

The character of the flow inside the nose is essentially determined by the inflow condition prescribed. Whereas the natural respiration process is characterised by an unsteady volume rate at the inlet plane, we simplified the problem by setting a constant volume rate of 22.2 litre of air per minute, which corresponds to an inflow velocity of 2 m/s. The Reynolds number computed with the local velocity and a typical local hydraulic diameter is listed in table 1 for three positions. The numbers suggest a laminar flow and therefore no turbulence model is activated in the THETA code.

Table 1. Reynolds number for a volume rate of 22.2 litre per minute at different locations

location	Re number
inlet	2174
inner region	570
trachea	2505
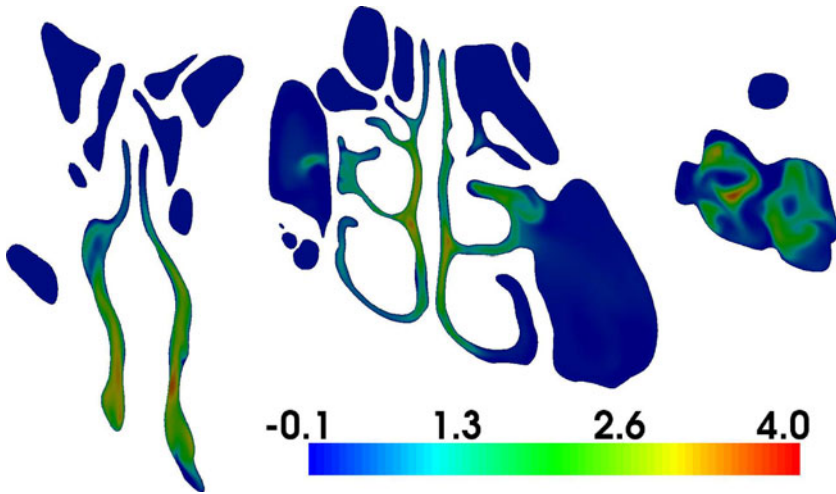
Fig. 2. Time-averaged y-velocity in slices at x = 0.03, x = 0.06 and x = 0.09
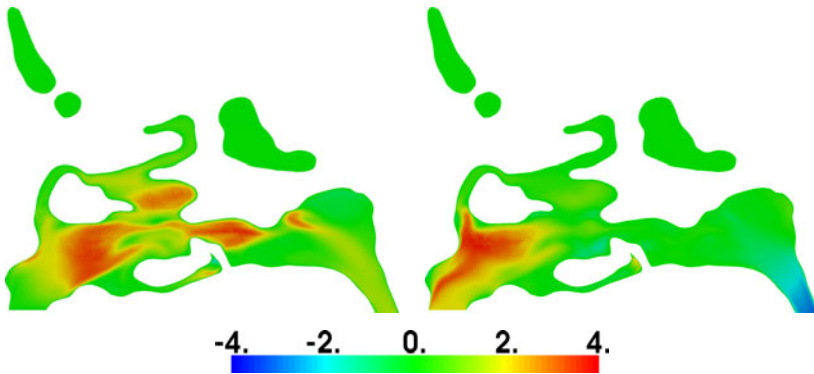
Fig. 3. Time-averaged y-velocity (left) and x-velocity (right) at y = 0.044

Contours of the y-component of the time-averaged velocity at three transversal cuts are shown in Fig. 2. The flow is highly asymmetric which is caused by the asymmetry of the geometry itself. Maximum velocities of nearly 4 m/s can be found at some positions of the nasal cavity, whereas the velocities inside the paranasal sinuses are small. A longitudinal cut is shown in Fig.3. Several regions of high velocities alternate with regions of lower speed. Due to the twisted nasal cavity, the longitudinal cutting plane touches near wall regions, which leads to observed strong variation of the velocity in these plots.

The temporal behaviour of the flow is quit complex. Near the inflow plane and in the narrow parts of the nasal cavity in the middle region of the nose, we observe steady flow or small oscillations. The oscillatory behaviour can be explained by local vortex
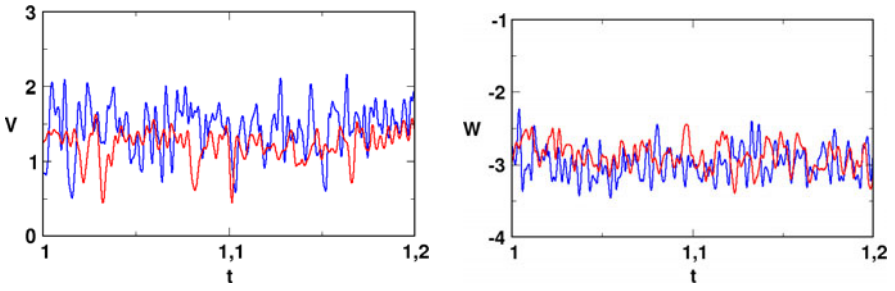
Fig. 4. Temporal behaviour of the y- and z-component of the velocity The monitor points (see Fig. 5) are located after the conjunction of the nasal cavities (left) and near the outflow plane (right). The red and blue curves indicate different transversal positions
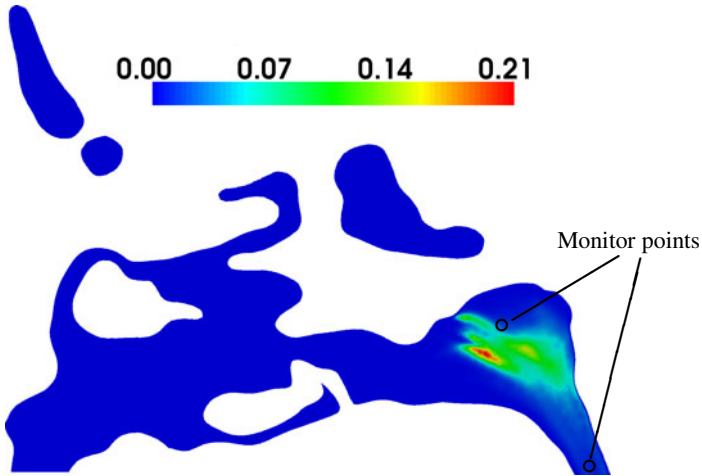
Fig. 5. Contout plot of the mean square of the velocity fluctuations in the plane x = 0.044

shedding phenomena in the highly warped nasal cavity. In the rear part of the nose, the left and right nasal cavities join and the geometry widens. Here we detect a strongly unsteady, nonperiodic flow. The temporal behaviour can be seen in the plots of Fig 4. The plot on the left hand side shows the y-component of the velocity at two positions right after the conjunction of the two parts of the nasal cavity. The fluctuation part of the velocity exceeds 70% of its averaged value. The z-component of the velocity near the outflow boundary is shown in the right plot. Here the fluctuations do no even exceed 40% of the averaged value. This damping is caused by the acceleration of the flow near the crossover of the nose to the trachea. The mean square of the velocity fluctuations

$$V'^2 = \frac{1}{2}\left(u'^2 + v'^2 + w'^2\right)$$

can be seen in the contour plot of Fig 5. A region of high fluctuations is indicated by the red and green spots near the rear part of the nose, whereas an almost steady flow can be observed upstream this region.
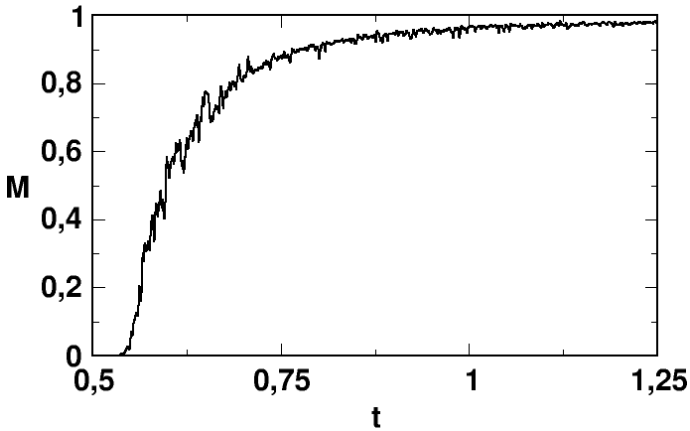
Fig. 6. Time-dependent behaviour of the mixture fraction M at the outflow plane

3.3   Fluid Mixing

The results presented above give no information about the mixing of the nearly station-ary fluid in the paranasal sinuses and the fluid flow passing through the nasal cavities. Therefore, we made a numerical experiment using two fluids with identical physical properties. This is realised in the simulation by solving an additional transport equation for the mixture fraction M. A value of zero indicates the fluid A while a value of one is related to the marked flow (fluid B).

The simulation is initialised with fluid A. After a transient phase of 0.5 seconds, the flow is fully developped and we switch to the marked fluid B at the inlet plane. The time-dependent behaviour of the mass fration at the outflow plane is shown in Fig. 6. Up to $t = 0.55$, the mixture fraction remains zero, indicating a minimal flow-through time of about 0.05 seconds. After 5 minimal flow-through times ($\Delta t = 0.75$), 90% of fluid A is replaced by the marked fluid B at the outflow plane. A small fraction of 2% of the fluid A can be found at the ouflow plane even after a long time ($\Delta t = 0.75$). This fluid is entrained mainly by diffusion from the paranasal sinuses.

The spatial distribution of the computed instantaneous mixture fraction can be seen in Fig 7 at four different times. At t = 0.625, a strong mixing of both fluids can be observed in the rear part of the nose, resulting in a mixture fraction of about 0.5 at the outflow plane. Most of the nasal cavity is filled with fluid B after a Δt of 0.375 seconds. The diffusion process can be seen in some paranasal sinuses. Less than one second is sufficient to fill some smaller sinuses with up to 50% of the pass through fluid.
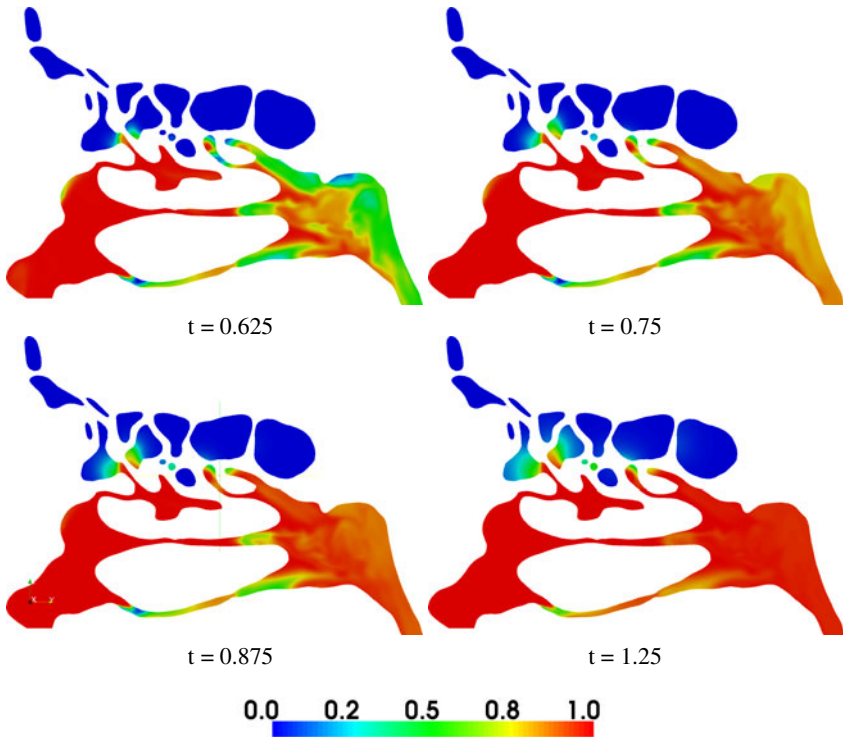
Fig. 7. Spatial distribution of the mixture fraction in a longitudinal cut at four different times. A mixture fraction of zero corresponds to the initial fluid A, a value of one indicates the fluid B

4   Conclusion

Starting from a high quality, body fitted hybrid grid, the DLR THETA code enables efficient simulation of the flow in a human nose. All essential features of the flow were captured by a first simulation on the initial grid. A single adaptation step refines the grid in regions of higher velocities and leads to grid independent numerical solutions. A further increase in efficiency could be obtained by starting with an even coarser grid followed by two or three adaptation steps.

The numerical results show steady flow regimes in the narrow parts of the nose and a highly unsteady flow after the conjunction of the right and left part of the nasal cavity. Different velocities in the various parts of the nose cavity lead to a strong mixing of the marked, inspired air and the unmarked air of the nasal cavity. Diffusion is mainly responsible for the mixing of flow-through air and the air inside the sinuses.

For an even more realistic simulation of the nose flow, effects like surface deformation, temperature transport and disturbances caused by small hairs probably have to be taken into account.

References

[1] Miki, T., Imai, Y., Nakamura, M., Iwamura, C., Ishikawa, T., Wada, S., Yamaguchi, T.: Image-Based Pulmonary Airflow Simulation using Cartesian Adaptive Mesh Generation. In: 5th European Congress on Computational Methods in Applied Sciences and engineering, Venice (2008)

[2] Pennecot, J., Krenkel, L.: An Automated Reconstruction of the Lungs for CFD Simulations. In: 5th European Congress on Computational Methods in Applied Sciences and engineering, Venice (2008)

[3] Knopp, T., Zhang, X., Kessler, R., Lube, G.: Enhancement of an industrial finite-volume code for the large-eddy-type simulation of incompressible high Reynolds number flow using near-wall modelling. Comput. Methods Appl. Mech. Engrg. (2009) (accepted for publication), doi:10.1016/j.cma.2009.01.005

Aerodynamics of the Wing/Fuselage Junction at an Transport Aircraft in High-Lift Configuration

Stefan Melber-Wilkending

German Aerospace Center (DLR), Institute of Aerodynamics and Flow Technology
Lilienthalplatz 7, D-38108 Braunschweig, Germany
Stefan.Melber@DLR.de

Summary

This paper presents the numerical simulation (DLR TAU-code) and the analysis of viscous high-lift flow around a complex wing/body configuration (DLR ALVAST) in landing configuration. The investigations aim for a better understanding of the aerodynamics at the wing root and the lift breakdown for such a configuration.

1 Introduction

The optimization of a transport aircraft at high incidence with respect to low speed take-off/landing capabilities and handling qualities near wing stall is a complex aerodynamic problem. The aerodynamic characteristic of such a high-lift configuration is determined by the type of high-lift devices and its settings. In addition there are some critical areas like the engine/nacelle integration or the wing/fuselage junction, which trigger premature flow separation. A triggered wing stall is usually advantageous for handling quality reasons, but it limits the maximum lift. The design of the AIRBUS A321 [1] is an example for such an optimization aiming on the wing root flow, especially on the inner slat-end/fuselage juncture. It was found that a small device at the inner slat end delays the wing root stall significantly [2].

The tools to study such aerodynamic effects are on one hand wind tunnel testing which provides mature measurement techniques and is therefore the basis of the industrial aircraft development. On the other hand fast low order design methods are used which however have only a limited accuracy in forecasting three-dimensional effects. Therefore increasingly higher order numerical methods like volume methods based on the Navier-Stokes-equations are coming into business [3] which compared to wind tunnel experiments hold the promise to significantly accelerate the aerodynamic design, save costs and give a detailed insight into the flow field.

This paper continues the investigations of the DLR ALVAST ("Aerodynamic Performance Improvement at Subsonic Transport Aircraft") wing/body transport aircraft configuration in high-lift condition [4], [5]. The focus is mainly on an improved understanding of the complex flow field, which is dominated by 3D effects. Another objective is the reproduction of the stall effects and the lift breakdown as found in wind tunnel tests depending from the variation of the geometry at the area of the wing/body junction.
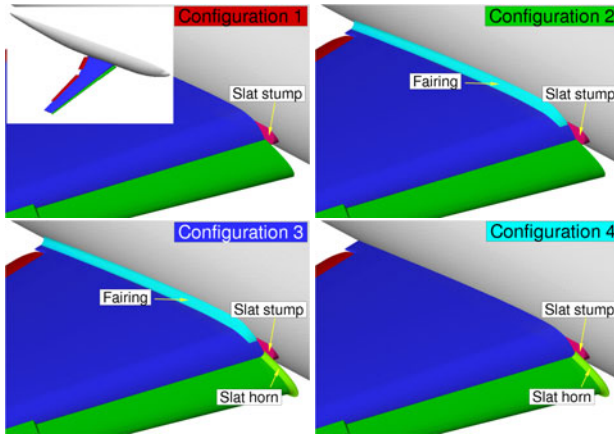
Fig. 1. ALVAST highlift configuration and its variation of the geometry in the area of the wing/body junction. Configurations *1-4*

2   Numerical Method, Geometry and Meshes

The solution of the Reynolds-averaged Navier-Stokes equations (RANS) is carried out using the hybrid unstructured DLR TAU code [6]. For the closure of the Reynolds-averaged equations the k-ω-SST turbulence model of Menter is used which combines robustness and the applicability to partly detached flows. Due to low Mach numbers and the resulting stiffness of the RANS equations low Mach number preconditioning is used. Also the laminar/turbulent transition is detected automatically [7] and accounted for the numerical simulations which also prevents the so called stagnation point anomaly of the k-ω-SST model. The central JST-scheme in combination with 80% matrix dissipation assures numerical flow solutions with low numerical dissipation. The numerical wind tunnel is used to remove uncertainties of half-model testing, wind tunnel corrections and angle-of-attack hysteresis [8].

The configuration considered in this paper is the ALVAST transport aircraft geometry (Figure 1), a generic configuration of a modern, two-engine transport aircraft like an AIRBUS A320 (scale 1 : 10). The slat on the landing configuration used here is deployed at 27.0^o, the single slotted flap at 32.0^o. The half-model was placed on a peniche (height $68~mm$) in the low-speed wind tunnel DNW-NWB (Braunschweig, cross-section $3.25~m \times 2.80~m$). The free-stream conditions are a velocity of $|V_\infty| = 60~m/s$ and a Reynolds-number of $Re_\infty = 1.435 \cdot 10^6$ with the mean aerodynamic chord $l_\mu = 0.41~m$ used as reference length. The hybrid unstructured meshes for the numerical simulations are generated using the grid generator *Centaur* of CentaurSoft [9], for details see [8].

3   Results

For the ALVAST-configuration a large number of measurements on national and also European level [10] are available. Concerning the achievable maximum lift and the

flow at the wing/body junction the following effects have been found: a flow separation at the wing-root section is the limiting factor for the maximum lift of the ALVAST-configuration. The flow separation can be considerably reduced and moved to higher angles of attack by closing the gap between the inboard slat-end and the fuselage and further with an reduced impact by a fairing on the upper-side of the wing. However on an real aircraft the gap cannot be closed because the slat has to be moved and therefore the effect of an end-plate including a fillet on the inboard slat end (slathorn) has been investigated, which shows nearly the same positive effect as closing the gap [10].

A variation of the geometry in the area of the wing/body junction during the wind tunnel test shows in Figure 1 the following sensitivity: while the geometry with slathorn and the wing/body fairing (*3*) reaches the highest maximum lift and with a small trade off the geometry with slathorn alone (*4*), both geometries without slathorn (*2* and *1*) have a significantly lower lift, compare Figure 2. In cases *2* and *1* the same small reduction can be found without a fairing. It can be found the slathorn has a considerable influence on the achievable maximum lift whereas the fairing has a supporting effect.

Further in Figure 2 the results of the numerical simulations are shown. Compared with the measurements the influence of the geometry variations at the wing/body junction for configurations *1-3* are correctly reproduced concerning the maximum lift whereas configuration *4* shows a clear deviation. A detailed investigation of the different influences like the turbulence model, the behavior of local flow separations, differences in the wind tunnel model-geometry compared to the CAD-model, the deformation of the wind tunnel model and the brakets of the slat- and flap-segments has been done. Because of the limited length of this paper this results cannot discussed here.
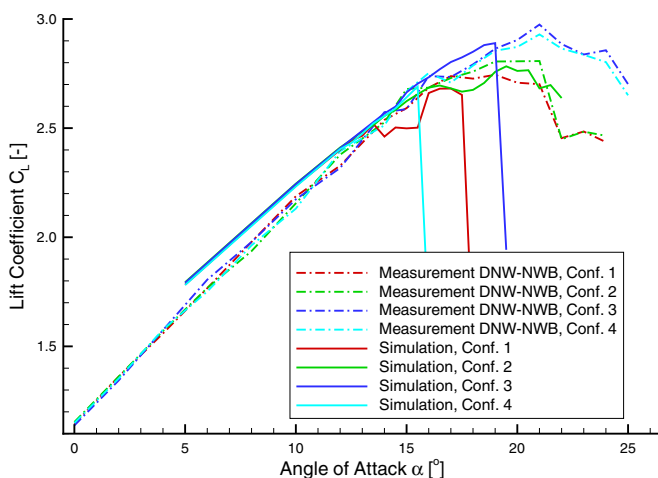
Fig. 2. Lift polars of the ALVAST highlift configuration *1-4*

In the following the differences in the flow fields will be traced back to the variations of the geometry and the mechanism of the maximum lift will be explained. In general

the lift breakdown does not take place immediatly after a topological change of the flow field but is commonly induced by an existing flow separation which spreads out with increasing angle of attack and leads to a final lift breakdown. Therefore in a first step flow separations of the ALVAST configuration have been detected and checked, if there exists a connection with the geometry variation. On the outboard wing starting with an angle of attack of $\alpha = 12^o$ a flow separation occurs on the trailing edge of the wing. The reason is a pressure rise in flow direction towards the trailing edge which is increased because of the missing flap in this area and finally overstressing the boundary layer. An area of flow with low kinetic energy can be found above both flaps without any contact to the surface starting with an angle of attack of $\alpha = 10^o$. This is caused by the pressure rise inside the slat- and wing-wakes in the flow field.

All flow separations discussed until now have no dependency with the geometry at the wing/body junction. However the fairing itself has a significant influence: if no fairing is placed already at lower angles of attack a flow separation spreading out from the trailing edge of the wing can be found. One reason is the low wing mounting with the occurring acute angle between wing and fuselage forms a channel, which is increasing in the direction to the trailing edge. The downwash of the wing and the spanwise flow is not sufficient to fill up the volume of the channel, after all the fuselage shields the downwash geometrically. Because of necessary movement of the flaps a part of the trailing edge of the inboard wing is not covered with a flap, which additionally increases the load on the boundary layer.

However the behavior found at maximum lift cannot be completely explained with the influence of the faring: The configurations *2* and *3* which both have a fairing but a completely different behavior of maximum lift (Figure 2). Although for configuration *2* at an angle of attack of $\alpha = 16.5^o$ a flow separation can be found in this area which does not spread out untill an angle of attack of $\alpha = 19.5^o$. Therefore there must be another mechanism which influences the maximum lift. To exclude the influence of the fairing, in the following configurations *2* and *3* will be considered, which both have a faring. Comparing the positions of the vortices (Figure 3) significant differences can be found in the position and also in the topology of the vortices in the area of the wing/body junction. To determine the influence of the vortices on the maximum lift, they should be discussed in more detail.

In the area of the wing/body junction the boundary layer of the fuselage hits the leading edge of the wing respectively the slat stump. A stagnation point occurs with a significant pressure rise stream-up, which cannot be overcome by the boundary layer of the fuselage and therefore it separates from the fuselage surface. This forms the so called horseshoe vortex, which diverts from the free stream around the wing-root (Figure 3) and increases its diameter on the upper wing because of the pressure rise behind the maximum thickness. In (Figure 3, colored in red) overall three (primary) horseshoe vortices can be identified at the wing/body junction: the primary slat stump horseshoe vortex in front of the slat stump, which runs along the fuselage and vanishes after a short distance because of its weakness. The slat-edge stump vortex is created on the spanwise outboard side of the slat stump and is strictly speaking no horseshoe vortex, because it is initiated by a local flow separation at the edge of the slat stump. Its rotation direction and behavior is however analogous to a horseshoe vortex. After

the generation on the edge it merges with the primary slat stump horseshoe vortex. The third primary horseshoe vortex is generated in front of the wing on the wing leading edge.

Because of the pressure difference from the upper- to the lower-side the flow is running around the inboard side edge of the slat creating a primary slatside edge vortex on the upper side edge and propagates on the upper wing to the trailing edge. The rotation direction on the upper wing is the same as for the horseshoe vortices. With increasing angle of attack the vortex strength is increased and moving steeper above the wing because of the free-stream flow. Inside the gap between the slat and the fuselage respectively the slat stump an accelerated flow occurs because of the reduction of the cross section. This jet-like flow moves in spanwise direction due to the low pressure in the area covered by the slat. Because of the interaction with the gapflow on the slat side-edge the secondary slat side-edge vortex with the same rotation direction as the primary slat stump horseshoe vortex, runs cross the free-stream with increasing distance to the upper wing and combines with the primary slat stump horseshoe vortex. In front and above the primary slat side-edge vortex on the surface of the fuselage the induced velocity leads to a redirection of the flow and additionally the vortex blocks partially the downwash of the wing, which induces finally a counter-rotating vortex. This secondary horseshoe vortex runs along the fuselage parallel with the inducing primary slat stump horseshoe vortex and moves downwards because of its own induced velocity.

On a swept wing creating lift the flow on the lower side is directed outboard because of the trailing vortices. Therefore in the slat-gap a spanwise outboards directed flow can be found with a magnitude comparable to the free-stream velocity. Regarding the flow running from the lower side in the slatgap the cove of the slat is a type of undercut and therefore the flow separates and forms a slatcove vortex. In the section of the inboard slatend this spanwise flow runs from the lower trailing edge of the slat in the slat cove while inside the cove the flow velocity increases because of the suction peak on the wing leading edge. The slatcove vortex is moved upwards because of this flow and leaves the slatgap on the upper side of the wing counter rotating compared to the horseshoe vortices (Figure 3, colored in blue).

Because of the additional volume needed for the described vortices along the fuselage the conclusion suggests itself this vortex-front has an influence because of its volume, its induced velocity and the shading of the downwash above the wing in the area of the wing/body junction and therefore influences the maximum lift of the configuration. A closer look on the cross-flow shows however that only in small distances from the vortex-front a significant induced flow velocity can be found and there the shading effect of the vortex front plays no significant role.

The differences in the position of the vortices for configuration *2* and *3* can be found already in the area of the slat- and wing-leading edge (Figure 3). A detailed analysis in this area shows in case of the configuration with slathorn (*3*) that the primary slat side-edge vortex leaves the surface earlier and has in spanwise direction a closer distance to the surface of the fuselage. At the same time the rollup of the vortex starts earlier on the slat side-edge, which indicates a stronger vortex compared to the case without the slathorn. The construction of the slathorn on a sheet of metal with a finite thickness reduces the gap between the slatside edge and the slat stump and the resulting
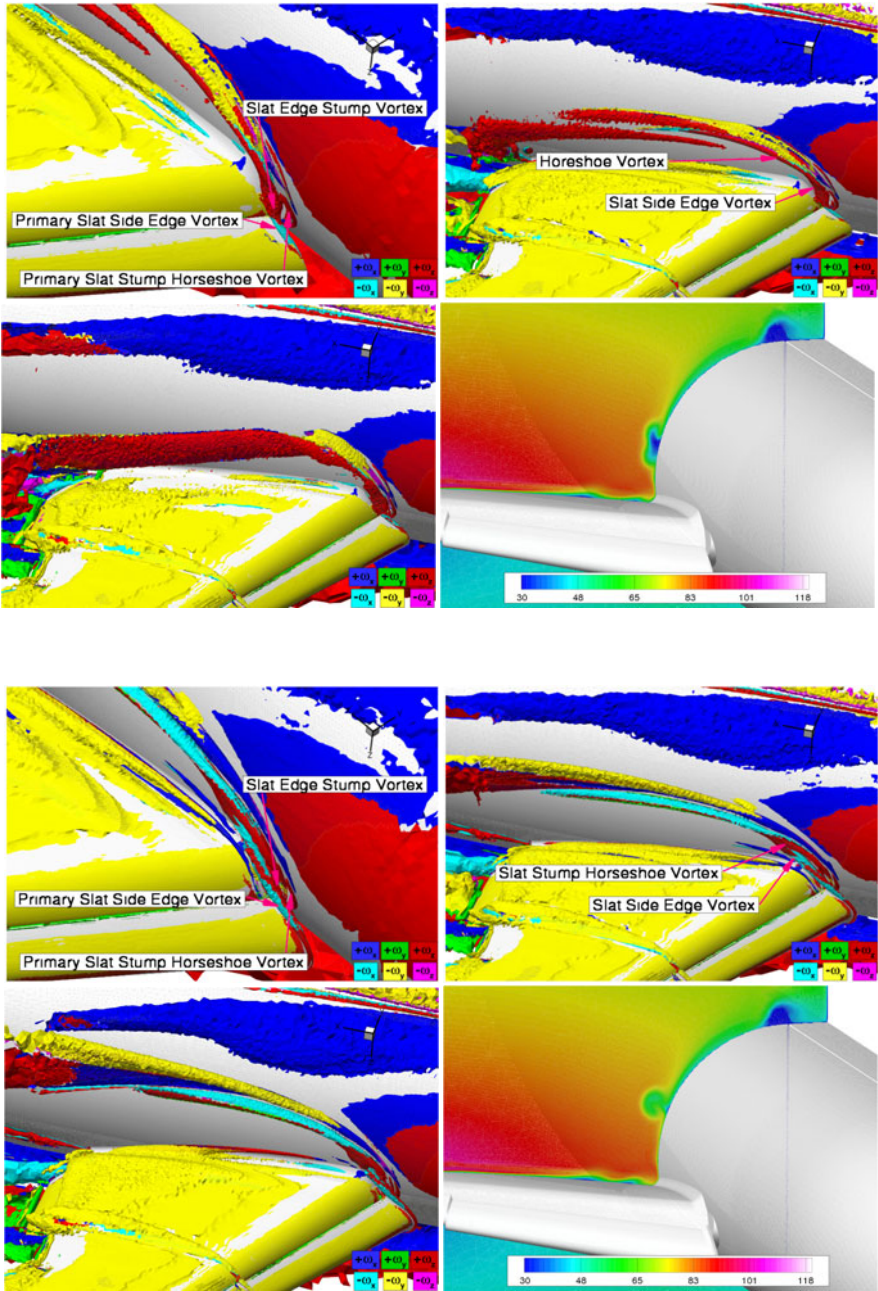
Fig. 3. Configuration 2 (top) and 3 (bottom): in each case vortex topology in the area of the wing/body junction colored with the rotation direction of the vortices and cut through the flow field perpendicular to the fuselage axis short before the wing trailing edge, magnitude of the velocity $|V|$ (lower right), angle of attack $\alpha = 14^o$ and $\alpha = 16^o$ lower left

channel in longer in flow direction. The increased drag in the channel reduces the flow velocity compared with a configuration without a slathorn, but the gap flow itself is more unified and moved farther towards the upper wing surface because of the smaller and longer channel. This leads to an additional deflection of the merged horseshoe vortices more upwards and more inboards compared to the slat side-edge. Further a better separation of the unified horseshoe vortices from the equal rotating primary slat side-edge vortex occurs. This separation is increased because of the jet-flow from the gap and the increased area of the slat side-edge. In the case with slathorn this leads to a delayed mixing of the primary slat side-edge vortex and the unified horseshoe vortices, so that these by vortices rotates enhanced rotation around each other (Figure 3).

This interaction of two vortices plays now an important role in the further discussion. The mixing behavior of two vortices rotating in the same direction depends among other things like the core radius, vortex Reynolds number and there distance on the circulation of each partner: in the case without a slathorn (*2*) the primary slat side-edge vortex is weaker as the unified horseshoe vortices and this leads to a fast mixing. In the contact area because of the opposite induced flow velocity additional dissipation occurs, which increases the size of the vortex and reduces the flow velocity in the resulting vortex core. In the case with slathorn (*3*) however both vortices have nearly the same strength and therefore thus rotate around each other with a bigger distance as in the case before. The increased distance reduces the dissipation on the contact surface significantly and over a much longer distance two separated vortices can be found in the flow field (Figure 3), whereas in the case without slathorn the increasing expansion and deceleration in the vortex core leads to vortex bursting (Figure 3). Further on in this Figure a cut of the velocity magnitude perpendicular through the fuselage-axis is shown for both configurations, which clearly shows the additional dissipation in the case without slathorn (*2*) because of the reduced flow velocity in the vortex core. At an angle of attack of $\alpha = 16^o$ (Figure 3) this behavior is clarified: in the case without slathorn (*2*) shortly after the mixing the resulting vortex bursts, whereas in the case with slathorn (*3*) no bursting can be found. In this case a slowly increasing vortex diameter of the secondary horseshoe vortex can be found, which is placed above the slowly mixing united horseshoe vortices and the primary slat side-edge vortex. Thereby the mixing point is moving slowly in the direction of the leading edge with increasing angle of attack, whereas the vortex front moves higher above the wing surface into the free stream direction.

In Figure 3 the different shifting of the vortex front on the upper wing between configuration *2* and *3* can be clearly seen. The difference is because the vortex front bursts early and has therefore only a small amount of induced flow velocity on the fuselage before bursting, clearly marked by the kink in the vortex path (Figure 3). In case of configuration *3* the vortex front runs much longer inducing itself a flow component directed upwards on the fuselage against the downwash of the wing. Further this behavior keeps the area of the wing/body junction free of any vortices. In case of the configuration without slathorn (*2*) the vortex front with its increased dissipation runs induced by the downwash of the wing in the area of the wing/body junction and leads to an additional weakening of the boundary layer. This finally leads to the earlier lift breakdown compared with configuration (*3*) with a slathorn.

For configuration *1* which has no slathorn like configuration *2* the shifting of the vortex front in the edge of the wing/body junction does not occur because the displacement of the flow separation. However because of the missing fairing a flow separation already exists which leads to the early lift breakdown.

4   Conclusion

With a systematic analysis of the complex three-dimensional flow topology of the ALVAST high lift configuration representing a transport-aircraft configuration the influence of geometric details in the area of the wing/body junction on the achievable maximum lift was demonstrated using the numerical wind tunnel. It was found that without a slathorn the early mixing of the primary slat-side edge vortex with the united horseshoe vortices leads to an increased dissipation and finally to a bursting of the vortex-front whereas with a slat horn this effect can be considerably reduced. The bursted vortex front degradates the flow between the wing and the fuselage and leads to an earlier stall of such a configuration. A fairing in the area however supports the flow in this area. The wind tunnel measurements in case of the already mentioned example of the AIRBUS A321 coincide with the flow topology of the ALVAST configuration [1], [2].

References

[1] Flaig, A., Hilbig, R.: High-Lift Design for Large Civil Aircraft. In: AGARD-CP-515, pp. 31-1–31-12 (September 1993)

[2] Schwetzler, D.: Improvement of Maximum Lift in Flight by Optimization of Vortex Flow. In: High-Lift and Separation Control Conference Proceedings, Univ. of Bath, United Kingdom, M"arz 29-31, pp. 4.1–4.10 (1995)

[3] Reckzeh, D.: Aerodynamic design of the high-lift-wing for a Megaliner aircraft. In: Aerospace Scienence and Technology, vol. 7, pp. 107–119. Elsevier, Amsterdam (2003)

[4] Rudnik, R., Melber, S., Ronzheimer, A., Brodersen, O.: Aspects of 3D RANS Simulations for Transport Aircraft High-Lift Configurations, AIAA paper 2000-4326 (2000)

[5] Melber, S.: 3D RANS Simulations for High-Lift Analysis of Transport Aircraft Configurations. Notes on numerical fluid mechanics, vol. 77. Springer, Heidelberg (2002)

[6] Kroll, N., Rossow, C.-C., Schwamborn, D., Becker, K., Heller, G.: MEGAFLOW - A Numerical Flow Simulation Tool for Transport Aircraft Design. In: 23rd ICAS Congress, ICAS 2002, Toronto, pp. 1.5–10.5 (2002)

[7] Melber-Wilkending, S., Schrauf, G., Rakowitz, M.: Aerodynamic Analysis of Flows with Low Mach- and Reynolds-Number under Consideration and Forecast of Transition on the Example of a Glider. In: 14th AG STAB/DGLR Symposium, November 16-18 (2004)

[8] Melber-Wilkending, S., Wichmann, G.: Project ForMEx - A new CFD approach for transposition of Wind Tunnel data towards Flight Conditions. In: 15th AG STAB/DGLR Symposium Darmstadt, November 29-December 1 (2006)

[9] Kallinderis, Y.: Hybrid Grids and Their Applications. In: Handbook of Grid Generation, pp. 25-1–25-18. CRC Press, Boca Raton (1999)

[10] Puffert-Meissner, W.: ALVAST Half-Model Wind Tunnel Investigations and Comparison with Full-Span Model Results. DLR IB 129-96/20 (1996)

Numerical and Experimental Investigation of a Stalling Flow-Through Nacelle

Axel Probst[1], Sonja Schulze[2], Rolf Radespiel[1], and Christian J. Kähler[2]

[1] TU Braunschweig, Institut für Strömungsmechanik
Bienroder Weg 3, 38106 Braunschweig, Germany
[2] UniBw München, Institut für Strömungsmechanik und Aerodynamik
Werner-Heisenberg-Weg 39, 85577 Neubiberg, Germany

Summary

Flow separations in the inlet of a recently constructed flow-through nacelle are studied by means of experiments and numerical simulations. First measurements in a low-speed wind tunnel at Re = 1.3 Mio. comprising oil film pictures and static surface pressure are used to validate time-averaged results of URANS simulations with a near-wall Reynolds stress model (RSM) based on an ε^h-equation. The simulations are performed with the DLR-TAU solver in an angle-of-attack range up to the onset of inlet separations around $\alpha = 21.5°$. Besides investigations on the role of transition, comparisons of experimental and numerical results show that both tested RSM capture the initial stage of stall in good agreement with the measurements.

1 Introduction

Flow separations in the inlet of jet engines represent a limit of the safe flight conditions of transport aircrafts, as the resulting disturbances in the onstream to the subsequent compressor stages may cause the engine to run unstable [1]. Reliable numerical predictions of the onset, size and topology of inlet separations at varying angles of attack are therefore important for the design process, but they are complicated by the well-known problem to accurately model turbulence in separated flow [14]. Recent improvements in the prediction of trailing-edge separations on airfoils around maximum lift [12] with a near-wall ε^h-Reynolds stress model [8] have motivated the present work to apply such models to the problem of inlet separations.

To assess the accuracy of this simulation approach, high-quality experimental data of well-defined test cases including the unsteady structures of the separated flow are needed, but currently not available in the literature. For this reason, a wind tunnel model of a flow-through nacelle for Reynolds numbers around Re = 1.3 Mio. was designed which mimics the basic stall behaviour of realistic, powered engines of modern transport aircrafts [13]. Results of the first measurement campaigns in the MUB wind tunnel (Modell-Unterschallwindkanal Braunschweig) are presented, including pressure distributions, oil visualization and investigations of the transition tripping mechanism. So far these data comprise the initial stages of the nacelle's stall and represent the basis for ongoing validation efforts of URANS simulations with advanced Reynolds stress turbulence models.

2   Experimental Setup

The wind tunnel model of the axisymmetric flow through nacelle is equipped with static pressure taps and control points for unsteady pressure measurements. The application of plexiglas as a material allows good optical access for PIV measurements (Fig. 1). According to the dimensions of the reference LARA nacelle [13] the flow-through nacelle has a length of 400 mm and a leading edge diameter of 240 mm. Transition is brought about by blowing out normal to the wall which ensures a good reproducibilty. A transition strip could hardly be fixed in the same place twice. Thus the inner nacelle features 160 blow-out orifices at a chord length of $x/c = 0.004$. The orifices' diameter of 0.4 mm and the radial distance of $2.25°$ were chosen according to the work of Horstmann et al. [6]. The orifices were originally placed in the suction peak at $x/c = 0.02$ according to foregoing numerical simulations [13]. The wind tunnel model, however, turned out to separate at higher angles of attack than expected which is why the orifices were shifted towards the leading edge in order to avoid a placement in the pressure rise. The orifices are connected to one of 20 settling chambers which allow a variation of the blow out amplitude (Fig. 1). The inlet of the nacelle can be detached from the aft part, rotated around the longitudinal axis and mounted back on in 20 different positions (every $18°$). This makes it possible to integrate all the needed measurement techniques in just one model. 48 static pressure taps are placed from 5% chord length on the nacelle's outside to about 60% chord length on the inside. The inlet also features 5 wall bounded transducers for unsteady pressure measurements of the type Kulite XCQ-093. The entire model is finally connected via a support to a traverse underneath the wind tunnel (Fig. 1). All experiments are undertaken at 50 m/s, corresponding to Re = 1.3 Mio. in the low speed wind tunnel MUB which is a closed return atmospheric tunnel with a test section of 1.3×1.3 m^2.
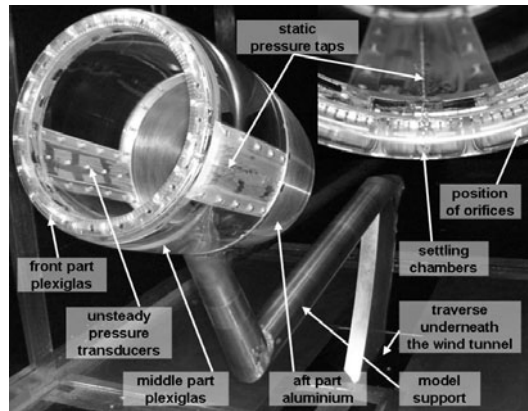
Fig. 1. Wind tunnel model of the nacelle

2.1   Transition Tripping Method

In order to introduce transition in a reproducible way, one has to be able to adjust a specific blow-out velocity via a defined volume flow rate which was regulated with the help of valves and a 500 l reservoir of compressed air at 8 bar.

The first objective in the experiments was to determine the right ratio of blow-out velocity to the onstream velocity in order to avoid overtripping. If the ratio becomes too large the flow in the nacelle's inlet will separate at too small angles of attack and thus causes bigger separated regions than expected. This effect can be observed in Fig. 2 which shows the static pressure distributions in the bottom section of the inlet for different blow-out ratios compared to numerical simulations [13] with the Spalart-Allmaras

turbulence model with Edwards Modification. Apparently the static pressure distributions resemble the numerical solution the better the smaller the blow-out ratio becomes. The boundary layer at 0.4% chord length is assumed to be so thin that only very small blow-out velocities need to be applied. In this case even the irregularities in the surface finish from drilling the orifices seem to be sufficient to trip the flow. Note that with a completely smooth surface without blowing orifices laminar leading edge stall occurs at much smaller angles of attack (not shown here). Thus it was decided to continue the experiments without blowing out in order to avoid overtripping. The above investigations were undertaken for equivalent blow-out velocities at all orifices. The initial idea was, however, that a variation of the blow-out amplitude over the circumference of the nacelle might be favourable. Oil film and infrared pictures showed that the inlet flow could be easily disturbed in its symmetry to the xz-axis if staggered blow-out amplitudes were used. This is probably due to small inaccuracies in the manufacturing process of the orifices and the nacelle's contour. Evenly spread blow-out amplitudes on the other hand resulted in symmetric flow fields which is why this way of introducing transition was chosen.
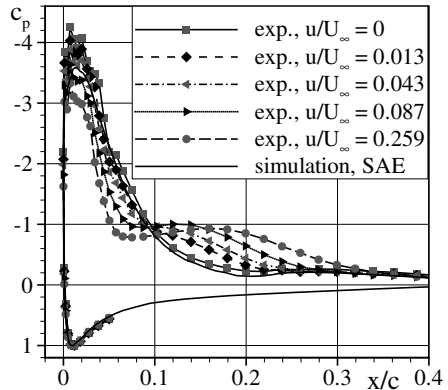
Fig. 2. Influence of the blow-out ratio on the pressure distribution, $\alpha = 20°$

3 Numerical Method

The present numerical approach to model the turbulent fluctuations is based on the solution of the Reynolds stress equations, reading in incompressible form:

$$\frac{D\overline{u_i u_j}}{Dt} = P_{ij} + \Phi_{ij} - \varepsilon_{ij} + D^{\nu}_{ij} + D^{t}_{ij} \quad . \tag{1}$$

Only production P_{ij} and viscous diffusion D^{ν}_{ij} of the Reynolds stresses can be computed exactly, whereas the pressure-strain correlation Φ_{ij}, the dissipation rate tensor ε_{ij} and the turbulent diffusion D^{t}_{ij} require suited modelling approximations.

3.1 The Near-Wall ε^h-Reynolds Stress Model

The ε^h-Reynolds stress model [8] is a variant of the ε-based near-wall HJ Low-Re RSM [7]. Both models employ a linear pressure-strain correlation:

$$\Phi_{ij} = -C_1 \varepsilon a_{ij} - C_2 \left(P_{ij} - \frac{2}{3} P_k \delta_{ij} \right) + \Phi^w_{ij} \quad , \tag{2}$$

comprising the wall-reflection model Φ^w_{ij} according to Gibson and Launder [4]. To account for near-wall effects, the coefficients in Eq. (2) are formulated as functions of characteristic turbulent parameters, such as the anisotropy invariants A and E, and are calibrated with the aid of DNS data of wall-bounded flows.

To directly capture the correct dissipation profile near walls, the length scale equation is written in terms of the homogeneous part ε^h of the total dissipation rate ε:

$$\frac{D\varepsilon^h}{Dt} = -C_{\varepsilon 1}\frac{\varepsilon^h}{k}\overline{u_i u_j}\frac{\partial U_i}{\partial x_j} - C_{\varepsilon 2}f_\varepsilon\frac{\varepsilon^h \tilde{\varepsilon}^h}{k} + C_{\varepsilon 3}\nu\frac{k}{\varepsilon^h}\overline{u_j u_k}\frac{\partial^2 U_i}{\partial x_j \partial x_l}\frac{\partial^2 U_i}{\partial x_k \partial x_l} + D_{\varepsilon^h} \ . \quad (3)$$

This equation is conventionally calibrated with constant coefficients $C_{\varepsilon 1}$, $C_{\varepsilon 2}$, $C_{\varepsilon 3}$ and a damping function f_ε. The dissipation rate tensor ε^h_{ij}, which departs from its isotropic state only near walls, is computed via an implicit algebraic relation.

For a comprehensive model description the reader is referred to [8], [12].

Extensions for Non-Equilibrium Flows. In flows with adverse pressure gradients, ε-(and ε^h-)based turbulence models are known to underestimate the dissipation rate and therefore delay the onset of separation [14]. To better sensitize the ε^h-RSM to pressure gradients, an additional source term in the length scale equation according to Apsley et al. [2] is applied, which is dependent on the irrotational strain in a streamline coordinate system and has been extended to the present 3D case as [12]:

$$S_{\varepsilon 4} = -C_{\varepsilon 4}^*\frac{\varepsilon^h}{k}\left(\overline{u_s^2}\frac{\partial U_s}{\partial x_s} + \overline{u_{n1}^2}\frac{\partial U_{n1}}{\partial x_{n1}} + \overline{u_{n2}^2}\frac{\partial U_{n2}}{\partial x_{n2}}\right) \quad \text{with} \quad C_{\varepsilon 4}^* = 1.16 \ . \quad (4)$$

A further weakness of ε-based RSM is a too rapid increase of the turbulent length scale l_t around separation and reattachment points which can cause unphysical streamline patterns [5]. This behaviour can be compensated by another source term S_l in the ε^h-equation, which directly counteracts large gradients of l_t [5]:

$$S_l = \max\left\{\left[\left(\frac{1}{C_l}\frac{\partial l_t}{\partial x_n}\right)^2 - 1\right]\left(\frac{1}{C_l}\frac{\partial l_t}{\partial x_n}\right)^2; 0\right\}\frac{\varepsilon^h \tilde{\varepsilon}^h}{k}A \quad \text{with} \quad C_l = 2.5 \ . \quad (5)$$

3.2 Numerical Setup for the Nacelle Computations

The ε^h-RSM with both extra terms $S_{\varepsilon 4}$ and S_l has been implemented into the DLR-TAU code [10] which is used to simulate the nacelle flow. A hybrid mesh in o-topology with 2.7 Mio. grid points (Fig. 3) has been generated with Gridgen V15, neglecting wind tunnel walls and installations for now. Its near-wall structured part comprises 380 points in streamwise, 76 points in wall-normal and 80 points in circumferential direction. The expected region of separated flow at the lower inner front is resolved with 135 streamwise points along the first 20% chord length and the initial wall-normal spacing of

380x76x80 struct.
2.7 Mio. total

Fig. 3. Hybrid mesh for the nacelle

$1.6 \cdot 10^{-6}$ m ensures $y_n^+ < 1.5$. The simulations employ a central scheme with scalar dissipation and low Mach number preconditioning. Unsteady results are obtained via

a dual-timestepping scheme and averaged over a sufficient time span. As reference, the computations are also performed with the models k-ω SST [11] and SSG/LRR-ω RSM [3].

Transition Modelling. Even small laminar regions in the nacelle's inlet were found to significantly influence the tendency to separation. This is illustrated in Fig. 4, which shows a noticeable variation of the minimum skin friction in the critical region around $x/c \approx 0.15$ of the bottom section, if transition in the simulation is specified at different locations (Fig. 4). This is achieved by switching off the turbulence model's source terms in the respective laminar regions. As transition locations could neither be reliably fixed, nor exactly measured in the experiments, the further simulations employ TAU's e^N-

Fig. 4. Influence of the transition location on the skin friction in the inlet, ε^h-RSM

method to predict transition [9]. A comparably low critical amplification factor of Tollmien-Schlichting waves, $N_{\mathrm{crit}} = 3.5$, is chosen. On the one hand this is supposed to roughly account for the disturbances induced by the blow out orifices (chap. 2.1), and on the other hand it suppresses the formation of laminar separation bubbles which were found to deteriorate convergence for $\alpha > 19°$. As reference, Fig. 4 also shows the transition location computed this way. Future experimental studies on the transition locations and on the existence of separation bubbles will show if this approach is justified.

4 Comparison of Experimental and Numerical Results

In both the experiments and the numerical simulations no indication of flow separation in the nacelle's inlet is observed until about $\alpha = 20°$. Accordingly, computed and measured pressure distributions in the lower cut section ($\Theta = 180°$) agree equally well for all three turbulence models at $\alpha = 17°$ (Fig. 6). The only significant deviation from measurements is observed around the suction peak at the inlet's lip, where besides some irregularities in the measured data, an offset of about

Fig. 5. Influence of inviscid wind tunnel walls on the pressure distribution

$\Delta c_p \approx 0.5$ occurs. While the former is attributed to the fabrication of the blow-out orifices (see also chap. 2.1), the latter is subject to further investigation. In a preliminary study, slip wall boundary conditions were introduced to model the inviscid wind

tunnel effects, but had virtually no influence on c_p (Fig. 5). Thus, further investigations are planned to include the tunnel wall boundary layers as well as installations. Another potential source of error are deviations between the design and the manufactured wind tunnel model. These are to be studied by comparing experimental results from the current and the new nacelle model (see chap. 5), as well as by measurements of the contour.

Although the flow is still attached at $\alpha = 20°$, the results of the ε^h-RSM begin to deviate slightly from the other models in the nose region. Apart from this, the agreement between experiment and simulation is still good (Fig. 6). Further increasing the angle of attack to $\alpha = 21°$, the oil film pictures yield first indications of separation onset, but there is still a clear pressure recovery in the critical region between the suction peak and $x/c = 0.2$. The slope of the pressure rise is slightly underestimated by the ε^h-RSM, and the wall streamlines (not depicted here) already show a small, owl-eye formed separation which is not observed in the experiments. The SSG/LRR-ω RSM, on the other hand, still matches the measured pressure well and shows only a very small separated region similar to the experimental results. By contrast, the k-ω SST model computes clearly too strong separation onset, which results in the breakdown of both the suction peak and the pressure recovery.
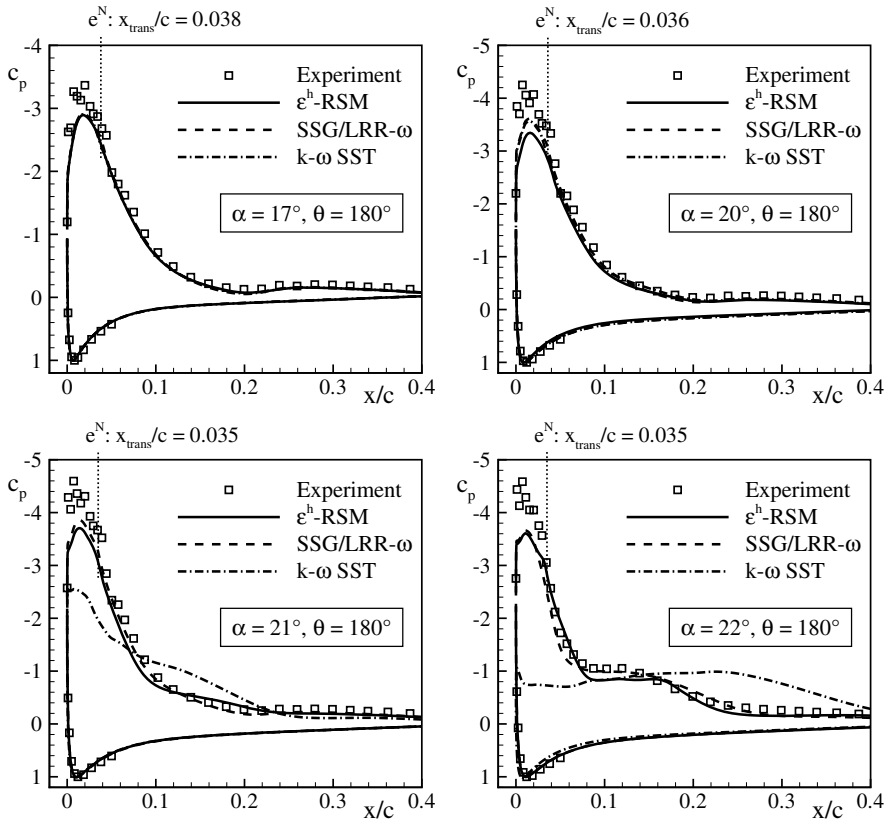
Fig. 6. Computed and measured pressure distributions in the lower cut section of the nacelle's inlet around separation onset. Computed transition locations for the ε^h-RSM

In the experiment first considerable separations occur around $\alpha = 22°$, which is evident from the stagnating suction peak and a pressure plateau around $x/c = 0.1$ (Fig. 6). While the k-ω SST model yields large deviations from the measured c_p distribution due to massive separation, both RSM, particularly the SSG/LRR-ω RSM, still agree well with the measured data. Although flow visualizations in Fig. 7 reveal that the separation topology computed by the ε^h-RSM compares well to the oil film picture, it is however larger and the vortex core is shifted outwards. This confirms that the model predicts separation onset at about $\Delta\alpha \approx 0.5° - 1°$ too early.

Fig. 6 also contains the transition locations computed via e^N for the ε^h-RSM. Despite their physically reasonable correlation with the development of the suction peak and the subsequent pressure rise, their actual accuracy remains unclear until further experimental validation. Besides this, the current simulation procedure of the sensitive stall process suffers from erroneous numerical flow field distortions, which are introduced by increasing the angle of attack in finite steps. On the other hand, their influence on the final results is small according to our experience so far, while the experiments did also not show any significant hysteresis effects.
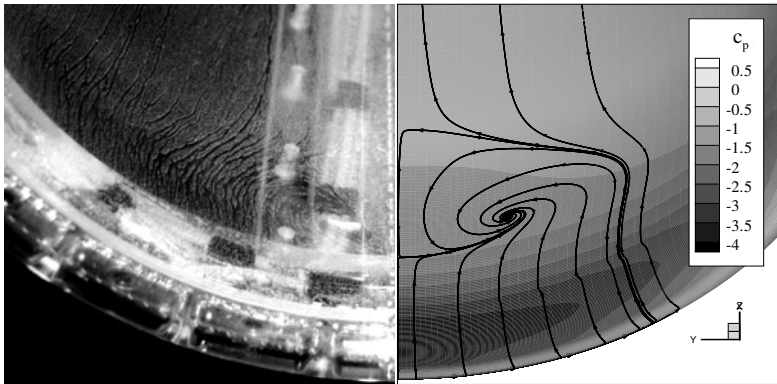
Fig. 7. Oil film picture (left) and computational result of the ε^h-RSM (right) at $\alpha = 22°$

5   Conclusions

A joint numerical and experimental investigation to study the onset of separation in a flow-through nacelle at Re = 1.3 Mio. was conducted with the aim to validate URANS simulations with a near-wall ε^h-Reynolds stress turbulence model. The initial approach to fix transition in the experiment by wall normal blowing was found to cause over-tripping, and the roughness distributed by the blowing orifices was sufficient to trip the flow. Transition locations for the simulations were then obtained from a coupled e^N-method. With this approach the computations of the initial stage of stall with both the ε^h-RSM and the SSG/LRR-ω RSM compare quite well to measured pressure and oil film pictures, and particularly better than the k-ω SST model, although separation onset is predicted at slightly too low angles of attack.

In the present case, the ε^h-RSM does not seem to clearly benefit from its careful near-wall and length scale modelling as compared to the SSG/LRR-ω RSM, since separation occurs close behind the leading edge and is strongly affected by transition. Future numerical studies are therefore aimed at improved transition modelling and will be extended to the fully stalled case. They are accompanied by further wind tunnel campaigns with unsteady pressure measurements, PSP, and different PIV methods, as well as a new, optimized wind tunnel model for the facilities of UniBw München to provide deeper insight into the transition process, the individual Reynolds stresses, and the unsteady behaviour of the inlet separation.

Acknowledgements

References

[1] Engine response to distorted inflow conditions. AGARD CP No. 400 (1986)

[2] Apsley, D.D., Leschziner, M.A.: Advanced Turbulence Modelling of separated flow in a diffuser. Flow, Turbulence and Combustion 63, 81–112 (2000)

[3] Eisfeld, B.: Numerical Simulation of Aerodynamic Problems with SSG/LRR-ω Reynolds Stress Turbulence Model Using the Unstructured TAU Code. Notes on Numerical Fluid Mechanics and Multidisciplinary Design, vol. 96. Springer, Berlin (2007)

[4] Gibson, M.M., Launder, B.E.: Ground Effects on Pressure Fluctuations in the Atmospheric Boundary Layer. J. Fluid Mech. 86, 491–511 (1978)

[5] Hanjalić, K., Jakirlić, S., Hadzić, I.: Expanding the limits of "equilibrium" second-moment closures. Fluid Dynamics Research 20(1), 25–41 (1997)

[6] Horstmann, K.H., Quast, A.: Widerstandsverminderung durch Blasturbulatoren. DLR Forschungsbericht FB 81-33, Braunschweig (1981)

[7] Jakirlić, S., Hanjalić, K.: A Second-Moment Closure for Non-Equilibrium and Separating High- and Low-Re-Number Flows. In: Proc. 10th Symposium on Turbulent Shear Flows, The Pennsylvania University, USA, August 14-16 (1995)

[8] Jakirlić, S., Hanjalić, K.: A new approach to modelling near-wall turbulence energy and stress dissipation. J. Fluid Mech. 539, 139–166 (2002)

[9] Krimmelbein, N., Radespiel, R.: Transition prediction for three-dimensional flows using parallel computation. Computers & Fluids 38(1), 121–136 (2009)

[10] Kroll, N., Rossow, C.-C., Schwamborn, D.: The MEGAFLOW-Project - Numerical Flow Simulation for Aircraft. In: Progress in Industrial Mathematics at ECMI 2004. Springer, Heidelberg (2005)

[11] Menter, F.R.: Zonal Two Equation k-ω Turbulence Models for Aerodynamic Flows. AIAA Paper 93-2906 (1993)

[12] Probst, A., Radespiel, R.: Implementation and Extension of a Near-Wall Reynolds-Stress Model for Application to Aerodynamic Flows on Unstructured Meshes. AIAA-2008-770 (2008)

[13] Schulze, S., Kähler, C., Radespiel, R.: On the Comparison of Stalling Flow-Through Nacelles and Powered Inlets at Take-Off Conditions. In: 1st CEAS European Air and Space Conference, Berlin, Germany, September 10-13 (2007)

[14] Wilcox, D.C.: Turbulence Modelling for CFD, 2nd edn., DCW Industries, La Canada (1998)

Minimal Induced Drag for Non-planar Lifting Surfaces with Moderate and Small Aspect Ratio

Th. Streit[1] , K. Visser[2], and C. Liersch[1]

[1] Institute of Aerodynamics and Flow Technology, DLR Braunschweig, Lilienthalplatz 7, 38108 Braunschweig, Germany
Th.Streit@dlr.de
[2] Clarkson University, Potsdam, NY, 13676, USA

Summary

The induced drag of non-planar wings is compared to that of planar wings which result from unfolding the non-planar ones. It is shown that due to the induced lift, there exist non-planar configurations with positive span camber that have an overall aerodynamic performance increase in comparison to the planar ones. The induced lift and increment of aerodynamic performance increases with decreasing aspect ratio. The effect is opposite for configurations with negative camber. Without the induced lift, the positive non-planar configuration would have more induced drag. Analysis is performed using a lifting line method, which takes into account the induced lift, and using Euler solutions. For the inviscid solutions, the induced drag is obtained with a far-field drag analysis method.

1 Introduction

The induced drag for non-planar wings is a classical aerodynamics problem, which through the years continuously has been the subject of several studies [1-3,5-6,8, 10-12,14-19]. Today, there is renewed interest due to improved analysis with more accurate analysis methods, but also due to the fact that optimum design of realistic wings at cruise and critical flight conditions does not consider only aerodynamics but uses a multidisciplinary approach which leads to or improves non-planar wings [18-19].

In nature, birds when they glide, do not adopt a planar wing shape. Their non-planar flying shape results from a compromise in which energy is minimized by trading the work done against induced drag and the consumption of muscle energy. As for birds, an optimum aircraft wing is a compromise between structure and aerodynamic requirements. In comparison to a planar extension, winglets offer the advantage that they provide a larger aerodynamic benefit for a given root bending moment increase. For tip extensions, if structure can be neglected, it is commonly believed, that the largest aerodynamic performance increase is achieved with a planar extension. This assumption is reinforced by some of the optimum induced drag results

[3,14-16] based on Munk's theorem for non-planar wings [17], which neglects the induced lift. If their results are applied to planar and non-planar wings of same unfolded span, the planar wing has the smallest induced drag. However, as shown by Eppler [5], if induced lift is taken into account, there are non-planar wings with less induced drag than the planar one, the difference being very small.

In this work, planar and non-planar wings are compared in the strict sense, i.e. the corresponding planar wing results from unfolding the non-planar wing, so that the compared wings have the same surface and unfolded span. In addition, analysis is performed with methods which take into account the induced lift. A previous parametric study performed by the authors for non-planar wings showed that there are non-planar wings with less induced drag than that of a planar configuration [12]. As shown below, the influence of induced lift becomes larger with decreasing aspect ratio. Therefore, in this work the analysis was extended to wings of smaller aspect ratio. The used geometries are shown in Figure 1. Geometries with positive and negative span camber were considered. Results were obtained using the lifting line code LIFTING_LINE (LILI) [13] as well as numerical Euler solutions on structured meshes obtained with the DLR-FLOWer code [9]. Since the LILI code provides the induced lift and induced drag components, their dependence on aspect ratio can be studied within lifting line theory. For the Euler solutions, induced drag was obtained using the ffd70 [4] far-field (FF) analysis method from ONERA. For minimum drag, a twist distribution was found using a steepest gradient optimization.

2 Background

A review of subjects concerning induced drag optimization and non-planar wings is found in references [2,10]. In this section, some known results for non-planar wings are mentioned and some theoretical arguments are given and derived, which indicate the relevance of induced lift for non-planar wings. Non-planar wings differ from planar wings since: a) They have transversal forces, b) There is induced lift due to induced velocities in freestream direction, c) For minimum drag, the downwash is not constant but proportional to the cosine of the local dihedral angle τ of the lifting line according to Munk´s theorem:

$$V_{Normal} = \text{constant} \cdot \cos(\tau) \qquad (1)$$

d) The circulation distribution for minimum induced drag is not necessarily elliptical. Within linear theory and based on Munk´s theorem there are several analytical and computational solutions [3,14-16] for minimum drag of non-planar wings. Most studies, however, compared planar and non-planar wings of the same projected span b. This is illustrated in Figure 2, where Cone´s [3] original comparison of the induced drag efficiency factor k, $k = C_L^2/\pi A C_D$ for a non-planar wing (with projected span b´) with a circular arc shape is given for the case of same projected span, i.e. b´=b(planar wing) as function of the camber factor β, with β=d/(b´/2). With increasing β, the efficiency of the non-planar wing increases up to a maximum value of 1.5 when the circular arc becomes a semicircle (β = 1). Additionally, Figure 2 shows the
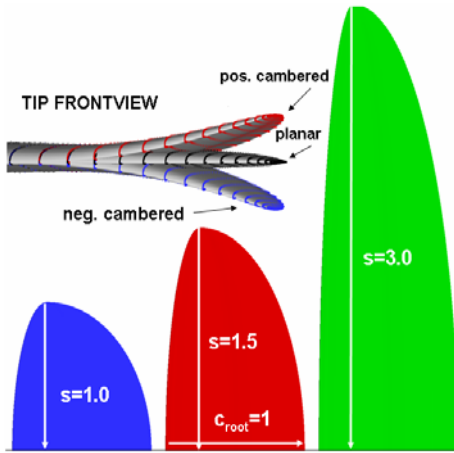
Fig. 1. Geometry: frontview and planform (planar) for considered planar and non-planar wings. Analysis performed for a fullspan, halfspan, and thirdspan configuration with, planar, positive, and negative cambered tip.
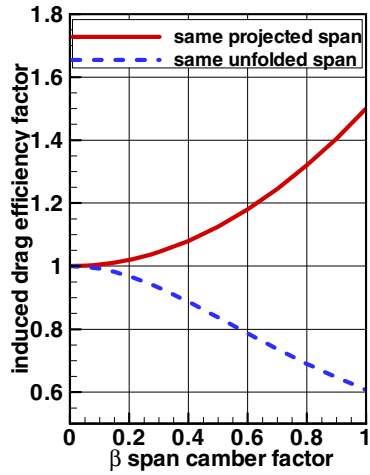
Fig. 2. Induced drag efficiency factor k for a non-planar circular arc wing as function of span camber. Comparison to a planar wing with same projected span or same unfolded span

comparison of non-planar circular arc wings, which unfolded have the same span as the planar wing. Note that contrary to the previous case, with increasing β the non-planar wing has a decreasing efficiency as compared to the planar one. Similar results are obtained if the efficiency is compared for a non-planar wing with an elliptical arc.

Results based on Munk´s theorem neglect the induced lift. They are independent of the non-planar wing having a positive or negative dihedral. As noted by Cone [3] this situation changes if the induced lift is not neglected. Horstmann [8] and Leyser [11] considered the induced lift in their numerical methods for non-planar wings. Eppler´s work [5] also pointed out the favourable effect of induced lift for the aerodynamic efficiency for upward pointed wingtips, whereas Bourdin [1] obtained a better performance for wingtips pointing downwards. Figure 2 suggests that for small span camber, a sufficient favourable positive induced lift may lead to an overall better efficiency compared to the planar wing. Defining the overall efficiency factor $k_{\Delta L}$ as:

$$k_{\Delta L} = \frac{(C_L + \Delta C_L)^2}{\pi A C_{Di}} \quad , \qquad (2)$$

an expression for the overall $k_{\Delta L}$ efficiency factor can be derived to evaluate the efficiency at minimum induced drag by:

$$k_{\Delta L} = k\left(1 + \frac{1}{2\pi} \frac{C_L}{A} D\right)^2 \qquad (3)$$

Equation (3) is derived using Cone's [3] expressions for the induced lift, the fact that the induced velocities parallel to the freestream velocity do not alter the induced drag, as well as introducing non-dimensional variables. D is a dimensionless constant, which is a functional of the circulation distribution function $\Gamma_{min}(\gamma)$, for the non-planar wing for minimum induced drag. For a planar wing, $\Gamma_{min}(\gamma)$ is the elliptical load distribution; for non-planar wings, Cone´s theory can be used to obtain $\Gamma_{min}(\gamma)$. The sign of D determines if efficiency is increased or reduced (positive, respectively negative sign), D is given by:

$$
D = \frac{\int_{-1}^{1} \frac{\Gamma_{min}(\gamma)}{\Gamma_0} \left[\int_{-1}^{1} \frac{\Gamma_{min}(\gamma)}{T_0} \frac{\vec{t} \times \vec{r}}{r^3} \frac{ds´}{d\gamma} d\gamma' \right] \cos \tau \frac{ds}{d\gamma} d\gamma}{\left(\int_{-1}^{1} \frac{\Gamma_{min}(\gamma)}{\Gamma_0} \cos \tau \frac{ds}{d\gamma} d\gamma \right)^2}
\tag{4}
$$

Note that according to Equation (3), the overall efficiency factor $k_{\Delta L}$ is proportional to k (the efficiency factor without considering induced lift) and to a factor which includes: aspect ratio (geometrical quantities) and lift coefficient. The above given expression indicates that the effect of induced lift will be larger with increasing lift coefficient and for decreasing aspect ratio wings. Note also that the above defined $k_{\Delta L}$ is the efficiency factor which considers the induced lift, but as it is evaluated at minimum drag, it does not provide the overall optimized efficiency, i.e. considering $(C_L + C_{\Delta L})/C_{Di}$.

3   Geometry, Flow Conditions and Used Numerical Methods

The present study is based on the non-planar "S_16_07" geometry found in [12]. It has a planar wing up to 70% semispan and the tip is rotated 16° upwards. The unfolded planar wing has an elliptical planform with the tip placed at $^1/_4{}^{th}$ root. Span is 6, root chord is 1, and aspect ratio is 7.6. Initial geometry is untwisted. Corresponding configurations with aspect ratio $^{7.6}/_2$ and $^{7.6}/_3$ are obtained by scaling the leading edge arc-length by a factor $^1/_2$ and $^1/_3$. Chord length and section airfoil thickness are kept constant. Symmetric configurations with negative camber are obtained by bending the unfolded planar wing downward. Initially, a NACA 0012 airfoil was used; later, a cambered airfoil with droop nose was used for the wing sections. The new airfoil reduces the large suction peaks which occur especially at the tip and which become larger for the reduced aspect ratio configurations. All Euler solutions were obtained at M=0.3 and C_L=0.8.

    The initial studies were carried out using incompressible LILI [13] solutions. This was followed by the use of the structured Euler code FLOWer from the DLR. Structured meshes for Euler solutions were generated using an OO-topology 1-block batch mesh generator for planar wings. The grid generation method is based on a

transfinite interpolation method. The meshes for the non-planar wings were obtained by using the deformation tool of Heinrich [7]. For the FF drag analysis the ONERA-ffd70+ code [4] was used, which breaks down the drag in its components: induced drag, viscous drag, and wave drag. It also provides an estimation of the numerical error, given by the difference between FF and near field (NF) drag prediction, which is denominated spurious drag. The use of FLOWer and ffd70+ for the here considered configurations was validated in [13] by performing mesh refinement studies. The meshes used for the aspect ratio variation study had a wing surface with 257x65 (chordwise) x (spanwise) points, the corresponding mesh had a size of 257x65x97 points. The numerical error for these meshes was reduced by: using the new airfoil, a rediscretization of points in the nose region and a finer mesh discretization in the direction normal to the wall. Results with the same quality regarding spurious drag were obtained, as the ones obtained within the mesh refinement study performed in [12], for the finest mesh with 513x193x193 points. While the absolute value for the FF drag and NF drag agreed for the finer meshes, the drag difference between planar and non-planar agreed already for the coarse meshes. Optimization was applied for both, the LILI and FLOWer results in order to find a twist distribution which minimizes drag. Twist was changed at 30 (16) sections, spanwise distributed with a cosine distribution for LILI (FLOWer) For FLOWer, a steepest descent gradient optimization method was used. The FF drag provided by ffd70+ was used as objective function. Coarse Euler meshes with 129x33x48 points were used for the optimization. Finer meshes were generated with the resulting twist distribution. LILI results were also obtained with a gradient based optimization.

4   Results

Results were obtained for the wings with positive camber, planar and negative camber for spans $b/b_0 = {}^1/_3$, ${}^1/_2$ and 1, with $b_0 = 6$ as span of the unfolded planar S-16-07 configuration. Figure 3 shows minimum drag results obtained with LILI: For the non-planar configuration with positive camber, the aerodynamic efficiency and the induced lift ΔL are increasing for smaller span. For the planar configuration, C_D agrees with $C_{D\ ellip} = C_L^2/\pi A$ up to the fourth significant digit. Since the induced lift ΔL comes from induced velocities which do not produce induced drag, the aerodynamic efficiency factor k can be determined for k(L) and for k(L+ ΔL). The obtained k(L) value is smaller than 1, indicating that the non-planar wing without the induced lift has more induced drag than the planar one. However, due to the induced lift ΔL, an overall increased aerodynamic efficiency is obtained for the non-planar wing. For the non-planar wing with negative camber, a negative ΔL is obtained, with its absolute value increasing for smaller span. Therefore, it has more induced drag than the planar configuration.

According to linear theory for a planar untwisted wing with elliptical planform, the minimum drag should be obtained for an elliptical circulation distribution. However, for the finite wings with moderate or small aspect ratio considered here, results
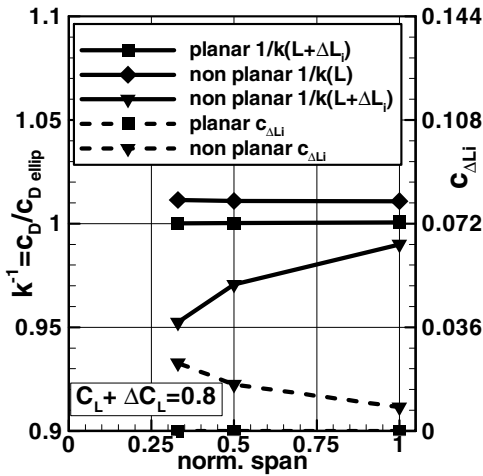
Fig. 3. LILI results: Ratio C_D/C_{Dellip} (FF) and induced lift $C_{\Delta Li}$ as function of wing span. For the non-planar wing, $C_D/C_{D\ ellip}$ is shown with and without taking into account induced lift.
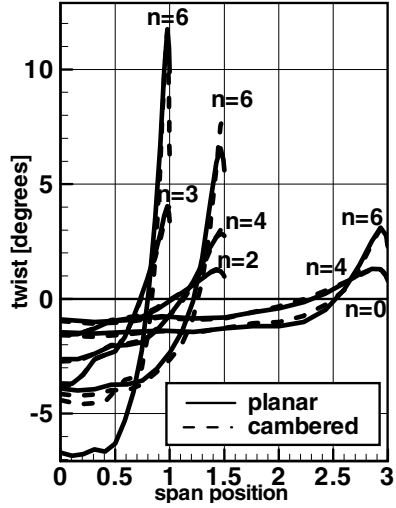
Fig. 4. Twist distribution for the fullspan, halfspan, and thirdspan wings for different optimization iterations n.

(obtained either with LILI or with Euler solutions) do not lead to minimum drag for the distributions, obtained in the drag minimization process for the Euler solutions for the planar and positive span camber wing cases. The resulting twist distribution develops a peak at the tip, while the root sections are twisted down. The large twist at the tip leads to large local lift values, which goes along with an increased numerical error. As a consequence, the optimization was stopped at the iteration in which $\Delta c_D(FF)$ and $\Delta c_D(NF)$ between planar and cambered wing began to differ. The Euler results (FF drag) for the planar case have a minimum drag which is lower than the theoretical value $C_{D\ ellip}$. However, it is interesting to note that the FF drag for twist distributions with circulations close to the elliptical circulation also gives the theoretical induced drag value. In that case, for the fullspan, halfspan and thirdspan configuration the values, 1.0009, 0.9982, and 1.007 were obtained for $C_D/C_{D\ ellip}$. LILI optimization was performed with 30 variables till convergence, showing similar twist distributions. Despite the large twist values, the induced drag difference to the untwisted value is very small. Figure 5 shows the absolute drag (left) and the relative (cambered minus planar) drag (right) as function of span for the considered wings. Twisted and untwisted results are shown. Similar as LILI, the Euler results show that the induced drag for the positive cambered configuration is reduced with decreasing aspect ratio, but to a less extent. The negative cambered configuration shows larger drag than the planar one, this effect being larger with reduced aspect ratio. The differences between twisted and untwisted are larger for Euler. The twisted result has
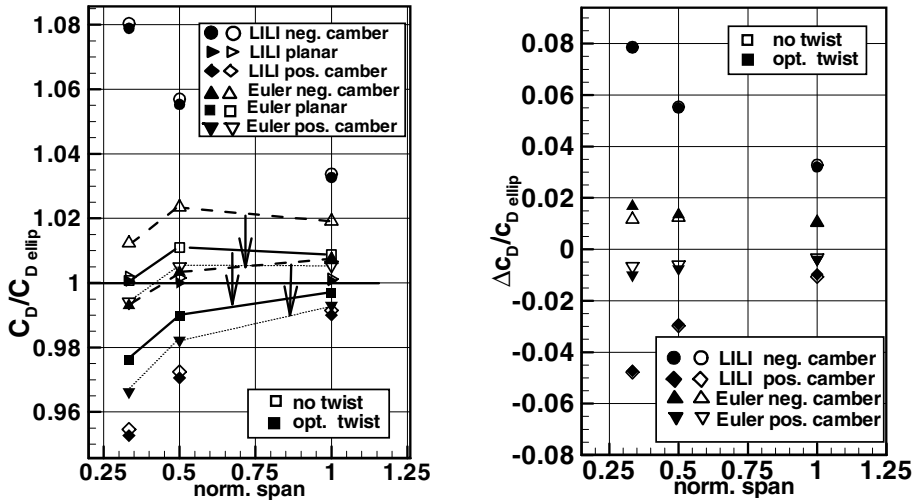
Fig. 5. Induced drag ratio (left) and non-planar to planar relative induced drag ratio (right) as function of span. Twisted results with filled symbols and untwisted results with unfilled symbols.

reduced drag for both: planar and cambered, so that their difference for the twisted and untwisted case is similar.

5 Conclusion

In this work the aerodynamic efficiency between corresponding non-planar and planar configurations is compared using lifting line theory and Euler solutions. For Euler solutions, drag was determined using a far-field analysis. Optimization of induced drag leads to twisted configurations with smaller induced drag than the untwisted ones. For the finite planar twisted configurations considered here, the obtained induced drag value is less then the theoretical values obtained for a planar wing with elliptical circulation. Within linear theory, it is shown that owing to induced lift, non-planar wings with positive camber can have a better aerodynamic performance than the corresponding unfolded planar wing. With Euler solutions an improvement in aerodynamic performance was also obtained, but to a smaller extent. With reduced aspect ratio, a further increase of aerodynamic performance is obtained.

Acknowledgment

References

[1] Bourdin, P.: Numerical Predictions of Wing-Tip Effects on Lift Induced Drag, Thermal Control, Design, and Operation. In: ICAS 2002, Congress, pp. 223.1–223.10 (2002)

[2] Büscher, A.: Flügelendformen zur Leistungssteigerung eines Langstrecken-flugzeuges, ZLR, Forschungsbericht 2008-06

[3] Cone, C.D.: The Theory of Induced Lift and Minimum Induced Drag of Nonplanar Lifting Systems, NASA Technical Report R-139 (1962)

[4] Destarac, D.: Far-Field / Near-Field Drag Balance and Applications of Drag Extraction in CFD. In: CFD-based Aircraft Drag Prediction and Reduction, Hampton (VA), November 3-7. VKI Lecture Series (2003)

[5] Eppler, R.: Induced Drag and Winglets. Aerospace Science and Technology (1), 3–15 (1997)

[6] Gold, N., Visser, K.: Aerodynamic Effects of Local Dihedral on Raked Wingtip. In: 40th Aerospace Science Meeting & Exhibit Reno, NV, AIAA-2002-0831

[7] Heinrich, R., Wild, J., Streit T., Nagel, B.: Steady Fluid-Structure Coupling for Transport aircraft, Deutscher Luft- und Raumfahrtkongress 2006, Braunschweig (2006)

[8] Horstmann, K.H.: Ein Mehrfach-Traglinienverfahren und seine Verwendung für Entwurf und Nachrechnung nichtplanarer Flügelanordnungen, DVFLR-FB 87-51 (1987)

[9] Kroll, N., Fassbender, J.K. [Hrsg.]: MEGAFLOW – Numerical Flow Simulation for Aircraft Design. Notes on Numerical Fluid Mechanics and Multidisciplinary Design (NNFM), vol. 89. Springer, Heidelberg (2002)

[10] Kroo, I.: Nonplanar Wing Concepts for Increased Aircraft Efficiency. VKI lecture series on Innovative Configurations and Advanced Concepts for Future Civil Aircraft, June 6-10 (2005)

[11] Leyser, J.: Kraftberechnung an der nichtplanaren tragenden Fläche, Dissertation, Universität Stuttgart (1966)

[12] Liersch, C., Streit, T., Visser, K.: Numerical Implications of Spanwise Camber on Minimum Induced Drag Configurations. In: 47th AIAA Aerospace Science Meeting, Orlando FL, AIAA 2009-898

[13] Liersch, C., Wunderlich, T.: A fast aerodynamic tool for Preliminary Aircraft Design. In: 12th AIAA/ISSMO Multidisciplinary Analysis and Optimization Conference, Victoria, BC (September 2008) AIAA-2008-95901

[14] Lowson, M.: Minimum Induced Drag for with Spanwise Camber. Journal of Aircraft 27(7), 627–631 (1990)

[15] Lundry, J.L., Lissaman, P.B.S.: Minimum Induced Drag on Non-planar Wings. J. Aircraft 5(1), 17–21 (1968)

[16] Mangler, W.: Die Auftriebsverteilung am Tragflügel mit Endscheiben. Jahrbuch deutsche Luftfahrt-Forschung, S1149–S1157 (1938)

[17] Munk, M.: Isoperimetrische Aufgaben aus der Theorie des Fluges. Inaugural-Dissertation, Göttingen (1919)

[18] Ning, A., Kroo, I.: Tip Extensions, Winglets and C-Wings: Conceptual Design and Optimization. In: 26th AIAA Applied Aerodynamics Conference, Honolulu, Hawai, AIAA 2008-7052

[19] Streit, T., Himisch, J., Heinrich, R., Nagel, B., Horstmann, K.H., Liersch, C.: Design of a Retrofit Winglet with Assessment of Cruise and Ultimate Structural Loads. In: 15th STAB/DGLR Symposium, Darmstadt. Notes on Numerical Fluid Mechanics and Multidisciplinary Design, vol. 96 (2006)

Vortex-Generator Pairs for Vortex-Induced Heat-Transfer Enhancement in Heat-Exchanger Channels

Markus Rütten and Lars Krenkel

German Aerospace Center, Institute of Aerodynamics and Flow Technology,
Bunsenstrasse 10, Göttingen, Germany
Markus.Ruetten@dlr.de
http://www.dlr.de/as

Summary

The objective of the presented work is to investigate possibilities for increasing the heat-transfer in heat-exchanger channels for aircraft applications by using flow-manipulating devices. Focal point of the investigation are different arrangements of vortex-generator pairs within a generic heat-exchanger channel. The DLR URANS CFD solver THETA has been used to carry out numerical simulations of the laminar flow within a rectangular channel with integrated vortex generators. In particular, the analysis of the interaction of generated vortices with the stratified thermal boundary layer, the impact of vortical flow structures on heated walls and the enforced mixed-convection flow is of special interest. The final goal is the evaluation of the applicability of oppositely arranged vortex-generator pairs for the enhancement of vortex-induced heat-transfer.

1 Introduction

The increase of fuel prices and the general increasing environmental awareness together with the demand for unlimited, fast and cheap air transport enforces the aircraft manufactureres to cut the full potential of all aircraft sub-systems to guarantee an economical success. One possibility to reduce the specific fuel consumption of modern aircraft is to increase the performance of the environmental control system (ECS), mainly by increasing the performance of the cooling capacity of its heat exchangers. A higher cooling capacity might allow for reducing the size of the heat exchangers, which may also enlarge the space envelope for the ducting of the cooling channel giving leeway for flow optimization. Therefore, the scientific goal of the work is, firstly to improve the understanding of the effect of large scale vortical flow structures on mixed thermal convection and, secondly to reveal possibilities to enhance the heat transfer in heat-exchanger channels while avoiding or minimising additional drag and pressure losses. The enhancement of heat transfer in energy-conversion systems is subject of extensive ongoing research. One way to achieve an enhancement of heat transfer is to utilize additional devices in heat exchanger channels in order to generate or amplify sufficiently

strong longitudinal vortices [10]. These vortices interact with the thermal boundary layer [1]. They disturb the stratification of the thermal boundary layer near the heated walls [7]. Eventually the transport of hot fluid perpendicular to the heated wall and its mixing with colder fluid is intensified by transporting external momentum into the internal boundary layer region. A completely different approach to enhance the heat transfer is the usage of dimples or additional surface concavities [2], welts or buckles in the wall material of the heat-exchanger channel. They increase the net surface. Additionally depending on size and geometry of such concavities flow instabilities in the boundary layer are enforced, a laminar flow undergoes an earlier transition to the turbulent flow regime. In turbulent boundary layers the energy transfer from large to small turbulent scales is amplified, and, therewith, also the mixing of cold and warm fluid.

2   Related Work

Depending on the application flow manipulating devices differ in their geometry, dimensions and integration. Micro devices like roughness elements, dimples or surface concavities are often used in small heat exchangers i.e. for electrical power systems, cpu coolers or biomass reactors [6]. Macro devices like guiding plates, fins, diverters, strakes or delta shaped winglets are utilized in large-scale heat exchangers, i.e. for cars, power transformators and turbines. Fiebig et al. [4], Gentry et al. [5] and Jacobi et al. [7] examined the flow effects of fins or winglets to improve the heat transfer on plates, in tubes or channels. Those types of flow manipulating vortex-generator devices are enhancing the heat transfer efficiently with the drawback of additional parasitic drag and significantly increased pressure losses.

Instead of considering large scale flow devices Isaev et al. [6] investigated the influences of small spherical dimples on flow ducts and micro pipes, while Lambert [8] and Ligrani et al. [9] examined the effects of depression depths on channel flows and even turbine components. Micro devices are especially designed for a certain flow regime, whereas in off-design operation cases they might loose their performance. Unfortunately, the overflown hot or cold wall has to have a certain minimum length otherwise the flow disturbances initiated by the micro devices can not take effect. Therefore, a shortening of channels is hard to realize. Texture like embossed vortex generators are a mixture of both, large-scale vortex generators and small-scale surface concavities. Dupond et al. [3] showed that cascades of such devices allow for realising compact and efficient heat exchangers, in particular, for a certain design point, nevertheless, a minimum channel length has also to be accepted. Bearing in mind the goal to decrease the size of the heat exchanger of the ECS pack, which means decreasing the length of the flow channel, and incorparating the constraint to design the heat exchanger for a wide operation range instead of surface concavities primarily vortex generators should be used. In the civil transport aircraft ECS application conventional industrial flat plate heat exchangers are used. They consist of stacks of thin plates. Flow control devices are embossed on the thin plates, and then many plates having the same embossing are stacked up. The distance between the plates is small in order to let the thermal layers grow together. However, there is a drastical increase of drag and pressure loss when the thermal layers are fusing [4]. Therefore, the distance between the plates, and therewith,

the heat-exchanger channel height is limited in order to avoid an immoderate increase of additional drag and pressure losses. A performance loss on the heat exchanger side has to be compensated by following ECS systems, i.e. by a jet pump or a duct fan in the cooling channel or by the turbo compressor in the fresh-air supply channel. Hence, in the case of the ECS application heat-transfer enhancement can only be realised by devices which generate only a small amount of additional pressure losses. Although the basic principles for controling vortices are known, not all aspects of the physical mechanisms are satisfyingly understood. Hence, in order to improve the design of compact heat exchangers a better understanding of the generation of suitable flow structures is mandatory. Since the vortex-induced heat-transfer enhancement depends strongly on the shape and position of vortex generators the subject of ongoing research is now to find design strategies for shape optimization.

3   The Generic Vortex-Generator-Pair Configuration

As mentioned above one possibility to enhance heat transfer is to use small flow-manipulating devices to generate additional vortices in order to increase the mass and heat transport between the temperature layers. According to the specific application and the used fluid, applied devices differ extremely in shape, dimension and function. Subject of the present study are vortex-generator devices generating longitudinal vortices, since they seem to perform best if resulting heat transfer and drag are taken into account. Futhermore, they are also less sensitive to an off-design mode. However, in contrast to the conventional heat-exchanger channel design in the considered configuration the channel height has been increased to avoid a fusing of thermal layers. The increased height can be compensated by interacting vortices generated by vortex generators. In order to generate a combination of interacting clockwise and counter-clockwise vortices vortex generator pairs are arranged facing one another: one pair is placed on the lower wall, one on the upper opposite channel wall. The lower pair generates an induced secondary dominant vorical flow between the vortex generators redirecting fluid away from the wall, the so called common flow-up flow structure. The other pair generates a common flow-down vortical flow structure, directing fluid towards the wall. This leads to an enforced transport of fluid from one wall to the other, moreover, one vortex pair is feeding and enforcing the other vortex pair leading to a better mixing of hot and cold air. In this numerical study geometrical variations of vortex-generator pair arrangements have been considered in order to find promising configurations and, even more, principles for the design of such flow control devices. Fig. 1 shows the examined generic heat-exchanger channel. The channel has a lenght of 200 mm, a height of 20 mm and a variable width. After an inflow lenght of 50 mm the vortex generators have been mounted. The length, thickness and heigth of the delta type winglets are the most important design parameters. Their length amounts to 13 mm, their height has been fixed to 6 mm, their thickness has been set to 1 mm. Also the angle of attack and the sweep angle are crucial design parameters, the angle of attack is set for the first configuration to $24°$, later set to $40°$. The sweep angle has been set to $20°$. Although the delta winglets have the same geometry their arrangement is essential, in particular the distance between the winglets has a huge effect on the vortical flow structure. In this

study the distance between the delta-type winglets of one pair measured at the winglet tips has been varied from 2 mm, over 8 mm and 14 mm to 18 mm, (heat-exchanger configurations 1, 4, 5 and 6). The heat-exchanger configuration 2 possesses rectangular and the configuration 3 trapezoidal winglets. The distance between the generator pairs has been the wall distance from ground to the cover plate of 20 mm. In Fig. 1 and 2 an impression of the heat-exchanger-channel geometry and the surface triangulation at the vortex-generator section is given. The number of grid points depends on the configuration, it varies from 4 to 6 Mio. points, the number of prismatic and tetrahedral elements ranges from 13 to 19 Mio.
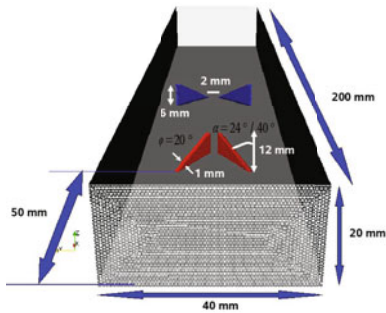
Fig. 1. Heat-exchanger channel with integrated delta winglet vortex generators
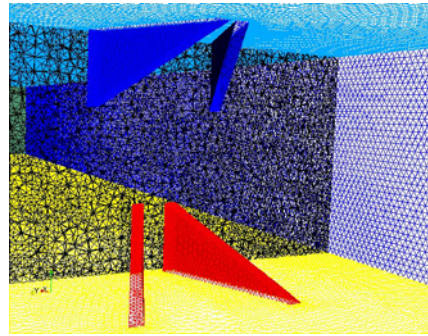
Fig. 2. View on the surface triangulation, oppositely arranged delta winglets

4 The Numerical Simulation Setup

For the heat-exchanger-configuration study numerical flow simulations were performed. The DLR code Theta has been used to conduct the unsteady flow simulations. Based on the well-known DLR-TAU code THETA is a finite volume code for incompressible flows. Due to its dualgrid approach it works on hybrid, unstructured grids consisting of a variety of types of polygonal elements. A SIMPLE algorithm has been applied for an efficient velocity pressure coupling. The well-known chequerboard instability of the pressure has been eliminated by a 4th-order stabilisation term. The spatial discretisation is done by using a second order quadratic upwind differencing scheme. The GMRES algorithm has been applied for solving the linear equations. For the unsteady simulations a 2nd-order implicit time integration scheme has been chosen, the time-step has been set to 0.005 s. The matrix free formulation of THETA has been applied to reduce the computational memory amount. The multigrid approach has been used to accelerate the solving of the linear equations even on fine grids. An efficient balancing algorithm for domain decomposition has been utilized to perform efficient computations on a DLR Linux-cluster.

5   Configurations and Dominant Thermal Flow Structures

In order to visualize and analyze the mixing flow initiated by the interacting dominant vortices first a generic configuration with a warm ground plate and a cold cover plate has been considered. The temperature of the warm plate and of the associated vortex generators has been set to 343.15 K. The other walls has been set adiabatic having an initial temperature of 293.15 K. The inflowing air has a temperature of 293.15 K and a velocity of 0.2 m/s. The Reynolds number, calculated with the channel height, was 200.

In Fig. 3 the vortical flow structure, result of the generated interacting vortices, is shown. The normalized helicity density criterion helps to distinguish between clockwise and counter-clockwise rotating vortices, in Fig. 3 isosurface of the helicity density are shown. The yellow coloured flow regions represents vortices with counter-clockwise rotational sense (isovalue 0.3), clockwise rotating vortices are coloured silver (isovalue -0.3). The extension of the shown flow regions indicates that the lower vortices are enforcing the upper vortices. In Fig. 4 stream ribbons and temperature contour plots on slices are used to visualise the convective transport of heat from the lower near wall region to the middle channel region.
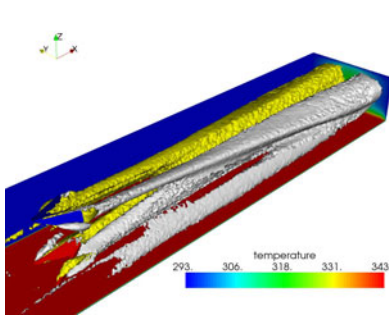
Fig. 3. Interacting vortical flow structure, isosurfaces of helicity density
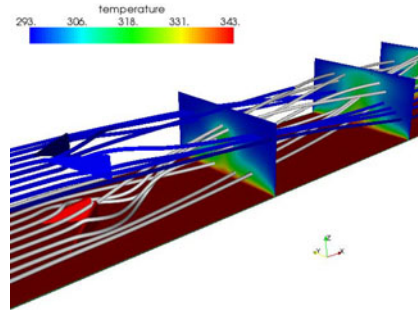
Fig. 4. Streamlines and temperature on slices illustrating the heat convection

Next, a more realistic flow condition has been examined, the cover plate and the associated mounted winglets are also considered as hot walls. In the numerical simulation they are defined as isothermal viscous walls, having a fixed temperature of 313.15 K. The velocity has been increased to 5 m/s, leading to a Reynolds number of 3000. Therefore, the k-ω SST model has been applied although an only weak turbulent flow has been assumed. The resulting flow structures for the heat-exchanger channel config. 1 and 2 are depicted in Fig. 5 and 6. The delta winglets are generating a stronger vortical flow structure than the rectangular winglets, the temperature distribution on the cut plane (background) shows more concentrated hot flow regions corresponding to the vortex cores. In contrast the rectangular winglets are stronger overflown, therefore, the temperature distribution on the cut plane is spread out and expanded. A further impression of heat exchanger channel flow fields is given in the Fig. 7 and 8. Here, the inplane
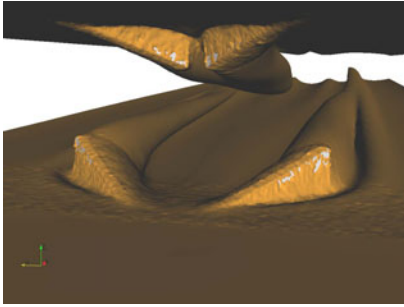
Fig. 5. Delta winglet heat exchanger, the temperature isosurface (265.15K) illustrates the vortex generation
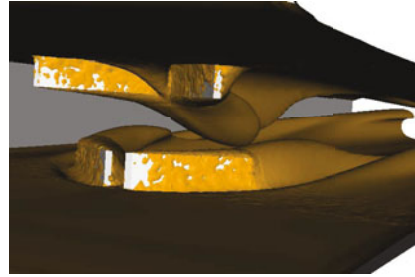
Fig. 6. Rectangular winglet heat exchanger, the temperature isosurface (265.15K) indicates the overflow of the winglets

vector plots show also the differences of the flow structures of the configuration 2 and 3. The vortical flow structure for configuration 2 is unstable and after two vortex generator lenghts destroyed. In contrast the trapezoidal vortex generators are generating a stable flow structure with distinguished hot temperature spots on the cut planes. The convective transport of hot air into the middle channel region is visible: Mushroom like temperature colour plots on the cut planes are indicating the "common flow-up".
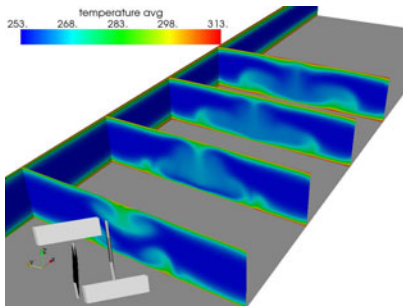
Fig. 7. Rectangular-winglet heat exchanger, temperature contour on cut planes
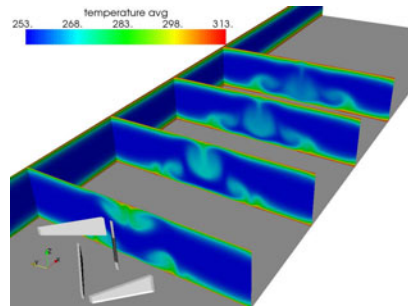
Fig. 8. Trapezoid-winglet heat exchanger, temperature on cut planes

6 Heat-Transfer Performance Evaluation

For the evaluation of the heat tranfer the integrated averaged surface temperature has been calculated for a cascade of 15 streamwise cross sections. The results for each configuration are visualized as line plot in Fig. 9. The first cross section cuts the heat-exchanger channel just before the vortex generators, the second section cuts the channel 5 mm behind the generators, all next cut planes follow in a consecutively distance of 10 mm. Then, the efficiency of the mixing process of cold with hot air is measured on these cross sections in order to determine the optimal length for the heat-exchanger

channel. For this purpose the temperature on each cutplane has been summed up and area weighted. The curves of the integrated and averaged cut plane temperature show that there is a temperature jump just behind the vortex generators. Further downstream the integrated and averaged temperature develops like in the undisturbed heat-exchanger channel case. A further crucial information in the evaluation of the ECS performance is
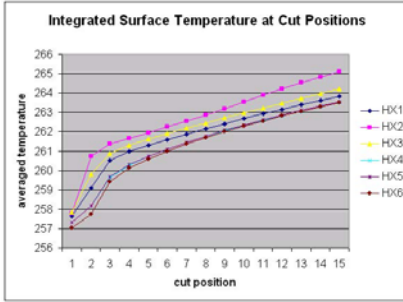
Fig. 9. Integrated surface temperature at cut planes by heat exchangers
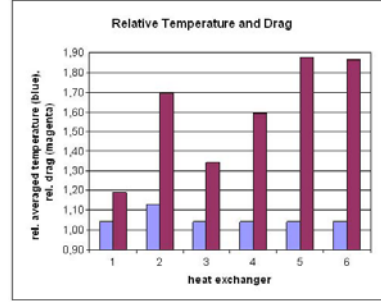
Fig. 10. Relative temperature and drag by heat exchangers

the drag which correlates with the pressure losses of the flow. The latter has an essential impact on the design of other ECS systems following the heat exchanger. In Fig. 10 the considered heat-exchanger configurations are compared with respect to relative drag (magenta) and relative integrated temperature (blue). For normalization the drag and integrated temperature of a heat-exchanger channel without any vortex generators has been chosen as reference. For the evaluation the values have been taken from the last cut plane. The channel with the rectangular winglets reveals the bests heat transfer, but also a comparatively high drag. The delta winglets and trapezoidal heat exchanger channels show better drag behaviour and moderate heat transfer. Taking drag as the main evaluation parameter then the first configuration is the most promising one since its drag is comparatively low and its relative temperature is moderately increased. Unfortunately a final evaluation can't be done, since an advanced cost function is not formulated. However, it could be shown that a huge optimisation potential in regard to the geometrical design of vortex generators exists.

7   Conclusion

For a specific vortex-generator pair arrangement it has been shown that the enforced vortex pair enhances the mixing of cold and warm fluid in the flow channel significantly. The analysis of the vortical flow field and the associated temperature field has shown that an additional heat transfer with relatively low additional pressure loss can be achieved when cold air surrounds a generated tube of hot air in the middle part of the heat-exchanger channel. Thereto, different flow visualization techniques are applied to analyse the vortical flow structure. The vortices have been detected by the normalized helicity which has also been used to distinguish clockwise and counter-clockwise

rotating vortices. Their fingerprints on the flow and their effect on heat transfer is examined by the resulting temperature distribution and the heat flux depicted on cut planes. Additionally, the usage of streamline integration and vortex detection algorithms has yielded a better understanding of the vortical structures and associated heat transfer. Due to the large number of parameters affecting the efficiency of the vortex induced heat-transfer enhancement further simulations have to be carried out. The main goal will be the reduction of the design parameters and to set-up an optimization process to find the best vortex-generator-pair configuration.

References

[1] Biswas, G., Torii, K., Fujii, D., Nishino, K.: Numerical and Experimental Determination of Flow Structures and Heat transfer of Longitudinal Vortices in a Channel Flow. J. Heat Mass Transfer 39(16), 3441–3451 (1996)

[2] Bunker, R.S., Donnellan, K.F.: Heat Transfer and Friction Factors for Flows Inside Circular Tubes with Concavity Surfaces. In: Proc. ASME Turbo Expo 2003 - Power for Land, Sea and Air, Atlanta, Georgia, USA (2003)

[3] Dupond, F., Gabillet, C., Bot, P.: Experimental Study of the Flow in a Compact Heat Exchanger Channel with Embossed-Type Vortex Generators. J. Fluids Eng. 125, 701–708 (2003)

[4] Fiebig, M.: Vortices, Generators and Heat Transfer. Chem. Eng. Res. Design 76(A2), 108–123 (1998)

[5] Gentry, M.C., Jacobi, A.M.: Heat Transfer Enhancement by Delta Wing Vortex Generators on a Flat Plate: Vortex Interactions with Boundary Layer. Exp. Thermal Fluid Sci. 14, 231–242 (1996)

[6] Isaev, S.A., Leontiev, A.I., Kudryavtsev, N.A., Pyshnyi, I.A.: The Effect of Rearrangement of the Vortex Structure on Heat Transfer under Conditions of Increasing Depth of a Spherical Dimple on the Wall of a Narrow Channel. J. High Temperature 41(2), 229–232 (2003)

[7] Jacobi, A.M., Shah, R.K.: Heat Transfer Surface Enhancement Through the Use of Longitudinal Vortices: A Review of Recent Progress. Exp. Thermal Fluids Sci. 11, 295–309 (1995)

[8] Lambert, S., Morrison, J.F.: Fundamental Study of Active Dimple. In: TSFP-4 Conference proceeding, Williamsburg, VA, USA, vol. 1, pp. 283–288 (2005)

[9] Ligrani, P.M., Harrison, J.L., Mahmmod, G.I., Hill, M.L.: Flow structure due to the dimple depressions on a channel surface. Phys. Fluids 13(11), 3442–3451 (2001)

[10] Yanagihara, J.I., Torri, K.: Enhancement of laminar boundary layer heat transfer by longitudinal vortices. In: Heat and Mass Transfer, University of New South Wales, Sydney (1991)

[11] Yun, Y.L., Lee, K.S.: Influence of design parameters on the heat transfer and flow friction characteristics of the heat exchanger with slit fins. Int. J. Heat Mass Transfer 43, 2529–2539 (2000)

Radiation Heat Transfer in Mixed Convection Flows

Markus Lambert and Roland Kessler

German Aerospace Center (DLR), Institute of Aerodynamics and Flow Technology
C^{2}A^{2}S^{2}E - Center for Computer Applications in Aero Space Science and Engineering
Bunsenstraße 10, 37073 Göttingen, Germany
markus.lambert@dlr.de, roland.kessler@dlr.de
http://www.dlr.de/as/

Summary

In this paper the influence of radiation heat transfer in mixed convection buoyant turbulent flows is considered. The results show that in thermal driven flows radiation heat transfer is an essential part of the total flow system and must be considered for accurate flow predictions. A parallel Discrete Transfer Radiation Method (DTRM), which simulates surface to surface radiation heat transfer, is coupled with the DLR THETA code, an unstructured incompressible Navier-Stokes-Solver developed by the German Aerospace Center (DLR). The THETA code supports convective heat transport, very large grids, high complex geometries and massive parallel computations.

1 Introduction

Many numerical studies [3], [2] and [10] are focused on two dimensional natural convection problems with simple geometries. The interest is in the basic effects of surface heat radiation on thermal driven flows. However numerical simulations of industrial relevant applications can require a very large number of grid points due to complex three dimensional geometries. Thus stringent requirements for the efficient use of memory and code performance are required. Moreover, an efficient parallelization strategy for the numerical radiation heat transfer method is necessary. Most of the flows over heated surfaces (like human bodies, installed wall lamps etc.) in closed rooms or rooms with air conditioning (like air-plane-, train- or car-cabins) are unsteady. Due to the unsteadiness it is necessary to couple the radiation module with the flow solver each time-step. This dictates that memory and CPU-time requirements for the radiation solver should ideally not exceed that of the Navier-Stokes-Solver itself. Additionally, the radiation module must be included in the parallelization concept of the Navier-Stokes-Solver.

We choose the Discrete Transfer Radiation Method (DTRM) for the simulation of the surface to surface radiation heat transfer. It shares similarities with the well known Radiation Simulation Monte Carlo Method [17] based on the transfer of independent radiative energy particles. These particles are emitted from each surface point in the computational domain but use only a finite number of fixed directions. In a preprocessing

step the boundary surfaces of the computational grid which are located in these directions are found and stored. During the simulation we directly transfer the radiative energy from surface to surface without tracing the trajectory of the energy particles. Because the DLR THETA code uses a domain decomposition approach for parallel computations, we decompose the stored surfaces such that each processor has a list of all boundary surfaces which can be reached from a boundary surface of its own domain. During the simulation we compute the DTRM step locally on each processor and then exchange the data in one communication step to avoid performance reduction due to communication. For very large grids the list of reachable boundary surfaces, which have should be retained in memory, can be large. Therefore we restrict the number of discrete directions we choose for the DTRM. In order to reduce statistical errors, a smoothing algorithm is used for the radiative energy distribution on the boundary surface. This method leads to accurate and smooth heat flux distributions even for a small number of discrete directions. In the above mentioned preprocessing we use an efficient ray-tracer algorithm [15], which is based on an element-to-element list thus avoiding element searches.

2 The Governing Equations and the Numerical Method

We consider the Reynolds-averaged (RANS) formulation of the non-stationary, incompressible ($\rho \neq \rho(p)$) Navier-Stokes-equations in a bounded domain $\Omega \in \mathbb{R}^3$ and in a time interval $(0, \tau)$

$$\frac{\partial (\rho \boldsymbol{v})}{\partial t} + \boldsymbol{\nabla} \cdot (\rho \boldsymbol{v} \otimes \boldsymbol{v}) - \boldsymbol{\nabla} \cdot (2 (\mu + \mu_{\mathrm{t}}) \mathbb{S}(\boldsymbol{v})) + \frac{2}{3} \rho k \mathbb{I} + \boldsymbol{\nabla} p = \rho \boldsymbol{f}$$

$$\frac{\partial \rho}{\partial t} + \boldsymbol{\nabla} \cdot \rho \boldsymbol{v} = 0.$$

Here $\boldsymbol{v}$ denotes the velocity, p the pressure, ρ the density, $\boldsymbol{f}$ the force density of external forces like gravity, $\mu > 0$ the physical viscosity, $\mu_{\mathrm{t}} > 0$ the turbulent viscosity and k the turbulent kinetic energy. $\mathbb{S}(\boldsymbol{v}) = \frac{1}{2} \left(\boldsymbol{\nabla} \boldsymbol{v} + \boldsymbol{\nabla} \boldsymbol{v}^T \right)$ is the symmetric deformation velocity tensor and $\mathbb{I}$ denotes the unit matrix. Additional boundary and initial conditions have to be formulated. Within this framework the standard k-ω turbulence model [16] with universal wall functions [8] and the standard buoyancy modification [11] are used. To simulate the influence of thermal convection, the temperature transport equation is solved

$$\frac{\partial (\rho T)}{\partial t} + \boldsymbol{\nabla} \cdot (\rho T \boldsymbol{v}) = \boldsymbol{\nabla} \cdot \left(\left(\frac{\kappa}{c_{\mathrm{p}}} + \frac{\mu_{\mathrm{t}}}{Pr_{\mathrm{t}}} \right) \boldsymbol{\nabla} T \right) \tag{1}$$

for the temperature T. In this equation c_{p} denotes the specific heat capacity, κ the thermal conductivity and Pr_{t} the turbulent Prandtl number. Appropriate boundary conditions, e.g. a von Neumann boundary condition at walls

$$\boldsymbol{n} \cdot \left(\left(\frac{\kappa}{c_{\mathrm{p}}} + \frac{\mu_{\mathrm{t}}}{Pr_{\mathrm{t}}} \right) \boldsymbol{\nabla} T \right) = \frac{\|\boldsymbol{n}\|}{c_{\mathrm{p}}} (q_{\mathrm{w}} + q_{\mathrm{rad}}) \tag{2}$$

with the boundary normal vector $\boldsymbol{n}$, a fixed wall heat flux q_{w} and the radiation heat flux q_{rad} are implemented. The radiation heat flux q_{rad} due to surface to surface heat

radiation is computed by the DTRM. Variable density due to buoyancy is modeled using the Boussinesq approximation [4] $\rho = \rho(T) = \rho_\infty \left(1 - \beta(T - T_\infty)\right)$ with the reference Temperature T_∞, the reference density ρ_∞ and the thermal expansion coefficient β. The DLR THETA code uses a finite volume approach [9] for solving the Navier-Stokes equations and additional scalar equations like k-ω turbulence model equations or the temperature transport equation (1). It provides inter alia the well known pressure correction projection method [6], [5], [13] for velocity pressure coupling and uses the multi-grid approach [7], [14] for solving the pressure equation of the pressure correction projection method.

3 Surface Heat Radiation

Any surface at a temperature above $0\ K$ radiates energy. The amount of energy E, per unit surface area and in unit time, a solid surface of a so called Gray Lambert radiator emits is given by the Stefan-Boltzmann law

$$E(T) = \varepsilon(T)\sigma T^4, \ \sigma = 5,67051 \cdot 10^{-8} \frac{W}{m^2 K^4}. \tag{3}$$

Here σ is the Stefan-Boltzmann constant and

$$\varepsilon(T) = \frac{1}{\sigma T^4} \int_0^\infty \int_0^{2\pi} \int_0^{\frac{\pi}{2}} \varepsilon_\lambda^{\mathrm{d}}(\theta, \phi, \lambda, T) I_{b,\lambda}(\lambda, T) \cos(\theta) \sin(\theta) \, d\theta \, d\phi \, d\lambda$$

is the emissivity. It is defined by integration over all directions θ, ϕ and all wavelengths λ of the so called directional spectral emissivity $\varepsilon_\lambda^{\mathrm{d}}(\theta, \phi, \lambda, T) = \frac{I_\lambda(\theta, \phi, \lambda, T)}{I_{b,\lambda}(\lambda, T)}$. The directional spectral emissivity describes the ratio of the emissive radiation intensity I_λ of some body and the emissive radiation intensity $I_{b,\lambda}$ of a black body, which have the same temperature. The emissive power emitted uniformly in all directions from an infinitesimal area dA into a solid angle $d\Omega$ is described by Lambert's cosine law

$$dq = I_\lambda(\theta, \phi, \lambda, T) \cos(\theta) \, dA \, d\Omega, \ d\Omega = \sin(\theta) \, d\theta \, d\phi. \tag{4}$$

The proportionality factor $I_\lambda(\theta, \phi, \lambda, T)$ is the directional spectral intensity of radiation. A more detailed description of the radiation heat transfer physics can be found in [1]. For each boundary wall surface F of the computational grid we compute a fixed number of directions for the DTRM in the following way. First we choose equidistant distributed numbers $R^i = \frac{i}{n_\phi}, R^j = \frac{j}{n_\theta} \in (0, 1), i = 0 \ldots n_\phi - 1, j = 1 \ldots n_\theta, n_\phi, n_\theta \in \mathbb{N}$. Let $\boldsymbol{n}_F$ be the surface normal and $\mathcal{R}_{\boldsymbol{n}_F}$ the rotation matrix, which rotates the vector $(1, 0, 0)^T$ into the direction of the surface normal, i.e. $\mathcal{R}_{\boldsymbol{n}_F}(1, 0, 0)^T = \frac{\boldsymbol{n}_F}{\|\boldsymbol{n}_F\|}$. Since the directional distribution must fulfill Lambert's cosine law (4), we set $\phi^i = 2\pi R^i, \theta^j = \arccos\left(\sqrt{1 - R^j}\right)$ and get in spherical coordinates $\boldsymbol{d}_F^{i,j} = \mathcal{R}_{\boldsymbol{n}_F} \boldsymbol{d}^{i,j}$, $\boldsymbol{d}^{i,j} = \left(\sin\theta^j \cos\phi^i, \sin\theta^j \sin\phi^i, \cos\theta^j\right)^T, d_F^{0,0} = \mathcal{R}_{\boldsymbol{n}_F}(1, 0, 0)^T = \frac{\boldsymbol{n}_F}{\|\boldsymbol{n}_F\|}$. Then we send rays in these directions and trace them through the computational domain. If they hit a boundary surface we store this surface number in a special surface list associated to the sending surface. For each radiative wall surface we have finally the above-named list of goal surfaces, which can be reached by a ray emitted by this
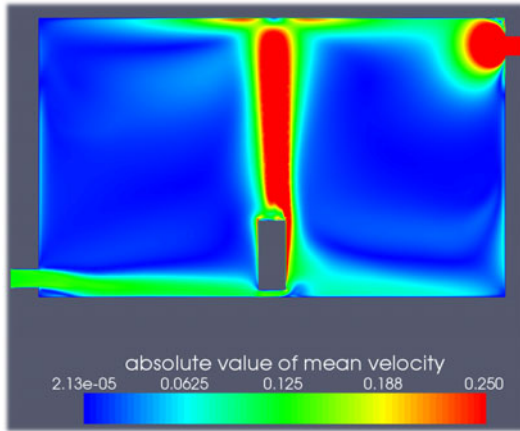
Fig. 1. Time averaged mean velocity without radiation heat transfer

surface. These lists are stored. We consider each radiative boundary surface F of the computational grid as a Gray Lambert radiator and send a fixed number N_P of energy-particles, which carries uniformly distributed radiation heat energy given by (3), i.e. each particle transfers the energy $e_P = \frac{\varepsilon \sigma T_F^4 \|\boldsymbol{n}_F\|}{N_P}$. Randomly one of the surfaces from the list of goal surfaces is chosen and the energy of the particle is added to the received energy of this surface. Since each surface is a member of the goal surface list of several other surfaces we sum up all received energy of one DTRM step. Let E_F^0 denote this sum of received energy. Then εE_N^0 is absorbed by the surface and $(1 - \varepsilon)E_F^0$ is reflected. So finally a so called wall reflection iteration is done, i.e. a fixed number N_{iter} of additional surface heat radiation steps by DTRM with the energy $e_P^{n+1} = \frac{E_F^{n+1}}{N_P}, E_F^{n+1} = (1 - \varepsilon)E_F^n, 0 \leq n < N_{iter}$ are performed.

4   Results

We simulate the mixed convection flow in a closed room (figure 5) (cubic measures: 3m x 4m x 5m). A small outflow of 10cm x 10cm is located under the top of the room at the eastern wall. An air supply over almost the complete length of the wall is located over the bottom of the western wall. A cylinder of 75 cm height and 30 cm diameter, which is heated with 100 W from inside, is placed in the middle of the room. We set a supply air flow rate of 300 $\frac{m^3}{h}$. The in-flowing air have a temperature of $291.35K$. To set the thermal boundary conditions at the cylinder surface (2) is used. The valid value q_w according to the 100 Watt heating is calculated using the surface area of the cylinder. We get $q_w = 107.22\frac{W}{m^2}$ for the shell and $q_w = 171.25\frac{W}{m^2}$ for the top and bottom of the cylinder. Additional isothermal room walls at temperature $293.45K$ are assumed. Due to unsteadiness of the considered flow [12] we couple the radiation module with the flow solver each time-step. For the DTRM we use 257 fixed directions per wall boundary surface in the computational grid (16 for zenith angle times 16 for azimuth angle plus the surface normal direction). Per time step we make 100 DTRM steps and
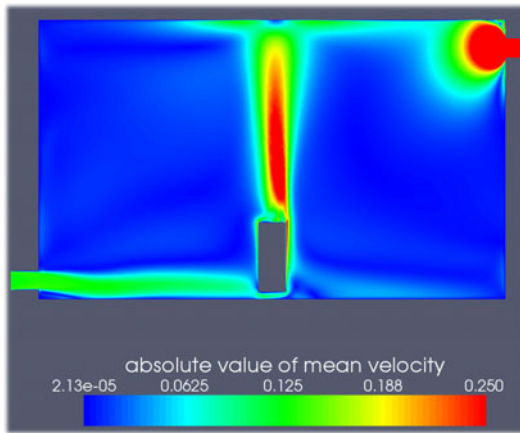
Fig. 2. Time averaged mean velocity with radiation heat transfer
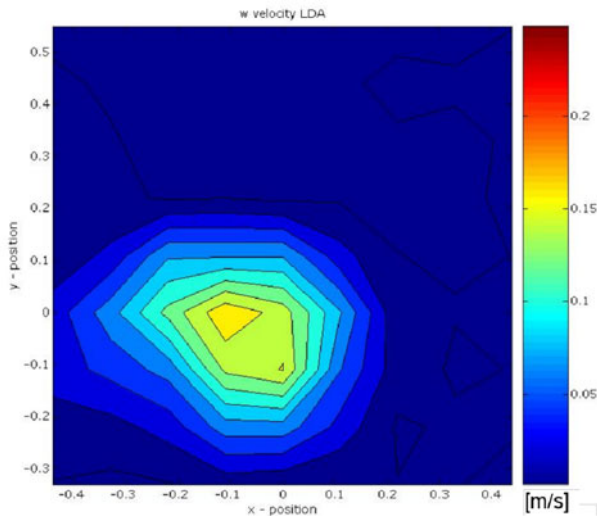
Fig. 3. Measurement z-component of the velocity over the cylinder in height 1.125 m

average the radiation heat flux over this 100 steps to reduce the statistical errors. In each DTRM step we send 50 rays per surface. We simulate a physical time of $300s$ and time average the quantities we are interested in over an interval of $150s$. Averaging is started after $150s$ of simulation. The computations are done on two unstructured, hybrid grids of 1 million (coarse grid) and 5.4 million (fine grid) points. We do a parallel computation on 16 (coarse grid) and 64 (fine grid) processors. Since the differences in the results comparing the fine and the coarse grid are less then 3.3 percent, we show the results on the fine grid. Figures 1, 2 show the results of the velocity distribution
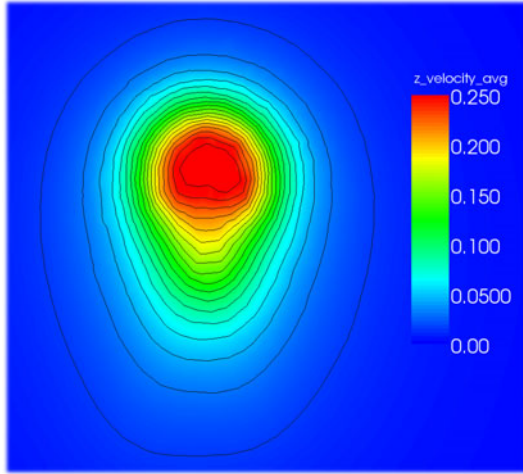
Fig. 4. Time averaged z-component of the velocity over the cylinder in height 1.125 m
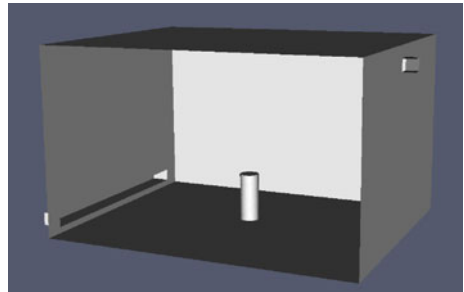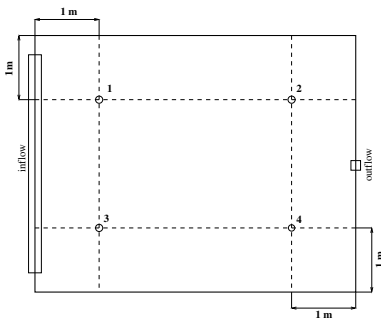
Fig. 5. Measurement positions (l) and geometry (r) of the test case

Height in cm	temperature $[^\circ C]$			
	1	2	3	4
10	19.21	19.40	19.30	19.52
50	19.56	19.68	19.75	19.66
100	20.14	20.12	20.05	20.2

(a) experiment

Height in cm	temperature $[^\circ C]$			
	1	2	3	4
10	18.20	18.34	18.20	18.34
50	19.03	18.77	19.03	18.77
100	19.44	19.33	19.44	19.33

(b) simulation

Fig. 6. Temperature at 10, 50 ,100 cm vertically above position 1, 2, 3 and 4

with and without radiation heat transfer. One can see that the plume over the cylinder have lower velocity in the radiation heat transfer case due to the additional transport of heat via the radiation. Comparing measurements [12] and simulation figure 3 shows the z-component of the velocity above the cylinder in the height $1.125m$. The maximum of the z-component of the velocity above the cylinder is about $0.16\frac{m}{s}$ in the measurements and about $0.274\frac{m}{s}$ in the simulation. Due to these differences the influence of the chosen turbulence model on the computed solution requires further investigation. Additionally, LES computations may provide a baseline against which further RANS computations can be validated.

5   Conclusions

A successful coupling of a DTRM with the DLR THETA Code was done. The memory and CPU-time requirements of the radiation computations do not exceed that of the Navier-Stokes-Solver itself. The radiation module is well parallelized and embedded in the parallelization concept of the DLR THETA code, which is based on a domain decomposition approach. Coupling the radiation module with the flow solver each time-step is possible and done. Unsteady flows over heated surfaces (like human bodies, installed wall lamps etc.) in closed rooms or rooms with air conditioning (like air-plane-, train- or car-cabins) can be done. The results show that radiation heat transfer is an essential part of the total flow system in thermal driven flows and must be taken into account to get accurate flow predictions.

Acknowledgments

References

[1] Baehr, H.D., Stephan, K.: Wärme- und Stoffübertragung. Springer, Heidelberg (2008)

[2] Bahlaoui, A., Raji, A., Hasnaoui, M.: Multiple steady state solutions resulting from coupling between mixed convection and radiation in an inclined channel. Heat and Mass Transfer 41(10), 899–908 (2005)

[3] Balaji, C., Venkateshan, S.P.: Correlations for free convection and surface radiation in a square cavity. International Journal of Heat and Fluid Flow 15(3), 249–251 (1994)

[4] Boussinesq, J.: Théorie Analytique de la Chaleur. L'École Politechnique, Paris 2, 224 (1903)

[5] Chorin, A.J.: Numerical solution of the Navier-Stokes equations. Math. Comp. 22, 745–762 (1968)

[6] Goda, K.: A multistep technique with implicit difference schemes for calculating two- or three-dimensional cavity flows. J. Comput. Phys. 30, 76–95 (1979)

[7] Hackbusch, W.: Multi-Grid Methods and Applications. Springer, Heidelberg (1985)

[8] Knopp, T.: Model-consistent universal wall-functions for RANS turbulence modelling. In: Proceedings Intern. Conf. BAIL 2006, Göttingen (July 2006)

[9] Kröner, D.: Numerical Schemes for Conservation Laws. Wiley/Teubner (1997)

[10] Ridouane, E.H., Hasnaoui, M., Campo, A.: Effects of surface radiation on natural convection in a Rayleigh-Bernard square enclosure: steady and unsteady conditions. Heat and Mass Transfer 42(3), 214–225 (2006)

[11] Rodi, W.: Turbulence models and their application in hydraulics - a state of the art review. In: International Association for Hydraulic Research, Delft, 3rd edn., Balkema (1993)

[12] Streblow, R., Rank, R., Müller, D.: An analyses of thermal plumes above a cylindrical heat source in a room with a vertical temperature gradient. In: Proceedings of Roomvent 2007, Helsinki, vol. 3, pp. 145–151. Gummerus Printing, Finnland (2007)

[13] Timmermans, L.J.P., Minev, P.D., Van De Vosse, F.N.: An approximate projection scheme for incompressible flow using spectral elements. Int. J. Numer. Methods Fluids 22, 673–688 (1996)

[14] Trottenberg, U., Oosterlee, C.W., Schüller, A.: Multigrid. Academic Press, London (2001)

[15] Widhalm, M., Ronzheimer, A., Meyer, J.: Lagrangian Particle Tracking on Large Unstructured Three-Dimensional Meshes. In: American Institute of Aeronautics and Astronautics, 46th AIAA Aerospace Sciences Meeting and Exhibit, Reno, Nevada, U.S.A., [2008-01-07 - 2008-01-10] AIAA Reno 472

[16] Wilcox, D.C.: Turbulence Modeling for CFD, DCW Industries, Inc. (November 2006)

[17] Yang, W.J., Taniguchi, H., Kudo, K.: Radiative Heat Transfer by the Monte Carlo Method. In: Advances in Heat Transfer, vol. 27. Academic Press, London (1995)

Flow Structure Formation of Turbulent Mixed Convection in a Closed Rectangular Cavity

D. Schmeling, A. Westhoff, M. Kühn, J. Bosbach, and C. Wagner

German Aerospace Center (DLR), Institute of Aerodynamics and Flow Technology,
Bunsenstraße 10, D-37073 Göttingen, Germany
Daniel.Schmeling@dlr.de
http://www.dlr.de/as

Summary

An experimental investigation of flow structure formation in turbulent mixed convection in a closed rectangular cavity with an aspect ratio of $1 : 1 : 5$ and air as working fluid is presented. Mixed convection at $Re = 1.1 \cdot 10^4$ and $Ra = 3.0 \cdot 10^8$ is studied under well-defined conditions by combination of forced and thermal convection. The resulting flow structures strongly depend on the ratio of inertia and buoyancy forces. A 2D mean wind, which can be approximated by a solid body rotation, is found at pure forced convection. With increasing Archimedes number (Ar), realized by a temperature gradient between bottom and ceiling of the convection cell, this structure becomes instable. Leading to four convection rolls for $Ar = 3.4$, which are oriented in longitudinal direction of the cell, are observed.

1 Introduction

In fluids usually no long range order exists between the atomic or molecular species. As a consequence convection serves as an additional transport mechanism for thermal energy beside heat conduction and heat radiation. In convective flows the fluid transports thermal energy in terms of intrinsic energy. Usually three regimes of convection are distinguished: Thermal convection, which is driven by thermally induced density gradients, forced convection, which is induced by an externally applied force and mixed convection, here as a superposition of the first two cases. Convection is an often occurring phenomenon, which is the driving mechanism in e.g. cloud formation and important for the transport of thermal energy in stars. Additionally it is responsible for plate tectonics in the bowels of the earth or the allocation of warm air in a heated room. Of particular importance is turbulent convection, which appears in many technical applications and occurs often in nature, e.g. heat exchanger, interior climatisation, meteorology, astrology or geology, [5] [6] and [9]. Turbulent mixed convection is a frequently-studied phenomenon, but many research groups concentrate on complex geometries with technical interest, like aircraft cabins [2], heat exchanger [9] or different arrangements of heat sources [1]. Some groups also provided detailed studies of velocity and temperature

distributions and the heat flux in purely thermal convection based on numerical [4] and experimental [3] investigations. But the basic physical mechanisms of the structure formation in mixed convection are not completely understood. In order to study the superposition of pure forced and thermal convection with optical measurement techniques under well-defined boundary conditions, a rectangular convection cell was developed. In this cell investigations of flow structure formation in turbulent mixed convection were performed. In this paper the results of the two-component, two-dimensional (2C-2D) and three-component, two-dimensional (3C-2D) particle image velocimetry (PIV) obtained for two different flow conditions are presented and discussed.

2   Dimensionless Parameters

In order to characterise mixed convective flows, at least three dimensionless parameters, which can be obtained by dimensional analysis, are needed. The ratio between inertia and friction force is given by the Reynolds number: $Re = \frac{U \cdot L}{\nu}$. Thereby U is the mean velocity, L is a characteristic length and ν is the kinematic viscosity. The ratio of buoyancy and friction forces is described by the Grashof number, which is defined by $Gr = \frac{g \cdot \beta \cdot \Delta T \cdot L^3}{\nu^2}$, with g the acceleration of gravity, β the thermal expansion coefficient and ΔT a temperature difference. The Prandtl number describes the ratio of momentum transport by friction and heat transport by conduction. It just depends on the fluid properties and not on flow parameters. It is given by $Pr = \frac{\nu}{\kappa}$, where κ denotes the thermal diffusivity. These three dimensionless parameters in combination with the geometry and the boundary conditions completely characterise mixed convection as long as no further forces are acting on the fluid. In addition to these numbers, one often refers to the Rayleigh number, which can be expressed as the product of Grashof and Prandtl number: $Ra = Gr \cdot Pr$.

Another parameter for the description of mixed convection is the Archimedes number, which is defined by $Ar = \frac{Ra}{Re^2 \cdot Pr}$. It is the ratio between buoyancy and inertia forces. In the region $Ar \gg 1$ thermal convection and in the region $Ar \ll 1$ forced convection dominates. Somewhere between these limiting cases mixed convection occurs.

3   Experimental Setup

In order to provide a test environment for the study of mixed convection under well-defined conditions a rectangular convection cell with the aspect ratios $\Gamma_{zy} = \frac{\text{length}}{\text{height}} = 5$ and $\Gamma_{xy} = \frac{\text{width}}{\text{height}} = 1$ is built. A sketch of the convection cell with the dimensions of $2500 \times 500 \times 500 \, \text{mm}^3$ (length × width × height) is shown in Figure 1. The heating plate at the bottom consists of five parts and is actively heated via a controlled water heating (volume flow rate $\dot{V} \approx 35 \, \text{litre} \cdot \text{minute}^{-1}$). The cooling plate at the top is passively cooled to room temperature via five air-air heat exchangers. The side panels are a double-wall system of polycarbonate plates in order to guarantee good optical access as well as a minimum of heat transport (heat transmission coefficient of the double-wall system: $k \approx 0.96 \, \frac{\text{W}}{\text{Km}^2}$). By operating the heating plates a vertical temperature gradient can be applied to the fluid and thus thermal convection can be generated.

An air inlet (height: $25\,\mathrm{mm}$) at the top and an air outlet (height: $15\,\mathrm{mm}$) at the bottom allow to superimpose forced convection by an externally driven volume flow. The volume flow is measured via the pressure drop at a standardised orifice and adjusted by a rotary speed controlled fan.
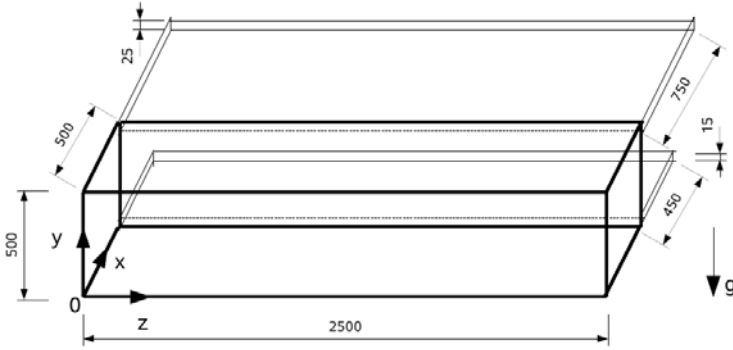
Fig. 1. Sketch of the convection cell, with an air inlet installed at the upper cooled plate and an air outlet at the bottom heated plate

As characteristic length of our system the height of the cell is chosen. With a maximum temperature difference of $60\,\mathrm{K}$ and air ($Pr \approx 0.72$) as working fluid characteristic numbers of $0 < Ra \lesssim 10^8$, $0 < Re \lesssim 10^5$ and $0 < Ar < \infty$ can be realized.

Temperature measurements are carried out with 62 Pt100 (1/3 DIN B) temperature sensors at a sample rate of $f \approx 1/6\,\mathrm{Hz}$. Cooling (index: c) and heating (index: h) plate are each equipped with 25 sensors, showing spatial temperature deviations of $\Delta T_{\mathrm{c,rms}} = 1.2\%$, $\Delta T_{\mathrm{c,max}} = 1.4\%$ and $\Delta T_{\mathrm{h,rms}} = 1.1\%$, $\Delta T_{\mathrm{h,max}} = 1.6\%$. The temperature of the incoming air is measured by three sensors: $\Delta T_{\mathrm{in,rms}} = 0.7\%$ and $\Delta T_{\mathrm{in,max}} = 0.9\%$. The indicies rms and max denote root mean square and maximal values of the variations. All deviations are normalised with the mean temperature difference between heating and cooling plate $\Delta T = 21.16 \pm 0.07\,\mathrm{K}$. To measure the temperature deviations of the outcoming air, nine sensors are installed equidistantly over the full lenght of the outlet.

In order to measure instantaneous velocity fields 2C-2D and 3C-2D (stereoscopic) PIV is applied. For further information on this measurement technique see [8]. As tracer particles small oil droplets with an average diameter $d \approx 2\,\mu\mathrm{m}$ are used. The particles are illuminated by a dual cavity Nd:YAG laser with a pulse energy of maximal $340\,\mathrm{mJ}$. The light pulses are shaped into a light sheet with a thickness between 2 and $5\,\mathrm{mm}$ by a telescope and a cylindrical lens. In case of 2C-2D PIV image acquisition is realized with one and in case of 3C-2D PIV with two CCD-cameras (pco.4000, PCO) with a resolution of 4008×2672 pixel. For 2C-2D and 3C-2D PIV the cameras are equipped with a $f = 100\,\mathrm{mm}$ lens (Planar T*2/100, Zeiss) without Scheimpflug adapter and two $f = 85\,\mathrm{mm}$ lenses (Planar T*1.4/85, Zeiss) with Scheimpflug adapters, respectively. For each series of mixed convection 4800 and for each series of forced convection

500 image pairs are acquired with a frequency of $1/1.5\,\mathrm{Hz}$. The arrangement of the measurement planes is shown in Figure 2. The evaluation of the 2C-2D images is realized with PIV*view*2C [7] with a single pass algorithm using double correlation and a three-point Gaussian fit for detection of the correlation maximum with sub pixel accuracy. As long as not mentioned differently, the interrogation window size is 32×32 pixels large and the overlap is set to 50%, which leads to 150×150 vectors in the measurement plane. This corresponds to a two-dimensional velocity vector field with a spatial resolution of $3.3\,\mathrm{mm}$ in each direction. For evaluation of the 3C-2D images an interrogation window size of 96×96 or 128×96 pixels is used at an overlap of 75%, which leads to a vector spacing of $6\,\mathrm{mm}$. From the instantaneous velocity maps the mean velocity fields are calculated, which are presented and discussed in the following. The results of two different flow conditions at $Re = 1.1 \cdot 10^4$ are presented in this paper. First pure forced convection at $Ar = 0$ and second mixed convection at $Ar = 3.4$ are discussed.
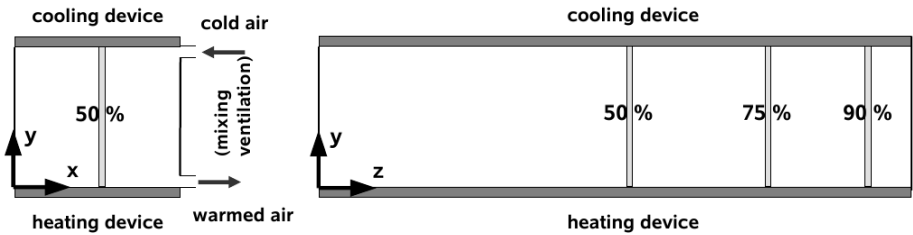
Fig. 2. Positions of the 3C-2D PIV longitudinal section (left) and the 2C-2D PIV cross sections (right)

4   Results

In this section the mean velocity fields measured with PIV in different measurement planes for $Ar = 0$ and $Ar = 3.4$ are presented and discussed. In subsection 4.1 and 4.2 the results for forced and mixed convection, as determined with 2C-2D PIV in the $x - y$ measurement planes are reviewed, respectively. In subsection 4.3 the flow structures measured with 3C-2D PIV in a longitudinal cross section are compared to the PIV results in the other cross sections.

4.1   Forced Convection

The mean velocity field of pure forced convection, i.e. with the heating plate switched off, in a cross section at 50% of the cell length is depicted in Figure 3 (left). A wall jet is generated by the incoming air, which is forced to separate and reattach at the corners of the cell. The jet thus follows the ceiling, the side wall and the floor of the cell. Due to entrainment the average jet velocity decreases and the mass flow rate increases as the jet moves downstream. Therefore only a part of the expanded jet leaves through

the outlet while the remaining part recirculates and interacts with the incoming air jet. As a result a counter clockwise rotating mean wind develops in the cell. In order to further analyse the roll structure velocity line scans of the v-component in y-direction are extracted at $y = 250\,\mathrm{mm}$ and depicted in Figure 3 (right) for three investigated measurement planes. First it should be noted that the velocity profile can be characterised by a constant angular velocity in all three measurement planes. Consequently the mean wind can be approximately described by a two-dimensional solid body rotation under forced convection conditions. The small offset of the line scans in x-direction is due to the additional volume flow in the downward oriented part of the wall jet in the front of the cell.
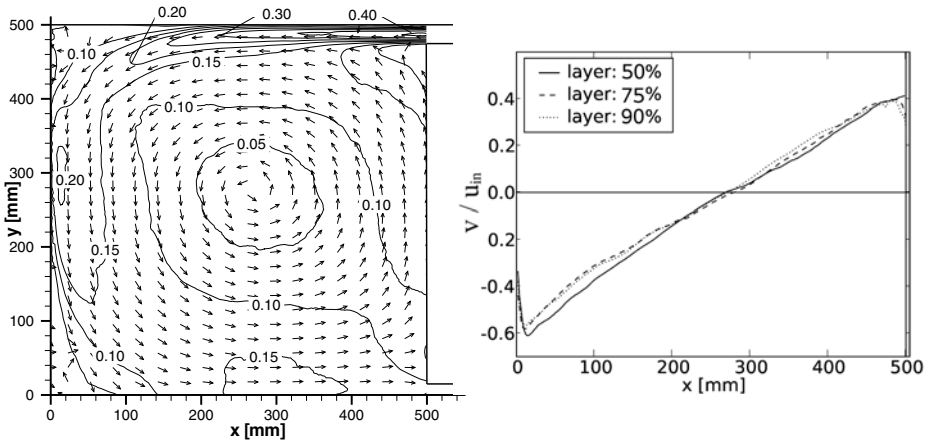
Fig. 3. Mean velocity field with isolines (showing the magnitude, unit: m/s) in the centre cross section evaluated for a window size of 24×24 pixels (every 12th, 8th vector is shown in x, y direction, respectively) (left) and profiles of the mean velocity field at three positions in longitudinal direction (right) obtained for $Re = 1.1 \cdot 10^4$ and $Ar = 0$

4.2 Mixed Convection

Figure 4 (left) shows the mean velocity field obtained for the mixed convection conditions. The flow field in the measurement plane deviates strongly from that observed in purely forced convection. Upon the onset of thermal convection the structure of the wall jet has changed dramatically. As a consequence the core of the mean wind is shifted with respect to the cell centre. The jet separation in the corners of the cell occurs further downstream, which leads to a decrease of the size of the recirculation zones in the corners of the cell as compared to forced convection. Again the velocity line scans of the v-component are extracted at $y = 250\,\mathrm{mm}$, see Figure 4 (right). Clearly a breakdown of the solid body rotation can be detected. Both, the structure of the wall jet and the location of the mean wind core is different in every cross section. Further a strongly three-dimensional nature of the flow can be deduced from the line scans, which differ considerably for the two investigated measurement planes.
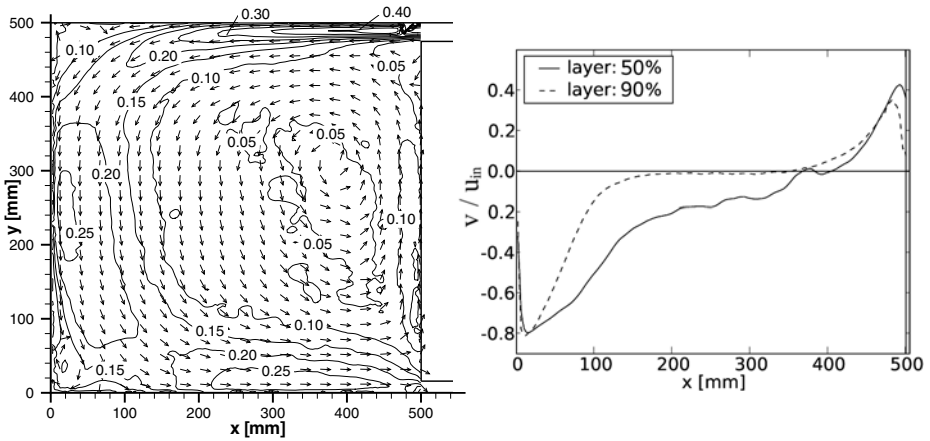
Fig. 4. Mean velocity field with isolines (showing the magnitude, unit: m/s) in the centre cross section (every 8th, 6th vector is shown in x, y direction, respectively) (left) and profiles of the mean velocity field at two positions in longitudinal direction at $y = 250\,\text{mm}$ (right) obtained for $Re = 1.1 \cdot 10^4$ and $Ar = 3.4$

4.3   Comparison of Flow Structures

In order to shed some more light on the three-dimensional characteristics of the flow stereoscopic PIV is conducted in a longitudinal section, see Figure 2 (left). In Figure 5 the u-component, which is oriented perpendicular to the measurement plane, is presented using contours superimposed with the v-w vector field. Under absence of buoyancy forces (see Figure 5 (top)) the u-component only depends on the position in y-direction (height) and in this measurement plane the v and the w-component are negligible. Below the ceiling of the cell the flow leaves the air inlet and is directed towards the front window of the convection cell. Above the cell floor the air flows back to the air outlet. A homogeneous flow, which is almost independent of the z-coordinate, indicating a very two-dimensional mean wind, is observed. The presence of buoyancy forces leads to a breakdown of the two-dimensional mean wind. More precisely the flow changes into a superposition of the incoming air jet with smaller flow structures. Figure 5 (bottom) shows the velocity field at an Archimedes number of $Ar = 3.4$ in the longitudinal measurement plane. The deviation to the flow field shown in Figure 5 (top) pinpoints the influence of the buoyancy forces, i.e. velocity components oriented parallel and opposite to the applied temperature gradient establish. Regions of fast upward and downward oriented motion, which are ascribed to the organisation of thermal plumes, can be observed. The encountered flow field suggests a superposition of the wall jet of incoming air with four induced rolls, their rotation axis being oriented in x-direction, see Figure 6. The rotational direction is an effect of the non-adiabatic side panels. In slightly cooler wall zones downdraughts are encouraged, purporting a clockwise and counter clockwise rotating roll in the right and left region of the convection cell, respectively. Corresponding to these additional flow structures a spatial temperature allocation of the outcoming air is detected. Two warmer regions are found at $z \approx 30\%$ and $z \approx 75\%$ of the cell length well-fitting to the areas of rising air.
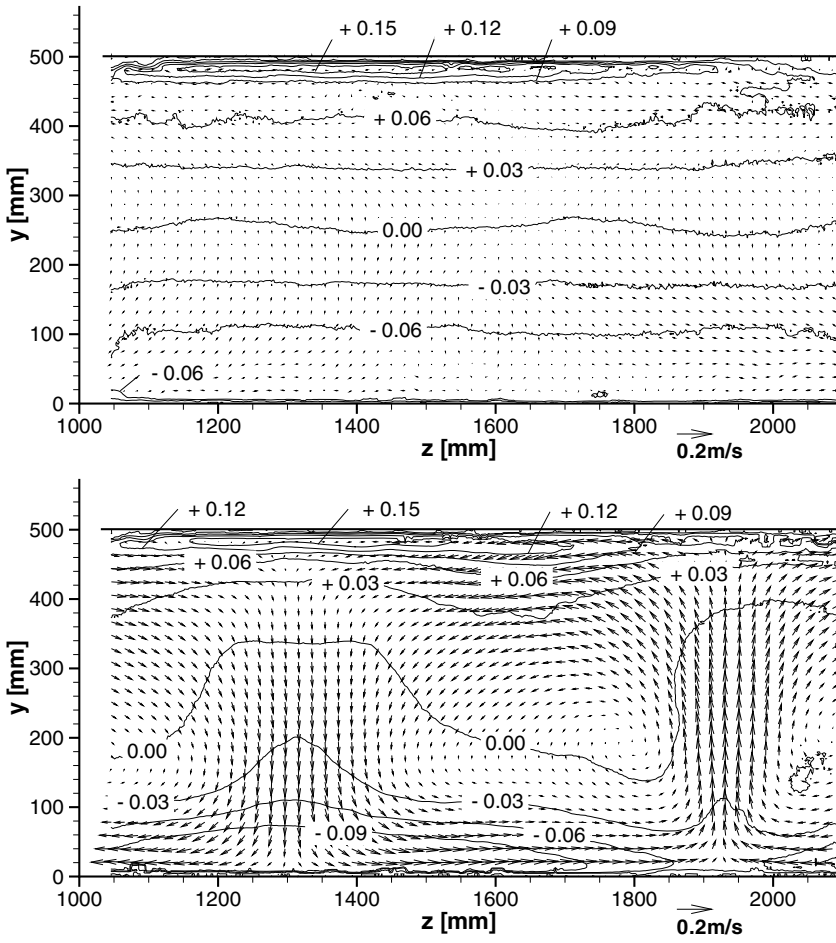
Fig. 5. Mean velocity fields (isolines show u-component, unit: m/s) in the longitudinal section obtained for pure forced convection ($Re = 1.1 \cdot 10^4$, $Ar = 0$) (top) and mixed convection ($Re = 1.1 \cdot 10^4$, $Ar = 3.4$) (bottom), (every 8th vector is show in each direction)
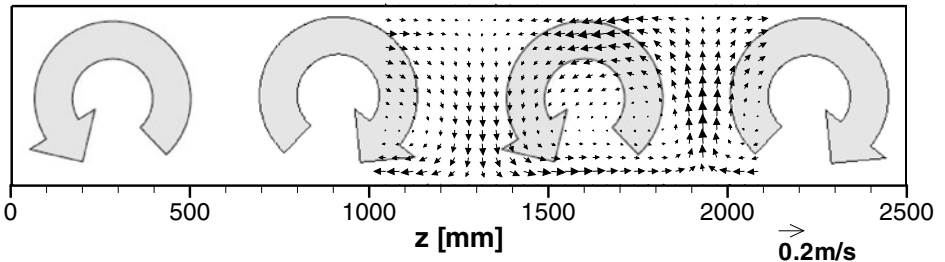
Fig. 6. Sketch of the four mean convection cells in longitudinal direction overlayed with the mean velocity field presented in Figure 5 (bottom). Every 18th velocity vector is plotted

5   Conclusion

Mixed convection has been investigated under precisely controlled conditions in a rectangular convection cell. Two flow cases have been studied: pure forced convection at $Re = 1.1 \cdot 10^4$ and $Ar = 0$ and mixed convection at $Re = 1.1 \cdot 10^4$ and $Ar = 3.4$. 2C-2D and 3C-2D PIV has been used in order to study the flow in three cross sectional and one longitudinal measurement planes. The resulting velocity fields revealed a strong dependence on the ratio of inertia and buoyancy forces. At pure forced convection it was found that the flow is governed by a two-dimensional solid body rotation of the fluid in the cell, that is driven by the externally applied air flow. Upon the onset of thermal convection, i.e. at $Ar = 3.4$ a collapse of the 2D mean wind was observed, as well as a formation of four convection rolls in longitudinal direction, which interact with the wall jet generated by the incoming air. The observed flow structures are in good agreement with temperature measurements in the air outlet, which reveal a characteristic fingerprint of the flow structures in the temperature profiles.

As the next steps the dynamics of the interaction between wall jet and convection rolls will be investigated in evaluations of the instantaneous velocity fields by means of proper orthogonal decomposition as well as time resolved temperature measurements at distinguished positions in the cell. Furthermore, application of advanced optical field- and volumetric measurement techniques to capture instantaneous temperature fields as well as the three-dimensional structure of the mean wind are under way.

References

[1] Baskaya, S., Erturhan, U., Sivrioglu, M.: Experimental investigation of mixed convection from an array of discrete heat sources at the bottom of a horizontal channel. Int. Journal of Heat Mass Transfer 42, 56–63 (2005)

[2] Bosbach, J., Kühn, M., Wagner, C.: Large scale particle image velocimetry with helium filled soap bubbles. Experiments in Fluids 46, 539–547 (2009)

[3] Ebert, A., Resagk, C., Thess, A.: A Experimental study of temperature distribution and local heat flux for turbulent Rayleigh-Bénard convection of air in a long rectangular enclosure. Int. Journal of Heat and Mass Transfer 51, 4238–4248 (2008)

[4] Kaczorowski, M., Wagner, C.: Analysis of the thermal plumes in turbulent Rayleigh-Bénard convection based on well-resolved numerical simulations. J. Fluid Mech. 618, 89–112 (2008)

[5] Kupka, F.: Convection in Stars. In: Proceedings International Astronomical Union Symposium, vol. 224, pp. 119–129 (2004)

[6] Linden, P.F.: The Fluid Mechanics of Natural Ventilation. Annu. Rev. Fluid Mech. 31, 201–238 (1999)

[7] http://www.pivtec.de

[8] Raffel, M., Willert, C.E., Wereley, S.T., Kompenhans, J.: Particle Image Velocimetry - A practical Guide, 2nd edn. Springer, Heidelberg (2007)

[9] Sillekens, J.J.M., Rindt, C.C.M., Van Steenhoven, A.A.: Developing mixed convection in a coiled heat exchanger. Int. Journal of Heat Mass Transfer 41, 61–72 (1998)

Numerical Determination of Nozzle Admittances in Rocket Engines

Daniel Morgenweck[1], Jutta Pieringer[2], and Thomas Sattelmayer[3]

[1] Technische Universität München, Boltzmannstr. 15, 85747 Garching, Germany
morgenweck@td.mw.tum.de
http://www.td.mw.tum.de
[2] Audi AG, Ingolfstadt, Germany
[3] Technische Universität München, Boltzmannstr. 15, 85747 Garching, Germany
sattelmayer@td.mw.tum.de

Summary

A numerical method in the time domain is introduced to assess the stability with respect to the nozzle's geometry in liquid rocket engines. A boundary condition for the injector plane in a combustion chamber is presented, where the mass flow fluctuations are set to zero. Thus the acoustic flux over the injector plane is zero even when there is mean flow normal to the boundary. Two ways of assessing the nozzles stability are shown. The first is to characterize the decaying of pressure oscillations means by the decay coefficient and the second is to determine the nozzle admittance. The procedures for obtaining both are described and the results are compared with the available experimental and analytical data.

Nomenclature

In the following all physical quantities are normalized by a set of characteristic quantities namely a characteristic length scale, a characteristic pressure and a characteristic velocity. The following nomenclature is used throughout the article:

f	frequency
$\underline{I}$	acoustic flux
$\bar{q}$	mean quantity (e.g. $\bar{\rho}$, $\underline{\bar{u}}$, $\bar{p}$, $\bar{a}$)
q'	perturbation quantity (e.g. ρ', $\underline{u}'$, p')
$\hat{q}$	complex quantity in the frequency domain (e.g. $\hat{\underline{u}}$, $\hat{p}$)
Y	admittance
α	decay coefficient
ω	angular frequency $2\pi f$

1 Introduction

Oscillating instabilities are still today a major thread for liquid rocket engines. Those high frequency oscillations can cause structural damage to the nozzle and combustion

chamber and also to the periphery. The increased heat exchange to the wall can cause thermal failure and threatens also the success of the mission. On from the beginning of modern rocket design there was the need to understand the mechanism of those instabilities. Crocco [3] did a fundamental investigation on this field at a very early stage. The ratio between the input of acoustic energy through the combustion process and the loss of acoustic energy mainly by transport through the nozzle are influencing the stability in the rocket engine. Marble and Candel [6] offered an analytic relation for admittances of short nozzles. It can be used to describe the stability of a nozzle depending on the Mach number. In a semi numerical and an experimental approach Bell and Zinn [1], [11], [2] surveyed nozzle admittances for 3D acoustic waves. The admittances characterize the reflection behavior of the nozzle and thus the energy flux over the nozzle.

In the work presented here the stability in rocket engines depending on the geometry will be surveyed numerically by evaluating the decay coefficient and the nozzle admittances. The numerically evaluated nozzle admittances are validated against the experiments of Bell [1].

2   Numerical Method

For the numerical evaluation given in this report the time dependent solver PIANO-SAT is used. The base code PIANO is provided by the DLR Braunschweig [4]. Special adaption for stability assessment in rocket nozzles are applied. PIANO-SAT works in the time domain and utilizes special discretization schemes commonly used in the field of aero-acoustic. It is a time explicit finite difference scheme of higher order. To assess the onset of acoustic oscillations in operating rocket engines a simple model for coupling combustion fluctuation and acoustic fluctuation was implemented [8]. The numerical method solves the **L**inearized **E**uler **E**quations (LEE) or the **A**coustic **P**erturbation **E**quations (APE) [5]. Thereby the primitive quantities for density, pressure and velocity are split into a mean part and a perturbation part. PIANO-SAT only solves for the perturbation part. The mean quantities are input to the solver and originate from a CFD computation.

The investigations below are based on the solution of the APEs. The mean flow field comes from a steady state Euler calculation. All quantities are normalized by a set of normalization factors.

3   Boundary Condition for the Nozzle Head

Following the argument of Pieringer [9] a special boundary condition needs to be considered at the nozzle's head. The exact flow field in this area is rather complex and hard to include in an acoustic computation. A simplifying approach is to take a block mean flow profile at the inlet, which means the mean velocity is constant at and normal to the injector plane in the rocket engine. Thus the mesh at the injector plane can be coarse enough to achieve results in a reasonable time. However by applying a non-zero mean flow over a boundary, it has to be made sure, that there is no acoustic flux over that

boundary, to guarantee an energy neutral acoustic boundary. In the following a possible way to impose such a boundary is described.

The balance for the acoustic energy can be written

$$\Delta E = \int\limits_A \langle \underline{n} \cdot \underline{I} \rangle \, dA. \tag{1}$$

Morfey [7] gave a formulation for the acoustic flux $\underline{I}$ in an isentropic potential flow

$$\underline{I} = p'\underline{u}' + \frac{p'^2 \bar{\underline{u}}}{\bar{\rho}\,\bar{a}^2} + \bar{\rho}(\bar{\underline{u}} \cdot \underline{u}')\underline{u}' + \frac{p'}{\bar{a}^2}(\bar{\underline{u}} \cdot \underline{u}')\bar{\underline{u}}. \tag{2}$$

For zero acoustic flux at the inlet boundary it has to be assured, that $\langle \underline{n} \cdot \underline{I} \rangle = 0$. Looking at equation 2 it becomes apparent, that it is not enough to set the perturbation velocity normal to the boundary to zero $\underline{u}' \cdot \underline{n} = 0$. In that case the second term on the right hand side of equation 2 will still give a contribution to the energy balance. Verhaar [10] showed, that a vanishing mass flow fluctuation at the boundary $\dot{m}' = 0$ does not contribute to the acoustic energy balance also for a boundary with normal mean flow components

$$\dot{m}' = 0 = \bar{\rho}\underline{n} \cdot \underline{u}' + \rho'\underline{n} \cdot \bar{\underline{u}}. \tag{3}$$

For isentropic flows the perturbation density in equation 3 can be substituted and the equation can be reformulated

$$\underline{n} \cdot \bar{\underline{u}} \frac{p'}{\bar{\rho}\,\bar{a}^2} + \underline{n} \cdot \underline{u}' = 0. \tag{4}$$

Inserting equation 4 into equation 2 it can indeed be proofed that a vanishing mass flow fluctuation leads to no acoustic flux at the boundary.

In a first 2D generic test case a circular domain with homogeneous mean flow is excited by a pressure pulse. On all outer boundaries of the domain the mass flow fluctuations are set to zero. In the left plot of figure 1 the instantaneous absolute value of the mass flow fluctuation is given. It can be seen that there is no fluctuation of the mass flow at the outer boundaries. The same can be observed on the right side of figure 1 for a nozzle with a no-mass flow condition at its head.

4   Determination of the Decay Coefficient

A criteria for stability in rocket engines is the decay coefficient. Thereby the exponential decay of pressure fluctuations are determined. In case no other source of acoustic energy exists and acoustic energy is not lost over other boundaries than the nozzle itself, the decay coefficient is a characteristic quantity for the stability in rocket engines. Unlike the admittance it also accounts for convective loss of acoustic energy through mean flow.

A first step to obtain a decay coefficient is to analyze the eigenmodes in the combustion chamber, which modes participate in the pressure oscillations. One way finding the
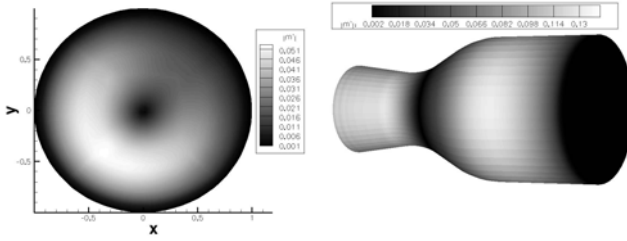
Fig. 1. Absolute value of the mass flow fluctuation, left 2D generic test case, right 3D nozzle with zero-mass flow boundary at the injector plane
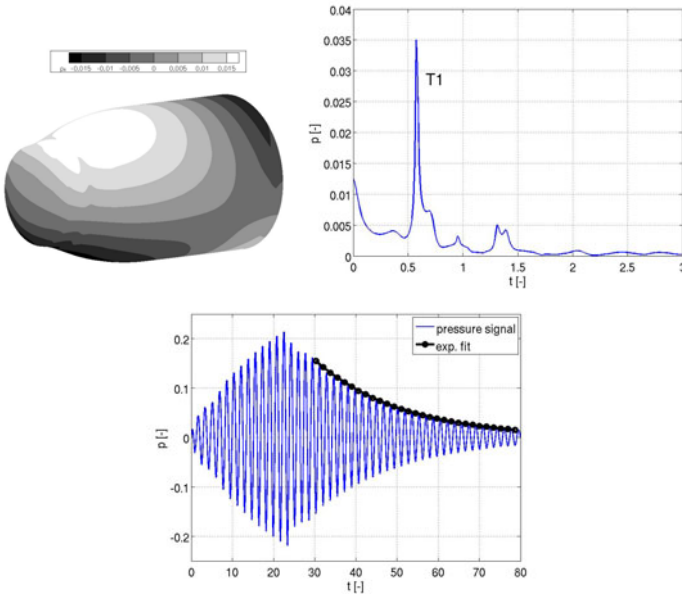
Fig. 2. Initially excited rocket engine, left contour plot for the dimensionless time t=40 [-], right dimensionless pressure amplitude over the dimensionless frequency, bottom pressure oscillation for determining the decay coefficient

dominating modes is to initially excite the the oscillation in the chamber and recording the decay of the pressure perturbation. This is done by setting a Gaussian pressure pulse at some point in the computational domain. The center of the Gaussian pulse is situated at some distance away from the axial axis to ensure also transverse modes are excited. In principle the excitation mechanism has an influence on how strong certain modes are excited. The recorded pressure signal is therefore dependent on the excitation. However it can be said, that a Gaussian pressure pulse has the ability to excite a broad band of frequencies. Thus the main eigenfrequencies will be excited and can be observed in the

pressure signal. The left plot of figure 2 shows the instantaneous pressure at the boundaries of the combustion chamber with the nozzle. The flow is only calculated until the Mach 1 isosurface. Only regions with Mach numbers lower than 1 can have an impact on the acoustic field in the combustion chamber. Pressure waves in areas with Mach numbers greater than 1 can only travel downstream. The circular plane on the left of the plot marks the throat of the nozzle, whereas the circular base area on the opposite marks the injector plane (not visible in the plot).

The right plot of figure 2 gives the FFT of the pressure signal. It is apparent that the oscillation is dominated by pressure fluctuations of a dimensionless frequency of $f = 0.58$ $[-]$. This corresponds to the first transverse mode. Usually in rocket engines the transverse modes are more noticeable than longitudinal ones. The longitudinal modes are more damped. Thus the transverse modes are often causing stability problems in rocket engines.

After the dominating mode is identified, the damping of the first transverse mode needs to be evaluated. Therefore, the combustion chamber will be excited only by the frequency corresponding to that specific mode ($f = 0.58$ $[-]$). A periodic source with the shape and position of the Gaussian pulse above is used for the excitation. After a few cycles the periodic source is switched off and the decay of the pressure oscillation is measured at several points in the domain. The Hilbert transformation of the recorded pressure signal delivers the envelope of the pressure oscillation. The decaying part of the envelope is approximated by an exponential function. The bottom plot of figure 2 shows the pressure signal with active and inactive periodic source. Furthermore the exponential function for the decaying signal is given. The decay coefficient of the best fitted exponential function characterizes the stability of the system. Applying this method to the rocket engine given in figure 2, a dimensionless decay coefficient for the first transverse mode of $\alpha = 0.048[-]$ could be obtained.

5   Comparison of Nozzle Admittances

Another way to characterize the nozzle's impact on stability is to evaluate its admittance. It provides information on how much acoustic energy is lost through the nozzle. Furthermore the admittance is used in more comprehensive stability analysis (e.g. means by network models) concerning the overall propulsion system to describe the influence of the nozzle. Zinn [11] found a semi analytical approach to describe the nozzle admittances. Bell and Zinn [2] computed three-dimensional nozzle admittances and compared them to experimental results of Bell [1]. Thereby they parameterized the nozzle through several radii and the angle of the convergent part of the nozzle (see figure 3). Furthermore the entry Mach number of the flow to the nozzle, the shape of the mode and the speed of sound are input to a program evaluating the nozzle's admittance.

Similar cases were surveyed in a numerical simulation with PIANO-SAT. Two configurations for longitudinal modes were investigated. The first calculation was done by Pieringer [9] for a nozzle with $15°$ apex angle, an entry Mach number of 0.08 and a radius ratio of 0.44 between the radius of the cylinder before the nozzle and the transition radius between cylinder and nozzle and between the convergent and divergent part of the nozzle (see figure 3). The second case surveys a nozzle at Mach 0.16 an apex angle
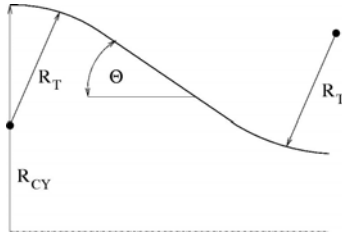
Fig. 3. Characteristics of the nozzle as suggested by Bell
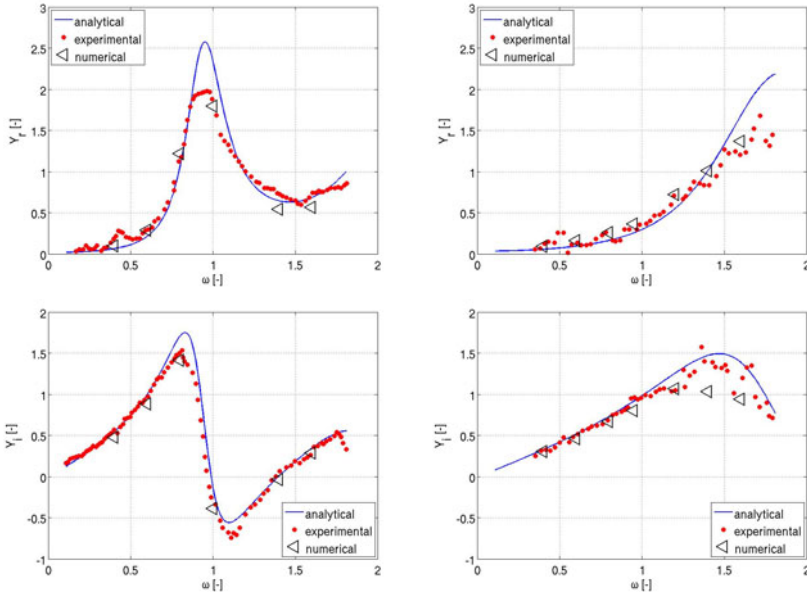
Fig. 4. Dimensionless admittances over dimensionless frequency for the first (left) and second (right) configuration

of $30°$ and a radius ratio of 1. In both calculations the pressure oscillation were excited by a periodic oscillating plane with a fixed angular frequency some way upstream the nozzle. At the nozzle entrance fluctuation velocity and pressure were recorded. The time signals of both are transformed into the frequency domain and the ratio between perturbation velocity and perturbation pressure at the excitation frequency is taken

$$Y = \bar{\rho}\,\bar{a}\,\frac{n \cdot \hat{u}}{\hat{p}}. \tag{5}$$

Considering figure 4, it is apparent that the numerical simulation in both configurations meet quite well the experimental results of Bell [1]. The left column shows the real and imaginary part of the admittances for the case with $M = 0.08$, apex angle $15°$ and radius ratio of 0.44. The deviation between numerics and experiment are small. Only

at higher frequencies the results diverge a little. A possible reason for this might be the onset of higher acoustic modes. The analytical solution shows a greater difference from the other two especially around $\omega = 0.9$. The analytical approach does only account for 1-dimensional mean flow. In the right column the results for the case with $M = 0.16$, apex angle $30°$ and radius ratio of 1. are given. Again the numerics matches quite well the experimental results. The numerical values lie within the scatter range of the experimental data. Only for ω around 1.4 some differences between numerics and the experiment occur in the imaginary part of the admittance. A possible explanation for the divergence is linked to the position, where the acoustic quantities are recorded in the numerical simulation. The calculation of the admittance proofed to be very sensitive to that position. This might cause inaccuracy.

6   Conclusion

A boundary condition was presented that causes no flux of acoustic energy over the boundary even when there is a mean flow through it. The results showed the validity of the boundary condition. Later on the boundary condition was used to survey the damping behavior of the rocket engine. A procedure for evaluating the decay coefficient of the declining acoustic oscillations of the first transverse mode was described and the results were shown. In a second study the admittances for two configurations were determined and compared to analytical and numerical results. The results agreed quite well with the experimental data. Both methods can be used in the state of design of a new rocket engine. The decay coefficient is a good measure of stability and provides information for the comparison with existing databases. Whereas the admittance is used in more comprehensive stability analysis of the overall engine means by network models.

References

[1] Bell, W.A.: Experimental Determination of Three-Dimensional Liquid Rocket Nozzle Admittances. PhD thesis, Gerorgia Institute of Technology, Atlanta (1972)
[2] Bell, W.A., Zinn, B.T.: The prediction of three-dimensional liquid-propellant rocket nozzle admittances. NASA CT-121129 (1973)
[3] Crocco, L., Cheng, S.I.: Theory of combustion instability in liquid propellant rocket motors. Butterworths Science Publication, note: AGARDOGRAPH N 8 (1956)
[4] Delfs, J.W., Grogger, H.A., Lauke, T.G.W.: Numerical simulation of aeroacoustic noise by DLR's aeroacoustic code PIANO. Technical report, DLR Braunschweig (2002)
[5] Ewert, R., Schröder, W.: Acoustic perturbation equations based on flow decomposition via source filtering. Journal of Computational Physics 144, 365–398 (2003)
[6] Marble, F.E., Candel, S.M.: Acoustic disturbance from gas non-uniformities convected through a nozzle. Journal of Sound and Vibration 55(2), 225–243 (1977)
[7] Morfey, C.L.: Acoustic energy in non-uniform flows. Journal of Sound and Vibration 14(2), 159–170 (1970)
[8] Pieringer, J., Sattelmayer, T.: Simulation of thermo-acoustic instabilities including mean flow effects in the time domain. In: ICSV13, Vienna (2006)

[9] Pieringer, J.E.: Simulation selbsterregter Verbrennungsschwingungen in Raketenschubkammern. PhD thesis, Technische Universität München (2008)

[10] Verhaar, B.: On thermo-acoustic stability analysis of gas turbines. Master's thesis, TU Eindhoven (1997)

[11] Zinn, B.T.: Review of nozzle damping in solid rocket instabilities. In: AIAA/SAE 8th Joint Propulsion Specialist Conference, New Orleans, Louisiana (1972)

Analysis of Vertical Axis Wind Turbines

Merim Mukinović, Gunther Brenner, and Ardavan Rahimi

Clausthal University of Technology, Institute of Applied Mechanics,
Adolph-Roemer Str. 2A, 38678 Clausthal-Zellerfeld, Germany

Summary

The present paper contributes to the modeling of unsteady aerodynamics of Vertical Axis Wind Turbines (VAWT). A Double Multiple Stream Tube (DMST) model as an engineering approach for design and optimization of VAWT is presented. The unsteady flow around a H-type rotor is investigated numerically in two and three dimensions using Computational Fluid Dynamics (CFD).

1 Introduction

In recent years an increasing demand in decentralized power plants is observed renewing the interest in Vertical Axis Wind Turbines (VAWT). Compared to Horizontal Axis Wind Turbines (HAWT), VAWT presents several advantages such as lower sound emission, its insensitivity to yaw and wind direction and its increased power output in skewed flow. Due to their simpler configuration, the production costs and service effort are potentially lower than for HAWT. These observations also have driven the promotion of small scale VAWT for the residential environment. In some sense, the price paid for structural simplicity is aerodynamic complexity; VAWT aerodynamics is inherently unsteady and beyond the limits of classical airfoil theory. However, recent developments in computational methods and the capability of predicting in detail the unsteady flow in such rotating machinery greatly increase the understanding of VAWT aerodynamics.

The object of investigation is the so called H-rotor, consisting of two straight NACA-4418 airfoils which are connected with the shaft at both ends, as shown in Figure 1a. From Figure 1b it is obvious that during one rotor revolution, the relative velocity at the airfoil W as well as the angle of attack α is changing significantly. The blades are then operated in a stalled condition most of the time.

For the design and analysis of Darrieus wind turbines, the Double Multiple Stream Tube (DMST) model was found to be very efficient [3]. The DMST model instantly delivers global parameters of the turbine, such as the power coefficient of the turbine and blade loads, all depending on geometrical details of the configuration or operating conditions. It is based on simplified one-dimensional aerodynamic consideration and with the model from Gormont [1] includes the dynamic stall effects. Although validated for the Darrieus wind turbine, the DMST model with the Gormont model does not give
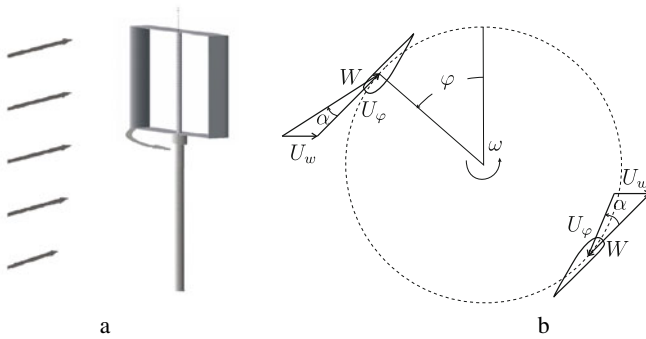
Fig. 1. Sketch of the turbine (a) and horizontal cross-section of the rotor with velocity triangles at the airfoils (b)

satisfying results for the existing H-Rotor design. The reason for that is the fact that the implemented dynamic stall model is based on empirical observations which are valid only for a certain class of airfoils, i.e. slender, symmetric profiles. The presented results are a step towards the development of models to include dynamic stall effects of particular airfoil types as well as the effect of finite airfoil span and the rotor traverse parts into the DMST model.

2   Aerodynamic Model

The basic principle of the DMST model is explained in following. A more detailed description may be found e.g. in [2]. The rotor swept area is divided into a series of adjacent stream-tubes. The loading on a blade element passing the stream-tube depends on the local relative velocity, which is the resultant of the local wind speed $U_{u,d}$ and the rotational motion ωR. But $U_{u,d}$ depends on how much the turbine has retarded the ambient wind, which in turn is a function of the blade load. To break this circular cycle of dependence, the DMST model uses a combination of actuator disc and blade element theories. As depicted in Figure 2, each stream tube intersects the airfoil path twice; once on the upwind pass, and again on the downwind pass. At these intersections we imagine the turbine replaced by a tandem pair of actuator discs, upon which the flow may exert force. The DMST model simultaneously solves two equations for the stream-wise force at the actuator disk; one obtained by conservation of momentum and other based on the aerodynamic coefficients of the airfoil (lift and drag) and the local wind velocity. These equations are solved twice; for the upwind and for the downwind part of the rotor.

The uncertainties of the model are due to the aerodynamic coefficients which are typically available only for a small range of static change of angle of attack. The empirical model of Gormont [1], implemented in the DMST model found to be successful in the analysis of Darrieus wind turbines. In the present model, static aerodynamic coefficients for the NACA-4418 available in [4] are used. These coefficients are experimentally obtained for the Reynolds number $Re = 850000$ and the range of the angle of attack $\alpha = \pm 90°$.
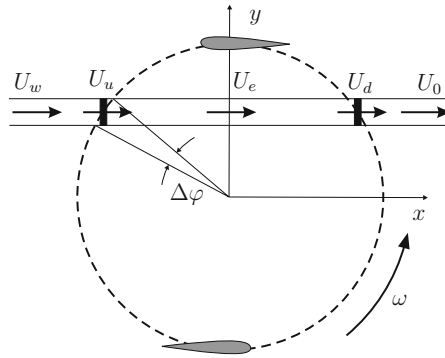
Fig. 2. Plane view of the rotor. A stream-tube, together with the actuator discs and appropriate velocity vectors are depicted

3   Computational Model

In the CFD analysis of unsteady rotor dynamics two different software packages are used: the commercial package ANSYS-CFX and the TAU code developed at the German Aerospace Center - DLR [5]. Both codes numerically solve Reynolds Averaged Navier-Stokes (RANS) equations. Various turbulence models are available in both packages. In this work, the $k-\omega$ SST turbulence model in association with the ANSYS-CFX simulation cases and the Spalart-Almaras turbulence model in association with the TAU simulation cases are used.

4   Results

One of the parameters which characterize VAWTs is the Tip Speed Ratio (TSR) which represents the ratio of the airfoil tip speed U_φ and the undisturbed wind velocity U_w

$$\lambda = \frac{U_\varphi}{U_w}. \tag{1}$$

For the rotor geometry and wind velocity given in the Table 1, results presented in the following subsections are referenced to λ.

Table 1. Parameters of the rotor and free stream conditions

airfoil	cord c [m]	span H [m]	rotor radius R [m]	wind velocity U_w $\left[\frac{m}{s}\right]$
NACA 4418	0.5	2.2	1.73	10
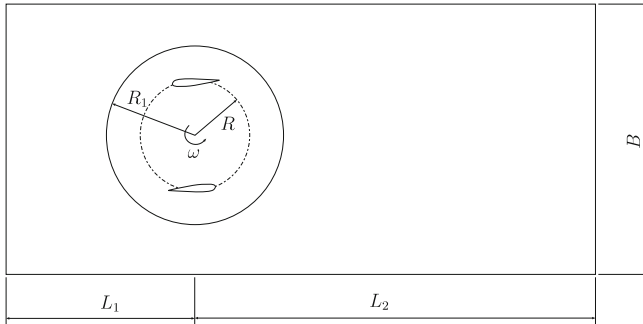
Fig. 3. Sketch of the ANSYS-CFX computational domain. $R_1 = 2R$, $L_1 = 15R$, $B = 2L_1$, $L_2 = 50R$

4.1 Two Dimensional Rotor Approximation

The appropriate two dimensional (2D) CFD model is sketched in Figure 3. The solution domain consist of two sub-domains: the inner rotating part and the outer stationary part. The numerical schemes solve the three dimensional RANS equations. Thus, symmetry boundary conditions are imposed at the top and bottom face of the computational domain consisting of one layer of prismatic and hexagonal cells. At the left face, a constant velocity inflow is imposed and at the right side outflow boundary conditions are imposed. At the airfoil, appropriate boundary conditions depending on the turbulence model with scalable wall functions are imposed.

The efficiency of the turbine is expressed by the power coefficient

$$C_P = \frac{P}{\frac{1}{2}\rho U_w^3 A} \tag{2}$$

where P is the average power of the turbine, ρ is density of the undisturbed wind and A is the vertical cross-section area of the rotor. Figure 4 shows a comparison of the DMST model and the CFD predictions. A quite good agreement of C_P is observed for $\lambda < 2$ (Figure 4a). Large deviations for larger values of λ may be explained with the dynamic stall effect which is not included in the present model. This is obvious from Figure 4b where the normalized moment of the single airfoil is compared. For the rotor position in the vicinity of $\varphi = 0°$, CFD predicts significantly higher negative moment. This may be not explained with the inappropriate aerodynamic coefficients. The angle of attack is significantly below the static stall angle where the sensitivity of the aerodynamic coefficients with respect to the Reynolds number is quiet low. The only explanation may be found in the dynamical change of the angle of attack and the dependence of the aerodynamic coefficients on it.

The above presented results clearly shows that the dynamic change of the angle of attack must be included in the DMST model. This effect is investigated using the CFD simulations presented in the following subsection.
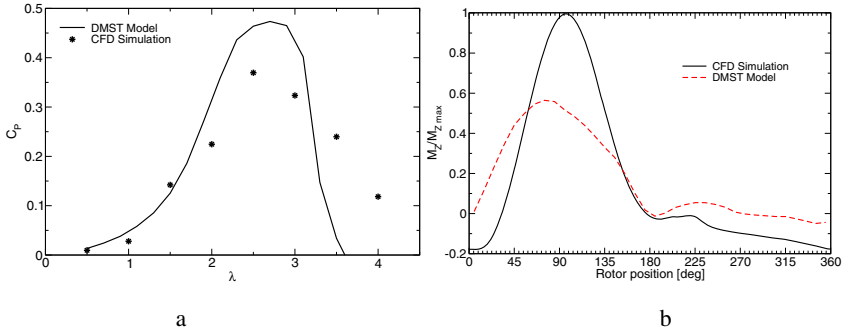
Fig. 4. The power coefficient of the rotor (a) and normalized moment of the single airfoil with respect to the rotor position (b)
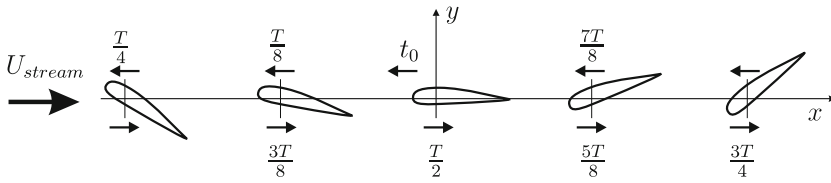
Fig. 5. The airfoil motion in the stream field.

4.2 Moving and Oscillating Airfoil

As explained previously, the profile in Darrieus motion is subjected to a strongly varying angle of attack and velocity magnitude (see Figure 1b). In order to investigate the aerodynamic forces at a single airfoil, this motion is decomposed in an approximate way as a combination of rotational and linear oscillation. Neglecting the retardation of the flow due to momentum change at the airfoil, the variation of angle of attack is approximated as

$$\alpha_0 = \alpha_{max}\sin(\omega \cdot t), \tag{3}$$

where α_{max} is the maximal angle of attack (pitching amplitude), $\omega = \lambda U_w/R$ is the angular velocity of the rotor and t is time. Similarly, the effective wind velocity at the airfoil W may be approximated with as

$$W_0 = U_w \left(\lambda + \cos\left(\omega \cdot t\right)\right). \tag{4}$$

Equations 3 and 4 may be described with the model depicted with Figure 5. In the stream field $U_{stream} = \lambda U_w$, the airfoil moves periodically with the period $T = 2\pi/\omega$. The airfoil velocity in x direction and the angular velocity around the quarter cord point are respectively:

$$U_x = U_w\cos\left(\omega \cdot t + \pi\right), \tag{5}$$
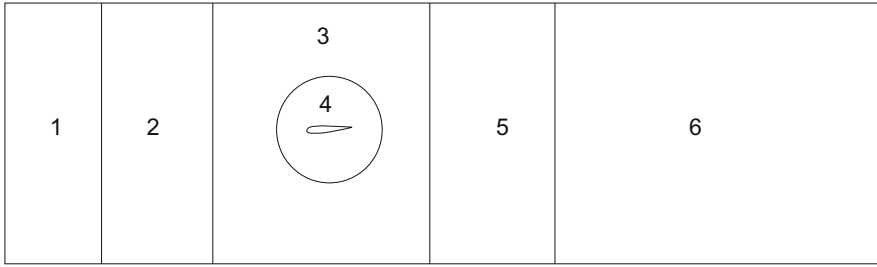
Fig. 6. Solution domain for moving airfoil

a

b
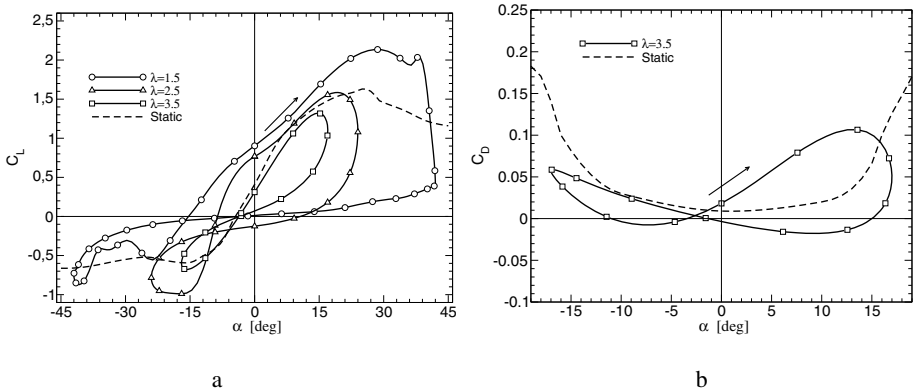
Fig. 7. C_L for various λ (a) and C_D for $\lambda = 3.5$ (b). $\alpha_{max}(\lambda = 3.5) = 42°$, $\alpha_{max}(\lambda = 2.5) = 22°$ and $\alpha_{max}(\lambda = 1.5) = 17°$

and

$$\omega_0 = \alpha_{max} \cos(\omega \cdot t + \pi)\,\omega. \tag{6}$$

The above described motion is modeled using the mesh deformation technique available in ANSYS-CFX. As shown in Figure 6, the solution domain is divided in 6 sub-domains. The mesh in sub-domain 4 rotates with the angular velocity ω_0 and moves (together with the mesh in sub-domain 3) with the velocity U_x. Sub-domains 1 and 6 are defined as stationary and the displacement of sub-domain 4 is compensated with the mesh deformation in sub-domains 2 and 5. The velocity U_{stream} is prescribed at the inlet boundary and other boundaries are defined as in subsection 4.1. The aerodynamic coefficients are defined in term of the relative wind velocity at the airfoil $U = U_{stream} - U_x$. The angle of attack α defined at the rotor is the reversed angle of attack defined in Equation 3.

The predicted aerodynamic coefficients are shown in Figure 7. For various λ and α_{max}, the lift coefficient is plotted together with the lift coefficient of a stationary profile in Figure 7a. The predicted lift coefficients are strongly dependent on the pitching amplitude. As expected, at large angle of attack beyond static stall angle stall delays. The dynamic stall with the hysteresis effect is obvious in all cases. The deviation of lift in the upstroke motion as compared to the static values is not clear and needs to be
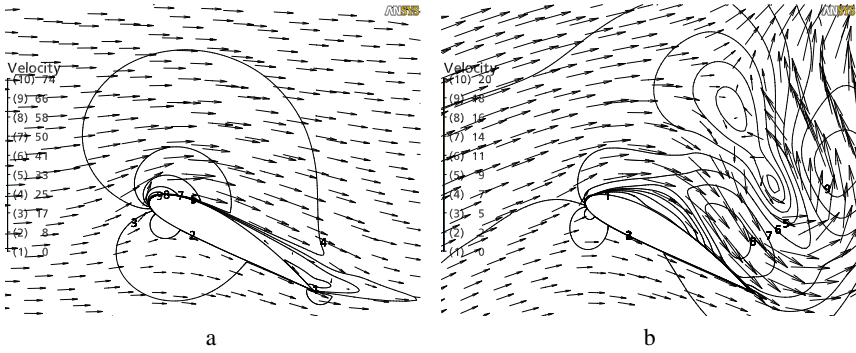
Fig. 8. Velocity [m/s] (relative to airfoil), isolines and vectors for $\lambda = 1.5$ and $\alpha = 28.5°$. a: $t < \frac{T}{4}$, b: $t > \frac{T}{4}$
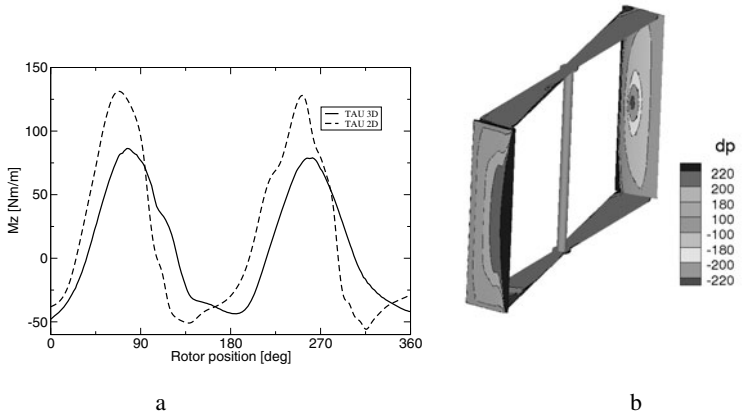
Fig. 9. Moment of the rotor per airfoil unit length (a) and pressure difference dp [Pa] at the solid surfaces for $\lambda = 2.5$ (b)

investigated. Figure 7 shows the predicted drag coefficient for $\lambda = 3.5$. It is observed, that during the hysteresis loop negative drag - the thrust appears.

The predicted dynamic stall is depicted in Figure 8. When the airfoil moves increasing α towards α_{max}, flow separation appears on the trailing edge of the airfoil (Figure 8b) and grows. Moving back decreasing α towards α_{min}, the separation stays in the vicinity of airfoil resulting in a rapid loss of the lift.

4.3   Three Dimensional Rotor Simulations

The results presented in subsection 4.1 are obtained for a simplified 2D rotor configuration. In order to quantify the influence of the rotor shaft and the traverse, full three dimensional (3D) simulations are required. For $\lambda = 2.5$ the 3D rotor is simulated using the TAU code. Exploiting the symmetry of the rotor with respect to the horizontal

plane, the 3D simulation model is discretized with 14.5 million hexagonal cells. The one layer of cells at the symmetry plane is used as an equivalent 2D TAU simulation model. The 3D rotor simulation causes an enormous computational effort. The simulation of one revolution using 96 CPU cores in parallel requires about 40 hours. The results presented in this subsection are predicted during the second revolution period while the flow is not yet fully developed.

Figure 9 shows the comparison of 2D and 3D model results. The moment of the rotor is presented in Figure 9a where the difference in the peak moment is remarkable. This is mainly due to the influence of the finite span and the drag of the traverse. Pressure difference contours presented in Figure 9b illustrate the influence of the finite span. The non-continuous distribution in spanwise direction results in decreased moment as compared to the 2D simulation. A further analysis of the 3D simulations allows to quantify the contribution of the traverse with respect to the overall drag moment. For the present configuration, 15% of the drag is due to this traverse.

5   Conclusions

In the present work the incompressible, time dependent and turbulent flow past a vertical axis wind turbine (VAWT) was simulated in two and three dimensions as well as the oscillating motion of the single NACA-4418 airfoil. These results serve to validate and improve the DMST parameter model suitable for the particular H-rotor type. The presented results help to quantify rotor aerodynamics and to contribute to the improvement of design tools.

Acknowledgments

References

[1] Gormont, R.: An Analytical Model of Unsteady Aerodynamics and Radial Flow for Application to Helicopter Rotors. Technical Report 72-67, U.S. Army Air Mobility Research and Development Laboratory (1973)

[2] Homicz, G.F.: Numerical Simulation of VAWT. Stochastic Aerodynamic Loads Produced by Atmospheric Turbulence: VAWT-SAL Code. Technical Report SAND91-1124, Sandia Laboratory (1991)

[3] Paraschivouiu, I.: Wind Turbine Design With Emphasis on Darrieus Concept. Polytechnic International Press, New York (2002)

[4] Paulsen, U.: Aerodynamics of a Full-Scale, Non Rotating Wind Turbine Blade Under Natural Wind Conditions. Technical Report Risø-M-2768, Risø National Laboratory, Denmark (1989)

[5] Schwamborn, D., Gerhold, T., Heinrich, R.: The DLR TAU-Code: Recent Applications in Research and Industry. In: Wesseling, P., Oñate, E., Périaaux, J. (eds.) European Conference on Computational Fluid Dynamics, ECCOMAS CFD 2006, TU Delft, The Netherlands (2006)

Numerical Analysis of the Influence of Tip Clearance Width in a Semi Open Centrifugal Compressor

Andreas Lucius and Gunther Brenner

Clausthal University of Technology,
Adolph-Roemer Str. 2A
38678 Clausthal-Zellerfeld, Germany
andreas.lucius@tu-clausthal.de,
gunther.brenner@tu-clausthal.de
http://www.itm.tu-clausthal.de

Summary

In the present investigation the influence of tip clearance height in a centrifugal compressor was analysed using CFD. The tip clearance was varied from 1 to 4 percent of the mean blade height. All results were compared to the theoretical case without clearance. It is shown, that the efficiency continuously increases with decreasing clearance height. An optimal value for clearance was not found although the clearance was very small. The increase in shaft power is calculated using dimensional analysis. Another observation is, that a local mass flow distribution of the leakage flow exists, which may be used for further improvement of performance.

1 Introduction

Centrifugal compressors are found in a wide range of applications. They are used for example in the process industry or as turbochargers. Depending on the special requirements two different types of compressors exist: The rotor may be shrouded or unshrouded at the blade tip. Centrifugal compressors with high rotational speed are ususally designed as unshrouded impellers due to high stresses in the shroud. These machines have a small gap between the blade tip and the stationary casing. The difference in static pressure between pressure side and suction side of the blade enforces a leakage flow, which interacts with the main flow in the channel. It is well known that efficiency decreases due the leakage flow [1]. For this reason tip clearance effects have been studied by several researchers e.g. [2], [9]. Harada [5] compares the performance of shrouded and unshrouded impellers. A review is found in [10]. In more recent investigations CFD is used to study the flow field, as for example in [3]. Van Zante et al. [12] have studied the influence of different approaches to include tip clearance effects in a CFD model. They give recommendations on grid size for sufficient resolution of tip clearance flows in axial compressors.

The aim of the present study is to determine the decrease of efficiency in a centrifugal compressor due to tip clearance. The usage of CFD as a tool for analysis is helpful, since the theoretical case of zero clearance can be modeled. This is impossible in experimental investigations. For axial machines optimum values of tip clearance are reported [1] and there are hints that this might also be the case for centrifugal machines [8], [4]. In addition to that, dimensional analysis will be used to determine the additional shaft power for different values of tip clearance.

2   Tip Clearance Flows

In this section a short overview of origin and effect of the tip clearance flow will be given. For a more detailed description we refer to the literature [1], [7]. There are three main factors influencing the mass flow over the blade tip. These are: Blade loading, clearance height, and the relative movement between rotor blades and stationary casing. Usually the effect of the leakage flow is separated into two parts. The major effect is, that in addition to the mass flow from inlet to outlet, the leakage flow must be transported. This effect increases the shaft power. The second effect is, that the interaction of the leakage flow with the main flow causes entropy generation and decreases efficiency. This loss is mainly a mixing loss in shear layers. In hydraulic machines it is a common practice to distinguish between overall machine efficiency and hydraulic efficiency of the blading [8]. For this purpose the power to transport the leakage flow is subtracted from the total power input. When flowing over the blade tip, the leakage flow usually separates at the suction side of the blade tip. The flow contracts to a jet, which at least partially mixes out over the blade tip. A contraction coefficient can be definded to determine the pressure recovery. The contraction coefficient is mainly determined by the ratio of blade thickness and clearance height. There have already been attempts to influence the contraction coefficient with different blade tip configurations [6]. In unshrouded impellers the relative movement of the wall causes an additional mass flow through the gap.

3   Dimensional Analysis in Turbomachines

As we will make use of dimensional analysis to determine the additional input shaft power, this section is used to introduce to some non dimensional numbers used in turbomachinery. The characteristic curve of a compressor usually displays pressure (or energy) rise over flow rate. This curve depends on the rotational speed. Dimensional analysis allows to derive only one characteristic curve independent from the rotational speed. The pressure coefficient $\Psi_{s,tot}$ is defined according to equation 1, where Δh is the enthalpy rise. The index s,tot indicates total isentropic thermodynamic state, u_2 is the circumferential velocity at outlet diameter d_2.

$$\Psi_{s,tot} = \frac{2\Delta h_{s,tot}}{u_2^2} \tag{1}$$

The flow coefficient is a nondimensional number for the volumetric flowrate in the suction pipe $\dot{V}_0$

$$\varphi = \frac{\dot{V}_0}{\frac{\Pi}{4}d_2^2 u_2} \tag{2}$$

Efficiency is also a non dimensional number, defined as

$$\eta_{s,tot} = \frac{\Delta h_{s,tot}}{\Delta h_{tot}}. \tag{3}$$

Since the power input is also of interest in this investigation, a power coefficient is defined accoring to equation 4. Here P_{shaft} is the mechanical input power and ρ_0 is the density in the suction pipe.

$$\lambda = \frac{P_{shaft}}{\rho_0 \frac{\Pi}{4}d_2^2 u_2 u_2^2} = \lambda = \frac{\Psi_{s,tot}\varphi}{\eta_{s,tot}} \tag{4}$$

With the given relations it is possible to reduce the different speed dependent characteric curves for pressure rise, efficiency and shaft power to single curves $\Psi_{s,tot}(\varphi)$, $\eta_{s,tot}(\varphi)$ and $\lambda(\varphi)$.

4   Numerical Model and Problem Setup

For the present investigation an industrial compressor was analysed using CFD. The compressor is designed for a pressure ratio of 1.2 at a flow rate of 1.1 kg/s. The tip speeds are 183 m/s at leading edge and 375 m/s at trailing edge, the Mach numbers built with tip speed are 0.52 and 0.97 respectively. Performance measurements were conducted by the manufacturer. The results are used to validate the numerical model. For the analysis of the flow field only one blade pitch was simulated, using periodic boundary conditions in the circumferential direction. The computational model contains 3 domains, the inlet, the rotor and a vaneless diffuser. For comparison with experiments a complete $360°$ model with volute was simulated.

The simulations were conducted using the general purpose CFD code ANSYS CFX. The turbulence was modelled using the SST k-ω model. For ω-based turbulence models CFX provides an automatic wall treatment, which allows Y^+ to be in the range of 0 - 200. The model switches from wall functions to a low Reynolds wall formulation for very small values of Y^+, with a smooth transition in the intermediate region. In all computations the steady flow field was calculated. A convergence criterion of 10^{-4} for the maximum residuals could be reached in most of the cases. The used grid is block structured; the influence of grid resolution was analysed using 3 different grids. As displayed in table 1 only a minor change in pressure rise is observed. Since there were remarkable changes in the size of the separated region inside the tip gap, the fine grid of 1.1 million control volumes was chosen for further investigation. In table 1 the leakage flow rate is normalised with the machine flow rate. Due to the small differences in pressure coefficient and efficiency, the coarsest grid was applied for the calculation of the $360°$ setup. A comparison with experimental performance measurements shows good

agreement in the range of the design point (figure 1). At high flow rates the difference in pressure rise increases. This may be due to the neglection of surface roughness in the volute. The built machine has a relative tip clearance of 2.1% based on the mean blade heigth.

Table 1. Grid convergence

number of cells [10^6]	nodes in gap	$\Psi_{s,tot}$	$\eta_{s,tot}$ [%]	$\dot{m}_{gap}$ [%]
0.36	9	1.242	84.94	7.47
0.69	13	1.243	85.07	7.71
1.1	20	1.247	85.26	7.8
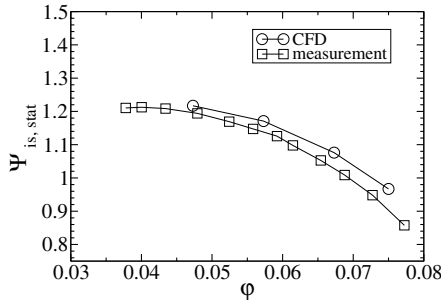
Fig. 1. Comparison of experimental and computational results

5   Results

In this section the influence of tip clearance on efficiency, pressure rise and input power will be analysed. Four different configurations are compared: $\delta = 0$ (theoretical case), 1%, 2.1% and 4.1%. The clearance height s is normalised with the average of blade height at inlet and outlet b_1 and b_2.

$$\delta = \frac{2s}{(b_1 + b_2)} \tag{5}$$

The key parameter in turbomachinery is efficiency. It is generally expected that efficiency is eroded with increasing tip clearance. There is a numerical study [4], which shows an optimum value of efficiency for $\delta > 0$ for a large low speed centrifugal compressor. The maximum efficiency was reported at 0.9 % of exit blade height. The case δ 1% in the present investigation corresponds to 3.2% relative tip clearance based on the exit blade height. The rotor in the present investigation is a small high speed compressor, which makes it impossible to reach such low clearances in practice.
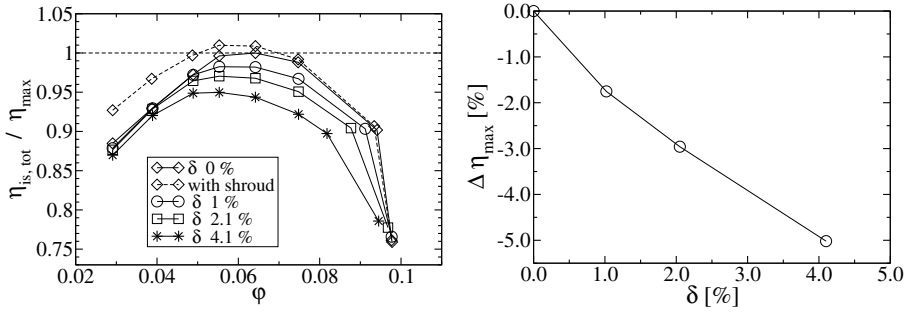
Fig. 2. Influence of δ on efficiency map and maximum efficiency

In figure 2 the change of efficiency due to tip clearance is shown. All values are normalised with the maximum efficiency for $\delta = 0$. It is remarkable, that the influence is rather small at low loads and quite high at design point and high flow rates. The influence of tip clearance is also to shift maximum efficiency to smaller flowrates. Although the clearance was made very small (ca. 0.3 mm) for δ 1% a continuous decrease in efficiency is observed. Maximum efficiency is found at zero clearance. In order to analyse the influence of shroud wall movement another configuration was modelled with rotating wall. This configuration corresponds to a shrouded rotor with zero clearance between shroud and casing. The shrouded impeller shows by far best perfomance at low flow rates and is still about 1% better at design conditions.

5.1   Influence of Tip Clearance on Pressure Rise

The computed characteristic curves show a strong degradation of the pressure coefficient for larger tip clearance (figure 3). The difference is smaller at low flow rates and increases up to 20% at high flow rates. The curve for the shrouded rotor is quite close to the curve for the unshrouded rotor with zero clearance. The pressure rise with shroud is slightly inferior at high flow rates and superior at part load.
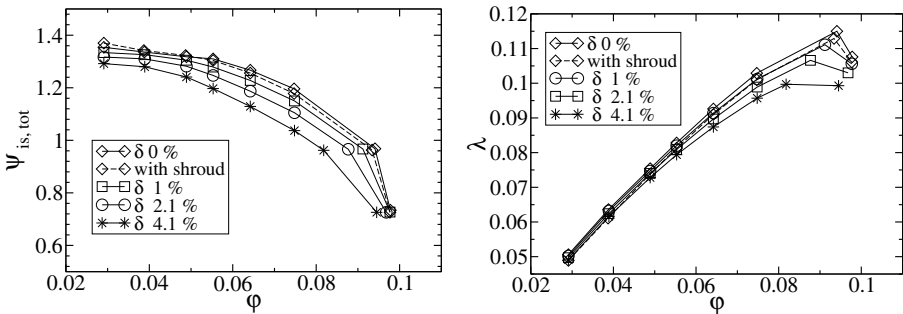
Fig. 3. Computational results for pressure coefficient (left) and power coefficient (right)

Table 2. Additional power input and change in rotational speed depending on tip clearance

$\delta[\%]$	ΔP [%]	Δn [%]
1	1.2	1.04
2.1	2.5	2.15
4.1	4.6	3.94

5.2   Influence of Tip Clearance on Shaft Power

As already mentioned in section 2 the input power at the shaft is expected to increase if δ grows. This is not obvious from the computed power coefficient displayed in figure 3. The diagram suggests, that input power decreases with growing tip clearance. For a correct interpretation of the data it should be noted, that the energy transferred to the fluid depends on δ (figure 3). Considering the same flow rate, the pressure rise is lower at bigger clearances. In order to compare the power input with the ideal rotor with $\delta = 0$, pressure rise and flow rate must be the same. To match the same operational condition the rotational speed has to be increased for configurations with tip clearance. Combining equations 2 and 3 a relation $u = f(\dot{V}_0, \Delta h_{s,tot})$ can be derived for each value of δ via curve fit. With the given rotational speed u^* the corresponding operational point $\Psi_{s,tot}^*$, φ^*, λ^* and finally the shaft power can be determined. As shown in table 2 the additional power input increases up to 4.6% for the biggest clearance.

5.3   Flow Inside the Tip Clearance

In this section the development of the flow between blade tip and shroud is analysed in more detail. As already mentioned in section 2 separation appears at the pressure side of the blade tip. Whether the flow mixes out or not in the gap depends on the blade thickness. In the present investigation relative clearance normalised with blade thickness gives the following values : 12.5, 25 and 50%. For small clearance only a small separated area appears, the contracted jet mixes out completely after a short distance. For the largest clearance the separation appears over ca. 50 % blade thickness. Figure 4 displays the separation inside the tip clearance near the trailing edge at design point.

Since the leakage flow strongly influences the primary flow field, it is of special interest to know the amount of flow passing through the tip clearance and its local distribution. The evaluation of the mass flow showed, that up to 20% of the machine mass flow passes the clearance of the main blades. Since the load is higher at low flow rates leakage flowrate is high at part load. Splitter blades are shorter, which causes the leakage flow rate over the splitter blade tip to be smaller. As expected, the local distribution shows high values near the trailing edge (figure 5), since the pressure rises approaching the outlet. Another peak is observed at the leading edge, where large deceleration of the relative flow appears. This matches with the observations of Sitaram [10], who pointed out that a narrow clearance at the leading edge is advantageous. Thus it appears that the clearance height needs to be small near the leading edge and trailing edge. It can be advantageous to have a profile of the clearance, and not a constant clearance as in our case.
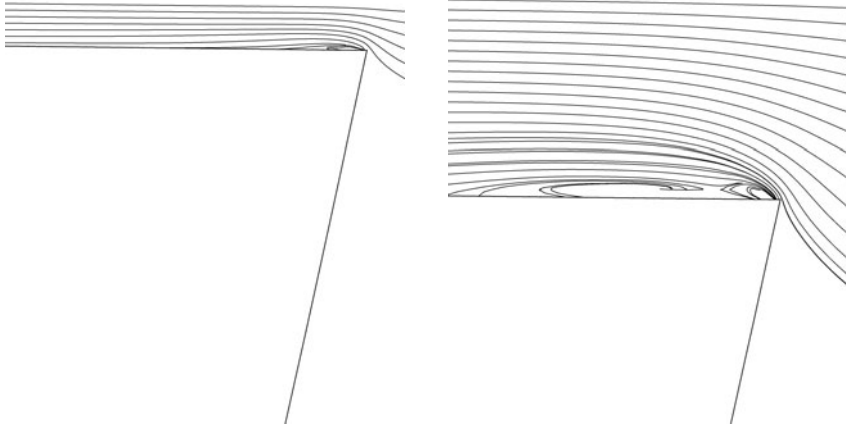
Fig. 4. Streamlines at pressure side of tip clearance, left δ= 1%, right δ= 4.1%
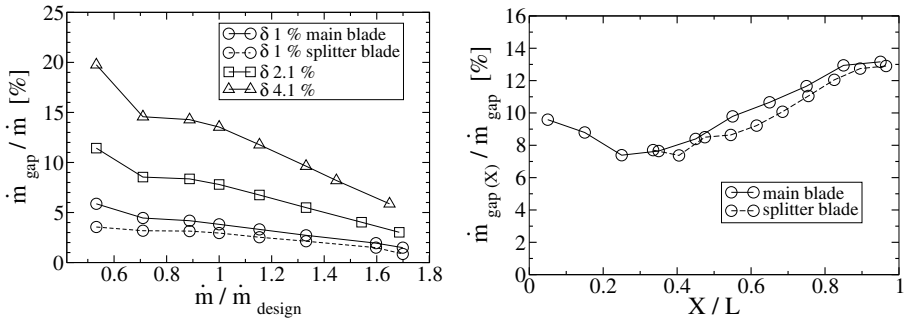
Fig. 5. Mass flow through the tip clearance and its local distribution at δ 1%, design point

6   Conclusions

In the present study the influence of tip clearance on the performance of a centrifugal compressor was analysed using CFD. The results show a continuously decreasing efficiency. An optimum clearance considering maximum efficiency was not observed, although the clearance was made very small. With the help of dimensional analysis the additional power input was calculated.

Another important result is, that the leakage flow rate is not constant over the blade length, but showing peaks at leading edge and trailing edge of the blading. With this knowledge and considering the local deformation (structural Finite Element analysis) it may be possible to derive a profile of the clearance height, which minimises leakage flow. In addition to that a change of geometry at the blade tip could help for further improvement. This is the objective in a further investigation.

Acknowledgements

References

[1] Denton, J.D.: Loss Mechanisms in Turbomachines. Journal of Turbomachinery 115, 621–656 (1993)

[2] Engeda, A.: Correlation and prediction of efficiency of centrifugal pumps due to tip clearance effects. Proceedings of the Institution of Mechanical Engineers Part A 209, 111–114 (1995)

[3] Engin, T.: Study of tip clearance effects in centrifugal fans with unshrouded impellers using computational fluid dynamics. Proceedings of the Institution of Mechanical Engineers Part A 220, 599–610 (2006)

[4] Gao, L.-M., Xi, G., Wang, S.-J.: Influence of Tip Clearance on the Flow Field and Aerodynamic Performance of the Centrifugal Impeller. Chinese Journal of Aeronautics 15(3) (2002)

[5] Harada, H.: Performance Characteristics of Shrouded and Unshrouded Impellers of a Centrifugal Compressor. Journal of Engineering for Gas Turbines and Power 107, 528–533 (1985)

[6] Ishida, M., Ueki, H., Senoo, Y.: Effect of Blade Tip Configuration on Tip Clearance Loss of a Centrifugal Compressor. Journal of Turbomachinery 80, 14–18 (1989)

[7] Lakshminarayana, B.: Fluid Dynamics and Heat Transfer of Turbomachinery. John Wiley and sons Inc., Chichester (1996)

[8] Pfleiderer, C., Petermann, H.: Strömungsmaschinen, Auflage, vol. 4. Springer, Heidelberg (1972)

[9] Senoo, Y., Ishida, M.: Pressure Loss Due to the Tip Clearance of Impeller Blades in Centrifugal and Axial Blowers. Journal of Engineering for Gas Turbines and Power 108, 32–37 (1986)

[10] Sitaram, N.: Review: Recent Investigations on Tip Clearance Flows in Centrifugal Compressors. International journal of turbo and jet engines 17, 65–78 (2000)

[11] Traupel, W.: Thermische Turbomaschinen, Auflage, vol. 3. Springer, Heidelberg (1977)

[12] Van Zante, D.E., Strazisar, A.J., Wood, J.R., Hathaway, M.D., Okiishi, T.H.: Recommendations for Achieving Accurate Numerical Simulation of Tip Clearance Flows in Transsonic Compressor Rotors. Journal of Turbomachinery 122, 733–742 (2000)

Aerodynamic Analysis of a Helicopter Fuselage

Florian Vogel, Christian Breitsamter, and Nikolaus A. Adams

Technische Universität München, Lehrstuhl für Aerodynamik, Boltzmannstr. 15, D-85748
Garching, Germany

Summary

This paper presents the analysis of the flow around a helicopter fuselage. The
numerical simulations were performed with an implicit, parallel Navier-Stokes solver.
The numerical accuracy of the solver was investigated by doing a grid study. A mesh
optimisation was accomplished to increase the quality of the flow prediction, in
particular, the flow topology in the fuselage wake. The results of the numerical
simulations were compared with experimental data. To achieve a good mapping of the
vortex structures in the wake, a well resolved mesh in this area in combination with a
hybrid turbulence model is needed. Based on numerical and experimental results the
vortex structure behind the helicopter fuselage is analyzed.

1 Introduction

The flow around a helicopter fuselage has very complex characteristics. Several
regions of flow separation around the body are responsible for that. These separations
build a wake with different coherent vortical structures and a strong unsteady
behaviour.

Depending on the flow incidence, the fuselage wake can impinge on components
of the helicopter tail, like the tailboom, the empennage or the tail rotor. This
interaction of the wake with these components can have different effects. One of them
is the reduction of the aerodynamic efficiency of the empennage, which is responsible
for lateral aerodynamic stability of the helicopter in forward flight. Another effect of
the wake-tail interaction could be the appearance of flow induced structural dynamic
loads, caused by the highly unsteady wake.

Former studies were focusing on the prediction of aerodynamic forces, mostly the
drag, [3]. Therefore grid studies were made to increase the prediction quality of the
aerodynamic forces. The influence of the Reynolds number on the flow around a
helicopter fuselage was accomplished, [2]. The effect of the angle of attack and
sideslip on the fuselage flow was investigated and also the influence of the strut for
model mounting, [4]. Different turbulence models were used and compared with
experimental results of wind-tunnel tests, [1].

The aim of this work is to get more information of the flow behaviour around the
fuselage, in particular in the tail section. The investigations are concentrated on the
flow separation and the wake which occurs in the lower part of the fuselage tail. One

interest is the improvement of the numerical model, like mesh optimization and turbulence modelling, to get a better prediction of flow in this specific area. But also the consequence of that improvement on the prediction quality of the aerodynamic loads is investigated.

For this study, several steady state, fully turbulent calculations with different mesh densities have been performed. Unsteady simulations with a hybrid type turbulence model and a RANS model were used for an optimized mesh. For validating the numerical results, a wind-tunnel campaign was conducted including force-, pressure- and velocity-measurements.

2   Numerical Setup

The geometry used for this study is a fuselage-tailboom configuration of a light weight transport helicopter (**Figure 1**). The fuselage has a symmetric shape with respect to the XZ-plane. The lower side of the fuselage tail has a strongly curved shape, to realise a large cargo volume in the helicopter interior. The tailboom consists of the empennage and the tail rotor mount. The asymmetry of the empennage and the tail rotor mount with respect to the XZ-plane is responsible for a yawing moment in cruise.
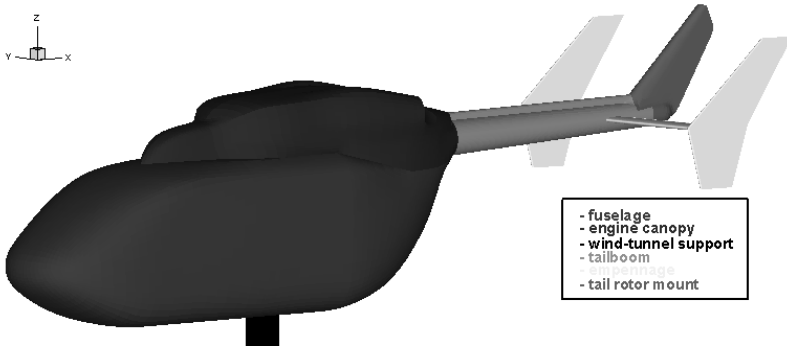
Fig. 1. Model setup

The computational domain is of spherical shape, with a diameter of eleven times the fuselage length. The strut of the helicopter is modelled as well. The free stream velocity at the domain boundary was set to 40 m/s which corresponds to a Mach number of 0.116 and a Reynolds number of $0.678 \cdot 10^6$. The Reynolds number was built with the square root of the projection area of the fuselage as reference length l_{ref}=0.262m.

Structured meshes were created with IcemCFD Hexa [10]. The generation of the mesh is based on a block structured method, but it is treated as unstructured within the code (**Figure 2**). The mesh is built by 643 blocks. The near wall area is resolved by 20 mesh layers and a stretching factor of 1.4, to realise a y^+ -value around the helicopter body of less then y^+=0.5. Additional information for the different meshes can be seen in **Table** 1.

Table 1. Mesh characteristics

Mesh type	Number of nodes	y^+_{max}	Number of near wall layers	average cell length l_c/l_{ref} in wake area
course	3021442	0.51	25	0.035
medium	4992742	0.56	25	0.027
fine	10759436	0.53	25	0.021
optimized	6878589	0.57	33	0.014

local mesh refinement
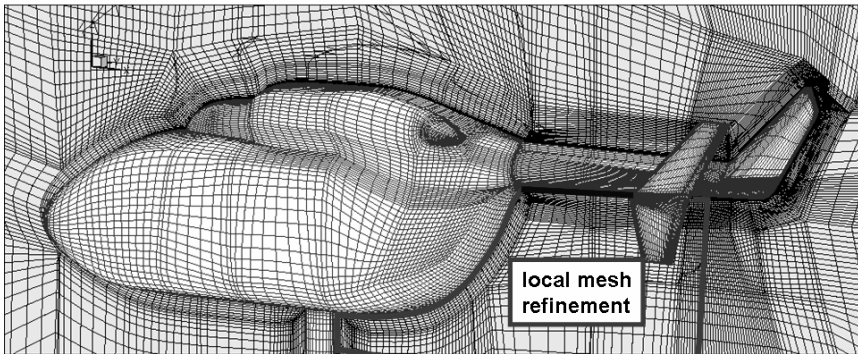
Fig. 2. Surface mesh and XZ-Plane slide of coarse grid, zone of local mesh refinement of optimized grid

The computational model consists of a commercial finite volume Navier-Stokes solver [9]. The code is solving the Navier-Stokes equations with an isothermal energy model. The discretisation in space is based on a high resolution scheme, whereas the accuracy is between first and second order and is controlled by a blend factor [9]. The time discretisation is an implicit Second Order Backward Euler scheme. The turbulence model which was used for steady state calculation is the SST k-ω model developed by Menter, [9]. To investigate the influence of the turbulence model on the flow unsteady calculations with the SST k-ω model and the scale adaptive turbulence model (SST-SAS k-ω model [6]) were made. The time step for this run was defined with $\Delta t_{dimless}=0.01527$ ($\Delta t_{dimless}=(\Delta t \cdot V_\infty)/l_{ref}$), to capture relevant unsteady effects. The unsteady calculation runs for 2500 time steps to get averaged solutions for the aerodynamic loads, pressure and the velocity field. The averaging of the time depending quantities was started after 400 time steps of the unsteady calculation, when the transient oscillation decayed. A steady calculation was used for initialisation.

3   Experimental Setup

To compare the numerical simulations with experimental results a wind-tunnel campaign was conducted. A geometrically identical wind-tunnel model as used for the simulation

model was available for the experiments. The measurements were carried out in two different Göttingen type wind tunnels, with a maximum freestream turbulence intensity of 0.5% regarding axial, lateral and vertical test section velocity components. The measurement of the aerodynamic forces and moments acting on the fuselage was done by an internal six-component strain gauge balance. The experiments were conducted at a free stream velocity of $V_\infty = 40$ m/s (Re = $0.678 \cdot 10^6$) and the measured signals were averaged over t=33s. Surface streamlines were photographed on the model at a free stream velocity equal to the force measurements. Therefore a mixture of oil, gasoline and colour pigments was sprayed on the model. The velocity field was measured by hot-wire anemometry. The four wire probe is moved by a 3-axes traversing system in the wake of the helicopter fuselage. The acquisition was averaged over 6.4 s and the free stream velocity was $V_\infty = 25$ m/s which corresponds to a Reynolds number of $0.424 \cdot 10^6$.

4   Results

4.1   Grid Study

A grid study was performed to get more information about the influence of the mesh resolution on the prediction quality of the code concerning the aerodynamic forces and the flow topology downstream of the fuselage. The three different mesh sizes are based on the same block topology and the refinement for the three cases was globally accomplished. The course mesh case consists of 3 million nodes, the medium mesh of 5 million and the fine mesh consists of 10 million nodes. For the comparison steady state simulations were used. Regarding the SST k-ω turbulence model, the comparison of the aerodynamic forces and moments predicted by the three different cases (**Figure 3/Figure 4**) shows an improving trend for the pitching-moment by refining the mesh. All other components seem not to be influenced by the global mesh refinement.
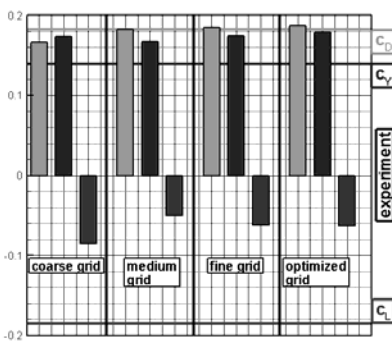
Fig. 3. Grid study – drag coefficient c_D, sideforce coefficient c_Y, lift coefficient c_L (steady state)
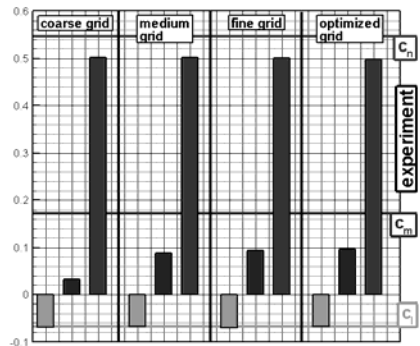
Fig. 4. Grid study – rolling moment coefficient c_l, pitching moment coefficient c_m, yawing moment coefficient c_n (steady state)

Including the SAS-SST turbulence model, the mesh was modified to concentrate the node-density in the separation zone and the direct connected wake area behind the fuselage tail, expecting a further improvement of the results. The maximum length of the cell edge to resolve the required vortex scales was $0.014 \cdot l_{ref}$ in the wake, according to the resolution of the velocity measurement technique. For the SST-SAS-simulation, a clear improvement of the lift was achieved (**Figure 5, Figure 6**). But there are still discrepancies in the pitching moment and side force. To identify the prediction problems for that, an analysis of the forces and moments acting on the different components of the helicopter model has been made. The negative pitching moment acting on the fuselage is highly over predicted by the simulation with the SST-SAS k-ω model in combination with the optimized mesh and the counter acting moment of the empennage under predicted (**Figure 8**). The analysis of the side force shows that the contribution of the empennage is too high in the simulation (**Figure 7**).
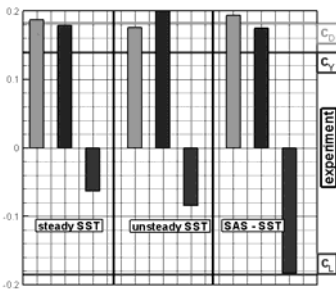
Fig. 5. Turbulence model study – drag coefficient c_D, sideforce coefficient c_Y, lift coefficient c_L
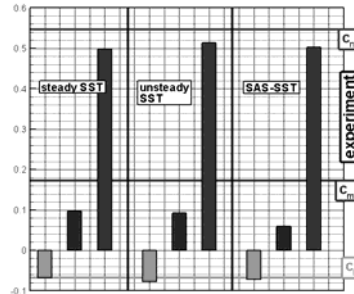
Fig. 6. Turbulence model study – rolling moment coefficient c_l, pitching moment coefficient c_m, yawing moment coefficient c_n
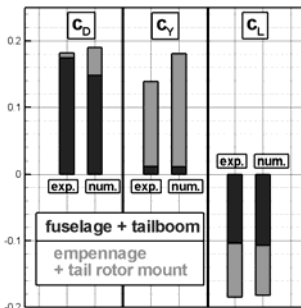
Fig. 7. Aerodynamic forces – drag coefficient c_D, sideforce coefficient c_Y, lift coefficient c_L (SAS-SST-turb.-model, opt. mesh)
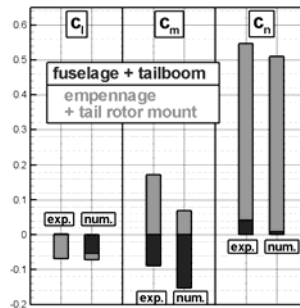
Fig. 8. Aerodynamic moments – rolling moment coefficient c_l, pitching moment coefficient c_m, yawing moment coefficient c_n (SAS-SST-turb.-model, opt. mesh)

The pressure distribution at the lower side of the fuselage (**Figure 9**) explains the under prediction of negative lift by the three steady simulations when using a too coarse mesh in the wake area. The suction peak directly behind the strut is not covered by the three steady simulations and leads to a higher pressure level in this area and so to lower down force.
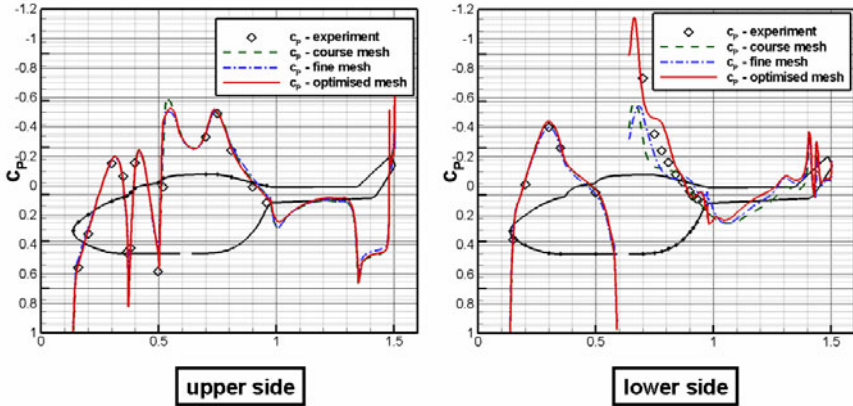
Fig. 9. Surface pressure distribution

4.2 Flow Topology

Based on the previous numerical results and the measured velocity fields and flow visualisations a first estimation of the flow topology in the fuselage wake can be made.

The strongly curved fuselage tail leads to flow separation in this area. Looking at the surface streamlines (**Figure 10**) the origin of a strong vortex pair under the connection
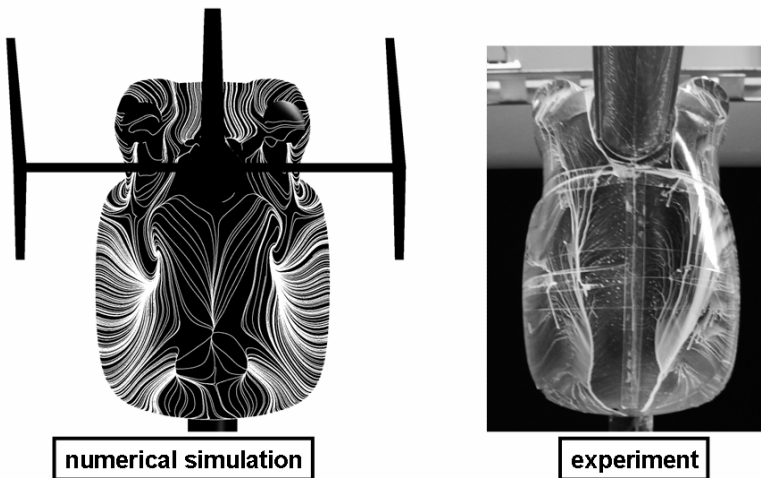
Fig. 10. Surface streamlines
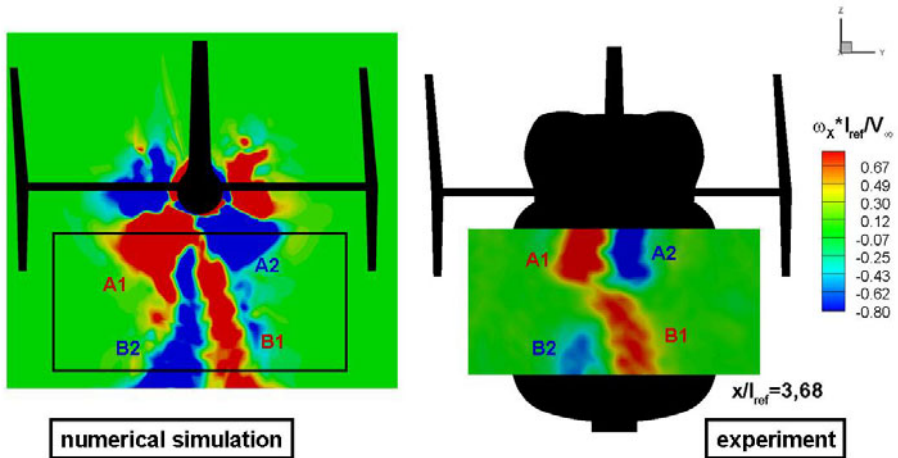
Fig. 11. Axial vorticity distribution

of the tailboom can be seen. The separation of the flow is well predicted by the simulation and can be localized with the numerically determined surface streamlines as well as with the oil-flow visualisation. Two counter rotating vortex pairs can be seen indicated by the vorticity field in the wake of the fuselage (**Figure 11**). Vortex pair A is generated below the connection of the tailboom and the fuselage, where the sidewise separation leads to the rollup of the corresponding shear layer. The origin of the vortex pair B can be localised at a lower area of the tail and it is developed along the curved section of the fuselage tail.

5   Conclusions

The flow around a helicopter fuselage was investigated numerically and validated with wind-tunnel test results.

Good agreement of the aerodynamic loads was achieved by using an optimized grid and a hybrid type turbulence model. The necessity of a well resolved wake area in combination with a DES-turbulence-model for predicting the forces and mainly the flow structure in the fuselage wake is demonstrated.

Based on the numerical and experimental results, the topology of the mean flow around the fuselage including the main vortical structures is identified.

Acknowledgement

References

[1] Le Chuiton, F., D'Alascio, A.: Computation of the Helicopter Fuselage Wake with the SST, SAS, DES and XLES Models. In: Advances in Hybrid RANS-LES Modelling, vol. 97, pp. 117–124 (2008)

[2] Filippone, A., Michelsen, J.A.: Aerodynamic Drag Prediction of Helicopter Fuselage. Journal of Aircraft 38, 326–333 (2001)

[3] Gleize, V., Costes, M.: Helicopter Fuselage Drag Prediction: State of the art in Europe. AIAA, 2001-0999

[4] Filippone, A.: Prediction of aerodynamic forces on a helicopter fuselage. The Aeronautical Journal, 175–184 (March 2007)

[5] Vogel, F., Breitsamter, C., Adams, N.A.: Aerodynamic investigations on a helicopter fuselage with rotor hub. In: 34th European Rotorcraft Forum (2008)

[6] Menter, F.R., Egorov, Y.: A Scale-Adaptive Simulation Model using Two-Equation Models. AIAA, 2005-1095

[7] Kapadia, S., Roy, S.: Detached-Eddy simulation over a reference Ahmed car model. AIAA, 2003-0857

[8] Roy, C.J., DeChant, L.J., Payne, J.L., Blottner, F.G.: Bluff-Body Flow Simulations using Hybrid RANS/LES. AIAA, 2003-3889

[9] ANSYS CFX-Solver Theory Guide, ANSYS CFX Release 11.0

[10] ANSYS ICEM CFD/AI*Environment User Manual

Truck Interference Effects on a Car during an Overtaking Manoeuvre: A Computational Study

B. Basara[1], S. Jakirlić[2,*], F. Aldudak[3], and C. Tropea[2]

[1] AVL List GmbH, Hans List Platz 1, 8020, Graz, Austria
[2, 3] Darmstadt University of Technology, Darmstadt, Germany
[2] Chair of Fluid Mechanics and Aerodynamics, 64287 Petersenstr. 30
[3] Chair of Fluid Dynamics, 64289 Hochschulstr. 1

Abstract

Numerical computations of an overtaking process approximated by fixing a truck model at characteristic stationary positions relative to a car model were performed. The reference database (geometry, operating parameters and surface pressure distribution) are adopted from an experimental investigation carried out in the wind tunnel of the BMW Group in Munich (Schreffl, 2008). Prior to the truck-car interaction during the overtaking manoeuvre the aerodynamics of the isolated car without the truck has been experimentally investigated to establish the reference pressure distribution for subsequent tests. The present computational study focuses on validation of some recently developed turbulence models for unsteady flow computations in conjunction with the universal wall treatment in such complex flow situations. The computational analysis includes both the isolated car and truck configurations in addition to their most critical relative position during the overtaking process corresponding to the largest drag coefficient.

1 Introduction

The evaluation of the aerodynamic properties of a car is traditionally based on the investigations conducted under the conditions of a steady oncoming flow. Large majority of the experimental and computational studies performed in the past relate to the steady flow past a car configuration situated in a wind tunnel. The aerodynamic forces obtained from such investigations served as a sole basis for decision to be made with respect to the aerodynamic properties. Accordingly, the possible time variation of the moments and forces have not been explicitly considered. The influence of their temporal changes on the aerodynamic properties is conventionally regarded to be negligible. The objective of the experimental study conducted by Schreffl (2008), whose results served as reference database for the present computational work, was to check this classical approach to estimate of the aerodynamic performances of a car configuration. The unsteady effects in question

---

* Corresponding author: s.jakirlic@sla.tu-darmstadt.de

originate primarily from the characteristics of the ongoing flow. The relevant configuration corresponds to the flow past a car which is situated in the wake of a truck, a situation encountered frequently during a highway passing manoeuvre. The aerodynamic effects pertaining to such an overtaking manoeuvre are still not completely clarified. To better understand these effects, a car-truck overtaking process has been experimentally investigated in the BMW wind tunnel at a 40% scale, Schreffl (2008).

2   Experimental Setup

As a first step the car has been measured without the truck to gain the reference pressure distribution for subsequent tests. This simplification to a 40% scaled model is acceptable and no significant discrepancies of the pressure field compared to that about the relevant full-scale car configuration are to be expected. The three-dimensional mapping of the surface pressure was realized by 54 surface-mounted pressure tabs; 13 pressure tabs were situated on each car-side; 14 on bonnet, roof and trunk. The resultant forces were measured with the wind tunnel balance. Tests have been performed at a velocity of 140 *km/h*, resulting in a Reynolds-number of 9×10^5. The subsequently investigated overtaking process has been experimentally realized by considering eight discrete (fixed) relative positions between the car and truck model, Fig. 1. By doing so the unsteady overtaking process has been approximated by a quasi-stationary process. The influence of the unsteady wake on the evolution of the drag coefficient with respect to the relative position $x \,/\, L$ of the car to the truck is presented in Fig. 1. The lower drag values correspond to the situation where the entire car is situated in the truck wake characterized by lower flow velocities. The truck exerts a suction effect on the car. After reaching the rear end of the truck (approximately at the position $x \,/\, L = -1$) the drag on the car increases up to its maximum value after the car front passed the front side of the truck at $x \,/\, L = 0.39$. The truck acts with a repulsive force on the car.

3   Computational Method

The main objective of the present study was the validation of the recently proposed computational method denoted as PANS – Partially-Averaged Navier-Stokes, Girimaji (2006). This method represent a hybrid RANS/LES (Large Eddy Simulation) scheme which should capture the unsteady flow features more accurately compared to the conventional URANS (Unsteady Reynolds-Averaged Navier-Stokes) method. The reference URANS calculations were performed with the $\zeta - f$ model, representing a more robust variant of the Durbin's $\overline{v^2} - f$ model. Prior to considering the most critical car-truck arrangement ($x \,/\, L = 0.39$) contributing to the largest drag coefficient ($C_x \approx 0.45$ compared to that of an isolated car $C_x \approx 0.3$, Fig. 1) the flow past a single passenger car configuration was analyzed in the present
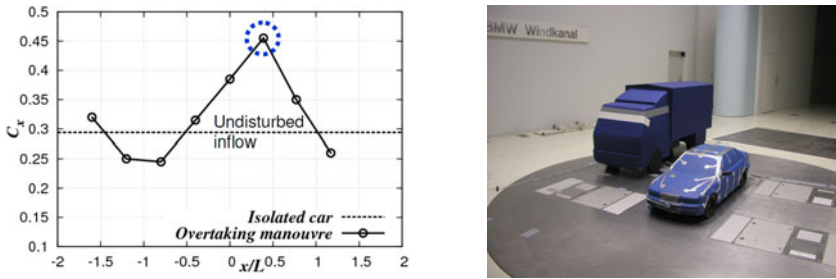
Fig. 1. Evolution of the drag coefficient in terms of the car positioning relative to the truck in the wind tunnel (left) and the most critical relative position ($x/L=0.39$) complying with the largest drag coefficient (right); from Schreffl (2008)

computational study. As a result of simulation detailed mean flow and turbulence fields are obtained and compared with experimental findings, thus enabling the study of forces, i.e. the aerodynamic coefficients (drag and lift coefficients, spatial wall-pressure distribution) on this ground vehicle as well as some unsteady flow phenomena in the car wake.

Both turbulence models applied are based on the eddy-viscosity concept which relies on the Boussinesq's correlation defining the Reynolds stress tensor $\overline{u_i u_j}$ in terms of the mean strain tensor S_{ij}: $-\rho \overline{u_i u_j} = 2\rho \nu_t S_{ij} - 2\rho k \delta_{ij} / 3$. Herewith, the modelling of the Reynolds-stress tensor is reduced to the modelling of the turbulent viscosity ν_t, defined as $\nu_t = 0.22 \zeta k \tau$ in the Hanjalic's et al. (2004) $\zeta - f$ model. Here, τ represents a switch between the turbulent time scale $\tau = k / \varepsilon$ and the Kolmogorov time scale $\tau_K = (\nu / \varepsilon)^{1/2}$. This model relies on the elliptic relaxation (ER) concept providing a continuous modification of the homogeneous pressure-strain process as the wall is approached to satisfy the wall conditions, thus avoiding the need for any wall topography parameter. The variable ζ represents the ratio $\overline{v^2} / k$ ($\overline{v^2}$ is a scalar property in the Durbin's $\overline{v^2} - f$ model, which reduces to the wall-normal stress in the near-wall region) providing more convenient formulation of the equation for ζ and especially of the wall boundary conditions for the elliptic function f. Readers are referred to the original publication for more details about the model.

The second model applied, the so-called Partially-Averaged Navier-Stokes (PANS) approach proposed recently by Girimaji (2006), enables seamlessly a smooth transition from RANS to the direct numerical solution of the Navier-Stokes equations (DNS) as the unresolved-to-total ratios of kinetic energy ($f_k = k_u / k$) and dissipation ($f_\varepsilon = \varepsilon_u / \varepsilon$) are varied. The equations governing the unresolved kinetic

energy k_u and corresponding unresolved dissipation rate ε_u are systematically derived from the $k - \varepsilon$ model:

$$\frac{Dk_u}{Dt} = \left(P_u - \varepsilon_u \right) + \frac{\partial}{\partial x_j} \left[\left(\nu + \frac{\nu_u}{\sigma_{ku}} \right) \frac{\partial k_u}{\partial x_j} \right] \tag{1}$$

$$\frac{D\varepsilon_u}{Dt} = C_{\varepsilon 1} P_u \frac{\varepsilon_u}{k_u} - C_{\varepsilon 2}^* \frac{\varepsilon_u^2}{k_u} + \frac{\partial}{\partial x_j} \left[\left(\nu + \frac{\nu_u}{\sigma_{\varepsilon u}} \right) \frac{\partial \varepsilon_u}{\partial x_j} \right] \tag{2}$$

Here, the eddy viscosity of the unresolved scales takes its standard form $\nu_u = C_\mu k_u^2 / \varepsilon_u$. The form of the functional dependency in the model coefficients is of decisive importance. This is especially the case with the coefficient multiplying the destruction term in the dissipation equation. The appropriate formulation is given by

$$C_{\varepsilon 2}^* = C_{\varepsilon 1+} \frac{f_k}{f_\varepsilon} \left(C_{\varepsilon 2} - C_{\varepsilon 1} \right); \ \sigma_{k,\varepsilon u} = \sigma_{k,\varepsilon} \frac{f_k^2}{f_\varepsilon} \tag{3}$$

Such a model coefficient form provides a dissipation rate level which suppresses the turbulence intensity towards the subgrid (i.e. subscale) level in the region where large coherent structures with a broader spectrum dominate the flow, allowing in such a way evolution of structural features of the associated turbulence. Herewith, a seamless coupling, i.e. a smooth transition from LES to RANS and opposite is enabled. The parameter f_k is formulated in terms of the grid spacing following Basara et al. (2008)

$$f_k = \frac{1}{\sqrt{C_\mu}} \left(\frac{\Delta}{\Lambda} \right)^{2/3} \tag{4}$$

where Δ is the grid cell size ($\Delta = \left(\Delta_x \times \Delta_y \times \Delta_z \right)^{1/3}$) and $\Lambda (= k^{3/2} / \varepsilon)$ is the turbulent length scale. In this derivation the equality $\varepsilon_u = \varepsilon$ resulting in $f_\varepsilon = 1$ was assumed. The PANS asymptotic behaviour goes smoothly from RANS to DNS with decreasing f_k. In the computational procedure used here, the lowest value of the parameter f_k is adjusted to the given grid as it was implemented as a dynamic parameter, changing at each grid node. The values obtained at the end of a time step are used in the following time step.

Both models are applied in conjunction with the so-called universal wall treatment. This method blends the integration up to the wall (exact boundary conditions) with the wall functions, enabling well-defined boundary conditions irrespective of the position of the wall-closest computational node. This method is especially attractive for computations of industrial flows in complex domains where higher grid flexibility, i.e. weaker sensitivity against grid non-uniformities in the near wall regions, featured

by different mean flow and turbulence phenomena (flow acceleration/deceleration, streamline curvature effects, separation, etc.), is desirable. Popovac and Hanjalic (2007) proposed the so-called compound wall treatment with a blending formula for the quantities specified at the central node P of the wall-closest grid cell as $\phi_P = \phi_\nu e^{-\Gamma} + \phi_t e^{-1/\Gamma}$, where '$\nu$' denotes the viscous and 't' the fully turbulent value. The variables ϕ apply here to the wall shear stress, production and dissipation of the turbulence kinetic energy. A somewhat simplified approach was introduced under the name "Hybrid Wall Treatment" in the numerical code AVL FIRE. Whereas the original compound wall treatment of Popovac and Hanjalic (2007) includes the tangential pressure gradient and convection, a simpler approach utilizing the standard wall functions as the "upper" bound is used presently.

Numerical Method. All computations were performed using the commercial CFD software package AVL FIRE (2006). The code employs the finite volume discretization method, which rests on the integral form of the general conservation law applied to the polyhedral control volumes. All dependent variables are stored at the geometric center of the control volume. The appropriate data structure (cell-face based connectivity) and interpolation practices for gradients and cell-face values are introduced to accommodate an arbitrary number of cell faces. The convection can be approximated by a variety of differencing schemes. The diffusion is approximated using central differencing. The overall solution procedure is iterative and is based on the SIMPLE-like segregated algorithm, which ensures coupling between the velocity and pressure fields.

Grid Details. Fig. 2-left displays the part of computational domain adopted. The car configuration was meshed with two grids containing 2.85 million (grid 1) and 4 million (grid 2) hexahedral cells. Coarser grids, comprising 1.3 and 2.5 million, cells were also tested. The near-wall region around the car body was appropriately refined. This was achieved by combining blocks of structured meshes connected with arbitrary interfaces. The finest grid provided y^+-values in the range of 10-30, while for other meshes y^+-values were in the range of 20-60 and above, Fig. 2-right. The solution domain comprising the truck configuration was meshed by 1.8 million grid cells.
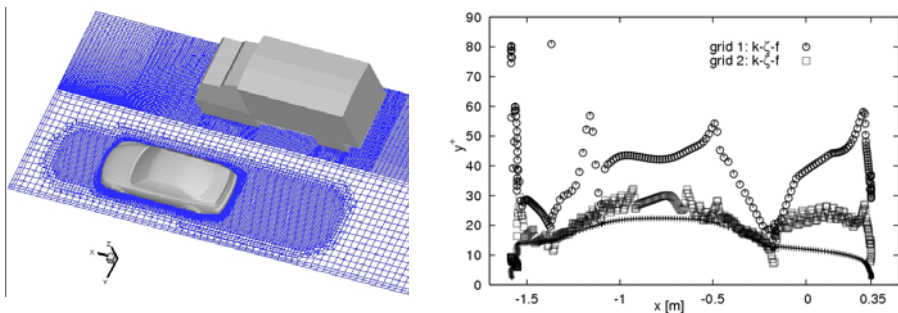
Fig. 2. Detail of the numerical grid applied (left) and y^+ values of the wall-closest grid nodes for the two grids used (right)
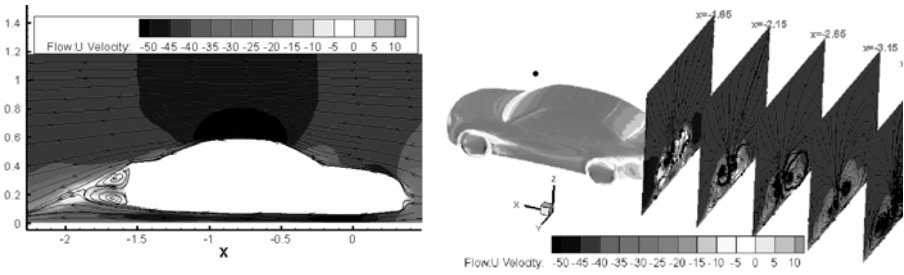
Fig. 3. Mean streamlines pattern at the center plane (left) and in the wake (right) of the isolated car coloured by the axial velocity component
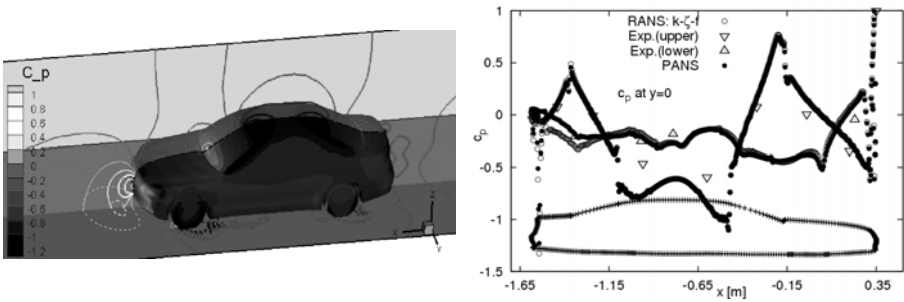
Fig. 4. Iso-contours of the mean pressure coefficient around the isolated car (left) and its evolution at the center plane (right)
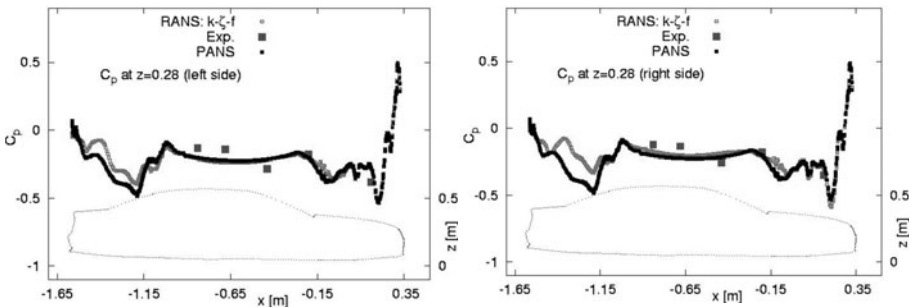
Fig. 5. Evolution of the mean pressure coefficient at the side plane z=0.28 of the isolated car

4   Results and Discussion

Figs. 3-6 illustrate the performance of the turbulence models applied to both configurations: unsteady flow past an isolated car (complying with steady inflow conditions) and a car-truck arrangement mimicking the overtaking process pertinent to the unsteady ongoing flow conditions.

The mean velocity field displayed in Figs. 3 exhibits an evolution typical to flow past a bluff body situated in the immediate wall vicinity characterized by a stagnation region at the front end and alternating acceleration and deceleration regions over the car surface. The near wake region (immediately after rear end of the car) is featured by a large recirculation zone exhibiting two counter-rotating vortices. The sizes of vortices vary in time. It is especially visible in Fig. 3-right displaying the blow-up of the streamline patterns behind the car body computed from the predicted mean velocity field at several y-z planes at an arbitrarily chosen time step. A strong asymmetry in the predictions (note that this is not a time-averaged result) can be observed, which confirms that there is a strong unsteadiness in the wake behind the car. The direct comparison with the measurements was made for the time averaged pressure coefficient C_P at the center plane of the model, Fig. 4. The pressure distribution along the car body is completely in accordance with the computed velocity field exhibiting total deceleration at the front part (stagnation region), followed by high acceleration at the strongly curved upper front surface of the car. The subsequent pressure rise complies with flow deceleration towards the front window. A further pressure drop reflects the effects of the favourable pressure gradient due to flow acceleration over the top surface. The final increase of the pressure coefficient featuring the adverse pressure gradient effect corresponds to the strong deceleration in the region of the rear window. A small separation zone in the transition region from the rear window to the rear end of the car (not visible in Figs. 3) is in accordance with the latter pressure increase. At the mid part of the car configuration, the calculated pressure coefficient is overpredicted on the upper side with both turbulence models. The only important difference between the two computational results is visible in the underbody region (lower side) close to the car rear end. The PANS results indicate a somewhat higher pressure pertinent to a stronger deceleration and a larger back-flow region. In Figs. 5 the predicted wall pressure distribution in the horizontal planes at $z=0.28$ is compared with the experimental findings. Some discrepancies can be observed at the rear part of the car model. A similar tendency and level of agreement is achieved at the other horizontal planes (not shown here). The global pressure at the side surfaces seems to be well predicted but clearly, there is no absolute agreement at all points. The differences between URANS and PANS results are in accordance with similar discrepancy displayed in Fig. 4-right. A larger recirculation region at the lower car surface obtained by PANS has as a consequence the flow acceleration in the upward direction along the side surfaces resulting in an appropriate pressure decrease. The predicted drag coefficient $C_x=0.331$ is somewhat higher compared to the experimentally obtained one $C_x=0.294$. This discrepancy indicates that the unsteady effects in the car wake are still not properly reproduced. Further computations with higher spatial and temporal resolution are in progress. On the other hand, the predicted lift coefficient $C_y=0.021$ is in a closer agreement with measurements $C_y=0.024$. The calculations as well as measurements show that the flow is not symmetric. It should be pointed out that the computational domain in this single car case is also asymmetric as this represents only one part of the entire flow domain (another part accommodates the truck), which could partially also be a reason for the afore-described aerodynamic coefficients behaviour. Figs. 6 show the pressure field in the case of the most critical car-truck constellation exhibiting the largest drag coefficient. A substantial pressure
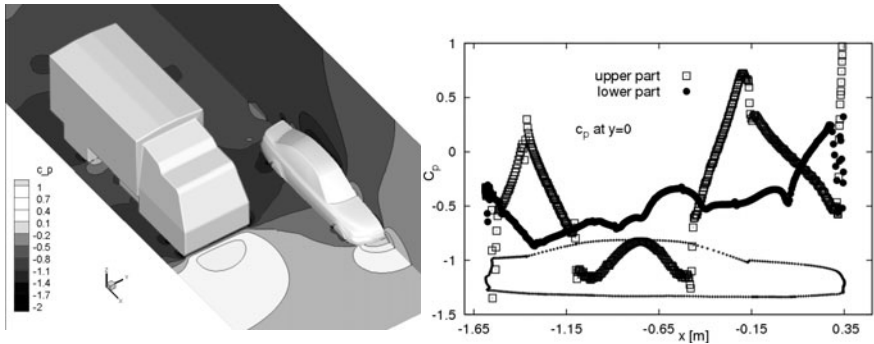
Fig. 6. Iso-contours of the mean pressure coefficient in the flow past a car-truck arrangement (left) and its evolution at the center plane (right) obtained by using the PANS method

decrease on the upper surface after reaching the front window is obvious. Similar pressure coefficient development is documented also on the lower surface. It indicates an appropriate increase of the pressure gradient and consequently a larger drag coefficient in accordance with the experimental observations (Fig. 1). The quantitative comparison was not possible as the computationally considered distance between the car and the truck doesn't exactly correspond to the experimental configuration.

5   Conclusions

The performances of two recently proposed turbulence models RANS-ζ-f and PANS-k-ε utilizing advantages of the universal wall functions for predicting the unsteady flow past a single car and a car-truck arrangement were illustrated. Three-dimensional wall pressure mapping covering the entire car surface (car sides, bonnet, roof and trunk) were obtained in reasonable agreement with available experimental database. The predicted flow characteristics reflect qualitatively correct the unsteady nature of the flow past a car body.

References

AVL AST, AVL Fire Manual 8.5, AVL List GmbH, Graz (2006)

Basara, B., Krajnovic, S., Girimaji, S.: PANS vs. LES for Computations of the Flow around a 3D Bluff Body. In: 7th Int. Symp. on Engineering Turbulence Modelling and Measurements, Limassol, Cyprus, June 4-6 (2008)

Durbin, P.A.: Near-Wall Turbulence Closure Modelling Without Damping Functions. Theoret. Comput. Fluid Dynamic 3, 1–13 (1991)

Girimaji, S.: Partially-Averaged Navier-Stokes Model for Turbulence: A Reynolds-Averaged Navier-Stokes to Direct Numerical Simulation Bridging Method. J. Appl. Mech. 73, 413–421 (2006)

Hanjalic, K., Popovac, M., Hadziabdic, M.: A robust near-wall elliptic-relaxation eddy-viscosity turbulence model for CFD. Int. J. of Heat and Fluid Flow 25, 1047–1051 (2004)

Popovac, M., Hanjalic, K.: Compound Wall Treatment for RANS Computation of Complex Turbulent Flows and Heat Transfer. Flow. Turbulence and Combustion 78(2), 177–202 (2007)

Schreffl, M.: Instationäre Aerodynamik von Kraftfahrzeugen - Aerodynamik bei Überholvorgang und böigem Seitenwind. PhD Thesis, Technische Universität Darmstadt (2008)

Author Index

Notes on Numerical Fluid Mechanics and Multidisciplinary Design

Volume 97: Shia-Hui Peng, Werner Haase (eds.): Advances in Hybrid RANS-LES Modelling - Papers contributed to the 2007 Symposium of Hybrid RANS-LES Methods, Corfu, Greece, 17–18 June 2007. ISBN 978-3-540-77813-4

Volume 96: C. Tropea, S. Jakirlic, H.-J. Heinemann, R. Henke, H. Hönlinger (eds.): New Results in Numerical and Experimental Fluid Mechanics VI - Contributions to the 15th STAB/DGLR Symposium Darmstadt, Germany, 2006. ISBN 978-3-540-74458-0

Volume 95: R. King (ed.): Active Flow Control - Papers contributed to the Conference "Active Flow Control 2006", Berlin, Germany, September 27 to 29, 2006. ISBN 978-3-540-71438-5

Volume 94: W. Haase, B. Aupoix, U. Bunge, D. Schwamborn (eds.): FLOMANIA - A European Initiative on Flow Physics Modelling - Results of the European-Union funded project 2002 - 2004. ISBN 978-3-540-28786-5

Volume 93: Yu. Shokin, M. Resch, N. Danaev, M. Orunkhanov, N. Shokina (eds.): Advances in High Performance Computing and Computational Sciences - The Ith Khazakh-German Advanced Research Workshop, Almaty, Kazakhstan, September 25 to October 1, 2005. ISBN 978-3-540-33864-2

Volume 92: H.J. Rath, C. Holze, H.-J. Heinemann, R. Henke, H. Hönlinger (eds.): New Results in Numerical and Experimental Fluid Mechanics V - Contributions to the 14th STAB/DGLR Symposium Bremen, Germany 2004. ISBN 978-3-540-33286-2

Volume 91: E. Krause, Yu. Shokin, M. Resch, N. Shokina (eds.): Computational Science and High Performance Computing II - The 2nd Russian-German Advanced Research Workshop, Stuttgart, Germany, March 14 to 16, 2005. ISBN 978-3-540-31767-8

Volume 87: Ch. Breitsamter, B. Laschka, H.-J. Heinemann, R. Hilbig (eds.): New Results in Numerical and Experimental Fluid Mechanics IV. ISBN 978-3-540-20258-5

Volume 86: S. Wagner, M. Kloker, U. Rist (eds.): Recent Results in Laminar-Turbulent Transition - Selected numerical and experimental contributions from the DFG priority programme 'Transition' in Germany. ISBN 978-3-540-40490-3

Volume 85: N.G. Barton, J. Periaux (eds.): Coupling of Fluids, Structures and Waves in Aeronautics - Proceedings of a French-Australian Workshop in Melbourne, Australia 3-6 December 2001. ISBN 978-3-540-40222-0

Volume 83: L. Davidson, D. Cokljat, J. Fröhlich, M.A. Leschziner, C. Mellen, W. Rodi (eds.): LESFOIL: Large Eddy Simulation of Flow around a High Lift Airfoil - Results of the Project LESFOIL supported by the European Union 1998 - 2001. ISBN 978-3-540-00533-9

Volume 82: E.H. Hirschel (ed.): Numerical Flow Simulation III - CNRS-DFG Collaborative Research Programme, Results 2000-2002. ISBN 978-3-540-44130-4

Volume 81: W. Haase, V. Selmin, B. Winzell (eds.): Progress in Computational Flow Structure Interaction - Results of the Project UNSI, supported by the European Union 1998-2000. ISBN 978-3-540-43902-8

Volume 80: E. Stanewsky, J. Delery, J. Fulker, P. de Matteis (eds.): Drag Reduction by Shock and Boundary Layer Control - Results of the Project EUROSHOCK II, supported by the European Union 1996-1999. ISBN 978-3-540-43317-0

Volume 79: B. Schulte-Werning, R. Gregoire, A. Malfatti, G. Matschke (eds.): TRANSAERO - A European Initiative on Transient Aerodynamics for Railway System Optimisation. ISBN 978-3-540-43316-3

Volume 78: M. Hafez, K. Morinishi, J. Periaux (eds.): Computational Fluid Dynamics for the 21st Century. Proceedings of a Symposium Honoring Prof. Satofuka on the Occasion of his 60th Birthday, Kyoto, Japan, 15-17 July 2000. ISBN 978-3-540-42053-8